

UC Berkeley

UC Berkeley Electronic Theses and Dissertations

Title

Engineering Properties and Geologic Setting of Old Bay Clay Deposits, Downtown San Francisco, California

Permalink

<https://escholarship.org/uc/item/7zx826gw>

Author

Parks, Margaret Clair

Publication Date

2019

Peer reviewed|Thesis/dissertation

Engineering Properties and Geologic Setting of Old Bay Clay Deposits, Downtown San
Francisco, California

By

Margaret Clair Parks

A dissertation submitted in partial satisfaction of the

requirements for the degree of

Doctor of Philosophy

in

Engineering – Civil and Environmental Engineering

in the Graduate Division

of the University of California, Berkeley

Committee in charge:

Professor Michael Riemer, Co-Chair

Professor Nicholas Sitar, Co-Chair

Professor Jonathan D. Bray

Professor Douglas S. Dreger

Summer 2019

Abstract

Engineering Properties and Geologic Setting of Old Bay Clay Deposits, Downtown San
Francisco, California

By

Margaret Clair Parks

Doctor in Philosophy in Engineering – Civil and Environmental Engineering

University of California, Berkeley

Professor Michael Riemer and Professor Nicholas Sitar, Co-Chairs

The Sangamon-aged, marine clay, locally known as the “Old Bay Clay” or the “Yerba Buena Mud” has an engineering significance due to its prevalence in the San Francisco Bay Area subsurface profile. Throughout the Bay Area, large-scale construction projects have been recently completed, begun construction, or are in planning that depend on understanding the small- to large-strain properties of deposits that were previously less affected by construction activities, deposits that include the Old Bay Clay. The construction of a transit center in Downtown San Francisco, California provided a direct opportunity to obtain unique data from a large, urban excavation 1500 feet long, 200 feet wide, and 65 feet deep. The excavation occurred in a densely constructed urban environment over a subsurface soil profile up to 240 feet thick, including a layer of Old Bay Clay approximately 80 feet thick. High quality samples were obtained at various depths and locations at the project site within the Old Bay Clay deposit, as well as in clay layers of other units in the subsurface. This work includes a multi-year study to document the laboratory properties of these clays.

The Old Bay Clay was characterized by contextualizing the deposit within the San Francisco Bay Area geologic setting, prior engineering geologic characterization, and with knowledge gained from subsurface exploration and sampling. The project site lies approximately on the southern limb of a Franciscan formation bedrock valley that dips to the northeast. Above the bedrock is the Alameda formation, which contains some interlayers of estuarine or marine clay. The Old Bay Clay overlies the Alameda and is remarkably consistent at the project site. Old Bay Clay is described as a Dark Greenish Gray, stiff to hard, fat clay, with water content from 33 to 44%, total unit weight from 105 to 117 pcf, 95 to 100% fines content, Liquid Limit from 60 to 68, and Plasticity Index from 37 to 44. The Old Bay Clay is a single transgression that was deposited during the last interglacial from a previous Bay that was deeper than the current San Francisco Bay. A microfossil study was performed that identified foraminifers and diatoms within Old Bay Clay samples that suggest the project site materials came from the lower units deposited in the

Sangamon San Francisco Bay. Above the upper erosional contact of the Old Bay Clay are late Pleistocene to Historic materials that contribute to the understanding of the Bay Area subsurface profile. The history of the development of the Bay Area subsurface profile is documented from the late 19th Century through present works, including the locations and significance of the engineering and geologic studies.

The deep, thick layer of the Old Bay Clay and deep clays within the Alameda formation prompted detailed study of compression parameters and stress history for this project. Ten Incremental Loading Consolidation (IL) tests and 21 Constant Rate of Strain Consolidation (CRS) tests were performed with all IL tests paired with one or more CRS tests. A particular focus was on recompression and secondary compression properties of the materials, so many cycles of unloading and reloading were performed for each test at various stress states. The Old Bay Clay soils were found to be moderately to slightly overconsolidated. For the Old Bay Clay, preconsolidation pressure ranged from 6.3 to 9.0 kg/cm² and OCR ranged from 1.6 to 2.4. In Old Bay Clay, compression index was found to be from 0.51 to 1.06, recompression index from 0.01 to 0.07, secondary compression index from 0.019 to 0.34, and coefficient of consolidation from 0.4 to 4.4 m²/yr. These compression parameters were compiled and compared with Young Bay Mud and Alameda clays. A sample quality assessment was made of the Old Bay Clay specimens, which was Very Good to Excellent (Lunne et al., 2006), which was important to justify the value of the other small strain testing performed.

Testing these materials also led to a focus on how consolidation testing methods and results unique for deep, stiff clays is different than for routine tests. The importance of a large soaking stress to prevent swelling was documented. Six methods of preconsolidation pressure were assessed and three methods routinely used in order to characterize dependence of methodology on estimates of preconsolidation pressure. Compression index was shown to vary depending on certain characteristics of compression curves. Recompression index was compiled at various stress states to show the dependence on unloading magnitude and stress level. Secondary compression was compiled for every unload and reload increment to show dependence on stress history. The coefficient of consolidation was compared between IL and CRS testing for understanding of instantaneous coefficient of consolidation estimates in CRS testing.

Monotonic and dynamic testing was performed on project samples with several different test types in order to explore small strain stiffness properties of the Old Bay Clay. Ten Anisotropic-Consolidated Undrained Triaxial (CKoUTX) tests were performed that involved a suite of tests, including bender elements, cyclic loading, and/or small to large strain compression and extension tests. A group of five CKoUTX tests were performed under special “lateral unloading” conditions to understand shear behavior and measure stiffness values at various stress states. Using the UC Berkeley high-performance triaxial cell in combination with a graphical user interface version of Georobot, small strain properties were meaningfully measured on high quality specimens fully characterized with index testing. Specimens were consolidated past their in-situ preconsolidation pressure and then anisotropically consolidated to field values of OCR and K_o . Values of G_{max} , from the several testing types, ranged from 57.2 to 133 MPa (1190 to 2780 ksf) with a mean value of approximately 80 MPa (1680 ksf). Results of small strain properties, including G_{max} , V_s , and modulus reduction curves, appear consistent with results of other research on the Old Bay Clay as well as for similar clay materials.

TABLE OF CONTENTS

Table of Contents	i
List of Figures	v
List of Tables	ix
Glossery and Symbols Used	x
Acknowledgements	xii
1 Introduction	1
1.1 Motivation	1
1.2 Scope and Research Objectives	2
1.3 GOALI and Transbay project	2
1.3.1 Transbay Transit Center and Construction	2
1.3.2 GOALI Project and Scope	4
2 Characterizing the Old Bay Clay	11
2.1 Geologic Setting	11
2.1.1 Regional and Bedrock Geology	11
2.1.2 Quaternary Site Geology	12
2.2 Engineering and Geologic Studies of Holocene and Pleistocene Bay Deposits	16
2.2.1 Late 19 th Century and Early 20 th Century Geology	17
2.2.2 Mid-Century Bay Crossings	18
2.2.3 Post-Loma Prieta Earthquake (1989)	23
2.2.4 To Present: Extensive and Deep Construction Projects	25
2.3 Nomenclature for Holocene and Pleistocene Bay Deposits used in this Study	26
2.4 Field Sampling	27
2.5 Determination of Field Stress	29
2.6 Composition and Index Properties	30
2.7 Subsurface Conditions	31
2.7.1 Project Site Description	31
2.7.2 Site Subsurface Conditions	32
2.7.3 Fossils at the TTC	36
2.8 Microfossil Study	38
2.8.1 Sample Preparation	38
2.8.2 Observations	39

2.9	Conclusions	41
3	Consolidation Testing.....	66
3.1	Introduction	66
3.2	Incremental Loading Consolidation Testing	67
3.2.1	Specimen Preparation, Testing Equipment, and Testing Procedure	67
3.2.2	Data Processing	69
3.3	Constant Rate of Strain Consolidation Testing.....	71
3.3.1	Specimen Preparation, Testing Equipment, and Testing Procedure	71
3.3.2	Data Processing	73
3.4	Compression Curves and Terminology	74
3.4.1	Comparison between IL and CRS Compression Curves.....	75
3.5	Conclusions	76
4	Consolidation Results and Interpretation.....	94
4.1	Introduction	94
4.2	Preconsolidation Pressure	94
4.2.1	Methods of Evaluating Preconsolidation Pressure.....	94
4.2.2	Results.....	105
4.2.3	Implications to Stress History	107
4.2.4	Discussion	109
4.3	Compression Index	110
4.3.1	Data processing.....	110
4.3.2	Compression Index Dependence on Field Curve Construction.....	110
4.3.3	Compression Index and Secondary Compression Relationship to Predicted Settlement.....	111
4.3.4	Results.....	112
4.3.5	Discussion	113
4.4	Recompression Index.....	114
4.4.1	Defining the Recompression Index	114
4.4.2	Hysteresis loops and Effects on Recompression Index	116
4.4.3	Recompression Index Dependence on Stress Level	117
4.4.4	Data Processing	119
4.4.5	Results.....	119
4.4.6	Discussion	121

4.5	Secondary Compression Index.....	121
4.5.1	Data Processing	121
4.5.2	Results.....	122
4.5.3	Secondary Compression Relationship to Stress History	122
4.5.4	Discussion	123
4.6	Coefficient of Consolidation.....	124
4.6.1	Data Processing	124
4.6.2	Coefficient of Consolidation dependence on Stress and Test Type.....	125
4.6.3	Results.....	126
4.6.4	Discussion	126
4.7	Sample Quality	126
4.7.1	Background and Data Processing	127
4.7.2	Results.....	127
4.7.3	Discussion	127
4.8	Conclusions	128
5	Small Strain Stiffness Testing.....	175
5.1	Monotonic and Cyclic Triaxial Testing	175
5.1.1	Specimen Preparation.....	175
5.1.2	Testing Equipment	176
5.1.3	Bender Elements.....	176
5.1.4	Testing Procedures	177
5.1.5	Results.....	178
5.2	Lateral Unloading Triaxial Testing	179
5.2.1	Specimen Preparation and Testing Equipment.....	179
5.2.2	Testing Procedures	179
5.2.3	Results.....	180
5.3	Small Strain Stiffness Properties	181
5.4	Conclusions	182
6	Conclusions, Recommendations, and Future Work	197
6.1	Conclusions	197
6.1.1	Significance of Old Bay Clay	199
6.1.2	Engineering Properties of Old Bay Clay in Downtown San Francisco	200

6.2	Recommendations for Consolidation Testing in Deep, Stiff Clays	200
6.3	Recommendations for Future Work	201
7	References	203
8	Appendix A	210
8.1	Samples	210
8.2	Incremental Consolidation (IL) Consolidation Tests	213
8.3	Constant Rate of Strain (CRS) Consolidation Tests.....	237
9	Appendix B	280
9.1	Anisotropically Consolidated Triaxial (CK _o UTX) Tests	280
9.2	Lateral Unloading Triaxial Tests.....	283

LIST OF FIGURES

Figure 1.1. Project site location within San Francisco Bay Area.	6
Figure 1.2. Project site location within San Francisco.....	7
Figure 1.3. In-progress photograph of excavation activities.....	8
Figure 1.4. Photograph of the full depth of excavation prior to construction of the train box.	9
Figure 1.5. Photograph of operations for construction of the buttress.....	10
Figure 2.1. Site plan showing exploration locations used in this study.	43
Figure 2.2 Project Site showing locations of proposed Parallel and Southern Crossings.	44
Figure 2.3. Cross section along Minna street.....	45
Figure 2.4. Cross section along Natoma street.	46
Figure 2.5. Cross sections along First Street and between Fremont and Beale Street.....	47
Figure 2.6. Epoxy-coated sample tube retrieved using Osterberg hydraulic piston sampler.	48
Figure 2.7. Specimen extruded using tube jack and showing tube weld.	49
Figure 2.8. Total Unit Weight and Moisture Content from tested specimens for Young Bay Mud, Old Bay Clay, and Alameda fm.	50
Figure 2.9. Initial void ratio of tested specimens from the Young Bay Mud, Old Bay Clay, and Alameda fm.....	51
Figure 2.10. Results of Atterberg Limits testing (ASTM Standard D4318).....	52
Figure 2.11. Cross sections overlain for comparison.....	54
Figure 2.12. Young Bay Mud with a bed of <i>Macoma nasuta</i> shells.	55
Figure 2.13. Colma sand excavated during construction of trainbox.	55
Figure 2.14. Specimen of Old Bay Clay prepared for testing.....	56
Figure 2.15. Specimen of clay from within Alameda fm.	56
Figure 2.16. Franciscan rock recovered from project site.	57
Figure 2.17. The <i>Mammuthus columbi</i> (Columbian Mammoth) tooth recovered at the project site.	58
Figure 2.18. Site plan showing locations where microfossil study was performed.....	59
Figure 2.19. Cross sections showing locations where microfossil study was performed.	60
Figure 2.20. Foraminifera and diatoms under microscope magnification.	61
Figure 2.21. SEM image of <i>Ammonia beccarii</i> forma <i>tepida</i> and <i>Elphidium excavatum</i> (forma <i>lidoensis</i>).	62
Figure 2.22. SEM image of <i>Elphidium excavatum</i> (forma <i>selseyensis</i>).....	63
Figure 2.23. SEM image of <i>Elphidiella hannai</i>	64
Figure 2.24. SEM images of <i>Arachnoidiscus</i> and <i>Isthmia nervosa</i>	65
Figure 3.1. Site plan showing borings with the corresponding consolidation tests noted.	79
Figure 3.2. Cross sections showing locations of consolidation testing.....	80
Figure 3.3. Oedometer rings from IL and CRS testing.....	81
Figure 3.4. IL test setup showing pneumatic piston system.	82
Figure 3.5. Comparison of EOP for the same ILC increment, using Procedure 1, the log of time method, and Procedure 2, the square root of time method.	83
Figure 3.6. Incremental Loading Consolidation test compression curve showing data processed using both ASTM Procedure 1 and 2.....	84
Figure 3.7. Time History Curve from an Incremental Consolidation increment where there is no clear break in slope between initial and secondary consolidation.	85

Figure 3.8. Time History Curve from an Incremental Consolidation increment where initial consolidation appears to continue and steepen with time.	86
Figure 3.9. Time History Curve from an Incremental Consolidation increment where secondary consolidation appears to steepen with time.	87
Figure 3.10. CRS load frame and oedometer.	88
Figure 3.11. Compression Curve from CRS test, showing typical shape of OBC test.	90
Figure 3.12. Compression Curve from CRS test, showing typical shape of Alameda test.	91
Figure 3.13. Compression Curve for IL test, showing two possible interpretations of the compression curve.	92
Figure 3.14. Comparison between CRS data and IL data, both excluding and including secondary compression.	93
Figure 4.1. Cumulative Work per Unit Volume plot for a CRS test.	130
Figure 4.2. Cumulative Work per Unit Volume plot for a CRS test, showing initial curvature in slope.	131
Figure 4.3. Oikawa (1987) method and Onitsuka et al. (1995) method for ILC test.	132
Figure 4.4. Oikawa (1987) method and Onitsuka et al. (1995) method for CRS test.	133
Figure 4.5. Consolidation Curve from a CRS test showing construction for the Boone (2010) method.	134
Figure 4.6. Consolidation Curve for CRS test, showing reload portion for known preconsolidation pressure analysis.	135
Figure 4.7. Preconsolidation Pressure and OCR from CRS testing.	136
Figure 4.8. Implied overburden based on consolidation testing.	137
Figure 4.9. Schematic of possible stress history of Old Bay Clay deposit.	138
Figure 4.10. Effect of phreatic surface on estimation of previous ground surface.	139
Figure 4.11. IL test with field curves for data excluding secondary and including secondary compression.	140
Figure 4.12. CRS test with field curve plotted.	141
Figure 4.13. IL test with field curves for data excluding secondary and including secondary compression.	142
Figure 4.14. Example settlement problem schematic using C_c from CRS and IL testing.	143
Figure 4.15. Compression Index (C_c) from consolidation testing of Young Bay Mud, Old Bay Clay, and Alameda.	144
Figure 4.16. Compression Index (C_c) results for Old Bay Clay and Alameda samples with depth.	146
Figure 4.17. Compression Index (C_c) plotted against moisture content (%) for OBC and Alameda samples.	147
Figure 4.18. “Typical curve of void ratio versus effective vertical stress,” from Leonards (1976).	148
Figure 4.19. Compression curve run with multiple unloading cycles to show recompression slope.	149
Figure 4.20. IL test showing various recompression slopes depending on the unloading increment.	150
Figure 4.21. An unloading loop, showing various points that can fit a straight line in order to define the recompression (C_r) index.	151
Figure 4.22. ILC test showing various calculations of recompression index (C_r).	152

Figure 4.23. CRS test showing calculation of recompression index for each full unload-reload cycle compared with magnitudes of unloading for the unloading loops.	153
Figure 4.24. Recompression index (C_r) is calculated for both a CRS test and IL test using factors of unloading.	154
Figure 4.25. Normalized recompression index ($C_{r_normalized}$) for a CRS test and IL test using factors of unloading.	155
Figure 4.26. Recompression index (C_r), normally consolidated, plotted with depth for Young Bay Mud, Old Bay Clay, and Alameda soils.	156
Figure 4.27. Recompression Index (C_r), normally consolidated, plotted for Old Bay Clay and Alameda soils.	157
Figure 4.28. Recompression index (C_r) for various stress states before unloading plotted with depth for Old Bay Clay and Alameda soils.	159
Figure 4.29. Secondary Compression Index from IL testing for Old Bay Clay and Alameda soils testing.	161
Figure 4.30. Ratio of secondary compression index to compression index with depth for Old Bay Clay.	162
Figure 4.31. Secondary Compression Index (C_α) from OBC soils plotted against stress for normally consolidated increments only.	164
Figure 4.32. Secondary Compression Index (C_α) for Old Bay Clay soils for recompression increments only.	165
Figure 4.33. Secondary Compression Index (C_α) for Old Bay Clay soils for recompression increments that have been overconsolidated by laboratory maximum past pressures.	166
Figure 4.34. Coefficient of Consolidation (C_v) estimates for paired CRS and IL consolidation tests.	167
Figure 4.35. Two plots of paired IL and CRS consolidation tests performed on OBC soil that show general agreement between calculated values of Coefficient of Consolidation (C_v).	168
Figure 4.36. Two plots of paired IL and CRS consolidation tests performed on OBC soil that show inconsistent calculated values of Coefficient of Consolidation (C_v).	169
Figure 4.37. Coefficient of Consolidation (C_v), normally consolidated, for project soils.	170
Figure 4.38. Measure of Sample Quality based on Lunne et al. (2006) criteria for Young Bay Mud, Old Bay Clay, and Alameda soils from consolidation testing.	173
Figure 4.39. Measure of Sample Quality based on Lunne et al. (2006) criteria for different Shelby tube materials: epoxy-coated, zinc, and steel.	174
Figure 5.1. Testing equipment used for Triaxial testing.	183
Figure 5.2. Example of Bender Element traces used for velocity measurements.	185
Figure 5.3. Example of Large Strain CUTX compression test showing small strain range.	186
Figure 5.4. Example of Large Strain CUTX extension test showing small strain range.	187
Figure 5.5. Cyclic Triaxial test showing time history and hysteresis loops.	188
Figure 5.6. Suite of Cyclic tests showing degradation.	189
Figure 5.7. Comparison of Monotonic and Shear tests showing small strains.	190
Figure 5.8. Measured Shear Modulus and Normalized Modulus results from Cyclic Triaxial Testing.	191
Figure 5.9. Schematic of soil element undergoing Lateral Unloading.	192
Figure 5.10. Stress paths during consolidation and unloading for Lateral Unloading test.	194
Figure 5.11. Stress path during Lateral Unloading test.	195

Figure 5.12. Strain Histories for Lateral Unload test.....	196
--	-----

LIST OF TABLES

Table 2.1. Specific Gravity testing (ASTM D854).....	53
Table 3.1. Incremental Load Consolidation testing per sample.....	77
Table 3.2. Constant Rate of Strain Consolidation testing per sample	78
Table 3.3. CRS Testing showing Loading Rate, Unloading Rate, and number of Loadings and Unloadings at which stress levels.	89
Table 4.1. Summary of Compression Index (C_c) and Compression Ratio (CR) Results from testing of Young Bay Mud, Old Bay Clay, and Alameda soils.....	145
Table 4.2. Summary of recompression index (C_r) and recompression ratio (RR) values for Young Bay Mud, Old Bay Clay, and Alameda soils for normal consolidation.	158
Table 4.3. Summary of recompression index (C_r) and recompression ratio (RR) values from Old Bay Clay testing at various stress states pressures at unloading.....	160
Table 4.4. Values of secondary compression index (C_{α}), normally consolidated, and the ratio of secondary compression to compression index for Old Bay Clay soils.	163
Table 4.5. Summary of Coefficient of Consolidation (C_v), normally consolidated, values for Young Bay Mud, Old Bay Clay, and Alameda soils	171
Table 4.6. Lunne et al. (2006) criteria for evaluating sample disturbance using $\Delta e/e_o$	172
Table 5.1. List Anisotropic Consolidated Undrained Triaxial testing for this project.	184
Table 5.2. Lateral Unloading Triaxial testing performed for this project.....	193
Table 6.1. Summary of Testing Results from index and consolidation on Old Bay Clay.....	200

GLOSSARY AND SYMBOLS USED

C_c	Compression index
CR	Compression ratio: compression index normalized by initial void ratio
C_r	Recompression index
$C_{r_normalized}$	Normalized recompression index
CRS	Constant rate of strain consolidation test
C_v	Coefficient of consolidation
C_α	Secondary compression index
Compression Curve	Curve of individual increments from IL testing or continuous data from CRS data, also called a consolidation curve or a lab curve by others
G_{max}	Low strain shear modulus
GDR	Geotechnical data report
Holocene	The current geologic epoch, beginning approximately 11,700 years before the present
IL	Incremental load consolidation test
K	Lateral earth pressure
K_o	In-situ lateral earth pressure
Maximum Past Pressure	Maximum past pressure of the soil due to laboratory loading history
OBC	Old Bay Clay, Pleistocene marine deposit of the San Francisco Bay
P_p	Preconsolidation pressure
Pleistocene	Geological epoch lasting from 2,588,000 to 11,7000 years before the present
P_p, σ'_p	Preconsolidation pressure: Maximum past pressure of the soil due to in-situ field conditions
Procedure 1	Incremental loading consolidation interpretation procedure based on the log of time (ASTM D2435)
Procedure 2	Incremental loading consolidation interpretation procedure based on the square root of time (ASTM D2435)
RR	Recompression ratio: recompression index normalized by initial void ratio
σ'_v	Vertical effective stress
Sangamon interglacial	Last interglacial period in North America, corresponds to roughly 75,000 to 125,000 years before present
Sample	Soil recovered from the ground, in a sample tube or from a bulk sample
Specimen	Soil that is tested, has been extruded, trimmed, or reconstituted from field sample
Test Method A	Incremental loading consolidation where the standard load increment is 24 hours (ASTM D2435)

Test Method B	Incremental loading consolidation where the standard load increment exceeds the time required to complete primary consolidation (ASTM D2435)
TTC	Transbay Transit Center
Wisconsin stage	Most recent glacial period in North America, corresponds to approximately 75,000 to 11,000 year ago
YBM	Young Bay Mud, Holocene marine deposit of the San Francisco Bay

ACKNOWLEDGEMENTS

This work would not be possible without the funding support from the National Science Foundation (NSF), Grant Opportunities for Academic Liaison with Industry, under award number 1101003. An especial thanks goes to Professor Youssef Hashash of University of Illinois at Urbana-Champaign, who was the Principal Investigator of this project and provided valuable guidance and a depth of knowledge. Thank you also to Arup, who were our Industry partners and provided many resources for this work.

Most importantly, I would like to thank my advisor, Dr. Michael Riemer. This was a long process and he was full of enthusiasm and encouragement for this work. Laboratory work requires so much detail-oriented planning and expecting of the unexpected, so I especially appreciate the guidance throughout suddenly unsaturated samples, late night equipment issues, and unexpected losses of power. I would also like to thank the other UC Berkeley faculty members for their knowledge and guidance through this process, including Professor Nicholas Sitar, Professor Jonathan D. Bray, Professor Raymond Seed, Professor Douglas S. Dreger, and Professor William Dietrich. I would also like to acknowledge Dr. Doris Sloan, who provided me amazing access to her wealth of knowledge of the Yerba Buena Mud as well as use of her samples and equipment. I would also like to thank Professor Lynn Ingram for use of her lab space.

I would like to acknowledge the individuals that would start me on the process towards this PhD. At UCLA, I was first introduced to geotechnical engineering and soil mechanics by Professor Mladen Vucetic and Professor Jonathan Stewart, who continues to be an encouragement through my career. I would especially like to thank Professor Abby Kavner, who first introduced me to laboratory work and inspired me to pursue my interests. I am hugely thankful to Carol Price, Dr. Daniel Chu, and Dr. Soumitra Guha, who all took a chance on a young engineering geologist and encouraged me to pursue my advanced degrees, and I am particularly grateful to have continued working with Old Bay Clay as Dr. Guha had previously studied.

A huge source of support came from the GeoBears: Dr. Christine Z. Beyzaei, Dr. Christie D. Hale, Dr. Roozbeh Geraili Mikola, Dr. Nick Oettle, Dr. Michelle Shriro, and so many other awesome people I have had the honor to meet at UC Berkeley. Last but not least, my fellow geology fans Dr. Mike George and Dr. Julien Cohen-Waeber, of whom I am so grateful for the years of friendship.

It was a journey to get to this point and having the inspiration and encouragement of my work family was so vital, so I give a big thanks to: James Allen, Uri Eliahu, Pedro Espinosa, Jeff Fippin, Dr. Bahareh Heidarzadeh, Randy Hildebrant, Janet Kan, Siobhan O'Reilly-Shah, and Phil Stuecheli.

I could not have done this without the encouragement and love from my friends and family: my sister Dr. Laura Heins, my father Walt Parks, my mother Geri Gail, my dad Mick Ehresman, my incredible friends Peggy Sinclair and Taline Khansa, and the knitting crew, Chris Roncall, Jenny Check, Eleyne Phillips, Nicole Hunter, and Lena Nilsson.

And a very special thanks to my rock, my husband, my love, Tim Clair. This would not have happened without your constant support and trust in me and my abilities.

1 INTRODUCTION

This dissertation presents results from a multi-year project in which laboratory testing and geologic context was used to characterize a locally significant geologic unit. This geologic unit can generally be described as a Sangamon-aged, marine clay, locally known as the “Old Bay Clay (OBC).” The Old Bay Clay has an engineering significance due to its prevalence in the San Francisco Bay Area.

1.1 Motivation

The motivation for this research was the planning and construction of the Transbay Transit Center (TTC) in San Francisco, California. The construction of the TTC was a massive undertaking that involved many years of planning and many partners in government, industry, and academia. This was a complicated engineering project that involved large-scale urban construction, soft soils, a permanently unloaded structure, and construction designed to minimize impact to adjacent structures.

Large-scale construction projects like the TTC can provide real-time case histories for many engineering questions. Past case histories that have previously been studied have provided insight into in-situ soil behavior, performance of engineered systems compared with construction, and opportunities to use real-time instrumentation to track construction activities and site response (Hashash, 1992; Hashash, Marulanda, Ghaboussi, & Jung, 2006; Hashash and Finno, 2008). As a large excavation in an urban environment, the TTC project provided a unique opportunity to study diverse engineering topics ranging from site characterization, instrumentation, design and performance of temporary components, and accuracy of estimated impacts from construction activities.

The highly built environment surrounding the excavation site was also a motivator for this study. The extensive infrastructure adjacent to the site, including the presence of existing buildings ranging from historic buildings on shallow foundations to large high-rises on deep foundations, and the requirements of an urban environment to maintain traffic flow and pedestrian access, was a large driver of the engineering planning and design.

Additionally, regional interest had been growing regarding soil properties of the subsurface in the Bay Area, partly due to increased construction of large developments on these deposits (Simpson, 2006; Espinosa, Pestana, Vahdani, and Heidarzadeh, 2017). While large infrastructure projects have been ongoing throughout Bay Area history, not the least including large reclamation projects and massive bridge construction, the deeper deposits were considered to have a less significant impact compared to the more shallow compressible deposits or they were avoided by deep foundations. The current phase of large projects in the Bay Area are more extensive, involve greater loads, and the engineering tolerances are less due to codes and the presence of other adjacent infrastructure.

1.2 Scope and Research Objectives

The scope of the effort described herein was to provide advanced laboratory testing to augment the field instrumentation and numerical modeling and to extract data from the previous exploratory work and contextualize it for use in modeling soil properties. The opportunity for advanced laboratory testing motivated the development of a new kind of testing, lateral unloading triaxial testing, as well as the validation and testing of the dynamic loading characteristics of the high performance triaxial cell and CKC Triaxial Control system (Li, Chan, & Shen, 1988). As the importance of settlement properties of these deposits became clear, a careful study was performed involving detailed oedometer testing for soil properties as well as for assessing testing procedures. Additionally, there was motivation to synthesize the geologic information of OBC and try to bridge the gap between the understanding of geologic and geotechnical importance.

1.3 GOALI and Transbay project

This dissertation concentrates on the properties of the Old Bay Clay specifically, but the soils testing performed was a component of a larger project. The larger research project was a National Science Foundation (NSF) Grant Opportunities for Academic Liaison with Industry (GOALI) project and was a joint partnership between the University of Illinois at Urbana-Champaign, University of California at Berkeley, and Arup. The goal of the greater research project was to document a large, urban excavation at an academic-research level, more than what would usually be necessary for engineering purposes. While the standard of care for a project like this is very high, for research purposes, more detailed sampling, instrumentation, and documentation was desired.

1.3.1 Transbay Transit Center and Construction

The Transbay Transit Center (TTC), now known as the Salesforce Transit Center, was officially open to the public in August 2018 and is a regional transit hub located in downtown San Francisco, California (Figure 1.1). It stretches five city blocks, from Beale Street to Second Street, and covers the entire block between Minna Street and Natoma Street (Figure 1.2). The structure is approximately 1,430 feet long by 165 feet wide and includes six levels. At the current time, the above-ground floors are being used as a bus terminal with space for retail use as well as a public garden on the upper level. The lower levels were built with the intent that they will be used in the future for Caltrain and California High Speed Rail service.

The geotechnical features of the construction for the center were particularly notable. The lower levels spanned the entire site, so the TTC excavation was very large: 1500 feet long, 200 feet wide, and 65 feet deep (Arup, 2016). While 65 feet is not an especially deep excavation in an engineering sense, at the TTC site groundwater is quite shallow and the site is underlain with both undocumented fills and soft Young Bay Mud. Further complicating excavation work was the urban environment, including adjacent buildings of varying foundation types and structural types. Adjoining structures ranged from tall, skyscraper-type modern towers on deep foundations to low-story but historic, brick buildings on shallow foundations. Also adjacent to the TTC excavation were major utilities that could tolerate very little movement. In addition to difficult constructability

of the project, considerations also had to be made for the permanent unloading of the soils under the TTC project, since the structure weighs less than the excavated soil removed.

Of note regarding this project is that, at the time of this writing, highly publicized litigation was filed relating to the differential settlement of an adjacent building at 301 Mission Street, called the Millennium Tower. The causes of the differential settlement will likely be debated and litigated in the engineering community for many years. This research project considered some elements of geomechanics related to excavation unloading; however, no part of this research project was used as a part of design for the TTC project. Nor was the author of this work involved in design or construction of the Millennium Tower. Any observations or conclusions regarding the mechanical behavior of the soils tested should not be considered a theory or suggestion regarding the differential settlement of the Millennium Tower.

As discussed, the underground construction for the TTC project was significant and noteworthy enough for use as a case history for engineering consideration. Construction of the TTC was begun in early 2011 with the demolition of the old Transbay Terminal and installation of shoring. Cement deep soil mixing (CDSM) method with soldier piles were used for the perimeter shoring wall. Non-structural CDSM panels were installed without soldier piles in order to hydraulically isolate the excavation into subzones for the dewatering activities. Four levels of cross-lot bracing were used to support the open excavation (Figure 1.3, Figure 1.4). Excavation began in the southwest corner of the site and was staged as the excavation progressed to the northeast corner of the project. A temporary bridge deck was constructed across the site to enable crane access for the excavation because of the tight footprint of construction space required by the urban environment. Additionally, as excavation progressed to Second Street and Fremont Street, temporary weekend street closures allowed the installation of bridges so that traffic could flow unobstructed across the excavation. Before foundations the trainbox was complete and foundations constructed, micropiles were installed at the base of the excavation for use as tie-downs to prevent buoyancy of the finished structure (Figure 1.4). The construction of the below grade structure began in early 2013 and all below-grade construction was completed by 2016.

Concurrently with the other more conventional staged construction and shoring activities in the southern end of the site, a large buttress was constructed in the northeast portion of the site between Beale and Fremont Streets (Figure 1.5). At the time the TTC was designed and constructed, there was awareness that further excavation-related shoring would be required adjacent to the Millennium Tower. The extra shoring involved a secant-pile buttress of overlapping 60-inch shafts drilled up to 260 feet below the ground surface into what was considered formational rock of the Franciscan sequence. The shafts were constructed of overlapping columns that alternated every-other shaft between high- and low-strength concrete. These large columns helped confirm the site stratigraphy due to the large amount of material excavated in each clamshell bucket. On-site engineers and geologists observed the shaft construction, so were able to confirm the properties of the site geologic formations. The shafts were also very deep, so information about the depth to rock and its competency was observed during construction. After construction of the shafts, the top 65 feet were excavated and braced like the rest of the project in a staged manner.

Importantly, an extensive pre-investigation study was performed with many deep borings, high quality testing, and compilation of other geotechnical data in the area (Arup, 2010). The data

containing this work is called the “Geotechnical Data Report” or the “GDR” as is referred to throughout this work because it contains a range of data collected for the project.

1.3.2 GOALI Project and Scope

This project intended to use the TTC construction as a real-time case study in excavation performance, limited to observing the construction sequence and activities without any input to design. As such, this study involved extra instrumentation and testing in order to fully characterize a case-study in order to answer specific research questions outside of what was necessary for the design of the project. The research project was able to leverage the significant work already performed for the project as well as include the direct participation of the project engineers. The research scope included:

- Review of all engineering reports and data packages, especially the GDR, prepared for the TTC project.
- Installation of field instrumentation designed to answer specific research questions as well as of novel construction, including: in-place inclinometers, flushable piezometers, multipoint borehole extensometers, bracing strain gauges, settlement monitors, building markers, and webcams. The instruments were linked to the Global Analyzer system in order to collect and store continuous data to be read remotely.
- Enhanced laboratory testing on samples taken at selected intervals during excavation of the instrument boreholes.
- Numerical modeling and inverse analysis of field and laboratory data.

Some of the general questions this research approached included the excavation bracing, such as how the very long (approximately 185 foot) cross bracing would perform as well as the asymmetrical building loads imposed on opposite sides of the excavation. Another consideration was the permanent excavation unloading of the underlying soils, including the seismic response of the soils and the excavation response of the dewatering. A third key consideration was the ground movements, including how well the estimates matched the observations during and after construction.

Of key focus in this study was more detailed engineering characterization of the properties of the OBC and further characterization of the Alameda deposit underneath. These two deposits were sufficiently characterized for design, but more detailed testing was desired to better complete the case history. A main goal of the supplemental testing project was to better understand the small strain and anisotropic behavior of the OBC as a function of confining pressure and under cyclic loading. To do so, static testing and dynamic testing was proposed. The static testing was intended give insight into the soil response under the specific stress paths anticipated during the excavation process, especially considering that the soils will be permanently unloaded. These properties were addressed by conducting anisotropically consolidated (K_0) Triaxial Compression and Extension tests under consolidated stress states that simulated field conditions. Dynamic testing, in order to investigate small-strain stiffness properties as well as the change in seismic response due to

unloading, included small strain compression and extension, cyclic triaxial, and bender element testing.

As the project progressed, there was renewed interest in consolidation properties of the OBC and Alameda. To explore this, detailed and multi-part paired Constant Rate of Strain (CRS) and Incremental Load (IL) oedometer tests were performed. A focus was on recompression and secondary compression properties as well as accurate stress history. Testing these materials also led to a focus on how consolidation testing methods influence results as well as the reflect the properties of deep, stiff clays.

The results of the supplementary laboratory testing are addressed and summarized in the rest of this work.

General geology and the geologic setting of the materials involved has been studied and given context by the testing and more thorough understanding of the subsurface profile, as documented in Chapter 2. The first phase of testing involved the characterization of the materials with index and consolidation tests, especially to provide stress history for later testing. Index Tests are included in Chapter 2 and consolidation tests are included in Chapter 3 and 4. Chapter 4 also includes explanations of how consolidation testing methods and results reflect the properties of the deep, stiff clay materials tested. The next phase involved strength testing, including monotonic and dynamic triaxial testing. This testing included bender element testing as well as a special triaxial tests called the “lateral unloading” triaxial test. Small strain strength testing is included in Chapter 5.



Figure 1.1. Project site location within San Francisco Bay Area.
Project site is shown in blue (Google Earth, 2019)

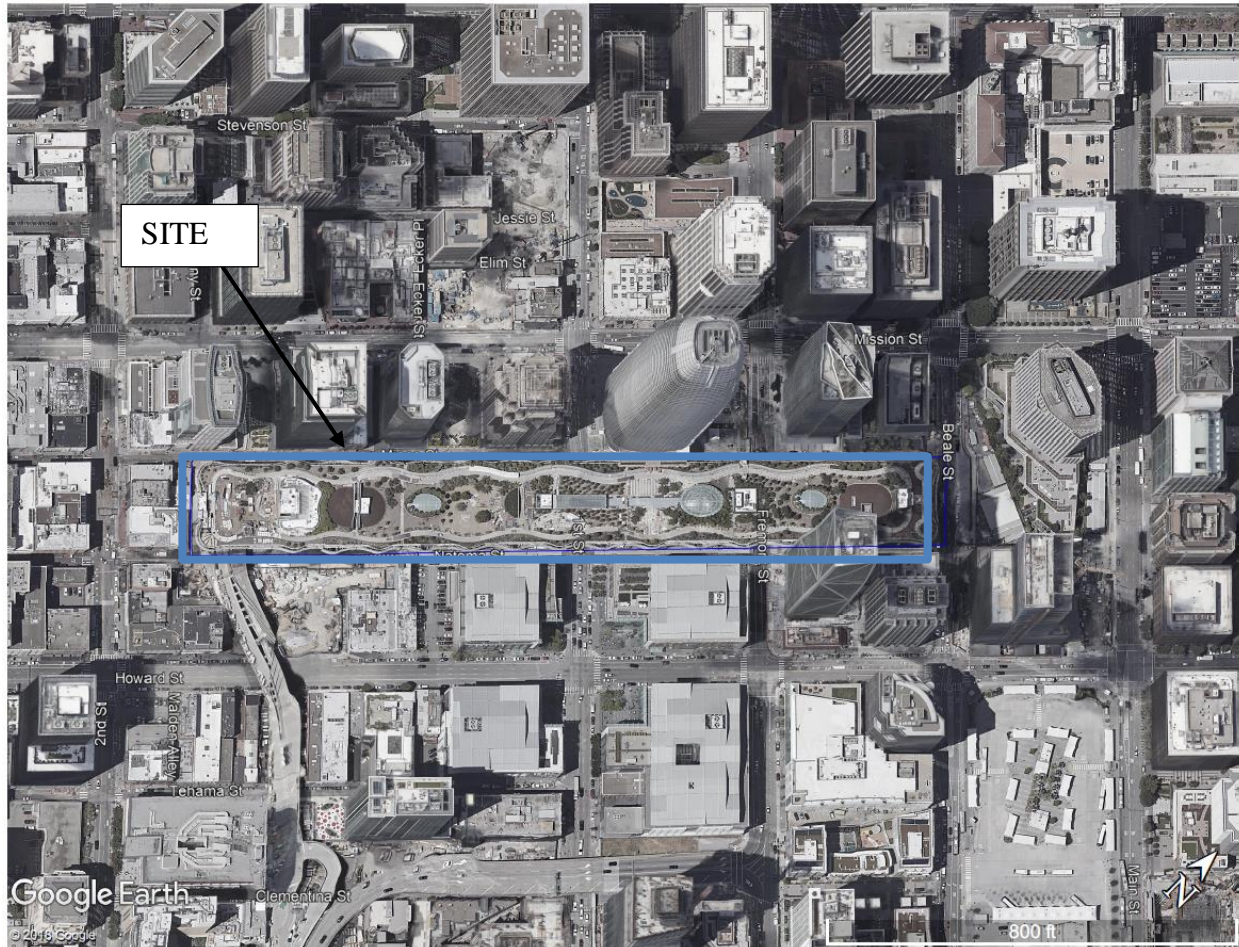


Figure 1.2. Project site location within San Francisco.
Project site is outlined in blue, Transbay Transit Center (Salesforce Transit Center) is visible. (Google Earth, 2008)



Figure 1.3. In-progress photograph of excavation activities.

Top row of bracing visible in the foreground, further rows of bracing and deeper excavation activities in the background. On the right is a temporary bridge built for crane access. Also visible in the background is a temporary bridge spanning the excavation. Photo taken by the author (2013)



Figure 1.4. Photograph of the full depth of excavation prior to construction of the train box. Visible are four levels of bracing, the soldier pile walls surrounding the excavation, and micropile tie-downs. Surface material is sand as discussed in Chapter 2. Wire has been placed just prior to pouring of rat slab. Photo taken by the author (2013)



Figure 1.5. Photograph of operations for construction of the buttress.

On the left side of photo is crane with clamshell bucket used during excavation. On the right are 6-foot casings, which are being installed in the left side of photo. Also pictured on the right are reinforcing cages used in the completed secant piles. Photo taken by the author (2011)

2 CHARACTERIZING THE OLD BAY CLAY

The following sections explore the geologic context of the project site as well as Old Bay Clay as a regional geologic formation. The geologic setting of the site is summarized, including regional bedrock geology and quaternary geology. Geologic and engineering geology studies are summarized because they are the basis for the general knowledge, geologic history, and geotechnical properties of the Old Bay Clay as it is known. A short discussion follows regarding the terminology of the Old Bay Clay and related deposits. Subsurface exploration, field sampling methods, sample handling and storage, and index testing on specimens are then summarized. Project subsurface conditions are explained using the guidance from regional knowledge and prior studies combined with subsurface geology from this research project. Lastly, a study of microfossils is explained within the context of the larger work.

2.1 Geologic Setting

2.1.1 Regional and Bedrock Geology

The study area is located on the northeast edge of the San Francisco peninsula within the Coast Ranges Geomorphic province (Norris and Webb, 1990). The Coast Ranges geomorphic province is characterized by a series of Northwest-trending ranges and valleys, generally formed due to the transpressional motion of the Pacific Plate moving relative to the North American Plate along the San Andreas fault zone. The Coast Range province is bounded by the Cascadia and Klamath zones to the north, the Sierra Nevada province to the East, and the Transverse Ranges to the south.

The Bay Area, encompassing the San Francisco peninsula, has complex geology with a complex geologic history. Some of the oldest rocks found in the region are the Franciscan formation, which is a diverse assemblage of rocks that generally were a part of the subduction complex that formed on the margins of the Pacific and Farallon plates from the Late Jurassic through the Miocene. At that time, the Pacific Plate was being subducted under the Farallon plate in an east-dipping convergent margin. Most oceanic rocks are generally subducted into the mantle, but due to the complex nature of subduction, some of the oceanic and wedge rocks were obducted onto the overriding plate. These oceanic rocks included ophiolite sequences of pillow basalts with gabbros intruded at depth, and overlying submarine sedimentary deposits of graywackes and cherts. As a result of passing through the subduction zone and being obducted, many of the Franciscan rocks show some degree of metamorphism, generally high-pressure/low-temperature metamorphism, including blueschist facies. Metamorphism ranges from low amounts of shearing or hydrothermal alteration all the way through being metamorphosed into low-grade metamorphic rocks. Serpentinite and greenstone, for example, are the low-grade metamorphic rocks formed from metamorphosed gabbros and shales. Thus, the Franciscan rocks are not one particular type of rock nor do they represent one type of geologic environment and can span a large range of age. Instead, rocks of the Franciscan formation generally share a similar geologic history. The Franciscan formation is mostly shales and sandstones with lesser amounts of basaltic volcanic rocks, chert, serpentinite, and some limestone (Wakabayashi, 2004).

The Franciscan formation forms the basement rocks of many locations within the San Francisco Bay Area, it is a major source material for clastic deposits throughout the region, and its properties contribute to the topography of the area. The Franciscan formation underlies the project site and contributes to the unique geomorphology of the San Francisco peninsula. The peninsula is characterized by a number of resistant bedrock knobs that create steep hills interspersed with valleys and plains. These hills surround the site and include Rincon Hill a third of a mile to the south of the site and Nob Hill, Russian Hill, and Telegraph Hill to north of the site. Further to the southwest of the site is the group of hills that make up the interior of the San Francisco peninsula and include Twin Peaks, Mount Davidson, and Mount Sutro. On the regional geologic map of Schlocker (1985), these resistant knobs are mapped as outcrops of Franciscan rock. As more research has been made into the various terranes that make up the Franciscan formation, the location and extent of subsurface rock assemblages as well as Franciscan structure has been identified. The Hunter's Point Shear Zone is mapped crossing the San Francisco peninsula southeast to northwest but to the south of the project site (Wakabayashi, 2004). This shear zone is not an active tectonic structure like the San Andreas Fault zone, but is an intra-Franciscan structural horizon that reflects the complicated nature of the subduction complex. Based on the bedrock encountered in deep borings, as discussed in Section 2.7.2, the project site is possibly underlain by the Hunter's Point Shear Zone, even though Alcatraz terrane is mapped at Nob Hill to the north and Rincon Hill to the south.

In addition to the remnant structure from the previous subduction, there is active faulting across the region, including the San Francisco peninsula. The active tectonism also contributes to the Bay Area geomorphology. The San Francisco Bay itself is a down-dropped basin, formed due to the interactions of the San Andreas fault to the West and the Hayward fault to the east. The project site is almost equidistant between the State of California-designated active fault zones of the San Andreas 9 miles to the west-southwest and the Hayward 9 miles to east-northeast (Jennings, Bryant, Saucedo, and CGS, 2010). The basin in between these fault zones has become an accumulation zone for sediments in the topographic low. The San Francisco Bay area is currently active tectonically, both with strike-slip and transpressional movement on the Bay Area faults, but also active uplifting in parts of the San Francisco peninsula and East Bay Hills.

Bedrock maps of the Bay Area highlight the resistant rock knobs discussed previously, as well as revealing the erosion surfaces before the present sediments were deposited. While San Francisco Bay itself is a basin filled with accumulating sediment, based on bedrock surfaces, it also appears that the project site resides within a bedrock valley. The bedrock map by Schlocker (1974) shows that the project is on the approximate axis of a northeast-trending bedrock valley. The deepest part of the valley is over 250 feet below sea level immediately adjacent to the site, which was observed in borings as described in Section 2.7.2. The ridgeline of the drainage area containing the bedrock valley appears to include the upland resistant knobs of the San Francisco peninsula, including Nob Hill, Alamo Heights, Dolores Heights, and Potrero Heights. This deep bedrock valley may help to explain the complicated subsurface geology at the site and subsurface materials observed there.

2.1.2 Quaternary Site Geology

The surficial geology at the site mapped by Schlocker, Bonilla, and Radbruch (1958) and by Blake, Graymer, Jones, and Soule (2000) shows surficial deposits are mapped as artificial fill. While

much has been learned about Bay Area geology, not least because of development and recognition of Plate Tectonics theory, surficial mapping is well known at the project site. This is because the history of the artificial fill placed at the site is mostly documented and the project site has been developed within a built, urban environment from when settlement of San Francisco began. While the surface has been well known, as can be shown on the Schlocker, Bonilla, and Radbruch (1958) map, the subsurface is an equally or more important aspect of site geology. In the Schlocker, Bonilla, and Radbruch (1958) map, subsurface profiles are listed from various boreholes around the site. In the years since publication of that map, more has been learned about the subsurface in this area, but, more importantly, the subsurface has had a greater impact on development in the area.

The project site is situated south of Mission Street and north of Howard Street between Fremont Street and Beale Street in downtown San Francisco (Figure 1.2). The project site was originally situated in Yerba Buena cove, which was the site of the original Spanish settlement of Yerba Buena in the 18th century that would become the city of San Francisco after the Mexican-American war. Some of the very first survey maps of the area extend back to 1852, which helps to constrain the original shoreline of Yerba Buena cove. This shoreline is noted throughout the text as the “1852 Shoreline” because it is a documented boundary that locates what would have been offshore and what would have been onshore at the time. That shoreline was located just east of First Street and roughly transects the site. However, because of difficulties comparing datums through time, this boundary should be taken to be somewhat inexact. As can be seen in Figure 6 to the north of Yerba Buena cove, even in the 1850’s the shoreline was rapidly being filled in to create new land for settlement. With time, Yerba Buena cove was entirely filled in as San Francisco developed. The materials used to infill the bay and create new land were variable, including debris from ships, buildings, rubble, and surficial soils from surrounding areas. In addition to infilling Yerba Buena cove, general surficial grading occurred to create flat land. Original survey maps show sand dunes and grades 10 to 15 feet higher than present in the western edge of the site. So while only the eastern half of the site was reclaimed from the Bay, the entire site is underlain with fill. The GDR documents more extensive history at the site since the 1850’s because there was extensive development that contributed to approximated 15 to 20 feet of fill at the site, including everything from Redwood timber piles to 1906 Earthquake debris to tar flats.

Prior to infilling, Yerba Buena cove was situated on the east side of the San Francisco peninsula and opened east to the San Francisco bay. Yerba Buena cove was bounded by Rincon Hill to the south and Nob Hill to the north and west. Similar to other portions of undeveloped San Francisco Bay shoreline, Yerba Buena cove was likely an estuarine depositional environment, with disposition of marine clays in offshore areas and deposition of fluvial and eolian deposits onshore and at the shoreline. As a part of an estuarine depositional environment, tidal mud flats and tidal channels would have been present with active deposition of both sands and clays. The most significant recent deposit at the site is the Young Bay Mud, which is well-known to Bay Area geologists and geotechnical engineers. It is an estuarine to marine clay that is currently being deposited within the Bay and is present in the axis and along the margins of the Bay in deposits up to over 100 feet thick (Rogers and Figuers, 1991).

Within the Quaternary Period, even though the Bay Area is undergoing active tectonics, the bedrock topography would have been very similar to today. Rather than seismicity, the dominant

geologic force in the Bay Area during the Quaternary Period has been global sea level change due to glaciation. Due to variation in the extent of glacial ice sheets and the global sea level, the shoreline in the vicinity of San Francisco has varied considerably. Within the downdropped basin, a sequence of sediments have been deposited that generally reflect the recent history of the California coastal margin.

The most recent glacial period in North America is the Wisconsin stage, which lasted from approximately 75,000 to 11,000 years before present (yr BP), with the Last Glacial Maximum, when the global ice sheets were at their maximum, considered to be 26,500 yr BP. Continental ice sheets never extended into California, though glacial stages were observed in the Sierra Nevada mountains through advancing and retreating alpine glaciers. The two most recent latest named stages in California are the Tahoe and the Tioga, with the Tioga being the youngest. The Tioga has been considered to be correlative to the late Wisconsin glaciation, with the greatest extent at approximately 20,000 yr BP (Gillespie, Burke, Clark, 1999). The Tahoe is older, around 50,000 yr BP, which would make it middle Wisconsin age (Gillespie, Burke, Clark, 1999). But with more exact dating techniques, it seems like these Sierran glacial stages have been reassessed, suggesting the last glacial retreat was approximate 19,000 yr BP and a penultimate retreat was at approximately 145,000 yr BP (Rood, Burbank, and Finkel, 2011). At times, the Sierran glacial stages seem to conflict with what is known about global glaciation. This context matters for understanding the Bay Area deposits because their presence depends strongly on global sea level change. The Sierran stages of glaciation are also used by workers who have studied the subsurface deposits of the Bay Area, as discussed below, so a contemporary understanding of these stages is important for understanding previous studies.

During the Last Glacial Maximum, the shoreline was approximately 300 feet lower and was located approximately 40 miles to the west near the Farallon Islands. During that time, the San Francisco peninsula would have been of greater relief than the surrounding area and was covered in sand dune fields. These dune fields were supplied by sand that had been transferred by eolian processes from the paleochannel of the Sacramento-San Joaquin River (Peterson, Stock, Meyer, Kaijankoski, & Price, 2015). These dune fields were still prominent features of San Francisco at the time of mid-1800's development, recorded in historical accounts and observed in early topographic maps. These dune field would have been dynamic and oriented due to the direction of the prevailing winds. Dune deposits are still present in portions of the San Francisco peninsula, as observed in the vicinity of the project site on the geologic maps of Schlocker et al. (1958) and Blake et al. (2000). They are also present at depth under fill materials and under Young Bay Mud, as observed in borings, excavations, and piles. One of the most well-known sand deposits in the Bay Area is the Colma Sand, which is a unit commonly applied to subsurface sand deposits. The Colma formation is named after a type section observed at the Presidio in San Francisco that lies just below latest Pleistocene and Holocene deposits (Schlocker, 1974). While portions of the Colma formation are eolian, much of the formation appears to have been deposited by water and gravity (Schlocker, 1974). While there were extensive dune fields present during the last glacial stage, there was active deposition in many forms, especially alluvial and colluvial. While surficial deposits of Colma formation are fairly well understood, it is possible that subsurface deposits may not be as well defined or correlative.

After the Last Glacial Maximum, sea level rose to the present levels over a period of time. In the process, the alluvial and eolian materials in areas that became submerged would have been re-worked and re-deposited. As a result of these periods of high and low stands of sea level and the complicated dynamics of estuarine deposition, interfingering layers of sands and clays are observed in the Holocene and upper Pleistocene deposits underlying the site. The interlayered deposits include eolian sands deposited during the last glacial period, sands that have been re-worked and re-deposited as the global sea level fluctuated, marine clays deposited in estuarine and offshore environments, and sands deposited in channel and offshore environments. In Yerba Buena cove itself, there is evidence that during the Holocene the global sea level was higher than present and that the shoreline extended further inland than the historic shoreline described in mid-1800's records (Meyer, 2015). Meyer (2015) maps various Holocene shorelines that are higher than the historic 1852 shoreline (Figure 2.1). These shorelines are based on a study involving C-14 dating of plant materials found in and around the TTC excavation as well as stratigraphy based on fossil remains at the site and in adjacent areas on the San Francisco peninsula. Meyer suggests several models for sea level rise and inundation, one of which could have been due to "still stands" or "near still stands" in sea level rise. This could have been a local phenomena or possibly more widespread, but resulted in the deposition of Young Bay Mud further inland than the 1852 shoreline. So rather than a layer cake of deposits from the glacial stage being overridden by Holocene deposits, there are interfingers in these deposits or possibly one transgressive-regressive sequence within these deposits. The combined Holocene and late Pleistocene layers beneath the Young Bay Mud range from 25 to up to 100 feet thick (Rogers and Figuers, 1991).

Prior to the last glacial stage was an interglacial period, a time of warmer temperatures that separates glacial states similar to our current Holocene interglacial period, assuming there is a future glacial stage. The last interglacial period was the Sangamon Stage, corresponding to Marine Isotope Stage 5, which is approximately 75,000 to 125,000 yr BP. Because the topography was largely the same as now, at that time a paleo-San Francisco Bay was present, likely with sea level much higher than present (Sloan, 1992). These deposits would have been deposited prior to the late Pleistocene to Holocene deposits, with some volume of Sangamon deposits eroded or re-worked during the late Pleistocene to Holocene. During the Sangamon interglacial, a thick accumulation of estuarine to marine clays were deposited. These marine clay deposits are what is commonly referred to as the Old Bay Clay or the Yerba Buena Mud and are prevalent across the Bay Area, over 100 feet thick in places (Rogers and Figuers, 1991). The Old Bay Clay is a characteristic deposit at the project site, which is why it is a main focus of this study. More detailed background study of the Old Bay Clay is discussed in the following sections, especially as related to the work of Sloan (1982) and Sloan (1992).

Prior to the Sangamon interglacial was the North American Illinoian Stage of glaciation, which lasted during the middle Pleistocene from approximately 191,000 to 130,000 yr BP. Prior to the Illinoian, there were several other cycles of interglacial and glacial stages reaching through the beginning of the Quaternary Period. Below the Sangamon Old Bay Clay, in the Bay Area subsurface column there, is not a clear correlation between deposits and named interglacial or glacial stages. There is a tuff encountered in boreholes that have been dated (Atwater, Hedel, & Helley, 1977), but subsurface layers that correlate to glacial stages appear to end with the Old Bay Clay. Below the Old Bay Clay are interfingering layers of sand and clays extending to the bedrock surface. Some of these clays appear to be estuarine or marine, which have been observed at the

project site. It is possible that these deposits may reflect many cycles of glacial and interglacial deposition prior to the previous interglacial period. Or it is possible that previous cycles of glacial and interglacial depositions have been eroded. Particular locations within the Bay Area may even retain deposits from certain glacial or interglacial periods but not others. Common names for these deposits below the Old Bay Clay include the Alameda formation, the Merced formation, the Santa Clara formation, and portions of the San Antonio formation. These names and their correlations are discussed further in the next section.

2.2 Engineering and Geologic Studies of Holocene and Pleistocene

Bay Deposits

As discussed in the previous section, there is a progression of Quaternary deposits that appear to correlate well with what is known about the previous glacial and interglacial stages. But because the majority of these units are only observed in borings, excavations, and pier drilling, these relationships are not readily apparent and have been a source of study since the beginnings of Bay Area geologic exploration. Some of the confusion comes from the gap between geologic and geotechnical studies. Because many of the subsurface deposits are identified in geotechnical studies within borings, they have been given unit names that correlate with geologic place names. Other times, the unit names describe the engineering properties gained through previous experience. Sometimes the units are given place names and then later correlated due to geologic or geotechnical similarities.

The Old Bay Clay (OBC) is a unit that most Bay Area geotechnical consultants are familiar with, but the literature does not contain many papers describing its properties. The main study of the unit is by Sloan (1982), who focused mostly on the geology of the unit as could be learned from microfossil study. Other workers in the area, as discussed below, have documented the Old Bay Clay within the context of other geotechnical and geologic studies. Most likely the knowledge of properties that consultants have is based on in-house information and lessons learned from previous projects. Thus, it can be useful to study the entirety of published works, which contain important contemporaneous observations of tested materials and which tend to be incremental continuations of previous research. Moreover, there is constant interdependence between published geological and geotechnical studies. Geotechnical studies tend to be project-focused and produce testable samples, but often require insight by geologists to give the studied materials context. It is also notable that the majority of published studies of Bay Area subsurface stratigraphy, including of the Old Bay Clay, only come from a handful of publicly available studies. These studies are thorough, but because they only represent particular locations, they may represent limited geographic coverage. Thus, there is no one source of definitive subsurface geology and geotechnical engineering for the Old Bay Clay. Published work that has been performed on the OBC roughly corresponds to several phases of interest: early characterization of Bay Area geology in the early 20th Century, work related to the bridge crossings across the Bay that were planned in the mid 20th Century, and seismic characterization of Bay deposits after the Loma Prieta earthquake. There is currently a new, fourth, phase in process due to the demands of construction in the Bay Area that requires more extensive characterization of the subsurface because the construction is more complicated and more extensive than it has been in the past.

2.2.1 Late 19th Century and Early 20th Century Geology

When understanding Bay Area geology, it helps to return to one of earliest papers describing Bay Area geology, which is informative to this day, Sketch of the San Francisco Peninsula (Lawson, 1895). In it, Lawson covers the hard rock geology of the Bay Area, giving very detailed descriptions of Bay Area stratigraphy and petrology. While he does not specifically address the quaternary Bay sediments, he does recognize that the exposed bedrock represents an eroded terrane and that there may have been periodic changes in sea level that contributed to the incised and infilled valleys.

One of the first published works that characterized the subsurface stratigraphy of the Bay was Lawson's 1914 *San Francisco folio*. Lawson identified the Young Bay Mud, which he called "salt marsh deposits," the Merritt sand, the San Antonio formation, and the Alameda formation. While he mostly limited his descriptions to outcropping geology, he had some information from East Bay well drilling, which penetrated the deeper bay sediments.

In his folio, Lawson gives the name San Antonio formation to the sequence of alluvial deposits emerging from the East Bay hills. The place name is derived from the San Antonio township, which was an original part of the land grant of Rancho San Antonio, also called the Peralta Grant, that would later become the town of Brooklyn before being incorporated into greater Oakland. Lawson separates the San Antonio formation into an upper member that contains fragments of Miocene Claremont chert and a lower member without those chert fragments. He thus suggests that the lower member was formed before streams had eroded the Claremont chert that outcrops in the Berkeley Hills. Further, he suggests that the San Antonio formation correlates with the uplift of the Berkeley Hills.

Lawson's San Antonio formation does not appear to include any clayey or marine materials, but later authors have used his formation name and have expanded that formational name to include materials which appear similar to what this study calls Old Bay Clay. It can be confusing to keep track of the formational names of Bay deposits, because various authors reuse names while changing what materials should be included. The materials that Lawson describes as the San Antonio formation would not be included in the current study of the Old Bay Clay because he mostly describes what would be quaternary alluvial deposits.

Lawson gives the name of the Alameda formation, a place name that reflects the city of Alameda, to all the quaternary materials lying beneath the East Bay alluvial deposits, including the San Antonio formation. He describes the Alameda formation as existing "practically everywhere beneath the slopes of Berkeley and Oakland," of predominantly marine origin, and having a thickness on the order of several hundred feet. In several places, the Alameda is described as "yellow sandy clay, of very uniform fine texture" that includes beds of marine shells and discontinuous fluvial gravel beds, possibly indicating a delta formation of alternating marine and estuarine deposition. He also describes that in several wells and at an outcrop in West Berkeley, a blue clay is encountered in the Alameda formation. The blue clay that Lawson describes is very characteristic of what is called the Old Bay Clay in this study. The description of "yellow sandy clay" maybe due to the formation's oxidized appearance. So, whereas others have included the Old Bay Clay in descriptions of the San Antonio formation and Lawson is one of the first to denote

the San Antonio formation, Lawson's description of the Alameda would likely include the Old Bay Clay.

2.2.2 Mid-Century Bay Crossings

Most of what is known about Bay sediments is based on work from the next phase of publications, which is work related to a number of contemporaneously proposed bridge crossings across the Bay. In the mid-twentieth century, engineering exploration at locations in the San Francisco Bay provided a wealth of information about stratigraphy and engineering properties of deeper sediments. The work at that time was of a very high quality, such that the observations from that time are still considered the state of the practice in the Bay area. Some of the samples taken at the time were even preserved for later study, which produced a number of papers discussed below. Trask and Rolston (1951) and Louderback (1951) published their observations about the engineering properties and geology, respectively, gleaned from these explorations. Trask and Rolston's work, in particular, is referenced in later papers, such as Treasher (1963), Goldman (Ed.) (1969), and Bonaparte and Mitchell (1979), which are still referenced by the greater engineering community. The samples from the bridge investigations also have a big impact in the 1970's when the California State Department of Public Works, Division of Bay Toll Crossings (Caltrans) donated approximately 5,000 specimens to the United States Geological Survey (USGS). Investigations utilizing these specimens include Atwater et al. (1977), Ross (1977), and Sloan (1982) and focused mostly on the geologic and biological properties of the sediments.

Trask and Rolston's 1951 paper is worth highlighting, because it is the root paper that many later investigations expand upon. Their work also includes many still important insights into the engineering properties of the described materials. Their work was based on investigation for two proposed crossings of the Bay, the "Parallel Crossing," which would have been built just south of the present Bay Bridge, and the "Southern Crossing," which would have connected Alameda and Potrero Hill area of San Francisco (Figure 2.2). The Webster Street Tube, in fact, was built as a portion that would have continued on to the proposed Southern Crossing. The exploration for the two crossings involved 60 borings, where California and Shelby tube samples were obtained for laboratory testing that included index testing, consolidation tests, unconfined compression, direct shear, and consolidated quick shear. As part of their paper, Trask and Rolston also summarized previous investigations for construction projects in the Bay. Thus, their paper provides a valuable characterization of the deposits and their engineering properties in the central part of the San Francisco Bay.

Trask and Rolston divided the stratigraphy of the subsurface Bay sediments into five formations: the Bay Mud, the Merritt sand, the Posey formation, the San Antonio formation, and the Alameda formation. Each of those formations is separated by an unconformity. Their description of the San Antonio formation closely matches what is called the Old Bay Clay for this study. Trask and Rolston note that there are two upper members within the San Antonio, a silty clay and a "persistent shell and sand" with silty clay layer, that are present in the eastern part of the Bay that are not well developed in the west, where this study is focused. The lower part of the formation is described as a gray and greenish-gray clay, with zones of sand and gravel as well as alternating layers of fine sand and clay. Trask and Rolston suggest that their description of San Antonio formation correlates with the lower member of San Antonio formation described by Lawson. Lawson's upper member

of the San Antonio appears to correlate with Trask and Rolston's Posey formation. It is noted that Trask and Rolston do not describe the Colma formation anywhere in their work, as that formation appears similar and possibly was deposited synchronic with the Merritt Sand unit. It is possible that due to the focus on the East Bay stratigraphy, unit names based on that side of the Bay were projected across based on stratigraphic position. It is also possible that the Colma actually pinches out before the Bay. At the project site, as discussed in Section 2.7.2, the Colma does appear to pinch out.

In describing the unconformities between formations in the study area, Trask and Rolston help to explain the paleogeography that lead to their deposition. They indicate a slight unconformity between the Posey and San Antonio formations, though in some places it was apparent that upper portions of the San Antonio have been eroded in presumably the western portion of the Bay. Between the San Antonio and Alameda formations, they conclude that considerable material was likely removed, as indicated by the absence of almost 50 feet of formation from the western part of the Southern Crossing. This is notable for later observations of stratigraphy of overburden stresses in this deposit. Additionally, they indicate that the variation between the sloping contact between the San Antonio and Alameda compared to the gentle slope of deposition suggests that the central Bay may be downdropped since the time of Alameda deposition.

Two of the more prescient observations that Trask and Rolston made about the San Antonio Formation is that it can consolidate appreciably when loaded past its preconsolidation pressure and that there are local variations in properties within the formation. In their lab testing program, they found that the preconsolidation pressure ranged from approximately 1.5 to 3 tons per square foot (approximately 144 to 287 kPa) and that there was a relatively high coefficient of consolidation. Thus, they indicated a large amount of potential settlement for the proposed sand islands that were a part of the proposed Southern Crossing project. Likewise, they highlight the local variation in the San Antonio. There were large variations in the thickness of the San Antonio across their study area, where thickness ranged from 15 to 120 feet. They found that there were variations in compressibility, with the stiffest material near the Webster Street Tube and the softest material just east of Yerba Buena Island. That location was also the thickest section of San Antonio found in their study.

While Trask and Rolston covered the engineering properties of the sediments at the Bay crossing locations, Louderback (1951) provides a complementary geological context. The paper was written without the context of plate tectonics, so the descriptions of the structural development of the Bay Area and surrounding uplifted terranes are not consistent with our current understanding; however, Louderback recognizes the influence of global sea level cycles in the deposition of the Quaternary sediments. At the time, there was debate whether the Bay sediments represented a subsiding/rebounding regime. He correlates the most recent development of the San Francisco Bay to the rise of sea level resulting from melting of the ice sheets to Wisconsin-age glaciation. He also recognized that there were a "succession of stages of ice-sheet development separated by intervals of recession." And that during the "great interglacial interval in mid-Pleistocene time, when less glacial ice existed than at present, it might be expected that the sea level would have risen higher than it is today." However, he suggests that these deposits would be found at higher elevations, rather than in lower elevations in boreholes consistent with the current range of the Old Bay Clay. He also places this period at a mid-Pleistocene period of from 400,000 to 240,000 yr

BP, rather than during Sangamon time. Louderback points out some interesting fossil discoveries that helped correlate the ages of Bay sediments, such as a bison jaw fossil found at 180 feet below sea level in a Bay Bridge East Span excavation east of Yerba Buena Island and a Mammoth tooth found about 1000 feet to the east in the same horizon.

Another often-cited paper relating the Bay Area sediments is Treasher's 1963 work. The paper reflects plans by the State of California to construct barriers across the bay in order to conserve fresh water. The engineering study for that plan included excavation of ten deep borings drilled between the Richmond-San Rafael bridge and the San Francisco Bay Bridge as well as compilation of logs from over 3,000 older core logs. Treasher's work is important because he ties the engineering properties of the sediments to their geologic setting and history. He also includes a number of useful maps of the Bay Area that contour the top of bedrock, the top of the "older bay mud," and the top of the younger bay mud. Similar contour maps are included in a number of important papers regarding Bay Area subsurface materials, because they can help other workers to understand a site prior to exploration or to fill in gaps of knowledge at a site where there is limited subsurface information available. Treasher combines all sediments above bedrock and below the sand units, including the Merritt sand, into his unit, "Older Bay Mud." This unit is described as "a stiff to very stiff, firm clay, which contains varying amounts of silt, and lenses of sandy clay, sand and gravel." He notes that various lenses observed in the boring logs do not lend themselves to correlation, that the grain-size of the nearshore materials is very similar to the deep materials, and that the Older Bay Mud is overconsolidated relative to the current overburden. He suggests that the top surface is deeply eroded, indicating a major stream drainage network. The uppermost stiff clay of his Older Bay Mud unit appears to correspond to the Old Bay Clay of this study. While this grouping of disparate sediments is supported by the lack of correlation below the uppermost stiff clay, as is also observed at the project site and discussed in Section 2.7.2, it leads towards a flattening of distinction between deep sediments. In the original GDR at the project site, the deep sediments were called, "Old Bay Clay, Unit II," which strongly harkens back to this study. However, because the units below the upper fat clay called the Old Bay Clay are actually very heterogenous, the "Old Bay Mud" name is a misnomer and not helpful to reflect the wide range of materials to which it refers.

Treasher expands upon Louderback's hypothesis of global sea level change related to glaciation and suggests three separated glacial advances. He proposed that a first glacial advance, possibly representing Illinoian Glaciation, that lowered sea level and eroded the Bay valley. The valley would then be flooded to a depth of at least 200 feet in order to allow deposition of a soft mud that would be consolidated into the Older Bay Mud. The second glacial advance he proposes, correlating to Wisconsin Glaciation, would expose the Older Bay Mud and lead to desiccation and overconsolidation. Once that period of glaciation ended, another high water event would involve deposition of the sand members and a lower, overconsolidated unit of Young Bay Mud. He proposes that a third event of limited glacial advance, also presumably Wisconsin-aged, led to desiccation and overconsolidation of the lower Young Bay Mud. The final interglacial even would then lead to the current deposition of normally consolidated, soft Young Bay Mud. This idea does not conform to our knowledge of global glacial epochs, but harkens to the Sierran glaciation of the Tahoe and the Tioga, which both would have occurred during the Wisconsin stage. At the project site, as discussed below, there may be present either a transgressive-regressive-transgressive

sequence or some sort of “still stands” or “near still stands” in sea level rise. More than one source suggests secondary retreats and advances within the Wisconsin glaciation in the Bay Area.

A similar work to Treasher’s and Atwater et al. (1977), discussed below, is Goldman (Ed.) (1969), which is also a compilation of borings from Bay Toll Crossings and the libraries of Dames and Moore and Woodward-Clyde-Sherard consultants. Especially notable are a series of scale maps of contours of subsurface units, including bedrock, the bottom of the Younger Bay Mud, and the thickness of the Younger Bay Mud, which plates are still in use by some Bay Area consultants.

Many later studies have been performed on the same Bay Toll Crossing samples collected in the 1950’s and 1960s, which were donated to the USGS in 1970’s. These studies include Atwater et al. (1977), Ross (1977), and Sloan (1982 and 1992), which all included investigations of microfossils within the marine clays in order to constrain age relationships and explore paleostratigraphy.

Atwater et al. (1977) published a USGS Professional Paper that summarized a large number of Bay Toll Crossing samples collected going back to 1946 that were then donated to the USGS for study. In addition to compiling the Bay Toll Crossing samples, the paper summarizes much of what is known from previous Bay Area geotechnical and engineering geologic studies into a very clear chronology and stratigraphic column. Their study contextualizes what we now understand about Bay Area stratigraphy, as described in Section 2.1.2. Unlike earlier studies, they refrain from applying the colloquial engineering names, such as Young Bay Mud and Old Bay Clay, or the geological formational place names, such as San Antonio or Alameda formations. They also make a distinction between the stratigraphy column in the North San Francisco peninsula and the South San Francisco peninsula, as well as on-shore versus Bay sediments. This helps to emphasize that materials were deposited synchronously throughout the Bay that were not deposited in the same geologic environment, thus producing dissimilar materials. In their study, Old Bay Clay would be included in the unit “Estuarine deposits (late Pleistocene),” corresponding to the Sangamon interglacial. Of particular note in this study are a series of generalized cross sections spanning the northern Bay at approximately Alameda, in the central Bay at approximately Hayward, and in the south Bay at approximately Fremont. This helps to contextualize the variation in Bay deposits as exhibiting the various geologic environments that would have been present at any one time in the Bay and thus show variation in space and time of the resulting deposits. The paper also includes a detailed microfossil study of the Holocene clays, documenting sea level rise and the changes in depth and salinity of the Bay through the Holocene. Lastly, they discuss evidence documenting subsidence of the South Bay, which was previously suggested by Lawson (1914) and Louderback (1951).

A similar study to Atwater et al. was Bruce Ross’s 1977 Master’s thesis. His thesis included a study of soil samples donated by the Bay Toll Crossing from a 1955 study along the Southern Crossing (Figure 2.2), focusing on the paleostratigraphy of pre-Holocene materials. His conclusions regarding Bay Area stratigraphy agree with Atwater et al. As a part of his study, he identified microfossils and shell fragments within what he calls “Unit C,” Sangamon estuarine deposits, which are equivalent to this study’s Old Bay Clay. His work would be further expanded in the work of Doris Sloan, explained below.

Sloan (1982, 1992) studied in detail the upper Pleistocene estuarine deposit of the standard Bay Area stratigraphic column. This was the most in-depth study to date of the unit referred to in this research project as the Old Bay Clay. Sloan gives the unit the name “Yerba Buena mud member” of the San Antonio Formation, named after Yerba Buena Island. The Yerba Buena mud correlates within the San Antonio formation of Lawson (1914) and Trask and Rolston (1951). Sloan’s work also utilized the Bay Toll Crossing samples along the proposed Southern Crossing alignment, though her specimens were younger and better preserved than the samples in the Atwater et al. (1977) and Ross (1977) studies. Sloan’s work was a biostratigraphic study of the sediments, which involved identifying the presence of foraminifers, sand-sized diatoms, seeds, fish remains, shells, and other microfossils within specimens. The presence of those microfossils and, in particular, their assemblages were used to indicate the environmental conditions at the time of deposition. Samples were washed and sieved with the sand-sized ($>63\ \mu\text{m}$) materials retained for study using paleontological and sedimentological methods of quantitative analysis. Additionally, observations were made of mineral content, sedimentary structure, and color. Bulk density and shear strength data was available from the original investigation when the samples were collected and was also used for stratigraphic interpretations.

As others have also previously observed, Sloan correlated the Yerba Buena Mud as a single transgression deposited during the Sangamon stage. The stratigraphy observed is consistent with what others have previously found, where the Yerba Buena Mud is deposited upon a Pleistocene alluvial disconformity and is overlain by layers of Holocene and Upper Pleistocene estuarine, aeolian, and alluvial deposits. The upper surface of the Yerba Buena Mud is an erosional surface and Sloan notes that the most complete section of Yerba Buena Mud is from the central portion of the alignment. In the western portion of the alignment, a deep channel has been eroded into the Yerba Buena Mud, also removing the upper layers of the identified biofacies units. It is noted the difficulties in constraining the age of the Yerba Buena Mud because of the lack of material for radiometric dating and the inconsistent results from dating *Macoma* shells fragments from within the deposit. Based on constraining age dating from some deeper ash beds, as well as the general stratigraphic position, thickness, and extent of the Yerba Buena Mud, the age is consistent with marine oxygen-isotope Stage 5 (Sangamon Stage).

Sloan breaks the transgression into five units, representing a deepening Bay. The lowermost biofacies is Biofacies A, which is the thickest unit and includes a low frequency of microfossils, bony fish remains, estuarine microfossils, and the most plant material. Biofacies A indicates “marsh, intertidal, and shallow-subtidal environments at brackish to normal salinities,” representing a Bay-margin, estuarine-type environment (Sloan, 1992). Biofacies B is present in much of the eastern and central alignment and in scattered locations along the western alignment. This biofacies has a “[h]igh diversity and abundance of estuarine foraminifers and diatoms...there is little plant material other than seeds” (Sloan, 1992). Biofacies B was likely deposited in moderate depth and salinity, similar to conditions throughout much of the current San Francisco Bay. Biofacies C is present in the central portion of the alignment and in several scattered borings in the eastern portion. This biofacies is noted to contain a high variety of microfossils, many of which are marine, and rarely contain plant material. The biofacies C depositional environment was more saline and in deeper, colder water than for Biofacies A and B, equivalent to conditions along the outer California coast at the present. Biofacies D and E are only present in a small group of samples. Biofacies D was correlated to a “high energy environments at close to coastal-marine

salinity” and Biofacies E was correlated to the null zone or an environment like outside the Golden Gate where there is increased upwelling and transport of sediments from the Bay (Sloan, 1992). The environments represented by the uppermost biofacies is suggested by Sloan to reflect the opening of the Colma Strait or another deep water channel that allowed deep, cold water into the Bay. The progression from Biofacies A to Biofacies E represents a bay transitioning from an estuarine to a fully marine environment, which is consistent with the observation that the Sangamon bay was deeper and more extensive than the present limits. That the microfossil record supports the other stratigraphic evidence is an important addition to what is known about these deposits. A small microfossil study was performed as part of the research project to correlate with Sloan’s work and it is discussed in Section 2.8.

Bonaparte and Mitchell’s 1979 study was performed on samples collected at the Hamilton Air Force Base (Hamilton) site over a period of time for research study. It is unique in that the project site is located in the North Bay Area of the San Francisco Bay on the western shore of San Pablo Bay. Bonaparte and Mitchell distinguish five sedimentary units comprising the San Francisco Bay sediments: Bay Mud; Merritt Sand; the Posey formation; the San Antonio Formation; and the Alameda formation. While the information about Bay Mud is closely detailed, not much is specified about the properties of the material grouped together as the “Older Bay Mud,” which include Posey, San Antonio, and Alameda formations, other than they comprise “a competent foundation material.” Bonaparte and Mitchell attribute their material descriptions to Trask and Rolston (1951). They describe the Posey formation as being “a mixture of sand and sandy clay up to 50 feet thick.” The Posey is described as overlying the San Antonio formation, which is described as “a sequence of moderately firm clays, sands, and gravels between 15 and 120 feet thick.” The Alameda formation is described as varying “from very firm clay through sandy clay to sand and gravel...[i]t varies up to 200 feet in thickness.” The grouping of heterogenous layers below the Young Bay Mud in this study is consistent with Treasher (1963) as well as future work like in the original GDR. As explained previously, the grouping of heterogenous layers under the label “Mud” or “Clay” is a misnomer that can cause confusion.

2.2.3 Post-Loma Prieta Earthquake (1989)

Several studies of subsurface geology were performed after the 1989 Loma Prieta earthquake, especially focusing on the Oakland and the East Bay Area. In that area, there was unexpected ground motion amplification in deep, stiff soil sites, which was possible amplification due to the deep sediments (Bray, Chameau, & Guha, 1992). These studies focused on understanding the extent and properties of deep sediments.

Rogers and Figuers (1991) summarized the findings of over 200 deep borings in the greater Oakland area and correlated the site stratigraphy with observed ground motions from the Loma Prieta (1989) earthquake. The borings came from Bay Toll Crossing borings, Woodward-Clyde records, and Rogers/Pacific records. While the Lawson (1914) study that gave many of these sediments their names focused mostly on East Bay subsurface stratigraphy, the published studies since then had been based on insights from Bay Crossings as well as the San Francisco peninsula. This study was a shift in focus back to the East Bay. It was also a more rigorous recognition of various properties of deep sediments in order to understand their seismic response with respect to localized ground motion amplification. A main result of their study was structural contour maps

of the basement rock and of the overlying Pleistocene and Holocene sediments as well as several idealized cross sections spanning the Bay from Berkeley to San Leandro. Their units are a continuation of the works cited above and correlate the Old Bay Clay of this study with Sloan's Yerba Buena Mud, but, in fact, call it the Old Bay Mud. They find that the Old Bay Mud is more widespread than Young Bay Mud and found further inland than the Young Bay Mud extent, suggesting a deeper, bigger bay. Deposited on the erosional surface of Alameda, they suggest that the unit involved the infilling of two paleo channels, which has also been suggested by earlier workers based on contouring the base of the unit. They note a widespread shelly and sandy layer in the middle of formation, possible temporary lowering or transgression. This layer or layers within the unit are noted in other parts of the central and East Bay, but not observed in the current project study area. Contouring the top of the unit suggests that the upper surface represents just one channel at the east span of Bay Bridge, representing a closed depression up to 100 feet thick.

Beneath the Old Bay Clay and above the Franciscan basement rocks, Rogers and Figuers map the Alameda as both continental and marine units representing a number of older interglacial periods of sea level rise and intervening glacial ages. Rogers and Figuers found the Alameda formation to be much deeper in the Oakland area than in other studies discussed previously, ranging from 400 to over 900 feet thick. In their work, they also include illustrations providing geomorphologic schematics for deposition of the Old Bay Clay, which includes two paleo channels, through the east span of the Bay Bridge, flowing south, and through the San Mateo bridge, also flowing south for a southern drainage through the San Bruno Channel. This is similar to the Colma Strait theory of Sloan (1982). They suggest a pull-apart basin to explain the thickness of units in the central portion of the bay. Above the Old Bay Mud, they group the Posey and Merritt formations with the non-marine portions of the San Antonio formation as described by Trask and Rolston (1951). In the East Bay study area, these materials comprise many different despositional environments, including alluvial fans, flood plain, lacustrine, and beach deposits, which they note are discontinuous and difficult to correlate.

One of Rogers and Figuers main conclusions, consistent with observation of current research work, is the problem of utilizing formation names. They state, “[h]istorically, the use of a formation name has tended to imply a specific set of parameters that may not have any relationship to the particular locality in question. As the entire East Bay margin has long been an interface area between continental and marine depositional environments. Formation names should, therefore, be used with caution, recognizing that the environment of deposition and the mechanical properties may be different than what is commonly implied by a formation name.”

Also originating from renewed interest after Loma Prieta, was Guha (1995) and Guha et al. (1997), which involved soil sampling at two sites in Emeryville and Oakland, with laboratory testing of dynamic soil properties within the Old Bay Clay. This study was predominantly a geotechnical study of the laboratory properties of the Old Bay Clay. He performed resonant column tests and cyclic triaxial tests for dynamic properties as well as index testing, Incremental Load (IL) consolidation testing, and isotropically consolidated undrained triaxial testing (CUTX). Additionally, downhole suspension logging was performed in one Oakland borehole in order to provide velocity profiles with depth and to compare with laboratory measurements of shear wave velocity, V_s .

Subsurface stratigraphy used for the Guha study came from the project borings with context from the work of Rogers and Figuers (1991). The Old Bay Clay layer extended from approximately 42 to 180 feet below the ground surface (ft bgs) at the Oakland site and from approximately 38 to 250 ft bgs at the Emeryville site. Both sites included some interlayers of granular materials, sandy silt layers approximately 4 feet thick at the Oakland site and a sandy to gravelly layer approximately 24 feet thick at the Emeryville site. At both these East Bay sites, the Old Bay Clay vary from the profile observed at the project site for this study, which was deeper, less thick, and had few if any significant interlayers of granular materials.

Samples tested in this study came from depths of 48 to 190 ft bgs. Tested specimens had water contents that ranged from 15 to 48.8 % with most in the 20 to 25 % range and Plasticity Index (PI), of 9 to 42 with most in the 15 to 25 range, corresponding to a generally CL to CL-CH material. OCRs ranged from 1 to 4, with average values between 2 and 3 and generally decreasing with depth. Compression index ranged from 0.055 to 0.328 and recompression index ranged from 0.006 to 0.029. When compared with the Old Bay Clay tested for the current research project, the Old Bay Clay of the Guha study generally had lower water contents, lower PIs, higher OCRs, and were less compressible in both initial compression and recompression. Dynamic testing in the Guha study produced estimates of low-strain shear moduli, G_{max} , normalized modulus reduction curves (G/G_{max} v. shear strain, γ), and low-strain damping ratios, D_{min} . These properties were correlated with plasticity, void ratio, magnitude and duration of confinement, and consolidation stress history. In addition, the in-situ estimates of G_{max} were used to evaluate the effects of sample disturbance and aging effects.

Another study of dynamic soil properties prompted by the Loma Prieta Earthquake was Gretchen Rau's PhD dissertation (1999). She performed cyclic simple shear testing on Young Bay Mud from Hamilton Fields, the same site as Bonaparte and Mitchell's (1979) study. The study involved monotonic, cyclic, and post-cyclic loading in simple shear in order to assess strength degradation of Young Bay Mud under earthquake loading. Rau also aggregated Young Bay Mud properties from different sites in the Bay Area as well as compare Young Bay Mud with the deeper Old Bay Clay of the Guha (1995) study.

2.2.4 To Present: Extensive and Deep Construction Projects

The current phase of subsurface investigation of the deeper deposits of the San Francisco Bay appears to be driven by construction in the Bay Area that involves more extensive development, deeper loads, and more stringent requirements for performance than has been previously been considered. During this phase, several consulting companies have published case histories that have documented their understanding of the subsurface. This study, itself, falls in this category, as a case study inspired by an unprecedented construction project in the Bay Area.

Simpson (2006) describes case studies in Mission Bay, San Francisco, from a large redevelopment project involving many parcels and structures. The Mission Bay Area is approximately a mile to the south of the TTC project site along the eastern side of the San Francisco peninsula, though on the opposite side of the Rincon Hill bedrock divide. Mission Bay has a similar history as Yerba Buena Cove, as it was previously a large estuarine bay that was filled during the 19th through early 20th century. She provides a summary of subsurface conditions based on six projects in Mission

Bay as well as the foundation solutions used for the construction at the site, generally pile foundations. The simplified stratigraphy presented groups the materials into four named groups: fill, Bay Mud, Colma Formation, and Old Bay Clay, as well as unnamed sand and clay. Surprisingly, there is very large variability between the six cross sections included in the paper. The Mission Bay appears to have a wide variability in the thickness of the subsurface layers. Fill ranges from 8.5 to 38.5 feet thick, Bay Mud from 9.5 to 127 feet thick, Colma formation from 0 to 61.5 feet thick, and Old Bay Clay from 0 to 27 feet thick. The Bay Mud is described as soft, weak, and compressible and is thinnest along the former shoreline and thickest at the easternmost edge of Mission Bay, where the deepest part of the former bay would have been. The Colma formation is described as medium dense to very dense sand, silty sand, and clayey sand, and thickens to the east and south parts of Mission Bay. The Old Bay Clay is described as a medium stiff to hard clay that is overconsolidated and, though the degree of OCR is not noted, it appears to be thinnest in the south part of Mission Bay. Bedrock was found at depths from 5 to 210 feet bgs. For an area so close to Yerba Buena cove that also had such similar recent history, the differences in subsurface profile is striking. From Schlocker et al. (1958), the bedrock topography in Mission Bay is much more variable than the bedrock valley underlying the TTC site. This may, then, reflect the variability of the overlying deposits, even though an initial assumption may be that these sites would have similar “layer cake” sequences of Bay deposits.

Espinosa, Pestana, Vahdani, and Heidarzadeh (2017), in the context of the proposed re-development of Treasure Island, performed a the seismic deformation analysis of its shoreline. Treasure Island is approximately 2 miles to the northeast of the project site, laying entirely within the San Francisco Bay to the north of Yerba Buena Island, which is a resistant bedrock knob. The Espinosa et al. study involved detailed subsurface investigation. Similar to the TTC site, the upper Holocene to late Pleistocene layers are complicated and unlike a “typical” layer cake. Beneath the artificial fills that construct the island is a unique deposit called the “Shoals,” which are silty sands and have an impact on seismic response as well as construction techniques at the island that involve densification. Beneath the Shoal are many layers of Young Bay Mud interbedded with silty to clayey sand layers. At Treasure Island, the equivalent unit to this study’s Old Bay Clay is called the Old Bay Deposits, because the unit is much less homogenous than is observed at the TTC site and has scattered layers of interbedded sands. Similar to Mission Bay, the Treasure Island site is fairly proximate to the research project site but appears to have different relationships between units as well more heterogeneity.

2.3 Nomenclature for Holocene and Pleistocene Bay Deposits used in this Study

As can be observed in the previous sections, there are a lot of names for the subsurface deposits in the San Francisco Bay Area and variation between different published authors. A large disconnect, in particular, exists between the colloquial engineering names that consultants use and the geological formation names that imply age and paleoenvironment.

As discussed above, there are a lot of names that describes the geologic unit of interest at the project site: the San Antonio, the Yerba Buena Mud, the Alameda, the Old Bay Mud, Old Bay

Clay, Old Bay Deposits, and likely many more. There is frustration and confusion for some who have to make sense of these names, especially when they must identify whether a soil fits into a known formation. Various ways of identifying the Old Bay Clay include looking for the succession of typical Bay Area deposits, such as calling the first soft marine clay the Young Bay Mud, then the underlying sands the Merritt or Colma Sands, and then any clays below that are by definition the Old Bay Clay. Others will denote any overconsolidated clay along the Bay margins the Old Bay Clay.

While no name will ever be perfect, this study chooses to call the deposit the Old Bay Clay due to its use in local engineering practice. It is a commonly used name by both engineers and geologists in the Bay Area to describe a stiff Pleistocene estuarine or marine clay. The Yerba Buena formation is also a good and appropriate name for the deposit. This name correctly includes interlayers that may have been deposited within the Sangamon, but are not clays. However, the name Yerba Buena formation is most useful in a geologic sense and when speaking with geologists. When used in a geotechnical sense, Old Bay Clay tends to be restricted to only the clay members of the deposit. Within the geotechnical engineering and engineering geology practice in the Bay Area, Old Bay Clay is already a known and established unit, so the name is useful as long as a soil is labeled correctly.

Another very important consideration is that there are likely many “Old Bay Clays” around the Bay Area. In a geologic sense, the Old Bay Clay is a Pleistocene estuarine to marine clay deposited during the Sangamon interglacial period. Because of the complex topography of the Bay Area, local conditions matter and stress history may be place-dependent. So while estuarine and marine clays were deposited in many part of the Bay Area, they may not all have the same stratigraphy, stress history, or engineering properties.

Some of the desire to identify the Old Bay Clay in geotechnical practice may be to identify the unit as a geotechnical material with prescriptive properties. It may be reassuring to identify the unit at a new project site, usually through borings, and assume similar properties as at other locations. However, by definition, the Old Bay Clay is not a geotechnical material, but rather a geological formation that describes similar materials deposited under similar conditions during the same geologic stage. Identifying Old Bay Clay is important for classification, but it can lead to a false sense of surety regarding its properties. In most cases, site-specific knowledge is paramount and published knowledge of Old Bay Clay should be used for reference or as a starting place.

2.4 Field Sampling

As discussed in Chapter 1, detailed subsurface exploration was previously performed to develop the Geotechnical Data Reports (GDR) for the TTC project. This study involved additional field instrumentation and sampling to supplement the findings in the GDR for use in the research project. The additional instruments and sampling were intended to be used for research and were not intended to be used to provide feedback for the construction activities. Samples were taken during excavation of instruments, with depths targeted for testing based on the findings of the GDR, including stratigraphy and material properties as well as where additional information was desired. Sample locations are presented on Figure 2.1 and cross sections with all the sample

locations are plotted in Figure 2.3, Figure 2.4, and Figure 2.5. A full list of collected samples are included in Table A-1 in Appendix A.

The locations without the “BH” designation were the locations drilled for this research project. These borings were drilled using mud rotary drilling techniques. The research samples were retrieved from July 2011 through March 2012. The prefix on the boring name describes the instrument installed at that location: “DSM” for deep settlement marker, “EX” for extensometer, “I” for inclinometer, and “P” for piezometer. Because the samples were taken from borings drilled for instruments, the borings were straight drilled to sample depths. Subsurface stratigraphy was confirmed by logging cuttings and noting material transitions, which were consistent with the subsurface findings from the GDRs. As a result, samples collected were targeted to be “representative” of the subsurface units, which included the soft clay deposits in Young Bay Mud, non-desiccated Old Bay Clay units, and clay layers within the Alameda formation.

The samples with the “BH” designation were obtained in June 2013 as a part of concurrent site exploration. As shown on Figure 2.1, these samples were taken at a site between Mission and Minna Streets and Fremont and First Streets, adjacent to the TTC site. These samples were collected during subsurface exploration for an adjacent project and were donated to the research project instead of being disposed after that project testing was complete. These samples are situated within the greater area characterized in the GDR report, so stratigraphy and material properties of the collected samples were consistent with earlier subsurface models.

As noted in Table A-1, there were several sampler types and sample tubes used to collect project samples. The majority of the samples collected for the research project were obtained with custom epoxy-coated steel Shelby tubes. In the deep, stiff clays of the OBC and Alameda fm., the samples were obtained using an Osterberg fixed piston sampler with the custom epoxy-coated tubes (Figure 2.6). The custom Shelby tubes were 3-inches in diameter, nominally 36-inches in length, and had a wall thickness of 0.065-inch. The Shelby tubes were modified to have no turned edge, with an inside clearance ratio of zero, as defined in ASTM Standard D1587, 2015. The ends of the tubes were filed to make a very sharp cutting edge in order to further reduce sample disturbance. The area ratio, defined by Hvorselv (1949), is,

$$C_a = \frac{100 \cdot (OD^2 - ID^2)}{ID^2}$$

Where C_a is area ratio, OD is the outside diameter, and ID is the inside diameter. The tubes used in this study had an area ratio of 9.26%. The epoxy coating was approximately 0.01 mm thick. Three tubes, from I-9, were collected in zinc-coated tubes in an early test-run of the sampling techniques. These tubes tended to have a welded seam that reacted to the clay specimens, causing the specimens to tear during extrusion (Figure 2.7), so the epoxy-coated tubes were used for the rest of the research project.

The epoxy-coated tubes were found to produce good-quality specimens for testing. The epoxy coating was non-reactive with the clays, so extrusion was smooth with little tearing or shearing of the samples (Figure 2.7). This meant that most of the consolidation and shear testing could be performed without much trimming or handling. Additionally, because the epoxy coating did not

rust, the samples could be kept in a wet room without oxidizing or reacting to the clays. So specimens were kept moisture-conditioned over the several years-long testing period. More discussion of sample quality is detailed in 4.7.

The “BH” samples also included custom epoxy-coated Shelby tubes, mainly in deep Alameda fm. samples. Traditional steel Shelby tubes were used to collect samples in the Young Bay Mud and the Old Bay Clay at that site. These sample tubes had also been modified to remove a turned edge and have no clearance ratio. Some “BH” samples were retrieved in “Modified California” (MC) samplers. These samples, especially in cohesive materials, are considered to be disturbed and were not used for consolidation or strength testing. The MC samples were only used for soil classification, which included stratigraphic logging, index testing, and microfossil studies.

After samples were retrieved to the ground surface, excess water and drilling fluids were removed, samples were labelled, and tubes were sealed with plastic caps and electrical tape. In order to minimize disturbance, samples were gently transported in an upright position as quickly as possible to the UC Berkeley Geotechnical laboratory because there was no on-site moisture-conditioned storage. Most often these samples were transported in a vehicle, but several samples were carried onto Bay Area Rapid Transit (BART) directly from the site to UC Berkeley. Once at the UC Berkeley Geotechnical Laboratory, samples were placed upright into a temperature- and moisture-controlled soil storage room.

As shown on Table A-1, the bulk of sampling was concentrated in the OBC and Alameda fm. clay layers. Thirty-seven samples were taken in the OBC, with 33 of those samples being Shelby tube samples. Twenty-eight samples were taken in the Alameda fm., with 30 being Shelby tube samples. Seventeen samples were collected of YBM, including one sample in “Upper Bay Mud,” three samples in “Lower Bay Mud,” and the remaining samples in Young Bay Mud west of the 1852 shoreline. The “Upper Bay Mud” and “Lower Bay Mud” samples were collected outboard of the 1852 shoreline where there is a sand layer between two thick units of Holocene marine clay, as described in Section 2.7.2. Samples were targeted to cover the site spatially, especially over the length of the project alignment, and at various depths within the OBC.

Boring logs from these project borings were not made by the field engineer collecting the samples because they were straight drilled to targeted depths based on GDR subsurface information. Thus, these were not regular samples taken for logging like in traditional geotechnical borings. Because of the density of the subsurface explorations in this area and the proximity to previously logged borings, stratigraphic information was projected from GDR data.

2.5 Determination of Field Stress

For laboratory testing, it was important to understand in-situ effective stresses. Because of the extensive subsurface exploration and laboratory testing in the GDR, it was possible to compile per-boring estimates of subsurface effective stresses based on the stratigraphy at each exploration location and unit weight of the various subsurface materials. While there was a range of unit weights, assumed values were generally median values of in-situ effective stress, while evaluating potential high and low values, which did not tend to be significant once evaluated. Transitory ground water conditions were not considered when estimating field stresses. So any estimates of

soil conditions are assumed to be “pre-construction,” before any further loading, unloading, or dewatering due to the TTC or adjacent project construction. Estimates of field stress are included in Appendix A.

2.6 Composition and Index Properties

Descriptions of the soil units underlying the project site are given in Section 2.7.2, which include visual descriptions and density estimates from blowcounts and sampling in clay horizons. All tested specimens routinely had unit weight (ASTM Standard D7263, 2018), moisture content (ASTM Standard D2216, 1998) tested, and initial void ratio measured. In addition, Atterberg limits (ASTM Standard D4318, 2017), sieve and hydrometer testing for grain size (ASTM Standard D6913/D6913M and D7928, 2017), and specific gravity measurements (ASTM Standard D854, 2014) were performed as supplemental testing on some specimens. Because of the large volume of index testing performed for the GDR, these additional index tests were to verify that the tested materials were consistent with what was expected from earlier phases of testing. The index testing performed for this research project was strongly correlative with values observed from the GDR, which reinforced the assumptions made from prior testing about the subsurface materials tested in this research project.

Total unit weight and moisture content are plotted in Figure 2.8 and initial void ratio in Figure 2.9 for tested samples from the Young Bay Mud, Old Bay Clay and Alameda fm. The Young Bay samples testing in this project were consistent with GDR data. Importantly, samples from West Bay Mud differed from samples from Upper and Lower Bay Mud as observed in tested samples from the GDR and this difference be discussed throughout this testing program. The West Bay Mud samples tended to have lower water contents that were below the liquid limit as compared with the Upper and Lower Bay Mud that had higher water contents that were above the liquid limit. The total unit weight of all the Young Bay Mud units tended to be similar. From this project testing data, the Young Bay Mud sample came from the West Bay Mud and had a moisture content from 66 to 70% and a total unit weight from 97 to 99 lbs/ft³. Worth discussing is a sample from 28 ft bgs that was tested in the research project. This sample received a field classification of Upper Bay Mud, from the area east of the 1852 shoreline. However, the moisture content (30%), total unit weight (116 lbs/ft³), and compression parameters were inconsistent with properties of Young Bay Mud and it was likely misidentified. The soil may have been within the “sandy clay” unit present in the stratigraphy at that location as discussed in Section 2.7.2 because the properties are consistent with testing data from the sandy clay unit within the GDR. However, because the sandy clay was not a focus of this study, this sample is not included in further testing summaries or descriptions in this work.

The Old Bay Clay total unit weight varied from 105 to 117 lbs/ft³ with a mean of 112 lbs/ft³, the moisture content varied from 37 to 54 % with a mean of 43 %, and the initial void ratio varied from 1.015 to 1.513 with a mean value of 1.172. The range of values for OBC was much narrower than from the GDR, but with very similar mean values, likely because of the quality of the samples tested and that they may have skewed toward the most homogenous fat clay samples. The tested samples within the Alameda, which were all from clay layers, have total unit weights that varied from 110 to 120 lbs/ft³ with a mean of 116 lbs/ft³, moisture content that varied from 33 to 44 %

with a mean of 40 %, and initial void ratio that varied from 0.873 to 1.233 with a mean of 1.041. In general, the research project data showed higher total unit weight, lower moisture content, and lower initial void ratio in the Alameda clays compared with the Old Bay Clay. This is consistent with other testing observations that would suggest that the Alameda is a more aged version of a similar material as the Old Bay Clay. Conversely, the GDR data has a very wide range of values for total unit weight and moisture content of the Alameda, likely because it includes the many heterogenous layers within the Alameda. There also does not appear to be as much difference between the Old Bay Clay and the Alameda clays in the GDR, possibly due to the scatter.

Atterberg limit testing (Figure 2.10) and sieve with hydrometer testing was performed on several samples. With the exception of the one sand sieve and hydrometer test, there were very similar results across the tested Young Bay Mud, Old Bay Clay, and Alameda samples tested. All tested samples were CH material with Liquid Limit, LL, ranging from 60 to 68 and Plasticity Index, PI, ranging from 37 to 44. All had between 90 to 100% passing the Number 200 Sieve. The sieve and hydrometer test exception came from a sand lens that was found approximately 6 inches below the tested clay specimen from the same sample tube. That sand lens was as a poorly graded fine sand with silt (SP-SM). Similar to the above total unit weight and moisture content tests, the data from this research project has a much narrower range in values and is more consistent than the broader data in the GDR. This is likely due to selectively testing homogeneous samples, while the GDR tested a wider range of materials present in the subsurface.

Table 2.1 lists the results of specific gravity testing for the project materials. For calculated parameters using specific gravity, the Young Bay Mud specific gravity was used as tested or from a proximate tested specimen in the GDR. Because of the consistency in tested specific gravity in the Old Bay Clay and Alameda specimens, it was assumed to be 2.75 when there was not a specific gravity test performed on the same sample.

2.7 Subsurface Conditions

In the previous sections, the generalized Bay Area subsurface stratigraphy was explained. But even with a typical type section, local conditions matter. At the project site, a relatively complete stratigraphic column exists that is close to an idealized profile. However, it is still unique in its geometry and properties. The following sections describe the site subsurface stratigraphy and geologic properties gained from site exploration.

2.7.1 Project Site Description

As described in Chapter 1, the area of interest is the area immediately surrounding and beneath the Transbay Transit Center (TTC) site. As shown on Figure 1.1, the project area is roughly bounded by Minna Street to the northwest, Beale Street to the northeast, Natoma Street to the southeast, and Second Street to the southwest. Figure 2.1 shows the project site with the borings used in this study, as well as the Holocene shoreline and 1852 shoreline discussed in Section 2.1.2. Ground surface at the site varies in elevation from approximately 13 to 24 feet (NAVD88). The site is relatively flat-lying but has a gentle dipping grade towards the Bay to the northeast. At the time of this writing, the TTC has been completed. The entire site and surrounding areas are a densely urban

environment. The area is built with steel and concrete high-rises, historic brick structures, roadways and sidewalks, and utilities.

As discussed in Section 2.1.2, the site has been in use since the founding of the settlement of Yerba Buena. Site use is generally well-known and contributes to the understanding of the subsurface because the upper 10 to 15 feet of the surrounding area is historic and artificial fill. Especially important is the 1852 historic shoreline (Figure 2.1) that characterizes the land that is outboard of the 19th century known shoreline to delineates the extent of infilling and land creation. More detailed site history is contained in the GDR. Of note also is the “Holocene shoreline” of Meyer, which represents a possible higher stand of water during the Holocene.

Groundwater levels at the site have been measured in borings and CPT soundings and they are generally even with sea level (0 ft NAVD88). However, there may be temporal variations in groundwater fluctuations due to the various active construction projects in the vicinity that involve dewatering.

2.7.2 Site Subsurface Conditions

Due to extensive investigation for both the TTC project, which was then supplemented with the additional explorations for this study, the GOALI project, a considerable amount is known about the geology at the project site. To some extent, the TTC site reflects the “layer cake” geology present at many locations around the bay. However, like any other site, local geology matters and there are some unique features. One significant feature is the 1852 shoreline, because some of the deposits and their properties are different from the east side to the west side of the site.

To summarize site subsurface conditions, four cross sections have been created and are plotted in Figure 2.3, Figure 2.4, and Figure 2.5 based on the data compiled and collected for this project. In Figure 2.3 and Figure 2.4, two sections are plotted that extend longitudinally across the site, one along Minna Street and one along Natoma Street, and in Figure 2.5, two sections are plotted that transect the site, one along First Street and one between Fremont and Beale Street. The longitudinal sections reach across the entire site length and help to understand the stratigraphy of the site between the portions that were onshore at 1852 and the portions that were offshore at 1852. The two transecting sections are perpendicular to the long sections. The First Street section is meant to generalize the perpendicular profile that was onshore at 1852 and the section between Fremont and Beale Street generalizes that profile that was offshore at 1852.

At the surface, as discussed in Section 2.1.2, are mapped deposits of fill. These deposits include historical fill, materials that have been removed and graded from their original deposits, and artificial fill placed as engineered fill. These deposits vary in thickness from approximately 11 to 33 feet at the site. The materials themselves are incredibly mixed, everything from historical building materials and artifacts, to dune sand and Young Bay Mud that has been excavated and placed as fill.

As shown on Figure 2.3, Figure 2.4, and Figure 2.5, there are a number of units underlying the Fill that are considered to be Holocene and late Pleistocene as consistent with the Wisconsin glacial stage through the current interglacial period, as discussed in Section 2.1.2. These units interfinger and are sometimes difficult to distinguish from the overlying fill because site grading has taken

place during historic time that involved the native soils. The non-fill upper materials have been subdivided into several layers: dune sand, sandy clay, marine sand, Upper Bay Mud, Lower Bay Mud, and West Bay Mud. A simplistic way of understanding the progression of sequences is that there is an onshore sequence west of the 1852 shoreline and an offshore sequence east of the 1852 shoreline. If only the ends of the longitudinal sections of Figure 2.3 and Figure 2.4 are isolated, two clear stratigraphic columns can be observed.

The West end of the project site has a somewhat typical Bay Area subsurface profile. Underneath the fill is a layer of dune sand that is a remnant of the more extensive dunes that were present at the site prior to site grading in the mid-19th Century. In-place upper dune sand material can be very difficult to distinguish from fill because historic site grading often used native materials loosely placed as fill. Beneath the dune sand is Young Bay Mud, which for this project is called the West Bay Mud in order to distinguish it from similar materials in the Eastern portion of the site. The West Bay Mud is a Bluish Gray fat clay, which corresponds to a OH to CH material (Figure 2.12). The West Bay Mud tends to be stiff to very stiff, with higher tip resistance from CPT than similar materials to the east. The Young Bay Mud contains occasional shell beds (Figure 2.12). The West Bay Mud lies inland of the 1852 shoreline, as discussed previously. As this material is an estuarine clay, its stratigraphic placement suggests a higher shoreline sometime during the Holocene (Meyer, 2015). This higher shoreline is plotted on Figure 2.1. However, it is noted that Young Bay Mud was encountered in some borings that were drilled outside the plotted line. As with the 1852 Shoreline, the extent and stratigraphy of subsurface materials is more complex than a single line. As with any natural system, especially one as dynamic as an estuarine environment, there is variation in the extent of materials due to either erosion or deposition.

Beneath the Young Bay Mud units across the site is a unit called the marine sand due to its similarity to Young Bay Mud, identified by its Dark Bluish Gray color. The marine sand has varying amounts of clay, ranging from a poorly graded sand to a clayey sand, with occasional clay stringers similar to Young Bay Mud. The marine sand varies from medium dense to very dense, but is distinguishable from the Colma sand discussed below by its relatively lower densities from blow counts.

The sand at the west end of the site that underlies the Young Bay Mud and the Marine Sand is identified as a member of the Colma formation and is referred to as such in this study and for the GDR. The Colma sand, when encountered is very distinctive due to its color, which ranges from Reddish Yellow to Yellowish Brown (Figure 2.13) and is distinct from the majority of upper subsurface materials that tend to be shades of gray, and by its density as measured by blow counts, which can vary from very dense to hard. The Colma sand is generally a silty fine sand with minor amounts of clay, which ranges in classification between SP, SM, and SC. As observed in Figure 2.3 and Figure 2.4, the Colma Sand is thickest in the Minna Street section and begins to pinch out or interfinger with other units near Fremont Street, which is roughly approximate to the 1852 Shoreline. In Figure 2.5, the Colma is still identifiable in the First Street section but has been eroded or pinches out in the middle portion of the Fremont and Beale Street Section. Again, the transition and interfingering of Holocene to late Pleistocene units is apparent from this lateral change of the Colma sand, Marine sand, and Young Bay Mud units.

The upper Holocene to late Pleistocene materials on the east end of the site are somewhat different than the west end and from the typical Bay Area profile (Figure 2.3 and Figure 2.4). Beneath the fills is a layer of Young Bay Mud, named the Upper Bay Mud to differentiate from similar materials. It is also a Dark Bluish Gray fat clay, but tends to be the less stiff Holocene clay on site, generally ranging from medium stiff to stiff with increasing stiffness with depth (Figure 2.12). Beneath this unit is a layer of marine sand similar to that in the western portion of the site. But beneath this marine sand layer is another fat clay layer that resembles Young Bay Mud and is called the Lower Bay Mud. It is more stiff than the Upper Bay Mud, but not as stiff as the West Bay Mud. It is at maximum approximately 20 feet thick and pinches out near Fremont Street, approximately where the 1852 Shoreline is located. Beneath the Lower Bay Mud is another layer of marine sand similar to what was described previously.

The presence of interfingering Holocene and late Pleistocene units complicates the standard “layer cake” model of Bay Area stratigraphy. The Upper Bay Mud, marine sand, Lower Bay mud, marine sand sequence in the eastern portion may suggest a possible transgressive-regressive-transgressive cycle due to sea level fluctuations or temporary still or high stands. The Young Bay Mud onshore of the 1852 Shoreline as well as the work of Meyer (2015) suggests several higher shorelines during the Holocene. This implies that the Late Pleistocene to Holocene deposition of materials is more complicated than a single transgressive sequence. Another explanation could be that there were changing currents or materials inputs into the basin that caused erosion and deposition or reworking of materials. An example of this explanation in the central portion of the site is a unit labeled as sandy clay (Figure 2.3 and Figure 2.4), which sometimes is called Sandy Bay Mud due to its similarity to Young Bay Mud, but higher coarse fraction, lower moisture content, and greater total unit weight. A sample that likely came from this unit was tested as explained in Section 2.6. The central portion of the site is clearly a transition zone, as observing the contrast between Sections in Figure 2.5. Some of these deposits may reflect reworking of other deposits or different material inputs at different times.

Beneath the dune sand in the western portion of the site and beneath the marine sand in the eastern portion of the site lies the Old Bay Clay, which is the main focus of this study. The unit is remarkably consistent across the project site, in contrast to the many interfingering layers that overlie the deposit. Across the site, the thickness of the deposit was generally 80 feet thick with some areas thinning to 65 feet thick. The top of the Old Bay Clay ranged in elevation from -65 to -85 ft (NAVD88). In Figure 2.11, the cross sections from Figure 2.3, Figure 2.4, and Figure 2.5, have been overlaid in order to compare the stratigraphy of Old Bay Clay, Alameda formation, and Franciscan bedrock contacts. While there are variations in places, the Old Bay Clay unit is very regular and resembles the “layer cake” stratigraphy of idealized cross sections of the Bay Area subsurface. In the GDR, the top surface and thickness of the Old Bay Clay was contoured based on the many explorations compiled in the GDR. The top surface of the Old Bay Clay dips gently to the north. The thickness of the unit tends to be at a maximum in the area between First and Fremont Streets and is less thick both to the west and the east ends of the site.

The Old Bay Clay is generally easy to identify in boreholes because there is a strong material contrast between the overlying sandy materials. The Old Bay Clay is a Dark Greenish Gray, stiff to hard, fat clay, which generally classifies as CH (Figure 2.14). At the upper contact in some places, the Old Bay Clay is a sandy clay or clay with sand and rarely a Dark Brown clay is

encountered. The upper several feet of the Old Bay Clay may be representative of a reworked material or a desiccated material exposed to erosion. These observations of an Old Bay Clay “crust” are consistent with the assumption that the upper surface is an erosional contact. Below this upper transition, the Old Bay Clay is remarkably consistent through the entire section as observed from blow counts, tip resistance from CPT, and velocity profiles from seismic studies. Even though the material was generally consistent, some scattered shell and organics horizons were encountered in places. This consistent profile of Old Bay Clay, both in geometry and material properties is a reason that the deposit is a good type section for study. As compared with other profiles of Old Bay Clay described from engineering projects in Section 2.2, the Old Bay Clay contains many fewer interbeds of coarse materials and appears to have consistent material properties with depth, excluding the upper crust materials.

Beneath the Old Bay Clay unit is the deposit that is being called the Alameda formation in this study based on correlations with prior studies documented in Section 2.2. The Alameda formation name is an extension of studies that defined the type section originating in Alameda, so the unit name is a kind of misnomer when used here. This unit has also been called the “OBC II” in early studies for the TTC project as well as in the GDR. The “OBC II” name was similar to the grouping of deposits by Treasher (1963). However, the “OBC II” name turned out to be a misnomer because of the presence of heterogeneous layers in the deposit. The name “Valley Deposits” was then used for reports that came after the GDR that covered the TTC construction, as well as for reports for some adjacent projects. The Valley Deposits name is a reference to the bedrock valley, described in Section 2.1.1, in which the unit is deposited. While in cross sections the Alameda appears similar to the Old Bay Clay because of its geometric consistency, the materials within the formation are extremely heterogeneous, as discussed further below. The top of the unit could also be contoured due to the density of subsurface explorations compiled in the GDR. Similar to the top of the Old Bay Clay, the top of the Alameda dips gently to the north. The elevation of the upper surface ranged from -130 to -155 ft NAVD88. Unlike the Old Bay Clay, the thickness was highly variable, likely because the unit drapes the bedrock and the underlying bedrock structure varies across the site. The thickness of the Alameda formation was from 10 to 80 feet.

The Alameda formation is generally easy to distinguish from the Old Bay Clay in boreholes because the Alameda is defined by a clear material change from the Dark Greenish Gray, stiff, fat clay that overlies it. Generally, the material change that defines the upper surface of the Alameda is a sand with silt to silty sand and, in some places, a sandy clay. The Alameda formation is a series of interlayered deposits, ranging from 5- to 20-foot thick layers, which do not have clear lateral relationships between layers. Because these layers are deep and were not a main focus of study, it may be possible to distinguish sublayers or possible relationships between layers with more detailed sampling. Especially because the deposit is very deep, frequent sampling for characterization can be difficult and time-consuming.

While the upper surface of the Alameda tends to be a sand or sandy clay, in several borings, stiff to very stiff Greenish Gray lean to fat clay layers were encountered that resembled the Old Bay Clay (Figure 2.15). Where possible, these clays were sampled in order to provide specimens for testing in order to compare with the Old Bay Clay. While these clays are similar to the Old Bay Clays, they tended to show more signs of oxidation, such as mottling or staining, and tended to range more from lean to fat clays when classified, corresponding to CL to CH materials. In some

layers there were significant minor amounts of sand as well as scattered gravels. In addition to these clay horizons, there were interlayers of Greenish Gray to Grayish Brown poorly-graded sand, sand with silt, silty sand, and clayey sand.

Within the Alameda formation and above the contact with bedrock, in several borings a layer of Greenish Gray clayey gravel with sand was encountered. The clasts within the deposit tended to be angular to subangular and reflect rock types that correlate with the Franciscan assemblage, including chert, sandstone, greenstone, and serpentinite. In several places, woody debris were encountered. This possible basal layer of the Alameda has been suggested to be a debris flow-type deposit. When the buttress was constructed, some of the clasts within this layer were cobble- to boulder-sized based on observations during excavation.

The bedrock underlying the site is the Franciscan formation. Based on bedrock contours, the rock appears to dip to the northwest and ranged in elevation from -150 to -220 ft NAVD88. The contours suggest that the site lies parallel to the southern limb of the bedrock channel identified by Schlocker (1974). While the bedrock all appears to dip to the northwest, there is an area of higher bedrock elevations between First and Second Streets. Thus, the longitudinal section along Natoma Street in Figure 2.4 shows a hill and valley topography of the bedrock surface, even though the entire surface is dipping generally to the northwest. In the overlain sections in Figure 2.11, the bedrock surface can also be observed to be dipping to the north.

The Franciscan bedrock underlying the site tended to be a *mélange* unit with irregular inclusions of hard sandstone and shale. In some places, greenstone and serpentinite was encountered (Figure 2.16). The *mélange* can be described as a Very Dark Gray, weak, completely weathered sandstone to shale. In many places, the Franciscan rock resembled a very hard clay with clasts of angular rock. This unit is likely a sheared member of the Franciscan assemblage. However, in some places there were inclusions of large blocks of less weathered and strong sandstone. No clear structural relationship between these blocks was identified, which suggests that this was a Block-in-Matrix Rocks (*bimrocks*) material that is observed in the Franciscan assemblage (Medley, 1994). While the project site area appears to plot within the Alcatraz terrane (Wakabayashi, 2004), this highly sheared rock is unlike the hard sandstones that are generally associated with that terrane. The bedrock underlying the site appears to be more consistent with the Hunter's Point Shear Zone rock assemblage (Wakabayashi, 2004).

2.7.3 Fossils at the TTC

To constrain geologic units with the fossil record is helpful for understanding the stratigraphic record. Many fossils have been encountered at the project site in the subsurface. During exploration and construction, fossils and other artifacts were encountered. As discussed, there is historical fill at the site, so during excavation, historic artifacts were encountered, and, in the deeper sediments, other fossils were also observed.

The Holocene Young Bay Mud contained several fossils, including a bed of *Macoma nasuta* shells (Allen, 2012a). This deposit was exposed during the excavation (Figure 2.12). These shells were encountered within the Young Bay Mud between Howard Street and Mission Street, and between Fremont Street and Beale Street about 25 to 30 feet below street level. Thus, they were likely in

the Upper Young Bay Mud deposit of the soils offshore of the 1852 shoreline. As identified by the paleontologist, the fossils have a geographic range “in the Eastern Pacific from Montague Island, Cooks Inlet, Alaska, south to Punta Rompiente, Baja California Sur, Mexico, from the intertidal zone to about 10 meters, usually on silt and (or) sand.” Additionally, it “ranges in age from Miocene to Holocene, although preservation and where it occurred argues for a latest Pleistocene to Holocene age.” This is consistent with what is known about the Young Bay Mud deposit, which helps to confirm its stratigraphic placement in time.

There were human remains encountered during excavation at the project site in 2014, as reported in contemporaneous news sources (Bay Area News Service, 2014; Nevius, 2014). According to the reported sources, the remains were found 60 feet below grade near Fremont Street. Based on observational data of construction progression, this reflects a depth of approximately -40 ft (NAVD88) and the corresponding deposit is likely the Lower Young Bay Mud. According to news sources, the skeleton was dated to 7,500 yr BP (Nevius, 2014). Further research on these remains has not been performed to the knowledge of the authors due to necessary permissions regarding human remains of Native persons of California. However, a preliminary age at 7,500 yr BP for materials at -40 ft is consistent with what is known and discussed regarding the Holocene deposits of the Bay Area and especially the Young Bay Mud (Meyer, 2015).

The most exciting find during construction of the TTC was a mammoth tooth (Figure 2.17). Based on contemporaneous news sources and contemporaneous documentation of the paleontologist of record (Allen, 2012b), the tooth was discovered during excavation of the buttress between Fremont and Beale Streets at the contact between Holocene to latest Pleistocene sands and Pleistocene clay, likely at the upper surface of the Old Bay Clay. The approximate depth at the time of excavation was 110 feet below street level, which corresponds to approximately -90 ft NAVD88. The deposit that the tooth was discovered within was described as “in dark-gray, silty mud to-clay” (Allen, 2012b). This depth and the stratigraphy described by the operator that discovered and identified the tooth suggests that it was found at the contact between overlying Holocene and latest Pleistocene deposits and the Old Bay Clay. The tooth was identified as *Mammuthus columbi* (Columbian Mammoth), the remains of which have been frequently identified throughout the Bay Area (Rodda & Baghai, 1993). The location of these remains may help to constrain the age of the upper erosional surface of the Old Bay Clay. At the time of publication of this project, this work had not yet been performed (J. Allen, personal communication, 2019).

Within the Old Bay Clay, a microfossil study was performed, which is discussed in Section 2.8. This study was motivated by age and facies correlation within the site Old Bay Clay with the Yerba Buena Mud of Sloan (1982). Samples of Young Bay Mud, Old Bay Clay, and Alameda recovered for this study were reviewed for microfossils.

During buttress construction, woody debris were discovered from deep deposits. The authors of this study were provided with a wood fragment recovered from 225 feet below the street level (approximately -210 ft NAVD88). The wood fragment was identified as *Sequoia sempervirens* (Coast Redwood), which unfortunately does not provide much of an age range due to the wide prevalence of the species in the Pleistocene (D. Erwin, personal communication, 2017). However, the common presence of woody debris found at depth in the named Alameda formation suggests a depositional environment for these materials. As discussed previously in this chapter, the bedrock

valley containing the project site had a defined drainage area. This drainage area is relatively compact and contains very steep bedrock grades. The presence of woody debris further supports the theory that these deep Alameda clayey gravel deposits are debris flow deposits in certain locations. Further age dating of the woody debris may be helpful, however, the fossils are likely pre-Sangamon, which makes Carbon-14 dating out of range.

2.8 Microfossil Study

As discussed in Section 2.2.2, Sloan performed a detailed study of microfossils within the Old Bay Clay, which she named the Yerba Buena mud (1982, 1992). Inspired by that work and with the assistance of Dr. Sloan, a small study of microfossils was performed within a set of project samples. Microfossils were present in some soil samples collected for this project and study of the assemblages of these microfossils can provide insight into the environment in which the soil was deposited. By noting the individual species of microfossils and in what combinations they are present, it can be inferred, for example, that the soil was deposited in a shallow and warm brackish environment or a deep marine setting. The motivation was to correlate the observed microfossils to any of the assemblages recognized by Sloan and, in particular, if any of the assemblages might correspond with her identified biofacies. In that way, the Old Bay Clay at the project site could be placed within the Bay depositional history.

In Sloan's earlier study and in this study, sand-sized microfossils were specifically observed due to the sorting methods described in Section 2.8.1, below. This is because the material studied is generally what is retained on the Number 120 sieve, which has a nominal opening of 0.0049 inches or 0.125 mm and is between very fine sand and silt sized particles. Many materials exist within estuarine and marine clays other than clastic particles and clay minerals at this small size. These include foraminifers (forams) shells, called tests, that are preserved in soils as the tests settle through the water column (Holbourn, Henderson, & MacLeod, 2013). Similarly, diatoms that produce silica *frustules* are preserved in soil (Smol & Soermer, 2010). In addition to forams and diatoms, sand-sized material other than mineral and rock clasts can be present in the samples. In the Old Bay Clay, these include shells and shell fragments, plant material including roots, stems, leaves, and seeds, Radiolaria, ostracods, and fish remains including scales and calcified cartilage (Sloan, 1982). Even the mineral and rock clasts can be helpful because they include clay agglomerates, mica, identifiable rock fragments, and glass shards.

2.8.1 Sample Preparation

The locations where samples for this study were selected are plotted on the site plan in Figure 2.18 and in the longitudinal cross sections in Figure 2.19. More detailed explanations of these cross sections are in Section 2.7.2. Once the samples were selected, they were prepared similarly to a sieve analysis. Between 40 and 100 g was partitioned from the sample, which in some cases the forams were visible due to their large size and white to translucent color. The specimens were soaked in distilled water for several days, then washed over No. 120 and 230 Sieves. The retained material from the different sieves was separately washed onto filter paper and left to dry. Afterwards, the material could be brushed into a sorting dish for use under a standard compound light microscope or stereomicroscope using 10X to 40X magnification. At that point, forams, diatoms, fish remains, shells, and seeds could be picked and sorted onto microscope slides for

identification and quantification. The three-dimensional shape of microfossils is very pronounced under the microscope and also sometimes necessary for identification (Figure 2.20). Different foram species may have similar features from some angles and may need to be turned to different surfaces to view the full microfossil. The portion of the sample from the 230 sieve was retained but not sorted for microfossils. This smaller fraction may also contain microfossils, which are often of interest to other researchers.

2.8.2 Observations

Compared to Sloan's study, this research study only observed a small number of samples and did not use quantitative techniques. The observations made were significant in that microfossils observed in Sloan's study were similarly observed in the samples from this research project. The samples used for the study came from various locations throughout the project site, but, due to the uniformity of the Old Bay Clay as discussed in Section 2.7.2, these locations were treated as a single profile with various depths represented by the different sample locations. This study focused primarily on the most identifiable microfossils within the samples, which ultimately were the same microfossils identified in Sloan's work. It should be noted that definitive identifications can oftentimes not be possible for young forams and for oxidized forams (Figure 2.20 and Figure 2.22).

Approximately 60% of samples that were prepared for microfossil identification contained microfossils. Of these, slightly less than half had an abundance of fresh, easy to identify forams, while the rest contained few, usually very oxidized forams. The specimens with the most microfossils and the best preserved forams came from samples at 99, 100, and 125 ft bgs, which corresponds with the upper and middle portions of the deposit. Samples from 110, and 135 feet contained few microfossils and/or oxidized forams. Figure 2.21 through Figure 2.23 includes SEM photos taken of microfossils from this study. All of the photos in the SEM images came from 99 feet except for the oxidized *E. excavatum* f. *selseyensis*, which came from 135 feet. Forams identified in the Old Bay Clay include *Ammonia beccarii* forma *tepida* (Figure 2.21 Top), *Elphidium excavatum* (forma *lidoensis*) (Figure 2.21 Bottom), *Elphidium excavatum* (forma *selseyensis*) (Figure 2.22), *Elphidiella hannai* (Figure 2.23), and *Elphidium gunteri* (not pictured). The *E. excavatum* in is an example of an oxidized foram present in some samples. The oxidation makes it difficult to distinguish the features that would help provide an identification, so some samples are identified as containing forams without clear identifications.

As discussed above, the observed microfossils were very similar to what was described by Sloan in her work. In particular, the majority of identified forams appeared to be within what Sloan called the *E. excavatum* association, where *E. excavatum* and *E. beccarii* make up >50% of the population with moderate frequencies of *E. hannai* and *E. gunteri*, as well as *Buccella frigida*, *Buliminella elegantissima*, and *Elphidium magellanicum*. Sloan places this assemblage in the lower part of the full thickness of Yerba Buena mud and associated it with a "marsh, intertidal, and shallow-subtidal environment," (Sloan, 1982), which is very similar to portions of the present-day San Francisco Bay. The units with low or absent forams in Sloan's study were the uppermost and lowermost samples. The same was observed in this study, with the uppermost sample without identified forams and the four deepest samples, two at 135 ft bgs, one at 165 ft bgs, and one at 170 ft bgs, having few oxidized forams or no forams. Sloan suggests that this could be due to dissolution of tests either post-deposition or after sampling, or that the depositional environment was absent of

large amounts of forams (Sloan, 1982). The depositional environment of these deepest samples is suggested as shallow bay margins with periodic low PH conditions that can dissolve the tests (Sloan, 1982).

Within the Old Bay Clay, the majority of samples contained diatoms, except for the uppermost sample at 96 ft bgs and the two lowermost samples at 165 and 170 ft bgs. Diatoms identified in the samples included *Campylodiscus* (Figure 2.20), *Arachnoidiscus* (Figure 2.24 Top), and *Isthmia nervosa* (Figure 2.24 Bottom). By far *Campylodiscus* was the most common diatom and easy to identify with its classic “potato chip” shape. Similarly, Sloan found *Campylodiscus* in 78% of diatom-bearing samples, with *I. nervosa* in 48 % and *Arachnoidiscus* in 48% of diatom-bearing samples (Sloan, 1982). Sloan defined four diatom associations, of which the observed specimens in these project samples appear to belong to the *Campylodiscus* association that is dominantly *Campylodiscus* with other taxa present. This association is present in “intertidal to shallow-subtidal areas of the Bay today” (Sloan, 1982).

For both the foram and the diatom associations, the Old Bay Clay at the project site appears consistent with Biofacies A and B as described in Section 2.2.2. These biofacies are the two lowermost and represent a transition from “marsh, intertidal, and shallow-subtidal environments at brackish to normal salinities” to a deeper bay similar to the current San Francisco Bay (Sloan, 1982). These lower two biofacies are in fact the only preserved biofacies remaining in the western portion of the studied alignment as defined by Sloan. She suggests that later biofacies were likely eroded. The project site is correlative with this western portion of the alignment, even though the proposed Southern Crossing is several miles to the south of the project site.

A sample of Upper Young Bay Mud and Alameda was also prepared for microfossil evaluation, but microfossils were not observed in either. The absence of material is difficult to assess, but as suggested above, microfossils may not be present or the tests dissolved in shallow bay margin environments. Abundant fibrous plant material was observed in the Alameda specimen. Sloan suggested that abundant plant material may represent marsh deposits (1982).

Further work with many more samples, using quantitative methods, and more expertise identifying the microfossils could provide much more information. At the time of this writing, portions of almost every project sample are preserved in moisture- and temperature-controlled storage, so such future work is possible.

The use of microfossils within soil samples may provide a type of signature for stratum or layers that have notable properties. Greater understanding of these microfossil relationships may also help to characterize Old Bay Clay stratum between larger areas of the Bay Area, such as in the South Bay where fewer studies have been performed.

Another possibility for microfossil study is to use isotope age dating. Such work is more common in climate studies and has been used for understanding the development of the Holocene San Francisco Bay (Ingram, Ingle, & Conrad, 1996; Schweikhardt, Sloan, & Ingram, 2010).

2.9 Conclusions

The Old Bay Clay was characterized by contextualizing the deposit within the San Francisco Bay Area geologic setting, prior engineering geologic characterization, and with knowledge gained from subsurface exploration and sampling. Most of what is known about the deposit comes from previous engineering and geologic subsurface studies. While the literature documenting the subsurface extends to the late 19th to early 20th Century, subsurface knowledge was somewhat limited. In the mid-20th century, several large bridge and cross-Bay studies performed and there was a large amount of work published using the samples. However, these studies generally came from the same alignments, so the understanding of the subsurface is constrained around several known transects. More work regarding the deeper parts of the subsurface profile was performed after the 1989 Loma Prieta Earthquake, mostly in the East Bay. A current phase of study, including this work, is underway due to current construction trends, which tend to involve projects with more extensive development, deeper loads, and more stringent requirements for performance based on codes or the presence of adjacent infrastructure. Several studies have been published about these projects, including in Mission Bay in San Francisco near this study site, but the subsurface appears to differ from the Bridge alignment studies as well as at this study site.

The previous sections show that the Old Bay Clay is a notable and defined unit within the Bay Area subsurface profile. The Old Bay Clay is a Dark Greenish Gray, stiff to hard, fat clay that is approximately 80 feet thick at the project site and shows characteristic consistency with depth. Based on microfossil studies, the Old Bay Clay is a single transgression deposited during the last interglacial from a previous Bay that was deeper than the current San Francisco Bay. A microfossil study was performed on Old Bay Clay samples from the project site that identified foraminifers and diatoms that suggest the project site materials came from the lower units deposited in the Sangamon San Francisco Bay. The upper surface of the Old Bay Clay is an erosional contact, which suggests that the original profile of Old Bay Clay was thicker.

Above the Old Bay Clay are Historic to late Pleistocene deposits that include fill, dune sand, Young Bay Mud, marine sands, and Colma sand. These deposits have a more complicated depositional history than the Old Bay Clay that represent the change in the San Francisco Bay from the previous glacial state, the Wisconsin, to the present interglacial period. During this time, sea level has risen approximately 300 feet and the deposition of material has transitioned from alluvial and eolian to estuarine and marine at the project site. Beneath the Old Bay Clay is the Alameda formation. This formation may represent various cycles of previous glacial and interglacial periods. Within the Alameda formation are some layers of clay that resemble the Old Bay Clay. These clay layers have been tested in order to understand similarities between the two units. From index testing, the Alameda clays tended to vary slightly to moderately from Old Bay Clay. Unit weight was greater, moisture content was less, though Alameda clays tended to have similarly high fines content and moderate to high plasticity as the Old Bay Clay.

While the Old Bay Clay is an excellent profile to study at the project site because of its consistent profile, from other studies it is clear that not all Old Bay Clay units have the same or similar properties. Other sites have different thickness of the unit, interlayers of coarse materials, and differing index properties. As has been noted previously, there may be a difference between the

West and East sides of San Francisco Bay due to fault activities, subsidence, and/or erosion. Understanding the Bay Area subsurface profile is helpful but does not replace site-specific understanding because of the variability of materials, even over very short distances. It is possible that work like the microfossil or isotope studies could provide insight into the different subunits with larger units like the Old Bay Clay. Additionally, further studies could provide additional insight especially if they are performed outside of the several well-known research areas in the Bay Area.

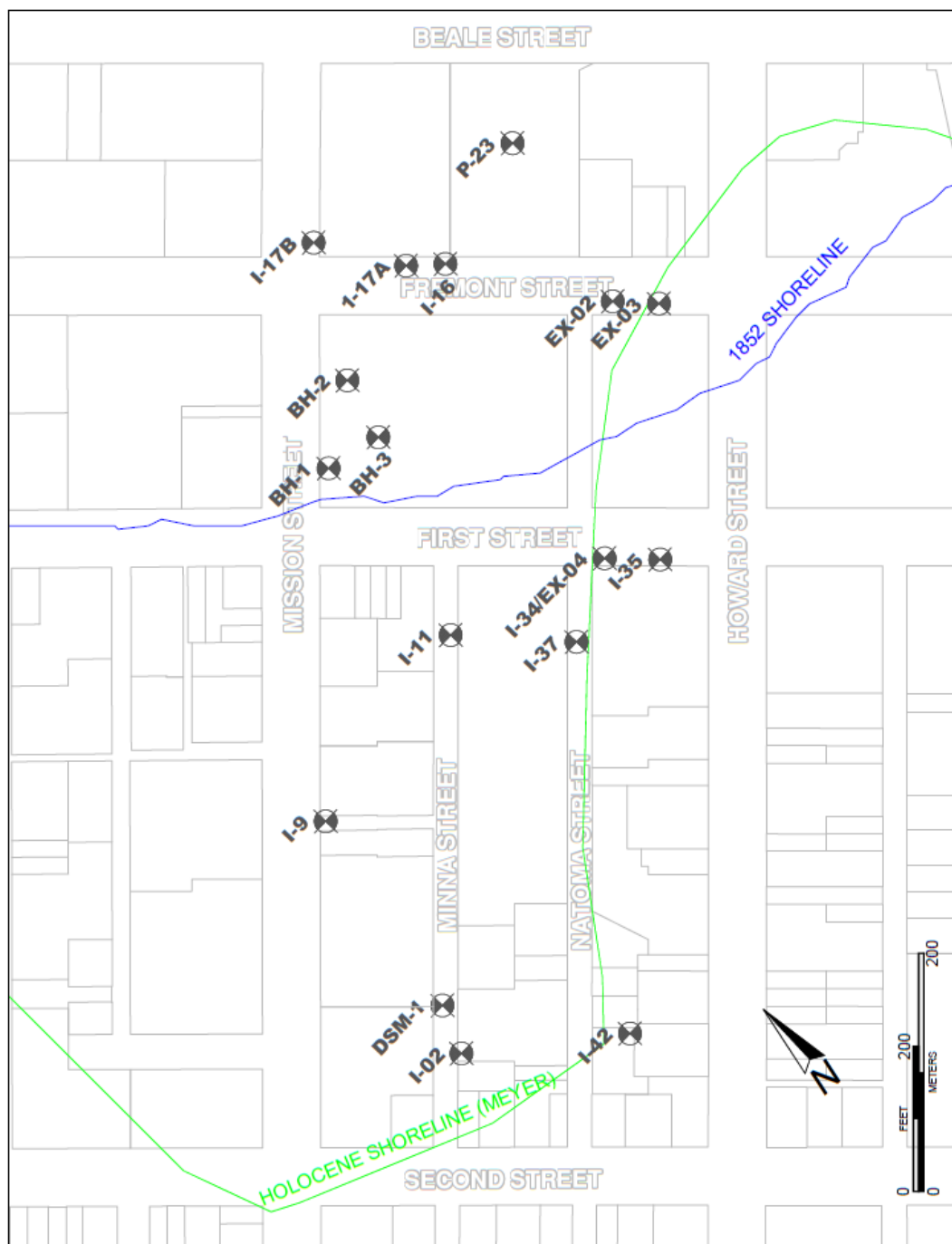


Figure 2.1. Site plan showing exploration locations used in this study. Holocene shoreline is plotted in green, and 1852 shoreline is plotted in blue



Figure 2.2 Project Site showing locations of proposed Parallel and Southern Crossings.
 Not to scale (Google Earth, 2018)

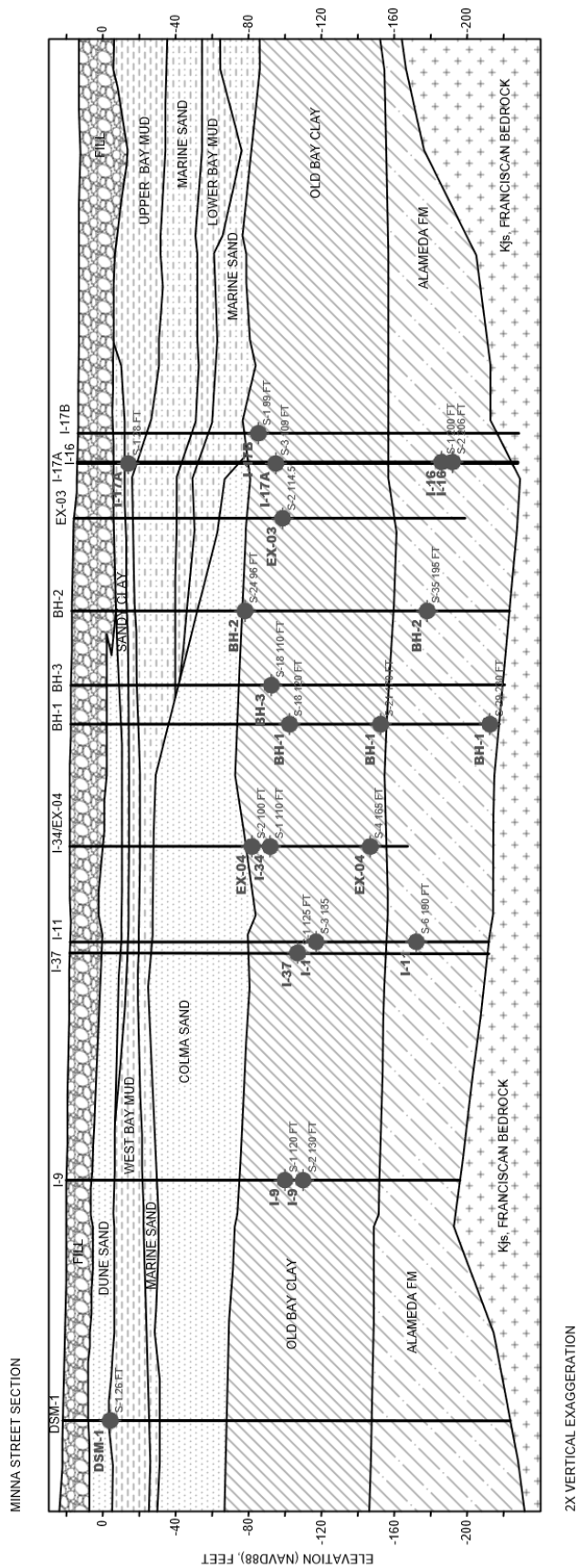


Figure 2.3. Cross section along Minna street.

The left side of the section corresponds to the west-southwest direction and the right side corresponds to east-northeast direction. Sample locations are noted. 2-times vertical exaggeration and not to scale.

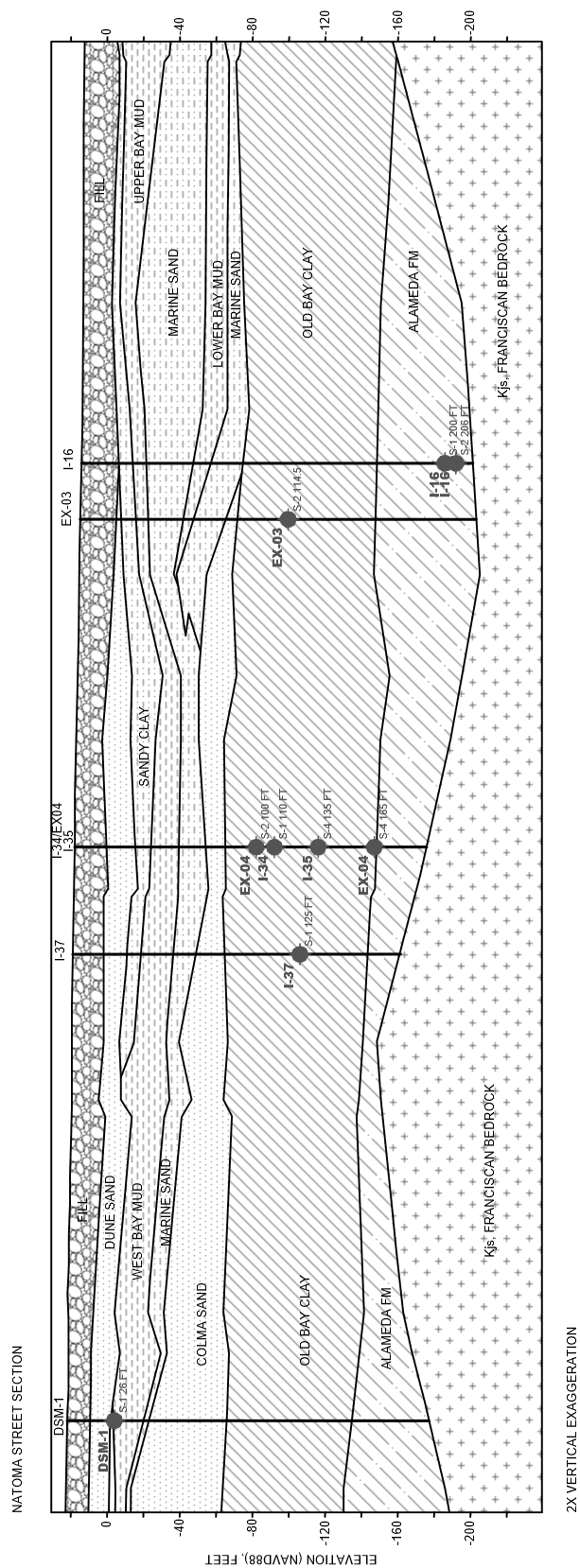


Figure 2.4. Cross section along Natoma street.

The left side of the section corresponds to the west-southwest direction and the right side corresponds to east-northeast direction. Sample locations are noted. 2-times vertical exaggeration and not to scale.

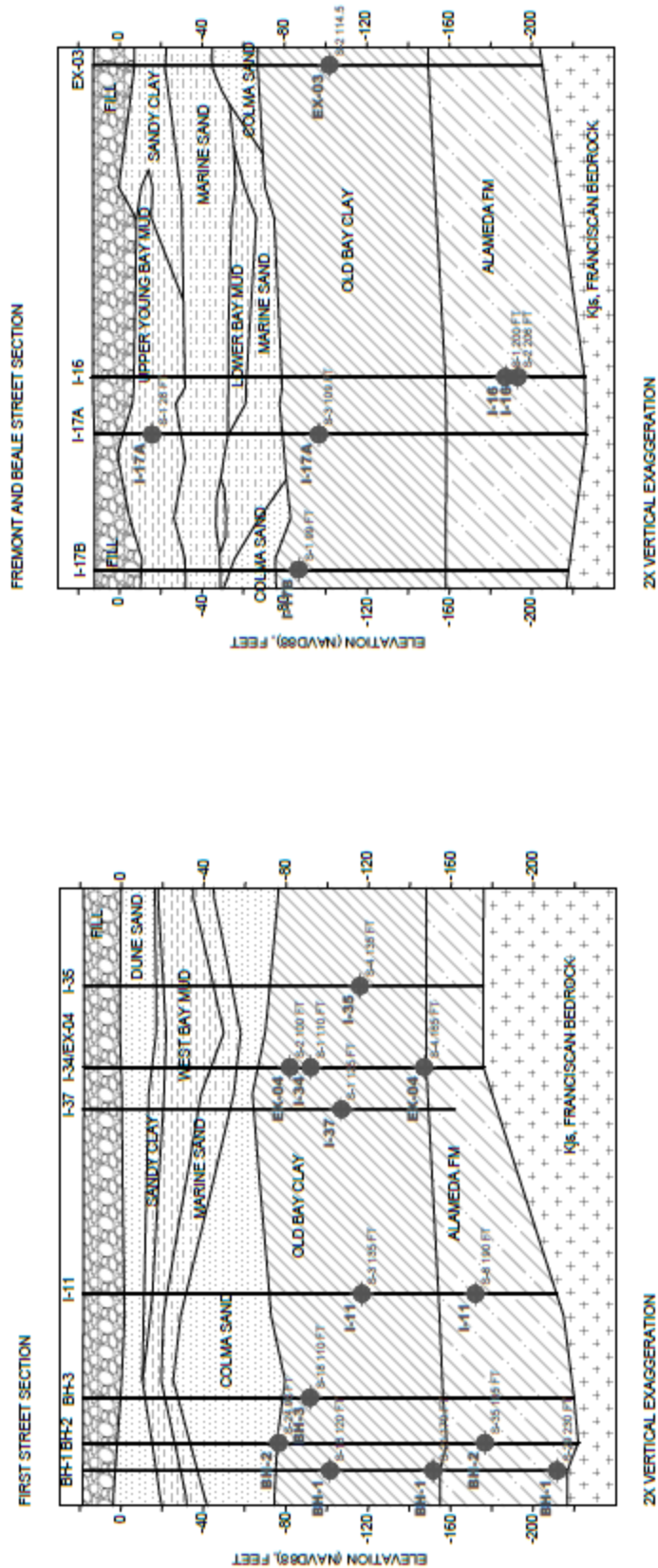


Figure 2.5. Cross sections along First Street and between Fremont and Beale Street. The left side of the sections corresponds to the west-northwest direction and the right side corresponds to east-southeast direction. Sample locations are noted. 2-times vertical exaggeration and not to scale



Figure 2.6. Epoxy-coated sample tube retrieved using Osterberg hydraulic piston sampler.

Left: The sample tube is slid inside the Osterberg sampler, then the entire device is lowered to the sample depth. The tube is forced from the sampler into the soil using water pressure from the drill rig. The sampler is rotated in order to break the bond with the in-situ soil and then the device is returned to the surface. In this photograph, the sample is within the Epoxy-coated tube and is being removed from the Osterberg device for handling and transport to the soils laboratory

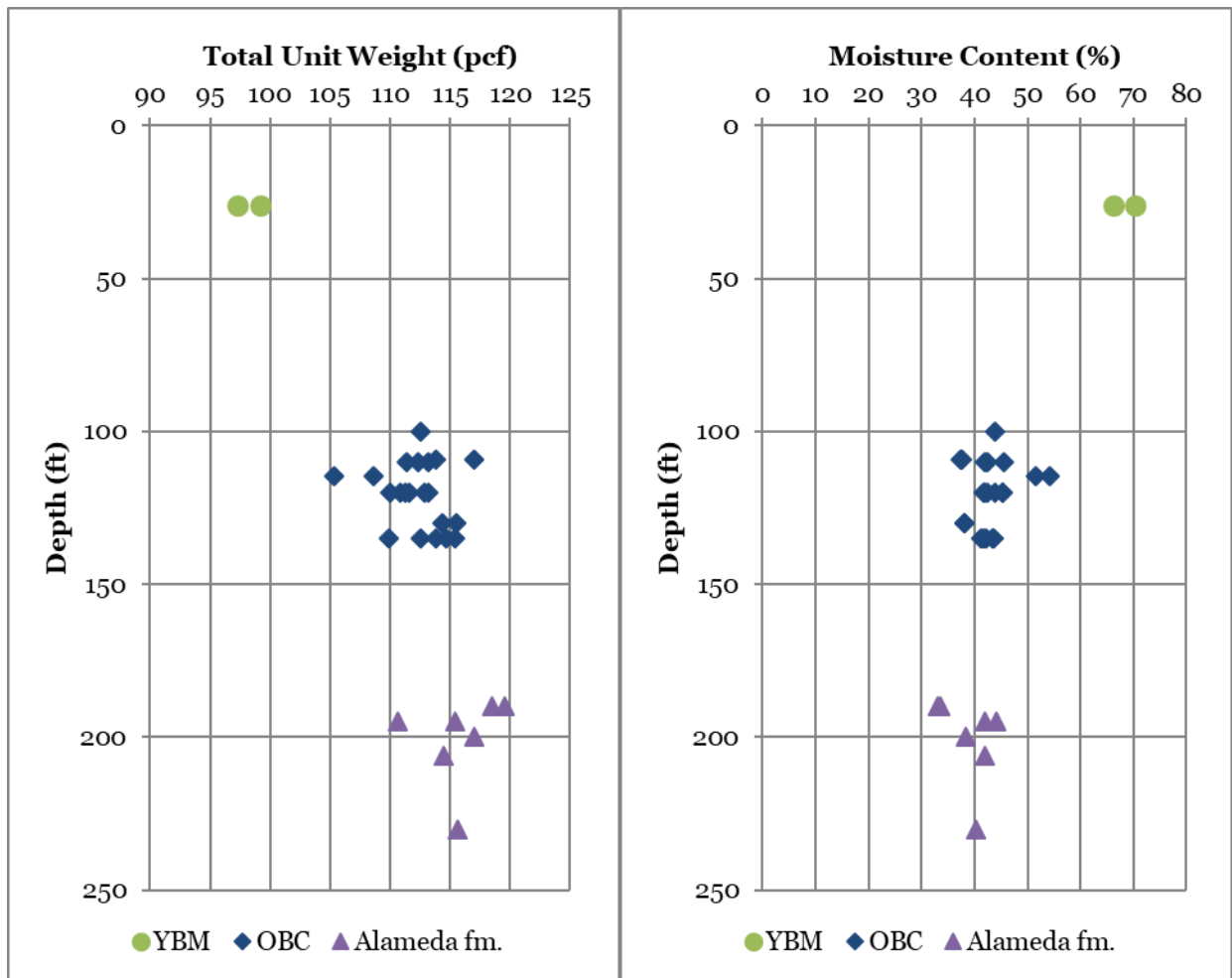
Right: The tube has been cleaned and plastic caps placed on either end. These caps will have been wrapped with tape for moisture retention. The sample tube was only briefly placed horizontal for handling. It was transported and stored upright

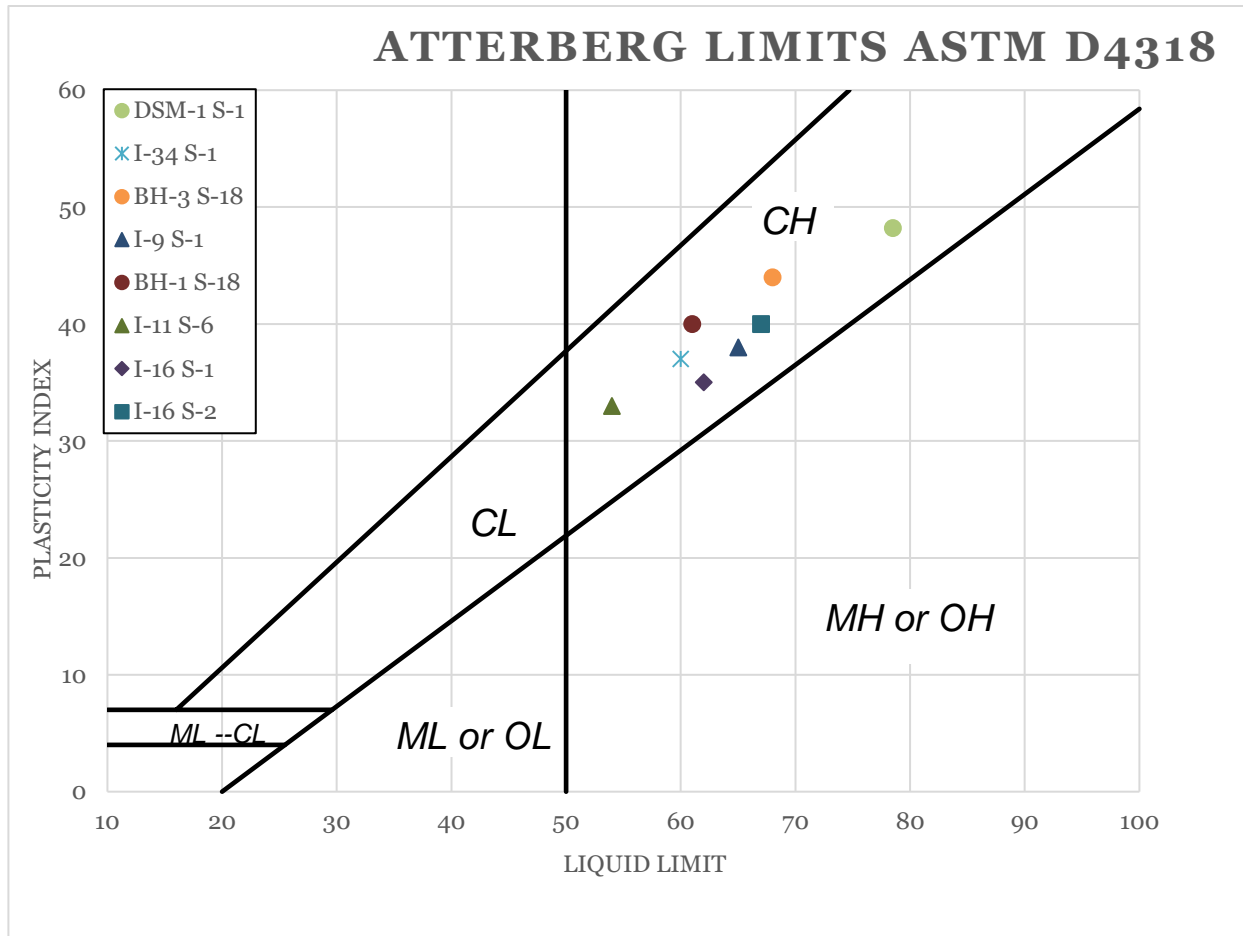


Figure 2.7. Specimen extruded using tube jack and showing tube weld.

Left: Specimen extruded from cut portion of epoxy-coated Shelby tube using tube jack. The sample tube had been cut using a pipe cutter with the tube reinforced by stiffening rings. The tube is deburred prior to extrusion in order to reduce sample disturbance

Right: Specimen in tube prior to extrusion showing slight gap along the weld that occurred in zinc-coated steel tubes





Sample Tube	Depth	Wc	LL	PL	PI	USCS
DSM-1 S-1	26.0	70%	78.5	30	48	CH
I-34 S-1	110.0	46%	60	23	37	CH
BH-3 S-18	110.0	42%	68	24	44	CH
I-9 S-1	120.0	42%	65	27	38	CH
BH-1 S-18	120.0	43%	61	21	40	CH
I-11 S-6	190.0	33%	54	21	33	CH
I-16 S-1	200.0	38%	62	27	35	CH
I-16 S-2	206.0	42%	67	27	40	CH

Figure 2.10. Results of Atterberg Limits testing (ASTM Standard D4318)

Table 2.1. Specific Gravity testing (ASTM D854).

Boring and sample	Depth (ft)	G _s
I-9 S-1	120	2.76
I-35 S-4	135	2.75
I-16 S-1	200	2.76
I-16 S-1	206	2.76

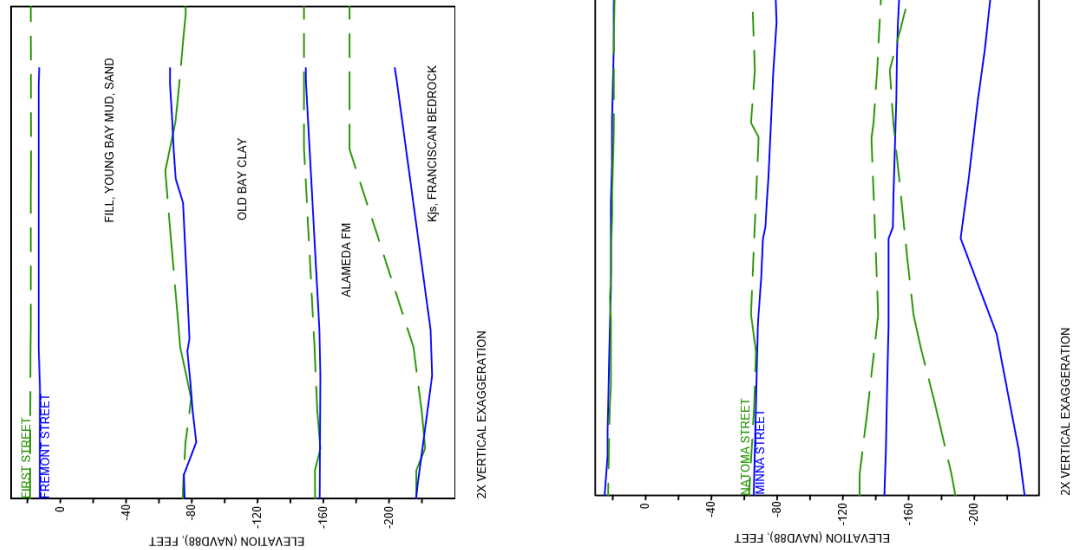


Figure 2.11. Cross sections overlain for comparison.

The two short sections that transect the site (Top) and the two long sections that parallel the site (Bottom) have been overlaid in order to compare the stratigraphy of the Old Bay Clay, Alameda formation, and Franciscan bedrock contacts



*Figure 2.12. Young Bay Mud with a bed of *Macoma nasuta* shells. Encountered during excavation of TTC trainbox.*



Figure 2.13. Colma sand excavated during construction of trainbox. Picture shows characteristic Reddish Yellow color of deposit, as well as some cross bedding.



Figure 2.14. Specimen of Old Bay Clay prepared for testing.

The top and bottom have been trimmed, but the sides are untrimmed and reflect the sample as extruded from the epoxy-coated Shelby tube. Slits have been excavated for bender element testing. The Old Bay Clay is a Dark Greenish Gray fat clay (CH)



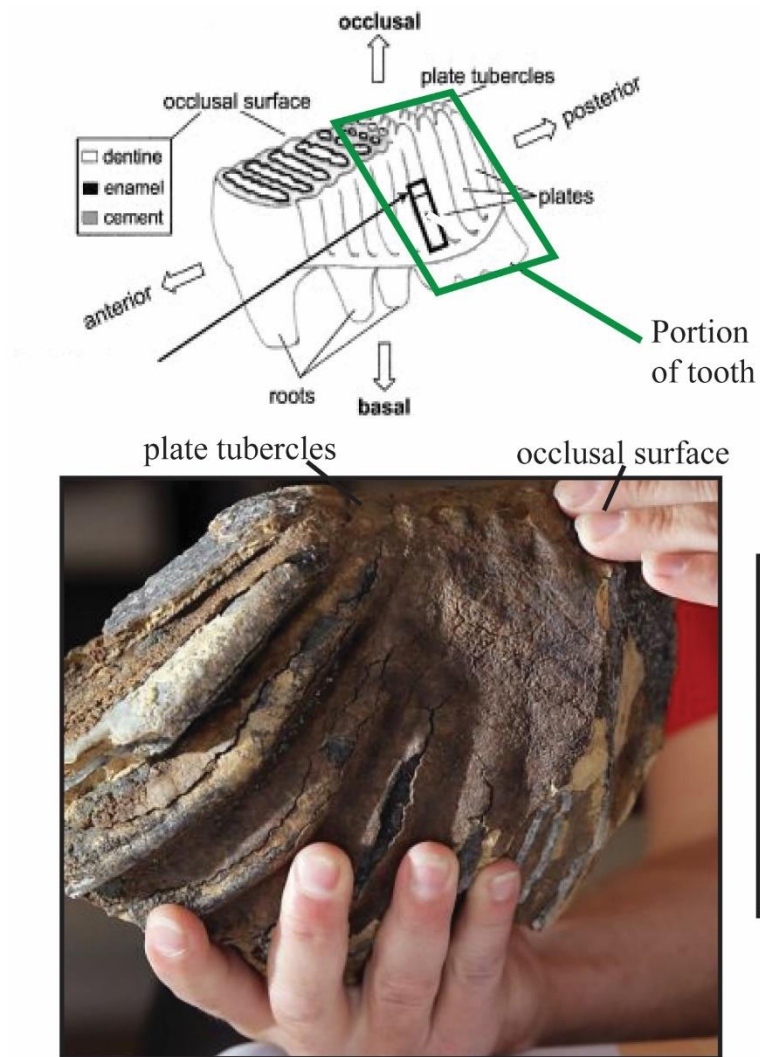
Figure 2.15. Specimen of clay from within Alameda fm.

The top and bottom have been trimmed, but the sides are untrimmed and reflect the sample as extruded from the epoxy-coated Shelby tube. Slits have been excavated for bender element testing. The clay within the Alameda resembles the Old Bay Clay but tends to have some oxidation



Figure 2.16. Franciscan rock recovered from project site.

Top: Serpentine, Bottom: greenstone, both recovered from excavation of buttress shafts into Franciscan bedrock



Fossil from Project.

Figure 2.17. The *Mammuthus columbi* (Columbian Mammoth) tooth recovered at the project site.
From Allen (2012b)

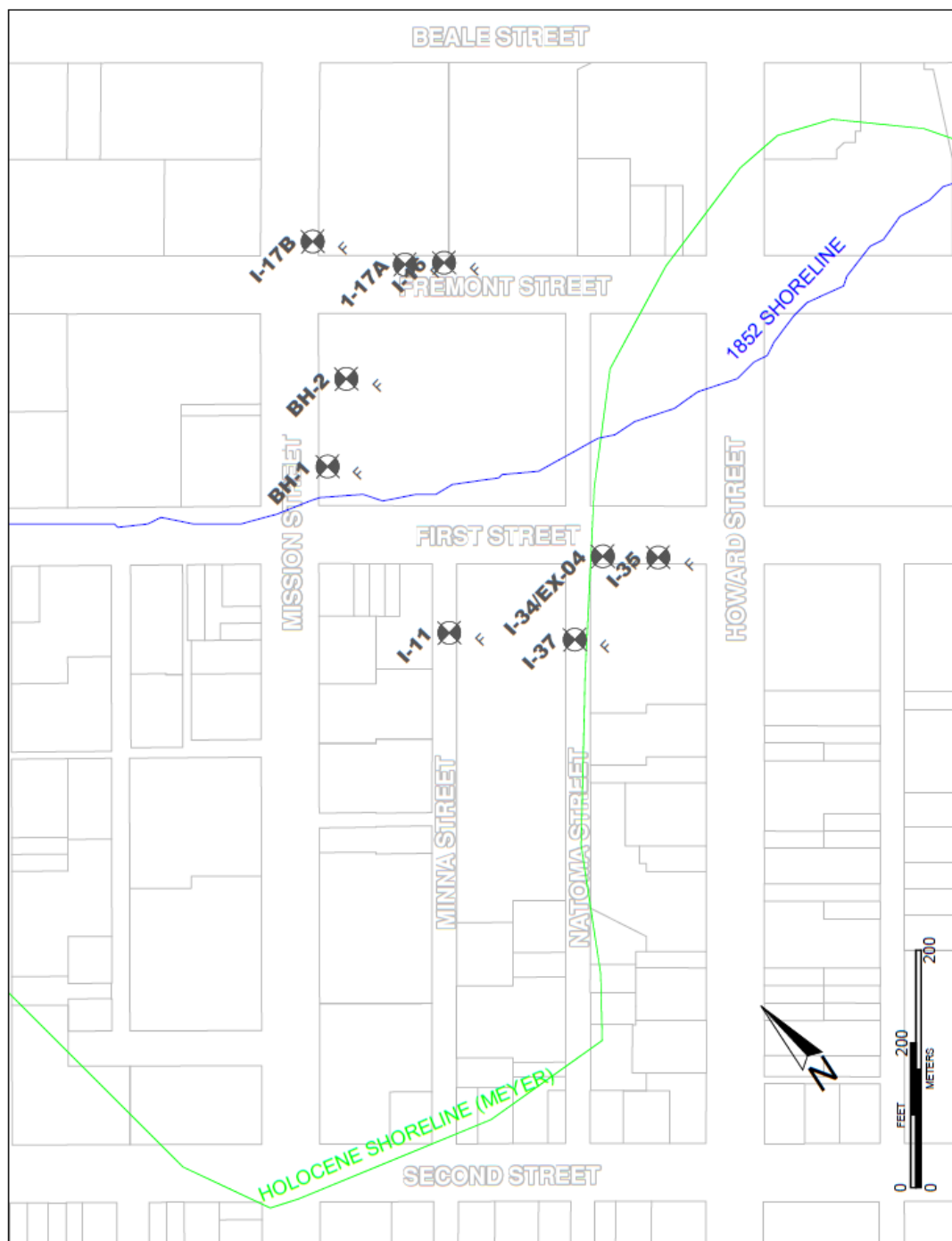


Figure 2.18. Site plan showing locations where microfossil study was performed.

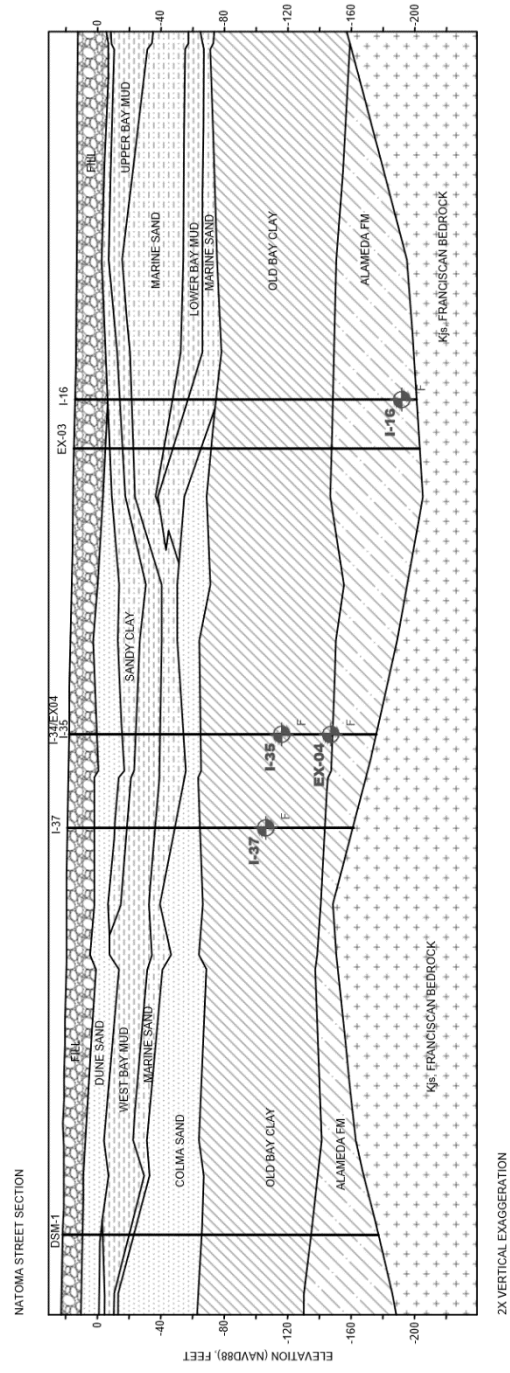
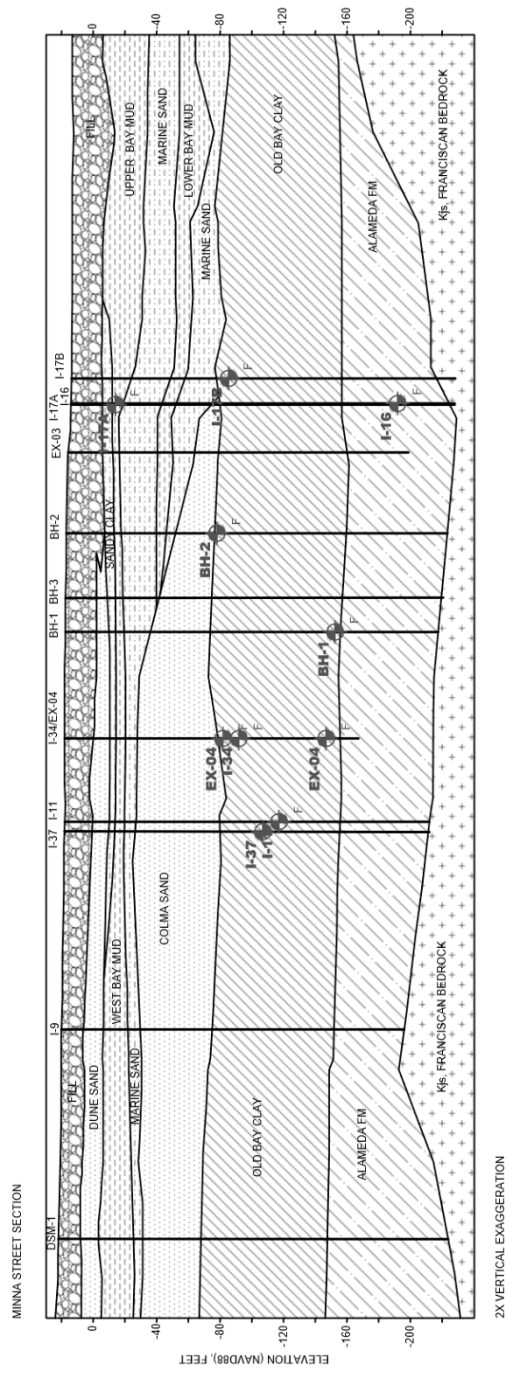


Figure 2.19. Cross sections showing locations where microfossil study was performed.

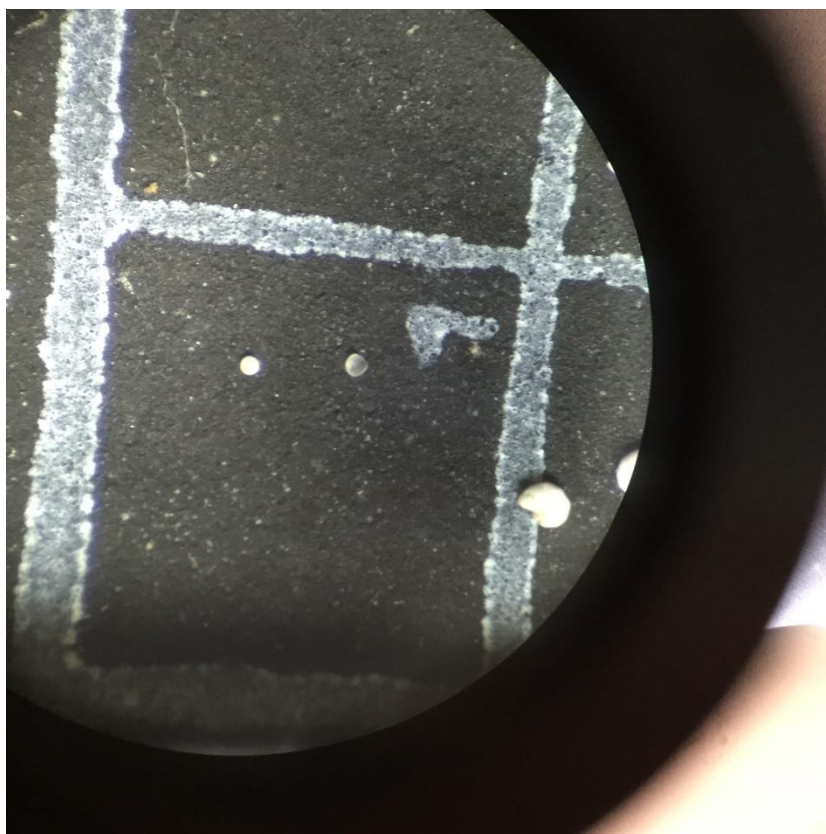
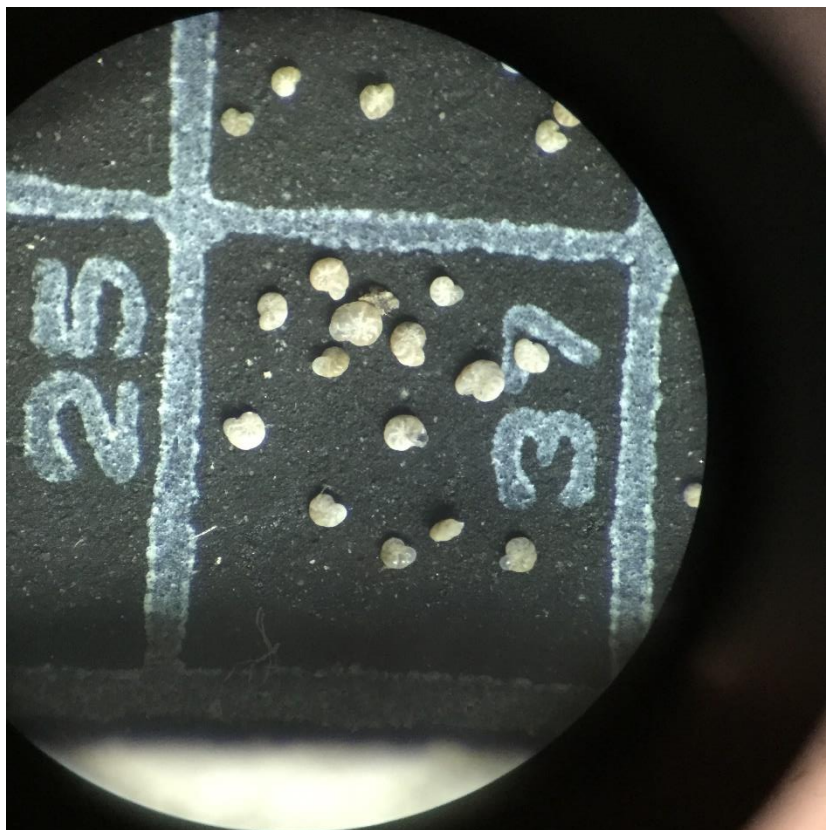


Figure 2.20. *Foraminifera and diatoms under microscope magnification.*
 Left: Forams, mostly *A. beccarii*, including juveniles. Right: Diatoms, with some forams in view at bottom.

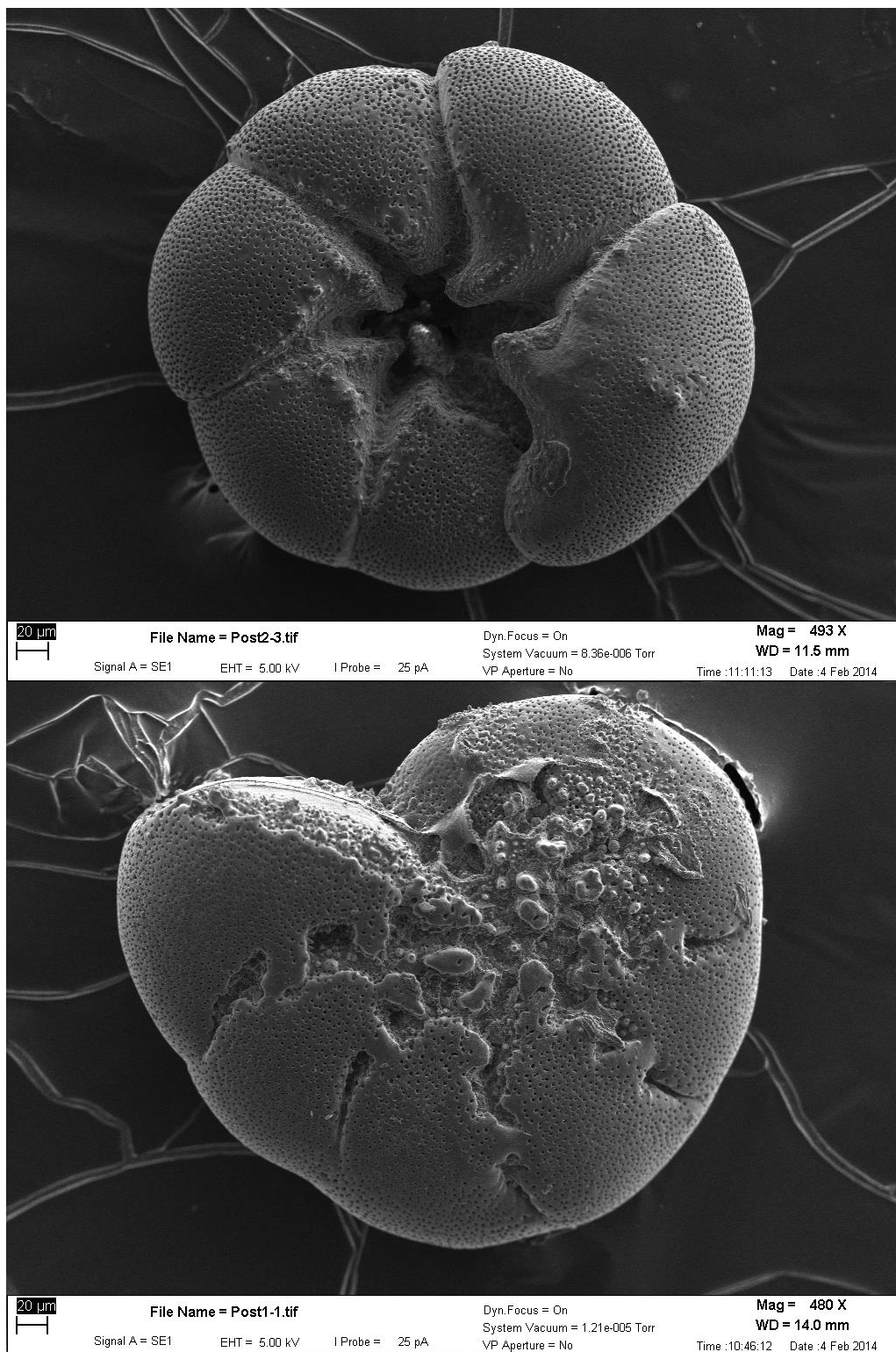


Figure 2.21. SEM image of *Ammonia beccarii* forma *tepida* and *Elphidium excavatum* (forma *lidoensis*).
A. *beccarii* f. *tepida* (Top) and E. *excavatum* f. *lidoensis* (Bottom). Images taken by the author.

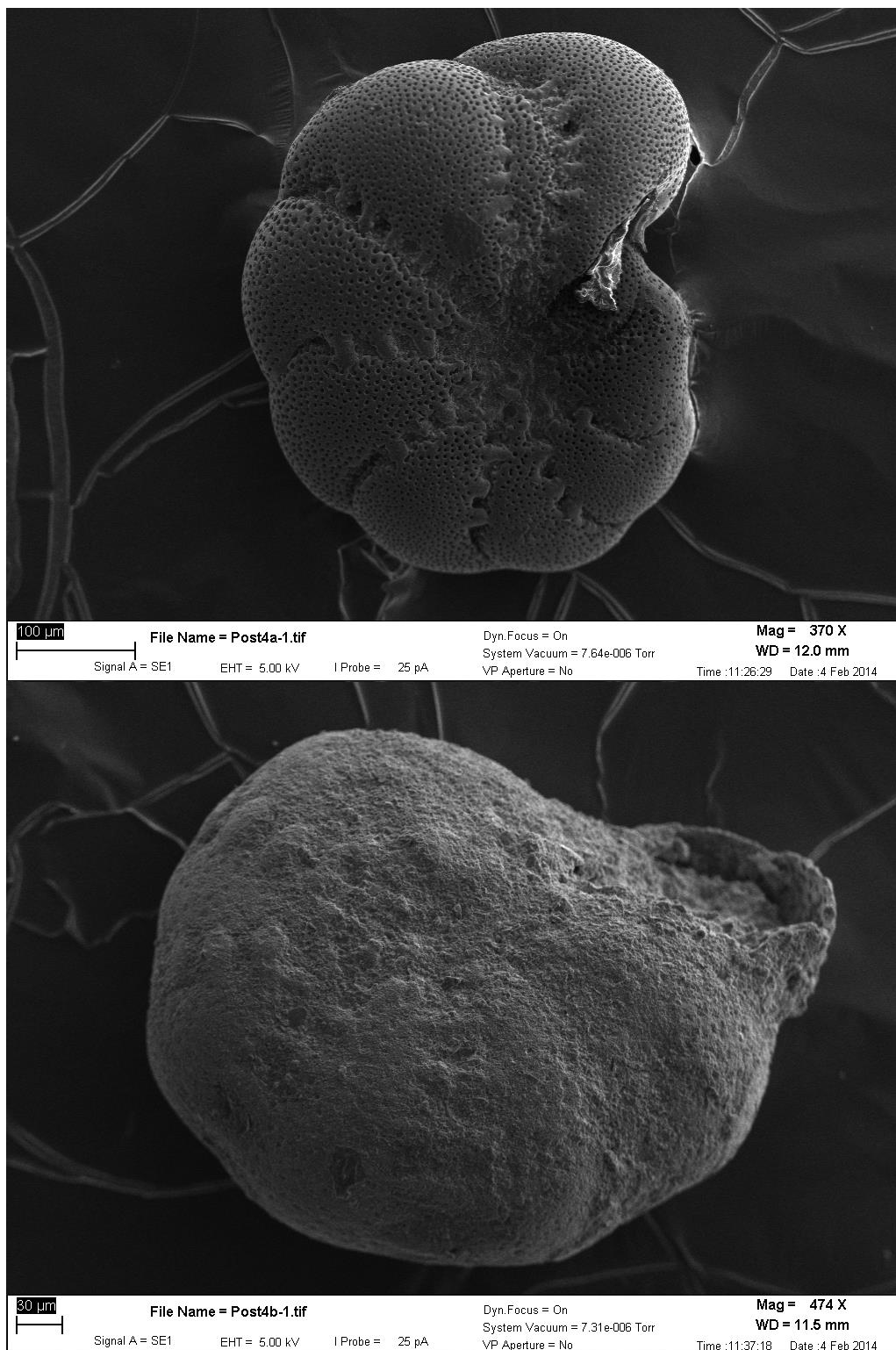


Figure 2.22. SEM image of *Elphidium excavatum* (forma *selseyensis*).

E. excavatum f. *selseyensis*: less weathered (Top) and weathered/oxidized (Bottom). Images taken by the author.

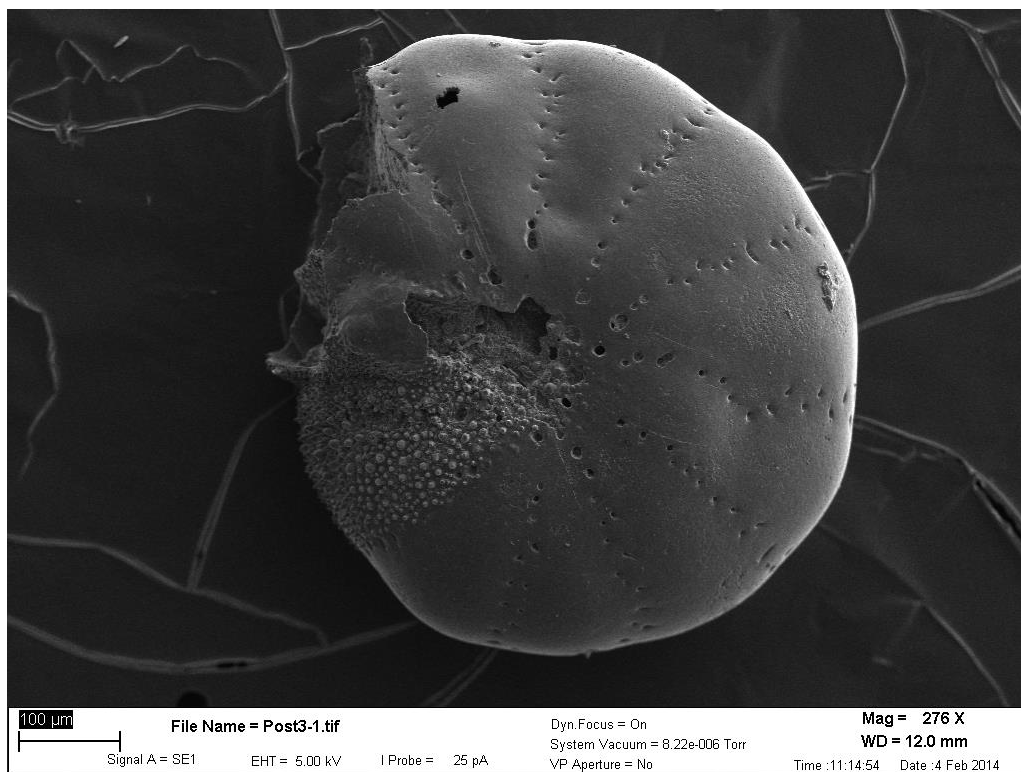


Figure 2.23. SEM image of Elphidiella hannai.
Image taken by the author.

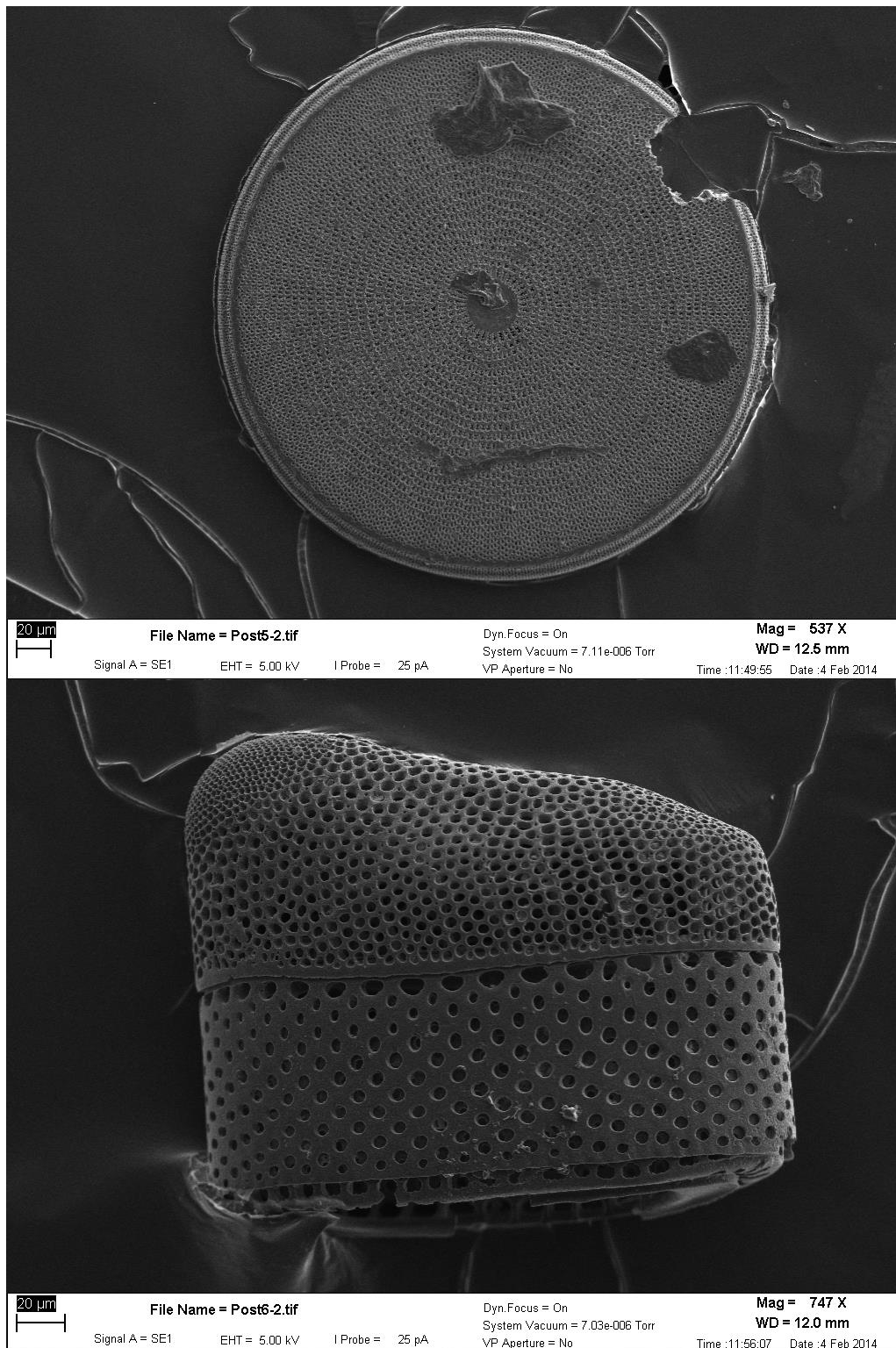


Figure 2.24. SEM images of Arachnoidiscus and Isthmia nervosa.
SEM images of (Top) Arachnoidiscus and (Bottom) Isthmia nervosa. Images taken by the author.

3 CONSOLIDATION TESTING

3.1 Introduction

In order to explore the long-term behavior of the clays in the study area, consolidation testing was performed with custom testing schedules. The following sections describe the tests performed and how testing was modified for this research study. The consolidation tests performed are listed in Table 3.1, Table 3.2, and Table A-2 and shown on Figure 3.1 and Figure 3.2.

In Figure 3.1, the locations of the samples used for consolidation are plotted in map view at the project site. As discussed in Section 2.4, the sample locations and depths were chosen prior to drilling to correspond to certain depths related to the proposed construction and instrumentation. The OBC samples taken were not necessarily evenly distributed across the site or across the unit thickness, because it was determined from the initial testing program and site characterization that the OBC was generally consistent throughout the OBC deposit at the site. For the YBM samples, consideration was made to collect samples from both East and West YBM. The Alameda formation samples were targeted based on prior explorations so that the clay horizons could be sampled. For the testing project, the samples that were chosen included the East and West YBM as well as the available Alameda samples. The OBC samples that were chosen for testing attempted both a spatial and depth distribution as much as possible. So the OBC samples do not attempt to develop particular soil profiles or particular site locations. As shown in Figure 3.1, consolidation testing was generally spatially distributed across the site from Second Street to Fremont Street and between Mission and Howard Street. There was a concentration in tested samples near Mission and Fremont Streets because more instrumentation and sampling came from this area. Figure 3.2 shows the locations of the tested samples in longitudinal cross sections along Minna and Natoma Streets. As can be seen, the YBM and Alameda samples come from limited depths because those locations were known beforehand to have probably recoverable samples. The OBC samples show much greater range in depth, from 100 to 135 feet below the ground surface in almost 5-foot increments.

As shown on Table 3.1, Table 3.2 and Table A-2, 31 consolidation tests were performed, with ten Incremental Loading Consolidation (IL) tests and 21 Constant Rate of Strain Consolidation (CRS) tests. Three CRS tests were performed on specimens from Young Bay Mud deposits, from both east and west of the 1852 shoreline. As discussed in Section 2.6, one sample retrieved from the Young Bay Mud layer was tested that showed characteristics of another material, so that test will not be included in data analysis for the Young Bay Mud. Thirteen CRS tests and nine IL tests were performed on OBC specimens. Six CRS tests and one IL test were performed on specimens from the Alameda formation. Ten tests are so-called “duplicate tests” because two of the same tests, either IL or CRS, were performed on specimens from the same sample tube. As described in following sections, the reasons for performing an additional test were either to confirm unexpected results or to rerun a test where equipment problems occurred. All ten IL tests also had CRS tests performed on another specimen from the same sample and those tests are noted as “paired IL and CRS test.”

3.2 Incremental Loading Consolidation Testing

Incremental loading consolidation (IL) was performed on ten specimens to obtain consolidation parameters, to investigate how loading and unloading effects consolidation parameters, and to investigate the relationships between secondary compression, C_α , and stress history and testing conditions.

3.2.1 Specimen Preparation, Testing Equipment, and Testing Procedure

IL specimens were prepared by extruding from the Shelby tube samples directly into an oedometer ring using a vertical hydraulic jack. The composite oedometer ring consisted of an outer portion stainless steel ring 6.7 mm thick and an interior Teflon lining 5.4 mm thick that reduced friction between the ring and the specimen (Figure 3.3). Interior dimensions of the ring were 7.275 cm in diameter and 2.590 cm in height, producing a specimen diameter-to-height ratio of 2.8, which is above the desirable minimum of 2.5 (ASTM Standard D2435, 2011). The top and bottom surface of the specimen were trimmed with wire saws and metal blades to produce a smooth surface even with the top and bottom of the ring (Figure 3.3). Rarely, minor voids were encountered during preparation. One source was the interaction with the metal weld of the sample tube for certain tube types, mainly zinc-coated steel tubes. The weld in these tubes appeared to contribute to a slight void along the weld seam (Figure 2.7). Other times, slight divots may have occurred during trimming. If present, these voids would be carefully backfilled with trimmings in order to accurately account for sample properties of a filled ring. The specimen dimensions were taken to be the interior volume of the ring. A preliminary water content was taken from trimmings, usually a slice of the sample taken adjacent to the tested specimen and from a complete slice of the sample.

Once trimmed into the ring, the specimen was placed into a basin on top of a large, dry porous stone. A dry porous stone sized to be slightly smaller than the inside diameter of the ring was centered on top of the specimen. A metal disk and a loading collar was then placed on the top stone in order to transfer load from the loading device.

IL specimens were loaded with a pneumatic piston system that included a return spring (Figure 3.4). In this system, a linear relationship between applied air pressure and resulting vertical load was developed during the testing program. A gauge pressure related to the desired load can be applied while the piston is clamped in place, such that when the piston is released, the load is instantaneously applied to the specimen. The loading frame was instrumented with a diaphragm-type load cell to continuously measure applied loads during the test. A linear variable differential transformer (LVDT) also continuously measured axial deformation of the specimen during testing. The load cell and LVDT data were passively collected with National Instruments VI logger software, version 4.0.0.3010.

Loading of the sample generally followed the ASTM procedure, however, there were a couple notable departures. The most significant were modifications to the ASTM proscribed seating load as well as the addition of a load referred to as the “soaking load” or the “soaking stress.” The ASTM procedure directs to apply a seating load that results in a total axial stress of about 5 kPa and then to apply additional load as needed to keep the specimen from swelling when the specimen is initially flooded with water. The seating load is meant to ensure that when load is applied to the

specimen, the load is transferred directly to sample strain instead to system compliance or emplacement of the porous stone. However, for the majority of deep samples in this study, that suggested stress was low with respect to the in-situ stresses. For example, for a sample from 120 feet below the ground surface, 5 kPa is approximately 1 to 2 % of the in-situ vertical effective stress. During seating, the data acquisition system collects real-time height and load data so it was possible to directly observe that system compliance and the seating of the stone occurred at higher stresses than the suggested 5 kPa. Height and load data for the specimen when fully seated will show a linear relationship, while the height and load data for the specimen prior to being fully seated will mostly show height change with little increase in load. It appeared that the seating load depended on both the in-situ vertical effective stress and the sample stiffness. It was found that the preferred seating load was approximately 5 to 15 % of the in-situ vertical effective stress, which ranged from approximately 30 to 60 kPa. This seating load is analogous to the seating load procedure used for CRS seating described in Section 3.3.1.

The addition of a “soaking stress” in this testing program also departs from the standard ASTM procedure. In general, the standard directs that stress during wetting is the same as the seating load, unless swelling occurs during wetting and it is determined that additional load should be applied. For this project, it was desired to avoid significant swelling of the sample. Low stresses, especially low stresses during soaking, would likely lead to significant swelling for these deep samples. After the seating stress was applied and the sample appeared stable at that stress, the initial height was based off the LVDT at the seating stress. A second, higher stress was then applied prior to soaking. The soaking stress was generally two-thirds of the in-situ vertical effective stress, so depended on the sample depth. This stress resulted in vertical strains around 0.5 %. It was found that this ratio of stress as based on field conditions contributed to negligible amounts of either swelling or collapse during the soaking increment. The time history was recorded during this process, so all changes in height of the specimen were tracked and documented. All deformations after the seating load were considered to be axial strain and were included in all strain computations for the consolidation test.

After applying the soaking load, flooding the specimen, and observing that the specimen was stabilized under that load, the incremental load testing would begin. As shown in Table A-2, various values of load increment ratio (LIR) were chosen, though the majority of testing was performed with a LIR of 0.5. Standard ASTM procedure suggests doubling the total axial stress each increment, which corresponds to an LIR of 1.0. The standard cautions that LIRs below 0.7, as well as load increments very close to the preconsolidation stress, “may preclude evaluation for the coefficient of consolidation, c_v , and the end-of-primary consolidation.” While some increments were somewhat ambiguous to interpret, discussed below in Section 3.3.2, there were benefits for this research project to use a low LIR. The lower LIR allowed for several loading increments below the preconsolidation pressure, especially as the relatively large soaking stress contributes to the first increment being close to the in-situ vertical effective stress. The lower LIR also allowed for more definition of the compression curve as well as more increments before the capacity of the testing equipment was reached. While many small load increments can contribute to an accumulation of secondary consolidation which can alter the shape and slope of the compression curve, this was less of a concern because one focus for these tests was to explore the nature and effects of secondary consolidation in the Old Bay Clay.

Loading increment timing was a modified version of ASTM Test Method B. Loads in this procedure are applied or removed once it had been observed that primary consolidation had finished and secondary compression was identified. ASTM Test Method A, on the other hand, prescribes 24-hour standard load increments. For this testing program, the length of the observation period of secondary compression varied greatly, as can be seen in Table A-2 in Appendix A. A main focus of the IL testing program was to study secondary compression, so timing of increments ranged from commonly used 12-hour increments, to as short as 3 hours for an overconsolidated increment, and to as long as 19 days for a normally consolidated increment. Because load and axial deformation were being continuously recorded, preliminary data could be downloaded during testing to check for the end of primary consolidation. Additionally, data sampling density was increased at the beginning of increments in order to fully characterize the rapid changes to axial deformation.

At the end of consolidation testing, the sample was fully unloaded and the solids extruded and collected for a final water content estimate and the determination of the dry mass of solids.

3.2.2 Data Processing

Data collected from the ILC tests included time histories of load and height, as well as index testing of the specimen. Recorded load and height were converted to stress and void ratio, respectively, for plots of both log time and square root of time, ASTM “Alternative Interpretation Procedures” 1 and 2, respectively. Both procedures were used in order to compare systematic differences in the results, as well as provide insight into increments where one method was ambiguous. From the Time History plots, end of primary (EOP) was determined, as well as calculations of the coefficient of consolidation, C_v , and the secondary compression index, C_{α} .

A systematic difference in EOP and C_v was observed between the log of time method, Procedure 1, and the square root of time, Procedure 2, methods. This is an observation also made by others (Holtz, Kovacs, and Sheahan, 2011, p. 394). As can be seen Figure 3.5, for the same normally consolidated loading increment, the EOP for the log of time method is at approximately 16,000 seconds while the EOP for the square root of time method is at approximately 4,356 seconds, almost four times shorter than the log of time method. As a result, the corresponding EOP void ratio for the log of time method is lower than for the square root of time method because the sample continued straining during the longer period of primary consolidation. The log of time method systematically predicted a later EOP than the square root of time method for all the testing in this research project. The most likely reason for this is that the log of time method construction depended on the later portions of the time history curve, while the square root of time method construction depended on the beginning of the curve. The focus on the two different portions of the curve then biases the answer towards those portions of the curve. The impact of this difference is twofold: the coefficient of consolidation, C_v , is lower for the log of time method and the cumulative strain and cumulative change in void ratio is greater for the log of time method, as discussed below. For the coefficient of consolidation, it is directly computed from the time curves, so the shorter time to EOP for the square root of time method is reflected in higher values of C_v because the sample appears to consolidate more quickly.

The resulting compression curve depends on the method used, as well as how the secondary compression strain is accounted for. For this research project, compression curves were constructed by data from individual increments where secondary compression strain or void ratio change was removed. This is how ASTM standard directs the construction of compression curves for Test Method B. Because of the later EOP, the log of time method included more vertical strain or void ratio change during individual increments. Figure 3.6 plots data from the same IL consolidation test using Procedure 1 and 2. Both methods are presented in two ways, with secondary compression removed and with secondary compression included. As can be observed, the compression curve from Procedure 2, the square root of time method, with secondary compression removed, shows the least total change in void ratio. Procedure 1, the log of time, with secondary compression removed, shows more change in void ratio. The two methods with secondary included show the most change in void ratio. With greater change in void ratio, the implied compression index, C_c , as derived from the field curve, is greater. The recompression index, C_r , also shows a slight increase, though the variability is much less than C_c variability. Using Procedure 1 or Procedure 2 may also have impacts on the evaluation of preconsolidation pressure, depending on the method for estimating preconsolidation pressure as explained in later sections.

Time curves for every increment in this research project were evaluated for secondary compression index, C_{α} . Data from every increment was compiled in order to assess C_{α} dependence on degree of consolidation, loading direction, and loading history and the results are discussed further in later sections. However, several special cases were observed and evaluated for their unique time history curves, as shown in Figure 3.7, Figure 3.8, and Figure 3.9. In Figure 3.7, there is no clear break in slope between the end of primary consolidation and secondary consolidation, even though the increment was allowed to run well past EOP consolidation as observed in previous and subsequent increments. Additionally, EOP consolidation was observed when plotting the time history using Procedure 2, the square root of time method. In this example and other similar testing increments, it was determined that the slope of C_{α} matched the maximum slope of the time history curve during primary consolidation. A common feature of these increments was that the applied stress was generally slightly above the maximum past pressure, up to approximately 20 % above that stress. In Figure 3.8, a similar behavior is observed, except that primary consolidation appears to continue and even steepen with time, even though previous and subsequent increments had EOP times much earlier than the total increment time of the example. The EOP time was also clearly observed in the square root of time method. In this case of apparently steepening primary consolidation, the increments were generally up to approximately 15 % below the preconsolidation pressure. These curves likely represent a transitional state in which the soil is straining from an overconsolidated condition to a normally consolidated one. Lastly, Figure 3.9 shows a consolidation time history curve that appears to have increasingly steepening C_{α} during secondary compression. In curves displaying this behavior, the stress of the increment was within a couple percent of the preconsolidation pressure, both above and below. This case is also likely transitional, moving from overconsolidated to normally consolidated, but the effects are more clearly seen in the secondary consolidation behavior rather than the primary consolidation portion of the curve.

After compiling the individual time increments, compression curves were constructed in order to evaluate the recompression index, C_r , to construct the field curve to derive compression index, C_c , and to estimate preconsolidation pressure, P_p . In general, the compression curve used was based

on individual points from Procedure 1, the log of time, with secondary compression strain or void ratio change removed. P_p was estimated using several methods, as explained in Section 4.2.

Sample quality estimates were made using the Lunne criteria (Lunne, et al., 2006) as explained in Section 4.7.

3.3 Constant Rate of Strain Consolidation Testing

Constant rate of strain consolidation (CRS) testing was performed on 21 specimens to evaluate sample quality by quantifying disturbance, to obtain consolidation parameters, to investigate how stress history effects consolidation parameters, and to compare with IL testing.

3.3.1 Specimen Preparation, Testing Equipment, and Testing Procedure

Specimen preparation for CRS was similar to IL up to the consolidometer set up explained previously in Section 3.2.1. The composite oedometer ring consisted of an outer portion aluminum ring about 14.2 mm wall thick, an inner stainless steel ring 5.7 mm thick, and an interior Teflon lining 5.2 mm thick that reduced friction between the ring and the specimen (Figure 3.3). The inside dimensions of the CRS ring was 7.280 cm in diameter and 2.535 cm in height, giving a diameter-to-height ratio of 0.35. The maximum height-to-diameter ratio that the ASTM standard recommends is 0.4 (ASTM Standard D4186, 2012). Unlike the IL ring, the CRS oedometer ring has a bottom gasket for sealing within the consolidometer. The ring with the specimen was attached to the base of the consolidometer cell with a confinement ring so that the bottom gasket seals around the bottom drain line in order to measure pore pressure. A porous stone sized just to the inside diameter of the oedometer ring was placed on top of the trimmed specimen. The trimmed specimen within the ring was then loaded via a piston through the top of the cell. The opening through the cell had linear ball bushings that allow the piston to move with very little friction and to constrain the piston to load purely vertically. Finally, the oedometer, stone, and loading piston were enclosed within an acrylic chamber and a sealed top cap, which allowed control of water levels and application of air pressure.

A Wykeham Farrance mechanical load frame with a uniform rate of loading was used for CRS testing. With the mechanical load frame, the loading table moves either up or down at a constant rate controlled by gears. Load can also be applied manually with a hand wheel. The loading table could be locked in place with a clutch, which allowed for the specimen to be held at a constant height. This loading device was strain-controlled as compared to load-controlled. The specimen itself was loaded via a piston that was centered under the cross arm of the load frame. Figure 3.10 shows the oedometer chamber situated within the load frame.

Air pressure could be applied both to the top of the chamber and as back pressure through the bottom drain line. The system was plumbed such that the chamber and back pressure were equivalent. The bottom drain line was attached to a differential pressure transducer that could measure pore pressures in the sample relative to the chamber pressure. With the bottom drain line open, pressure could be applied to the specimen for back pressure saturation. With the bottom drain line closed, the excess pore pressure at the base of the sample could be measured.

Continuous data was collected during testing with National Instruments VI logger software, version 4.0.0.3010. Strain was measured using a LVDT clamped to the piston and referencing the top of the chamber. This prevented the LVDT from measuring compliance of the load cell and load frame. However, some tests were run with the LVDT clamped to the mechanical load frame cross bar. In those tests, a compliance test was run for the testing configuration so that system compliance could be removed from the measured strain data. Load was measured with a load cell placed between the piston and mechanical load frame. Pore pressure at the base of the specimen was measured via the differential pressure transducer connected to the bottom drain line.

After being installed within the consolidometer, both a seating load and a soaking load were applied to the specimen prior to inundation, similar as described for IL testing. The seating load for this testing program depended on the sample stiffness and the in-situ vertical effective stress. Because of the hand wheel and the use of the clutch, seating the sample could be precise and deformations observed in real time with the data acquisition system. Similar to the seating load procedure described for IL testing in Section 3.2.1, height and load could be observed in real time during seating. The sample was considered to be seated when there was no further height change without a corresponding increase in load. The height under this seating load was recorded for the initial conditions of the sample. The seating load ranged between 5 to 15 % of the in-situ vertical effective stress, which corresponded to approximately 30 to 60 kPa. Unlike the ASTM procedure for IL testing, the standard for CRS testing directs only that “seating pressure must prevent swelling but not cause significant consolidation.” The standard also notes that this load depends on the stiffness of the soil and a “reasonable estimate is to use about 10 % of the in situ effective stress or causes about 0.2 % axial strain.” This is consistent with the observations and procedures of this testing program and similar to how IL tests were performed for this testing program.

After seating and before inundation, a higher soaking load was applied to the specimen. Similar to IL testing described previously, the soaking stress was taken to be approximately two-thirds of the in-situ vertical effective stress, thus dependent on the sample depth. The hand wheel was used to slowly load the specimen while height, load, and pressure were recorded. At the desired load, the sample was left to stabilize under constant height with the table clutch enabled. If the load dropped due to sample relaxation, the load table was gently raised until the sample maintained a stable load. At that time, the sample was inundated with de-aired water with the table clutch enabled to preserve constant height. While the sample was inundated, the bottom drainline was opened to allow water flow to or from the bottom porous stone. Shortly after inundation, chamber pressure was gently applied to the chamber in increments to ensure that there were no rapid changes in observed load from the sample. The sample was allowed to equilibrate with the data acquisition running in order to monitor any changes for a period of time. Total axial strain during the soaking increment was approximately 0.5 %. After the sample appeared to be equilibrated, the bottom drainage valve was closed and the sample was left in the consolidometer under constant height and pressure for a period of approximately 12 hours prior to testing. This process was similar to a back pressure saturation process as directed in the ASTM standard and yielded high saturation rates when saturation was tested. Back pressure saturation was checked by applying an undrained increment of chamber pressure and observing how long it took for sample pore pressures to equilibrate.

With the sample held under constant height, any swelling or collapse would be recognized by an increase or decrease in the measured load. Under the soaking stress during saturation, negligible amounts of either swelling or collapse were observed. After saturation, the specimens were consistently within approximately +/- 5 kPa of the original soaking stress. The time history was recorded during this process, so all changes in height of the specimen were tracked and documented. All deformations after the seating load were considered to be axial strain and were included in all strain computations.

For testing, a strain rate is chosen such that a base excess pressure ratio of 10% was not exceeded during loading, though generally the pore pressure ratio would stay below 5% for most of the normally consolidated range. The pore pressure ratio is defined as $\Delta u/\sigma_a$, where Δu is excess pore pressure measured at the base of the specimen and σ_a is the total axial stress. The ASTM standard notes that the desired pore pressure ratio is between 3% and 15%, suggesting that 5% is best. The pore pressure appeared to depend on both loading rate as well as stress history. In particular, high pore pressure ratios were observed during loading at stresses well above the current maximum past pressure as well as during unloading at low stresses much lower than the maximum past pressure. It was also observed that the deepest samples would exhibit greater pore pressures at lower stresses at the same rates as shallower samples, possibly due the materials having lower permeability. Thus, deeper samples from the Alameda formation were loaded at slower rates than shallower OBC samples. A rate of 0.00406 mm/hr (0.00016 in/hr), which corresponds to 0.93% vertical strain per hour, was found to be optimal for the OBC through this testing program. Generally, this was the same rate used for unloading. On some occasions, if high pressures were observed during unloading, the rate could be reduced by a factor of 5 by using a lower stud gear on the loading frame.

Several series of loadings and unloadings were performed in order to investigate how OCR and stress history affects consolidation parameters. Table 3.3 includes information about number of loadings and unloadings and over what stress range they were performed for the CRS testing. Generally, the first unload-reload cycle was performed at the estimated field stress, another when the sample had passed the preconsolidation pressure, and at additional larger stresses.

3.3.2 Data Processing

Data collected from the CRS tests included time histories of load, vertical displacement, and pore pressure at the specimen base, as well as index testing of the specimen. Void ratio was calculated with the height data, which was corrected for compliance as needed. The load and pore pressure data were used to calculate the “Average Effective Axial Stress” using the cubic formula,

$$\bar{\sigma}_{v_{avg}} = (\sigma_v^3 - 2 \cdot \sigma_v^2 \cdot u_h + \sigma_v \cdot u_h^2)^{1/3}$$

Where $\bar{\sigma}_{v_{avg}}$ is average effective stress, σ_v is the total stress, and u_h is excess pore pressure (Wissa, Christian, Davis, & Heiberg, 1971). Height, load, and pore pressure were also used to calculate the Coefficient of Consolidation, C_v ,

$$C_v = - \frac{H^2 \cdot \log \left(\frac{\sigma_{v2}}{\sigma_{v1}} \right)}{2 \cdot \Delta t \cdot \log \left(1 - \frac{u_h}{\sigma_v} \right)}$$

Where H is the height of the sample, σ_{v1} and σ_{v2} are the total stresses at times t_1 and t_2 , respectively, and Δt is $t_2 - t_1$ (Wissa et al., 1971). The C_v from CRS testing are presented as plots for individual tests in Appendix A.

The void ratio and average effective axial stress were used to construct a compression curve, which was used to find C_r , estimate P_p using various construction methods, and to construct a field curve in order to obtain C_c . Because of the many unload and reload loops, C_r was compiled for the various loading combinations and stress histories and is discussed in later sections. The various methods used to estimate P_p are discussed in Section 4.2.1, though several methods utilized the continuous CRS data and were calculated at the same time as the data was compiled. The Lunne criteria (Lunne, et al., 2006) was used to quantify sample quality as described in Section 4.7.

3.4 Compression Curves and Terminology

The consolidation tests in the research project were unique in several ways that reflect both the testing procedures as well as the specimens tested. The main distinction is that the OBC and Alameda soils are deep, moderately plastic marine clays. The common focus traditionally for consolidation testing are soft, shallow clays. The samples in this testing program, in contrast, required much larger stresses in order to overcome the Preconsolidation Pressure and to reach high enough stresses to clearly define normally consolidated behavior.

In particular for IL testing, the tests in this research project differed from standard IL procedures. Because a large focus of this testing was secondary compression behavior, many testing increments had significant amounts of secondary consolidation strain, so the handling of that displacement and which method was used to find the end of primary consolidation has an impact on plots of the compression curve as discussed in Section 3.2.2. Additionally, like all IL tests, the discontinuous data requires interpolation be made the discrete data points in order to use many of the methods for evaluating the preconsolidation pressure.

The CRS testing data was straight-forward to use because of the continuous data, but the shape of the tested curves was unlike more typical shallow, soft-soil compression curves. CRS data from tested OBC and Alameda specimens ranged from fairly well-behaved curves like Figure 3.11 to more rounded compression curves like Figure 3.12. As can be observed in the figures, many portions of the curve show some degree of curvature. This is a deviation from simplified bi-linear compression models, though not quite as curved as some very low plastic soils. The initial loading segments appear somewhat curved and as the stress approaches the preconsolidation stress, there is a diffuse change in slope. At around the “middle stresses,” most samples in this study did reach a portion of straight slope corresponding to the maximum slope for the normally consolidated region. But at large stresses, the compression curve is often observed to become concave upwards with a decreasing slope.

The somewhat rounded shapes of the initial portion of the compression curves tends to be correlated with disturbed samples or soils that have low plasticity, this is not the case with the samples tested in this study. Importantly, the soils tested in this project were moderately to highly plastic and, as discussed further in Section 4.7, had generally low disturbance. Thus, the slightly rounded initial slopes and lack of strong inflection points reflect the consolidation characteristic of the materials.

The concave upwards slope at the end of the compression curve is commonly associated with sensitivity. While that may be the case for these samples, it is suggested that the shape reflects increasing particle interaction at large stresses and a departure from the simplistic bi-linear consolidation model. The high stresses and densities reached in this project is likely the reason for the concave upwards shape of these compression curves. Generally, a shallow, soft soil will not be tested to such large stresses, so particle-to-particle interaction effects would not be commonly observed in other consolidation testing programs.

These characteristics of the actual compression curves emphasize that the bi-linear model is a simplistic representation for real consolidation behavior. They especially highlight the limitations of using IL data. The CRS curves provide insight into how the slope changes throughout the various stress ranges, but sparse IL data as shown on Figure 3.13 can be more easily interpreted in the bi-linear framework. With only a few points in the initial portion of the curve, it is easier to assume that the slope is a constant straight-line segment and ignore the gradually steepening slope as the preconsolidation pressure is approached. Likewise, the increasing slope after the preconsolidation pressure can be missed by fitting the sparse data points to a straight line.

Most importantly, sparse IL data tends to force the preconsolidation pressure estimate to be controlled by the chosen stress increments. As can be seen on the top plot of Figure 3.13, Point B is the inflection point. But if there was a continuous curve that could be measured, as drawn on the bottom plot of Figure 3.13, it is likely that the point of maximum curvature lies between Point B and Point C. The tendency of these approximations will push the preconsolidation pressure to the left, to lower stresses, as well as underestimate the slope of the normally consolidated region as discussed further in Section 4.2. This also impacts estimates for other parameters estimated with compression curve, like the recompression index, because the sparse data tends towards straight-line fits that are less clear on curved CRS compression curves.

For this research project, how to interpolate points was driven by what was known from the CRS data. It was clear from the tests on both OBC and Alameda clays that the compression curve had a gentle, rounded appearance. So individual test increments were connected by similar, gently curved lines. This is in contrast to introducing straight line segments or an obvious break in slope somewhere along the curve.

3.4.1 Comparison between IL and CRS Compression Curves

While continuous CRS data shows that compression curves should be more complex than the sparse IL compression curves, it is more difficult to assess what assumptions of IL curves are analogous to CRS curves. In Figure 3.14, data from a paired CRS and IL curve are plotted together. The IL data has been shifted, such that the initial void ratio corresponding with the IL data has

been made to equal the initial void ratio of the CRS data. While that specimens were adjacent in the sample tube, there still was slight variation in these index properties. There are two sets of IL data, both have been processed with Procedure 1, the log of time method, but one set has been processed to exclude secondary compression, like Test Method B, and the other includes all accumulated secondary compression. As can be seen Figure 3.14, the CRS data lies somewhere between the IL data without secondary and with secondary. This is possibly due to secondary compression accumulating during test, but there are also contributions to the shape of the CRS curve due to pore pressure generation from rate effects and soil permeability. When compared to IL data that has been processed with Procedure 2, the square root of time method, without secondary compression, like in Figure 3.5, will plot even higher than the log of time method, without secondary compression. This will impact comparisons between CRS and IL data for estimating parameters, which is discussed further in Chapter 4.

3.5 Conclusions

To understand the compression parameters and stress history of the deep, thick layer of Old Bay Clay and deep clays within the Alameda formation a detailed consolidation testing program was performed. Ten Incremental Loading Consolidation (IL) tests and 21 Constant Rate of Strain Consolidation (CRS) tests were performed with all IL tests paired with one or more CRS test. The consolidation tests included many cycles of unloading and reloading at various stress states to understand recompression and secondary compression properties. Because of the sample depths, a large soaking stress was routinely used for both IL and CRS testing to prevent swelling. Likewise, the IL testing was performed with many increments with small LIR in order to characterize the compression curve, as well as understand recompression and secondary compression dependence on stress state. Processing IL testing was explained, especially how End of Primary was determined and how secondary compression strain was treated. Lastly, a comparison of IL versus CRS compression curves was discussed. When CRS compression data is plotted with a paired IL compression test, the CRS data lies between IL data that includes secondary compression and excludes secondary compression, showing that some secondary compression is present in CRS compression curves.

Table 3.1. Incremental Load Consolidation testing per sample

Test	Unit	Sample ID	Depth (feet)
ILC-01	OBC	I-9 S-2	130
ILC-02	OBC	I-9 S-1	120
ILC-03	OBC	I-35 S-4	135
ILC-04	OBC	I-11 S-3	135
ILC-05	OBC	I-17A S-3	109
ILC-06	OBC	EX-03 S-2	114.5
ILC-07	Alameda	BH-2 S-35	195
ILC-08	OBC	BH-1 S-18	120
ILC-09	OBC	BH-1 S-18	120
ILC-10	OBC	BH-3 S-18	110

Table 3.2. Constant Rate of Strain Consolidation testing per sample

Test	Unit	Sample ID	Depth (feet)
CRS-08	OBC	I-9 S-2	130
CRS-09	OBC	I-9 S-1	120
CRS-10	OBC	I-9 S-1	120
CRS-11	Alameda	I-16 S-2	206
CRS-12	Alameda	I-16 S-1	200
CRS-13	YBM	DSM-1 S-1	26
CRS-14	YBM	DSM-1 S-1	26
CRS-15	Alameda	I-11 S-6	190
CRS-16	Alameda	I-11 S-6	190
CRS-17	Alameda	I-11 S-6	190
CRS-18	YBM	I-17A S-1	28
CRS-19	OBC	I-35 S-4	135
CRS-20	OBC	I-11 S-3	125
CRS-21	OBC	I-17A S-3	109
CRS-22	OBC	I-11 S-3	135
CRS-23	OBC	EX-03 S-2	114.5
CRS-24	OBC	I-34 S-1	110
CRS-25	Alameda	BH-2 S-35	195
CRS-26	OBC	BH-1 S-18	120
CRS-27	OBC	BH-3 S-18	110
CRS-28	OBC	EX-04 S-2	100
CRS-29	Alameda	BH-1 S-29	230

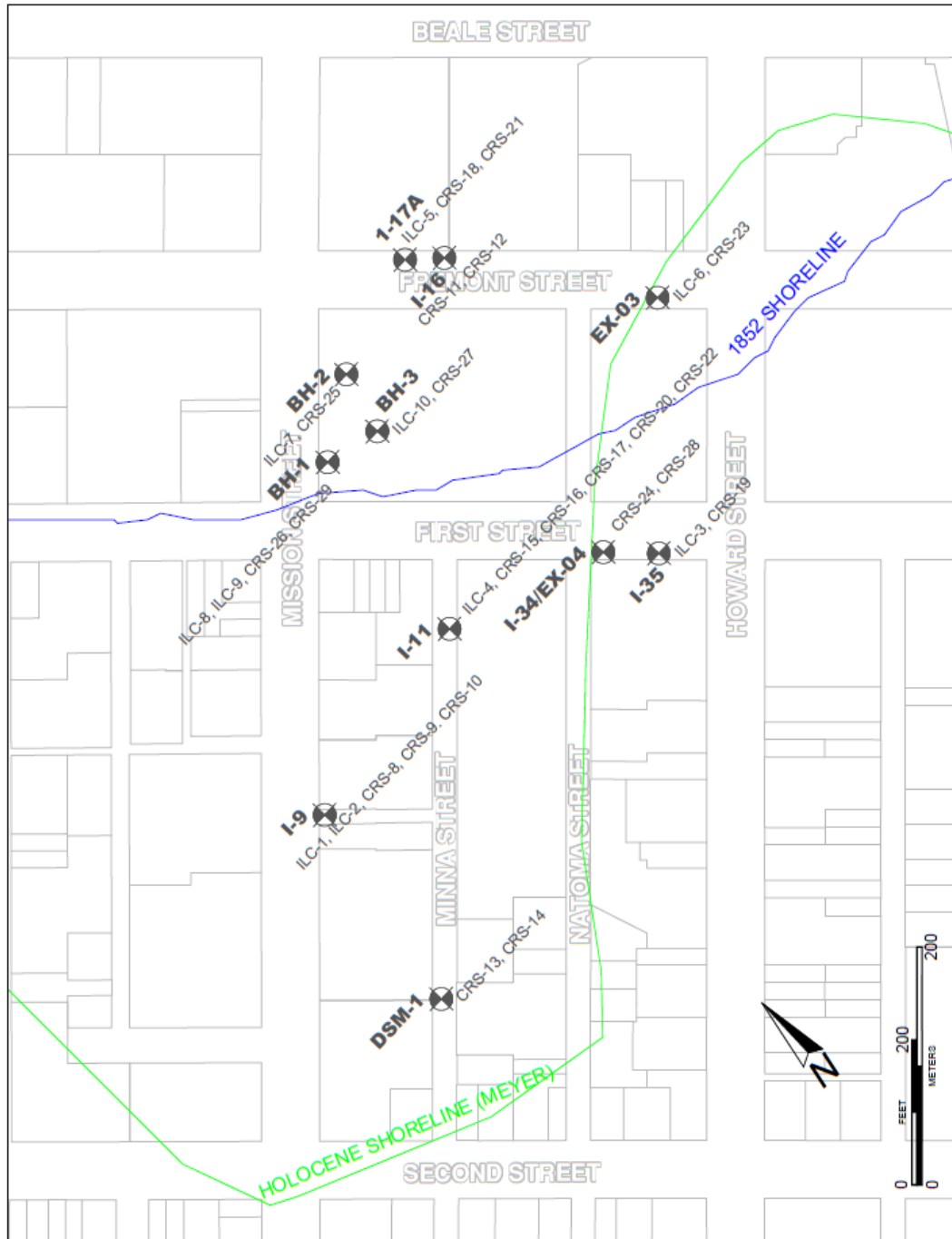


Figure 3.1. Site plan showing borings with the corresponding consolidation tests noted. The Holocene shoreline (Chapter 2) is marked in green and the 1852 shoreline is in blue

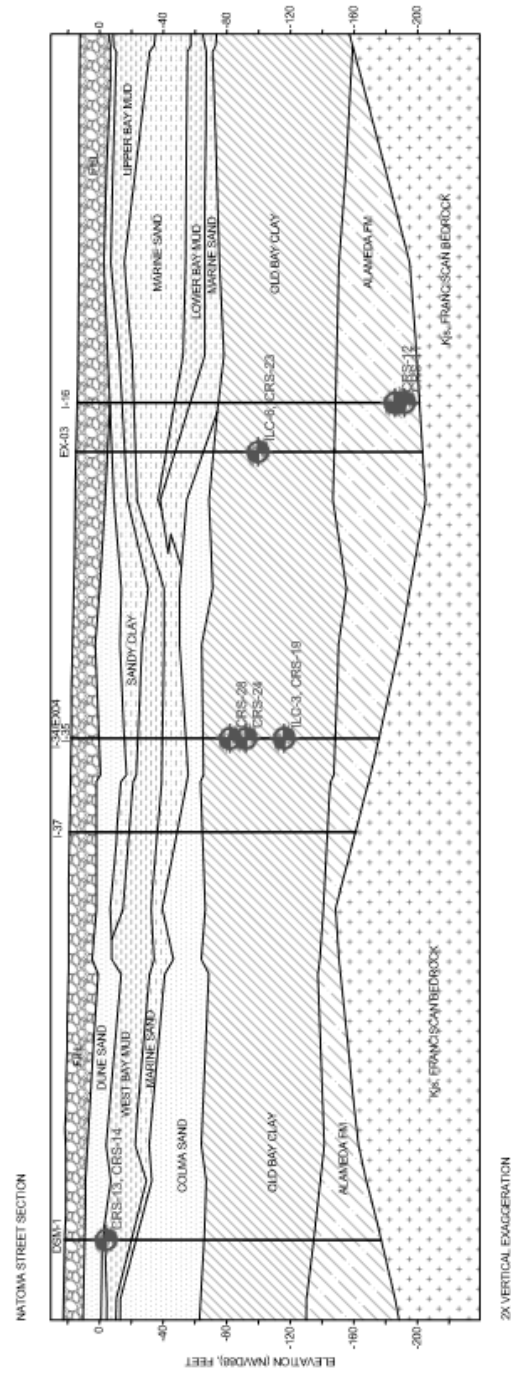
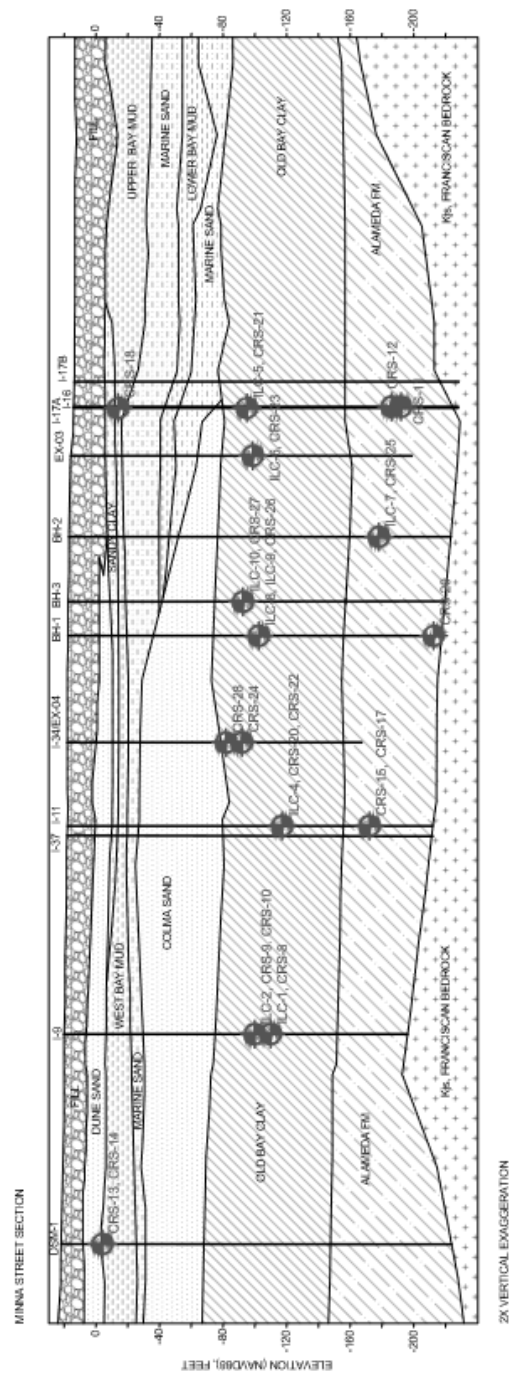


Figure 3.2. Cross sections showing locations of consolidation testing.



Figure 3.3. Oedometer rings from IL and CRS testing.
Top: IL ring on left and CRS ring on right. Bottom: CRS ring with trimmed Alameda specimen for testing

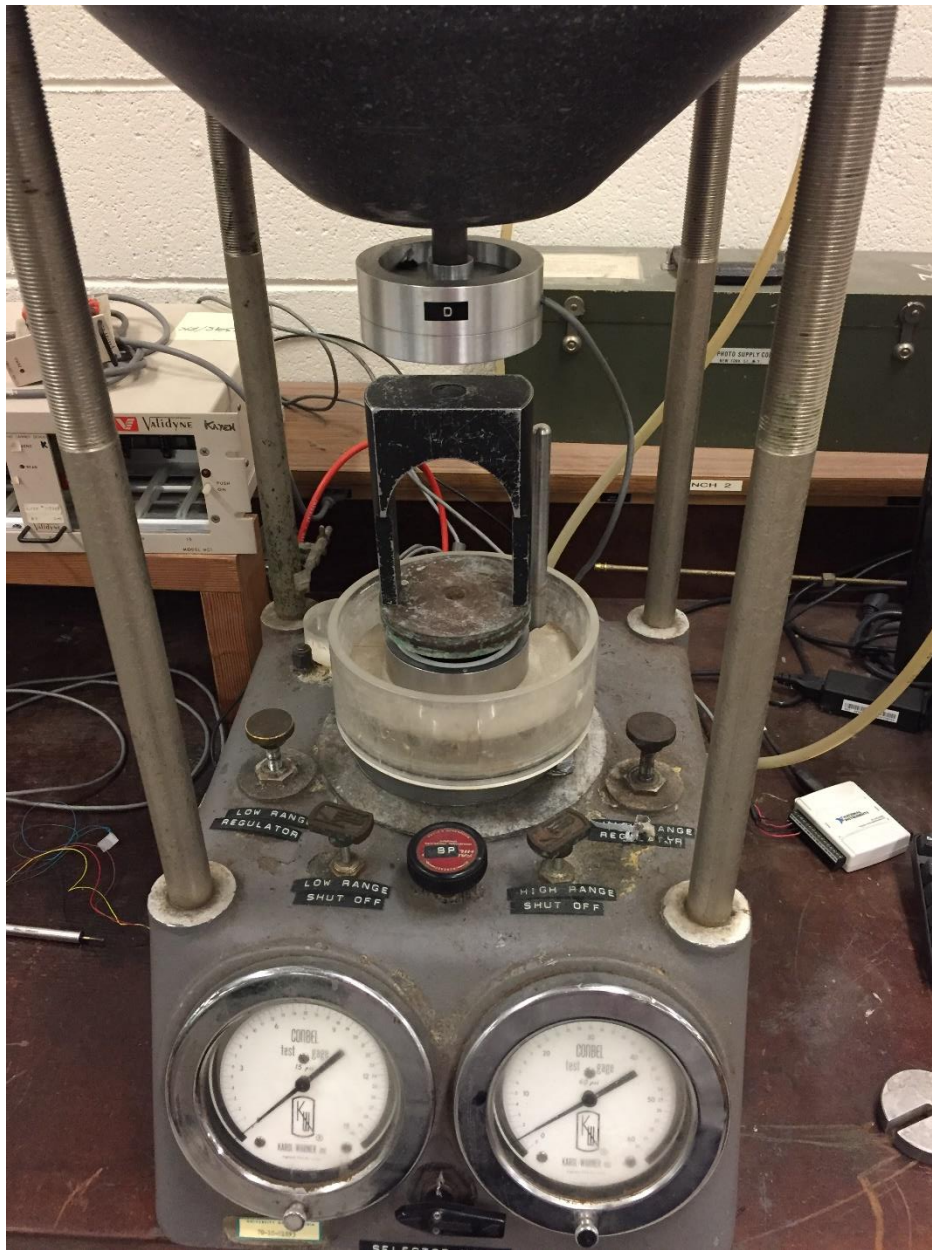


Figure 3.4. IL test setup showing pneumatic piston system.

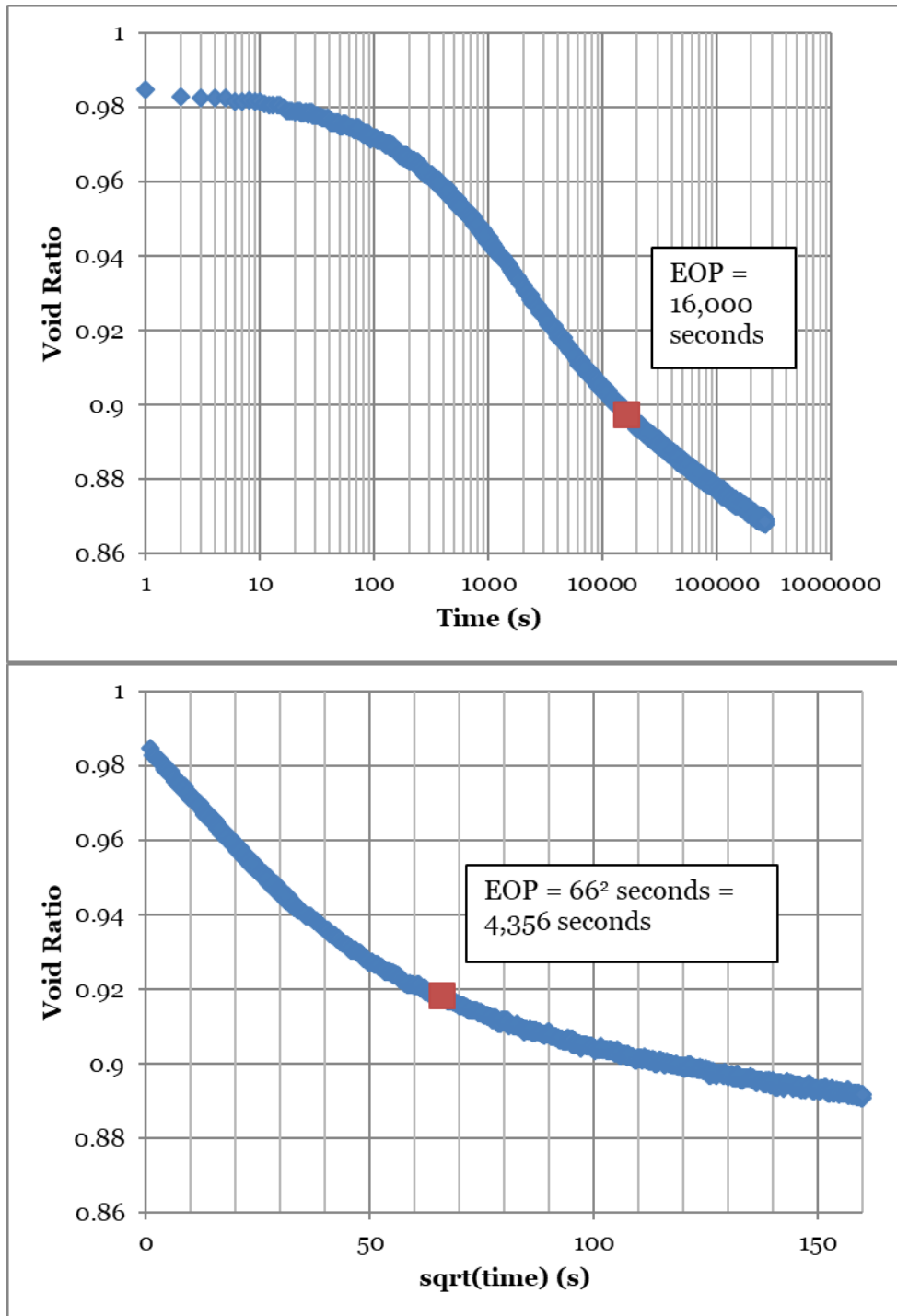


Figure 3.5. Comparison of EOP for the same ILC increment, using Procedure 1, the log of time method, and Procedure 2, the square root of time method.
 Top: Procedure 1, log of time method. Bottom: Procedure 2: square root of time method

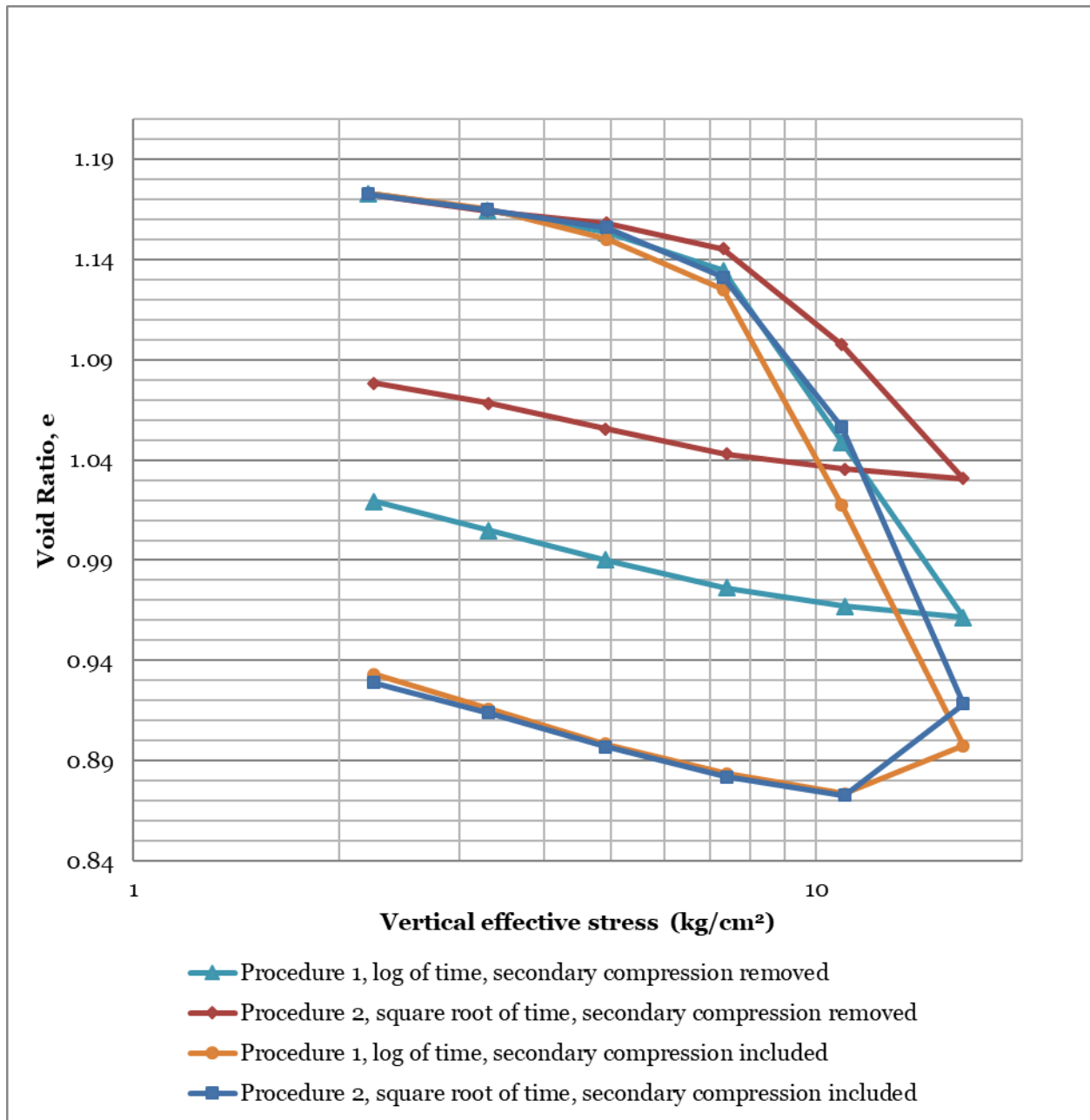


Figure 3.6. Incremental Loading Consolidation test compression curve showing data processed using both ASTM Procedure 1 and 2.

Procedure 1 and 2 are log of time and square root of time methods, respectively. Secondary consolidation has been removed and included for both methods, which roughly correlate to ASTM Test Method B and ASTM test Method A (ASTM D2435).

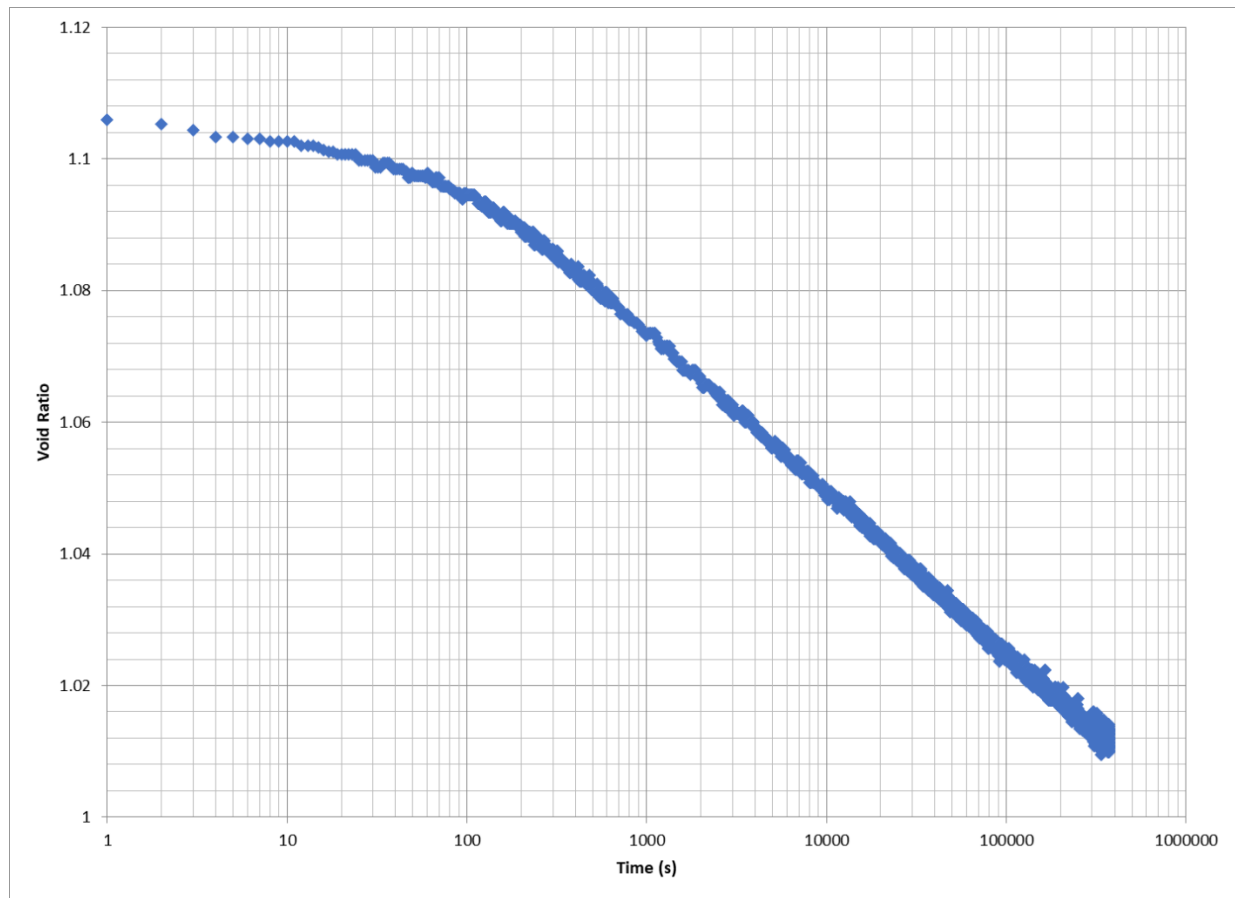


Figure 3.7. Time History Curve from an Incremental Consolidation increment where there is no clear break in slope between initial and secondary consolidation.

Test was LIR=0.5 and from an initial increment past the preconsolidation pressure.

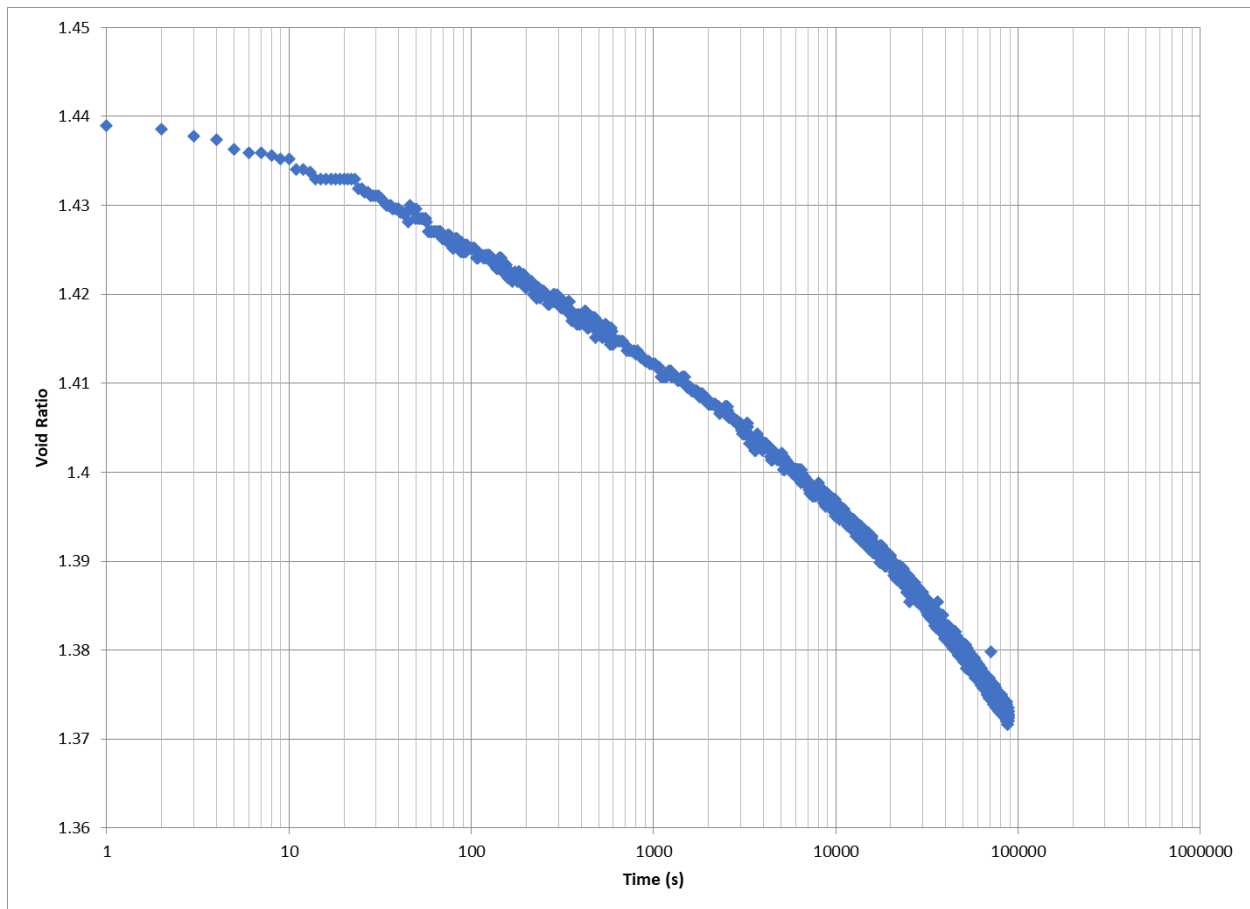


Figure 3.8. Time History Curve from an Incremental Consolidation increment where initial consolidation appears to continue and steepen with time.

Test was LIR=0.5 and from a “reset” increment below the previous maximum past pressure.

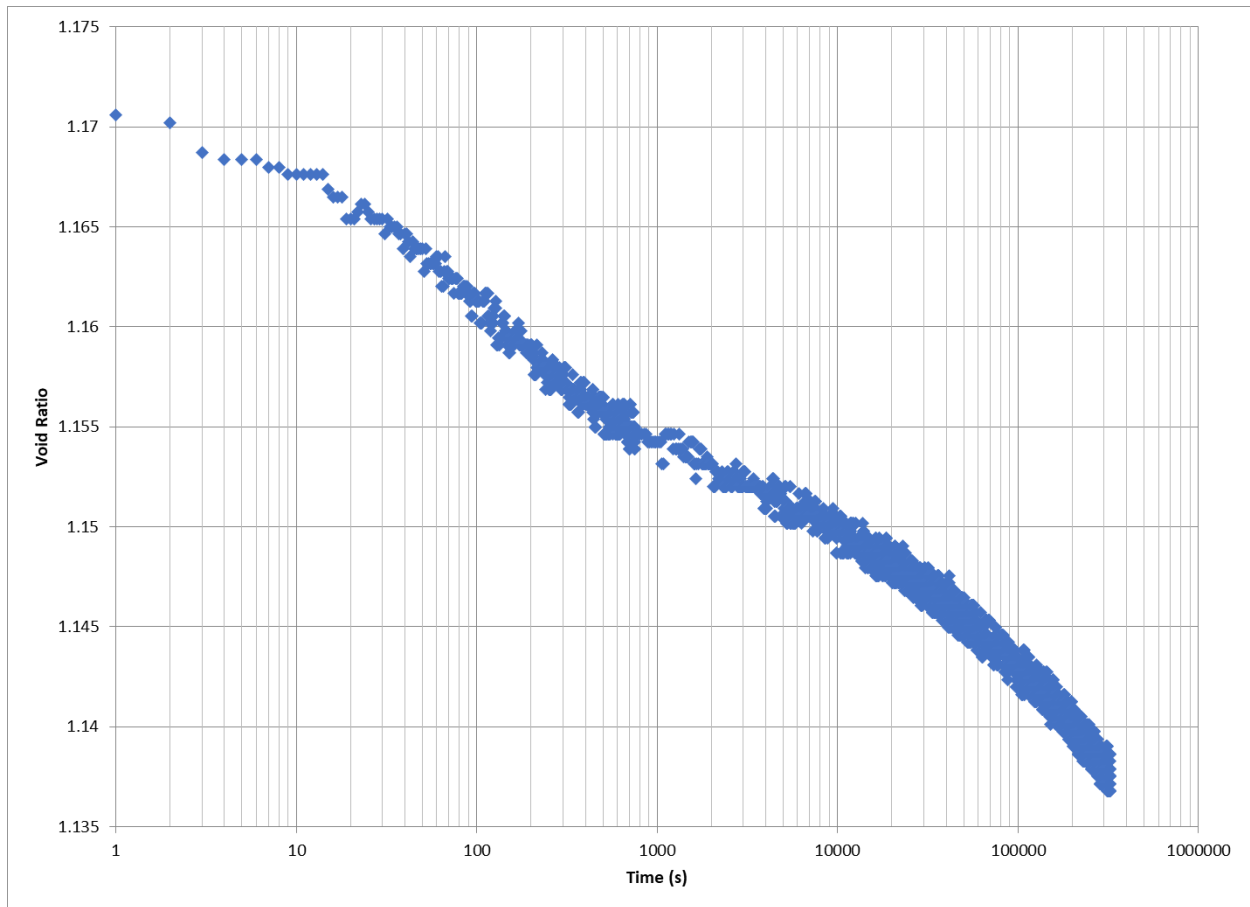


Figure 3.9. Time History Curve from an Incremental Consolidation increment where secondary consolidation appears to steepen with time.

Test was LIR=0.5 and from an initial increment below the preconsolidation pressure.

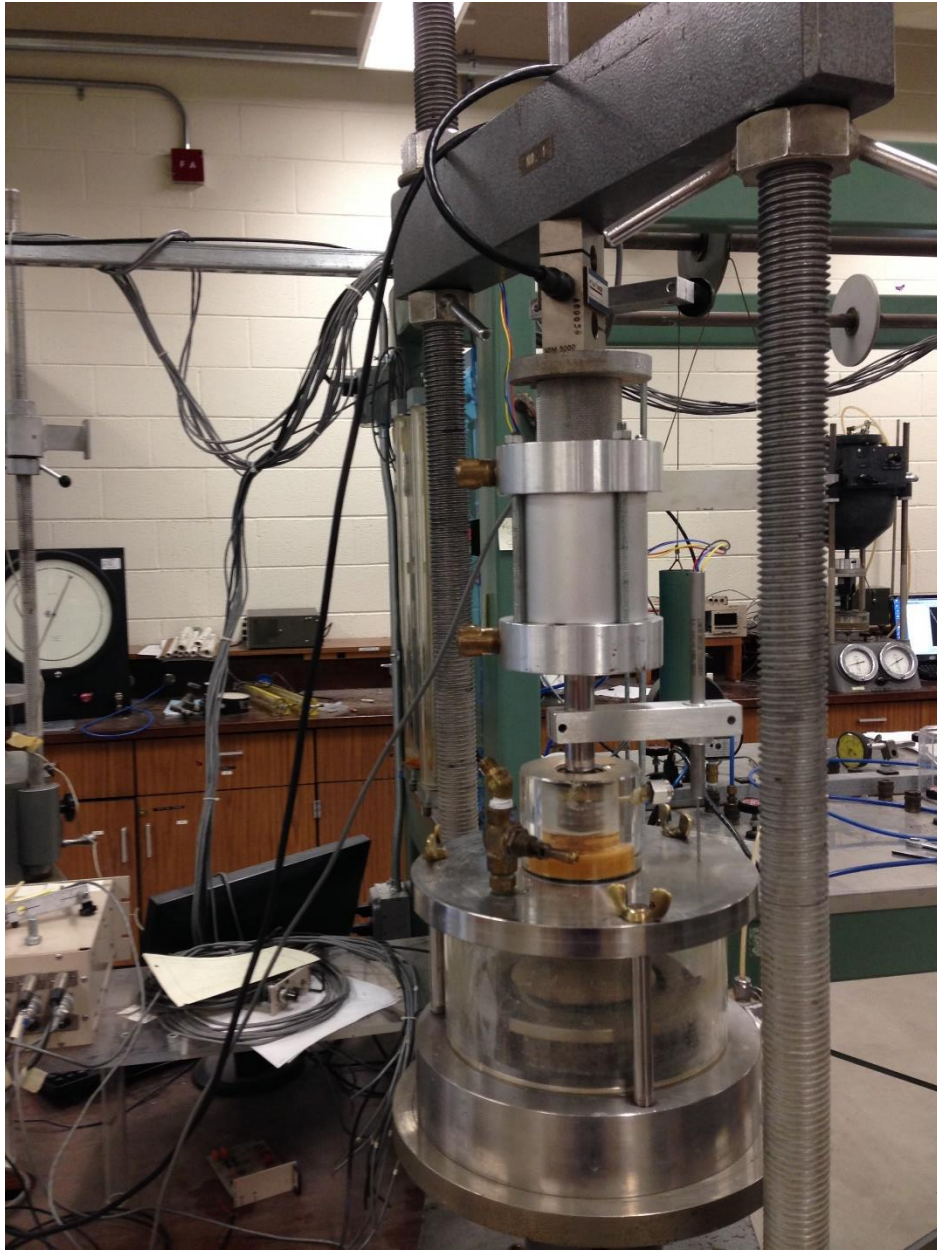


Figure 3.10. CRS load frame and oedometer.

In this set up, the LVDT is attached directly to the loading rod and a piston is installed between the load cell and the loading rod to measure secondary consolidation.

Table 3.3. CRS Testing showing Loading Rate, Unloading Rate, and number of Loadings and Unloadings at which stress levels.

Test	Loading Rate (in/min)	Loading Rate (%/hr)	Unloading Rate (in/min)	Unloading Rate (%/hr)	Unload/R ead below Pp	Low Strain Unload/R ead	Mid Strain Unload/R ead	High Strain Unload/R ead	Number of Loadings	Number of unloadings
CRS-08	0.000096	0.557	0.000096	0.557	0	1	1	0	3	2
CRS-09	0.00024	1.392	0.00024	1.392	0	0	1	0	2	1
CRS-10	0.00016	0.928	0.00016	0.928	0	0	0	1	2	1
CRS-11	0.00016	0.928	0.000032	0.186	0	0	1	1	2.5	1.5
CRS-12	0.00016	0.928	0.00016	0.928	0	0	1	0	2	1
CRS-13	0.00016	0.928	0.000032	0.186	0	0	1	0	2	1
CRS-14	0.000096	0.557	0.000096	0.557	0	0	1	1	3	2
CRS-15	0.00016	0.928	0.00016	0.928	0	0	0	1	2	2
CRS-17	0.00016	0.928	0.00016	0.928	0	0	0	1	2	1
CRS-18	0.00016	0.928	0.00016	0.928	0	0	1	1	2	2
CRS-19	0.00016	0.928	3.2E-5/1.6E-4	0.186/0.928	0	1	0	1	2	2
CRS-20	0.00016	0.928	0.00016	0.928	1	1	0	1	4	3
CRS-21	0.00016	0.928	0.00016	0.928	1	1	1	1	3	4
CRS-22	0.00016	0.928	0.00016	0.928	1	1	0	1	3	3
CRS-23	0.00016	0.928	0.00016	0.928	1	1	1	1	4	4
CRS-24	0.00016	0.928	0.00016	0.928	1	1	1	1	4	4
CRS-25	0.00016	0.928	0.00016	0.928	1	0	1	1	3	3
CRS-26	0.00016	0.928	0.00016	0.928	1	1	0	1	3	3
CRS-27	0.00016	0.928	0.00016	0.928	1	1	1	1	4	4
CRS-28	0.00016	0.928	0.00016	0.928	1	1	1	1	4	4
CRS-29	0.000024	0.139	0.000024	0.139	1	0	1	1	3	3

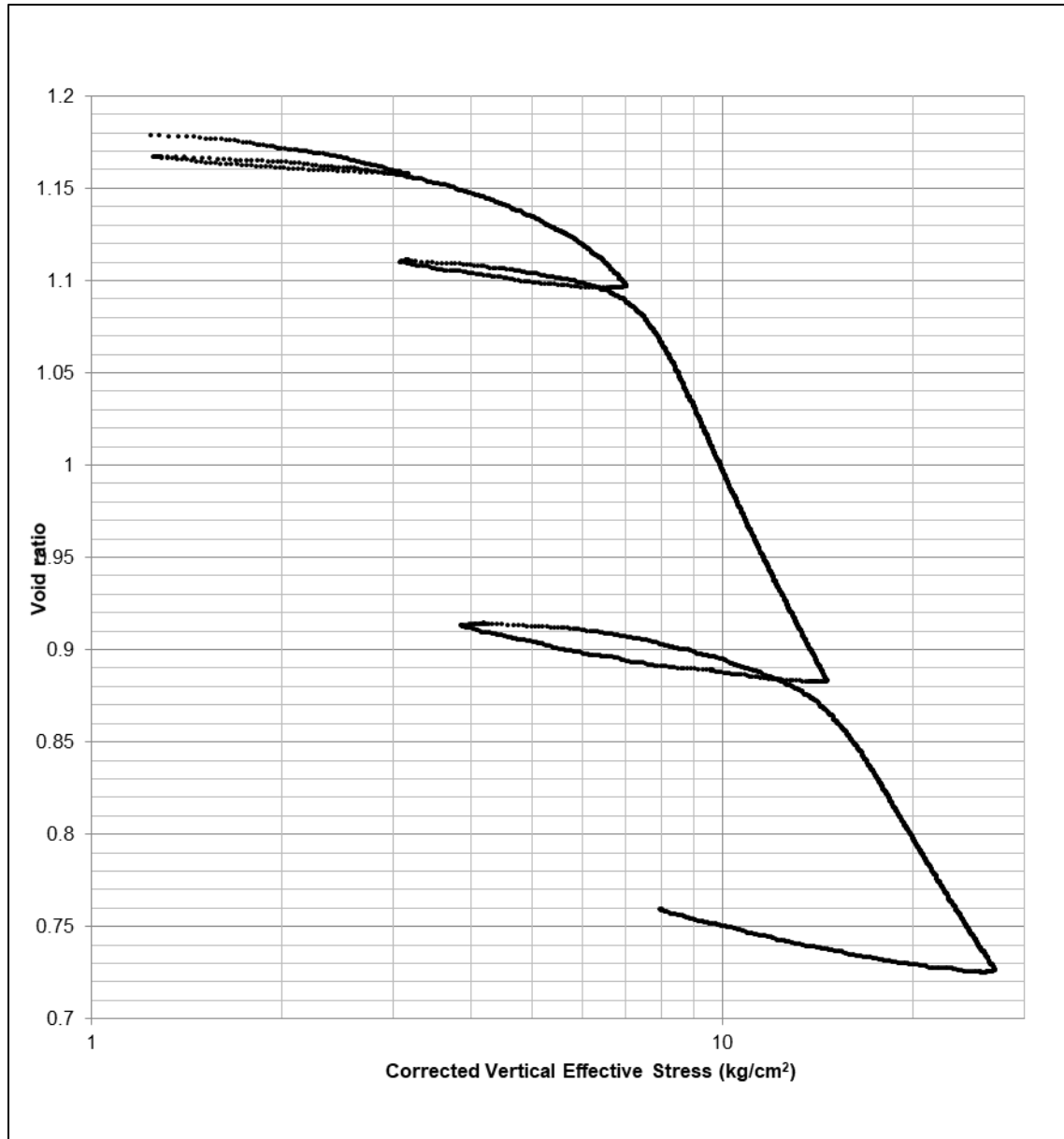


Figure 3.11. Compression Curve from CRS test, showing typical shape of OBC test.

CRS test showing initial curvature in recompression, a rounded curve around the preconsolidation stress, a generally straight-line slope in the middle stress range, and a concave upwards shape with decreasing slope at high stress. Additionally, unload-reload loops display increasing hysteresis at subsequent cycles.

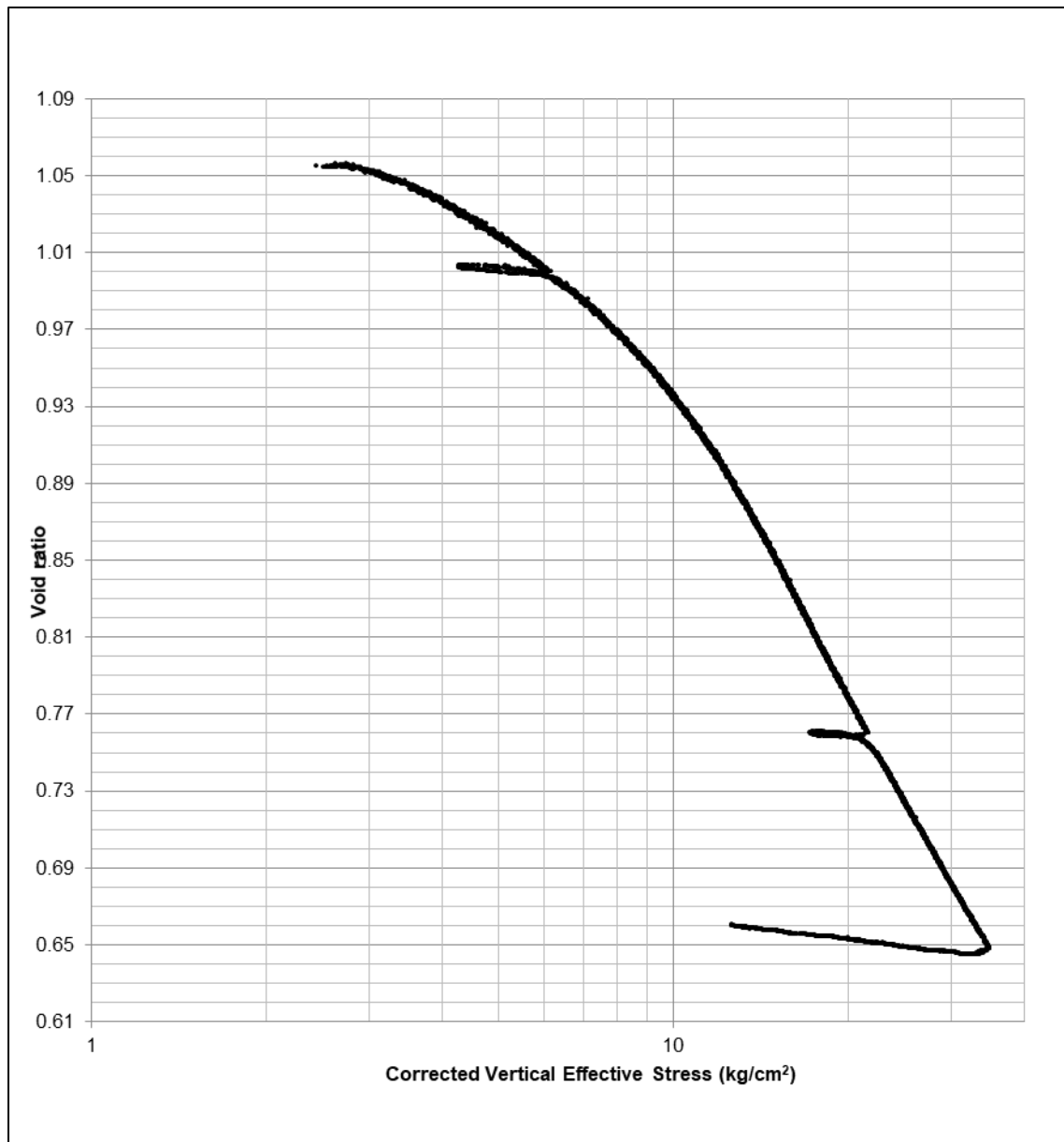


Figure 3.12. Compression Curve from CRS test, showing typical shape of Alameda test.
 CRS test showing more curvature at low stresses and a diffuse inflection around the preconsolidation stress.

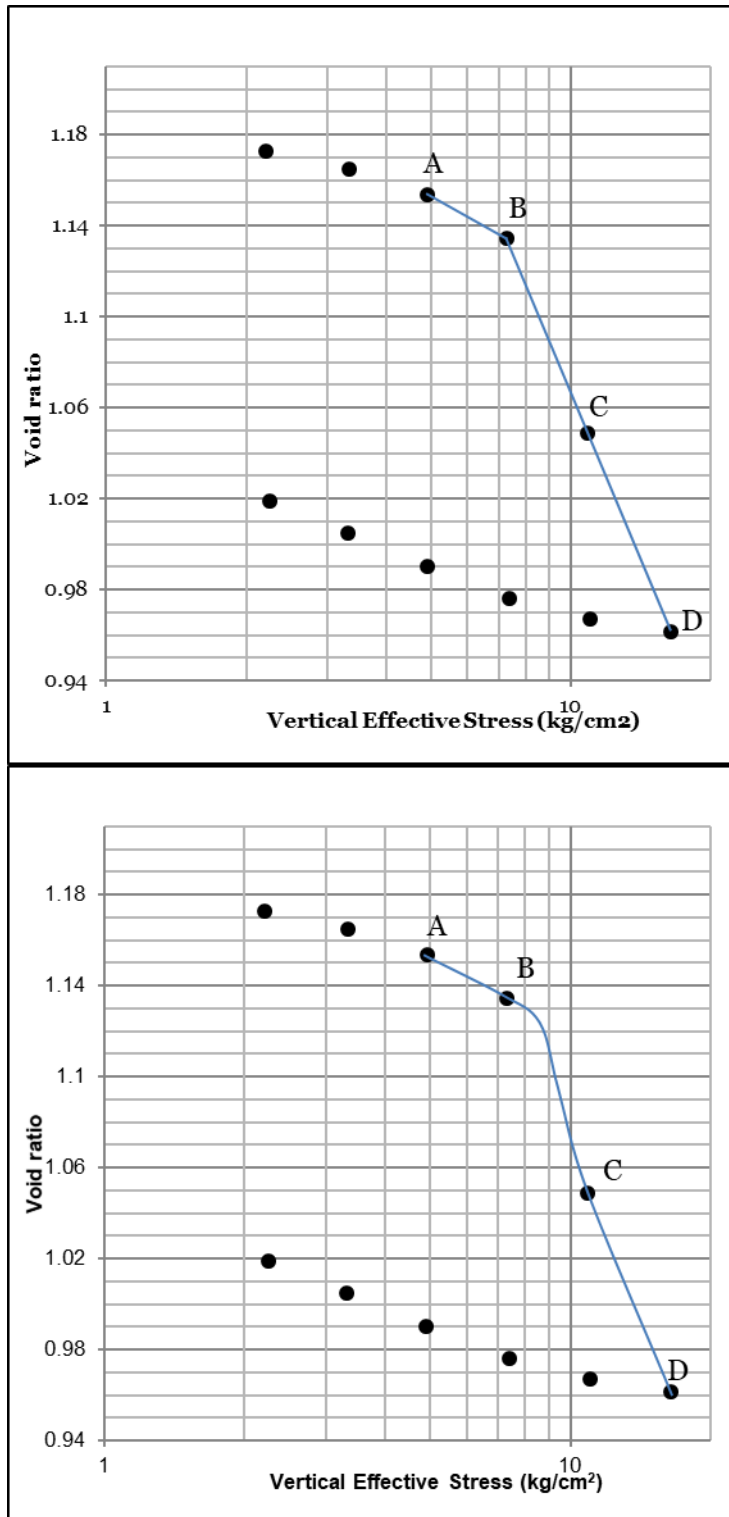


Figure 3.13. Compression Curve for IL test, showing two possible interpretations of the compression curve. Top: straight lines connect points A and B with points B and D and at point B there is an inflection point. Bottom: the curve reflects similar compression curves observed in CRS testing, with an inflection point lying between points B and C

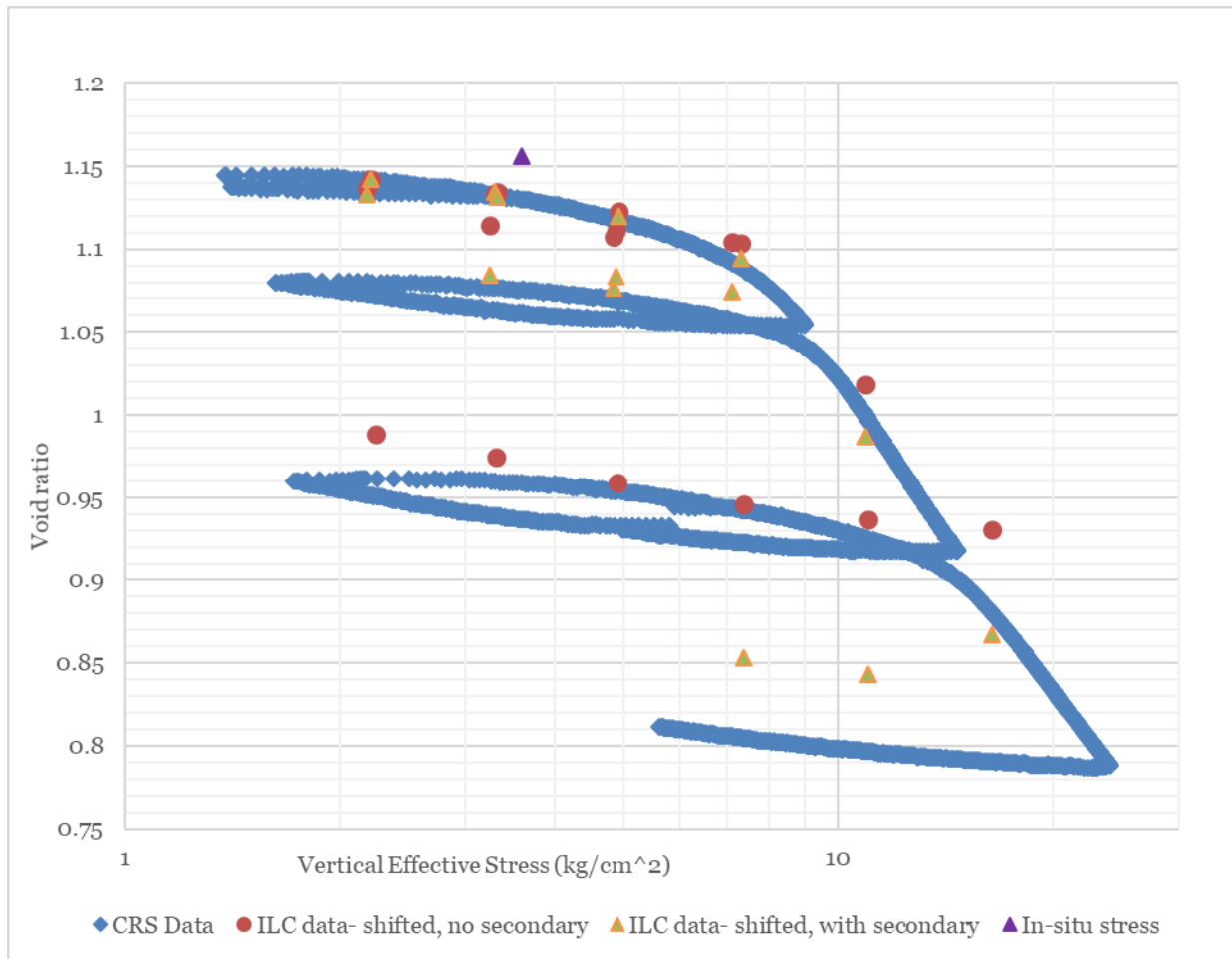


Figure 3.14. Comparison between CRS data and IL data, both excluding and including secondary compression. The IL data in this chart has been shifted, such that the initial void ratio is equal to the CRS data and the IL data is from Procedure 1, log of time increments

4 CONSOLIDATION RESULTS AND INTERPRETATION

4.1 Introduction

Stress history and consolidation parameters of OBC were a main focus of this research project. Paired CRS and IL tests were performed following the methods described in Chapter 3 so that complimentary consolidation data could be gathered from the same samples. The following sections describe the findings and the results from consolidation testing, in addition to insights gained regarding consolidation testing procedures for the project materials and the consolidation properties of the subsurface materials at the project site.

4.2 Preconsolidation Pressure

Of all the results derived from consolidation testing, an estimate of preconsolidation pressure is most often the primary focus of commercial testing and the main motivation for testing by industry. The following sections describe the methods used to evaluate preconsolidation pressure from the lab and testing results on the project materials, the accuracy of those methods, recommendations for using the methods with project materials, the results of the testing and how they compare with other testing, and implications regarding stress history of the materials.

4.2.1 Methods of Evaluating Preconsolidation Pressure

Even though preconsolidation pressure, P_p or σ_p' , is an important parameter for engineering design, the basis for our understanding of preconsolidation pressure is the simplistic bilinear model of soil consolidation behavior as presented by Casagrande (1936). More recently, some authors have described the preconsolidation pressure as a yield stress where, below this pressure, observed vertical displacements of the soil under stress are relatively small (Becker, et al., 1987; Onitsuka et al., 1995; Boone, 2010). And above the yield stress, the soil experiences greater stresses than it has previously undergone, so vertical displacements under these higher stresses will be greater. An example of a typical CRS test from this research project is shown in Figure 3.11 with the portions of the curve noted.

Determining an accurate value of the preconsolidation or yield stress is very important for many engineering problems and is also a component of calculating the Overconsolidation Ratio (OCR), which is a simple numerical characterization of the stress history. The OCR is used as an input parameter for a variety of engineering models and parameters, such as SHANSEP strength parameters (Ladd and Foott, 1974). Accuracy of preconsolidation pressure is thus important on its own but also as an input for other engineering problems. But preconsolidation pressure is often presented as a singular value determined by one method, the Casagrande method. In contrast, different methods or different ways of presenting the data may suggest a range of values of preconsolidation pressure.

While not as well known as the Casagrande method, there are a wide variety of methods available for evaluating the preconsolidation pressure. Other workers have evaluated the effectiveness of these methods while often also providing new methods [Becker, et al. (1987); Onitsuka et al. (1995); Grozic, Lunne, and Pande (2003); Boone, et al. (2010); Umar & Sadrekarimi, (2017)]. The methods generally are based on observations of bilinear consolidation behavior and involve a graphical construction. Where they differ is usually in how the consolidation data is plotted, which may be in semi-logarithmic space, bilogarithmic space, using calculated modulus values, or calculated work per unit volume values.

In this research project, several methods for evaluating preconsolidation pressure were used and evaluated. Because of the importance of stress history for the research project, multiple methods to determine preconsolidation were used for every test in order to assess variability and check the consistency of the data. Additionally, a set of data was evaluated with a wide range of methods, including Casagrande (1936), Pacheco Silva (1970), Becker et al. (1987), Oikawa (1987), Onitsuka et al. (1995), and Boone (2010). A set of data was also evaluated where the preconsolidation pressure was known due to stress imposed during testing. In the course of evaluating these methods, it was noted that some unique aspects of the specimens and the testing procedures can make preconsolidation pressure difficult to calculate. A discussion follows that explains the methods used and the results of the analyses using this research data.

It should be noted that this is not a definitive list of methods, as there are other notable past methods, like Janbu (1969) and Butterfield (1979), not discussed. Additionally, some workers are still developing new methodologies [Carneiro, Gerscovich, and Danziger, (2018); Soltani, Taheri, Deng, and Azimi, (2019)].

4.2.1.1 Characteristics of Compression Curves that Impact Preconsolidation

As discussed in Section 3.4, several aspects of the compression curves produced in this testing program make standard constructions and assumptions more difficult. These features include curvature throughout the compression curve rather than simple bi-linear behavior, a gentle break in slope around the preconsolidation pressure, and concave upwards behavior at high stresses. The compression curves from this project highlight the difficulties in using some preconsolidation methods and why they may not be preferable to use depending on testing conditions or soils.

4.2.1.2 Casagrande 1936

The Casagrande (1936) method is by far the most used and recommended method for finding preconsolidation pressure. This is because it is recommended in many design manuals (ASTM Standard D2435, 2011), as well as being the main, if only, method taught to students for evaluating consolidation tests. A general assumption by some practitioners is that it is the only method for evaluating preconsolidation pressure.

However, the Casagrande method has many drawbacks, particularly for the soils in this study. It is a graphical technique used in semi-logarithmic space that is based on identifying the point of maximum curvature of the compression curve. This has obvious issues when evaluating IL tests because the individual test increments are discontinuous on the compression curve (Figure 3.13). To evaluate the discontinuous data, one must interpolate the shape of the curve between the

discrete points. The subsequent steps of identifying the point of maximum curvature and constructing the graphical solution will depend on the result of the interpolation. Some practitioners will tend to choose the point of inflection at a data point while others may draw in a “reasonable” continuous compression curve to connect the data. The tendency to choose a data point, such as point B in Figure 3.13, may bias the preconsolidation pressure to a lower value.

Even for continuous CRS data, finding the point of maximum curvature can be difficult (Figure 3.12). In this research, some of the deep soils show a gentle curve where the soil moves from recompression to normally consolidated. No sharp inflection point can be easily identified, so one must choose an arbitrary point or possibly choose a range of values between which the inflection point lies. Due to the logarithmic scale, this can lead to a high degree of potential error. Additionally, an observation by Clementino (2004) shows that scale effects the construction, so the estimated preconsolidation pressure may even depend on the scale ratio to which the data is plotted.

The main advantage of the Casagrande method, and likely the reason that it is so commonly used, is that it only requires a compression curve to perform the construction. No other testing data is needed, like initial void ratio, in-situ vertical effective stress, computations of slope indices, etc. Nor does the data need to be reprocessed for something like work energy or does the data need to be re-plotted in another format. This has a consequence in the consulting industry because consultants often review test data from other consultants or laboratories and so do not have the full testing data. Additionally, even when consultants run tests, they still may only receive plots of consolidation data, often in strain format, and not the full testing data or electronic files. This is because many consultants do not run their own tests and outsource testing to outside labs. Even in-house testing may present similar outputs as outside laboratories because of the standards-based requirements of commercial laboratories.

The Casagrande method was used to process all the testing data in this research project because it is widely accepted in the consulting industry. As a benchmark value, it was important to calculate, but was not generally used to find other values or parameters. When compared to the Pacheco Silva (1970) and Becker et al. (1987) methods, the predicted values of preconsolidation pressure from the Casagrande method were generally higher. Of note is that both Casagrande and Pacheco Silva methods used the same straight line construction continued from the normally consolidated region. For the Casagrande method, the intersection point with the straight line is controlled by the estimated point of maximum curvature. For the Pacheco Silva construction, the intersection point with straight line is controlled by the initial void ratio. It is possible that these controls on the construction may bias the Casagrande estimate to later portions of the curve than the Pacheco Silva estimate. The value of preconsolidation for the Casagrande method, using the Pacheco Silva method as a baseline value, typically up to 10% higher.

4.2.1.3 Pacheco Silva 1970

The Pacheco Silva (1970) method as explained by Clementino (2004) is straightforward and easy to use on plotted data. It involves a construction that depends on knowing the initial void ratio and fitting a straight line to the normally consolidated portion of the laboratory compression curve. The method is quick to use, on plotted data as well as in a spreadsheet. The method is repeatable

and consistent between users (Clementino, 2004). The method works equally well for IL and CRS data, making comparisons between an IL test and a CRS test easier because additional uncertainty from the interpolation method itself has been removed. The Pacheco Silva method also skips over the recompression portion of the compression curve. This is advantageous because recompression should be where the greatest effects of disturbance are observed. Because the method does not depend on a recompression slope like in other methods, one avoids having to choose a recompression slope, whether from the in-situ vertical effective stress or at some other loading point. As discussed below in Section 4.4, there are many valid reasons for considering a best fit for a recompression slope, but it is not needed to perform the Pacheco Silva method.

However, several issues can make the Pacheco Silva method difficult to use. The initial void ratio must be known and it would be preferable to have the data plotted in void ratio-stress space instead of strain-stress space, which is often more popular in practice. Many practitioners assume that where strain equals zero corresponds to the initial void ratio. However, changes to the sample during seating or soaking may not be accounted for at the start of testing. It is possible to back-calculate a reference strain value that corresponds to the void ratio, but this can be a rough approximation as well as introduce uncertainty to the method.

While the method does work for both IL and CRS tests, it works much better on CRS tests because of the continuous data. With discontinuous IL data, one must still decide what the shape of the curve looks like between increments (Figure 3.6). This can add some additional uncertainty to the test, dependent of the unknown continuous shape of the IL compression curve.

Grozic, Lunne, and Pande (2005) in their reply to Clementino observe that there can be inconsistency in estimating the straight line portion of the compression curve for very rounded compression curves when using the Pacheco Silva method. In an experiment, they found that values of estimated preconsolidation pressure depended on individual interpretation of the method on testing data. It appears that the data with the most difficulty was from very highly overconsolidated samples. Boone (2010) also observed that some of the variability in fitting the straight line for this method may also be scale-dependent. For this research project, there could be some ambiguity in fitting this straight line because of the concave upward shape at high stress. But because the CRS data generally had a well-defined straight line segment in the normally consolidated range that represented the maximum slope, this is where straight lines were fit. As observed elsewhere, for IL testing with sparse data, more interpolation between points may underestimate the slope in the normally consolidated range. Fitting a straight line to the ILC data appears to give a very high degree of precision, but the accuracy of these constructions is unknown because the accuracy varies depending on relation between stress increments and the true preconsolidation pressure. The unknown accuracy of fitting these lines to IL data may contribute to discrepancies in calculating preconsolidation pressure on specimens from the same sample using the different test methods.

The Pacheco Silva method was used to evaluate all the of consolidation testing in this research project. A major advantage of the method is that it works well on both IL and CRS data and a key component of the research was to use both test methods together to fully evaluate consolidation characteristics of OBC and Alameda soils. This method also does not depend on the initial portion of the compression curve or a determination of a representative recompression index or slope. This

was advantageous because the majority of the tested specimens show a gradual slope between recompression and normal consolidation. It was also helpful not to have to choose a reconsolidation slope, because the variability of recompression slope is another topic evaluated in this project (Section 4.4).

The preconsolidation pressures calculated with the Pacheco Silva method also appeared to generally be an intermediate value, neither the lowest nor the highest, as compared to other methods. It is noted above that the Pacheco Silva method tends to produce lower estimate of preconsolidation pressure as compared to the Casagrande method, possibly because of the portions of the curve that the construction is controlled by.

For the reasons above, in this research project, the preconsolidation pressures calculated with Pacheco Silva were generally used to calculate further parameters and is the value used when another method is not quoted. It is possible that other choices may have been made depending on the motivations of the study. But as a general study of deep clay soils, OBC and Alameda in particular, this appeared to be the best method to use for this project.

4.2.1.4 Becker et al. 1987

The Becker et al. (1987) method for evaluating preconsolidation pressure consists of a calculation of work energy performed during consolidation testing and a construction plotted in cumulative work per unit volume versus effective stress space, an example of which is shown in Figure 4.1. The preconsolidation pressure is defined as the intersection of a straight line fit to the initial portion of the curve and a straight line fit to the post-preconsolidation pressure range of the curve. While this method is another that is dependent on a construction, it is appealing because it approaches preconsolidation differently than a compression curve construction. Because the method is based on a computation of work per unit volume, finding the preconsolidation pressure in this way allows for some variability in methodology versus other graphical methods. Additionally, the construction is performed in linear stress space, so the difficulty of accurately interpolating in logarithmic space is avoided.

In the original Becker et al. paper, IL data is used to document the methodology and the CRS testing techniques are not discussed. However, the Becker et al. method is commonly used with CRS testing data, likely because CRS data is continuous and a work energy plot can be easily programmed into a spreadsheet. However, there is no reason that discontinuous data from IL testing is incompatible with the method and would be a good additional method to use to determine preconsolidation pressure for IL testing.

The Becker et al. method is not that commonly used in consulting work for similar reasons noted previously. Key among them is that one must have the testing data to compute and plot the work per unit volume curves. When testing data is only provided as compression curve plots or when reviewing tests performed by others, this data is often not available.

In particular for this research project, the Becker et al. method has some features that appeal for deep samples, as well as some that make it more challenging to use for these materials. Interestingly, the paper notes the difficulty of using traditional methods like Casagrande for samples that have “rounded” compression curves. They note that the rounded curves have been

taken as evidence of soil disturbance, but suggest that “[t]his may not always be the case and rounded $e - \log$ stress curves may equally represent real soil behaviour.” In this research project, the rounded compression curves are present in many tested specimens with low sample disturbance values (Section 4.7), which supports this observation.

The Becker et al. method, like the other construction-based methods, does require that one fit straight lines to the curved portions of the work energy curves. Boone (2010) notes that “[t]he strain energy density (‘work’) approach is also somewhat subjective in the determination of the ‘best-fit’ linear interpretations of the cumulative straight energy density and stress plots.” He also notes that some scale effects can be observed when fitting lines to the data. This is observed in the research data where the concave upwards shape of the compression curve is reflected in the work energy plots as a concave downwards shape (Figure 4.1).

Curvature is apparent in the initial portions of the curve (Figure 4.2), especially depending on scaling. Becker et al. suggests that in the work method, for overconsolidated clays there is a portion of the work per unit volume plot between “pre-yield” and “post-yield” stresses that deviates from a linear trend around the in-situ vertical effective stress. Thus, the construction to find preconsolidation pressure for an overconsolidated clay should fit a straight line to the initial portion of the curve, below the in-situ vertical effective stress. This provides moderate help in fitting the initial line by constraining the segment to before the in-situ vertical effective stress, but even this portion shows curvature when zoomed in (Figure 4.2).

Just like in the compression curve plots, many of the tested specimens show a concave downwards shape in the work per unit volume plots in the “post-yield” portion of the test, as well (Figure 4.2). For the data in this project, there is a fairly consistent straight line segment of maximum slope that can be used for the construction. As long as the data is properly plotted, this portion of the construction is straight-forward for CRS data. As noted for other methods with sparse IL data, the straight-line segment may underestimate the slope.

Of particular note for using the Becker et al. method for this research project is that all the work energy should be accounted for beyond the seating stress. Because the soaking stresses were much higher than seating stresses and above the seating stress recommended in the ASTM methods, additional work was performed before the initial loading in CRS or the first increment in IL. This is a consideration for any deep samples that use a high soaking stress, but is easily accounted for by keeping track of all loads and height changes after the seating stress. The additional work should be added to the work calculated during the test. For this testing data, it was found that the effects of this additional work energy were low, less than about 5% the estimate of the preconsolidation pressure without the additional initial work. Accounting for the additional work energy at the initial portion of the test tended to give a slightly lower estimate of the preconsolidation pressure because of how the initial work shifted the curve.

The Becker et al. method was used to estimate preconsolidation pressure for all of the CRS testing and some of the IL testing for this research project. When comparing the Becker et al. method to the Pacheco Silva and Casagrande methods, there was some variability, but, generally, the preconsolidation pressure predicted by the Becker et al. method was lower than the other two

methods. The range was approximately up to 10% lower than the Pacheco Silva method, when normalized by the Pacheco Silva estimated value.

4.2.1.5 Oikawa 1987 and Onitsuka et al. 1995

The Oikawa (1987) and Onitsuka et al. (1995) methods may be grouped together as bilogarithmic construction methods and are based off the original method of Butterfield (1979). All three methods estimate the preconsolidation pressure at the point where a straight line fit to the initial portion of the compression curve and a straight line fit to the “post-yield” portion of the compression curve meet. Where they differ is that Butterfield plots the natural log of the void ratio on the y-axis and the natural log of stress on the x-axis, Oikawa plots the common log of the void ratio versus the common log of the stress, and Onitsuka et al. plots the natural log of void ratio on the y-axis and the common log of stress on the x-axis. Each of these methods have been modeled as improvements of the former, though others, (Umar and Sadrekarimi, 2016), have found the Oikawa method to provide the most accurate estimate. These methods are straightforward and easy to use, especially for IL plots. However, one must have the testing data for individual increments or continuous CRS data in order to do the construction. This may be a problem when one only has plotted testing data or is reviewing consolidation test performed by others.

Both Oikawa and Onitsuka et al. appear to be developed using IL testing and use IL testing to validate the methods. For this research project, it was found that the methods were straightforward to use and provided fairly non-ambiguous results for IL data (Figure 4.3). However, using the methods with CRS testing data was more complicated. As discussed in other sections, the CRS testing data is generally curved in all portions of semi-logarithmic space. When plotted in bilogarithmic space, portions of the curve remained curved, especially the initial loading segment before the “yield” stress. In particular, sometimes the very initial loading appeared nearly flat and somewhat linear (Figure 4.4). On inspection, it appears that the initial flat portion may represent loading effects related to the seating stress.

As a result, it is not clear how to fit the first straight line segment, to the initial portion of the curve, when doing the construction on CRS test data. In Figure 4.4, it can be seen that any number of straight line segments can be fit to the initial portion of the curve. Straight lines that fit just the very initial segment produce values that seem generally low compared to other methods for finding preconsolidation pressure. Fitting the line to this section appears to be incorrect, especially if the flat response is due to the effects of the soaking stress.

While no guidance is given by the authors as to how to proceed, in this study it was found that a straight line fit through the middle portion of the initial recompression curve produces an answer more consistent to other methods or for when the preconsolidation pressure is known. It is possible that this is because this portion of the curve that passes through the in-situ vertical effective stress. The in-situ vertical effective stress is significant in the stress history of the soil and important for the Becker et al. and Boone (2010) methods. Likewise, the initial void ratio is used as a part of the Pacheco Silva method, so initial field conditions may be a guide for analyzing consolidation data.

For this study, the Oikawa and Onitsuka et al. methods were found to be very easy to use for IL data and a good way to provide insight into preconsolidation pressure by using a variety of

methodologies. But because of the ambiguity in assessing the CRS testing data, it was not found to be a good way to evaluate these samples for preconsolidation pressure. Potentially, CRS testing data may be less ambiguous with shallower samples or samples that show more bilinear behavior in compression curve plots.

4.2.1.6 Boone 2010

Boone (2010) is one of the newer methods proposed for evaluating preconsolidation pressure. The method is also a construction-type method within semi-log void ratio and effective stress space. However, the method provides guidance on where to choose points for the construction and is based on computations that can be programmed for accuracy. Like many methods, the construction generally defines the preconsolidation pressure as a point where the intersection of a line through the initial portion of the compression curve meets a line drawn through the steepest portion of the curve beyond the “yield stress.” But unlike other methods, Boone carefully defines where to draw these lines and how to use actual data points to compute the preconsolidation pressure instead of interpolation. A potential downside of this method, as with the majority of methods described, is that one needs full access to the testing data and not just plots of the compression curve.

For the initial straight line segment, Boone defines it as passing through the portion of the curve at the in-situ vertical effective stress as a slope equal to the recompression index. The recompression index here is defined by an unload-reload cycle, “preferably conducted at stresses above and below σ'_{vo} and less than σ'_p ” at the approximate in-situ stress and before the preconsolidation pressure. Defining these points and slopes is an important distinction of the Boone method because other methods are less clear as to which points and slopes should be used to define the initial segments of the construction for a consolidation test. For IL testing, Boone provides further guidance as to how to interpolate for the void ratio at the in-situ stress if there is no increment including this point. Advantageously, the testing procedures in this research project for the majority of IL and CRS tests placed emphasis on in-situ vertical effective stress (Section 4.4). Thus, for the majority of project testing, the IL data includes an increment at the in-situ stress and both IL and CRS tests include an unload-reload cycle at the in-situ stress.

The Boone method makes no mention of CRS testing, but the method is easy to apply to the initial loading portion of consolidation as well, and it helps to avoid common issues of processing CRS data for preconsolidation pressure. As mentioned previously, in many of the CRS tests in this research project the compression curves have curvature at the initial portions of the test and at high stresses. Definition of the initial slope clarifies that ambiguity and the decision to focus on in-situ stress also means that the very initial portion of the curve is skipped over. This makes sense for this testing data, especially, because the very initial portion of the curves are possibly affected by the soaking stresses and are curved in a way that makes them difficult to fit a straight line. Additionally, the testing procedures for this project emphasized the in-situ stress, so most CRS tests have an unload-reload cycle at that point.

The second line segment is defined by the slope of the maximum compression index and passes through the final void ratio and stress of that increment. This definition makes the most sense for IL tests, but was adapted to use for CRS testing data. It also seems clear that Boone anticipated sensitive clay soils that show concave upwards shape at high stresses. In most of the CRS testing

data from this project, a fairly straight-line portion can be observed at “middle stresses” above the preconsolidation pressure. Thus, the second line for the Boone method was set using the maximum slope of this segment and the corresponding void ratio and effective stress at the end of the segment. This was simple to perform computationally by calculating a floating “compression index” using the continuous CRS data. However, it was noted that the data points that are a part of the construction should be plotted and visually verified. This is due to the continuous CRS data having fluctuations that may reflect instrument noise, especially depending on how rigorous the data filtering is performed (Figure 4.5). In this example, a local maximum slope was calculated from noisy data that does not reflect the median slope for the line segment.

The Boone method is a helpful modification of the standard construction methods in void ratio or strain versus stress space, especially because preconsolidation pressure can be computed as well as plotted graphically as a confirmation. The computed preconsolidation pressure is attractive because it can help preserve precision from the testing data. In the majority of the graphical methods, digital data, which is very precise, is used for a visual approximation of the preconsolidation pressure in semi-log space. Thus, data that has a high degree of precision from electronic instruments is reduced to a visual estimate that can vary greatly by how the person performing the construction decides to interpolate the result in semi-log space. Alternatively, the Boone method preserves the precision of the digital data. And because the construction can be plotted on the compression curve, the computed points can be verified to avoid potential outlier digital points from skewing the results. Thus, if an algorithm is set up to process the data, plotting the construction can help prevent a local maximum or minimum from erroneously being used to find the preconsolidation pressure.

The Boone method was found to work well with the data in this research project, though it required generally more data processing than the other methods. The Boone method made good use of both the precision of this research data as well as the detailed loading methods that allowed use of defined recompression indices and compression slopes.

4.2.1.7 Accuracy of Preconsolidation Methods

Most of the discussion in the previous section relates to using the methods for evaluating preconsolidation pressure on specimens of natural soils retrieved from field deposits. When evaluating this condition, the accuracy of the answer is unknown, though a likely range of values can be generally accepted based on correlations or compared with adjacent tested soils. In order to assess the accuracy of the estimate for preconsolidation pressure, many previous studies of clays are based on samples reconstituted from slurries. These slurry samples are consolidated to certain stresses to impose a stress history. This is a valid method that has been well studied, but the behavior will be different from testing a structured natural soil sample. When natural soils are used for evaluating preconsolidation, they tend to be from a handful of well-known clays, such as Leda clay or Chicago clay, and tend to be shallow samples. These clays have different consolidation properties from this study’s OBC and Alameda samples, which are deep and tend to have consolidation parameters similar to fat clays (Sections 4.3 through 4.6).

In order to evaluate the accuracy of different methods for determining preconsolidation pressure, a series of tests were evaluated using recompression loops where the preconsolidation pressure

was known. The known preconsolidation pressure was the maximum effective stress imposed on the specimen during the previous loading cycle. An example of such a test is shown in Figure 4.6. This specimen was loaded and unloaded four times: up to the estimated in-situ vertical effective stress, past the estimated preconsolidation stress to a “low-range” stress, to a “mid-range” stress, and to a “high stress.” The highlighted data consists of the third loading, from when the sample has already been loaded past the preconsolidation stress and unloaded back to the approximate soaking stress. The newly established preconsolidation pressure was 8.95 kg/cm^2 . The Casagrande (1936), Pacheco Silva (1970), Becker et al. (1987), Oikawa (1987), Onitsuka et al (1995), and Boone (2010) methods were all used to assess this known preconsolidation pressure from the subsequent reloadings and are discussed below.

While it would be assumed that using a reload loop would make determining preconsolidation easier because the disturbance was minimized, many of the methods were difficult to use in the same ways as when determining the in-situ preconsolidation pressure. As can be seen in Figure 4.6 above, the initial reconsolidation slope is still moderately curved. Methods that require a straight line fit to the initial portion of the curve can be difficult to use because of curvature, including the bi-linear methods of Oikawa and Onitsuka et al. and the work method of Becker et al. For this example, the reload loop chosen had a very linear slope in the normally consolidated region, which made the normally consolidated portion of the construction uncomplicated. If a reload loop was chosen where the normally consolidated portion of the curve exhibited either a steepening slope or concave upwards curvature, it would be important to be careful with the construction.

The preconsolidation stress predicted using the reload loops was fairly close to the known maximum consolidation pressure, ranging up to approximately 8% from the known value. The precision was better than when evaluating the in-situ preconsolidation pressure, likely because the reload loops were less disturbed than the initial loading loops, because the reload loops generally had a flat curvature. The Casagrande and Boone methods both appeared to generally overpredict the preconsolidation pressure while the Pacheco Silva, Becker et al., Oikawa, and Onitsuka methods all underpredicted to slightly overpredicted the preconsolidation pressure.

Other workers have also reviewed the accuracy of the various preconsolidation methods, including a recent paper by Umar and Sadrekarimi (2016). Similar to this study, they assessed the methods by using reload loops of natural soils as well as utilizing CRS testing in addition to IL tests. They performed 30 CRS and IL tests on three different natural Canadian silty clays, as well as included data from some prior studies to supplement their data because their data tended to have low plasticity. Umar and Sadrekarimi ranked the eleven methods evaluated in their study by their root mean square error (RMSE), though they avoided assessing the methods on usability depending on the samples or the testing data. They found the bilogarithmic methods, Oikawa in particular, to provide the most accurate estimations. Boone was also considered favorably. On the other hand, Becker et al., Casagrande, and Pacheco Silva were rated lower, with Pacheco Silva ranking in lower accuracy than Casagrande. Additionally, they found that all the methods overestimate preconsolidation pressure. This implies that all methods would be to some degree unconservative when used to predict consolidation settlement.

The results of Umar and Sadrekarimi are consistent with some of the results of this study, though the impact of the variation in soil specimens and testing techniques may explain where observations differ. As mentioned previously, some methods for determining preconsolidation are difficult to use or can produce a variety of estimates depending on how they are used with the testing data from this study. While a method may be classified as generally more or less accurate for a group of soils, it may be possible that a particular soil may have its own skew or methods that are more applicable to the data. Umar and Sadrekarimi's study includes samples that are generally less plastic, much shallower, and includes IL testing into their RMSE calculations, which may explain some of the differences from observations made in this study. Some of these samples will be more ambiguous to assess and possibly have lower sample quality as compared to this project's soils. As explained in previous sections, preferred methods for estimating preconsolidation pressure depend on the shape of individual compression curves. A method that may work well for one soil may not work as well for a soil with a different compression curve shape. Similarly, using RMSE to assess accuracy can overly weigh outliers. Outliers in geotechnical laboratory testing are quite common and may reflect many issues, especially sample quality. IL testing also encourages interpolation, which can contribute to inconsistencies. Thus, using RMSE to assess "more accurate" preconsolidation methods can be helpful but may also obscure that some methods will work particularly well for some soils, but not all.

4.2.1.8 Discussion

While an estimate of preconsolidation pressure is one of the main motivations for performing consolidation testing, often not much thought is put into the choice of method used or acknowledgement that testing conditions can have a large impact on the preconsolidation pressure estimate. While accuracy is the most important concern of any chosen method, for in-situ soils it can be almost impossible to be sure of the accuracy. It is critical to have a method that is repeatable and not arbitrary. A method should be recognized for its strengths and weaknesses depending on both the testing conditions, the sampling of the soils, and the characteristic compression curves for different kinds of soils. Lastly, even if a method may be considered to be accurate when assessed against laboratory built or well-sampled natural soils, it is possible that an engineer evaluating non-ideal consolidation tests of natural soils may seek a method that provides a generally reasonable, but conservative estimate of preconsolidation. A method that may tend to underpredict preconsolidation pressure may be preferable to one that generally overpredicts.

An aspect of consolidation testing particular to IL testing is how the compression curve is computed, whether Procedure 1 or Procedure 2 and how secondary compression is handled. As discussed in Chapter 3, Procedure 1, the log of time method, will produce compression curves with more strain or change in void ratio than Procedure 2, the square root of time method. Additionally, secondary compression that accumulates during individual consolidation increments will contribute to more strain or void ratio change in the compression curve if it is not removed. The estimates of preconsolidation pressure all rely on compression curves, so variability in how the curves are computed will also vary estimates of preconsolidation pressure. Because of the relationship between increasing strain or void ratio in curves, the lowest estimates of preconsolidation pressure will be with Procedure 2 curves with secondary compression removed. Procedure 1 curves with secondary compression removed will suggest slightly higher preconsolidation pressure. Lastly, both methods with secondary compression included will suggest

higher preconsolidation pressure, dependent on the amount of accumulated secondary compression during testing.

As noted in Chapter 3, the shape of CRS compression curves incorporates some amount of accumulated secondary compression. CRS curves plotted against IL curves from the same sample tend to lie somewhere between an IL curve with no secondary compression included and an IL curve with all the secondary compression included. Another contribution to uncertainty in estimating preconsolidation pressure can be this relatively unknown contribution of secondary compression strain to the shape of the compression curve.

Mentioned throughout the discussion of IL testing has been the limitations of sparse data due to the individual increments that make up a compression curve. However, sometimes the sparse data from IL testing can suggest uncomplicated conclusions. Constructions based on IL data can often appear to contain straight line segments. The same sample tested by CRS testing usually displays a much more complicated compression curve. IL compression curves should be understood to be simplistic representations of in-situ consolidation behavior. Constructions that fit IL data well may be precise to the tested data, but may not accurately represent the soil's consolidation behavior (Figure 3.13).

4.2.1.9 Recommendations

For best practices processing consolidation data, several methods should be attempted to understand the range in uncertainty. Using several methods helps prevent one aspect of the testing conditions or the resulting compression curve from overly influencing the preconsolidation estimate. Preconsolidation pressure is similar an epistemic parameter because the value is unknown and may depend on the model used. Similar to other fields that commonly deal with epistemic uncertainty, like seismic hazard analysis, a similar approach can be taken to address the epistemic uncertainty of preconsolidation pressure by using several models and combining the results using weighting factors.

Another best practice when assessing preconsolidation pressure is to take care that constructions are performed with precision. Because most data is now digital, constructions can also be performed digitally. In the past, scaling effects might be forgivable when plotting options were limited. In the current era of spreadsheets and numerical computing, data can be inspected at any scale and with a high degree of precision. Similarly, the result of a construction can easily be plotted along with the construction in order to confirm data interpolation, especially when in log space.

4.2.2 Results

Consolidation testing results showing preconsolidation pressure and OCR are plotted in Figure 4.7. The plots only include results from CRS testing and using the Pacheco Silva method for determining preconsolidation pressure. As discussed in Section 3.2.2 above, the IL testing performed included significant secondary compression, so the results of this testing were highly variable depending on the duration of increments, as well as how the data was processed and interpolated. Additionally, as discussed in Section 4.2.1.3, the Pacheco Silva method was used for these results because of its consistency and applicability to the tested data. Figure 4.7 includes a

generalized estimate of in-situ effective stress, however, as discussed in Section 2.5, less generalized values were used in the testing based on actual field conditions of each sample. In the following sections, comparisons are made with GDR data (Section 1.3). The testing in this research project was supplemental and more detailed than the testing performed for design. As such, comparisons between the two data sets are helpful because the total number of tests are much more in the GDR and show a wider range of values. One CRS test was performed on a specimen that did not reflect YBM properties (Section 2.6), so those results were not included in the following sections because the values were outliers.

Young Bay Mud (YBM) was not a main focus of this testing program, but several tests were run in order to compare with the results of the GDR as well as to compare with the well-known Hamilton Airfield YBM testing (Bonaparte and Mitchell, 1979). As can be seen, was a narrow range of results because of the small number of tests, with preconsolidation of approximately 4.2 kg/cm², and an OCRs of 4.2. This is consistent with the wide range in values observed in the GDR testing but in contrast to the Hamilton samples. Hamilton YBM as well as YBM encountered around the San Francisco Bay tends to have a several-foot-thick “crust” of overconsolidated clay, below which the profile tends to be normally consolidated and increase in strength corresponding to depth and overburden. Interestingly, a spatial distribution is observed within the YBM testing at the site and based on their relatively positions with respect to the historic 1852 shoreline. As discussed in Section 2.1.2, the 1852 shoreline is likely an arbitrary geographic reference point because the climate was changing throughout the Holocene epoch. Nevertheless, samples west of the 1852 shoreline clearly appear to be more overconsolidated than samples east of that line, with OCRs ranging from 1.6 to 3.7 in West YBM and 1.0 to 1.6 in East YBM. Samples east of the 1852 shoreline appear like Hamilton-type YBM and are even underconsolidated in places, possibly because of the in-filling actions in this area. The observations from this testing are consistent with the differences between “East-YMB” and “West-YBM” within the GDR data because these samples with relatively high OCR came from the western portion of the site.

The main focus of this research project was OBC. Preconsolidation pressure of the OBC samples ranged from approximately 6.30 to 9.0 kg/cm² with a mean value of 7.4 kg/cm². OCR ranged from approximately 1.6 to 2.4, with a mean value of 2.0. These values are consistent with the GDR values, which showed a wider range, with OCRs from approximately 1.2 to 3.6, but generally centered around similar mean values. A possible trend of high OCR values at the shallowest depths of OBC is observed in the GDR data. This could be a type of overconsolidated “crust” at the upper surface of the deposit. As described in Section 2.1.2 and below in Section 4.2.3, the OBC is in disconformable contact with the overlying deposits, so the upper surface is likely an eroded surface. As such, an overconsolidated crust might be expected. Below the layer of higher OCRs, which corresponds to elevations below approximately -90 ft (NAVD88), the OBC is fairly consistent, with OCR centered around approximately 1.7 but not showing a strong relationship to depth.

Consolidation testing data from the Alameda formation, which is called “OBC II” in the GDR, shows more variability than OBC data. For the research project, Alameda preconsolidation pressure ranged from 8.0 to 13.0 kg/cm² with a mean value of 9.9 kg/cm², while OCR ranged from 1.2 to 2.3 with a mean value of 1.7. These results are consistent with the GDR testing, which found OCR to range from 1.2 to 2.2 in this deposit. In Figure 4.7, it can be seen that there is variability

within the Alameda deposit, but it can be observed that there is possibly a trend of decreasing OCR with depth. Surprisingly, some samples appear to be only slightly overconsolidated within the GDR testing.

4.2.3 Implications to Stress History

Estimates of preconsolidation pressure from consolidation testing combined with what is known about local geologic history can give insight into the stress history of the site deposits. Most of the samples tested were slightly to moderately overconsolidated, which can be caused by many effects. These effects include: mechanical one-dimensional, such as changes in overburden or pore pressure; desiccation; drained creep or ageing; and physiochemical, such as cementation or weathering (Mitchell and Soga, 2005, p. 329). The last three effects are both difficult to conceptualize as well as difficult to test for, especially when features like cementation might be disturbed by sampling.

The stress history of the YBM is the most straight-forward of the site materials to understand because it was deposited during the Holocene epoch in what is assumed to be a single transgressive sequence. The Hamilton Field deposit of YBM is the clearest example of a single transgression of YBM, as the clay is generally normally consolidated and conformably deposited upon non-marine sands. Similarly, the East YBM at the site is normally consolidated and deposited upon sands at depth. It is important to note that there are “upper” and “lower” YBM in the Eastern portion of the site with sand deposited in between. But because there is no indication that in-situ stresses are anything but hydrostatic, the sands are likely conformably deposited along with the clays, possibly due to a change of currents or source deposits.

The stress history of the West YBM is more complicated, mainly because of its presence west of the historic 1852 shoreline. This portion of the San Francisco peninsula is not known for being uplifting and is likely a part of a subsiding block (Bürgmann, Hilley, Ferretti, & Novali, 2006). The San Francisco block has been a topographic low for at least the last several million years. Thus, the most likely explanation for the deposit is a local sea level regression that produced a “Mid-Holocene” shoreline further inshore than the present (Meyer, 2015). The overconsolidation in these samples from GDR testing makes sense, because they were likely exposed to desiccation and weathering effects. Additionally, historic topographic maps indicate that the elevation of this area was approximately 10 feet higher in the mid-19th century and likely contained sand dunes (Arup, 2010). This indicates that the overconsolidation observed can also be partially contributed to removed overburden.

Unlike the YBM, the OBC across the site is laterally more uniform and appears to show a fairly consistent OCR with depth. The OCRs, especially below approximately an elevation of approximately -70 ft (NAVD88), show a narrow and consistent range. Data profiles from both CPTs and Shear Wave Velocity testing also exhibit consistent profiles with depth. Sloan (1992) has shown that OBC was deposited in one transgressive sequence as the San Francisco Bay became deeper and colder than at present, during the last interglacial period (Sangamon). The upper contact of OBC is thought to be an erosional disconformity with the overlying materials. Thus, some of the original sequence of OBC has likely been eroded and because the OBC is not normally consolidated, the previous overburden must have been greater than the current overburden. The

project testing data supports the theory that OBC was deposited in a single, transgressive sequence with an erosional surface.

To determine how thick the original sequence of OBC may have been before the upper surface was eroded and subsequent materials were deposited, it is possible to use the estimated preconsolidation pressures from consolidation testing. To do so, many assumptions have to be made about unit weight as well as the presence of the phreatic surface. To simplify the problem, it is assumed that the OBC was deposited in a similar environment as YBM is currently being deposited. Thus, the unit weight for the estimate is a plastic marine clay with high water content and is fully submerged. With those assumptions, the depth of the overburden can be calculated using the estimated preconsolidation pressure from the individual consolidation tests. In Figure 4.8 (Left), the implied overburden from these simple calculations is plotted with depth. If the sample was normally consolidated, it would lie on the 1:1 line that is plotted. In Figure 4.8 (Right), the difference between the implied overburden and the actual depth of the sample is plotted with depth. This figure represents the additional depth of soil that would be above the current ground surface using the simple assumptions of unit weight and phreatic surface.

The YBM appears to be close to normally consolidated, so the implied overburden reflects what we understand about the depositional history of that deposit. As can be seen, there is a fair degree of variation within the OBC samples and Alameda samples. The Alameda samples show a great degree of variability, with some samples indicating less implied overburden than the OBC soils above. However, the Alameda, as discussed previously, has a complicated and mostly unknown stress history so the simple assumptions regarding unit weights and phreatic surface may not be valid.

For the OBC samples, the implied overburden thickness ranged from approximately 95 to 180 feet more than the current overburden depth with a median value of approximately 135 feet. While the implied overburden increased with depth, once the depth of the sample is subtracted there does not appear to be a strong dependence on depth, which supports the idea that the OBC was deposited in a single sequence. Importantly, it is estimated that sea level during the Sangamon interglacial was approximately 6 m (19.7 ft) higher than current mean sea level (Sloan, 1981). Additionally, as noted above, this portion of the San Francisco peninsula is not being uplifted. It is unlikely that an additional 135 feet of overburden was deposited and then removed because of these constraints. Thus, even if there was a high level of erosion during the Wisconsin stage, not enough material could have been deposited during the Sangamon, nor was the land uplifted from a lower position that would have allowed enough material to have been deposited and then eroded.

A more likely explanation for the overconsolidation of OBC is a change in phreatic surface. During the Last Glacial Maximum at the San Francisco Bay Area, the sea was more than 100 m (300 ft) lower than today, with the shoreline at the present Farallon Islands. The phreatic surface at the site could have persisted over a range of levels due to local variations in the water table and the presence of streams or seepage. However, the same assumptions used to create the profiles in Figure 4.8 can be used to model the possible phreatic surface. A schematic of two possible phreatic surfaces are plotted in Figure 4.9, as well as a schematic of the possible thickness of the original deposit of OBC and of the current conditions. The two phreatic conditions modeled are with groundwater lowered just to the top of the uniform profile of OBC, which was approximately -70

ft (NAVD88), and with groundwater lowered to some depth within the Alameda, which was set to approximately -160 ft (NAVD88). These two scenarios represent the two extreme cases for groundwater, with the OBC never below the phreatic surface and the OBC fully above the water table with the phreatic surface possibly within coarse layers of the Alameda. In Figure 4.10, the same simplified assumptions about unit weight of the overlying materials were made, however, the figure on the left has the phreatic surface at the top of the OBC and the figure on the right has the phreatic surface was set to within the Alameda formation. For the groundwater at -90 feet (NAVD88), the previous ground surface ranged from 6 to 92 feet from the present. In the case of the water table being in the Alameda, the difference in previous ground surface ranged from -12 to 34 feet from the present.

Either of the two groundwater cases may represent possible stress history scenarios, especially because some overconsolidation may be due to aging effects. Likely depositional history of the OBC at the site involved being deposited in a single transgressive sequence during the Sangamon, possibly to an elevation of 20 to 30 ft (NAVD88), for a total thickness of approximately 170 to 180 feet thick. The OBC would have been generally normally consolidated. During the Wisconsin stage, the groundwater dropped, possibly to -70 ft (NAVD88) or deeper. However, the OBC does not appear to have any characteristic oxidation that would have suggested it was ever unsaturated. When the water table was lower, there would have been erosion of the upper sequence of OBC. At this point, the OBC was overconsolidated. After this, there was deposition of the overlying materials, including the Colma sand, as well as eventually a return of a higher phreatic surface. Finally, the present Holocene sequence were deposited, but the overburden has clearly not exceeded the stresses of the original column of OBC.

The underlying Alameda deposit has experienced what both the YBM and the OBC have, with possibly additional cycles of phreatic changes and varying levels of overburden. Because of the variability in OCRs and the lack of trend with depth, it is hard to say if the Alameda represents a single depositional cycle or possibly many depositional cycles either deposited sequentially or disconformably.

4.2.4 Discussion

While preconsolidation pressure is a main goal of consolidation testing, often not a lot of care is taken regarding the assumptions made to estimate it. These include the variability between methods to estimate preconsolidation pressure, differences in constructing compression curves from IL data, and precision in estimates from graphical solutions. When presenting preconsolidation pressure results, some of this variability might be considered as an epistemic uncertainty.

Regarding OBC in particular, it seems likely from the stress history that the soil deposit is only moderately overconsolidated. Often deep clays with overconsolidation are considered to be incompressible, but OBC shows that the stress history may matter for this deposit, especially if it is loaded due to deep foundations or deep excavations.

The Alameda formation also has a surprising stress history, which is very close to normally consolidated in certain samples. While the stress increments required to put these soils into normal

consolidation are fairly high, it is possible that in the future these stresses may be a consideration. It may not be appropriate to consider that the clays within the Alameda are incompressible.

4.3 Compression Index

Compression index, C_c , is an important parameter to characterize clays because it helps to explain settlement behavior for normally consolidated materials. The following sections detail data processing and results for compression index derived from consolidation testing of YBM, OBC, and Alameda samples, as well as observations made.

4.3.1 Data processing

To find the compression index, the compression curves and estimates of preconsolidation pressure were used to construct field curves based on the Schmertmann (1955) method. For CRS consolidation, compression curves were from the testing data and the preconsolidation pressure used was estimated using the Pacheco Silva method. For IL data, there was great variation in compression curves depending on whether the log of time, Procedure 1, or square root of time, Procedure 2, was used, as well as how secondary compression was handled. For this testing data, the compression curves were constructed using increments from the log of time method, Procedure 1, with secondary compression removed. The Pacheco Silva method was used to estimate preconsolidation pressure.

4.3.2 Compression Index Dependence on Field Curve Construction

Variations in estimates of compression index from different testing methods could be observed during data compilation because IL and CRS data could be directly compared from specimens tested from the same sample. As noted in Section 3.4.1, when CRS compression curves are plotted with IL data, they tend to lie somewhere between IL data that does and does not contain secondary compression (Figure 3.14). Additionally, compression curves have more strain or void ratio change when using the log of time method, Procedure 1, to compute individual increments (Figure 3.5).

Special attention was made of constructions using the IL and CRS compression curves because of these observed differences. For finding the compression index, the Schmertmann (1955) correction for construction of the field curve is intended to correct for sample disturbance. There was the possibility that construction of the field curve might also compensate for some of the differences in lab compression curves from IL and CRS testing. In Figure 4.11 and Figure 4.12, field curves have been constructed for a paired set of IL and CRS data from the same sample. The field curves for the IL data in Figure 4.11 were computed using Procedure 1, the log of time method, and include data that excludes secondary compression and includes secondary compression. As can be seen, the resulting field curve is steeper for the data set that includes secondary. The corresponding compression index is also higher. Compression index from the field curve based on no secondary compression was 0.53 and from the field curve based on including secondary compression was 0.70. In Figure 4.12, the field curve for the paired CRS test is plotted, which produced a compression index of 0.72, which is greater than both of the estimates from the IL data even though as discussed in Section 3.4.1 that the CRS data tends to be intermediate between the spread of IL values. However, even though these specimens came from the same sample as each other, there

are still slight variations in index properties because of the natural variations in layered soils. Thus, with different values of initial void ratio, e_o , there are different values of $0.42e_o$, which both inform the field curve construction.

The other main input to the field curve is the estimate of the preconsolidation pressure, which, as discussed in Section 4.1, can vary due to method used as well as the shape of the compression curve. In Section 4.2, it was noted that IL tests tend to predict lower values of preconsolidation pressure as the paired CRS test from the same sample. This is likely due to the sparse data from IL testing biasing toward lower values. The data from Figure 4.11 included the preconsolidation estimate derived from IL data set and this value was lower than the estimate from the CRS data from the same sample. To see what effect this difference in preconsolidation estimate makes on the construction of the field curve, in Figure 4.13, the same IL data from Figure 4.11 has been plotted with field curve constructions using preconsolidation estimated from the CRS test in Figure 4.12. As observed in Figure 4.13, the resulting field curves produce slightly higher values of compression index, 0.55 and 0.74 for excluding secondary compression and including secondary compression, respectively. The estimate that does not include secondary compression is still significantly lower than both the estimate that includes secondary compression as well as the estimate from the CRS field curve. It should be noted that the magnitude of these differences are likely amplified by the long duration of the IL tests.

4.3.3 Compression Index and Secondary Compression Relationship to Predicted Settlement

The variation in estimated compression index depends on how the field curve was constructed, including whether the field curve was based on CRS or IL data, implies that settlement calculations using this data may also show variability. However, CRS testing involves some degree of secondary compression. It is possible that lower values of compression index derived from removing secondary compression effects might be compensated in settlement calculations with higher values of compression index. Conversely, using compression index from CRS testing for estimates of consolidation settlement and then adding additional secondary compression settlement may overestimate total settlements.

To test the significance of this, a parametric consolidation settlement study was performed. A 100-foot thick deposit of stiff clay was modeled to have similar properties as the mean values discussed for OBC in this chapter, which include: OCR (1.9), C_r (0.030), C_v (1.7 m²/yr), and C_α (0.027). From the paired tests of Figure 4.11 and Figure 4.12, compression index was approximated in two ways, from the IL test for increments where secondary compression is excluded and from CRS. To emphasize the point, all the scenarios that use C_c from the CRS test **do not** include additional secondary compression strain. Several loading scenarios were considered to capture the range of consolidation behavior. The most illuminating two scenarios ended up being a deeper deposit with a high load placed at depth and a shallower deposit with a lighter load placed at the surface (Figure 4.14).

The main difference between the scenario with the deeper deposit and the higher load and shallower deposit and the lighter load was what thickness of the stiff clay layer became normally consolidated. In these scenarios discussed, the deeper deposit with the higher load had a greater

thickness of the clay layer become normally consolidated, so settlement was greater and there was a longer predicted time for pore pressures to dissipate with no additional drainage modeled. As such, the contribution from secondary compression was a smaller proportion of the total settlement. Because the time to dissipate the excess pore pressure was longer, in an assumed 50-year design life approximation, the time period for secondary compression to accumulate was less. As a result, for the deep profile with a higher load, the total consolidation settlement predicted using the C_c from CRS testing without any secondary compression was approximately 10% **more than** the combined primary consolidation and secondary settlement predicted using the C_c from IL testing. Conversely, for the shallower profile with less loading, the total primary consolidation settlement predicted using the C_c from CRS testing was approximately 10% **less than** the combined secondary settlement and the total consolidation settlement predicted using the C_c from IL testing.

As with many issues surrounding soil settlement, there appear to be offsetting factors that sometimes cause the settlement estimate using C_c from CRS testing to be more conservative than the combined settlement estimate using C_c from IL testing and the estimate of secondary settlement. When there is a significant amount of primary consolidation settlement compared to the amount of secondary compression settlement, using just a settlement based on C_c from CRS testing may be more conservative. This is especially true when pore pressure dissipation is slow. For situations where there is less consolidation settlement, especially if the consolidation settlement has been rapid due to vertical drains or other systems, secondary compression becomes more significant than consolidation settlement. In that case, the estimate of combined consolidation settlement based on C_c from IL testing with the secondary settlement will be greater than only the estimate of consolidation settlement based on C_c from CRS testing. Combining the estimate of consolidation settlement based on C_c from CRS testing with the secondary settlement estimate should be sufficiently conservative in this case and likely not as overly conservative as using these combined estimates when there is a high level of consolidation settlement.

Secondary settlement estimates still matter when performing consolidation settlement calculations that use values of C_c from CRS testing. However, it may be the case that overly conservative values may be predicted depending on the loading conditions and the geology of the clay layers. Some of the disagreement between initial predictions of settlement compared with field observations can be attributed to design calculations tending to use only the most conservative parameters estimated from lab testing, as well as an accumulation of conservative estimates throughout the design process. More thorough parametric studies might shed further light into the conditions for which parameters estimated from CRS testing or from IL testing may best predict field observations.

4.3.4 Results

Compression Index, C_c , from consolidation testing of samples for this research project are shown on Figure 4.15, Figure 4.16, and Figure 4.17 and Table 4.1. Figure 4.15 presents compression index results for YBM, OBC, and Alameda, while Figure 4.16 present compression index results for OBC and Alameda, respectively, plotted with mean values, mean plus one standard deviation, and mean minus one standard deviation. Figure 4.17 plots compression index against water content

for OBC and Alameda. Table 1 summarizes these values and includes estimates of compression ratio, CR.

As previously discussed, testing of YBM was not a focus of this research project, though some tests were run in order to correlate with GDR results. As can be seen in Figure 4.15 and Table 4.1, compression index, C_c , ranges from 1.05 to 1.1, which correlates to compression ratios, CR, from 0.48 to 0.51. As compared to the GDR data, these values are high for the West Bay Mud. For the East YBM, a mean CR was found to be 0.29 with a standard deviation of 0.1 and, for the West YBM, a mean CR was found to be 0.24 with a standard deviation of 0.06. The data tended to be fairly scattered with no clear depth dependence. As compared to Hamilton Field YBM, C_c was 1.2 to 1.8 for normally consolidated samples and 0.8 to 0.9 for slightly overconsolidated samples (Bonaparte and Mitchell, 1979). As such, the YBM at this site appears to have high compression indices compared with the Hamilton Field YBM because of the OCR.

The OBC compression indices also show some scatter and do not appear to have a strong depth dependence. C_c for OBC was a mean of 0.73, with a standard deviation of 0.15 (Table 4.1). Equivalent values of CR show a mean of 0.34, and a standard deviation of 0.07. GDR data for OBC CR was a mean of 0.31 with a standard deviation of 0.09. These values appear consistent with some other published values for OBC, though possibly on the lower end. Holtz, Kovacs, and Sheahan (2011, p. 394) has San Francisco Old Bay Clay C_c as 0.7 to 0.9. To contextualize these values, they can be compared to published values of YBM mentioned above. The project values also reflect lower C_c than suggested by Holtz, Kovacs, and Sheahan (2011, p. 394). As can be seen in Figure 4.17, a fairly strong relationship between moisture content and compression index is observed.

Compression Index results from Alameda clays tend to show lower values than for either YBM or OBC. C_c for Alameda was a mean of 0.62, with a standard deviation of 0.09 and equivalent values of CR show a mean of 0.28 and a standard deviation of 0.04. GDR data for Alameda CR was a mean of 0.21 with a standard deviation of 0.07. This data also shows a degree of scatter without a relationship to depth, similar to the OBC. There did appear to be correlation between compression index and water content as plotted on Figure 4.17. While compression index for Alameda samples was not as high as either YBM or OBC, they still are higher than assumed values often given for “generic clays” for settlement calculations, such as a C_c of 0.2 to 0.5 (Holtz, Kovacs, and Sheahan, 2011, p. 394) or generally less than 0.5 (Soga and Mitchell, 2005, p. 325). This could be because of the relatively high PI of the Alameda clays tested, even though these are deep clays.

4.3.5 Discussion

Compression index is a hybrid parameter that depends on several constructions. The main construction is the Schmertmann (1955) field curve construction, which is rooted in the value of $0.42e_o$, as well as whatever construction is used to estimate the preconsolidation pressure. As discussed in Section 4.2, there is variability in how the preconsolidation pressure is constructed. There is also variability in how a field curve is constructed from IL testing, which is not necessarily the same as a field curve from CRS taken from the same sample (4.3.2). For deep clays like the OBC and Alameda, the $0.42e_o$ straight line projection of Schmertmann does not reflect the shape of compression curves that have concave upwards shapes at high loads and low void ratios (Figure

3.11, Figure 3.12, Figure 4.12). While the Schmertmann correction is an industry-wide standard, it is suggested that it may need modification for deep clays.

Compression index for OBC and Alameda soils can be estimated that is consistent with compressible soils. Both OBC and Alameda soils have often been considered to be incompressible, most likely because imposed loads are not significant enough for compression properties to matter. However, these soils are compressible, similar to other moderate PI soils. As increasing loads are more common, especially from deep foundations, the compressibility of OBC and Alameda soils is increasingly more significant.

Of note was the moderate to strong relationship between C_c and moisture content. This relationship could be helpful for other sites with Old Bay Clay and Alameda soils for identifying zones of higher compression.

4.4 Recompression Index

The recompression index, C_r , is used to characterize settlement and swelling behavior of overconsolidated clays. As most of the clay materials at the project site are overconsolidated, this data can provide insight into soil behavior both under added loads but also when overburden is temporarily or permanently removed. The following sections detail data processing and results for recompression index derived from consolidation testing for YBM, OBC, and Alameda, as well as observations made.

4.4.1 Defining the Recompression Index

The recompression index is often defined as an analogous property to the compression index, “except that it is the average slope of the recompression part of the e versus $\log \sigma'_{vc}$ curve” (Holtz, Kovacs, and Sheahan, 2011, p. 373). Leonards (1976) tends to be the definitive source on how to measure and define C_r , where “ C_r , should be evaluated over the range $p'_c + \Delta p$ [initial effective vertical overburden pressure plus the load increment]” as shown in Figure 4.18. However, in most commercial testing, loading-unloading cycles may be rare, usually beyond P_p and sometimes with only an unload cycle at the very end of the test. In that case, the recompression index tends to be defined as the slope of the final unloading because the initial loading in recompression is assumed to be disturbed, especially if the sample is normally consolidated.

However, it can be observed in consolidation testing with many unload-reload cycles that the slope of the recompression loops are not all equivalent. Figure 4.19 is an example of multiple unload-reload cycles on the same sample. The first unload was performed at the in-situ vertical effective stress, the second at a relatively low stress beyond the preconsolidation pressure, the third at an intermediate stress, and the fourth at a relatively high stress. The first three cycles were unloaded to the same total stress, while the last was terminated before that stress. This compression curve illustrates an apparent increase in slope of the recompression portions of the compression curve both before and after the P_p . An increase in recompression slope is observed in the loops as the maximum pressure at the point of unloading increases. An additional feature of the curves can also be observed in the last unloading, which was not unloaded to the same total stress as the others and also did not have a reloading cycle. The last unload appears to have approximately the same

slope as the previous unloading cycle, even though the maximum past pressure at unloading was higher. Also, the lack of an unloading cycle means that the straight line fit to the recompression segment appears to be inconsistent with how the straight line was fit to the other recompression loops.

The relationship between possibly increasing recompression index with increasing maximum past pressure is very important for understanding unloading behavior of clays. In this research project, this relationship was explored by performing many unload-reload cycles, at stresses below the preconsolidation pressure, as well as for several cycles past the preconsolidation pressure. Both CRS and IL testing included these many unload-reload cycles.

A subset of GDR testing also explored this relationship and defined the resulting recompression slopes as “Swelling Ratios.” In Figure 4.20, this parameter is explained for that testing program. In general, the Swelling Ratio, SR, (Intermediate Stress), correlates with the Recompression Ratio, RR, while the Swelling Ratio, SR, (Final Unloading), corresponds to the recompression slope at a high maximum past pressure. The data compiled for RR, SR (Intermediate Stress), and SR (Final Unloading) was then sorted depending on the tested stress range at unloading. In some cases, there was not more than one unloading, so that slope was taken as the RR.

The degree of unloading or number of unloading increments also appears to influence the estimate of recompression index. This is observed in Figure 4.20 where the recompression slope appears similar in the third unload loop and the final unload cycle even though these portions of the compression curve were unloaded to different values. This can be more apparent in IL testing, as shown in Figure 4.21. In this test, there were five unloading increments, at the same LIR. Lines fit from the maximum past pressure at unloading to the five different unloading increments illustrate the slope steepening with subsequent unloading increments. Any of these slopes could define a recompression index from this test. Bilgin, Tsimbelman, & Chernova (2017) have also observed this effect in IL testing and the dependence of the recompression index both on the location of the unload-reload cycle as well as the number of unloading steps. CRS data illustrates this aspect even more deeply, because continuous testing data can produce any amount of unloading. At any point of a CRS unload-reload cycle, the test can be terminated or the loading direction changed, which will define the recompression curve.

The same unload-reload cycle in a compression curve can define various recompression indices depending on how a line is fit to the data. In Figure 4.21, this can be illustrated by the differences in fit lines between the third unload loop and the final unload cycle. In the unload loop, the line has been fit to between the low stress end of the loop and a “crossover” point at the high stress end of the loop where the void ratio of unloading and reloading were the same. In Figure 4.22, this point is illustrated further. In this hysteresis loop, a straight line can be fit from the point of maximum stress to the point of minimum stress (Point A to B), from the “cross-over” point where the hysteresis meets to the point of minimum stress (Point C to B), a straight line fitted to the top (Point D) or bottom of the hysteresis (Point E). Different practitioners may even fit a straight line to a portion of the curve that appears to be a straight line, such as Point B to E or Point E to C. Or as noted above, a line could be fit to the final unloading of Figure 4.19. This issue was a focus by a paper by Vipulanandan, Guezo, Bilgin, Yin, and Khan (2008), where they highlighted the

differences in slope between these assumptions, even adding more possible fit combinations than listed above.

While recompression index is often seen as analogous to the compression index, it can be much more complicated to define. As stated by Vipulanandan et al. (2008), “of the consolidation test parameters, recompression index is the least investigated in the literature.” It appears to have dependence on stress degree, stress direction and history, as well as how a practitioner interprets the data. Importantly, an unacknowledged cause of this variability may be how the test method is performed and the choices taken by the person performing the test in regards to stresses and loading-unloading sequences.

4.4.2 Hysteresis loops and Effects on Recompression Index

The degree of hysteresis in unload-reload loops may be an unexplored contributor to the difficulty estimating the recompression index. The degree of hysteresis used in this context is how much of a lens-like shape is developed during unloading and reloading. In Figure 4.19, the first unload-reload cycle below the in-situ vertical effective stress appears to have a very low degree of hysteresis because it is like a flat line, where the unload and reload portions of the compression curve appear to have the same values and the reload joins the trajectory of the original curve without additional vertical strain. On the other hand, the third unload-reload shows a notable difference between the unload and reload portions of the compression curves. Those two portions of the curve only meet at two points, at the low stress of the cycle and at a crossover point below the maximum past pressure. Notable is that the reload portion of the curve does not have the same void ratio at the maximum past pressure before unloading. On unload-reload loops with a lot of hysteresis, this is often the case and there is more void ratio change before the reload portion of the curve meets the projected continuation of the normally consolidated portion of the curve.

Degree of unloading appears to effect recompression index estimates, due to its contribution to hysteresis, among several factors. As in Figure 4.19, the first loop shows less hysteresis than the third, but it was unloaded by a factor of 2.4 while the third was unloaded by a factor of 8.45. In general, unload-reload loops at low stresses may exhibit a low degree of hysteresis because the load cannot be reduced as much as an unload-reload loop at high stress.

The dependence on loading suggests that loading schedules matter. The ASTM standard for Incremental Loading Consolidation (ILC) directs that “unloading shall always include at least two decrements of total axial stress” (ASTM Standard D2435, 2011). Additionally, the ASTM directs that successive stress unloading level can be one-fourth as large as the proceeding stress level. This may be consistent with some general assumptions by practitioners to limit unloads to below a factor of 4. However, it is unclear if this matters for unloads that are less than 4 or even if most practitioners consider magnitude of unloading when processing data.

Some other testing conditions can strongly influence hysteresis. For CRS consolidation, pore pressure generation can have large effects. Pore pressure generation is related both to the natural hydraulic conductivity of a soil, but also the rate at which the test is run. The more pore pressure is generated, the larger the difference between total and effective stress in the sample. In unloading, the pore pressures will tend towards negative pore pressures, while loading will generate positive

pore pressures. Running a CRS test at a low speed in order to prevent pore pressure generation may not reduce the effect of hysteresis, because secondary compression is accumulated during CRS testing, as discussed in Section 3.4. A tradeoff between excessive pore pressure generation and an accumulation of secondary compression is a key component of CRS testing and also a contributor to hysteresis.

Even IL data shows hysteresis, which may be due to the issues discussed in Section 3.2.2 regarding the end of primary calculations and how they depend on Procedure 1 or Procedure 2 procedures as well as the accumulation of secondary compression. In general, Procedure 2, the square root of time method, produces less hysteresis. The accumulation of secondary also makes a difference in the shape of the unload-reload loops, so when it is removed from increments to generate the compression curve, they unload-reload portions will be flatter.

4.4.3 Recompression Index Dependence on Stress Level

While it appears that recompression index increases with increasing maximum past pressure at unloading, it is unclear if this is a phenomenon that reflects testing conditions and interpretations rather than intrinsic soil behavior. The first factor is that the stress level at unloading and the terminal stress of the unloading cycle can define the recompression index. The second factor is that the recompression index can be ambiguous because there are many ways to interpret the data. Lastly, how to describe relative stress level is difficult because distinctions like “low stress” and “high stress” can be dependent on the individual stress history of a soil as well as hard to define once a soil is normally consolidated.

To explore this concept, paired IL and CRS tests were interpreted in several ways to try to understand the dependence. In Figure 4.22, an IL test is plotted and, in Figure 4.23, a paired CRS test is plotted. These tests came from adjacent specimens in the same sample tube from the OBC. In Figure 4.22 and Figure 4.23, an estimate of recompression ratio is made that is calculated from the minimum to maximum stress for each unload-reload loop. As can be seen, the recompression ratio increases with increasing maximum past pressure, with the exception of the last unload curve from the CRS test, likely because it was terminated at a lower total stress than the other cycles. To understand the dependence on unloading magnitude, it is helpful to define a uniform way to quantify the degree of unloading. For IL tests, this is fairly straight-forward, especially if the same LIR is consistently use for the unloading increments. In Figure 4.22, the LIR was 0.5, so the first unloading magnitude shows an unloading magnitude of 1.5-times, which is the maximum past pressure divided by the increment stress. For the second unloading, the magnitude was 2.25-times unloading with respect to the maximum past pressure, because the second unloading was half the difference from the first unloading. In Figure 4.23, a similar concept is illustrated for CRS testing, however, because CRS test data is continuous, the factors can be interpolated from the data. In Figure 4.23, 2-times unloading and 4-times unloading are illustrated. The maximum past pressure is fixed, but the low pressure that corresponds to the loading magnitude can be queried in the data along with the corresponding void ratio. A recompression ratio can then be defined that corresponds to these points. Using these factors of unloading, the relative difference between the unloading loops can be explored by using similar values instead of the values arbitrarily imposed by the testing conditions.

In Figure 4.24, recompression index has been calculated for the IL and CRS tests of Figure 4.22 and Figure 4.23 using factors of unloading. In this example, the IL test, had unloading factors of 1.5-, 2.25-, 3.375-, 5-, and 7.6-times, but the first unloading only includes the 1.5-times and the second only includes the 1.5- and 2.25-times. For the CRS test, recompression index was calculated for 2-, 3-, 4-, and 5-times unloading. Because of the magnitudes of unloading, only certain loops had enough unloading for the 4- and 5-times unloading. To generalize the results, instead of plotting against the maximum past pressure at the point of unloading, these values were divided by the preconsolidation pressure. Values below 1 represent unloadings around the in-situ vertical effective stress. Values above the preconsolidation pressure can be more easily compared between tests where there are different ranges of testing pressures. Because these specimens came from the same sample, similar ranges of pressures were used, but the unload-reloads were performed at different stresses. Figure 4.24 presents the recompression index calculated using factors for both the ILC and CRS test plotted against the ratio of preconsolidation pressure. From this data, there does appear to be a trend of increasing recompression index both as the factor of unloading increases and the ratio of preconsolidation pressure increases. However, there appears to be less variation in the CRS testing data for the higher factors and the higher ratio of preconsolidation pressure. There also appears to be less variation between the same factor at multiple preconsolidation pressure ratios than the variability observed in Figure 4.22 and Figure 4.23 when the recompression ratio is calculated for the entire unloading loop. In Figure 4.24, the recompression index using factors are plotted against the magnitude of unloading using a log scale. The trend of increasing recompression index with magnitude of unloading is clear, though also emphasizes that the effect is strongest for the small factors of unloading. The variability between unloading loops also appears to be less than the variability within a loop at various factors of unloading. This correlation is not surprising, though, because the way that the recompression index calculated with factors incorporates the trend.

A more universal recompression index may be possible if the recompression index calculated with factors are then normalized. Figure 4.25 presents these values called recompression index, normalized ($C_{r_normalized}$), which are the values of recompression calculated as in Figure 4.24, but normalized by the unloading factors used in the calculations. In Figure 4.25, the $C_{r_normalized}$ values are plotted against the ratio of preconsolidation pressure explained in the previous paragraph. As can be observed, variability has been greatly reduced both within the unloading loops as well as between unloading loops. However, there are outliers, which include the ILC data at low unloading factors. And it is still clear that there is a positive trend between increasing ratio of preconsolidation pressure and increasing $C_{r_normalized}$. In Figure 4.25, the $C_{r_normalized}$ values are plotted against unloading factor on a log scale. However, a potential negative correlation between the $C_{r_normalized}$ values with increasing magnitude of unloading suggests an overcorrection to the positive correlation observed in Figure 4.24.

Across the plots for Figure 4.24 and Figure 4.25, it is interesting to focus on the low unloading factors as well as the unloading loops before the preconsolidation pressure. The recompression indices for these are the lowest calculated and generally represent the recompression index as defined by Leonards (1976). However, they are clearly less than values that will be observed if the recompression index is calculated at later portions of the test or for a higher degree of unloading. Focusing on the very initial portion of the unloadings, such as in Figure 23a, it is clear that the slope is less. However, for laboratory samples, some of flattening of the slope has to do with the

reversal of pore pressure as well as lingering effects of the accumulation of secondary compression during the normally consolidated loading just prior to unloading. Some of these effects may be present in the field, but may not have as strong an influence as in laboratory testing. Interestingly, across Figure 4.24 and Figure 4.25, the most consistent values of recompression index appear around the 3- to 5- times unloading factors for the CRS test. As mentioned in Section 3.2.1, some consultants suggest limiting unloading to a 4-times factor and this might give insight why. While not the lowest values, the values produced around an unloading factor of 3 may be more consistent and lack some of the testing effects that the 1- to 2-times factors produce.

This exercise in calculating recompression index shows that there is a correlation between maximum past pressure at unloading as well as the degree of unloading. Recompression index is a parameter with a high degree of variability, but not a lot of standardization in testing procedures or calculation. It is possible that some of this variability may be reduced if more consistency was introduced. CRS testing can be helpful in this way because recompression index can be calculated by the factors introduced in this section.

4.4.4 Data Processing

Like with other steps in processing consolidation data, this study has focused on processing the data consistently both within and between the tests. All of the CRS and ILC tests in this study have had recompression index, C_r , and recompression ratio, RR , values estimated by fitting a straight line through the unload loop and connecting the crossover point to the minimum stress value. For unloads when there is no reload, the straight line is fit between the minimum and maximum points. In general, the reported value of recompression index for a test is the lowest value, usually from the unload-reload cycle around the in-situ vertical effective stress. Recompression index was calculated for all loops and is reported in the Results section.

4.4.5 Results

Recompression Index, C_r , from consolidation testing of samples for this research project are shown on Figure 4.26, Figure 4.27, and Figure 4.28 and Table 4.2 and Table 4.3. Figure 4.26 presents recompression index results plotted with depth for YBM, OBC, and Alameda showing the low value as explained in the previous section. Figure 4.27 present lowest values of recompression index results for OBC and Alameda, plotted with mean values, mean plus one standard deviation, and mean minus one standard deviation. Figure 4.28 shows recompression index plotted with depth as calculated for OBC and Alameda at various levels of preconsolidation pressure at unloading. Table 4.2 summarizes the low values of recompression index, C_r , and recompression ratio, RR , for YBM, OBC, and Alameda. Table 4.3 summarizes recompression index, C_r , and recompression ratio, RR , values for OBC at various levels of preconsolidation pressure at unloading.

Most of the same considerations for compression index apply for the recompression index, as discussed previously in detail in Section 4.3.4. Because this research project did not involve extensive testing of YBM or of swelling ratios of YBM as defined in the GDR, there is limited data. As can be seen on Figure 4.26 and Figure 4.27 and in Table 4.2, recompression index, C_r , ranges from 0.08 to 0.09, which correlates to compression ratios, RR , from 0.036 to 0.041, which is consistent with West YBM. From the GDR, the East YBM had a mean RR of 0.025 with a standard deviation of 0.010 and the West YBM had a mean RR of 0.038 with a standard deviation

of 0.012. The data tended to be fairly scattered without clear depth dependence. As compared to Hamilton Field YBM, C_r was 0.10 to 0.15 (Bonaparte and Mitchell, 1979). As such, the YBM at this site appears to have lower recompression indices than the Hamilton Field YBM.

As with the estimates of compression index, the OBC recompression indices show scatter and do not appear to have a strong depth dependence. When only assessing the lowest value of recompression index, as explained in Section 4.4.4, C_r for OBC was a mean of 0.033, with a standard deviation of 0.022 (Figure 4.27 and Table 4.2). Equivalent values of RR show a mean of 0.015 and a standard deviation of 0.01. GDR data for OBC RR was a mean of 0.028 with a standard deviation of 0.012. The project data seems to conflict with the GDR data, but more insight is gained when the data is assessed against the various swelling ratios at different maximum past pressures at unloading.

In Figure 4.28 and in Table 4.3, the recompression ratios for OBC have been organized by maximum past pressure at unloading, which correlated to unloads before the preconsolidation pressure, at low stresses past the preconsolidation pressure, at moderate stresses past the preconsolidation pressure, and at high stresses past the preconsolidation pressure. There is a consistent correlation to higher recompression index as the stress at unloading increases. The same is observed in the GDR data, where swelling ratio, SR, is divided into low stress, intermediate stress, and high stress values. Low stress SR had a mean value of 0.017 with a standard deviation of 0.008, intermediate stress SR had a mean value of 0.023 with a standard deviation of 0.008, and high stress SR had a mean value of 0.038 with a standard deviation of 0.008. The low stress SR is very similar to this study's RR values taken from below the preconsolidation pressure, and the intermediate and high stress SRs are consistent with this study's medium and high stress RR values. There does appear to be clear trends in the recompression ratio values when stress at unloading is evaluated.

Lowest values of recompression index for Alameda are plotted on Figure 4.26 and Figure 4.27 and presented in Table 4.2. Similar to compression index trends, recompression index for Alameda appears less than values for YBM. There is also a fair amount of scatter and a lack of depth dependence. Recompression index for Alameda and OBC appear very similar with the mean value for Alameda actually higher than OBC, possibly because there is not enough testing data from the Alameda to show clear trends. When only assessing the lowest value of recompression index, as explained in Section 4.4.4, C_r for Alameda was a mean of 0.033, with a standard deviation of 0.014 (Figure 4.27 and Table 4.2). Equivalent values of RR show a mean of 0.016 and a standard deviation of 0.0061. Compared with GDR values for recompression ratio, the Alameda values in this study appear low. In the GDR data, too, the recompression ratio values are lower for Alameda than for OBC, which would make sense and it probably not observed in the project data because of the statistically smaller amount of data.

Recompression index for Alameda at various levels of maximum past pressure at unloading are plotted on Figure 4.28. Because there was less consolidation testing on the Alameda soils than the OBC soils and the degree of scatter in the data, there is less data to do a statistical measure of recompression index at different stress levels. The GDR did consolidation testing with enough data to estimate swelling ratios at low, intermediate, and high stresses. Low stress SR had a mean value of 0.020 with a standard deviation of 0.009, intermediate stress SR had a mean value of 0.019 with

a standard deviation of 0.011, and high stress SR had a mean value of 0.035 with a standard deviation of 0.013. The recompression ratio estimates from this study appear to be consistent with the low and intermediate stress SR values, though still on the lower end. For both the GDR and this study, there was less testing in the Alameda than the OBC, so possibly more testing data might exhibit clearer trends.

4.4.6 Discussion

Recompression index is an important parameter for all overconsolidated soils. However, the generally accepted procedures to calculate recompression index do not necessarily reflect how consolidation testing is commonly performed. There may be limited stresses that unloads are performed at and practitioners may have various ways of calculating recompression index from the same data. However, it is clear that there is a stress dependence to recompression index.

For recompression to be a meaningful parameter, it is suggested that more uniformity is used for calculation. In CRS testing, this is achievable because the continuous data can be queried for factors of unloading. With more research, a parameter that generalizes unloading data or reloading data to produce recompression index without bias from stress level and/or unloading factor may be possible. At the very least, practitioners should explain how they define recompression index, including how the straight line was fit, at what stress levels unloading was performed, and what unloading factors were used.

For calculations of settlement or swelling in overconsolidated clays, it is also suggested that these variations in recompression matter. In the testing data, unloading factors and stress level matter, so recompression index at various stress states or reflecting various stress histories may provide insight in real field behavior.

4.5 Secondary Compression Index

Secondary compression index (C_α) is a parameter that characterizes secondary compression, which occurs is continued volumetric straining constant effective stress. Secondary compression is always present in clay soils, but can have a big impact on engineering design when there are added fills or excavations, especially for staged construction and when there are preloads. Similar to the recompression index discussed in the previous section, there is observed variability in the secondary compression index dependent on stress history. The following sections detail data processing and results for secondary compression index derived from consolidation testing, as well as observations made.

4.5.1 Data Processing

Secondary compression index, C_α , was calculated for every increment of IL testing in this research project. While the testing equipment did allow for estimates of C_α from CRS specimens, it was not estimated as a part of this study. All the secondary compression results, therefore, are from IL tests and they are predominantly from Old Bay Clay soils. As discussed previously, stress history was a main focus for this study, so individual IL test contained many increments at various stress states. C_α is straight-forward to estimate, taken as the straight-line segment from the log time history

curves after the end of primary, EOP. There are several unique cases of time history curves as explained in Section 3.2.2 and the C_α value reported was taken as the greatest value when the slope appeared to steepen. When only one value of secondary compression index is reported for a full IL test, it is generally the highest value of C_α observed, which generally correlates to the portions of the compression curve in normal consolidation and at the higher stresses. Initial compression, unloading, and reloading increments produced smaller estimates of C_α .

4.5.2 Results

Figure 4.29 and Table 4.4 present secondary compression index results from testing in Old Bay Clay and Alameda soils. Figure 4.30 and Table 4.4 present values of the ratio of secondary compression index to compression index for the Old Bay Clay soils. Similar to compression index and recompression index, there is a degree of scatter and not strong depth dependence in these values.

The GDR did not compile C_α for the project soils, so direct comparisons with the calculated results must be made with published values. In Bonaparte and Mitchell (1979), C_α for the Hamilton Field YBM was 0.1 to 0.02. This appears to be a generally lower estimate than the OBC and Alameda soil, consistent with just the lowest values. In Holtz, Kovacs, and Sheahan (2011, p. 441), C_α for “San Francisco Bay mud” is given as 0.052. For the value of C_α/C_c , Terzaghi, Peck, and Mesri (1996) provide a value of 0.04 ± 0.01 for inorganic clays and silts and 0.05 ± 0.01 for organic clays and silts. Again, the OBC soils are consistent with the lower range of the estimate. From Figure 4.30 (Bottom), the relationship between C_α and C_c appears moderately correlated.

4.5.3 Secondary Compression Relationship to Stress History

As noted in the prior sections, secondary compression index is usually taken as the largest estimate calculated from IL testing, however, secondary compression is observed in every increment of IL testing. The values of C_α calculated across an IL test for the various reloading, unloading, and normally consolidated increments vary both because of differences in overconsolidated and normally consolidated behavior, but also appear to depend on loading direction. While secondary compression appears to be an intrinsic property of soils, present under constant stress conditions, it appears very sensitive to stress history during laboratory testing.

Looking more closely at C_α calculated from normally consolidated soils helps to emphasize the importance of stress history. In Figure 4.31 (Top), C_α estimates from normally consolidated increments are plotted against stress. There is much larger scatter in this data than suggested in Table 4.4 because Table 4 only includes the largest estimate of C_α from each test, which generally had several increments in the normally consolidated portion of the compression curve. The scatter in the data is reminiscent to the scatter in recompression index data, where it is not clear if larger estimates are due to the greater stresses or due to testing conditions. In Figure 4.31 (Bottom), C_α from normally consolidated increments are plotted, but this time only from increments succeeding another normally consolidated increment. In this plot, the scatter has been greatly reduced and there no longer appears to be a clear stress dependence to the C_α estimates. Rather, C_α appears to be influenced by the stress conditions of previous increments in the laboratory.

The relationship to stress history is even more clear in C_α estimates from unload and reload cycles. However, C_α estimates from overconsolidated increments can be confusing to understand, with a lot of scatter and unclear relationship to stress history. In Figure 4.32, all C_α estimates calculated from the OBC IL tests in overconsolidated increments is plotted, with Figure 4.32 (Top) containing the reloading increments and Figure 4.32 (Bottom) containing the unloading increments. In Figure 4.33, a subset of the data that only includes “reset” increments is plotted. In these increments, the maximum past pressure has been set by previous loading increments, so the OCR is known. Unlike in Figure 4.32, where the data is plotted against increment stress, in Figure 4.33, the data is plotted against the known OCR. A couple trends can be observed from these plots. For both reloading and unloading increments, the first increment appears to give the lowest estimate of C_α . Similar to normally consolidated increments that generally are at a maximum when the previous increment is also normally consolidated, in unloading and reloading increments, C_α is influenced by the previous increment when there is a stress direction reversal.

For both unloading and reloading, there also appears to be a dependence on OCR. As can be seen in Figure 4.33 (Top), there is a large jump in C_α estimates for reloading increments as OCR becomes close to 1. These C_α estimates correlate with some of the special cases of time history curves described in Section 3.2.2. While the lowest estimate of C_α occurs for the first increment when there is a stress reversal, for reloading increments there are moderate estimates of C_α after the first increment and below OCR=1. As the stress for a reload increment approaches the maximum past pressure, a higher estimate of C_α is observed, which still is generally not as high as the C_α from an increment that is fully within the normally consolidated portion of the compression curve. The higher estimate of C_α for reloading increments likely reflects the soil transition from an overconsolidated soil to a normally consolidated soil at the maximum past pressure.

The unloading increments also appear to depend on OCR as observed from Figure 4.33 (Bottom). Just as for reloading increments, the first increment is the lowest estimate of C_α , likely due to the stress reversal. After the first increment and then at increasing values of OCR, C_α estimates increase. While higher values of C_α are observed at high OCRs, there does appear to be less of a correlation around an OCR of about 4. It is possible that the unloading C_α reaches something like a maximum once the soil no longer feels the effects of the stress reversal and a significant enough load has been removed so that the soil is fully in an overconsolidated portion of the compression curve. The value of OCR equal to 4 is notable because it appeared to be a median value for C_r estimates.

4.5.4 Discussion

Understanding secondary compression is important to any engineering project that involves permanent loading or unloading, in particular when there is staged construction or preloading. However, there is generally little direction regarding what values of C_α to use during design. It is clear that there is a difference between C_α for an overconsolidated or a normally consolidated soil. Similar to recompression index, there is a lot of scatter in this type of data as well as influences to the data from the testing itself. From this study, it appears that stress history matters when evaluating C_α . Maximum estimates of C_α for both overconsolidated and normally consolidated increments are observed when there is no previous stress reversal and the soil is well above or below the maximum past pressure. However, for in-situ soils under intermediate stress conditions near the maximum past pressure, these observations may be helpful to understand potential

deformations. For example, a soil loaded to very close to the maximum past pressure may behave like an intermediate soil and produce more deformation than expected. Conversely, less deformation may be expected due to stress reversals when small unload or loadings occur to a soil that has been experiencing the opposite stress state.

4.6 Coefficient of Consolidation

The coefficient of consolidation is a parameter that characterizes the rate of consolidation. Coefficient of consolidation is important for engineering settlement analysis because it helps to understand timing of consolidation. This is a critical parameter for engineering construction involving permanent loading or unloading, especially for designing staged construction or any design that involves pre-loading. However, laboratory estimates of the rate of consolidation are known to be lower than observed rates of consolidation observed in the field. The following sections contain explanations for data processing and summarize results for the coefficient of consolidation derived from consolidation testing, as well as insights gained.

4.6.1 Data Processing

Coefficient of Consolidation was calculated per ASTM Standard D2435 and D4186 for IL and CRS consolidation testing, respectively for the sample data. Coefficient of consolidation was calculated for all increments of IL testing and all loadings cycles of CRS. As discussed in Section 3.2.2, there is a consistent difference between consolidation increments from IL testing that are processed with Procedure 1, the log of time method, or Procedure 2, the square root of time method. Procedure 2 produces consistently higher estimates of coefficient of consolidation because it estimates a shorter End of Primary (EOP).

Because there were many increments for each IL test and multiple unload-reload cycles for the CRS tests, there are many coefficient of consolidation estimates at various stress states. Generally, the value for coefficient of consolidation is taken as the smallest value from a test, which usually correlates to higher stress, normally consolidated portions of a consolidation test. For IL testing, there will be one estimate of C_v per increment, so one test has a range of C_v estimates. For CRS testing, C_v appears like a continuous curve similar to the compression curve. However, because C_v is estimated from differences in pore pressure measurements, as explained in Section 3.3.2, C_v calculated from CRS data often does not reach stable values until pore pressure is significant, stable, and shows consistent increases or decreases. In Figure 4.34, C_v estimates are plotted from a paired set of IL and CRS consolidation tests. As can be seen, the IL data corresponds to the discrete loading increments, while the CRS data is mostly continuous with stress. Of note is that there is no C_v data from the initial loading cycle of the CRS test that occurred below the preconsolidation pressure. Because there was very little pore pressure generated, the C_v estimates were unstable and appear erroneously high because the change in pore pressure generated is very low. This is very common when observing C_v data from CRS testing, as the values tend to stabilize after the preconsolidation pressure or the previous maximum past pressure and then stabilize and decrease in value as stress increases. For some loading cycles, a stable C_v value is not reached.

For the estimates of coefficient of consolidation presented in Section 4.6.3, the values of C_v are taken as the lowest estimate from the various increments of an IL test or from the lowest value

observed in the plot of C_v with stress from CRS testing. The values for all increments from IL testing as well as complete plots of C_v with stress from CRS testing are presented on the individual test data sheets in Appendix A.

4.6.2 Coefficient of Consolidation dependence on Stress and Test Type

As mentioned at the beginning of the section, laboratory estimates of coefficient of consolidation are known to differ from field estimates, with the rate of consolidation generally being greater in the field. There are strong geologic and hydraulic reasons for this, including interlayering of more permeable soils and preferential horizontal drainage paths. A contributing factor is that the estimate of coefficient of consolidation taken from laboratory testing is the lowest value, which usually correlates to normally consolidated soil at high stress.

A question that comes up for CRS testing is whether the plots of C_v with stress reflect something like an “instantaneous” C_v at the corresponding stress state or if they are intermediate values that represent the transient pore pressures during testing. As discussed in Section 3.3.2, the specimen undergoing CRS testing is experiencing a pore pressure gradient across the sample, with the top surface completely drained and the pore pressure measured by the testing equipment reflecting the undrained bottom portion of the specimen. At any moment in time during testing, there is a pore pressure gradient within the sample. The non-linear formula for C_v is a type of rate formula because it incorporates an arbitrary time period between points before and after the current state for the calculation. Thus, C_v represents a specimen experiencing changing pore pressures both within the specimen and over a window of time. If a very small difference in time is used for this calculation when there is little to no change in pore pressure state, large and unstable values of C_v are predicted. Similar results are observed if there is little to no pore pressure generation because either the specimen is highly conductive or the test speed allows for the pore pressure to dissipate. While C_v is estimated for any increment of IL testing, C_v appears to only be estimated under certain testing conditions during CRS tests.

In Figure 4.34, C_v estimates from the paired IL and CRS consolidation test are similar once the CRS test curve starts trending toward low values of C_v . At low stresses at the beginning portions of the loading curves, the estimates of C_v from CRS testing are very large, in the hundreds of meters squared per year. In this test, the preconsolidation pressure was estimated at 7.5 kg/cm², which corresponds with an intermediate value of C_v . Past the preconsolidation pressure and past the maximum past pressures in the reloading cycles, it takes some time for the C_v to reach a minimum value. The IL testing appears to confirm these intermediate values of C_v . However, IL testing emphasizes that the very high values of C_v predicted at low stresses are likely erroneous. Because IL testing does not have continuous pore pressure gradients like CRS, it seems more likely that the estimated values of C_v reflect the one-dimensional consolidation rate properties of the soil.

A way to explore whether the calculated C_v values from CRS testing reflect instantaneous C_v at various stress levels is to compare with values calculated from IL testing. In the majority of the paired consolidation tests, the C_v values calculated were generally consistent. Figure 4.35 presents two paired IL and CRS tests which show agreement between the calculated C_v values, even with CRS C_v and stress curves that are somewhat unusual in shape. On the other hand, several paired tests did not appear to show much agreement between the two test types, as shown on Figure 4.36.

Based on the project testing, it is not clear if the agreement between the IL and CRS tests calculated C_v values are coincidental. The calculated values of C_v appear to be consistent in magnitude between the IL and CRS tests. Because of the inconsistencies between laboratory and field values of C_v , the magnitude of C_v is often emphasized rather than more precise values. It is possible that the inconsistencies between the IL and CRS calculated results emphasize that magnitudes of C_v values may be the current best estimates.

4.6.3 Results

Figure 4.37 (Left) and Table 4.5 presents coefficient of consolidation values for Young Bay Mud, Old Bay Clay, and Alameda soils, taken as the lowest estimate from the test. Unlike some of the other parameters, there is no clear depth dependence or soil dependence. For the OBC soils, there is clear variability and higher values than for the other soils, but OBC was a main focus of this study and had more extensive testing. In Figure 4.37 (Right), all OBC consolidation tests are plotted, with the IL and CRS tests plotted separately and with the mean, mean plus one standard deviation, and mean minus one standard deviation plotted. The IL testing does appear to produce lower values of C_v than the CRS, but there is scatter within both data sets.

The GDR did not compile C_v for the project soils, so direct comparisons with the calculated results must be made with published values. In Bonaparte and Mitchell (1979), C_v for the Hamilton Field YBM was 8 to 10 ft²/yr (0.7 to 0.9 m²/yr). This appears consistent with the lowest values calculated from the project soils. In Holtz, Kovacs, and Sheahan (2011, p. 433), C_v for “San Francisco Bay mud (CL)” is given as 0.6 to 1.2 m²/yr. This value again tends to encompass the lowest calculated values. However, the OBC in both cases has higher mean values and scatter that tends towards even higher values.

4.6.4 Discussion

Coefficient of consolidation is a difficult value to determine for field response because it is known to be underpredicted in the lab. In general, it is hoped that field instrumentation can be used to provide more realistic estimates of C_v , but those values are usually not available until after initial phases of engineering design has been performed. It is notable that a range of C_v values are produced during consolidation testing, both for IL and CRS tests. It may be more helpful for design to use the intermediate rather than the lowest calculated values. In addition, more research may be helpful to understand if “instantaneous” C_v values from CRS C_v versus stress plots reflect values of C_v in the field under similar stress conditions.

4.7 Sample Quality

An estimate of sample quality is very important for evaluating the quality of laboratory strength testing, especially for small strain testing including bender element testing and cyclic strength testing. An assessment of sample quality was important for this research project both because great care was taken to take high quality samples (Section 2.4) but also because of the small strain testing performed during this study (Chapter 5).

4.7.1 Background and Data Processing

Sample quality was estimated as a part of consolidation testing using the Lunne criteria as presented in Lunne et al. (2006). Sample quality is quantified by the value of $\Delta e/e_o$, which is the difference between the initial void ratio and the void ratio at the in-situ vertical effective stress measured during consolidation testing on the compression curve. The greater this difference, the more disturbed the sample is presumed to be because it is assumed that the sample has undergone significant strain between its in-situ state and the same stress state during consolidation testing. This could be due to sampling, handling, preparation, etc. In Table 4.6, categories are presented from “Very good to excellent (1)” to “Very poor (4)” that depends on the estimate of $\Delta e/e_o$ as well the OCR of the sample, whether 1-2 or 2-4. This indicates that more overconsolidated samples should exhibit less strain than less overconsolidated materials if they are at the same degree of sample quality. Of note is that the Lunne et al. criteria is based on testing of Holocene clays from shallow depths, so the criteria does not reflect the depositional environment and stress conditions of the OBC.

For all the consolidation testing in this study, an estimate of $\Delta e/e_o$ was made. For CRS testing, the void ratio at the in-situ vertical effective stress could be queried from the continuous data. For IL testing, the void ratio usually had to be interpolated between increments on the presumed compression curve. It should be noted that, as discussed in the Section 4.2.2, OCRs for OBC almost exactly straddled the OCR=2 distinction of the Lunne criteria.

4.7.2 Results

Figure 4.38 presents estimates of sample quality from consolidation tests of YBM, OBC, and Alameda soils. The majority of samples from YBM and OBC would be classified as “Very Good to Excellent”, with one sample in YBM classified as “Poor” and several samples in OBC classified as “Good to Fair.” Alameda samples were mostly “Good to Fair” with a couple being classified “Poor.” From the sample data, a relationship between sample quality and depth is apparent.

In Figure 4.39, the various types of Shelby tubes that contained samples tested in this study have been plotted against sample quality. In general, Epoxy-coated sample tubes were used for project samples, but some samples tested came from zinc-coated steel Shelby tubes as well as standard steel Shelby tubes. All of the Shelby tubes were as described in Section 2.4, having no turned-in edge and a sharpened cutting edge. However, it was noticed with the zinc-coated steel tubes that a reaction with the soil and the tube weld occurred, which produced a very small gap on the side of the sample. In addition, both the zinc-coated and steel Shelby tubes tended to be more difficult to extrude and leave behind residual soil coatings on the sample tube after extrusion. It does appear that the epoxy-coated tubes as tested in the OBC soils had generally less disturbance than the other types, however, there was a lot of variability. It is possible that the dependence on tube material is not as strong as would be assumed from handling the samples. The dependence of depth appears to be greater than between Shelby tube materials.

4.7.3 Discussion

The Old Bay Clay samples used in this study were generally of Very good to Excellent sample quality. This is important for assessing the quality of the strength testing performed, but it also

helps to validate the practices involved in sampling, handling, and specimen preparation for testing. In particular, the various steps taken to prepare the samples for consolidation testing, including the large soaking increments, do not have a negative influence on the sample quality.

The Alameda samples varied in sample quality from Good to Fair to Poor. Based on the Lunne criteria, this is correct. However, the criteria does not account for deep samples as it does for less overconsolidated (OCR 1-2) versus more overconsolidated samples (OCR 2-4). Especially because the criteria is based on the strain that occurs between the in-situ vertical effective stress between the field and the laboratory, deeper soils will be somewhat penalized by this measure. It would be interesting to have a sample quality scale that considered sample depth so that a relative degree of sample quality could be assessed for deep samples. The deep Alameda samples in this study were handled the same as the relatively more shallow OBC samples, which showed Very good to excellent sample quality. It makes sense that a sample from 200 feet may be more disturbed from a sample from 20 feet, but more helpful may be a sample quality assessment comparing all samples obtained from 200 feet. That the majority of Alameda samples were classified as Good to Fair and Poor is not as helpful as a quantitative measure with other samples taken from depth.

One of the samples from shallow Young Bay Mud that was excluded had a relatively high sample disturbance. This specimen also produced other results that tended toward generally extreme values. The assessment of sample quality helped to contextualize these values that did not appear to conform and helped to determine not to include the parameters with the rest of the project data. For projects that produce copious testing data, in addition to doing statistical analysis, it might be helpful to also weigh the testing data by sample quality. For the case of the outlier YBM data, understanding that the sample was of Poor quality helped to understand that the results were negligible.

4.8 Conclusions

In this Chapter, the results of consolidation testing were discussed as well as insights gained into testing methodologies and how they impact the estimated parameters. Compression parameters from consolidation tests within the Young Bay Mud, Old Bay Clay, and Alameda clays were compared. The Old Bay Clay and Alameda soils were found to be moderately to slightly overconsolidated. The Old Bay Clay and Alameda soils were found to be compressible, consistent with their moderate water content and moderate plasticity. Compression parameters including compression index, recompression index, secondary compression, and coefficient of consolidation were compiled and compared with similar materials. There was also an assessment of sample quality in order to quantify disturbance from sampling, handling, and trimming techniques. Sample quality was found to be very good for Old Bay Clay and moderate for Alameda soils, which may be due to the substantial depth of the deposit and how sample quality can reflect depth.

Testing these materials also led to a focus on how consolidation testing methods and results are unique for some deep, stiff clays. For parameters that depend on constructions, including preconsolidation pressure, compression index, and recompression index, careful study was made regarding assumptions. Six methods of preconsolidation pressure were assessed and three methods routinely used in order to characterize dependence of methodology on estimates of

preconsolidation pressure. A small study was discussed using a known maximum past pressure in order to assess accuracy. For compression index, the difference in construction of field curves was discussed between CRS and IL compression curves, but also between IL compression curves with different constructions. An example settlement problem illustrated the variability of field curve construction on settlement estimates. Recompression index was compiled at various stress states to show the dependence on unloading magnitude and stress level. For recompression to be a meaningful parameter, it is suggested that more uniformity is used for calculation, as well as some ways to compute recompression index to compare between various unloading magnitudes and stress states.

While not dependent on constructions, secondary compression and coefficient of consolidation both produce a range of values in any given oedometer test. For secondary compression, values were compiled for every loading, unloading, and reloading increment to show dependence on stress history. For coefficient of consolidation, values were compared between IL and CRS testing for understanding of instantaneous coefficient of consolidation estimates in CRS testing as well as dependence on stress level.

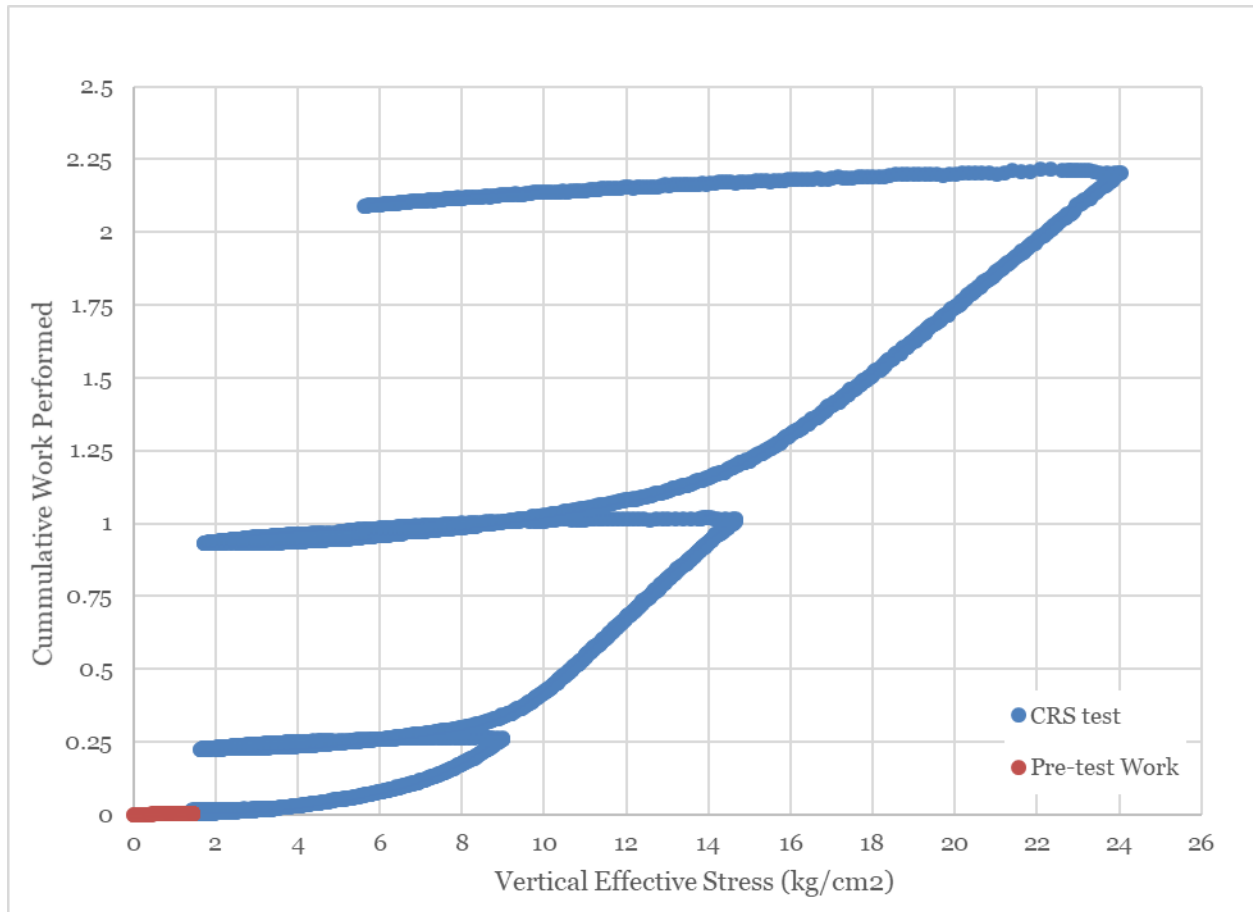


Figure 4.1. Cumulative Work per Unit Volume plot for a CRS test.

Cumulative Work per Unit Volume plot for a CRS test, showing curvature in slope at initial portion of the test and concave downwards shape at large stresses. Work performed after seating and before beginning of test is plotted in red. The estimated in-situ vertical effective stress is 3.6 kg/cm².

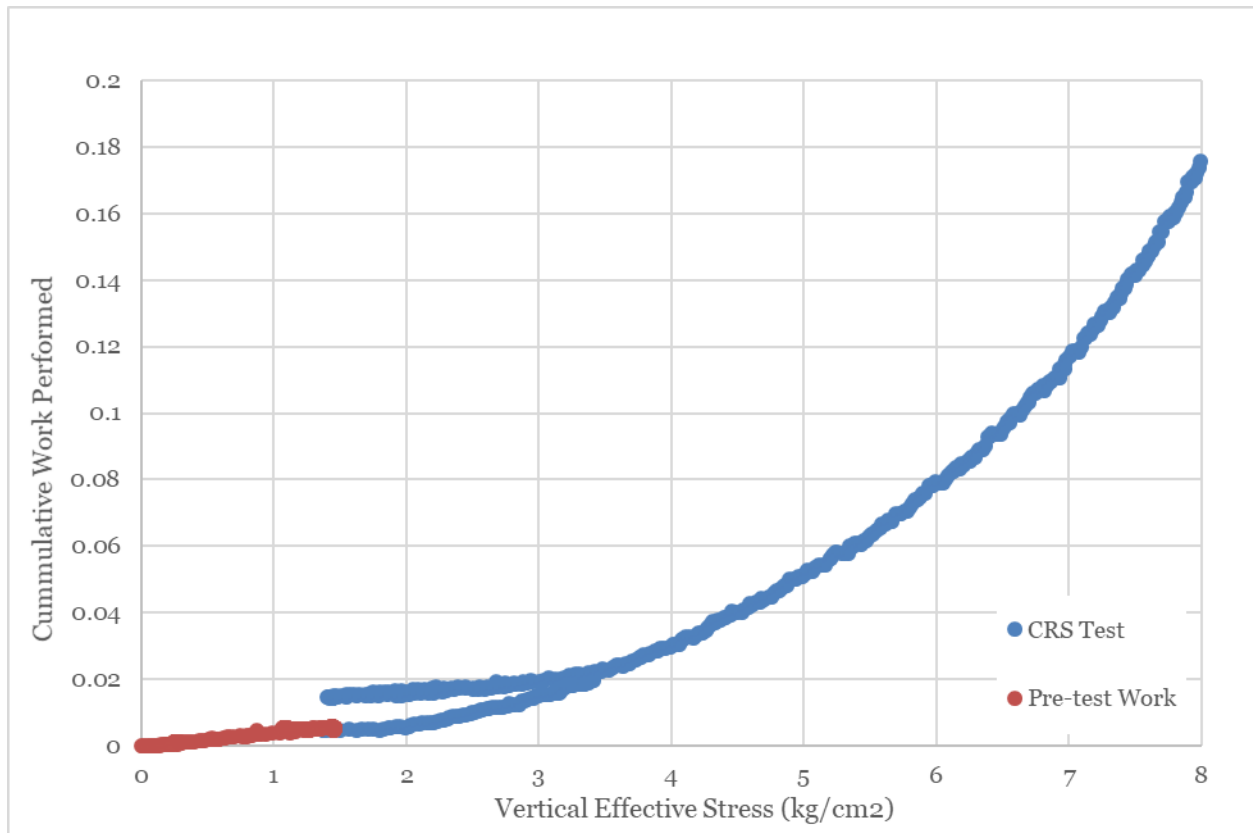


Figure 4.2. Cumulative Work per Unit Volume plot for a CRS test, showing initial curvature in slope. Work performed after seating and before beginning of test is plotted in red. The estimated in-situ vertical effective stress is 3.6 kg/cm².

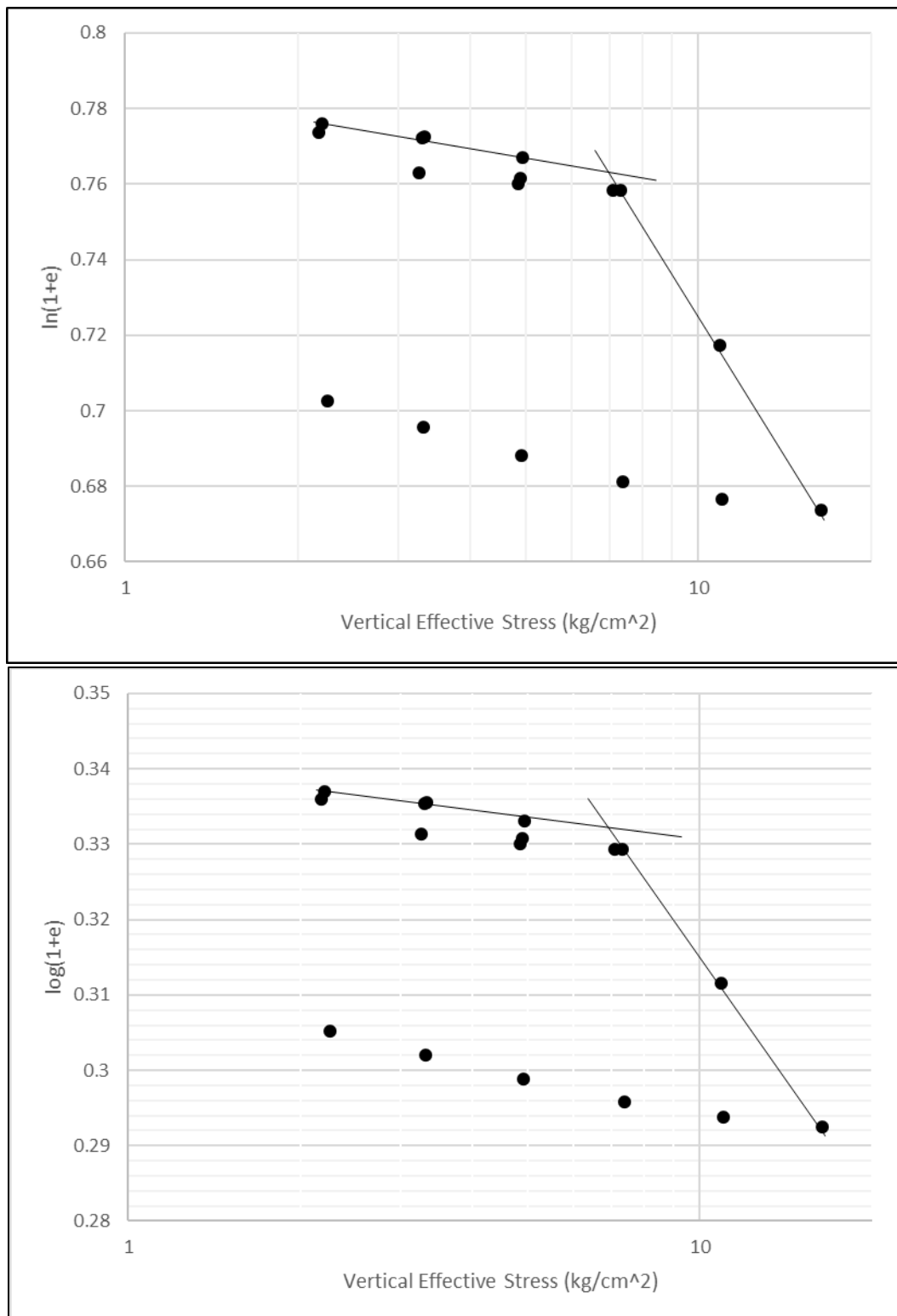


Figure 4.3. Oikawa (1987) method and Onitsuka et al. (1995) method for ILC test.
Top : Oikawa (1987), Bottom: Onitsuka et al. (1995)

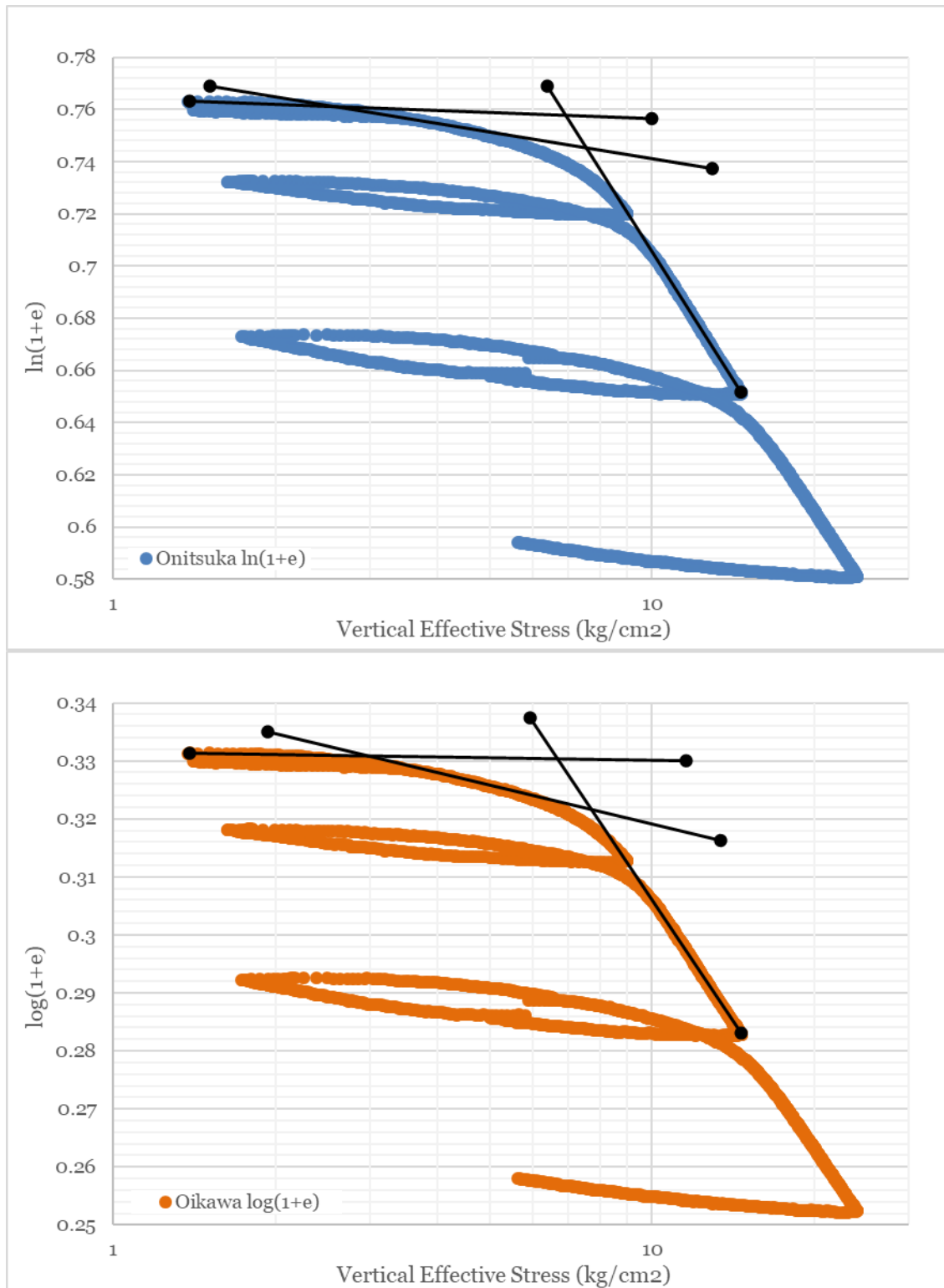


Figure 4.4. Oikawa (1987) method and Onitsuka et al. (1995) method for CRS test.
Top : Oikawa (1987), Bottom: Onitsuka et al. (1995)

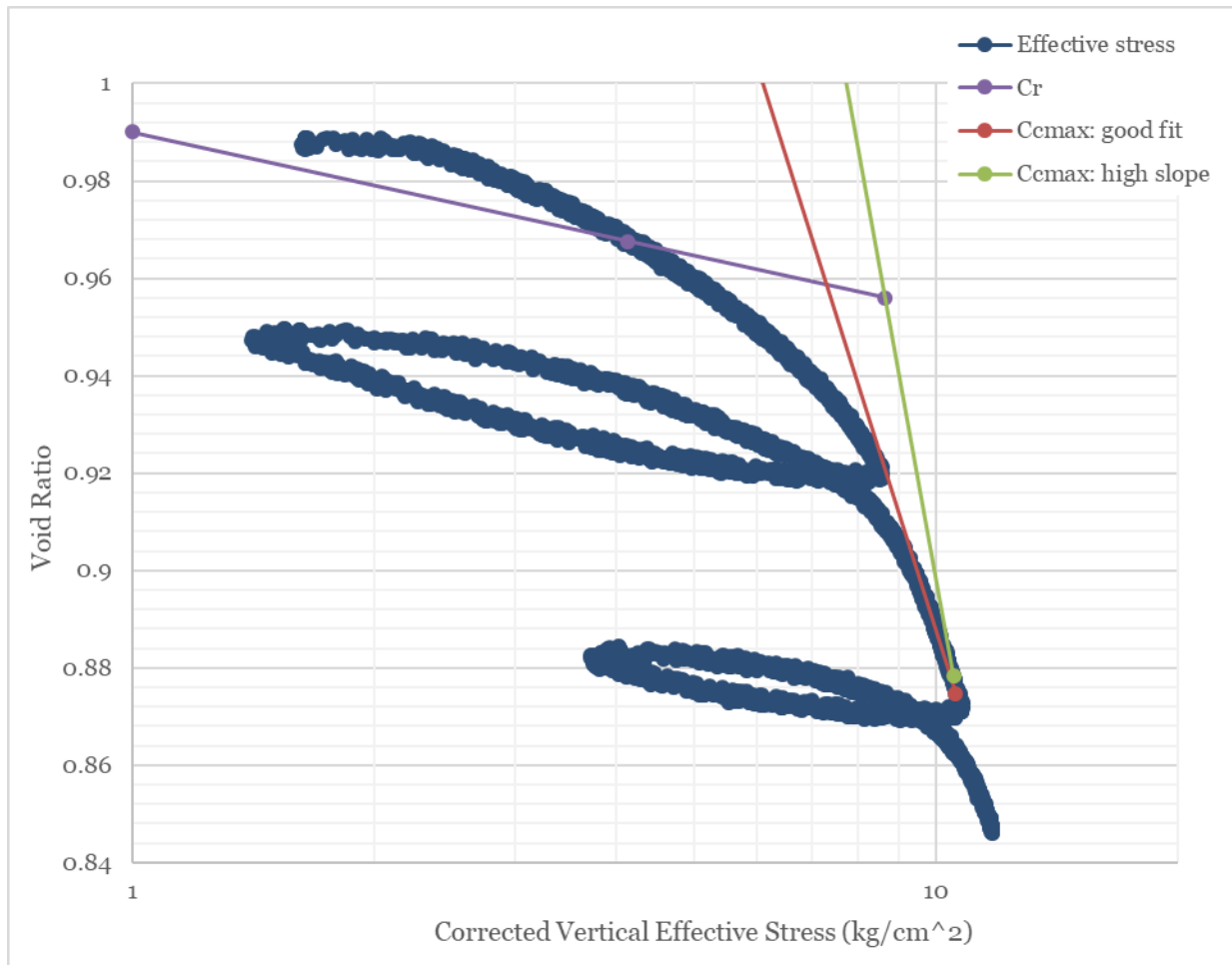


Figure 4.5. Consolidation Curve from a CRS test showing construction for the Boone (2010) method.

The red line is plot with a good fit to the slope of the actual data, the green line was plotted using an erroneously high slope value numerically identified from noisy data

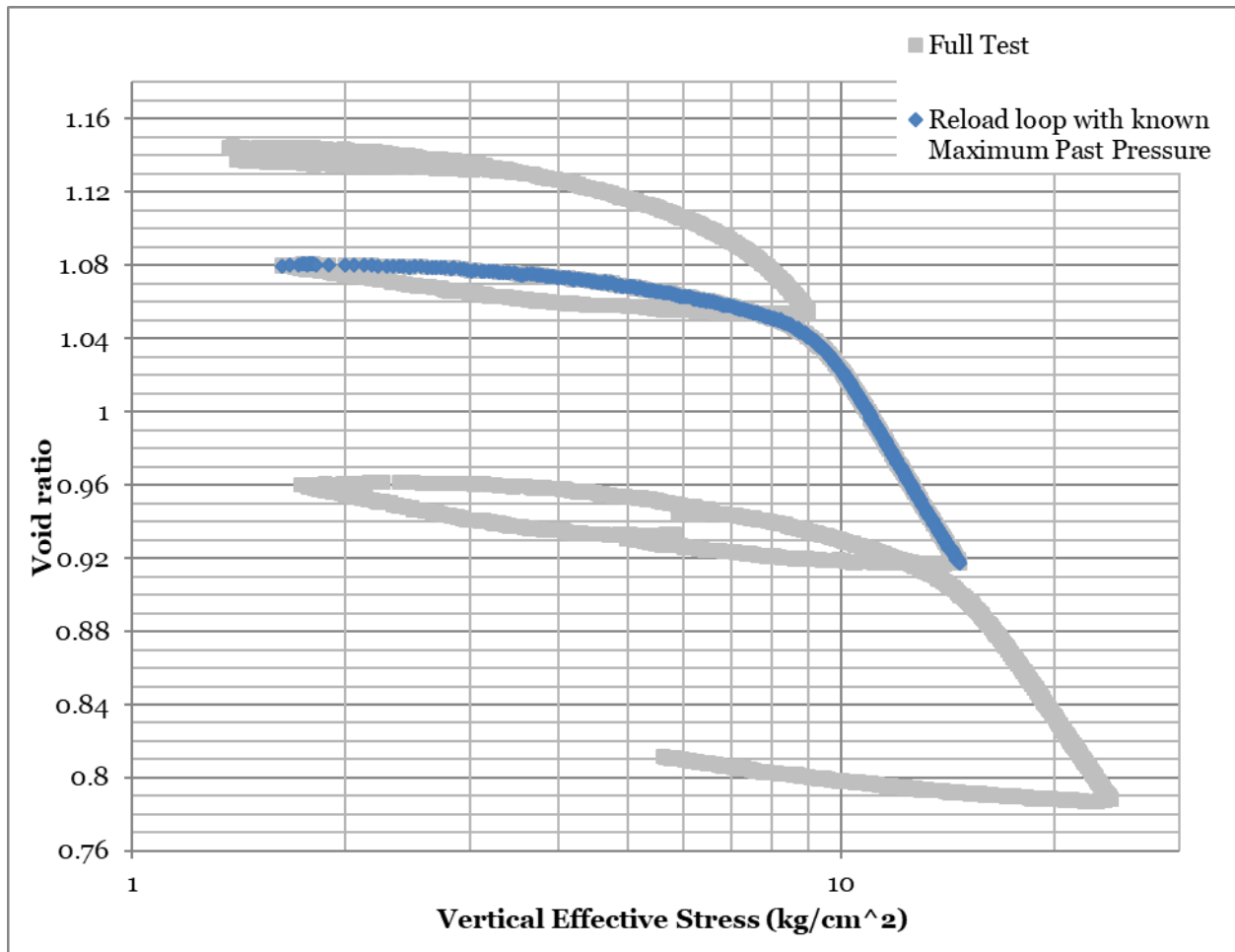


Figure 4.6. Consolidation Curve for CRS test, showing reload portion for known preconsolidation pressure analysis.

Full test is shown in gray, reload loop used for “known preconsolidation pressure” analysis is highlighted in blue

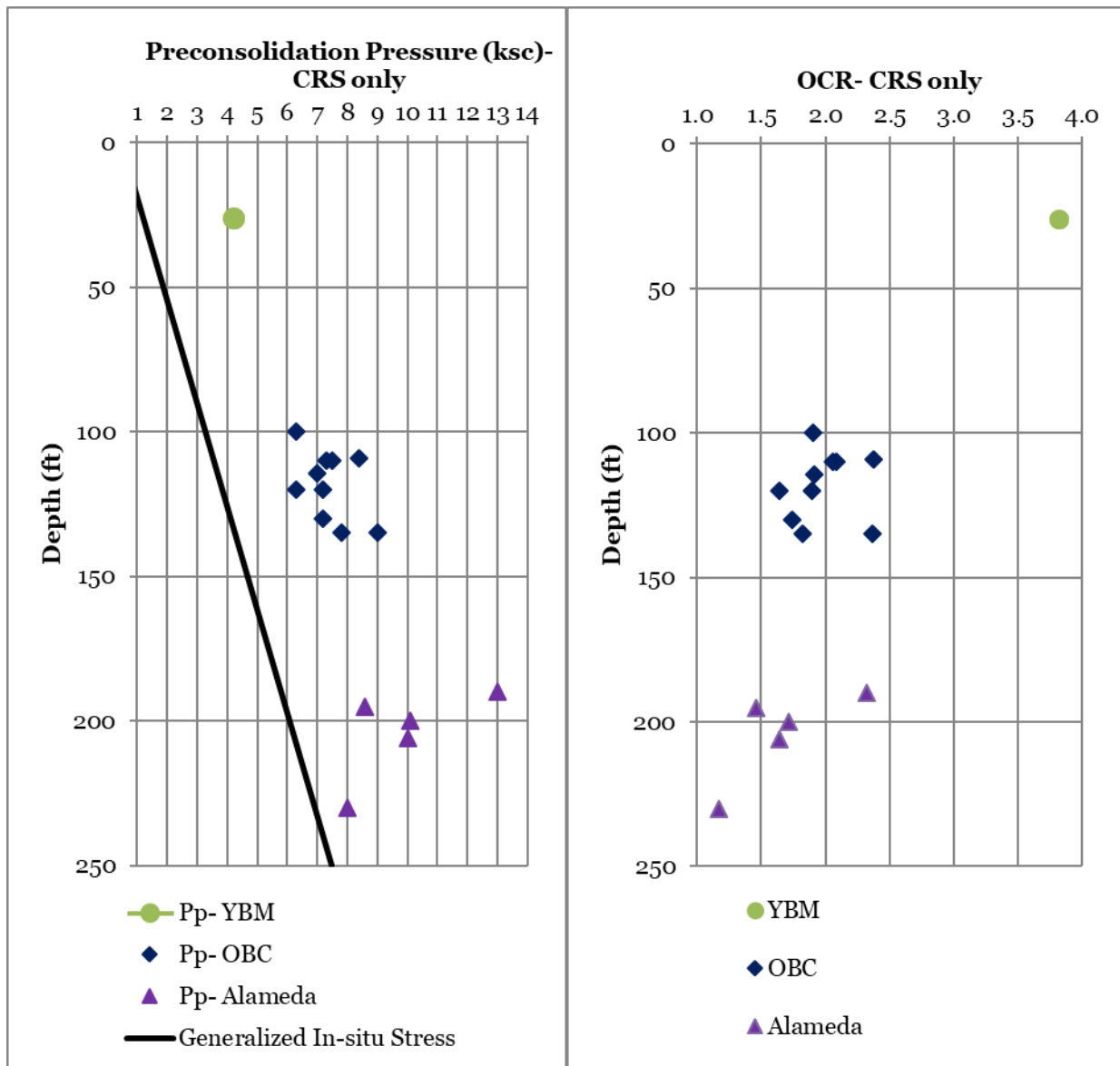


Figure 4.7. Preconsolidation Pressure and OCR from CRS testing.

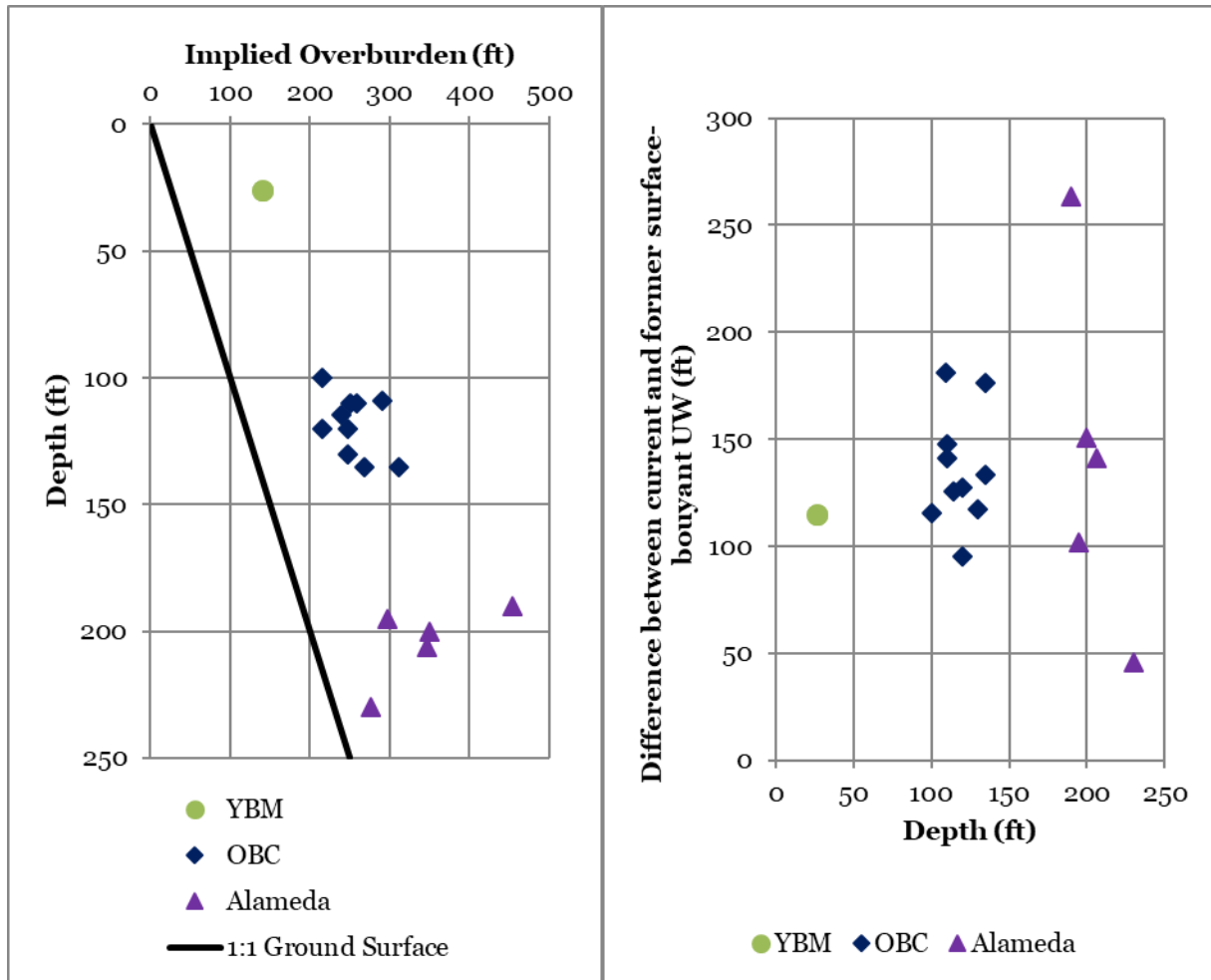


Figure 4.8. Implied overburden based on consolidation testing.

Left: Implied overburden if soil is submerged, marine clay, where the 1:1 line indicates the current ground surface.

Right: The difference between the implied overburden and the current ground surface. Positive values indicate a higher ground surface elevation than present

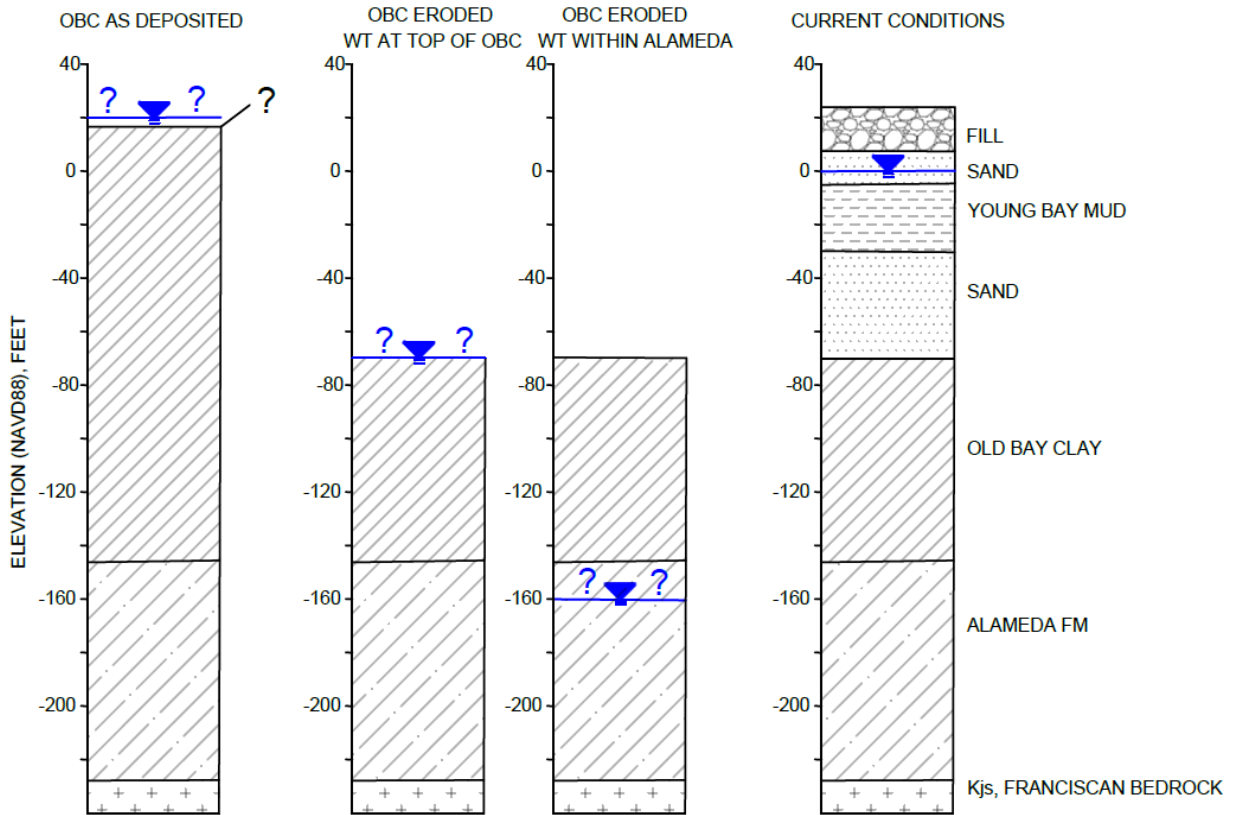


Figure 4.9. Schematic of possible stress history of Old Bay Clay deposit.

The stratigraphic column on the left represents the Old Bay Clay as deposited, with some unknown thickness and water table at the end of deposition. On the right are the current conditions. The two middle scenarios present Old Bay Clay after the upper surface has been eroded, with two groundwater scenarios: to the left, the water table is at the top of the Old Bay Clay and, to the right, the water table is within the Alameda formation.

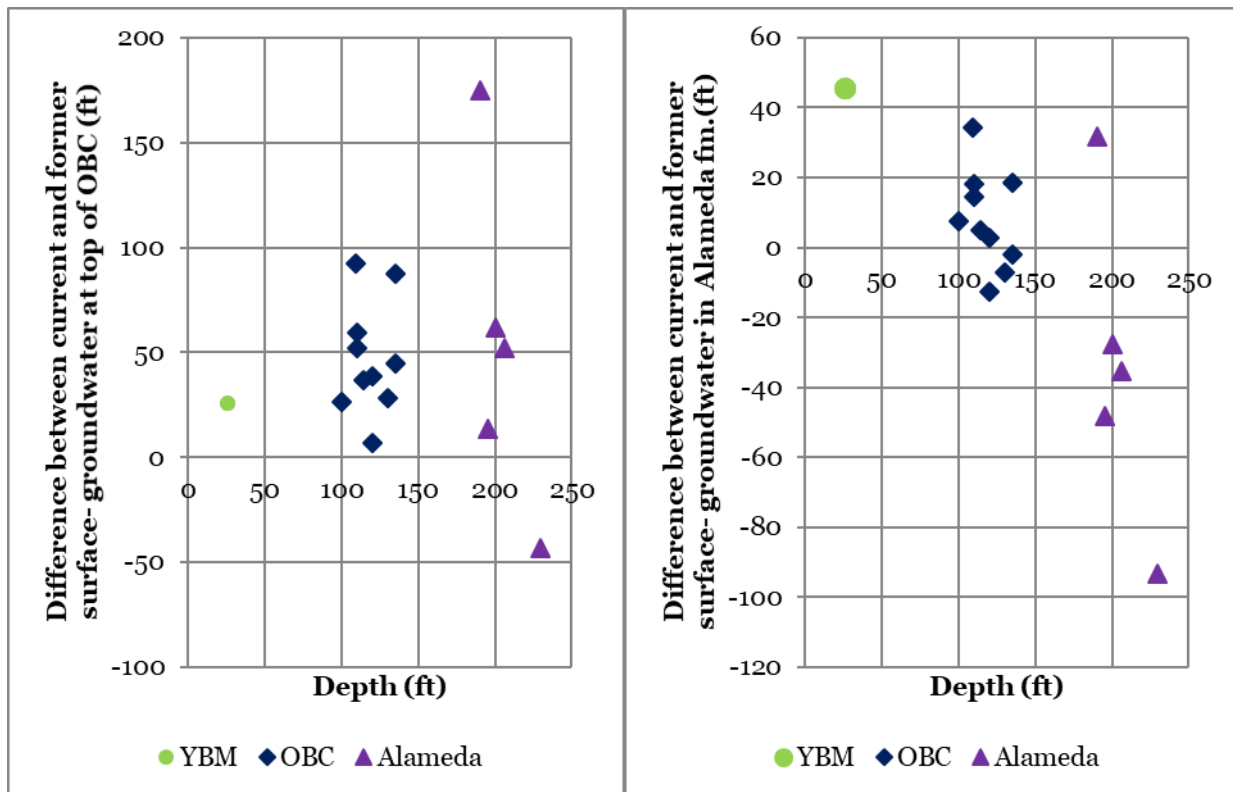


Figure 4.10. Effect of phreatic surface on estimation of previous ground surface.

The difference between the current and former ground surface, where positive values indicate a higher ground surface elevation than present, assuming: (Left) groundwater at the top of the Old Bay Clay, -70 feet (NAVD88) and (Right) groundwater within the Alameda fm., approximately -160 ft (NAVD88).

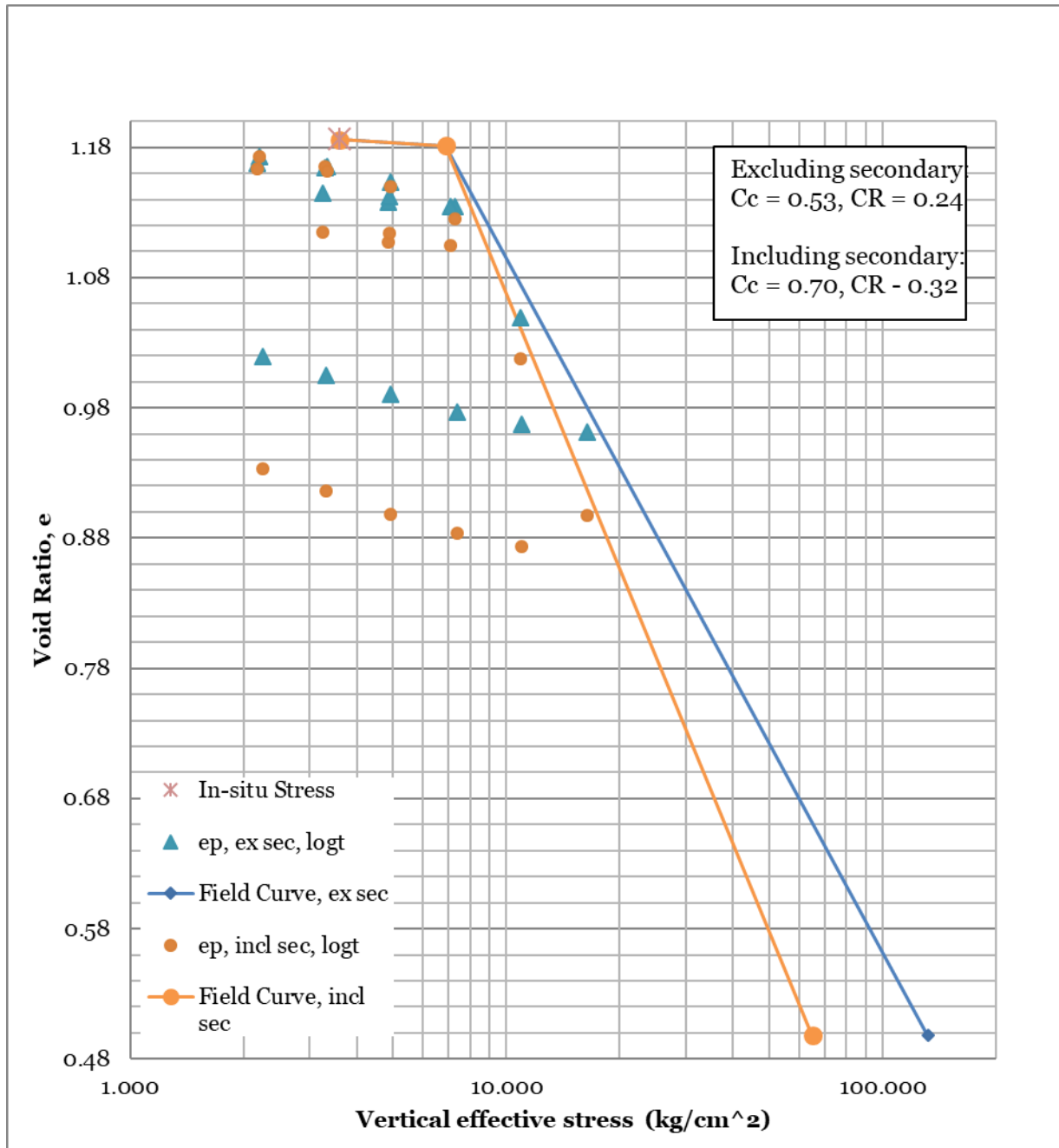


Figure 4.11. IL test with field curves for data excluding secondary and including secondary compression. Both sets of data were computed using the log of time method, Procedure 1

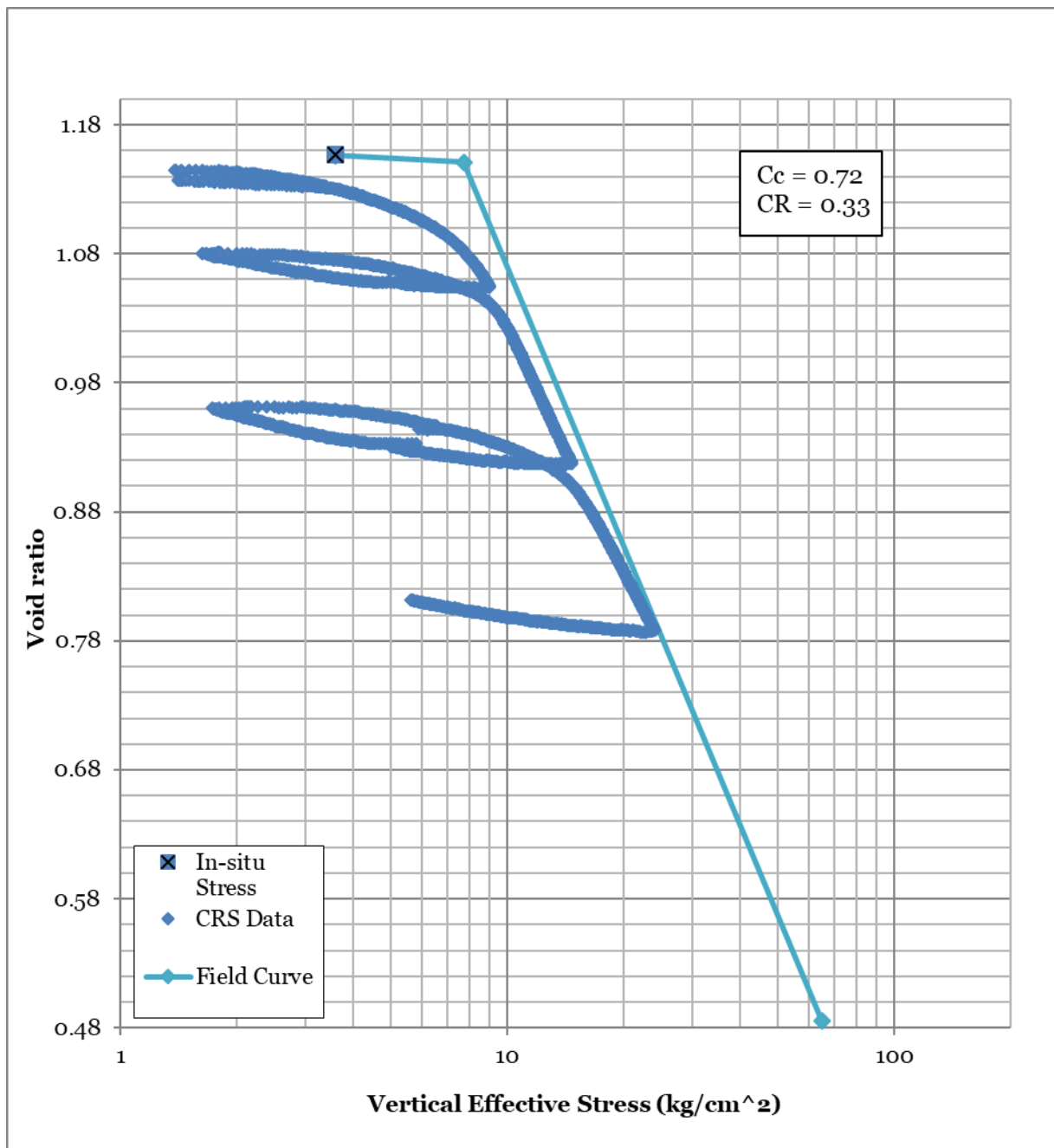


Figure 4.12. CRS test with field curve plotted.

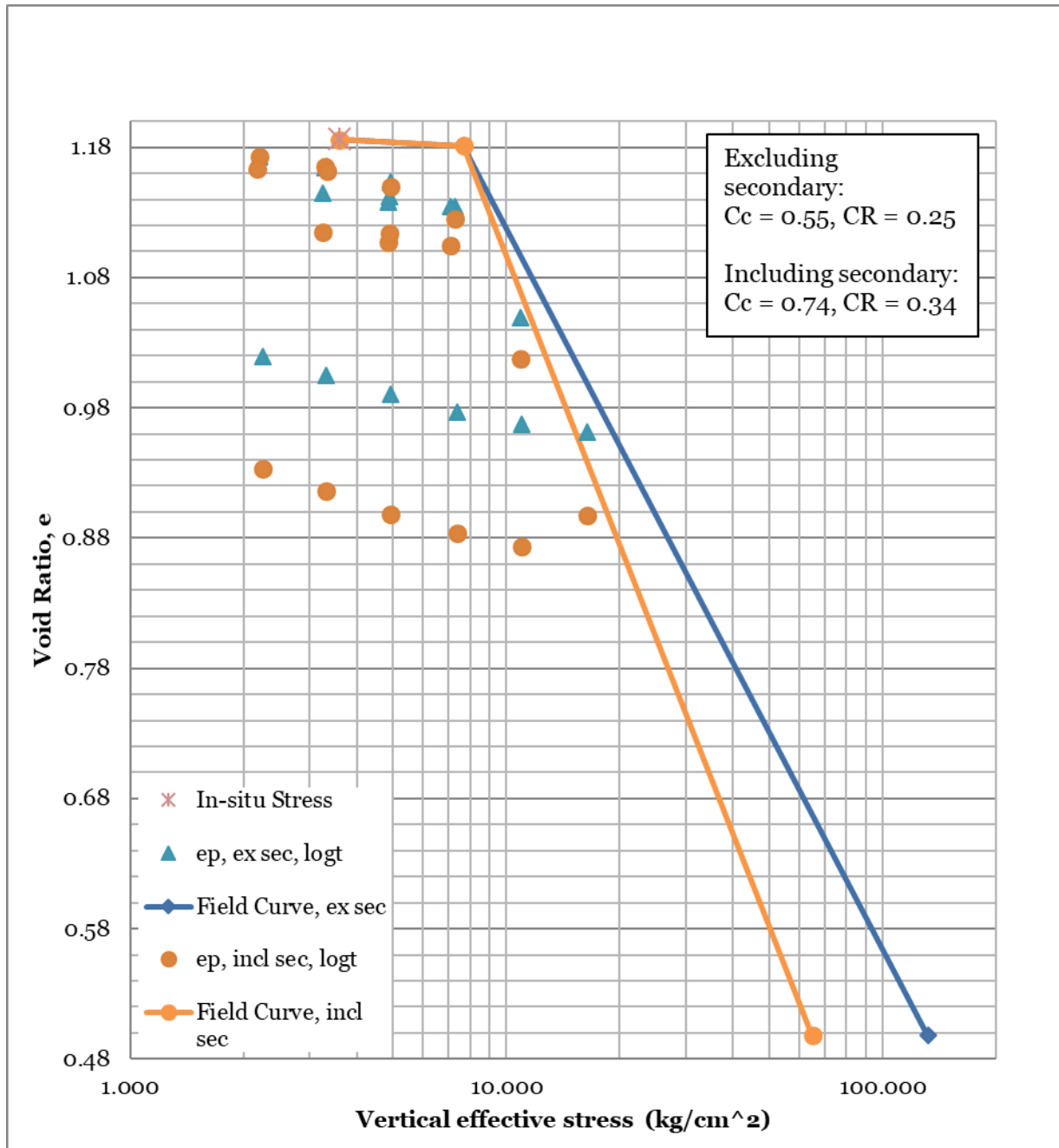


Figure 4.13. IL test with field curves for data excluding secondary and including secondary compression. Both sets of data were computed using the log of time method. These field curves have been calculated using the preconsolidation pressure determined from the paired CRS test, which yields higher values of compression index and compression ratio

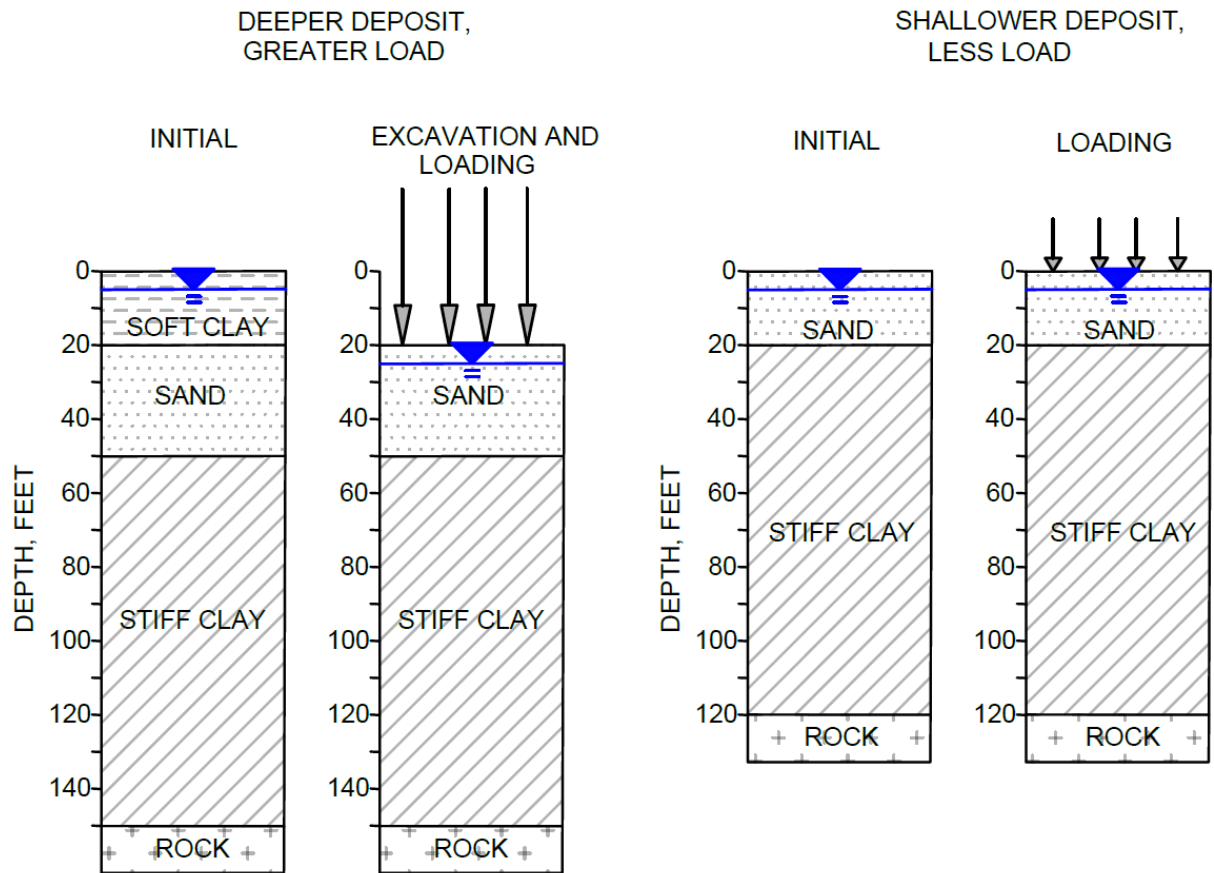


Figure 4.14. Example settlement problem schematic using C_c from CRS and IL testing.

The scenario on the left has a deeper deposit of stiff clay that under goes excavation and a large load placed at depth. The scenario on the right has a shallower deposit of stiff clay that has a smaller load placed at the ground surface.

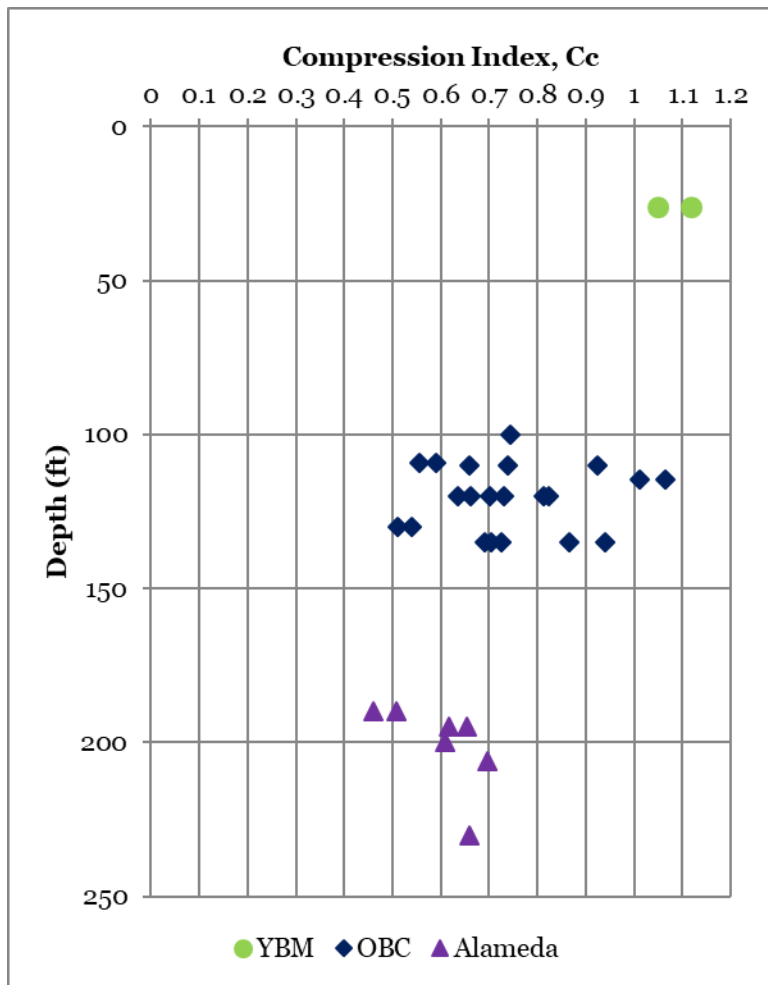


Figure 4.15. Compression Index (C_c) from consolidation testing of Young Bay Mud, Old Bay Clay, and Alameda.

Table 4.1. Summary of Compression Index (C_c) and Compression Ratio (CR) Results from testing of Young Bay Mud, Old Bay Clay, and Alameda soils.

	YBM		OBC		Alameda	
	Cc	CR	Cc	CR	Cc	CR
Min	1.05	0.48	0.51	0.23	0.46	0.21
Max	1.12	0.51	1.06	0.49	0.70	0.32
Mean	-	-	0.73	0.33	0.62	0.28
σ	-	-	0.15	0.07	0.09	0.04

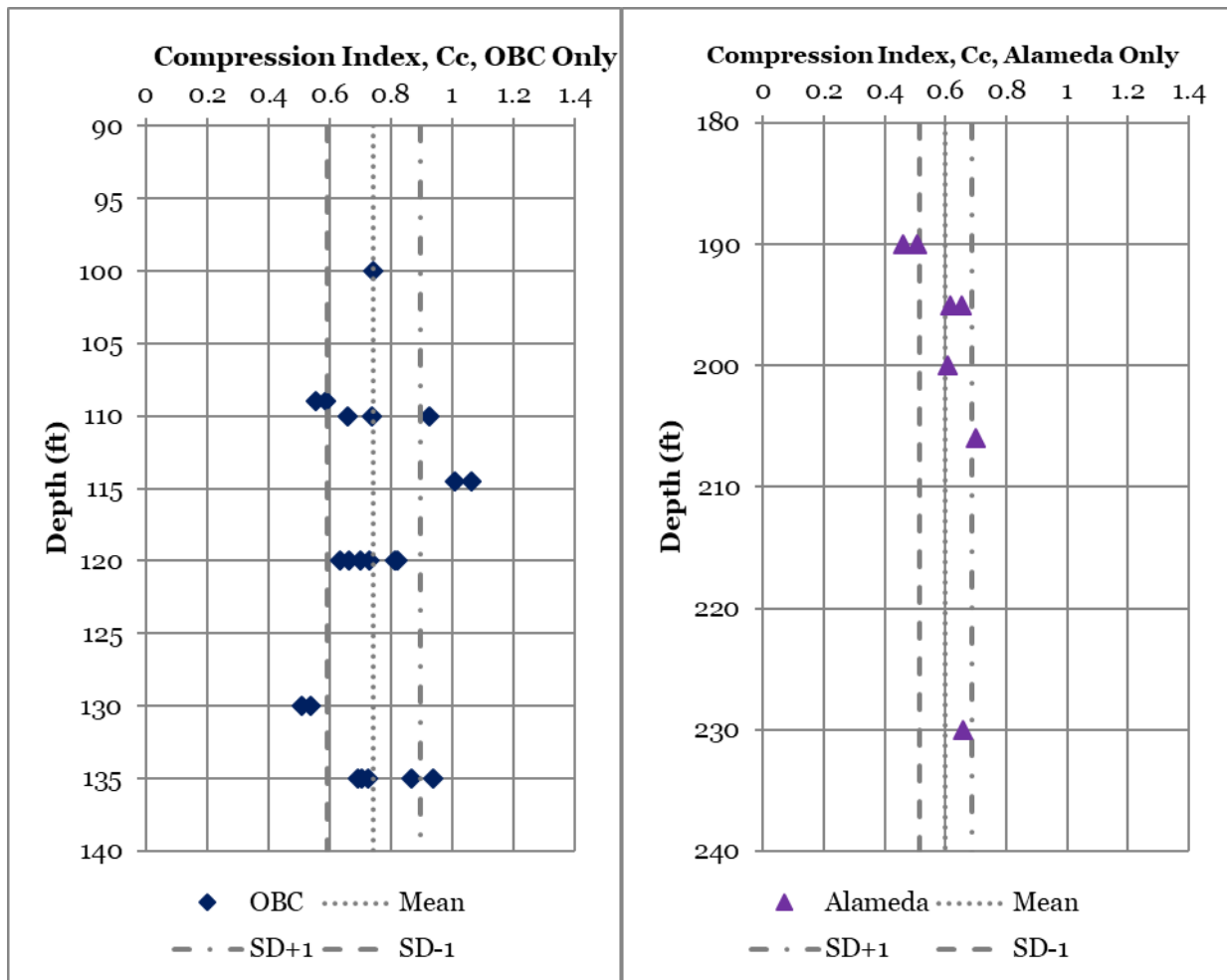


Figure 4.16. Compression Index (C_c) results for Old Bay Clay and Alameda samples with depth. Plots show Compression Index results for (Left) Old Bay Clay samples showing mean, mean plus on standard deviation, and mean minus one standard deviation from testing and for (Right) Alameda samples showing mean, mean plus on standard deviation, and mean minus one standard deviation from testing

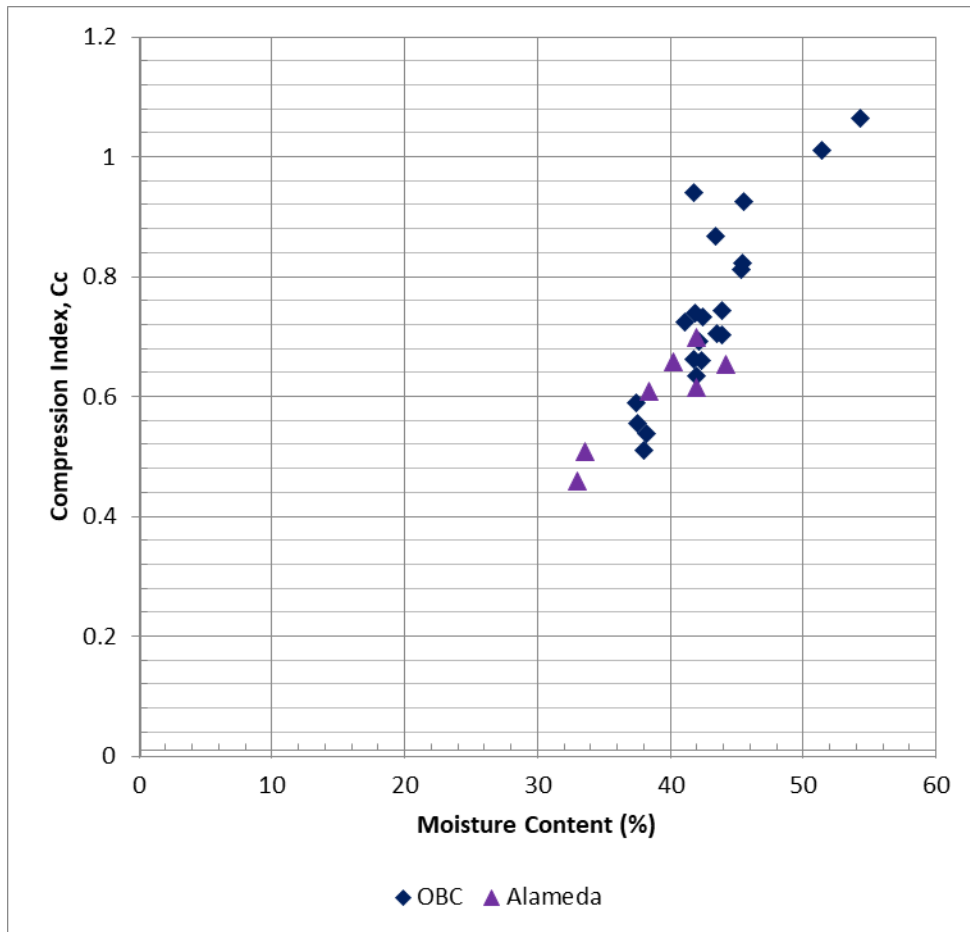


Figure 4.17. Compression Index (C_c) plotted against moisture content (%) for OBC and Alameda samples.

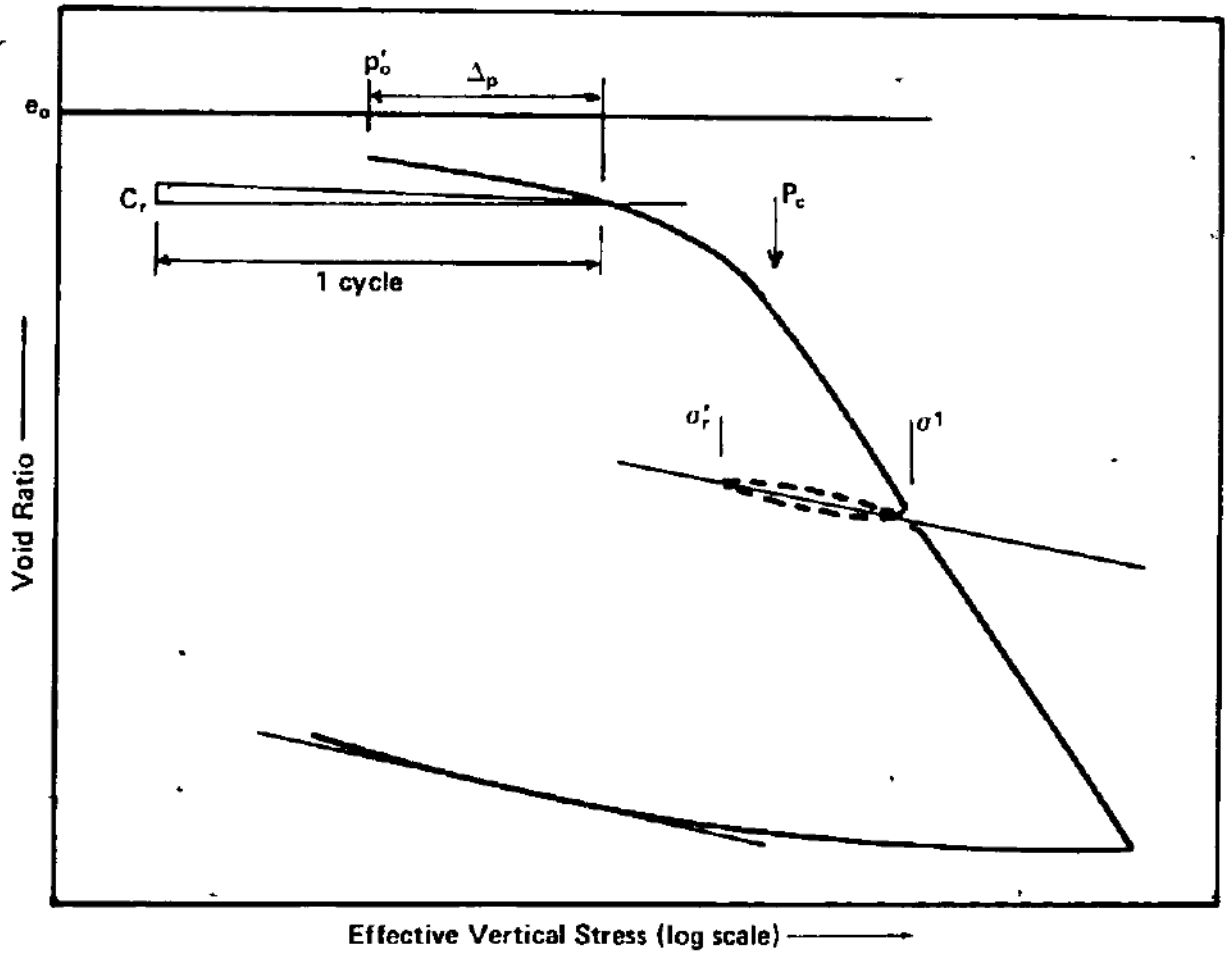


Figure 4.18. "Typical curve of void ratio versus effective vertical stress," from Leonards (1976).

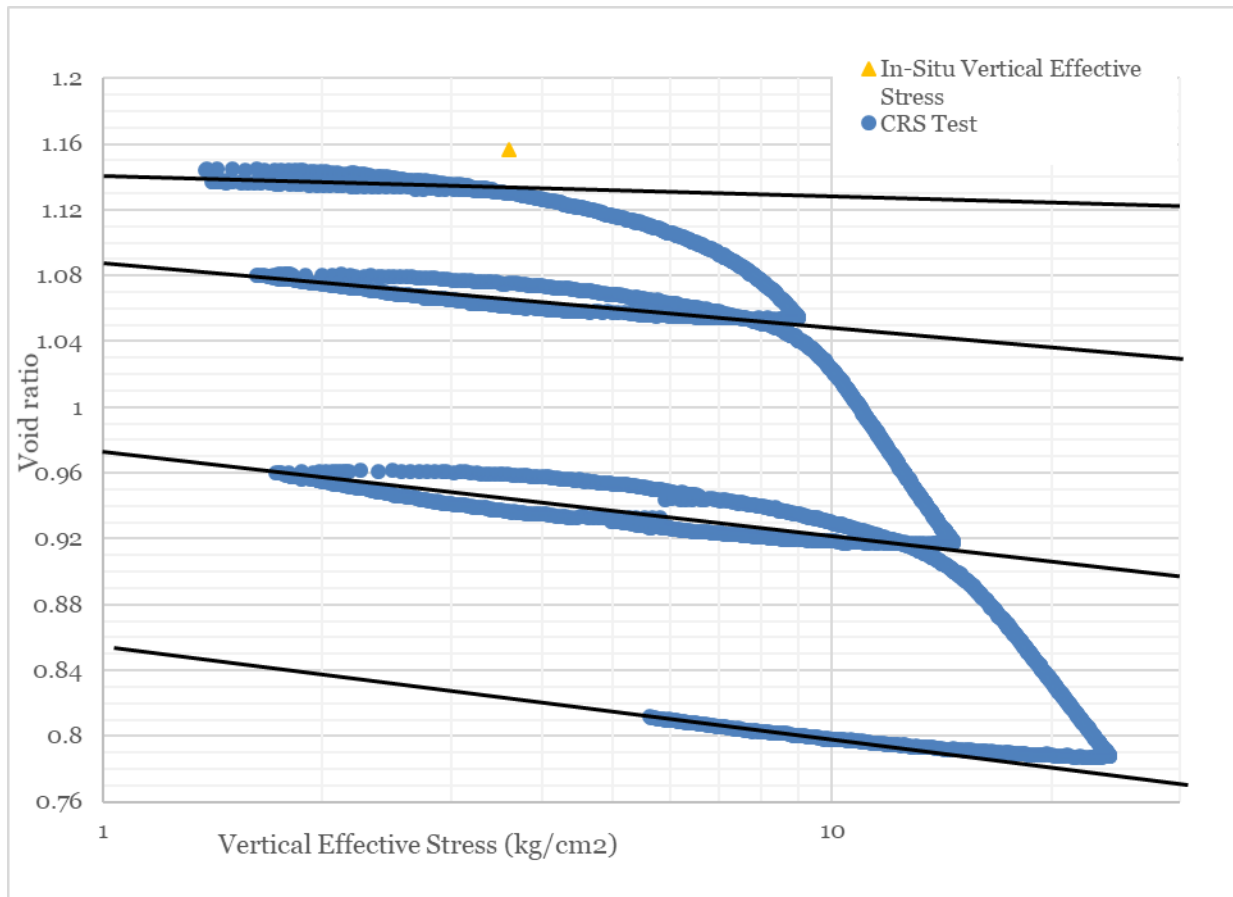


Figure 4.19. Compression curve run with multiple unloading cycles to show recompression slope. Plot shows the increasing slope of the recompression portions for each of the four unloading cycles of the compression curve.

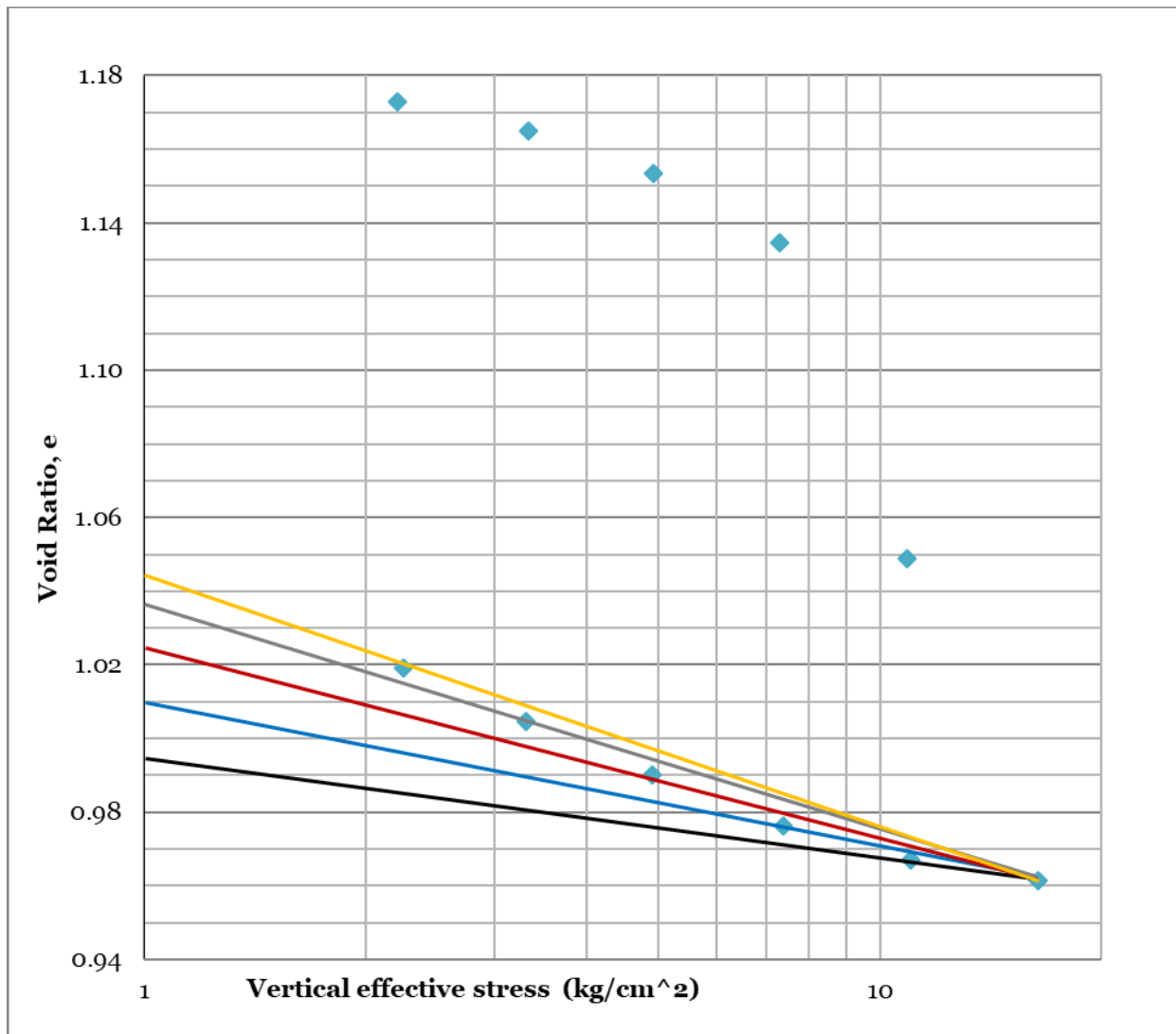


Figure 4.20. IL test showing various recompression slopes depending on the unloading increment.

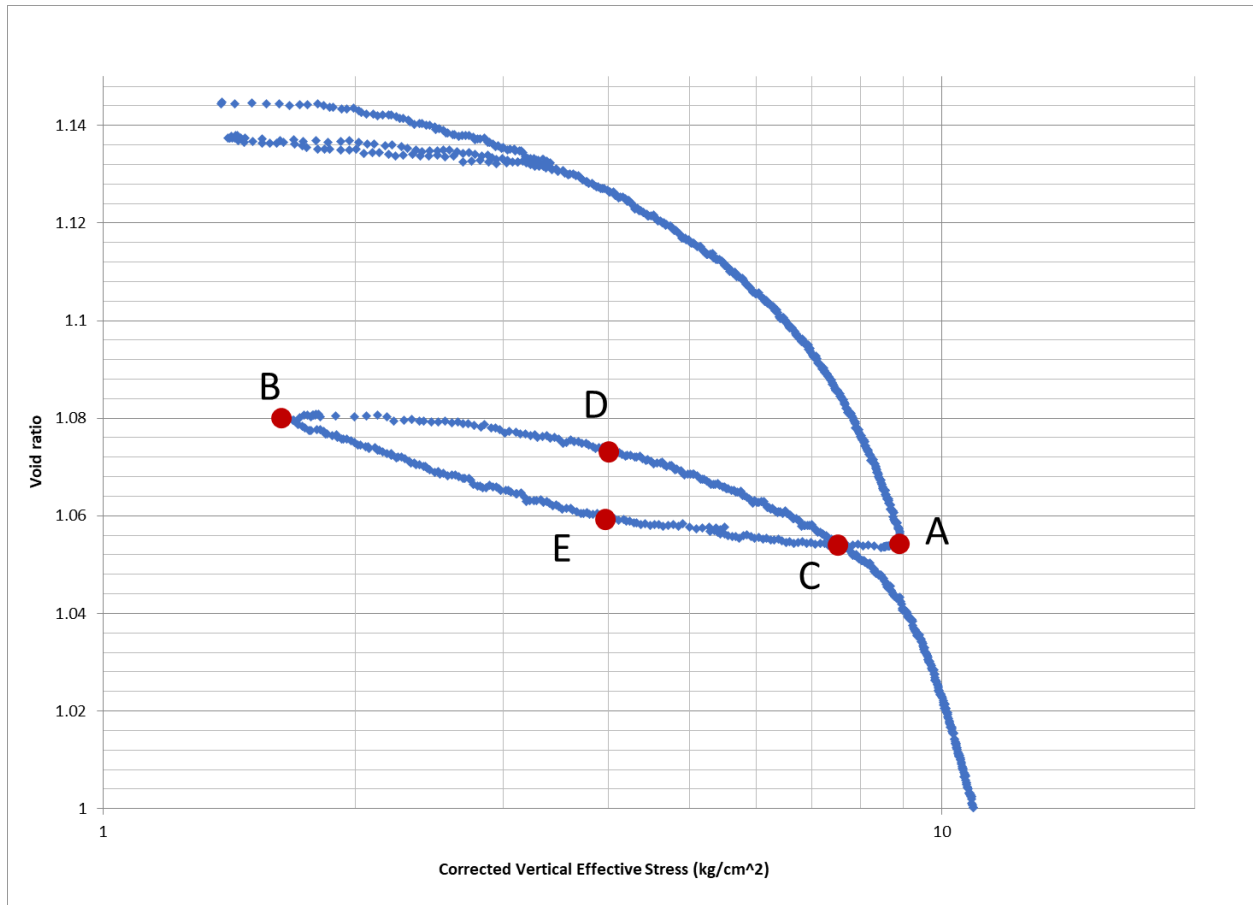


Figure 4.21. An unloading loop, showing various points that can fit a straight line in order to define the recompression (C_r) index.

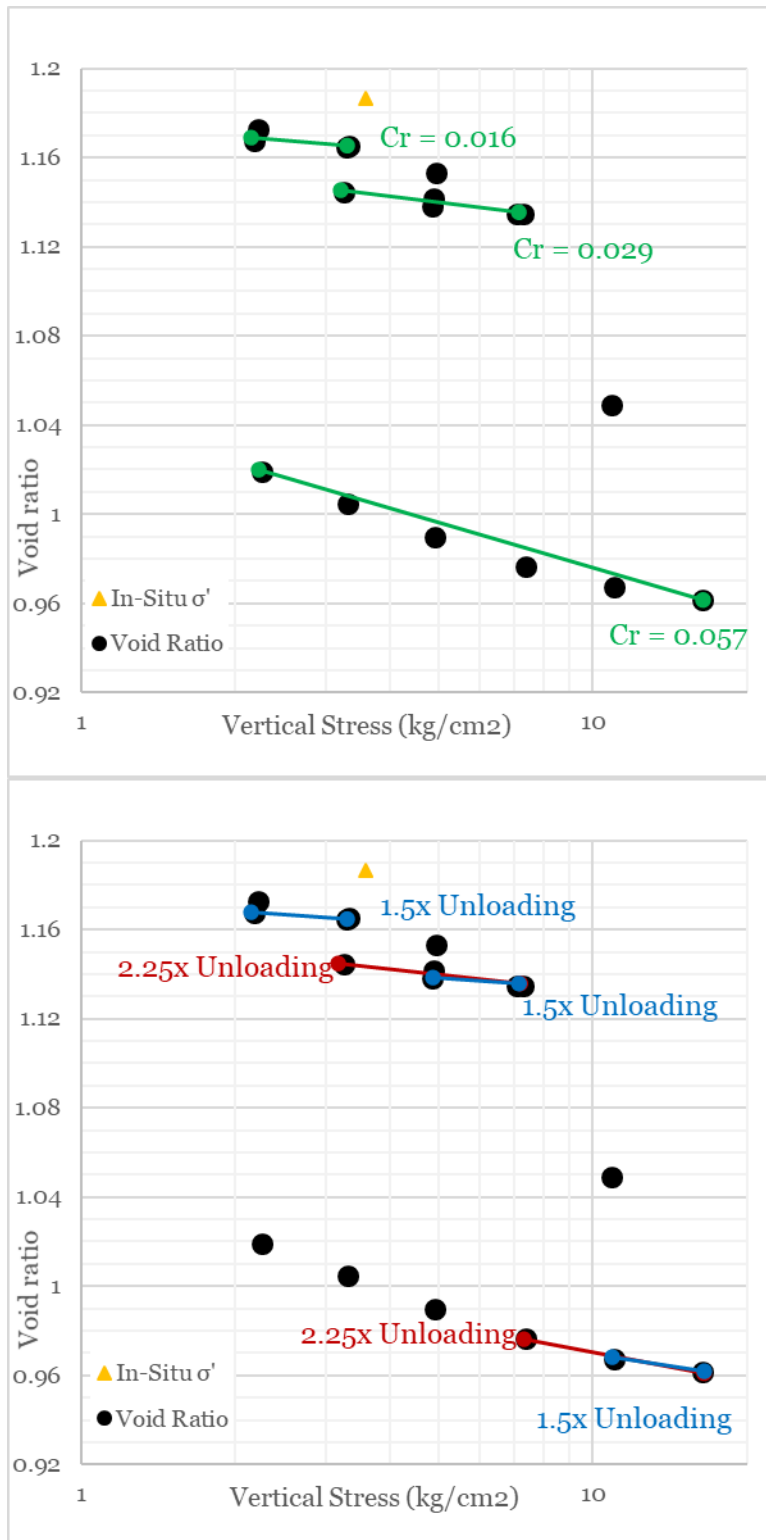


Figure 4.22. ILC test showing various calculations of recompression index (C_r).

Top: recompression index is calculated for each unload-reload cycle. Bottom: recompression index is calculated based on the magnitude of unloading

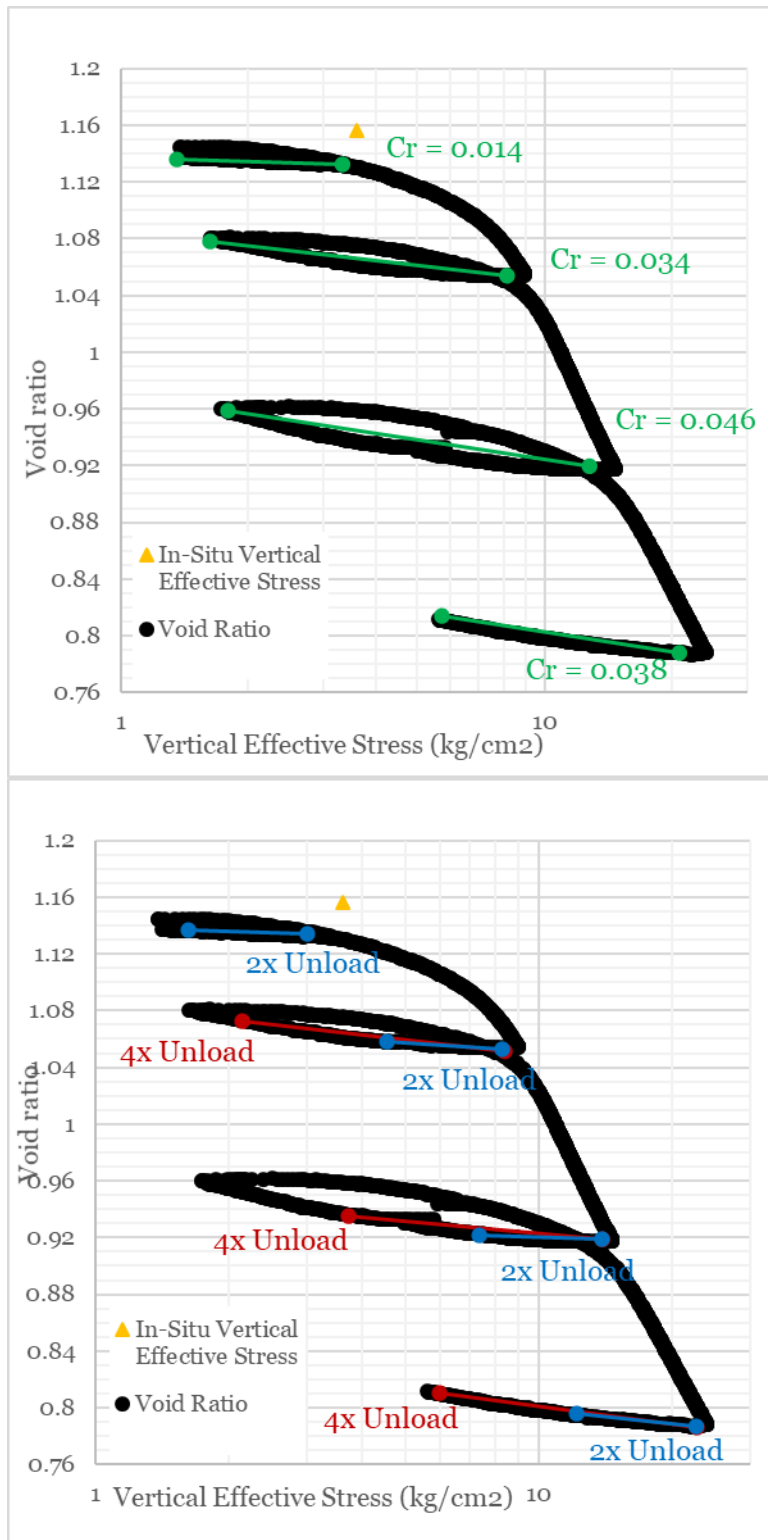


Figure 4.23. CRS test showing calculation of recompression index for each full unload-reload cycle compared with magnitudes of unloading for the unloading loops.

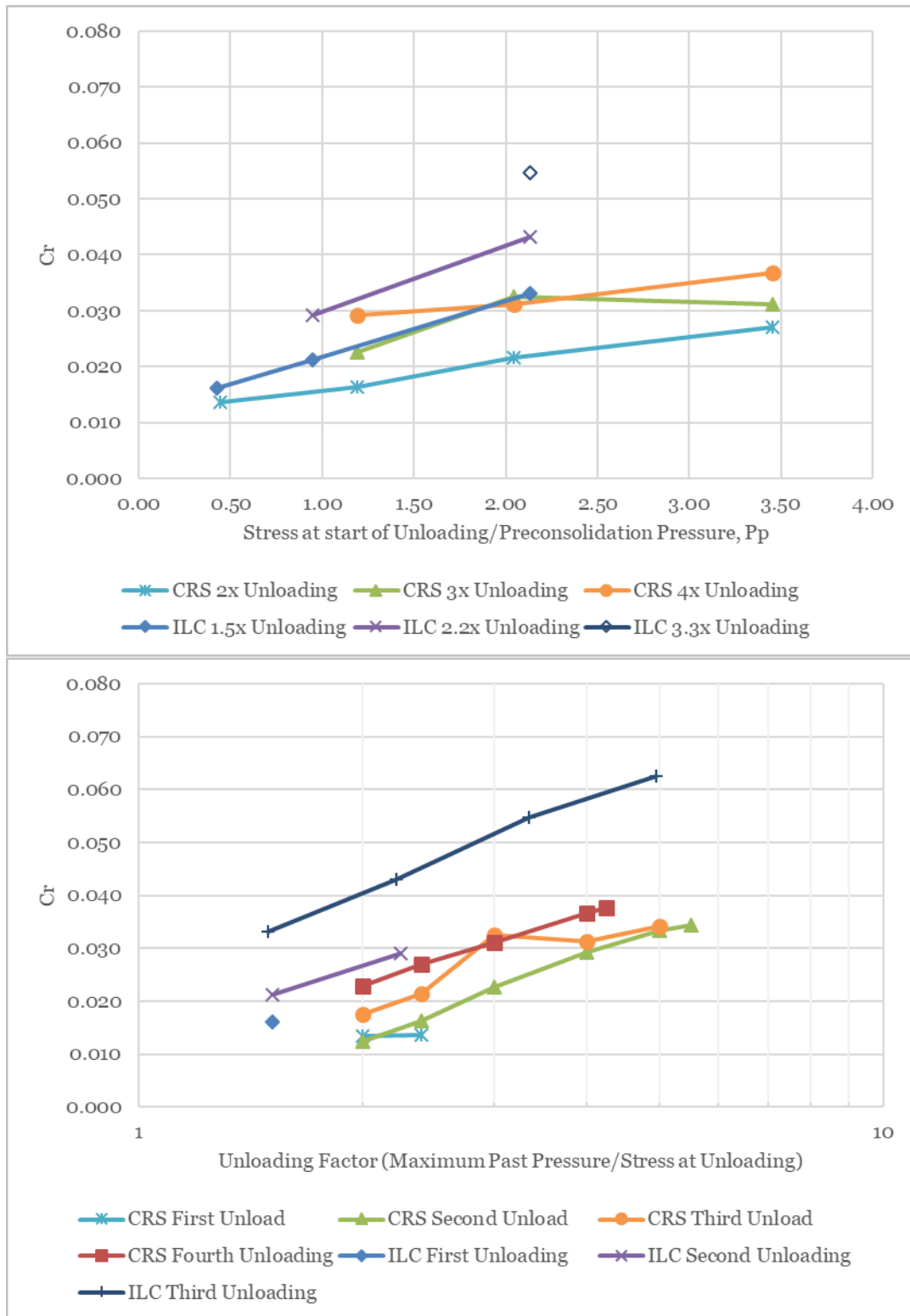


Figure 4.24. Recompression index (C_r) is calculated for both a CRS test and IL test using factors of unloading. Top: The recompression index is plotted against the ratio of preconsolidation pressure. Bottom: The recompression index is plotted against the unloading factor on a log scale

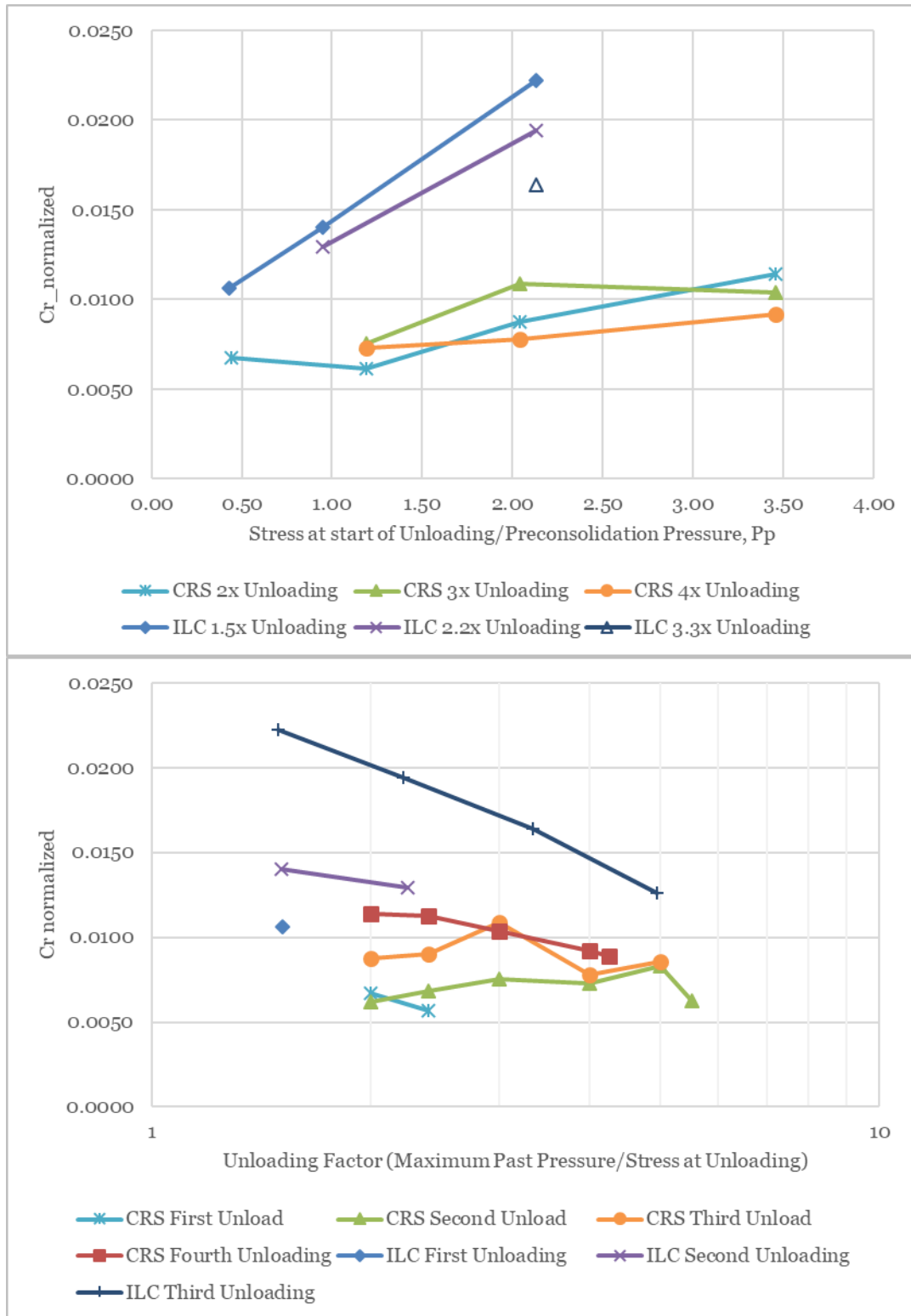
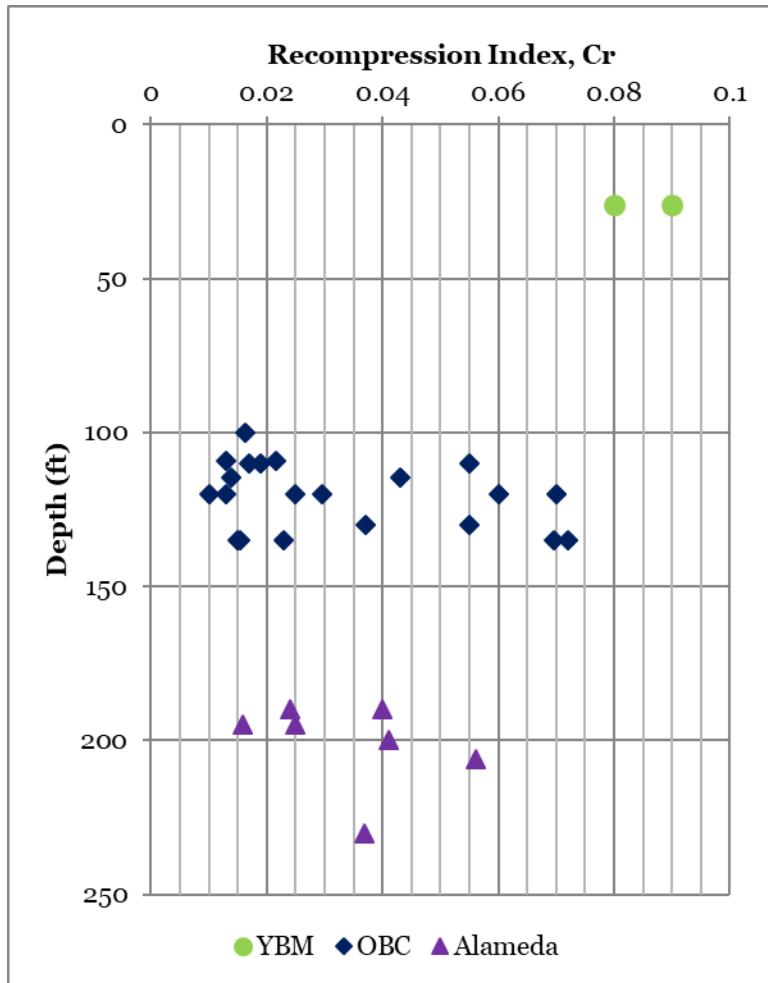


Figure 4.25. Normalized recompression index ($C_{r_normalized}$) for a CRS test and IL test using factors of unloading. Top: The recompression index is plotted against the ratio of preconsolidation pressure. Bottom: The recompression index is plotted against the unloading factor on a log scale



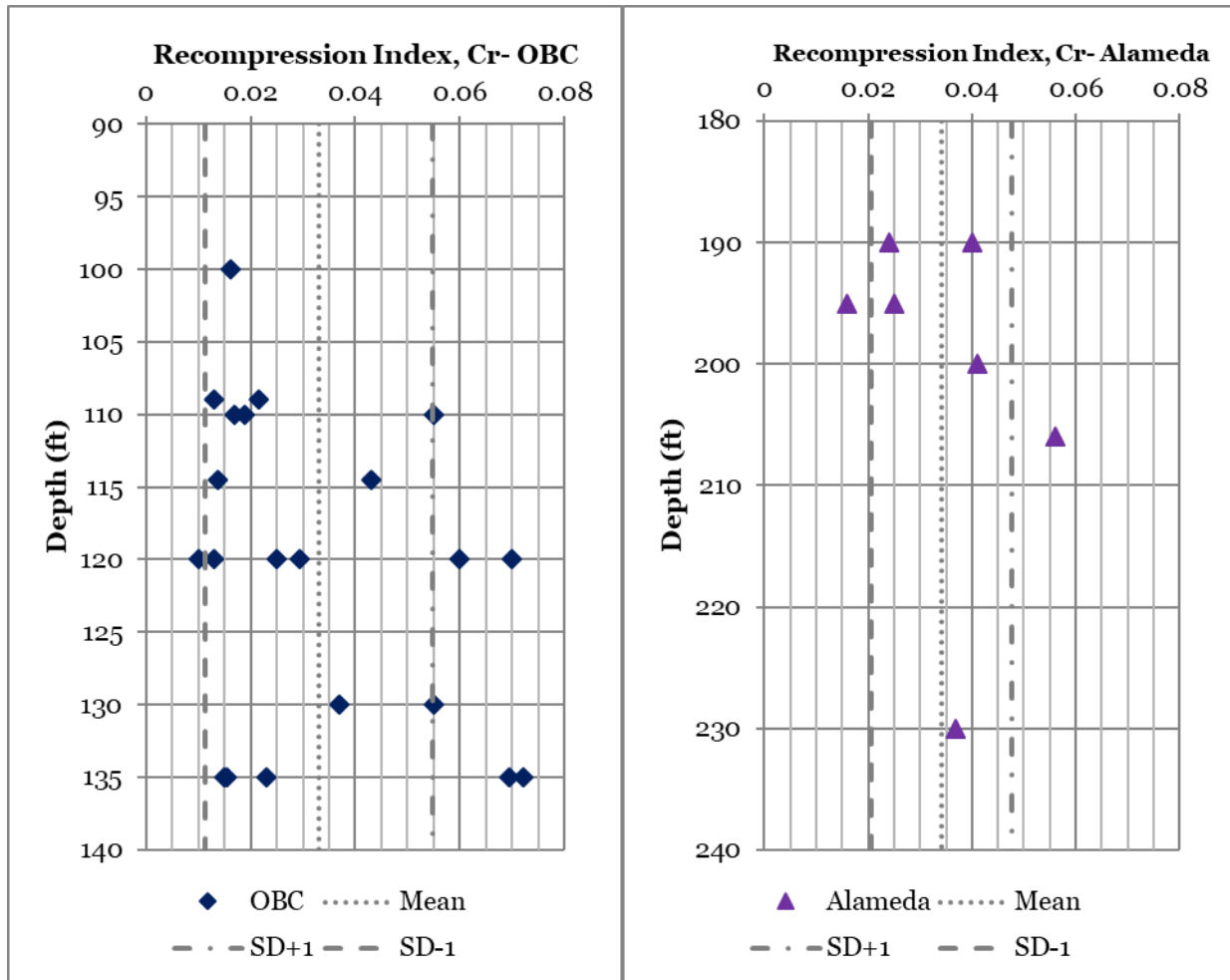


Figure 4.27. Recompression Index (C_r), normally consolidated, plotted for Old Bay Clay and Alameda soils. Plots show mean, mean plus one standard deviation, and mean minus one standard deviation from this testing data.

Table 4.2. Summary of recompression index (Cr) and recompression ratio (RR) values for Young Bay Mud, Old Bay Clay, and Alameda soils for normal consolidation.

	YBM		OBC		Alameda	
	Cr	RR	Cr	RR	Cr	RR
Min	0.080	0.036	0.0100	0.0046	0.0159	0.0073
Max	0.090	0.041	0.0720	0.0328	0.0560	0.0255
Mean	-	-	0.0330	0.0151	0.0341	0.0156
σ	-	-	0.0217	0.0099	0.0135	0.0061

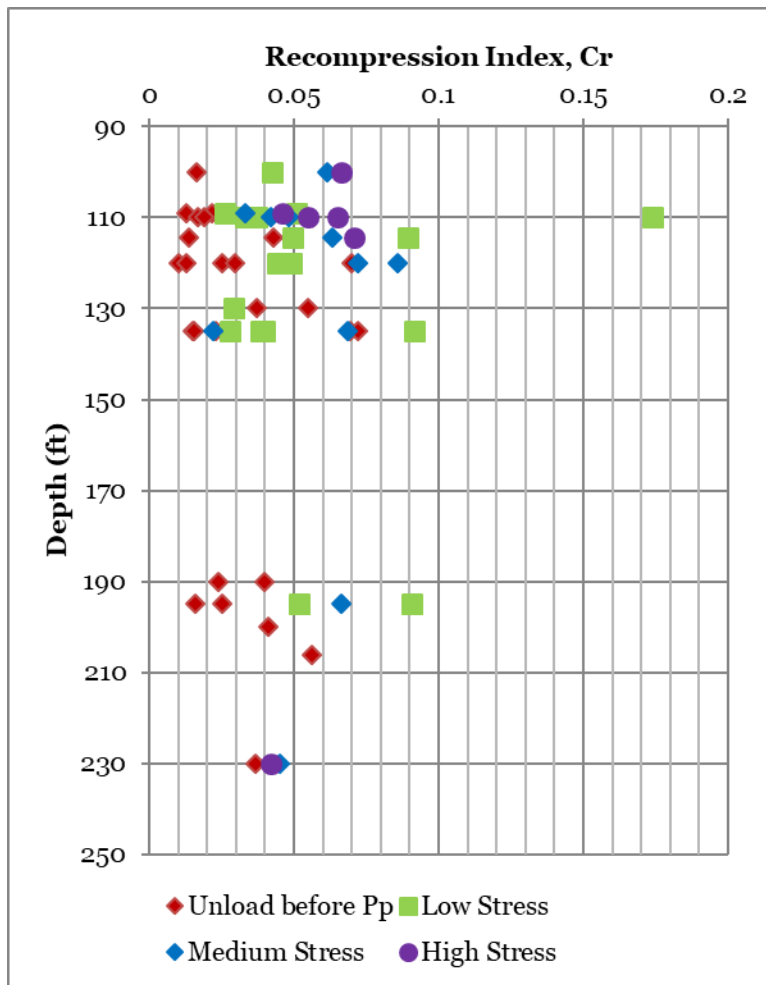


Figure 4.28. Recompression index (C_r) for various stress states before unloading plotted with depth for Old Bay Clay and Alameda soils.

Table 4.3. Summary of recompression index (C_r) and recompression ratio (RR) values from Old Bay Clay testing at various stress states pressures at unloading.

	OBC							
	Below P_p		Low Stress		Medium Stress		High Stress	
	Cr	RR	Cr	RR	Cr	RR	Cr	RR
Min	0.010	0.005	0.026	0.012	0.022	0.010	0.046	0.021
Max	0.072	0.033	0.174	0.079	0.086	0.039	0.071	0.032
Mean	0.032	0.014	0.055	0.025	0.055	0.025	0.061	0.028
σ	0.021	0.010	0.038	0.017	0.020	0.009	0.010	0.005

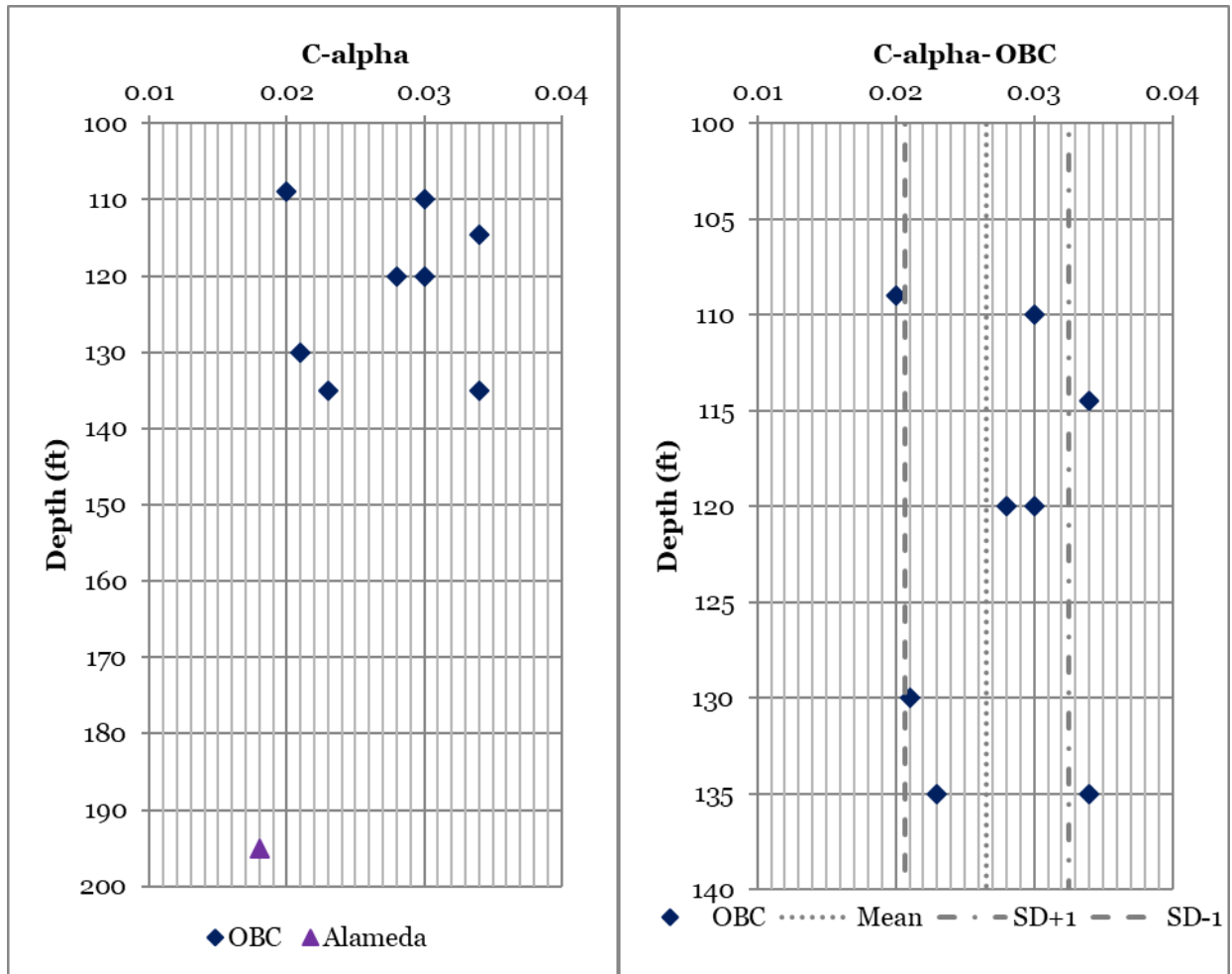


Figure 4.29. Secondary Compression Index from IL testing for Old Bay Clay and Alameda soils testing. Left: Combined results for Old Bay Clay and Alameda soils. Right: Old Bay Clay data showing mean, mean plus one standard deviation, and mean minus one standard deviation values from this testing data.

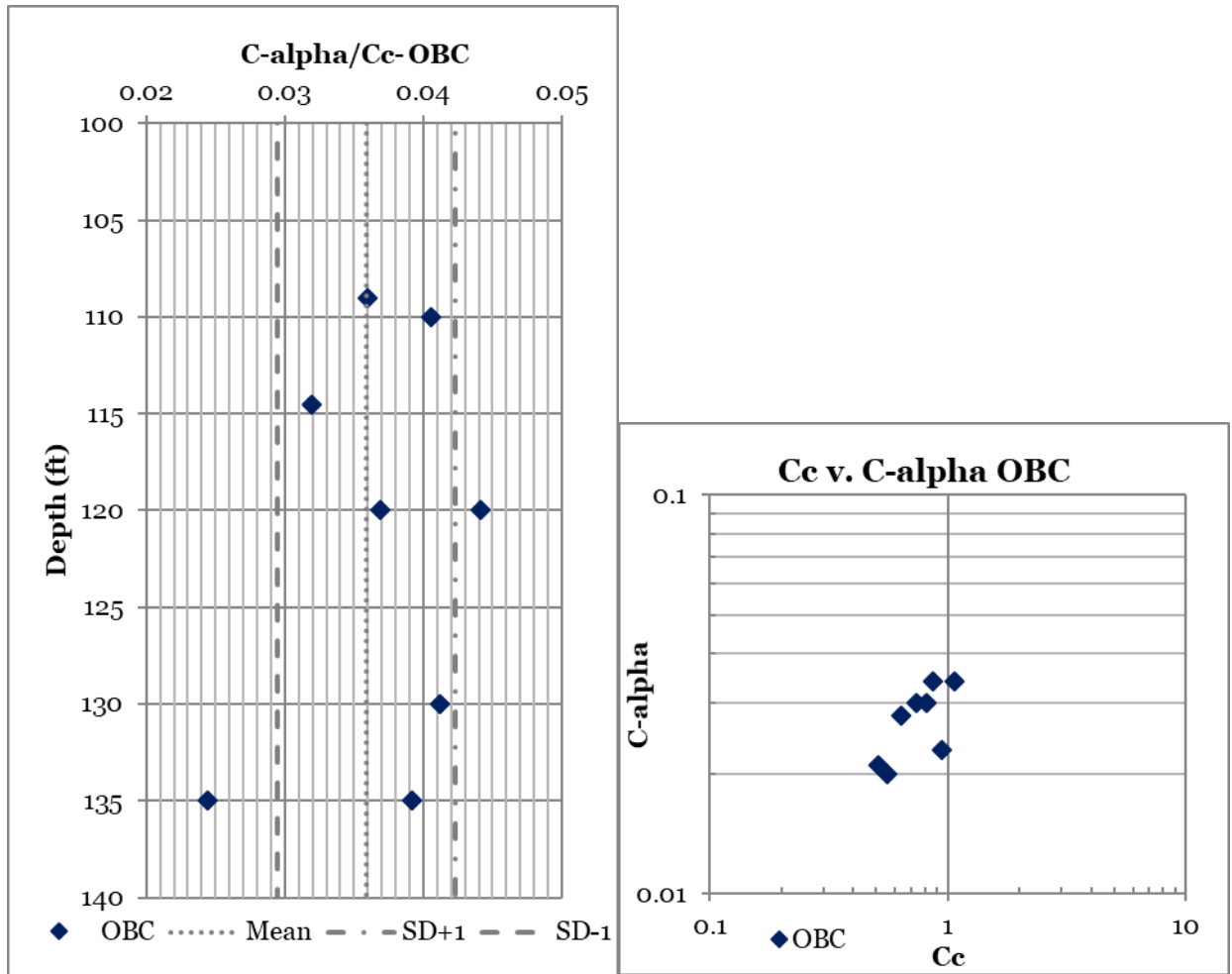


Figure 4.30. Ratio of secondary compression index to compression index with depth for Old Bay Clay.
 Left: Plot of ratio of secondary compression index (C_c) to secondary compression index (C_a) with depth for Old Bay Clay.
 Right: plot of compression index (C_c) against secondary compression index (C_a) for Old Bay Clay.

Table 4.4. Values of secondary compression index (C_{α}), normally consolidated, and the ratio of secondary compression to compression index for Old Bay Clay soils.

	C_{α}	C_{α}/C_c
Min	0.019	0.024
Max	0.034	0.044
Mean	0.027	0.036
σ	0.0059	0.0064

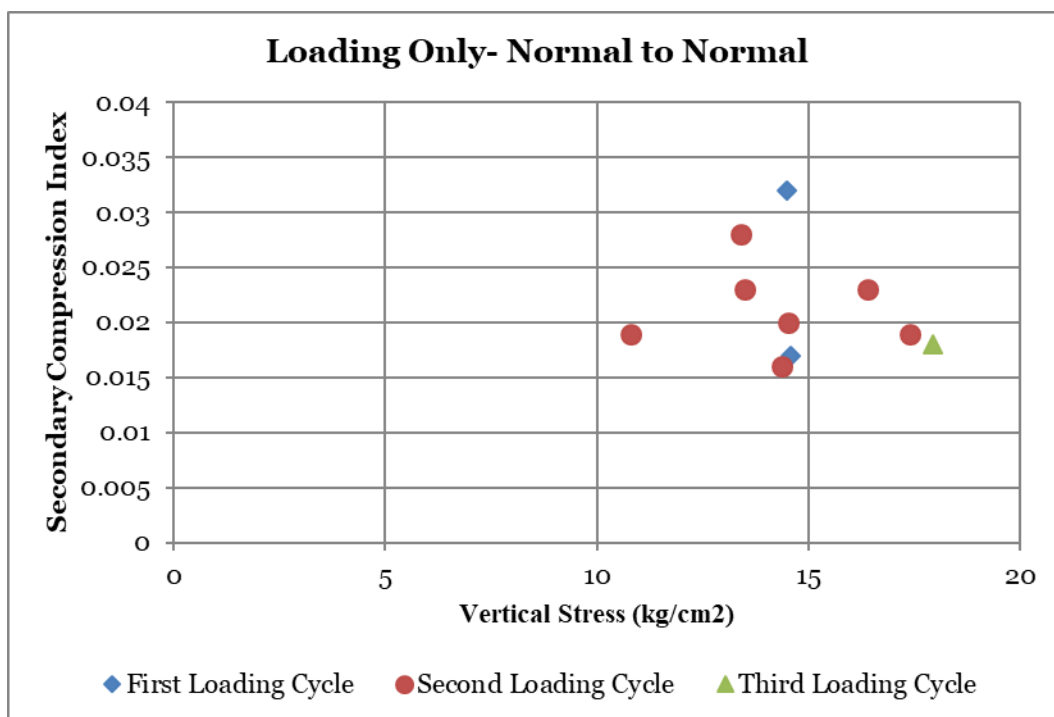
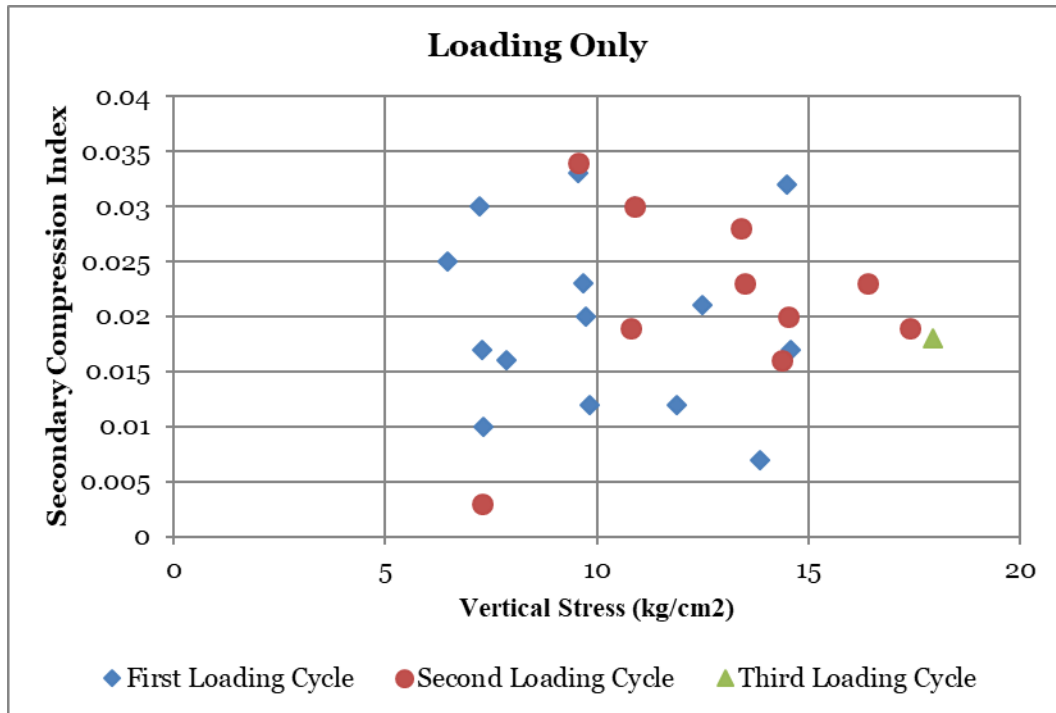


Figure 4.31. Secondary Compression Index (C_a) from OBC soils plotted against stress for normally consolidated increments only.

Top: all normally consolidated increments are plotted. Bottom: only increments where the prior increment was also normally consolidated are plotted

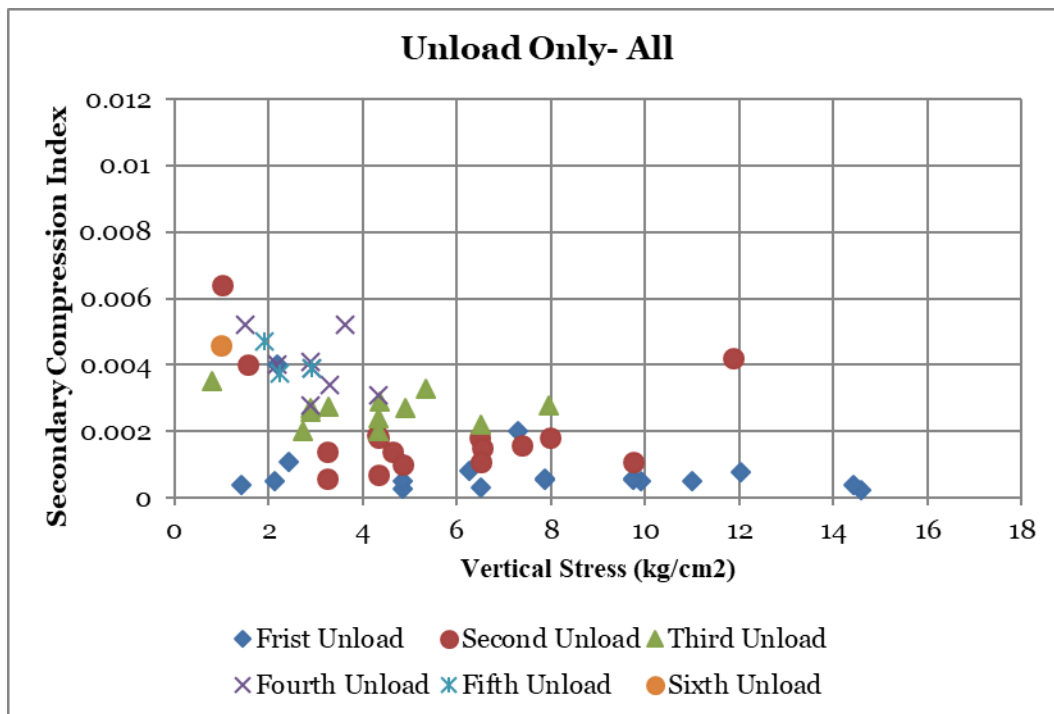
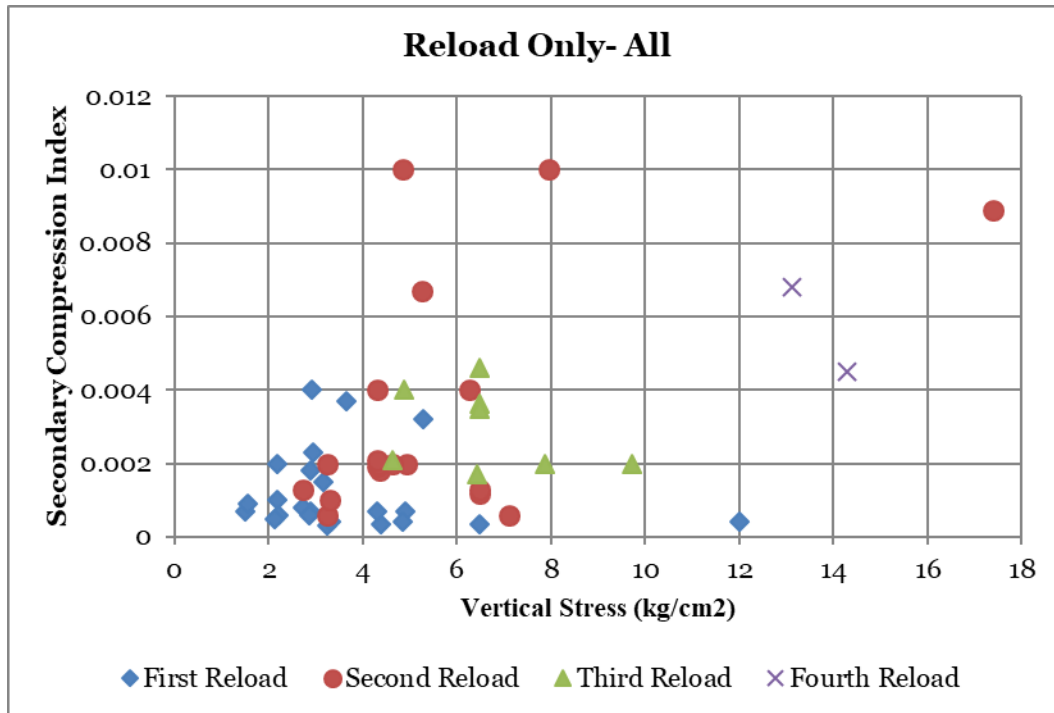


Figure 4.32. Secondary Compression Index (C_{α}) for Old Bay Clay soils for recompression increments only. Top: Secondary compression index plotted for reloading increments. Bottom: Secondary compression index plotted unloading increments.

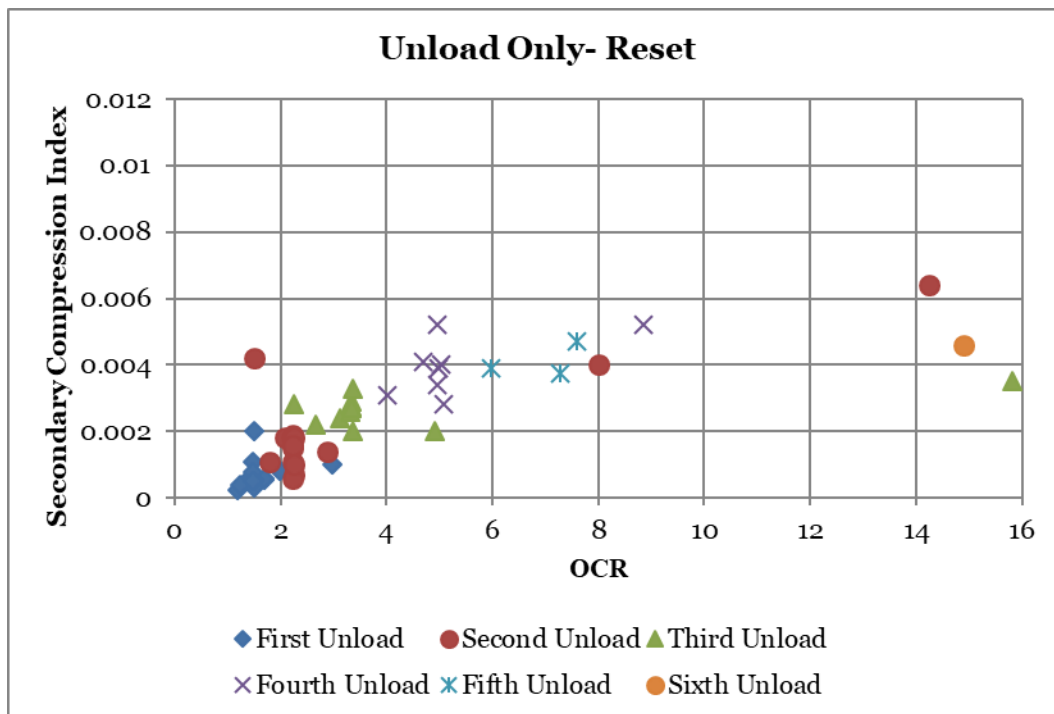
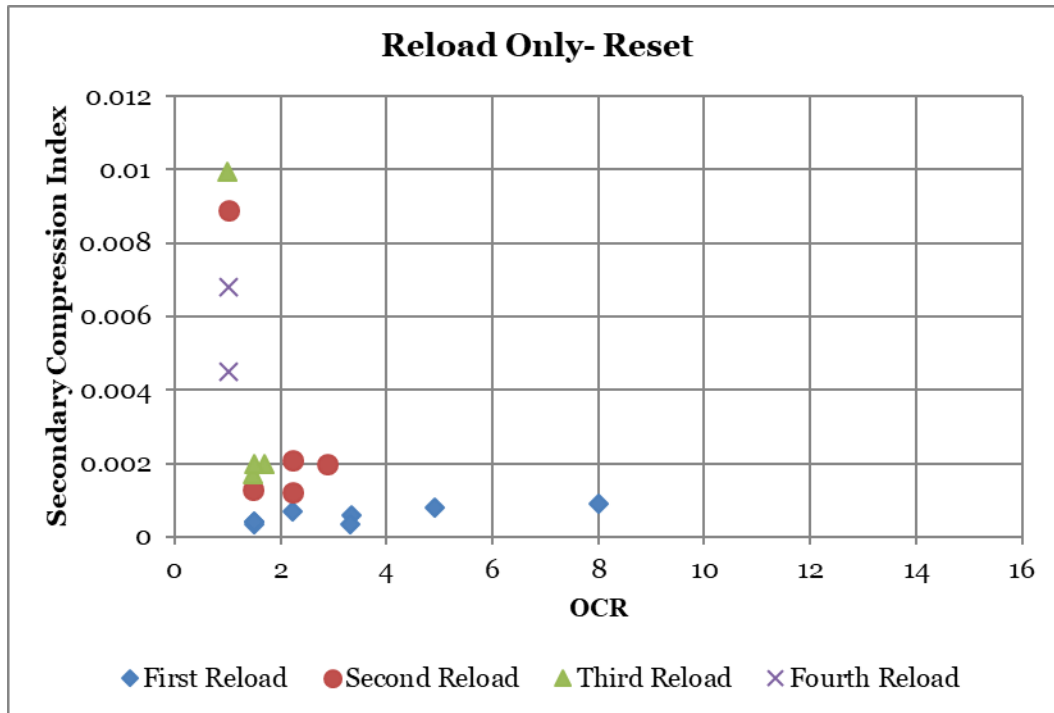


Figure 4.33. Secondary Compression Index (C_α) for Old Bay Clay soils for recompression increments that have been overconsolidated by laboratory maximum past pressures.

Top: Secondary compression index plotted for reloading increments. Bottom: Secondary compression index plotted for unloading increments.

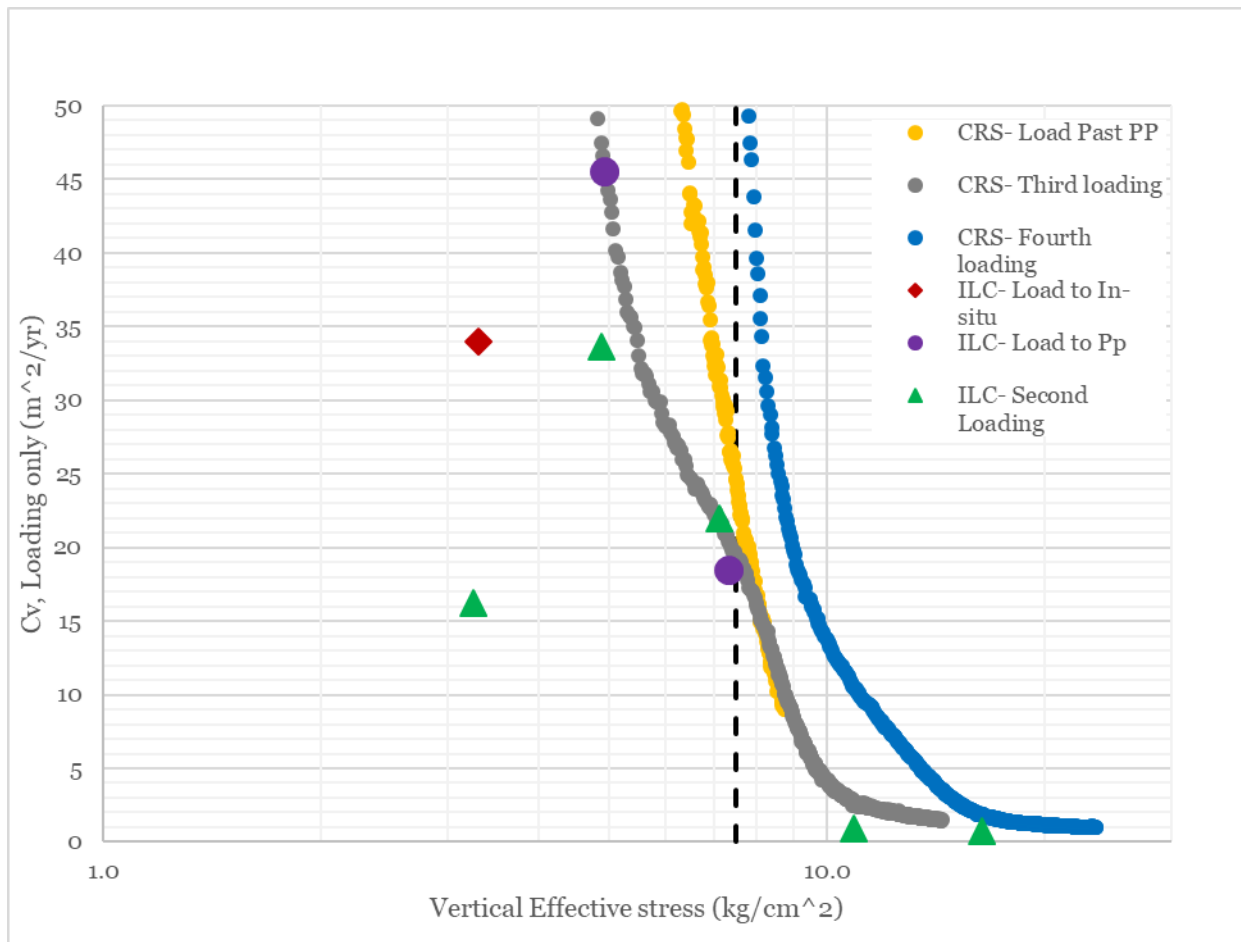


Figure 4.34. Coefficient of Consolidation (C_v) estimates for paired CRS and IL consolidation tests.

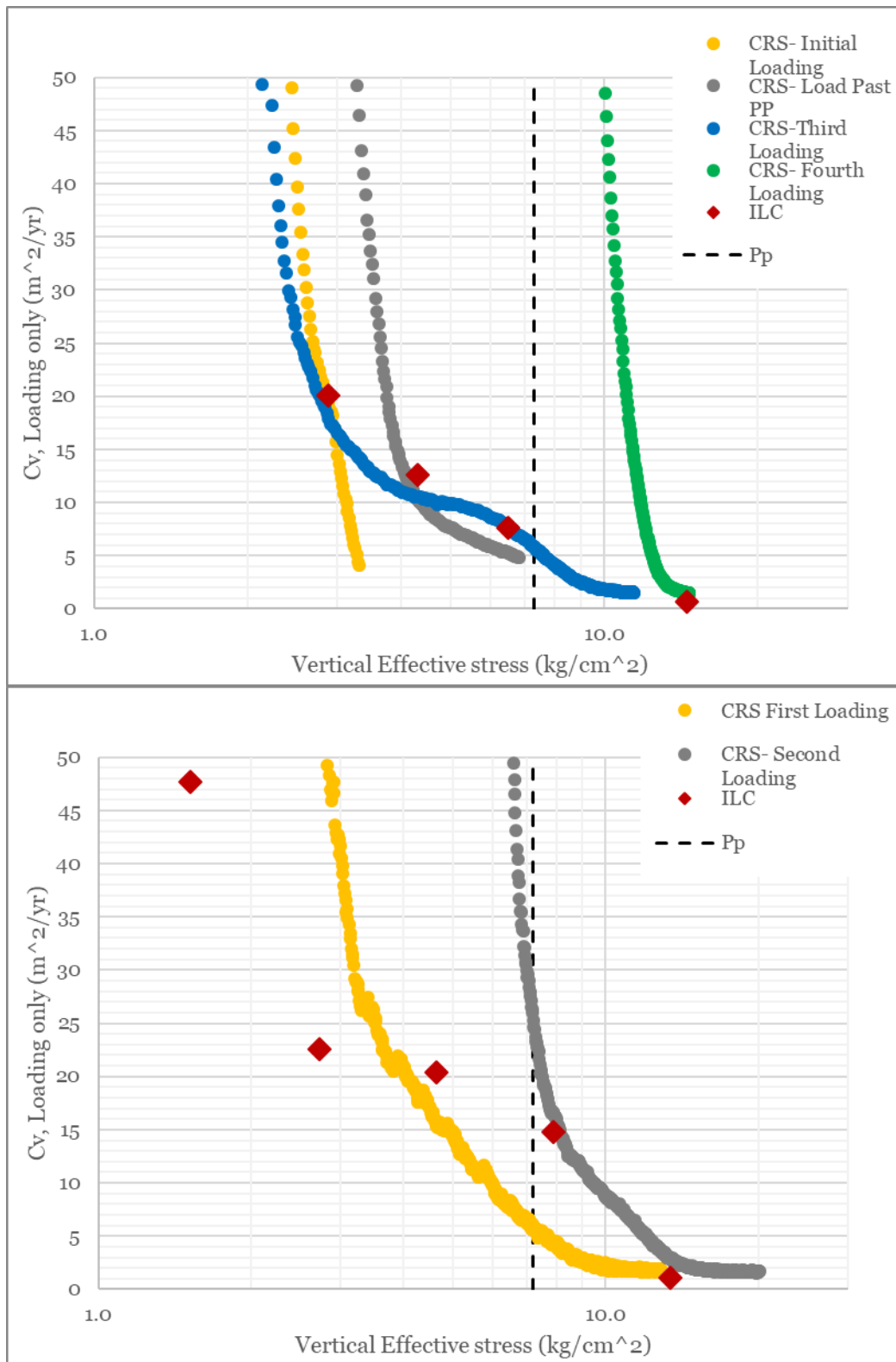


Figure 4.35. Two plots of paired IL and CRS consolidation tests performed on OBC soil that show general agreement between calculated values of Coefficient of Consolidation (C_v).

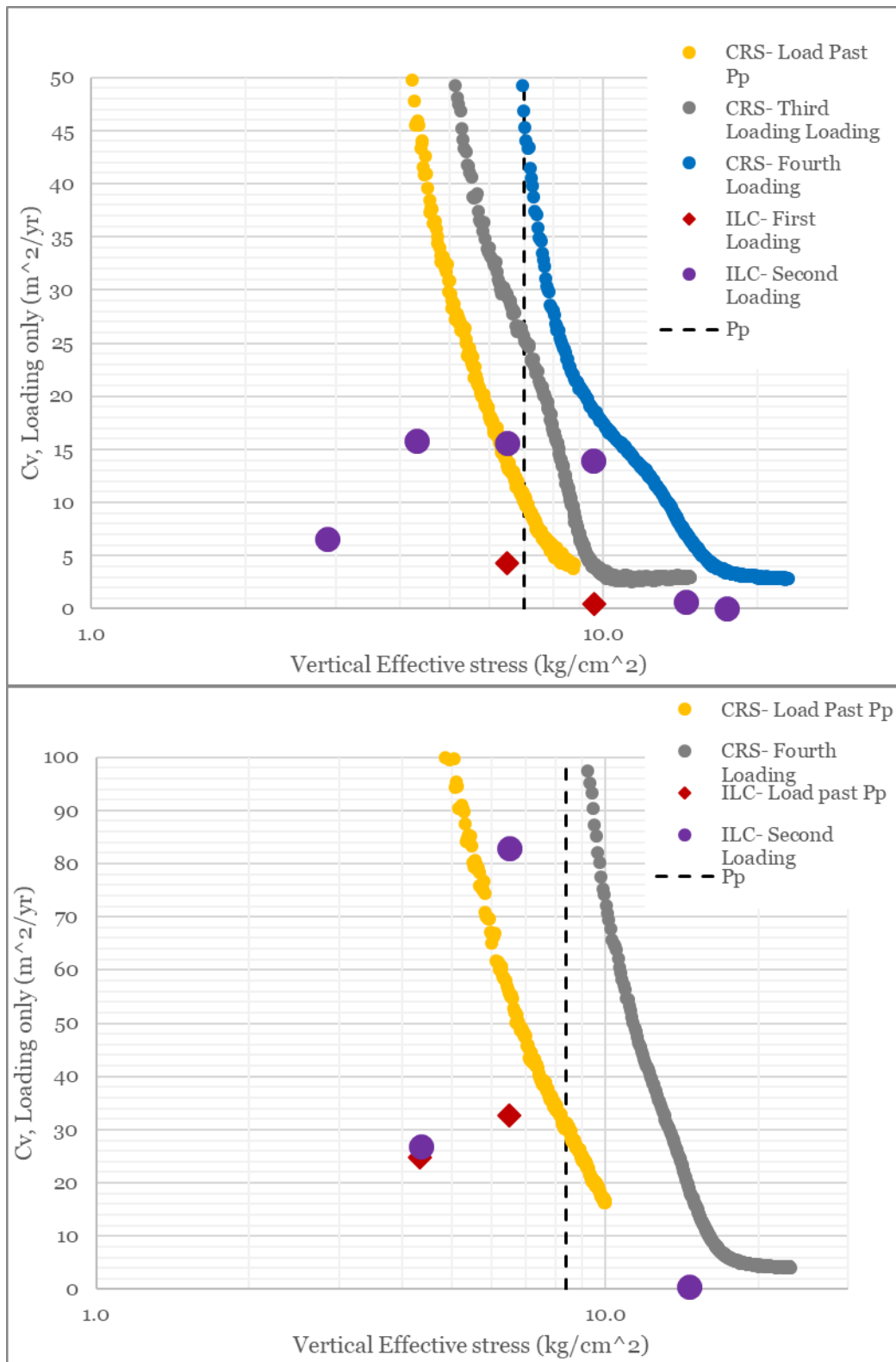


Figure 4.36. Two plots of paired IL and CRS consolidation tests performed on OBC soil that show inconsistent calculated values of Coefficient of Consolidation (C_v).

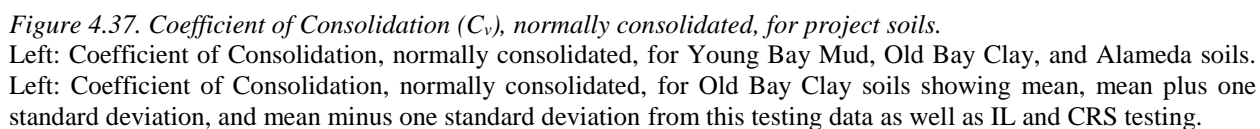
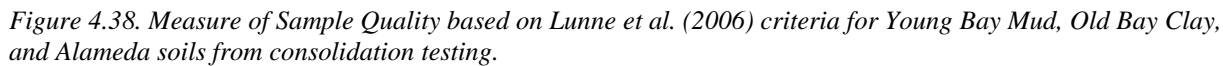


Table 4.5. Summary of Coefficient of Consolidation (C_v), normally consolidated, values for Young Bay Mud, Old Bay Clay, and Alameda soils

	YBM	OBC	Alameda
	C_v (m ² /yr)		
Min	0.3	0.43	0.50
Max	0.4	4.4	1.4
Mean	-	1.7	1.0
σ	-	0.92	0.29

Table 4.6. Lunne et al. (2006) criteria for evaluating sample disturbance using $\Delta e/e_o$.

	Sample quality category			
OCR	Very good to Excellent (1)	Good to Fair (2)	Poor (3)	Very Poor (4)
1-2	<0.04	0.04-0.07	0.07-0.14	>0.14
2-4	<0.03	0.03-0.05	0.05-0.10	>0.10



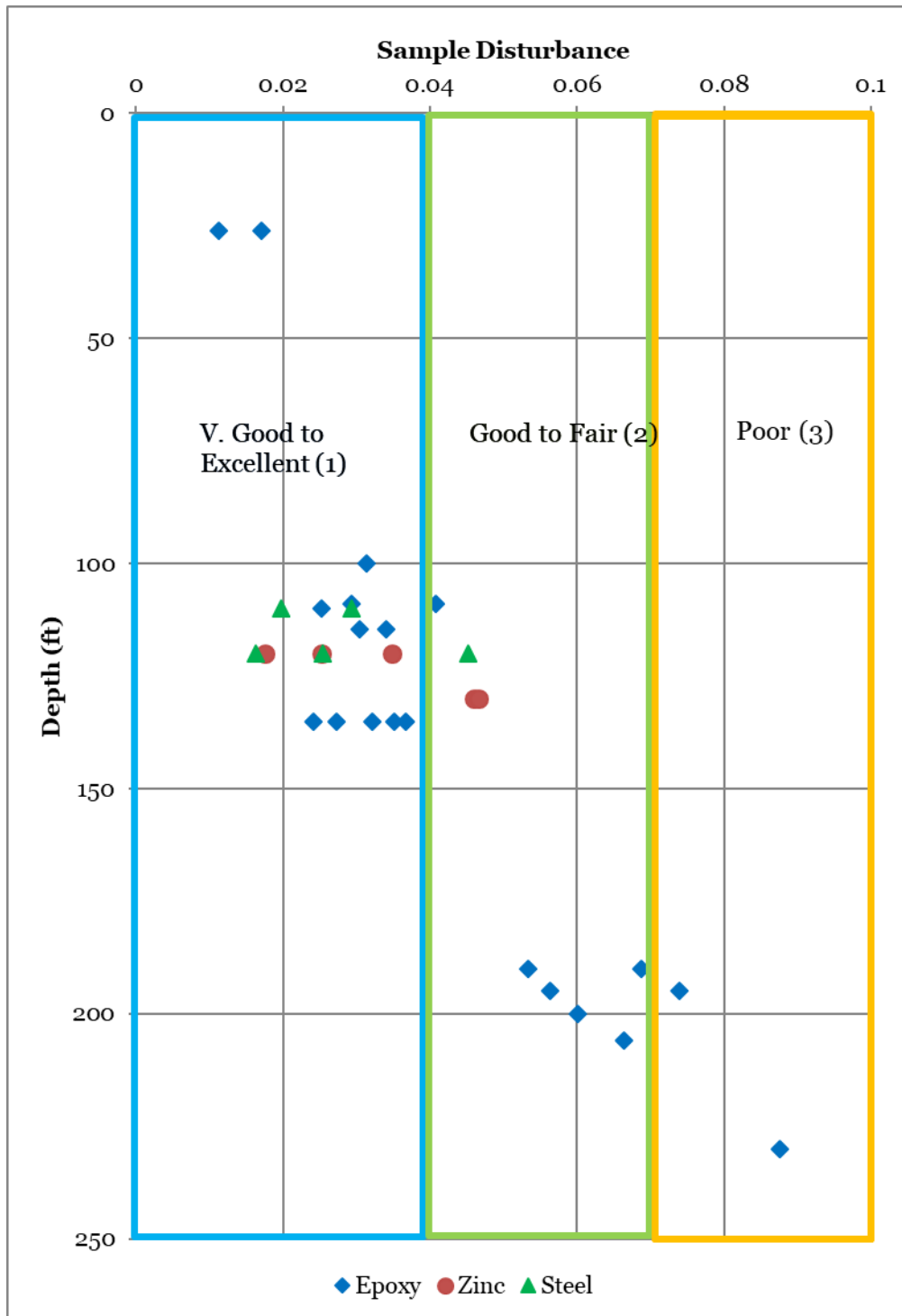


Figure 4.39. Measure of Sample Quality based on Lunne et al. (2006) criteria for different Shelby tube materials: epoxy-coated, zinc, and steel.

5 SMALL STRAIN STIFFNESS TESTING

Monotonic and dynamic testing was performed on project samples with several different test types in order to explore small strain stiffness properties of the Old Bay Clay. A number of Anisotropic-Consolidated Undrained Triaxial (CK_oUTX) tests were performed that involved a suite of tests, such as bender elements, cyclic loading, and/or small to large strain compression and extension tests. A small group of CK_oUTX tests were performed under special “lateral unloading” conditions to failure.

The initial motivation for this testing program was to develop a sophisticated numerical model with the project partners to model excavation unloading. Material-specific calibration of a numerical model can be performed by determining and matching the small-strain stiffness of the laboratory materials to deformation of project site materials. Ideally, the small-strain stiffness would come from the anisotropically consolidated stress state that simulates the field conditions. Thus, the majority of strength testing was intended to simulate field conditions. Oedometer testing prior to these tests provided stress history for each sample as well as confirming high sample quality for use in small-strain testing.

5.1 Monotonic and Cyclic Triaxial Testing

Triaxial testing was performed on 10 specimens in order to investigate small-strain stiffness behavior. Anisotropically Consolidated Undrained Triaxial (CK_oUTX) tests in compression and extension, as well as cyclic tests, were performed. Bender element testing was also performed on the specimens, concurrently with triaxial preparation and consolidation. These tests were generally anisotropically consolidated to stress states slightly above the maximum past pressures to remove disturbance and then unloaded to field conditions for testing.

5.1.1 Specimen Preparation

Triaxial specimens were prepared by extruding full-diameter Shelby tube specimens using a tube jack (Figure 2.7). The preparation was the same as for consolidation testing discussed in Section 4.2.1, however, the triaxial specimens were extruded to their full height, nominally 14.5 cm, instead of into an oedometer ring. As discussed in Section 3.1, the sample tubes had no turned edges, so the outer surfaces of specimens had low disturbance. CRS testing confirmed that the majority of Old Bay Clay samples were “Very Good to Excellent” quality and the Alameda samples were mostly “Good to Fair” quality (Section 4.7). Therefore, it was not necessary to trim the outer surface of the specimen. Specimen dimensions were 7.3 cm in diameter and ranged from 14.2 to 14.8 cm with a mean of 14.5 cm in height. The height to diameter ratio was approximately 2, which is within the desired 2 to 2.5 range as recommended by ASTM Standard D4767 (2011). The top and bottom surfaces were trimmed smooth with a wire saw and metal blade and then slots for bender elements were excavated in the ends using a template (Figure 2.14, Figure 2.15). Grooves for the bender elements had to be excavated due to the brittle nature of the soil, though care was taken not to over-excavate the slots to insure good contact between the soil and bender elements.

Whatman No. 54 filter paper was used for filter paper disks between the specimens and the caps and as vertical filter strips (Figure 5.1, Upper Right). Rubber membranes used were 6.86 cm in diameter and 0.320 mm in thickness. In some tests, two membranes with a layer of vacuum grease in between were used to attempt to maintain specimen saturation. Membranes were applied with a vacuum membrane expander. Once the specimen was placed on the caps and the membrane sealed to the caps with O-rings, the chamber could be filled with de-aired water.

5.1.2 Testing Equipment

The majority of triaxial testing in this study took place in a high-performance triaxial cell that has low friction and low leakage seals (Figure 5.1). The cell had both internal and external LVDTs, internal and external load cells, as well as bender elements in the caps. The internal high-resolution LVDTs could provide small-strain data for stiffness. The three LVDTs inside the cell consisted of one “coarse” LVDT that had a total stroke length of ± 12.7 mm and two “fine” LVDTs with a stroke length of ± 5.08 mm. The coarse LVDT tracked total strain during the entire test. The fine LVDTs were calibrated to be highly sensitive, with a span of approximately 2.4 mm across the voltage range. The fine LVDTs could resolve small strains, especially during cyclic testing, and were positioned to measure any rocking of the specimen during testing. However, because of the small total stroke length of the fine LVDTs, they had to be manually re-positioned when they went out of range during testing. Outside the triaxial cell was an additional LVDT that was also used to track total strain during the entire test and to help characterize equipment compliance and cell friction.

The internal load cell was a low-profile load cell with capacity of 500 lbs and the external load cell was a standard load cell with a capacity of 1000 lbs. The internal load cell was calibrated for use over a smaller range than its capacity and could resolve much smaller loads than the external load cell, which was important during small strain cyclic testing. Additionally, comparison between the internal and external load cells enabled estimation of cell friction, which was important during cyclic testing. This internal load cell was a system upgrade to the UC Berkeley high performance triaxial cell that was performed for this testing program.

The CKC Triaxial Control system (Li, Chan, & Shen, 1988) was used to run the triaxial tests. This system is an electropneumatic cyclic triaxial testing system. The system was controlled by a recently updated version of Georobot software. The external LVDT and external load cell were used as feedback control. The control system had a graphical user interface (UI) and controlled loading during all phases of testing, including saturation, consolidation, cyclic testing, and shearing. Loading was performed with a 101 mm diameter air piston, supplied by the building’s supply of air pressure.

One suite of tests was performed with a conventional triaxial cell, the CKC system, and an older, non-graphical UI version of Georobot, in order to investigate standard SHANSEP properties of the OBC. This conventional cell had only an external load cell and LVDT.

5.1.3 Bender Elements

The high performance triaxial cell was instrumented with bender elements. Cantilever-type, piezoelectric bender elements were installed in the top and bottom caps (Figure 5.1). One bender

element would be used to send a signal that was generated from a function generator, while the other bender element would be the receiver element. The signal received from the receiving bender was collected with an oscilloscope (Figure 5.2). The oscilloscope records were processed to get travel time of the impulse wave using cross-correlation between the input and output signals (Arulnathan, Boulanger, & Riemer, 1998). With the specimen height and density, this arrival time was used to find the small strain shear modulus, G_{max} , which could be related to the Shear Wave Velocity (V_s) by the following formula.

$$G_{max} = V_s^2 \cdot \rho$$

Where ρ is the density of the soil.

The bender element tests could be performed during many stages of triaxial testing. However, because of electrical interference between the instruments inside the triaxial cell, power to the internal LVDTs and load cell had to be turned off to perform the bender element test. Thus, bender element testing was not performed during active shearing or cyclic testing, rather it was run between stages of the multi-staged testing process.

5.1.4 Testing Procedures

Triaxial specimens were vacuum and back pressure saturated. Because of the relatively high field stress and preconsolidation pressure, specimens could be saturated with from 180 to 250 kPa of effective isotropic pressure, which corresponds to approximately two-thirds of the in-situ vertical effective stress. Axial displacements were monitored throughout saturation. The saturation stress was found to produce desirable saturation measurements without significant vertical strain being observed, thereby suggesting minimal swelling occurred. However, it is much higher than the maximum value of 35 kPa recommended in ASTM Standard D4767 (2011).

To begin, vacuum was supplied to the specimen through a vacuum water interface chamber using a vacuum pump, applying isotropic confining stress. An increment of chamber pressure would also be supplied to the cell in order to reach a saturation stress that was higher than could be applied with only the vacuum. After the vacuum was left on the specimen for a period of time, the vacuum was stepped down while the chamber pressure was stepped up to maintain constant saturation stress. Once the vacuum was removed, the CKC system was used to back pressure saturate the specimen while the height and volume of the specimen were monitored.

When sufficient back pressure stresses were applied to reach a desirable B value, K_o consolidation would begin. Because of the risk of shearing the specimen during K_o consolidation, consolidation was achieved in a series of steps with decreasing lateral earth pressure, K . The CKC system was programmed to add loads and pressures on a schedule, as well to record axial and volumetric strain. Once normal consolidation was reached, usually with a K of 0.55, the specimen would be unloaded to field conditions of sample OCR and K_o . OCR was based on consolidation testing on an adjacent specimen from the same sample tube. K_o was based on estimates from GDR testing based on in-situ testing.

The CKC system was also used for cyclic and monotonic testing. For each specimen, a unique series of cyclic and monotonic testing, extension and/or compression, was performed. In some

testing suites, the specimen would be re-consolidated and re-tested after a series of tests. Between stress states, cyclic testing could be performed. For example, a cyclic suite could be performed after initial consolidation with the specimen at an OCR=1 as well as after unloading with the specimen at an OCR=2.

5.1.5 Results

Table 5.1 includes a list of CK_oUTX tests performed on project specimens and lists the suite of tests that were performed on each specimen during testing. Tests CUTX-7, CUTX-8, and CUTX-9 were the more conventional CK_oUTX tests performed for SHANSEP estimations. These tests were back pressure saturated, anisotropically consolidated, unloaded, and then sheared to failure. Appendix B includes detailed testing schedules for each of the tests listed, as well as magnitude of stresses and stress ratios. Data from these tests are available electronically.

An example of the excellent small-strain data obtained from monotonic testing is plotted in Figure 5.3. In this test, a compression test was performed and terminated at moderate, 1.4%, strain, as shown in the Top plot. While the test had not yet reached failure at the strain level shown, the development of a nearly flat response in shear stress and excess pore pressure suggest a brittle response. In the Bottom plot, the same test is plotted with the initial small-strain response up to 0.05% shown. This is the raw, unfiltered data from the internal sensors on a scale at which the initial stiffness can be more clearly observed, and also illustrates the perturbations in load and deformation that can occur internally when the system is being controlled using external sensors for the feedback channels.

In addition to compression tests, small-strain data was obtained from extension triaxial testing. An example is shown in Figure 5.4, where the full extension test is plotted as well as the small-strain portion up to -0.01%. This extension test was to failure, with the specimen failure at -4% strain. In this test, previous moderate strain compression tests had been performed, with the specimen reconsolidated in between tests. Small strain stiffness could be measured from different modes and compared.

Figure 5.5 shows an example of cyclic triaxial testing. In the top plot of Figure 5.5, the time history of the cyclic test is shown, which was run at a rate of 0.25 Hz and had 4 cycles. This was a fairly typical loading schedule for the cyclic tests. As can be seen, many different channels recorded the data within the high performance triaxial cell. Instances of rocking and cell friction can be observed due to the many sensors. The resolution of the two fine LVDTs is apparent compared to the more granular data from the large external and internal LVDTs. The asymmetry of the cyclic loops was sometimes observed depending on the degree of anisotropy of the specimen, the testing pressures, and the feedback channels from the loading piston. Even though the cycles were asymmetric, they still produce characteristic hysteresis loops (Figure 5.5, Bottom), from which secant modulus, G , peak-to-peak strain, and damping ratio can be evaluated. In Figure 5.6, a suite of cyclic tests with strain of 0.001%, 0.026%, and 0.065% is plotted together showing cyclic degradation as strain increases.

The cyclic triaxial tests could be compared at small strains with the monotonic testing, as in Figure 5.7. In these paired tests from the same testing suite, a monotonic compression test is plotted with

a small strain cyclic test, with 0.005% strain, in the small-strain portion. There is good agreement between the cyclic modulus and the monotonic modulus, further validating the high performance triaxial cell. Improvements had been made during this testing program to reduce friction, which was greatly reduced with the internal load cell, as seen in the paired test of Figure 5.7. Further, this emphasizes the validity of the small-strain monotonic tests performed for modulus values.

Using the suites of cyclic testing at different strain levels as were plotted in Figure 5.6, modulus curves were constructed at various stress states. In Figure 5.8, modulus and normalized modulus, G/G_{\max} , curves are plotted at OCR=1 and OCR=2 for a triaxial test. The OCR=1 was after normal consolidation before unloading to the OCR=2 stress state. The OCR=1 curve shows higher modulus values, which become less of a contrast when the normalized modulus curve is plotted. As can be seen, a characteristic shape becomes clearer with cyclic testing data from higher strain values. At OCR=1, cyclic straining was kept low in order to prevent pore pressure re-distribution, so typically the cyclic testing suites contain cyclic tests at lower strain amplitudes.

5.2 Lateral Unloading Triaxial Testing

In order to understand details of unloading response of the OBC, which might control the response during the TTC foundation excavation, a special test was performed to simulate what a unit of soil adjacent to an excavation might experience, with a constant vertical effective stress and a decreasing horizontal effective stress. This test is referred to as the “lateral unloading triaxial” test. An example of this concept is illustrated in Figure 5.9, where an element of soil within the wall of an excavation is located at a sufficient depth relatively close to the face. This element of soil will generally experience a constant vertical effective stress but a reduction of horizontal effective stress. And because of the excavation sequence, this unloading would be in increments or step-wise. The following sections describe how this testing was performed and the results of the testing program.

5.2.1 Specimen Preparation and Testing Equipment

Like in the triaxial tests described in Section 5.1.1, specimens for the unloading triaxial test were extruded directly from Shelby tubes, with the same membranes and filter paper as well as slots for bender elements carved into the ends of the specimen. The high-performance cell described above was used. However, the CKC system was not used. Instead, loads and pressures were manually applied and continuous data was passively collected using National Instruments VI logger software, version 4.0.0.3010. Axial load was applied using an air piston supplied by house air pressures and chamber pressure was applied using pressure regulators.

5.2.2 Testing Procedures

Similar to the triaxial tests described above in Section 5.1.4, the unloading triaxial tests underwent vacuum and back pressure saturation prior to consolidation. Like the triaxial testing, these tests were anisotropically consolidated past their preconsolidation pressure in order to reduce sample disturbance effects and create a new stress state. This is illustrated in the stress path plotted in Figure 5.10 that shows the sample anisotropically consolidated from isotropic conditions in steps and then anisotropic consolidation past the maximum past pressure. Once the specimen was

normally consolidated, it was unloaded in steps to approximately field conditions, for both OCR and K_o . In the test plotted in Figure 5.10, the test was unloaded to stresses below the in-situ stress in order to measure the change in soil response for those stress states. At the various saturation, consolidation, and unloading stages, bender element tests were performed. These bender element tests were compiled to track how modulus changed with the imposed stresses.

After the specimen was unloaded to the desired testing stress, the “lateral unloading” triaxial test commenced. Figure 5.11 plots the stress path for lateral unloading test VS-5, which was tested at an OCR of 1.1. As described above, this test was meant to simulate decreasing lateral pressure, while maintaining constant vertical stress, which in triaxial test can be difficult to maintain. This is because in order to maintain a constant vertical stress, during each stage of unloading the chamber pressure must be reduced while simultaneously increasing the vertical load. A series of unloading steps was performed under drained conditions with volume change, vertical strain, and stress continuously recorded by the data logger system. Each loading stage was held at the chamber stress and deviatoric load imposed until observed deformations stabilized. Bender element tests were performed at each stage in order to measure the small-strain shear wave velocity, which could be used to calculate the change in modulus with stress state. After several stages, the specimen would creep to failure under sustained stress (Figure 5.12).

5.2.3 Results

Table 5.2 lists the Lateral Unloading tests. In VS-1, VS-2, and VS-3, consolidation and unloading was successful and bender element testing was performed. Thus, G_{\max} and V_s data was collected at various stress states and K for the specimens. However, the lateral unloading test was unsuccessfully performed. Successful complete lateral unloading tests were performed for VS-4 and VS-5. Appendix B contains testing schedules with magnitude of stresses and stress ratios for this testing program. Data from these tests is available electronically.

In VS-4, shearing to failure occurred in the 5th unloading increment and in VS-5, shearing occurred in the 8th unloading increment. Figure 5.11 and Figure 5.12 present data from VS-5, which is representative of other lateral unloading tests performed. As can be seen, unloading occurred in 10 kPa increments. After most increments, some compression or creep behavior was observed in the specimen but stabilized over a period of time. As more increments were performed, greater creep strain was observed while the time to stabilization increased. Eventually, the final failure increment would be observed to strain quickly and with an increasing rate as compared to earlier increments that would stabilize with time.

The main result from these tests were measures of G_{\max} and V_s at many stress states that could be used in conjunction with the CK_o UTX tests described in Section 5.1. The creep to failure is an interesting result, which seemingly occurred below the failure envelope. This mode of failure would be interesting to pursue, especially combined with numerical modeling of soil elements that might also be able to simulate the unique unloading sequence.

5.3 Small Strain Stiffness Properties

The monotonic and dynamic CK_oUTX tests and the bender element testing from both CK_oUTX testing and the lateral unloading triaxial testing produced a variety of small strain properties for many different modes and stress states. Much of this testing is most useful for use in material-specific calibration of a numerical model, but these values can be compared to other workers, as well. A key result from the study is the range in value of G_{\max} , which, summarized from the various testing types, ranged from 57.2 to 133 MPa (1190 to 2780 ksf) for samples that were anisotropically consolidated to field values of OCR and K_o . Using the relationship to V_s , the corresponding shear velocities would be 180 to 270 m/s (580 to 890 ft/s) with an average of 210 m/s (690 ft/s). The next section compares these results with values obtained by other researchers who have performed laboratory testing on similar clays as well as in-situ testing within the Old Bay Clay.

The work of Guha (1995) was specifically focused on small strain properties from resonant column and cyclic triaxial testing of samples of Old Bay Clay from two sites, in Oakland, California, and Emeryville, California (Section 2.2.3). Additionally, at the Oakland site, a velocity profile was obtained from downhole suspension logging. As discussed in Section 2.2.3, the soil profiles at the Oakland and Emeryville project sites were different than at this project site, in elevation of the Old Bay Clay, thickness of the Old Bay Clay, and the interlayers of coarse materials. Additionally, lab testing showed that the Oakland and Emeryville soils were generally lower moisture content, high total density, lower plasticity, and higher OCR than these project soils. The results for Lab G_{\max} from Guha's study ranged from 47.7 to 204.7 MPa. Which were 44.1 to 71.5 percent lower than the field estimates of G_{\max} from in-situ testing. So while the soil profiles and soil parameters differ moderately, the values from this study fit within the range of laboratory values estimated by Guha, so the laboratory estimates appear to be consistent. However, it is noted that these materials have different index properties and have different stress states in-situ and during testing.

Darendeli (2001) prepared a "family" of normalized modulus reduction correlations based on plasticity, confining pressure, and OCR for clays. These curves can be used to estimate site-specific modulus and damping once a site G_{\max} is estimated. In Figure 5.8 the normalized modulus reduction curve is plotted for one of the most complete modulus curves from this testing project. As mentioned previously, the bulk of data tended to be low-strain values, in the mostly elastic range. The curve in Figure 5.8 includes the corresponding curve from Darendeli, which was estimated using the sample parameters, $PI=40$, mean effective confining pressure $p'_c=3.0$ atm, and $OCR=2$. The fit between the curve from this data and the curve from Darendeli is very consistent. This suggests that the dynamic response of the OBC reflects assumptions from other similar clay materials.

Within the GDR, a number of in-situ and field tests were performed for small strain properties, including suspension velocity tests and direct simple shear (DSS) testing. From the in-situ testing, shear wave velocity within the Old Bay Clay was one of the distinguishing features of the unit because the results were generally so uniform across the site and showed a clear change from the materials above and below. Shear wave velocity in Old Bay Clay was generally between 650 to 750 ft/s (200 to 230 m/s), although there was variability in the measurements with some measured

values up to 380 m/s (1250 ft/s). Small strain shear modulus, G_{\max} , from GDR DSS testing ranged in value from 820 to 1542 ksf for Old Bay Clay specimens. These values were generally lower than what was observed from this research project, however, the comparison is between fairly different test types.

5.4 Conclusions

A suite of testing was performed on Old Bay Clay specimens that produced meaningful values of small strain stiffness for specimens that had been consolidated to eliminate disturbance effects and then unloaded to replicate field conditions. Testing involved a number of Anisotropically Consolidated Undrained Triaxial (CK_oUTX) tests, that included bender elements, cyclic loading, and/or small to large strain compression and extension tests. A small group of CK_oUTX tests were performed under special “lateral unloading” conditions to failure. Because of the precision and responsiveness of the testing equipment and the high-quality samples, small strain properties were meaningfully measured. Results of small strain properties, including G_{\max} and modulus reduction curves, appear to agree well with other workers within the Old Bay Clay as well as for similar clay materials.

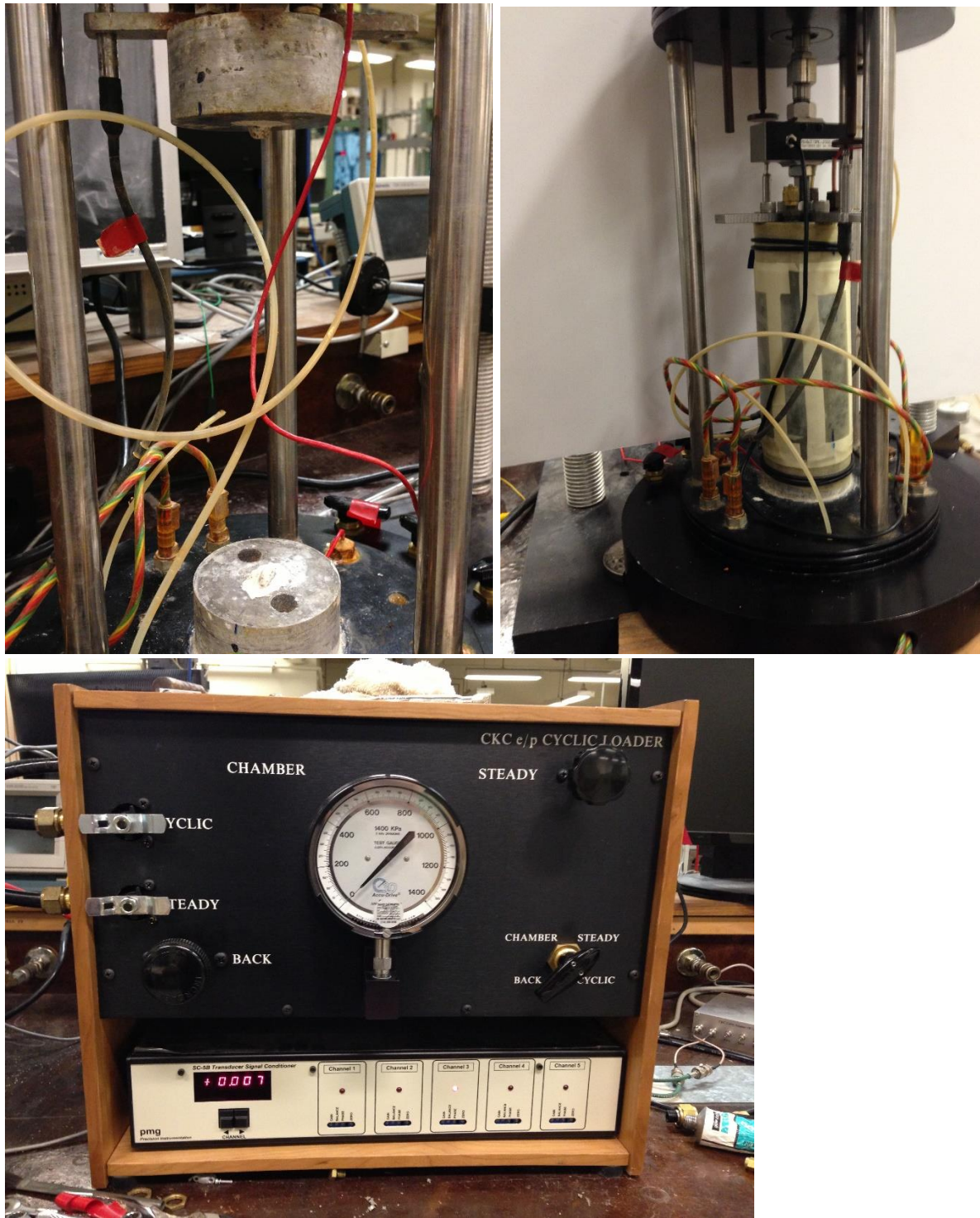


Figure 5.1. Testing equipment used for Triaxial testing.

(Upper Left) Caps showing embedded bender elements, (Upper Right) specimen placed on caps with membrane in place and internal load cell and three internal load cells aligned, and (Lower) CKC device for loading

Table 5.1. List Anisotropic Consolidated Undrained Triaxial testing for this project.

It is noted whether the test included any of the following: bender elements testing, cyclic testing, compression testing, and/or extension testing

Test	Unit	Sample ID	Depth	Bender Testing	Cyclic Testing	Compression Testing	Extension Testing
CUTX-1	OBC	I-9 S-2	120	Yes	2 Sets	2 Small Strain	1 Small Strain, 1 Large Strain
CUTX-2	OBC	EX-03 S-2	114.5	-	-	Large Strain	-
CUTX-3	Alameda	BH-2 S-35	195	Yes	4 Sets	Small Strain	Small Strain
CUTX-4	OBC	I-34 S-18	110	-	2 Sets	Small Strain	Large Strain
CUTX-5	OBC	I-35 S-4	135	-	1 Set	Small Strain	-
CUTX-6	OBC	BH-1 S-18	120	-	2 Sets	Small Strain	Large Strain
CUTX-7	OBC	BH-3 S-18	110	-	-	Large Strain	-
CUTX-8	OBC	BH-3 S-18	110	-	-	Large Strain	-
CUTX-9	OBC	BH-3 S-18	110	-	-	Large Strain	-
CUTX-10	OBC	BH-1 S-18	120	-	3 Sets	Large Strain	-

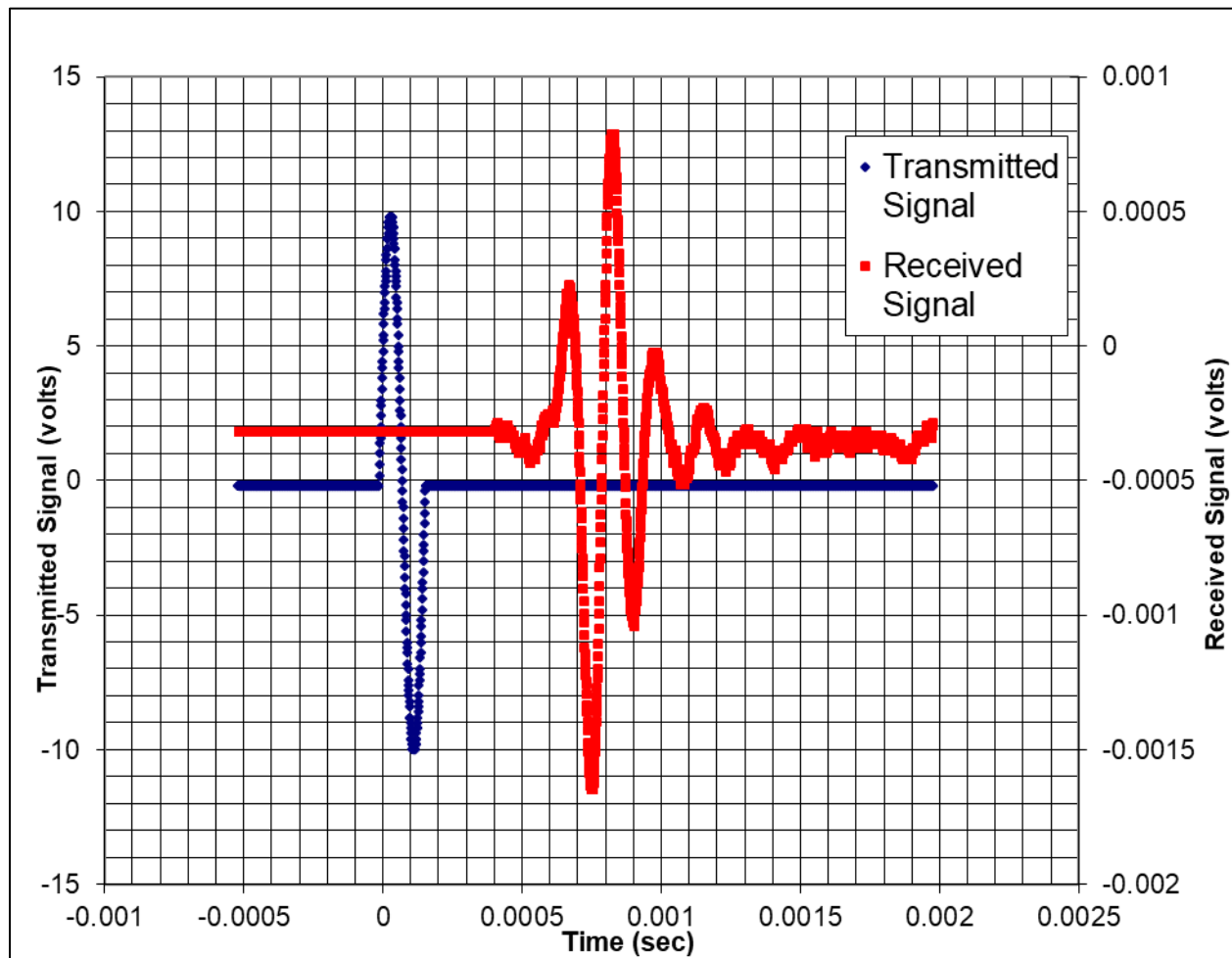


Figure 5.2. Example of Bender Element traces used for velocity measurements.

Data is from VS-5, performed during lateral unloading test

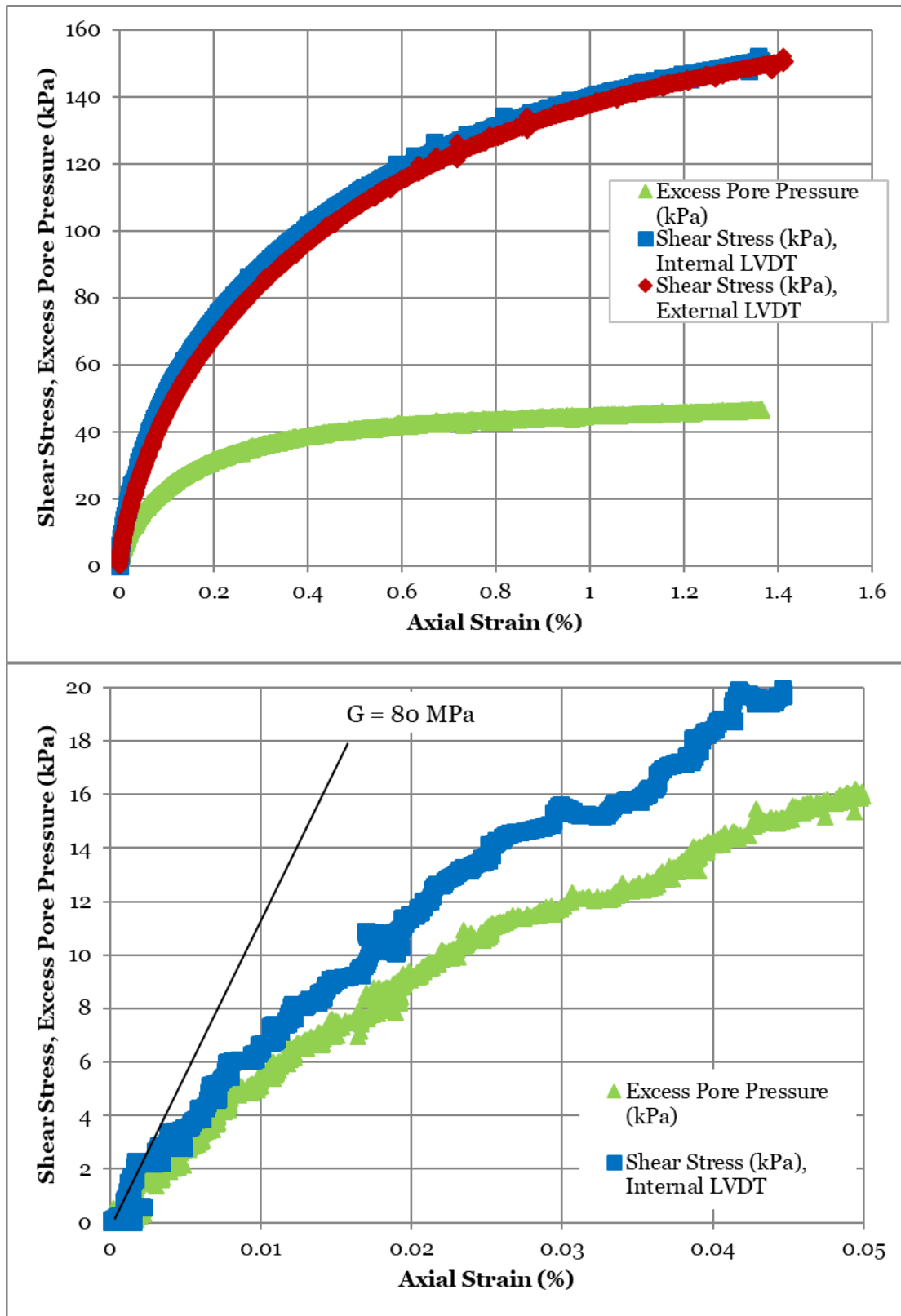


Figure 5.3. Example of Large Strain CUTX compression test showing small strain range.
Test shown is the large strain compression test from CUTX-4 (Top) and the small strain portion (Bottom)

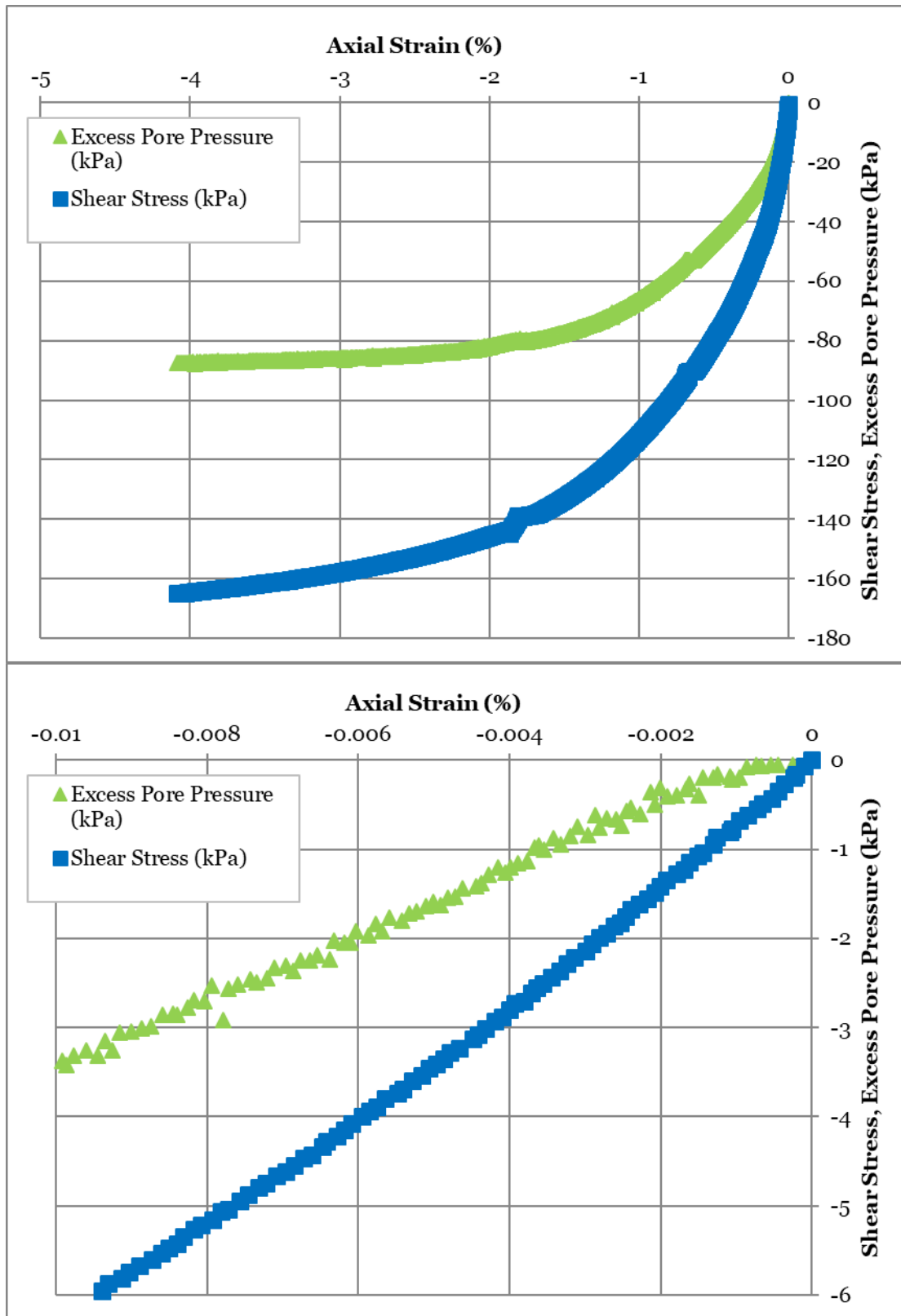


Figure 5.4. Example of Large Strain CUTX extension test showing small strain range.
 Test shown is the large strain compression test from CUTX-1 (Top) and the small strain portion (Bottom)

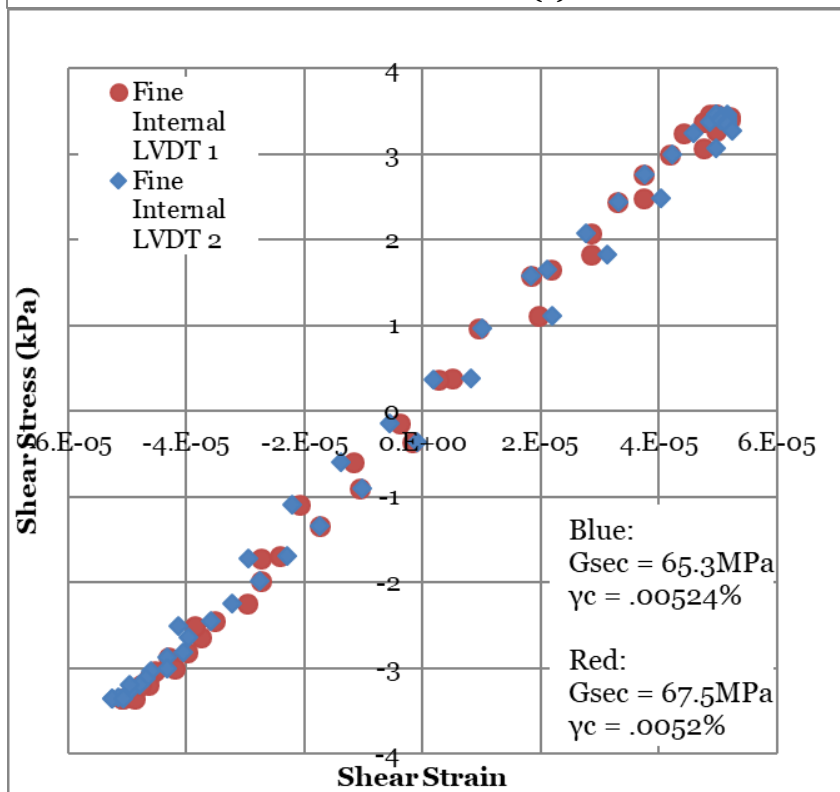
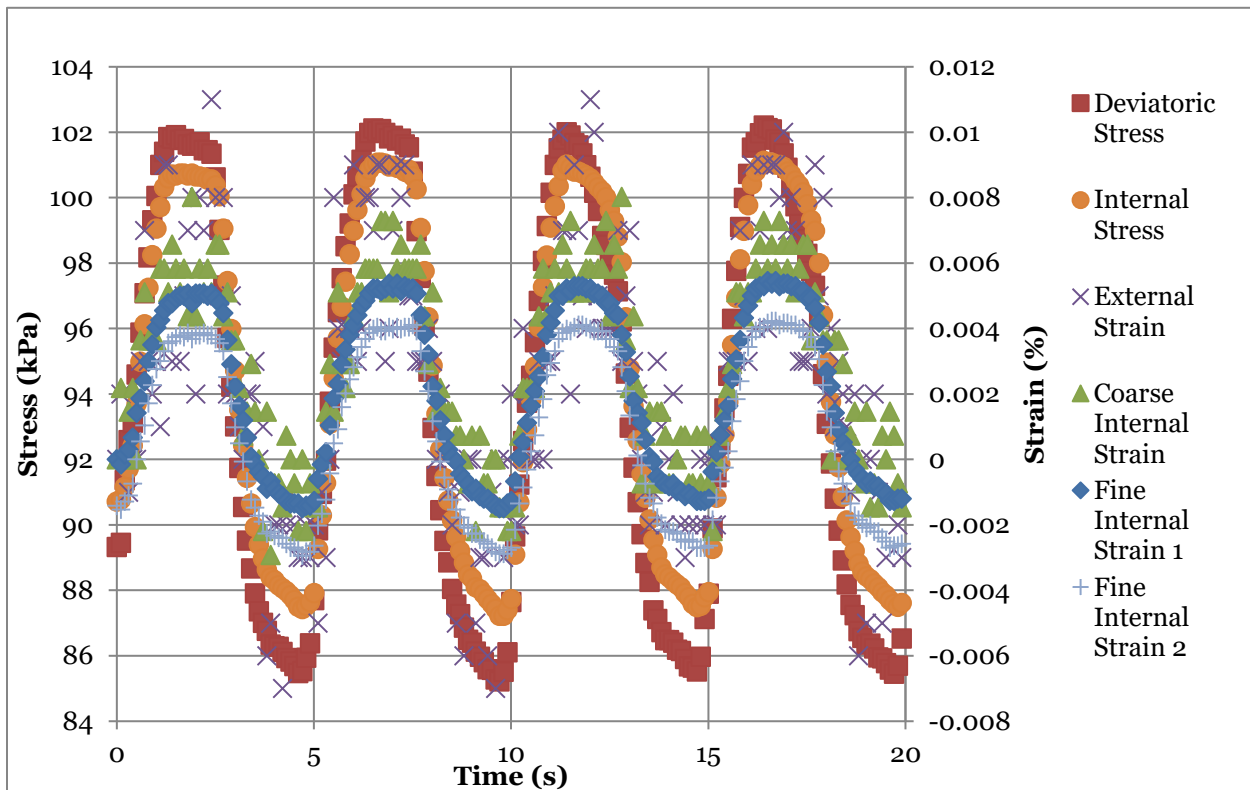


Figure 5.5. Cyclic Triaxial test showing time history and hysteresis loops.
From a dynamic suite for CUTX-10, (Top) is the time history and (Bottom) are the hysteresis loops

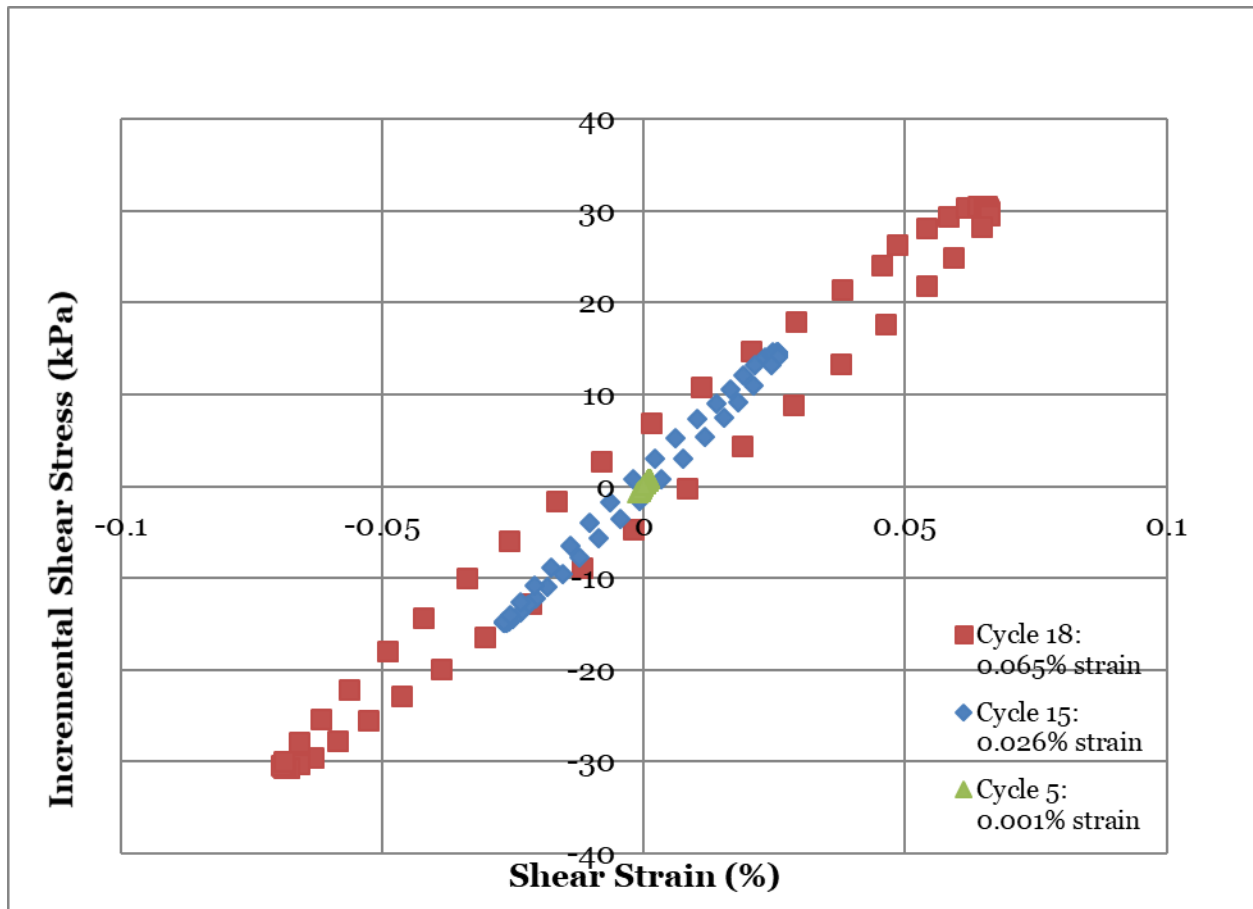


Figure 5.6. Suite of Cyclic tests showing degradation.

Cyclic testing suite showing loops for 0.001%, 0.026%, and 0.065%, with degradation observed at greater amplitudes.

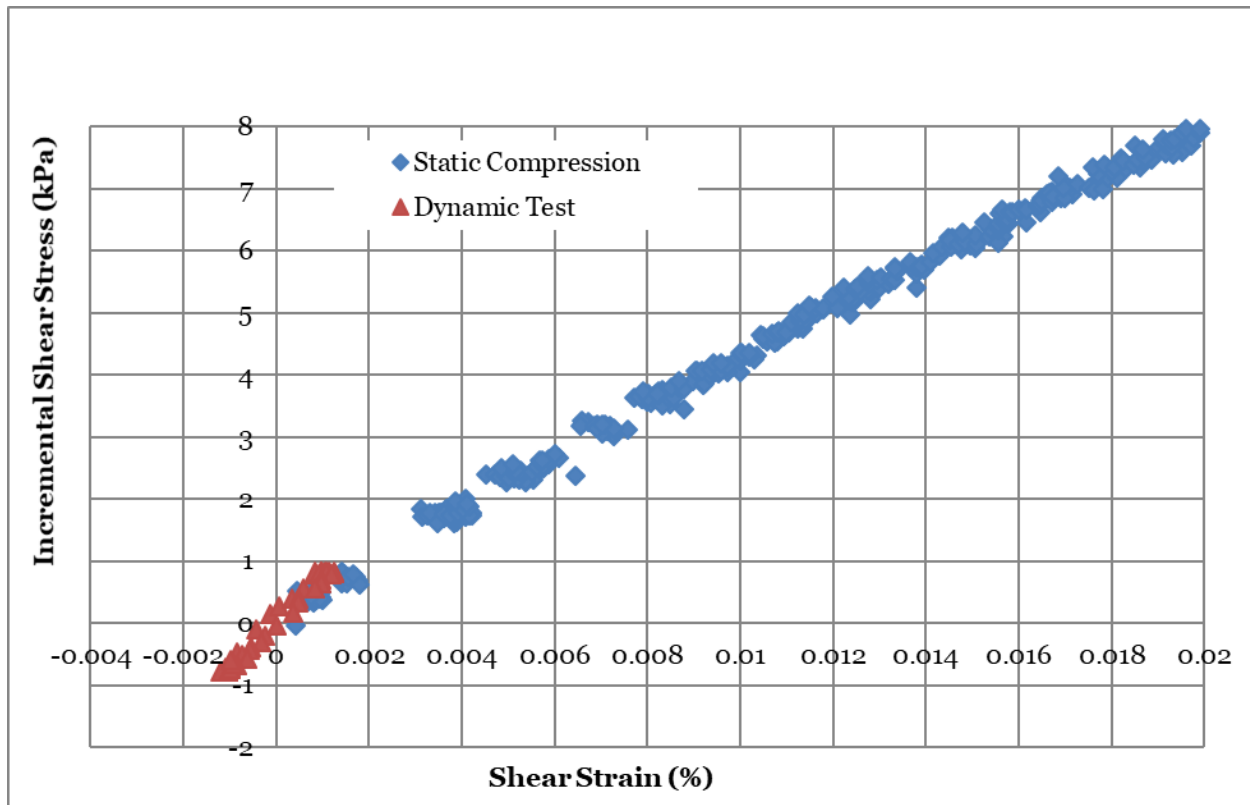


Figure 5.7. Comparison of Monotonic and Shear tests showing small strains.

Test shown is CUTX-10 showing the small strain portion of the monotonic shear test with a small-strain cyclic test, the 0.005% strain cyclic test shown on the previous figure.

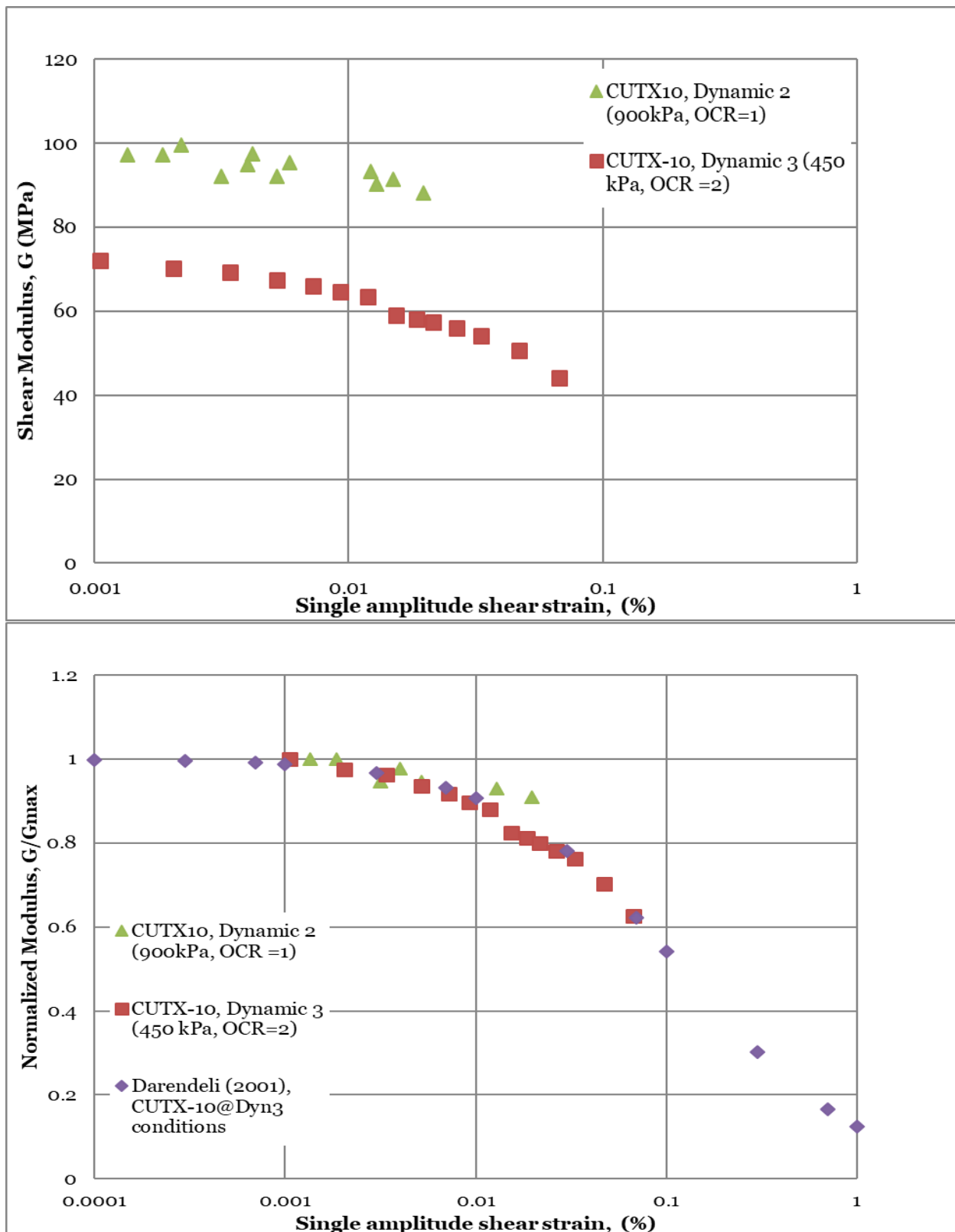


Figure 5.8. Measured Shear Modulus and Normalized Modulus results from Cyclic Triaxial Testing. From CUTX-10, values vary with strain level at two confining stresses. Reference curve from Darendeli (2001b)

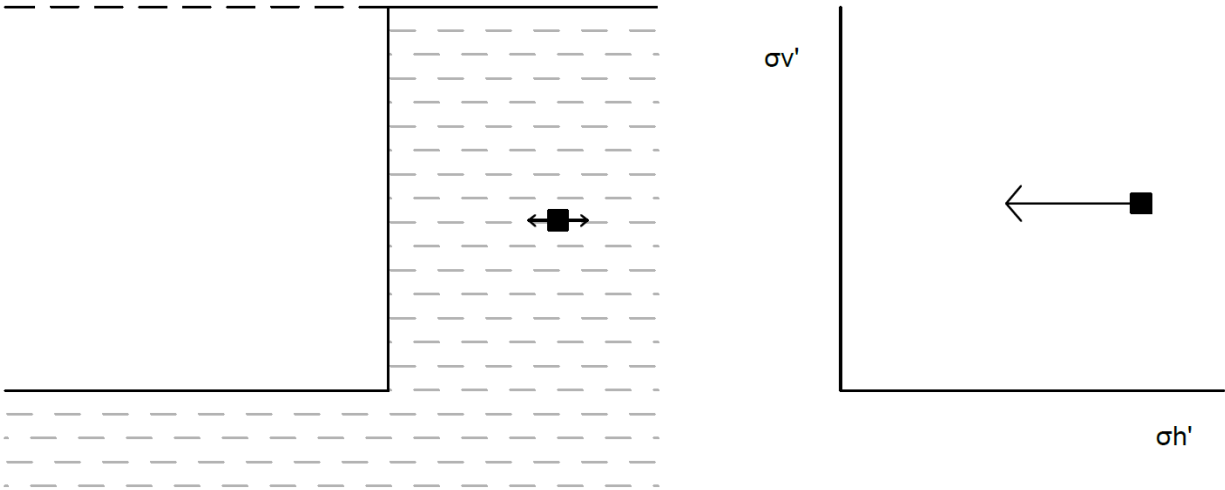


Figure 5.9. Schematic of soil element undergoing Lateral Unloading.

Schematic illustration of soil element undergoing lateral unloading: on the left, the overburden has generally remained constant while the lateral load has been removed due to excavation, and, on the right, the element in stress space.

Table 5.2. Lateral Unloading Triaxial testing performed for this project.

It is noted whether there was also bender element and/or cyclic testing performed

Test	Unit	Sample ID	Depth	Bender Testing	Cyclic Testing
VS-1	Alameda	I-16 S-2	206	Yes	Yes
VS-2	Alameda	I-11 S-6	190	Yes	-
VS-3	OBC	I-35 S-4	135	-	-
VS-4	OBC	I-9 S-2	130	Yes	Yes
VS-5	OBC	I-11 S-3	135	Yes	Yes

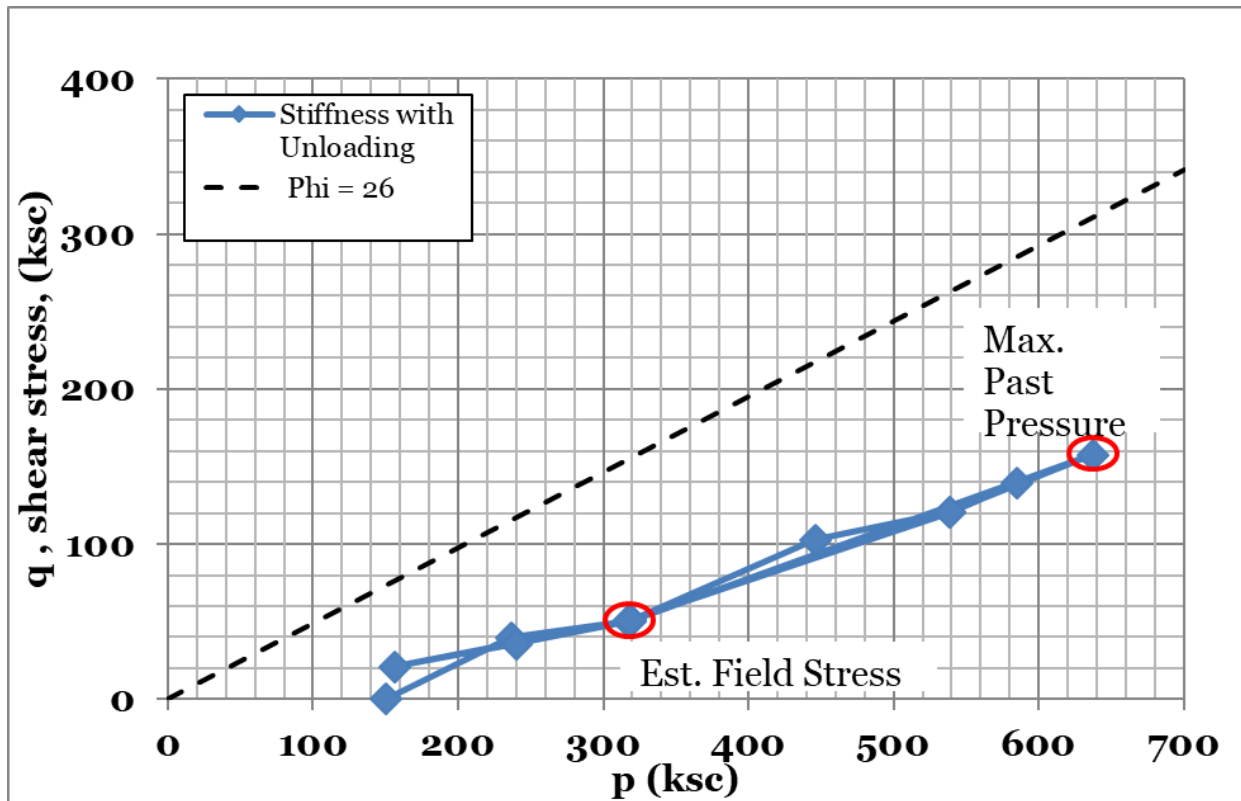


Figure 5.10. Stress paths during consolidation and unloading for Lateral Unloading test.

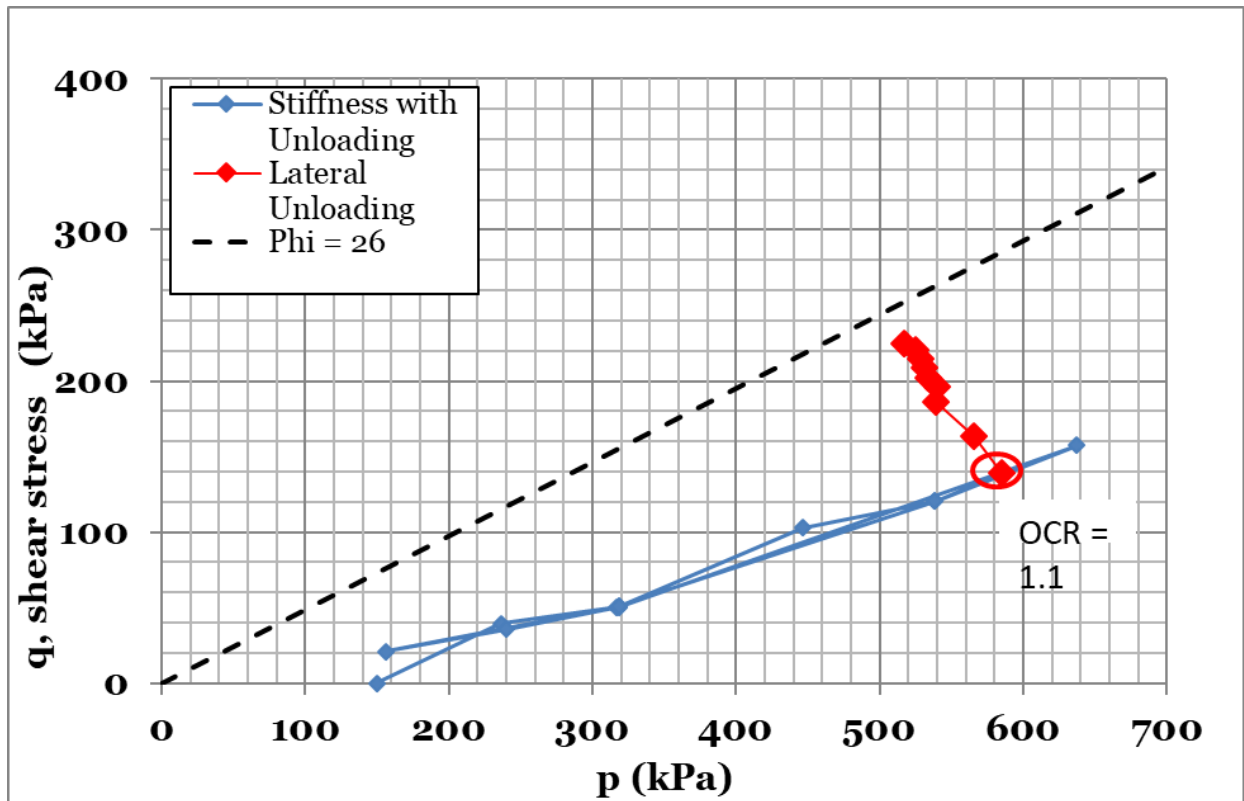


Figure 5.11. Stress path during Lateral Unloading test.

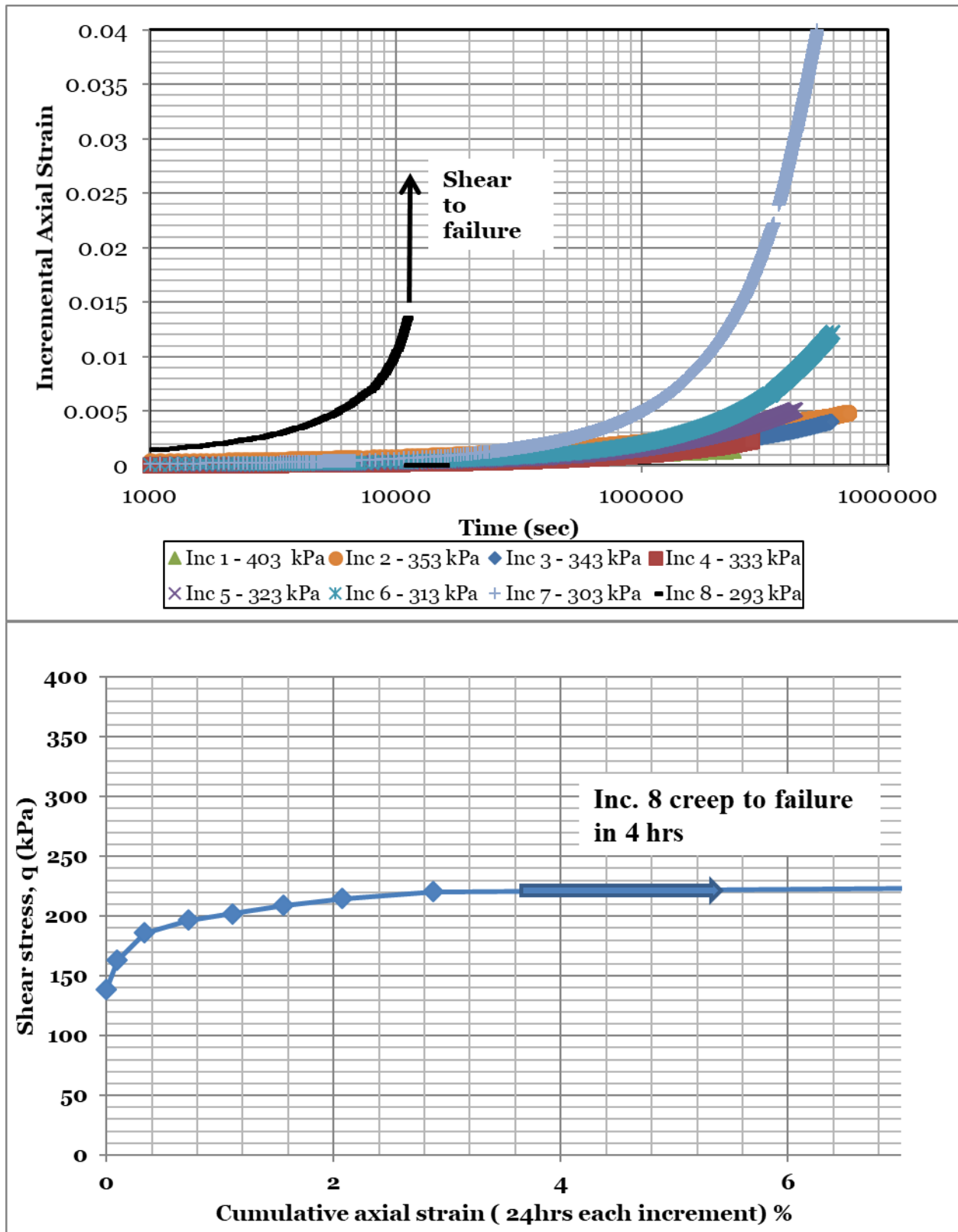


Figure 5.12. Strain Histories for Lateral Unload test.

From VS-5: (Top) all increments and (Bottom) final increment showing creep to failure

6 CONCLUSIONS, RECOMMENDATIONS, AND FUTURE WORK

6.1 Conclusions

This study has presented the geologic history, setting, and engineering properties of Sangamon-aged, marine clay, locally known as the “Old Bay Clay” or the “Yerba Buena Mud” as it exists in the South of Market area of Downtown San Francisco, California. This project was motivated by the construction of a transit center in Downtown San Francisco, California. The 1500 feet long, 200 feet wide, and 65 feet deep excavation occurred in a densely constructed urban environment over a subsurface soil profile up to 240 feet thick, including a layer of Old Bay Clay approximately 80 feet thick.

The Old Bay Clay was characterized by contextualizing the deposit within the San Francisco Bay Area geologic setting, prior engineering geologic characterization, and with knowledge gained from subsurface exploration and sampling. The geologic setting of the basement rocks, the Franciscan formation, was briefly explained and the bedrock morphology explained. The project site lies approximately on the southern limb of a bedrock valley that dips to the northeast. The Quaternary Bay Area history of deposition was summarized to include the deposition of the youngest to oldest subsurface units at the site, which are fill, dune sand, Young Bay Mud, marine sands, Colma sand, Old Bay Clay, and Alameda formation. The youngest units are from Historic time. The dune sand, Young Bay Mud, and marine sand were deposited as sea level rose during the Holocene from the Last Glacial Maximum when the shoreline was approximately 300 feet lower. During the last glaciation, the Wisconsin stage, which lasted from approximately 75,000, to 11,000 years before the present, the Bay Area would have been an area of alluvial or eolian deposition, possibly including the deposition of the Colma formation.

The Old Bay Clay was deposited during the last interglacial period, likely in a previous version of San Francisco Bay that was much deeper. The profile of Old Bay Clay at this site is very consistent, compared with other project materials, as well as to other subsurface profiles containing Old Bay Clay in the Bay Area. Old Bay Clay is described as a Dark Greenish Gray, stiff to hard, fat clay, with water content from 33 to 44%, total unit weight from 105 to 117 pcf, 95 to 100% fines content, Liquid Limit from 60 to 68, and Plasticity Index from 37 to 44. Based on microfossil studies, the Old Bay Clay is a single transgression deposited during the last interglacial from a previous Bay that was deeper than the current San Francisco Bay. A microfossil study was performed on Old Bay Clay samples from the project site that identified foraminifers and diatoms that suggest the project site materials came from the lower units deposited in the Sangamon San Francisco Bay.

Beneath the Old Bay Clay is the Alameda formation, which contains some interlayers of estuarine or marine clay that resemble the Old Bay Clay. Clay samples from the Alameda were tested for this project in order to compare with the Old Bay Clay properties. The Alameda clay engineering properties tended to vary slightly to moderately from Old Bay Clay. Unit weight was greater,

moisture content was less, OCR was less, and consolidation properties were less compressible. Alameda clays tended to have high fines content and moderate to high plasticity similar to the Old Bay Clay.

To understand the compression parameters and stress history of the deep, thick layer the Old Bay Clay and deep clays within the Alameda formation, a detailed consolidation testing program was performed. The Old Bay Clay and Alameda soils were found to be slightly to moderately overconsolidated. The Old Bay Clay and Alameda soils were found to be compressible, consistent with their moderate water content and moderate plasticity. Compression parameters including compression ratio, recompression ratio, secondary compression, and coefficient of consolidation were compiled and compared for and between Young Bay Mud, Old Bay Clay, and the Alameda clays. There was also an assessment of sample quality in order to quantify sampling, handing, and trimming techniques. Sample quality was found to be very good for Old Bay Clay and moderate for Alameda soils, which is likely due to the significant depth of these deposits and the variation of sample quality with depth. Sample quality was also important to justify the value of the small strain testing performed.

Testing of these clay materials led to a focus on how consolidation testing methods and results are different for deep, stiff clays than for the more conventional shallow materials often tested. For parameters that depend on graphical constructions, including preconsolidation pressure, compression index, and recompression index, careful study was made regarding assumptions. Six methods of preconsolidation pressure were assessed and three methods routinely used in order to characterize dependence of methodology on estimates of preconsolidation pressure. A small study was discussed using a known maximum past pressure in order to assess accuracy the of the estimates from different preconsolidation methods. For compression index, the difference in field curves was discussed between CRS and IL compression curves, but also between IL compression curves from the same test using different methodologies for assessing IL data. An example settlement problem illustrated the variability of field curve construction on settlement estimates. Recompression index was compiled at various stress states to show the dependence on unloading magnitude and stress level. For recompression to be a meaningful parameter, it is suggested that more uniformity is used for calculation, as well as some ways to compute recompression index to compare between various unloading magnitudes and stress states.

While not dependent on constructions, secondary compression and coefficient of consolidation both produce a range of values in any given oedometer test. For secondary compression, values were compiled for every unload and reload increment to show dependence on stress history. For coefficient of consolidation, values were compared between IL and CRS testing for understanding of instantaneous coefficient of consolidation estimates in CRS testing as well as dependence on stress level.

Lastly, a suite of testing was performed on Old Bay Clay specimens that produced meaningful values of small strain stiffness for specimens that had been reconsolidated to large stresses eliminate disturbance effects and then unloaded to replicate field conditions. Anisotropic-Consolidated Undrained Triaxial (CKoUTX) tests were performed that involved a suite of tests, including bender elements, cyclic loading, and/or small to large strain compression and extension tests. A group of CKoUTX tests were performed under special “lateral unloading” conditions to

understand shear behavior and measure stiffness values at various stress states. Because of the precision and responsiveness of the testing equipment and the high-quality samples, small strain properties were meaningfully measured that agree well with other research within the Old Bay Clay as well as for similar clay materials.

6.1.1 Significance of Old Bay Clay

The Old Bay Clay has engineering significance due to its prevalence throughout the San Francisco Bay Area. In the previous sections it has been characterized at the TTC site in Downtown San Francisco, where the profile is remarkably consistent. This makes it a good type study area for engineering properties. The Old Bay Clay at the site has moderate water content and plasticity as well as moderately compressible parameters from consolidation testing. When loading at a project site matters, Old Bay Clay should be considered within the soil profile. Old Bay Clay at the project site also has a clear and easy to understand geologic history, as a single marine transgression, which can help explain its context in other parts of the Bay.

However, many sites around the Bay Area have Old Bay Clay that differs from the material at the project site. Even some sites that are very close geographically. While the profile deposited at the project site during the Sangamon was an estuarine or marine sequence, not all areas of the Bay Area at that time would have been estuarine or marine. Because of the complex topography of the Bay Area, local conditions matter and stress history may be place-dependent. While estuarine and marine clays were deposited in many parts of the Bay Area, they may not all have the same stratigraphy, stress history, or engineering properties.

By definition, the Old Bay Clay is not a single geotechnical material, but rather a geological formation that describes similar clay materials deposited under estuarine to marine conditions during the Sangamon stage. Identifying Old Bay Clay is important for classification, but site-specific knowledge is paramount. Testing of on-site materials should always be performed to understand the properties, even when the site profile resembles a typical Bay Area subsurface profile.

6.1.2 Engineering Properties of Old Bay Clay in Downtown San Francisco

Table 6.1. Summary of Testing Results from index and consolidation on Old Bay Clay

Parameter	Value
Total Unit Weight	17.3-18.4 kN/m ³ 105-117 lbs/ft ³
Natural Water Content	33-44%
Liquid Limit, LL	60-68
Plasticity Index, PI	37-44
USCS	CH
Compression Index, C _c , CRS consolidation testing	0.54-1.01
Compression Ratio, C _R , CRS consolidation testing	0.25-0.46
Compression Index, C _c , IL consolidation testing	0.51-1.06
Compression Ratio, C _R , IL consolidation testing	0.23-0.49
Recompression Index, C _r	0.01-0.07
Recompression Ratio, R _R	0.005-0.03
Coefficient of Secondary Compression, C _α , normally consolidated	0.020-0.034
Coefficient of Consolidation, C _v , normally consolidated	1.4-1.7 m ² /yr 15-17 ft ² /yr
Overconsolidation Ratio	1.7-2.4
Specific Gravity, G _s	2.75

6.2 Recommendations for Consolidation Testing in Deep, Stiff Clays

Particular interest in this study was on consolidation testing of deep, stiff, overconsolidated clays in order to establish a typical range of parameters and, most importantly, to provide guidance for future test protocols for these materials. Some recommendations for testing these materials follows.

- High quality samples can be obtained in deep clays with Shelby tubes with no turned edge using an Osterberg-type hydraulic fixed-piston sampler. These tubes are recommended for use in order to reduce sample disturbance during extrusion and prevent unnecessary trimming.
- Application of a substantial soaking stress, recommended one-half to two-thirds of the in-situ vertical effective stress, can prevent swelling and will likely lessen sample disturbance.
- A sufficient unloading-reloading should be performed prior to the preconsolidation pressure.

- Unload/reload cycles should be performed with unloading factors between 2 and 4.
- For consistency, calculate C_r values at a constant unloading factor, such as 3.
- For CRS testing, pore water pressure generation needs to be significant enough to provide estimates of certain parameters, especially coefficient of consolidation, C_v . Depending on the accuracy and precision of the testing equipment, a pore pressure ratio between 3% and 8% will provide clear values of C_v and prevent unnecessary secondary compression from being included in the compression index.
- Several methods should be performed in order to estimate preconsolidation pressure, this helps to understand variability and to find the best method for the soil.
- Constructions should be performed digitally for accuracy with the digital testing data.
- For Recompression Index, C_r , consider the stresses at unloading relative to preconsolidation pressure and the unloading factor. Calculating several C_r values from consolidation test may be necessary to capture the range of behavior observed.
- Likewise, C_α may include several estimates from one test, including for loading, unloading, or reloading loops that are relevant for the stress history of the project.
- A range of C_v should be reported, especially if relevant stress conditions for the projects include soil in recompression or unloading.

6.3 Recommendations for Future Work

Much of the literature regarding properties of subsurface materials in the Bay Area only come from a handful of sites, generally Bridge and Bay crossing sites. More projects like this one, that characterize subsurface materials in various locations or across new transects would be tremendously helpful. More data could clarify the true variability of the Old Bay Clay. In particular, the relationship between the deposits in the West Bay and the East Bay as well as to the South Bay.

Moreover, these site studies could help develop site-specific or region-specific Cone Penetration Test (CPT) parameters for Old Bay Clay. The deep clays are different in enough ways from shallow, highly compressible clays that more guidance in the literature is needed.

The compression index, recompression index, secondary compression, and coefficient of consolidation values appear to vary both due to intrinsic soil variability, but also due to testing methods and data processing. A case study could be helpful to understand sources of variability in this data, especially to understand the role of data processing and data synthesis. A case study that incorporates field monitoring, a review early project data, and observations after construction is complete could assess the validity of the field monitoring and early project data. In that way, it could be evaluated what data may have been valid but did not reflect the project conditions prior to construction.

For parameters that require constructions, especially those that require a lot of judgement, especially preconsolidation pressure as well as compression index and recompression index, require a method for handling variability and for weighting the quality of the estimates. More study could be made of how much the variability in these tests is intrinsic or is due to data interpretations. This could be helpful for large projects with copious testing data.

Lastly, this dataset could be useful for numerical modeling. Either to calibrate a performance-based model or to build a soil model.

7 REFERENCES

- Allen, James. (2012a). Report on Referred Fossils, Field No.: JA91012A, Report Date: September 11, 2012. Form 9-1861, U.S. Department of the Interior Geological Survey.
- Allen, James. (2012b). Identification Report for the Mammoth Fossil Tooth at the Transbay Transit Center Project in San Francisco, California, dated October 26, 2012.
- American Society of Testing and Materials. (1998.) *ASTM D2216-98: Standard Test Method for Laboratory Determination of Water (Moisture) Content of Soil and Rock by Mass.*
- American Society of Testing and Materials. (2011a). *ASTM D2435/D2435M: Standard test methods for one-dimensional consolidation properties of soils using incremental loading.*
- American Society of Testing and Materials. (2011b). *ASTM D3999/D3999M-11^{el}: Standard Test Methods for the Determination of the Modulus and Damping Properties of Soils Using the Cyclic Triaxial Apparatus.*
- American Society of Testing and Materials. (2011c). *ASTM D4767-11: Standard Test Method for Consolidated Undrained Triaxial Compression Test for Cohesive Soils.*
- American Society of Testing and Materials. (2012). *ASTM D4186/D4186M: Standard test method for one-dimensional consolidation properties of saturated cohesive soils using controlled-strain loading.*
- American Society of Testing and Materials., (2013). *ASTM D5311/D5311M-13: Standard Test Method for Load Controlled Cyclic Triaxial Strength of Soil.*
- American Society of Testing and Materials. (2014). *ASTM D854-14: Standard Test Methods for Specific Gravity of Soil Solids by Water Pycnometer.*
- American Society of Testing and Materials. (2015a). *ASTM D1587/D1587M-15: Standard Practice for Thin-Walled Tube Sampling of Fine-Grained Soils for Geotechnical Purposes.*
- American Society of Testing and Materials. (2015b). *ASTM D2850-15: Standard Test Method for Unconsolidated-Undrained Triaxial Compression Test on Cohesive Soils.*
- American Society of Testing and Materials. (2017a). *ASTM D4318-17^{el}: Standard Test Methods for Liquid Limit, Plastic Limit, and Plasticity Index of Soils.*
- American Society of Testing and Materials. (2017b). *ASTM D6913/6913M: Standard Test Methods for Particle-Size Distribution (Gradation) of Soils Using Sieve.*

- American Society of Testing and Materials. (2017c). *ASTM D7928-17: Standard Test Method for Particle-Size Distribution (Gradation) of Fine-Grained Soils Using the Sedimentation (Hydrometer) Analysis*.
- American Society of Testing and Materials. (2018). *ASTM D7263-09: Standard Test Methods for Laboratory Determination of Density (Unit Weight) of Soil Specimens*.
- Arulnathan, R., Boulanger, R., & Riemer, M. (1998). Analysis of Bender Element Tests. *Geotechnical Testing Journal*, 21(2), 120-131.
- Arup North America. (2010). Final Geotechnical Data Report, Transbay Transit Center, prepared for Transbay Joint Powers Authority, Job Number 132242, dated February 23, 2010.
- Atwater, B. F., Hedel, C. W., & Helley, E. J. (1977). Late Quaternary depositional history, Holocene sea-level changes, and vertical crustal movement, southern San Francisco Bay, California. *U.S. Geological Survey Professional Paper*, 15.
- Bay Area News Service. (2014, February 26). Native American remains found buried at Transbay Transit construction site. *San Jose Mercury News*. Retrieved from <https://www.mercurynews.com/2014/02/26/native-american-remains-found-buried-at-transbay-transit-construction-site/>
- Becker, D. E., Crooks, J. H. A., Been, K., & Jefferies, M. G. (1987). Work as a Criterion for Determining *In Situ* and Yield Stresses in Clays. *Canadian Geotechnical Journal*, 24(4), 549–564.
- Bilgin, Ö., Tsimbelman, N., & Chernova, T. (2017). Variability in Recompression Index Obtained from Incremental Consolidation Tests. *19th International Conference on Soil Mechanics and Geotechnical Engineering, Seoul*, (1), 317–320.
- Bonaparte, R., & Mitchell, J. K. (1979). *The properties of San Francisco Bay mud at Hamilton Air Force Base, California*. Berkeley, CA: Dept. of Civil Engineering, University of California, Berkeley.
- Boone, S. J. (2010). A Critical Reappraisal of “Preconsolidation Pressure” Interpretations Using the Oedometer Test. *Canadian Geotechnical Journal*, 47(3), 281–296.
- Bray, J. D., Chameau, J. L., & Guha, S. (1992). Seismic Response of Deep Stiff Clay Deposits: Paper presented at Proceedings, First Canadian Symposium on Geotechnique and Natural Hazards, Vancouver, British Columbia, 167-174.
- Bürgmann, R., Hilley, G., Ferretti, A., & Novali, F. (2006). Resolving vertical tectonics in the San Francisco Bay Area from Permanent Scatterer InSAR and GPS Analysis. *Geology*, 34(3), 221–224.

- Butterfield, R. (1979). A Natural Compression Law for Soils (an Advance on $e - \log p'$). *Géotechnique*, 29(4), 469–480.
- Clementino, R. V. (2005). Discussion of “An Oedometer Test Study on the Preconsolidation Stress of Glaciomarine Clays.” *Canadian Geotechnical Journal*, 42(3), 972–974.
- Darendeli, M.B. (2001) Development of a New Family of Normalized Modulus Reduction and Material Damping Curves (PhD dissertation). University of Texas at Austin.
- Espinosa, P., Pestana, J., Vahdani, S., & Heidarzadeh, B. (2017). Seismic Deformation Analyses of the Existing Shoreline at Treasure Island: Paper Presented at Proceedings from 3rd International Conference on Performance-based Design in Earthquake Geotechnical Engineering, Vancouver, British Columbia.
- Gillespie, A.R., Burke, R.M., & Clark, M.M. (1999). Eliot Blackwelder and the Alpine Glaciations of the Sierra Nevada. In E.M. Moores, D. Sloan, & D.L. Stout (Eds.), *Classic California Cordilleran Centennial Concepts: A View from California* (pp. 443–452). Geological Society of America, Special Paper 338, Boulder, Colorado.
- Goldman, H. B. (Ed.). (1969). Geologic and engineering aspects of San Francisco Bay fill. *Special Report 97*. San Francisco Bay Conservation and Development Commission; California Division of Mines and Geology, plates 1:70,000.
- Gookin, W. B. (1998). The Combined Effects of Loading Frequency And Other Parameters On Dynamic Properties Of Reconstituted Cohesive Soils (Doctoral dissertation). University of California, Berkeley.
- Grozic, J. L. H., Lunne, T., & Pande, S. (2003). An Oedometer Test Study on the Preconsolidation Stress of Glaciomarine Clays. *Canadian Geotechnical Journal*, 40, 857–872.
- Grozic, J. L., Lunne, T., & Pande, S. (2005). Reply to the discussion by Clementino on “An Oedometer Test Study on the Preconsolidation Stress of Glaciomarine Clays.” *Canadian Geotechnical Journal*, 42(3), 975–976.
- Guha, S. (1995). Dynamic Characteristic of Old Bay Clay Deposits in the East San Francisco Bay Area (Doctoral dissertation). Purdue University.
- Guha, S., Drnevich, V. R., & Bray, J. D. (1997). Dynamic Characteristics of Old Bay Clay. *Geotechnical Testing Journal, GTJODJ*, 20(4), 383-393.
- Hashash, Y. M. A. (1992) Analysis of Deep Excavations in Clay (Doctoral dissertation). Massachusetts Institute of Technology, Cambridge, MA.

- Hashash, Y. M. A., & Finno, R. J. (2008). Development of new integrated tools for predicting, monitoring and controlling ground movement due to excavations. *Practice Periodical on Structural Design and Construction*, American Society of Civil Engineers, 13(1), 4–10.
- Hashash, Y. M. A., Marulanda, C., Ghaboussi, J., & Jung, S. (2006). Novel Approach to Integration of Numerical Modeling and Field Observations for Deep Excavations. *Journal of Geotechnical and Geoenvironmental Engineering*, 132(8), 1019-1031.
- Holbourn, A., Henderson, A. S., & MacLeod, N. (2013). *Atlas of Benthic Foraminifera*. Hoboken, NJ: John Wiley & Sons.
- Holtz, R. D., Kovacs, W. D., & Sheahan, T. C. (2011). *An Introduction to Geotechnical Engineering*. Upper Saddle River, NJ: Pearson.
- Hvorslev, M. Juul. (1949). *Subsurface Exploration and Sampling of Soils for Civil Engineering Purposes: Report on a Research Project*. American Society of Civil Engineers. The Engineering Foundation. Harvard University. The Waterways Experiment Station. Edited and Printed by: Waterways Experiment Station, Vicksburg, Miss.
- Ingram, B. L., Ingle, J. C., & Conrad, M. E. (1996). Stable isotope record of Late Holocene Paleosalinity and Paleodischarge in San Francisco Bay, California. *Earth and Planetary Science Letters*, 141, 237-247.
- Janbu, N. (1969). The Resistance Concept applied to Deformations of Soils. *Proc. 7th International Conference on Soil Mechanics*, 1(5), 191–196.
- Jennings, C. W., Bryant, W. A., Saucedo, G. J., & California Geological Survey. (2010). *Fault Activity Map of California*. Sacramento, Calif.: California Geological Survey.
- Kootahi, K. (2017). Discussion of “Accuracy of Determining Pre-Consolidation Pressure from Laboratory Tests.” *Canadian Geotechnical Journal*, 54(12), 1796–1798.
- Ladd, C. C., & Foott, R. (1974). New Design Procedure for Stability of Soft Clays. *Journal of the Geotechnical Engineering Division*, 100(7), 763–786.
- Lawson, A.C. (1895). *Sketch of the Geology of the San Francisco Peninsula*. Washington: Government Printing Office.
- Lawson, A. C. (1914). Description of the San Francisco District; Tamalpais, San Francisco, Concord, San Mateo, and Haywards quadrangles. *Geological Atlas Folio*. U. S. Geological Survey, Reston, VA.
- Leong, E., Yeo, S., & Rahardjo, H. (2005). Measuring Shear Wave Velocity Using Bender Elements. *Geotechnical Testing Journal*, 28(5), 488-498.

- Leonards, G. A. (1976). Estimating Consolidation Settlements of Shallow Foundations on Overconsolidated Clay. *Transportation Research Board Special Report*, (163), 13–16.
- Louderback, G. D. (1939). San Francisco Bay Sediments. Paper presented at Sixth Pacific Science Conference [i.e. Congress], Berkeley, California, 2, 783–793.
- Louderback, G. D., (1951). Geological History of San Francisco Bay. *Geologic Guide Book to San Francisco Bay Counties*. California Division of Mines and Geology, Bulletin 154.
- Lunne, T., Berre, T., Andersen, K. H., Strandvik, S., & Sjursen, M. (2007). Effects of Sample Disturbance and Consolidation Procedures on Measured Shear Strength of Soft Marine Norwegian Clays. *Canadian Geotechnical Journal*, 44(1), 111.
- Medley, E. W. (1994). The Engineering Characterization of Mélanges and Similar Block-in-Matrix Rocks (Bimrocks), (Doctoral dissertation). University of California, Berkeley.
- Meyer, J.A. (2015). Holocene Transformation of Yerba Buena Cove and San Francisco Bay. Presentation at the 2015 Society for American Archaeology Meeting, San Francisco, California.
- Mitchell, J. K., & Soga, K. (2005). *Fundamentals of Soil Behavior*. Hoboken, NJ: John Wiley & Sons.
- Nevius, C.W. (2014, October 20). Construction crew’s discovery of human remains can’t stay buried. *San Francisco Chronicle*. Retried from <https://www.sfgate.com/bayarea/nevius/article/Construction-crew-s-discovery-of-human-remains-5835634.php>
- Norris, R.M. & Webb, R.W. (1990). *Geology of California* (2nd ed.). Hoboken, NJ: John Wiley and Sons, Inc.
- Oikawa, H. (2011). Compression Curve of Soft Soils. *Journal of the Japanese Geotechnical Society, Soils and Foundations*, 27(3), 99–104.
- Onitsuka, K., Hong, Z., Hara, Y., & Yoshitake, S. (1995). Interpretation of Oedometer Test Data for Natural Clays. *Journal of the Japanese Geotechnical Society, Soils and Foundations*, 35(3), 61–70.
- Peterson, C. D., Stock, E., Meyer, J., Kaijankoski, P., & Price, D. M. (2015). Origins of Quaternary Coastal Dune Sheets in San Francisco and Monterey Bay, Central California Coast, U.S.A.: Reflecting Contrasts in Shelf Depocenters and Coastal Neotectonics. *Journal of Coastal Research*, 31(6), 1317–1333.

- Rau, G. A. (1999). Evaluation of Strength Degradation in Seismic Loading of Holocene Bay Mud from Marin County, California (Doctoral dissertation). University of California, Berkeley.
- Rodda, P., & Baghai, N. (1993). Late Pleistocene Vertebrates from Downtown San Francisco, California. *Journal of Paleontology*, 67(6), 1058-1063.
- Rogers, J.D., & Figuers, S.H. (1991). Engineering Geologic Site Characterization of the Greater Oakland-Alameda Area, Alameda and San Francisco Counties, California, Final Report to NSF, Grant No. BCS-9003785.
- Rood, D.H., Burbank, D.W., & Finkel, R.C. (2011). Chronology of glaciations in the Sierra Nevada, California, from (10)Be surface exposure dating. *Quaternary Science Reviews*, 30(5-6), 646-661.
- Ross, B. E. (1977). The Pleistocene History of San Francisco Bay along the Southern Crossing (Master's Thesis), San Jose State University.
- Sadrekarami, A. (2017). Reply to the discussion by Kootahi on "Accuracy of Determining Pre-Consolidation Pressure from Laboratory Tests." *Canadian Geotechnical Journal*, 54(12), 1799–1801.
- Schlocker, Julius, Bonilla, M.G., & Radbruch, D.H.. (1958). Geology of the San Francisco North quadrangle, California: U.S. Geological Survey, Miscellaneous Geologic Investigations Map I-272, scale 1:24,000.
- Schlocker, J. (1974). Geology of the San Francisco North quadrangle, California. *Professional Paper 782*. U.S. Geological Survey.
- Schmertmann, J. H. (1955). The Undisturbed Consolidation Behavior of Clay. *ASCE Transactions*, 120(1), 1201–1227.
- Schweikhardt, P., Sloan, D., & Ingram, B. (2010). Early Holocene Evolution of San Francisco Estuary, Northern California. *Journal of Coastal Research*, 26(4), 704-713.
- Simpson, L.A. (2006). Case Studies in Mission Bay, San Francisco: Deep Foundations in Challenging Soil Conditions. Paper presented at DFI Proceedings of the 31st Annual Conference on Deep Foundations, Washington, DC, USA.
- Sloan, D. (1982). Ecostratigraphic study of Sangamon Sediments beneath Central San Francisco Bay (Doctoral dissertation). University of California, Berkeley.
- Sloan, D. (1992). The Yerba Buena Mud; Record of the Last-Interglacial Predecessor of San Francisco Bay, California. *Geological Society of America Bulletin*, 104(6), 716-727.

- Smol, J., & Stoermer, E. (Eds.). (2010). *The Diatoms: Applications for the Environmental and Earth Sciences*. Cambridge: Cambridge University Press.
- Soltani, A., Taheri, A., Deng, A., & Azimi, M. (2019). A Note on Determination of the Preconsolidation Pressure. *Journal of Testing and Evaluation*, 47(6), 20170689.
- Terzaghi, K., Peck, R. B., & Mesri, G. (1996). *Soil Mechanics in Engineering Practice*. Hoboken, NJ: John Wiley & Sons.
- Treasher, R.C. (1963). Geology of the Sedimentary Deposits in San Francisco Bay. *Special Report 82*. California Division of Mines and Geology, 11-19
- Trask, P. D., & Rolston, J. W. (1951) Engineering geology of San Francisco Bay, California. *Bulletin of the Geological Society of America*, 62(9), 1079-1110.
- Umar, M., & Sadrekarimi, A. (2017). Accuracy of Determining Pre-Consolidation Pressure from Laboratory Tests. *Canadian Geotechnical Journal*, 54(3), 441–450.
- United States Coast Survey. (1852). City of San Francisco and Its Vicinity, California.
- Vipulanandan, C., Ahossin Guezo, Y. J., Bilgin, Ö., Yin, S., & Khan, M. (2008). Recompression Index (C_r) for Overconsolidated Soft Clay Soils. Paper presented at GeoCongress 2008: Characterization, Monitoring, and Modeling of GeoSystems, New Orleans, LA, (GSP 179, 68–75).
- Wakabayashi, J. (2004). Contrasting Settings of Serpentinite Bodies, San Francisco Bay Area, California: Derivation from the Subducting Plate vs. Mantle Hanging Wall? *International Geology Review*, 46(12), 1103–1118.
- Wissa, A.E., Christian, J.T., Davis, E.H., & Heiberg, S. (1971). Consolidation at Constant Rate of Strain. *Journal of the Soil Mechanics and Foundations Division*. 97 (10), 1393-1413.

8 APPENDIX A

8.1 Samples

Table A- 1. List of samples collected for research project, not all collected samples were tested. Sample types are as follows: Epoxy = epoxy-coated steel Shelby tube, MC= Modified California sampler 6-inch liner, Shelby = steel Shelby tube, Zinc = zinc-coated Shelby tube

Borehole	Sample No.	Depth BGS (ft)	Sample Type	Field Classification	Recovery (in)
DSM-1	S-1	26	Epoxy	Young Bay Mud - W	31.5
I-17A	S-1	28	Epoxy	Young Bay Mud - U	34
DSM-1	S-1	28.5	Epoxy	Young Bay Mud - W	30
BH-2	S-7	30.3	MC	Young Bay Mud - W	6
BH-2	S-8	30.8	MC	Young Bay Mud - W	6
DSM-1	S-2	32.5	Epoxy	Young Bay Mud - W	31
P-23	S-1	34.5	Epoxy	Young Bay Mud - W	29.5
DSM-12	S-1	37.5	Epoxy	Young Bay Mud - W	30
I-35	S-1	40	Epoxy	Young Bay Mud - W	30
EX-02	S-1	44.5	Epoxy	Young Bay Mud - W	27.5
EX-03	S-1	44.5	Epoxy	Young Bay Mud - W	29
P-24	S-1	44.5	Epoxy	Young Bay Mud - W	29
DSM-12	S-2	47.5	Epoxy	Young Bay Mud - W	29
BH-2	S-12	50	Shelby	Young Bay Mud - L	20
BH-3	S-11	50	Shelby	Young Bay Mud - L	32
I-35	S-2	50	Epoxy	Young Bay Mud - W	31
I-17A	S-2	69	Epoxy	Young Bay Mud - L	23
EX-04	S-1	80	Epoxy	Old Bay Clay	32
BH-2	S-23	95.5	MC	Old Bay Clay	6
BH-2	S-24	96	MC	Old Bay Clay	6
I-35	S-3	98	Epoxy	Old Bay Clay	30
I-17B		99	Epoxy	Old Bay Clay	36
BH-1	S-17	100	Shelby	Old Bay Clay	31
EX-04	S-2	100	Epoxy	Old Bay Clay	32
EX-02	S-2	104	Epoxy	Old Bay Clay	28
P-23	S-2	104.5	Epoxy	Old Bay Clay	31
I-17A	S-3	109	Epoxy	Old Bay Clay	30
BH-3	S-18	110	Shelby	Old Bay Clay	30
I-11	S-1	110	Epoxy	Old Bay Clay	12
I-34	S-1	110	Epoxy	Old Bay Clay	30
I-2	S-1	112	Epoxy	Old Bay Clay	32

Borehole	Sample No.	Depth BGS (ft)	Sample Type	Field Classification	Recovery (in)
EX-03	S-2	114.5	Epoxy	Old Bay Clay	28
BH-1	S-18	120	Shelby	Old Bay Clay	32
I-11	S-2	120	Epoxy	Old Bay Clay	32
I-9	S-1	120	Zinc	Old Bay Clay	29.75
I-2	S-2	122	Epoxy	Old Bay Clay	32.5
P-24	S-2	124.5	Epoxy	Old Bay Clay	28
I-37	S-1	125	Epoxy	Old Bay Clay	N/A
I-42	S-1	128	Epoxy	Old Bay Clay	20.5
BH-3	S-19	130	Shelby	Old Bay Clay	24
I-9	S-2	130	Zinc	Old Bay Clay	32
I-11	S-3	135	Epoxy	Old Bay Clay	32
I-35	S-4	135	Epoxy	Old Bay Clay	29
BH-1	S-19	140	Shelby	Old Bay Clay	31
I-9	S-3	140	Zinc	Old Bay Clay	36
BH-3	S-20	150	Shelby	Old Bay Clay	32
I-11	S-4	150	Epoxy	Old Bay Clay	32
I-35	S-5	158	Epoxy	Old Bay Clay	28
BH-1	S-20	160	Shelby	Old Bay Clay	31
BH-2	S-28	160	Shelby	Old Bay Clay	27
EX-04	S-3	160	Epoxy	Alameda fm.	21
EX-04	S-4	165	Epoxy	Alameda fm.	24
BH-1	S-21	170	MC	Old Bay Clay	6
BH-1	S-22	171	MC	Old Bay Clay	6
BH-2	S-30	171	MC	Alameda fm.	6
I-37	S-2	172.5	Epoxy	Alameda fm.	20
EX-02	S-3	174	Epoxy	Old Bay Clay	27
BH-2	S-31	175	Epoxy	Alameda fm.	29
BH-1	S-23	180	Epoxy	Old Bay Clay	31
BH-2	S-32	180	Epoxy	Alameda fm.	N/A
I-11	S-5	180	Epoxy	Alameda fm.	32
I-2	S-1	180	Epoxy	Alameda fm.	29.5
EX-02	S-4	189.5	Epoxy	Alameda fm.	28.5
BH-3	S-23	190	Epoxy	Alameda fm.	27
I-11	S-6	190	Epoxy	Alameda fm.	29
I-2	S-2	190	Epoxy	Alameda fm.	30
BH-1	S-25	191	MC	Alameda fm.	6
P-24	S-3	194	Epoxy	Alameda fm.	21
EX-02	S-5	194.5	Epoxy	Alameda fm.	24.75

Borehole	Sample No.	Depth BGS (ft)	Sample Type	Field Classification	Recovery (in)
EX-03	S-3	194.5	Epoxy	Alameda fm.	18.5
P-23	S-3	194.5	Epoxy	Alameda fm.	13
BH-2	S-35	195	Epoxy	Alameda fm.	29
I-11	S-7	195	Epoxy	Alameda fm.	5
I-16	S-1	200	Epoxy	Alameda fm.	24.5
P-24	S-4	204	Epoxy	Alameda fm.	11
EX-03	S-4	204.5	Epoxy	Alameda fm.	17.5
I-16	S-2	206	Epoxy	Alameda fm.	29.5
BH-2	S-40	215.4	MC	Alameda fm.	40
BH-2	S-42	225	Epoxy	Alameda fm.	30
BH-1	S-29	230	Epoxy	Alameda fm.	33
BH-3	S-26	231	Epoxy	Alameda fm.	12
BH-2	S-43	235	Epoxy	Alameda fm.	12

8.2 Incremental Consolidation (IL) Consolidation Tests

Table A- 2. Incremental Loading (IL) Consolidation Testing

Test	Increment	Effective stress (ksc)	LIR	Start Date and Time	Elapsed time of Increment (hr:min)
ILC-01	1	3.15		5/22/11 4:43 PM	17:02
	2	6.25	1.0	5/23/11 9:45 AM	26:15
	3	12.49	1.0	5/24/11 12:00 PM	22:00
	4	6.25	-1.0	5/25/11 10:00 AM	3:20
	5	1.56	-3.0	5/25/11 1:20 PM	4:20
	6	0.79	-1.0	5/25/11 5:40 PM	16:45
	7	1.56	1.0	5/26/11 10:25 AM	
ILC-02	1	1.51		6/4/12 12:50 PM	10:10
	2	2.73	0.7	6/4/12 11:00 PM	18:00
	3	4.64	0.7	6/5/12 5:00 PM	18:00
	4	7.88	0.7	6/6/12 11:00 AM	29:47
	5	13.39	0.7	6/7/12 4:47 PM	28:23
	6	7.88	-0.7	6/8/12 9:10 PM	12:25
	7	4.64	-0.7	6/9/12 9:35 AM	8:23
	8	2.73	-0.7	6/9/12 5:58 PM	15:06
	9	1.51	-0.7	6/10/12 9:04 AM	14:56
	10	2.73	0.7	6/11/12 12:00 AM	9:20
	11	4.64	0.7	6/11/12 9:20 AM	9:00
	12	7.88	0.7	6/11/12 6:20 PM	13:41
	13	13.13	0.7	6/12/12 8:01 AM	29:24
	14	7.88	-0.7	6/13/12 1:25 PM	10:35
	15	13.85	0.7	6/14/12 12:00 AM	

8 APPENDIX A

8.1 Samples

Table A- 1. List of samples collected for research project, not all collected samples were tested. Sample types are as follows: Epoxy = epoxy-coated steel Shelby tube, MC= Modified California sampler 6-inch liner, Shelby = steel Shelby tube, Zinc = zinc-coated Shelby tube

Borehole	Sample No.	Depth BGS (ft)	Sample Type	Field Classification	Recovery (in)
DSM-1	S-1	26	Epoxy	Young Bay Mud - W	31.5
I-17A	S-1	28	Epoxy	Young Bay Mud - U	34
DSM-1	S-1	28.5	Epoxy	Young Bay Mud - W	30
BH-2	S-7	30.3	MC	Young Bay Mud - W	6
BH-2	S-8	30.8	MC	Young Bay Mud - W	6
DSM-1	S-2	32.5	Epoxy	Young Bay Mud - W	31
P-23	S-1	34.5	Epoxy	Young Bay Mud - W	29.5
DSM-12	S-1	37.5	Epoxy	Young Bay Mud - W	30
I-35	S-1	40	Epoxy	Young Bay Mud - W	30
EX-02	S-1	44.5	Epoxy	Young Bay Mud - W	27.5
EX-03	S-1	44.5	Epoxy	Young Bay Mud - W	29
P-24	S-1	44.5	Epoxy	Young Bay Mud - W	29
DSM-12	S-2	47.5	Epoxy	Young Bay Mud - W	29
BH-2	S-12	50	Shelby	Young Bay Mud - L	20
BH-3	S-11	50	Shelby	Young Bay Mud - L	32
I-35	S-2	50	Epoxy	Young Bay Mud - W	31
I-17A	S-2	69	Epoxy	Young Bay Mud - L	23
EX-04	S-1	80	Epoxy	Old Bay Clay	32
BH-2	S-23	95.5	MC	Old Bay Clay	6
BH-2	S-24	96	MC	Old Bay Clay	6
I-35	S-3	98	Epoxy	Old Bay Clay	30
I-17B		99	Epoxy	Old Bay Clay	36
BH-1	S-17	100	Shelby	Old Bay Clay	31
EX-04	S-2	100	Epoxy	Old Bay Clay	32
EX-02	S-2	104	Epoxy	Old Bay Clay	28
P-23	S-2	104.5	Epoxy	Old Bay Clay	31
I-17A	S-3	109	Epoxy	Old Bay Clay	30
BH-3	S-18	110	Shelby	Old Bay Clay	30
I-11	S-1	110	Epoxy	Old Bay Clay	12
I-34	S-1	110	Epoxy	Old Bay Clay	30
I-2	S-1	112	Epoxy	Old Bay Clay	32

Borehole	Sample No.	Depth BGS (ft)	Sample Type	Field Classification	Recovery (in)
EX-03	S-2	114.5	Epoxy	Old Bay Clay	28
BH-1	S-18	120	Shelby	Old Bay Clay	32
I-11	S-2	120	Epoxy	Old Bay Clay	32
I-9	S-1	120	Zinc	Old Bay Clay	29.75
I-2	S-2	122	Epoxy	Old Bay Clay	32.5
P-24	S-2	124.5	Epoxy	Old Bay Clay	28
I-37	S-1	125	Epoxy	Old Bay Clay	N/A
I-42	S-1	128	Epoxy	Old Bay Clay	20.5
BH-3	S-19	130	Shelby	Old Bay Clay	24
I-9	S-2	130	Zinc	Old Bay Clay	32
I-11	S-3	135	Epoxy	Old Bay Clay	32
I-35	S-4	135	Epoxy	Old Bay Clay	29
BH-1	S-19	140	Shelby	Old Bay Clay	31
I-9	S-3	140	Zinc	Old Bay Clay	36
BH-3	S-20	150	Shelby	Old Bay Clay	32
I-11	S-4	150	Epoxy	Old Bay Clay	32
I-35	S-5	158	Epoxy	Old Bay Clay	28
BH-1	S-20	160	Shelby	Old Bay Clay	31
BH-2	S-28	160	Shelby	Old Bay Clay	27
EX-04	S-3	160	Epoxy	Alameda fm.	21
EX-04	S-4	165	Epoxy	Alameda fm.	24
BH-1	S-21	170	MC	Old Bay Clay	6
BH-1	S-22	171	MC	Old Bay Clay	6
BH-2	S-30	171	MC	Alameda fm.	6
I-37	S-2	172.5	Epoxy	Alameda fm.	20
EX-02	S-3	174	Epoxy	Old Bay Clay	27
BH-2	S-31	175	Epoxy	Alameda fm.	29
BH-1	S-23	180	Epoxy	Old Bay Clay	31
BH-2	S-32	180	Epoxy	Alameda fm.	N/A
I-11	S-5	180	Epoxy	Alameda fm.	32
I-2	S-1	180	Epoxy	Alameda fm.	29.5
EX-02	S-4	189.5	Epoxy	Alameda fm.	28.5
BH-3	S-23	190	Epoxy	Alameda fm.	27
I-11	S-6	190	Epoxy	Alameda fm.	29
I-2	S-2	190	Epoxy	Alameda fm.	30
BH-1	S-25	191	MC	Alameda fm.	6
P-24	S-3	194	Epoxy	Alameda fm.	21
EX-02	S-5	194.5	Epoxy	Alameda fm.	24.75

Borehole	Sample No.	Depth BGS (ft)	Sample Type	Field Classification	Recovery (in)
EX-03	S-3	194.5	Epoxy	Alameda fm.	18.5
P-23	S-3	194.5	Epoxy	Alameda fm.	13
BH-2	S-35	195	Epoxy	Alameda fm.	29
I-11	S-7	195	Epoxy	Alameda fm.	5
I-16	S-1	200	Epoxy	Alameda fm.	24.5
P-24	S-4	204	Epoxy	Alameda fm.	11
EX-03	S-4	204.5	Epoxy	Alameda fm.	17.5
I-16	S-2	206	Epoxy	Alameda fm.	29.5
BH-2	S-40	215.4	MC	Alameda fm.	40
BH-2	S-42	225	Epoxy	Alameda fm.	30
BH-1	S-29	230	Epoxy	Alameda fm.	33
BH-3	S-26	231	Epoxy	Alameda fm.	12
BH-2	S-43	235	Epoxy	Alameda fm.	12

8.2 Incremental Consolidation (IL) Consolidation Testing

Table A- 2. Incremental Loading (IL) Consolidation Testing

Test	Increment	Effective stress (ksc)	LIR	Start Date and Time	Elapsed time of Increment (hr:min)
ILC-01	1	3.15		5/22/11 4:43 PM	17:02
	2	6.25	1.0	5/23/11 9:45 AM	26:15
	3	12.49	1.0	5/24/11 12:00 PM	22:00
	4	6.25	-1.0	5/25/11 10:00 AM	3:20
	5	1.56	-3.0	5/25/11 1:20 PM	4:20
	6	0.79	-1.0	5/25/11 5:40 PM	16:45
	7	1.56	1.0	5/26/11 10:25 AM	
ILC-02	1	1.51		6/4/12 12:50 PM	10:10
	2	2.73	0.7	6/4/12 11:00 PM	18:00
	3	4.64	0.7	6/5/12 5:00 PM	18:00
	4	7.88	0.7	6/6/12 11:00 AM	29:47
	5	13.39	0.7	6/7/12 4:47 PM	28:23
	6	7.88	-0.7	6/8/12 9:10 PM	12:25
	7	4.64	-0.7	6/9/12 9:35 AM	8:23
	8	2.73	-0.7	6/9/12 5:58 PM	15:06
	9	1.51	-0.7	6/10/12 9:04 AM	14:56
	10	2.73	0.7	6/11/12 12:00 AM	9:20
	11	4.64	0.7	6/11/12 9:20 AM	9:00
	12	7.88	0.7	6/11/12 6:20 PM	13:41
	13	13.13	0.7	6/12/12 8:01 AM	29:24
	14	7.88	-0.7	6/13/12 1:25 PM	10:35
	15	13.85	0.7	6/14/12 12:00 AM	

Test	Increment	Effective stress (ksc)	LIR	Start Date and Time	Elapsed time of Increment (hr:min)
ILC-03	1	2.89		5/23/12 5:00 PM	15:48
	2	4.35	0.5	5/24/12 8:48 AM	12:48
	3	6.47	0.5	5/24/12 9:36 PM	12:54
	4	9.56	0.5	5/25/12 10:30 AM	103:50
	5	6.46	-0.5	5/29/12 6:20 PM	15:40
	6	4.31	-0.5	5/30/12 10:00 AM	9:00
	7	2.88	-0.5	5/30/12 7:00 PM	19:00
	8	1.94	-0.5	5/31/12 2:00 PM	69:05
	9	2.86	0.5	6/3/12 11:05 AM	75:15
	10	4.30	0.5	6/6/12 2:20 PM	24:20
	11	6.44	0.5	6/7/12 2:40 PM	384:27
	12	9.84	0.5	6/23/12 3:07 PM	116:36
	13	13.50	0.5	6/28/12 11:43 AM	54:47
	14	9.90	-0.5	6/30/12 6:30 PM	28:20
	15	6.48	-0.5	7/1/12 10:50 PM	13:25
	16	4.33	-0.5	7/2/12 12:15 PM	11:15
	17	2.88	-0.5	7/2/12 11:30 PM	
ILC-04	1	2.88		7/24/12 6:00 PM	16:30
	2	4.32	0.5	7/25/12 10:30 AM	11:30
	3	6.48	0.5	7/25/12 10:00 PM	12:00
	4	9.68	0.5	7/26/12 10:00 AM	457:45
	5	14.54	0.5	8/14/12 11:45 AM	119:35
	6	9.76	-0.5	8/19/12 11:20 AM	10:09
	7	6.53	-0.5	8/19/12 9:29 PM	13:16
	8	4.35	-0.5	8/20/12 10:45 AM	10:45
	9	2.92	-0.5	8/20/12 9:30 PM	12:15
	10	4.37	0.5	8/21/12 9:45 AM	24:15
	11	6.49	0.5	8/22/12 10:00 AM	24:20
	12	9.73	0.5	8/23/12 10:20 AM	23:30
	13	14.30	0.5	8/24/12 9:50 AM	23:35
	14	4.88	-2.0	8/25/12 9:25 AM	47:45
	15	1.02	-4.0	8/27/12 9:10 AM	

Test	Increment	Effective stress (ksc)	LIR	Start Date and Time	Elapsed time of Increment (hr:min)
ILC-05	1	2.91		1/15/12 3:20 PM	19:10
	2	4.33	0.5	1/16/12 10:30 AM	11:30
	3	6.49	0.5	1/16/12 10:00 PM	12:45
	4	9.75	0.5	1/17/12 10:45 AM	150:39
	5	6.51	-0.5	1/23/12 5:24 PM	16:26
	6	4.34	-0.5	1/24/12 9:50 AM	11:30
	7	6.48	0.5	1/24/12 9:20 PM	11:55
	8	9.60	0.5	1/25/12 9:15 AM	98:45
	9	14.60	0.5	1/29/12 12:00 PM	197:30
	10	9.75	-0.5	2/6/12 5:30 PM	16:30
	11	6.52	-0.5	2/7/12 10:00 AM	11:00
	12	4.34	-0.5	2/7/12 9:00 PM	12:30
	13	2.88	-0.5	2/8/12 9:30 AM	24:30
	14	1.92	-0.5	2/9/12 10:00 AM	24:00
	15	0.98	-1.0	2/10/12 10:00 AM	
ILC-06	1	2.95		5/21/13 12:15 PM	20:15
	2	4.31	0.5	5/22/13 8:30 AM	22:00
	3	6.48	0.5	5/23/13 6:30 AM	24:45
	4	9.57	0.5	5/24/13 7:15 AM	123:30
	5	6.49	-0.5	5/29/13 10:45 AM	11:45
	6	4.33	-0.5	5/29/13 10:30 PM	11:40
	7	2.89	-0.5	5/30/13 10:10 AM	12:20
	8	4.31	0.5	5/30/13 10:30 PM	12:30
	9	6.48	0.5	5/31/13 11:00 AM	11:30
	10	9.54	0.5	5/31/13 10:30 PM	66:15
	11	14.50	0.5	6/3/13 4:45 PM	162:45
	12	17.40	0.2	6/10/13 11:30 AM	193:41
	13	14.60	-0.2	6/18/13 1:11 PM	21:29
	14	9.74	-0.5	6/19/13 10:40 AM	10:20
	15	6.51	-0.5	6/19/13 9:00 PM	12:45
	16	4.33	-0.5	6/20/13 9:45 AM	11:00
	17	2.91	-0.5	6/20/13 8:45 PM	

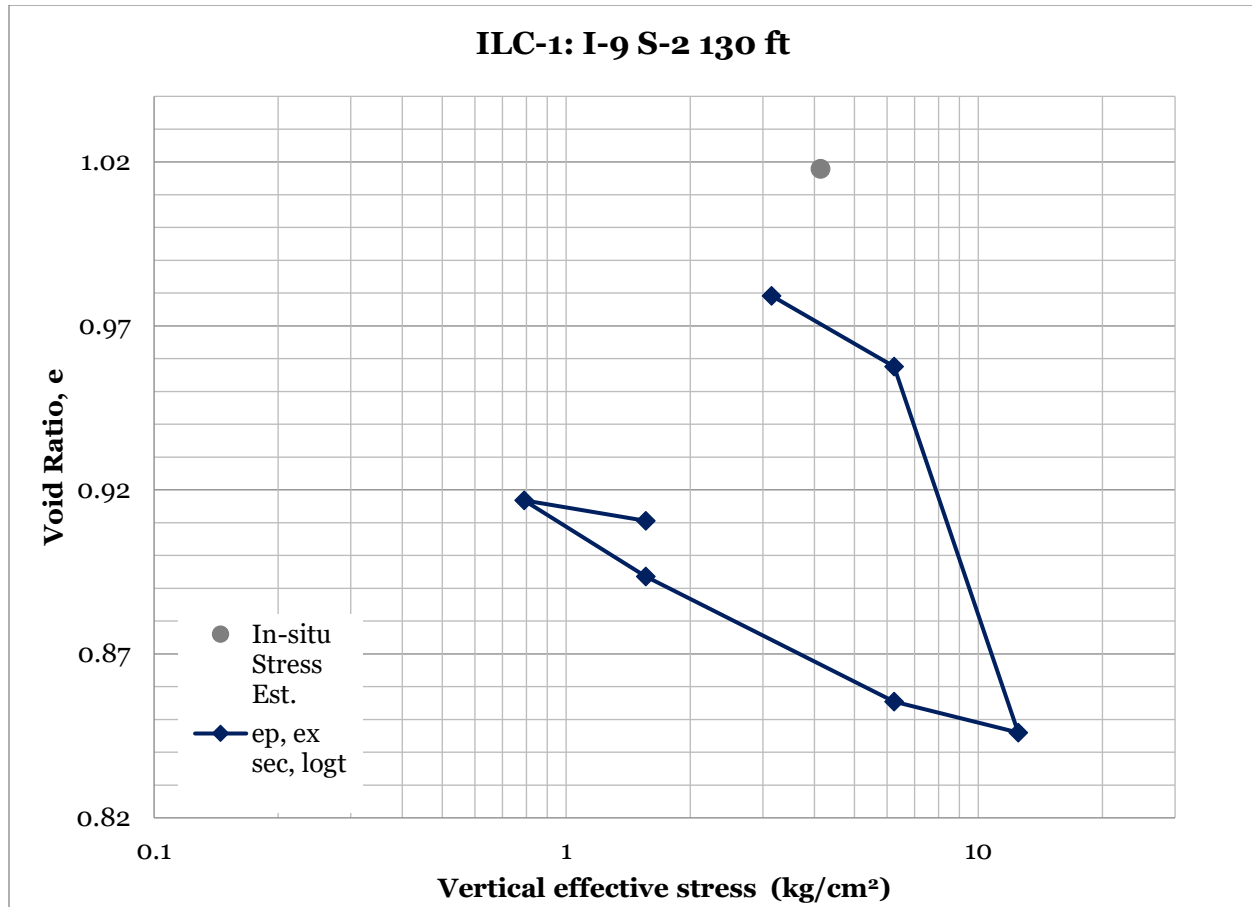
Test	Increment	Effective stress (ksc)	LIR	Start Date and Time	Elapsed time of Increment (hr:min)
ILC-07	1	3.64		9/27/13 5:30 PM	14:30
	2	5.26	0.4	9/28/13 8:00 AM	11:30
	3	2.42	-1.2	9/28/13 7:30 PM	13:30
	4	5.29	1.2	9/29/2013 9:00	12:00
	5	7.94	0.5	9/29/2013 21:00	13:00
	6	11.90	0.5	9/30/2013 10:00	75:15
	7	14.37	0.2	10/3/13 1:15 PM	124:00
	8	17.95	0.2	10/8/13 5:15 PM	113:30
	9	14.43	-0.2	10/13/13 10:45 AM	25:00
	10	11.86	-0.2	10/14/13 11:45 AM	8:45
	11	7.96	-0.5	10/14/13 8:30 PM	14:30
	12	12.00	0.5	10/15/13 11:00 AM	24:00
	13	17.39	0.4	10/16/13 11:00 AM	31:00
	14	12.04	-0.4	10/17/13 6:00 PM	16:00
	15	7.97	-0.5	10/18/13 10:00 AM	26:00
	16	5.35	-0.5	10/19/13 12:00 PM	21:00
	17	3.62	-0.5	10/20/13 9:00 AM	
ILC-08	1	2.17		1/7/14 5:50 PM	15:10
	2	1.43	-0.5	1/8/14 9:00 AM	4:00
	3	2.12	0.5	1/8/14 1:00 PM	4:30
	4	3.23	0.5	1/8/14 5:30 PM	16:33
	5	4.88	0.5	1/9/14 10:03 AM	10:17
	6	7.28	0.5	1/9/14 8:20 PM	111:40
	7	10.80	0.5	1/14/14 12:00 PM	

Test	Increment	Effective stress (ksc)	LIR	Start Date and Time	Elapsed time of Increment (hr:min)
ILC-09	1	2.17		2/12/14 3:05 PM	18:15
	2	3.23	0.5	2/13/14 9:20 AM	6:00
	3	2.13	-0.5	2/13/14 3:20 PM	17:40
	4	3.23	0.5	2/14/2014 9:00	7:00
	5	4.86	0.5	2/14/2014 16:00	15:20
	6	7.24	0.5	2/15/2014 7:20	133:10
	7	4.85	-0.5	2/20/14 8:30 PM	11:00
	8	3.25	-0.5	2/21/14 7:30 AM	13:30
	9	4.84	0.5	2/21/14 9:00 PM	12:00
	10	7.28	0.5	2/22/14 9:00 AM	8:30
	11	10.90	0.5	2/22/14 5:30 PM	88:30
	12	7.29	-0.5	2/26/14 10:00 AM	6:00
	13	4.86	-0.5	2/26/14 4:00 PM	6:00
	14	3.26	-0.5	2/26/14 10:00 PM	11:30
	15	2.17	-0.5	2/27/14 9:30 AM	
ILC-10	1	2.21		4/17/14 4:20 PM	4:55
	2	3.30	0.5	4/17/14 9:15 PM	13:00
	3	2.18	-0.5	4/18/14 10:15 AM	5:45
	4	3.33	0.5	4/18/2014 16:00	5:20
	5	4.93	0.5	4/18/2014 21:20	12:55
	6	7.31	0.5	4/19/2014 10:15	72:30
	7	4.84	-0.5	4/22/14 10:45 AM	5:30
	8	3.25	-0.5	4/22/14 4:15 PM	5:30
	9	4.89	0.5	4/22/14 9:45 PM	12:45
	10	7.10	0.5	4/23/14 10:30 AM	7:50
	11	10.90	0.5	4/23/14 6:20 PM	117:20
	12	16.40	0.5	4/28/14 3:40 PM	76:20
	13	11.00	-0.5	5/1/14 8:00 PM	14:00
	14	7.38	-0.5	5/2/14 10:00 AM	6:00
	15	4.91	-0.5	5/2/14 4:00 PM	6:00
	16	3.31	-0.5	5/2/14 10:00 PM	11:00
	17	2.25	-0.5	5/3/14 9:00 AM	

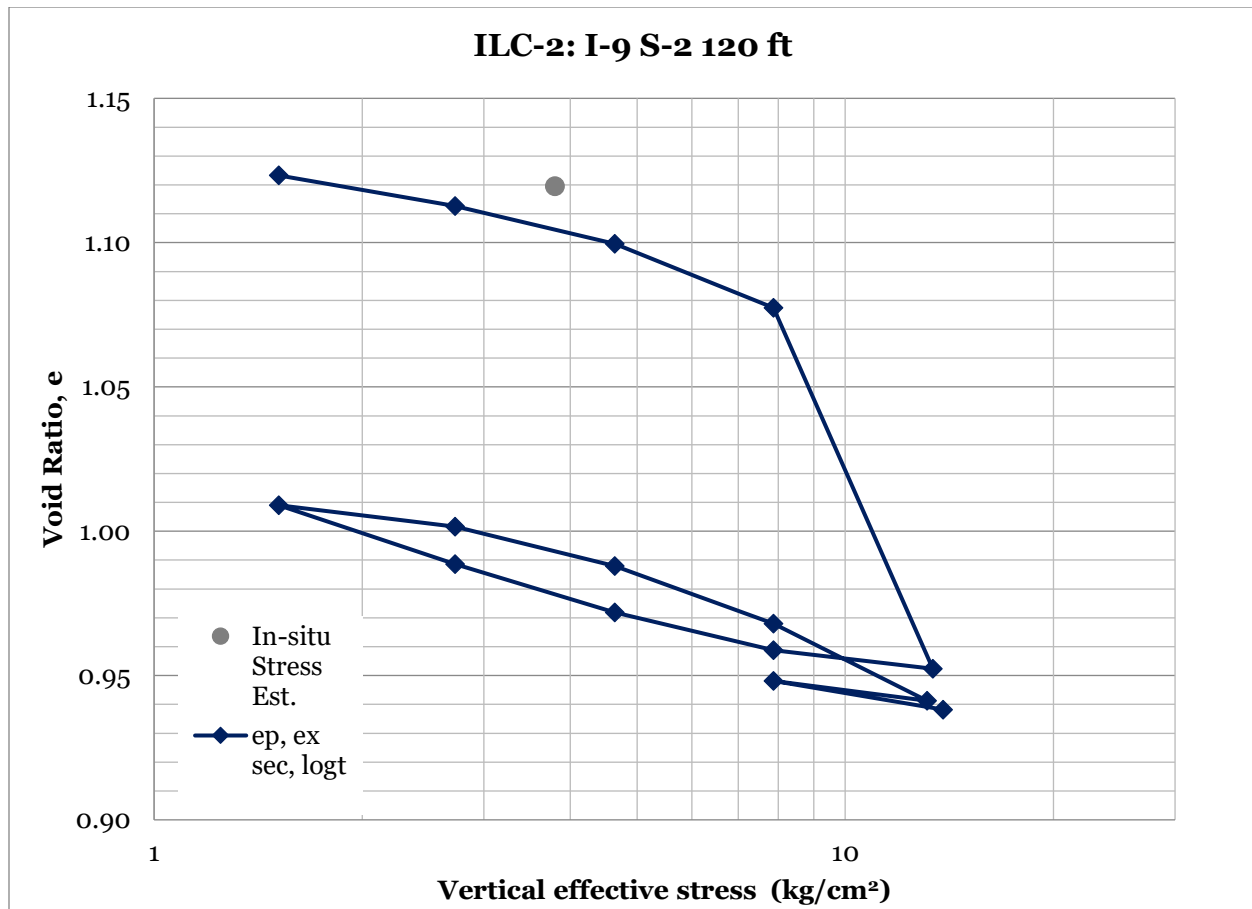
Table A- 3. Specimen properties and IL test results for individual tests.

Test*	Sample	Depth (ft)	Unit	e _o	WC (%)	Dry Density (g/cm ³)	Unit Weight (pcf)	In situ Stress (kg/cm ²)	Pp (Pacheco- Silva) (kg/cm ²)	C _c	C, norm. consol.	C _o , norm. consol.	C _v , norm. consol., (m ² /yr)
ILC-1	I-9 S-2	130	OBC	1.027	38.0	1.328	114.4	4.14	7.3	0.51	0.055	0.021	1.09
ILC-2	I-9 S-2	120	OBC	1.120	42.0	1.274	112.9	3.80	7.5	0.63	0.070	0.028	1.08
ILC-3	I-35 S-4	135	OBC	1.170	43.4	1.267	109.9	3.80	8.7	0.87	0.070	0.034	1.36
ILC-4	I-11 S-3	135	OBC	1.161	41.8	1.272	112.5	4.27	9.0	0.94	0.072	0.023	0.64
ILC-5	I-17A S-3	109	OBC	1.072	37.5	1.327	113.9	3.54	8.5	0.56	0.022	0.020	1.2
ILC-6	EX-03 S-2	114.5	OBC	1.513	54.3	1.094	105.3	3.66	6.3	1.06	0.043	0.034	1.72
ILC-7*	BH-2 S-35	195	Alameda	1.233	44.2	1.232	110.7	5.90	7.6	0.65	0.025	0.018	0.96
ILC-8*	BH-1 S-18	120	OBC	1.180	41.8	1.261	111.7	3.85	6.6	0.66	0.013	0.019	0.93
ILC-9	BH-1 S-18	120	OBC	1.267	45.3	1.213	110.0	3.85	6.3	0.81	0.030	0.030	0.79
ILC-10	BH-3 S-18	110	OBC	1.186	41.9	1.258	111.4	3.60	7.3	0.74	0.055	0.030	0.77

Most tests were processed using Procedure 1, the log of time method, with secondary compression removed. Tests marked with an () were processed using Procedure 2, the square root of time method.



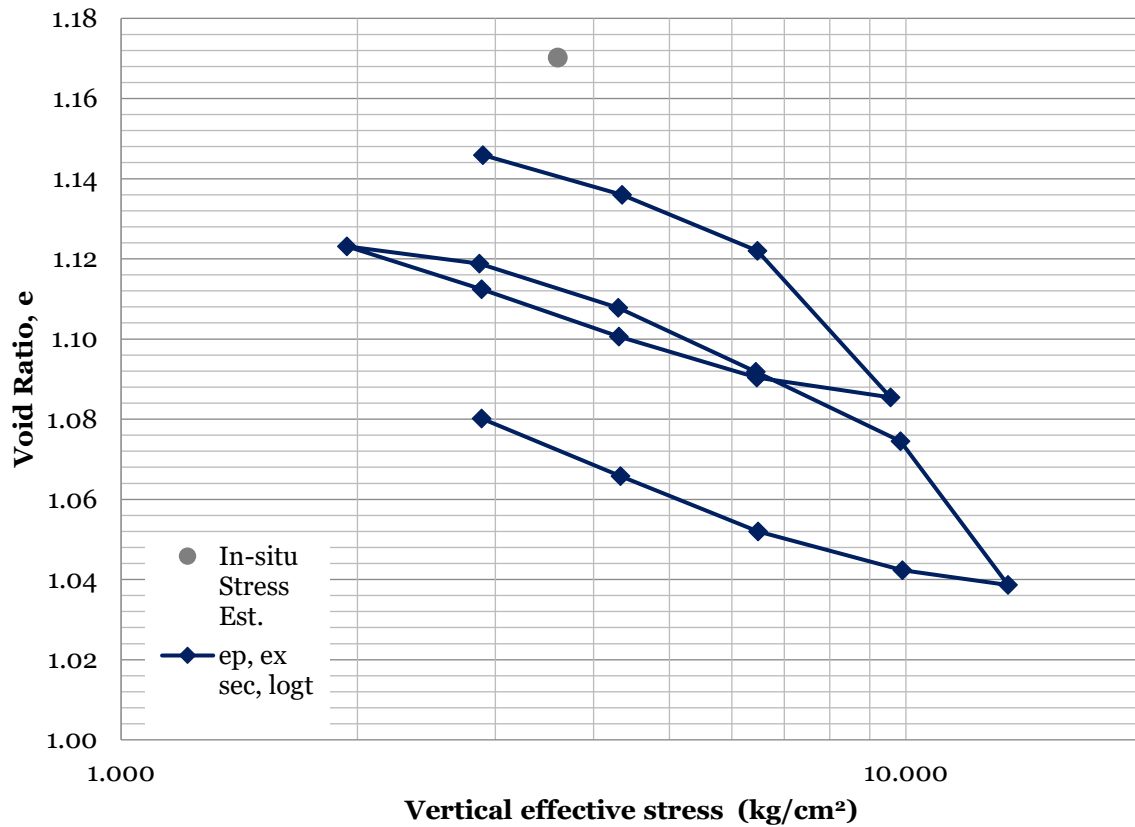
Increment	Effective stress (kg/cm ²)	LIR	e ₀	e ₁₀₀	e _p , excluding secondary	C _v (m ² /yr)	C _a
1	3.15		0.986	0.979	0.979	18.3	0.0015
2	6.25	1	0.975	0.954	0.958	14.8	0.004
3	12.49	1	0.944	0.832	0.846	1.7	0.021
4	6.25	-1	0.811	0.820	0.855	14.0	0.0008
5	1.56	-3	0.822	0.860	0.894	3.6	0.004
6	0.79	-1	0.863	0.886	0.917	1.1	0.0035
7	1.56	1	0.889	0.883	0.911	6.5	0.0009



Increment	Effective stress (kg/cm ²)	LIR	e ₀	e ₁₀₀	e _p , excluding secondary	C _v (m ² /yr)	C _α
1	1.51		1.126	1.123	1.123	47.7	0.00069
2	2.73	0.8	1.121	1.110	1.113	22.6	0.0013
3	4.64	0.7	1.106	1.093	1.100	20.3	0.0021
4	7.88	0.7	1.087	1.065	1.077	14.7	0.016
5	13.39	0.7	1.033	0.908	0.952	1.1	0.028
6	7.88	-0.7	0.879	0.885	0.959	7.9	0.00055
7	4.64	-0.7	0.887	0.900	0.972	4.7	0.0014
8	2.73	-0.7	0.904	0.920	0.989	2.9	0.002
9	1.51	-0.8	0.924	0.944	1.009	1.4	0.0052
10	2.73	0.8	0.948	0.941	1.002	6.5	0.0008
11	4.64	0.7	0.938	0.924	0.988	4.1	0.002

Increment	Effective stress (kg/cm²)	LIR	e₀	e₁₀₀	e_p, excluding secondary	C_v (m²/yr)	C_α
12	7.88	0.7	0.920	0.900	0.968	4.3	0.002
13	13.13	0.7	0.896	0.870	0.941	6.0	0.0068
14	7.88	-0.7	0.856	0.863	0.948	11.0	0.0006
15	13.8	0.8	0.863	0.853	0.938	15.3	0.007

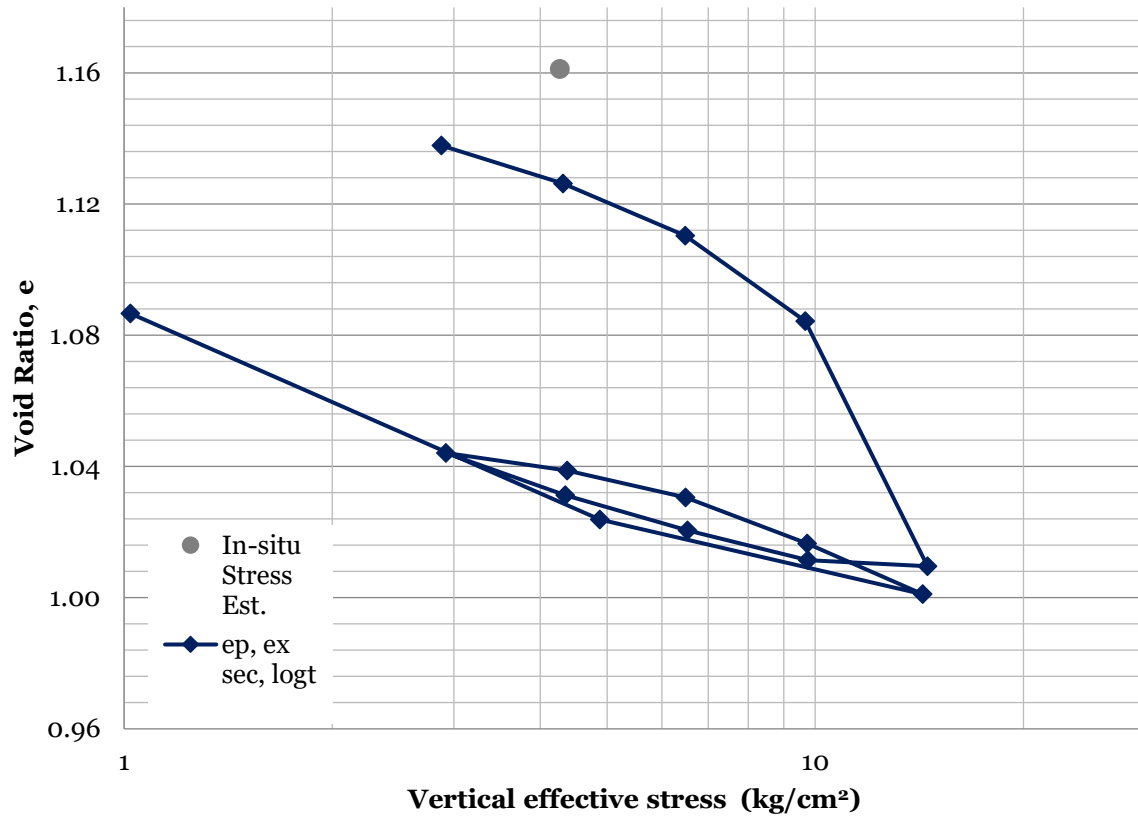
ILC-3: I-35 S-4 135 ft



Increment	Effective stress (kg/cm^2)	LIR	e_0	e_{100}	e_p , excluding secondary	C_v (m^2/yr)	C_a
1	2.89		1.153	1.146	1.146	11.2	0.00071
2	4.35	0.5	1.144	1.134	1.136	13.3	0.0018
3	6.47	0.5	1.128	1.114	1.122	7.9	0.003638
4	9.56	0.5	1.106	1.070	1.085		0.033
5	6.46	-0.5	1.011	1.016	1.090	17.2	0.007
6	4.31	-0.5	1.017	1.027	1.101	7.2	0.0019
7	2.88	-0.5	1.031	1.042	1.112	4.0	0.0027
8	1.94	-0.5	1.046	1.057	1.123		
9	2.86	0.5	1.065	1.061	1.119	12.9	0.00059
10	4.3	0.5	1.059	1.048	1.108	3.7	0.0021
11	6.44	0.5	1.045	1.029	1.092	4.4	0.0017
12	9.84	0.5	1.024	1.006	1.074		0.012
13	13.5	0.4	0.986	0.950	1.039		0.023

Increment	Effective stress (kg/cm²)	LIR	e₀	e₁₀₀	e_p, excluding secondary	C_v (m²/yr)	C_α
14	9.9	-0.4	0.907	0.911	1.042		0.00052
15	6.48	-0.5	0.913	0.922	1.052	4.6	0.0018
16	4.33	-0.5	0.925	0.939	1.066	2.6	0.0024
17	2.88	-0.5	0.942	0.956	1.080	1.7	0.0041

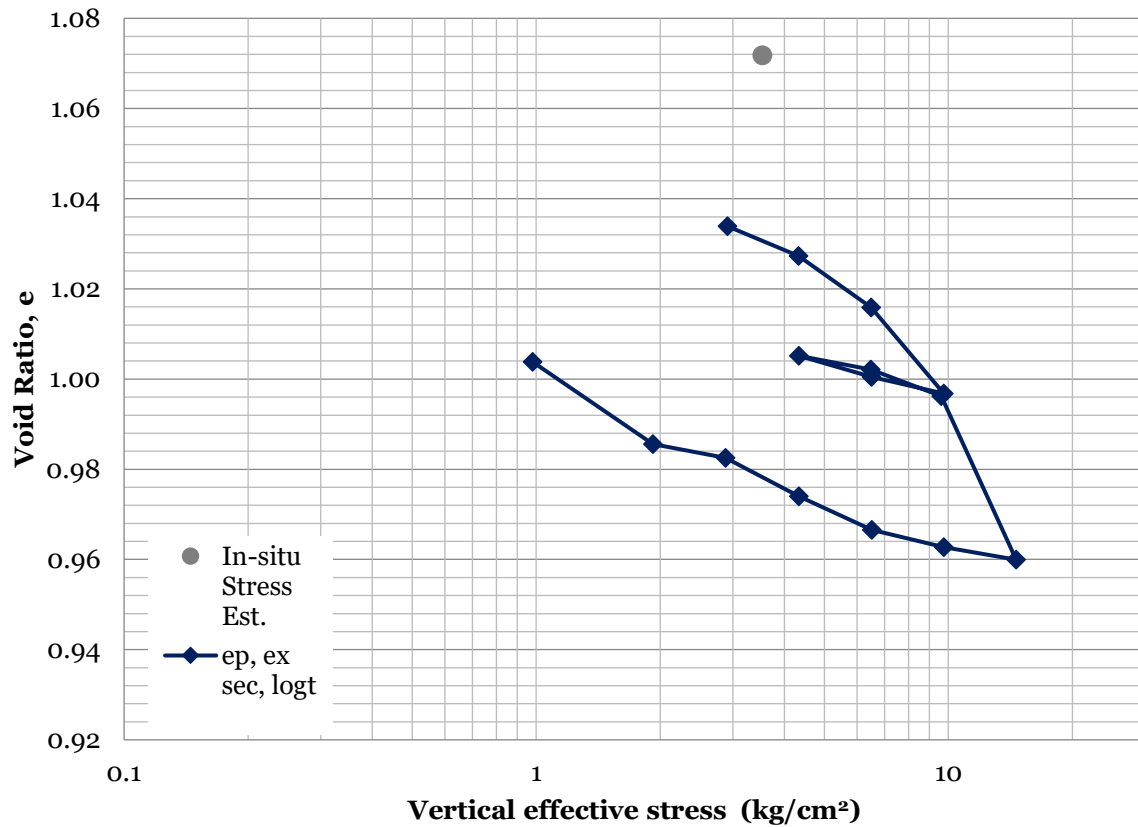
ILC-4: I-11 S-3 135 ft



Increment	Effective stress (kg/cm^2)	LIR	e_0	e_{100}	e_p , excluding secondary	C_v (m^2/yr)	C_a
1	2.88		1.145	1.138	1.138	20.1	0.0018
2	4.32	0.5	1.135	1.124	1.126	12.6	0.0019
3	6.48	0.5	1.117	1.102	1.110	7.6	0.0046
4	9.68	0.5	1.094	1.068	1.084		0.0230
5	14.54	0.5	0.984	0.909	1.010	0.7	0.0200
6	9.76	-0.5	0.837	0.838	1.011	7.5	0.0006
7	6.53	-0.5	0.842	0.851	1.021	5.1	0.0015
8	4.35	-0.5	0.855	0.865	1.031	2.9	0.0029
9	2.92	-0.5	0.869	0.882	1.044	2.4	0.0039
10	4.37	0.5	0.886	0.881	1.039	7.9	0.0003
11	6.49	0.5	0.878	0.870	1.031	4.1	0.0012
12	9.73	0.5	0.867	0.853	1.017	0.6	0.0020
13	14.30	0.5	0.849	0.833	1.001	4.2	0.0045

Increment	Effective stress (kg/cm²)	LIR	e₀	e₁₀₀	e_p, excluding secondary	C_v (m²/yr)	C_a
14	4.88	-1.9	0.830	0.853	1.024	3.4	0.0010
15	1.02	-3.8	0.855	0.918	1.087	1.1	0.0064

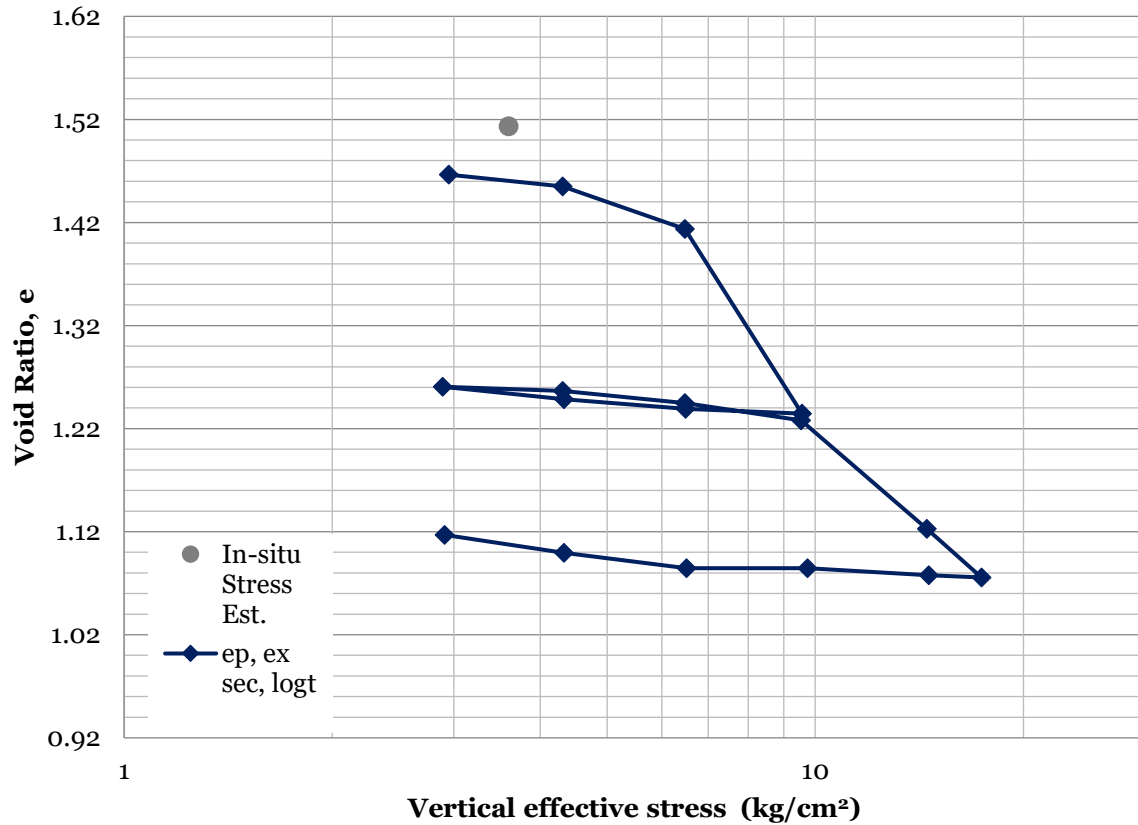
ILC-5: I-17A S-3 109 ft



Increment	Effective stress (kg/cm^2)	LIR	e_0	e_{100}	e_p , excluding secondary	C_v (m^2/yr)	C_a
1	2.91		1.037	1.034	1.034	167.5	0.0040
2	4.33	0.5	1.027	1.020	1.027	24.8	0.0020
3	6.49	0.5	1.015	1.004	1.016	32.7	0.0035
4	9.75	0.5	0.996	0.977	0.997		0.0200
5	6.51	-0.5	0.931	0.934	1.001	39.4	0.0003
6	4.34	-0.5	0.936	0.940	1.005	26.8	0.0007
7	6.48	0.5	0.942	0.939	1.002	83.0	0.0003
8	9.60	0.5	0.938	0.932	0.996		
9	14.60	0.5	0.924	0.888	0.960	0.6	0.0170
10	9.75	-0.5	0.827	0.830	0.963	27.0	0.0005
11	6.52	-0.5	0.831	0.835	0.967	20.4	0.0011
12	4.34	-0.5	0.838	0.846	0.974	7.5	0.0020
13	2.88	-0.5	0.850	0.858	0.983	4.0	0.0028

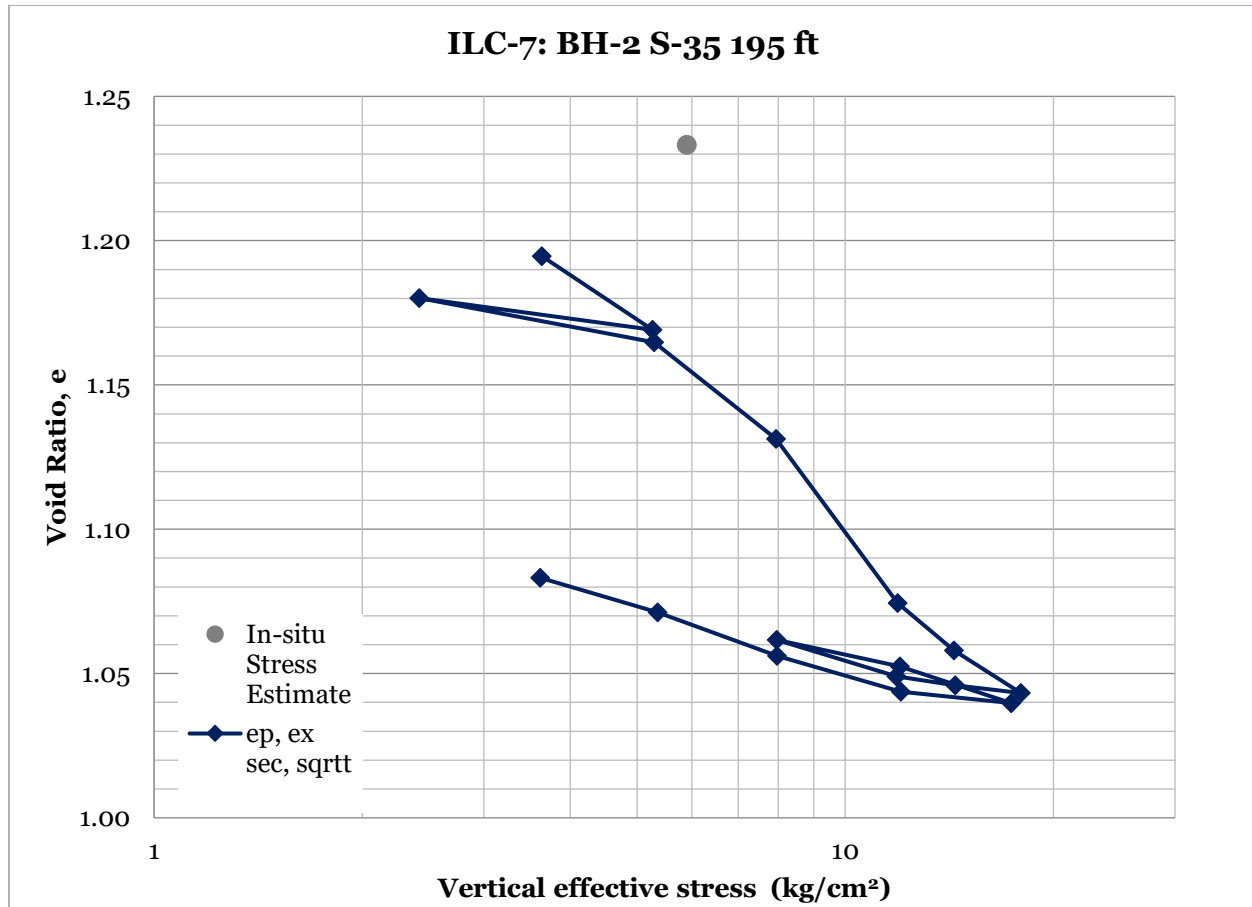
Increment	Effective stress (kg/cm²)	LIR	e₀	e₁₀₀	e_p, excluding secondary	C_v (m²/yr)	C_a
14	1.92	-0.5	0.862	0.865	0.986		0.0047
15	0.98	-1.0	0.877	0.895	1.004	1.2	0.0046

ILC-6: EX-03 S-2 114.5 ft



Increment	Effective stress (kg/cm ²)	LIR	e ₀	e ₁₀₀	e _p , excluding secondary	C _v (m ² /yr)	C _a
1	2.95		1.477	1.466	1.466	83.7	0.0023
2	4.31	0.5	1.461	1.450	1.455	55.0	0.0040
3	6.48	0.5	1.442	1.400	1.414	4.3	0.0250
4	9.57	0.5	1.375	1.196	1.235	0.4	0.0340
5	6.49	-0.5	1.156	1.161	1.239	30.8	0.0011
6	4.33	-0.5	1.163	1.172	1.249	12.9	0.0018
7	2.89	-0.5	1.175	1.187	1.261	6.6	0.0026
8	4.31	0.5	1.190	1.186	1.257	15.8	0.0007
9	6.48	0.5	1.185	1.173	1.245	15.6	0.0013
10	9.54	0.5	1.172	1.155	1.228	13.9	0.0100
11	14.50	0.5	1.139	1.034	1.123	0.7	0.0320
12	17.40	0.2	1.004	0.957	1.076	0.0	0.0190
13	14.60	-0.2	0.947	0.949	1.078	31.3	0.0003

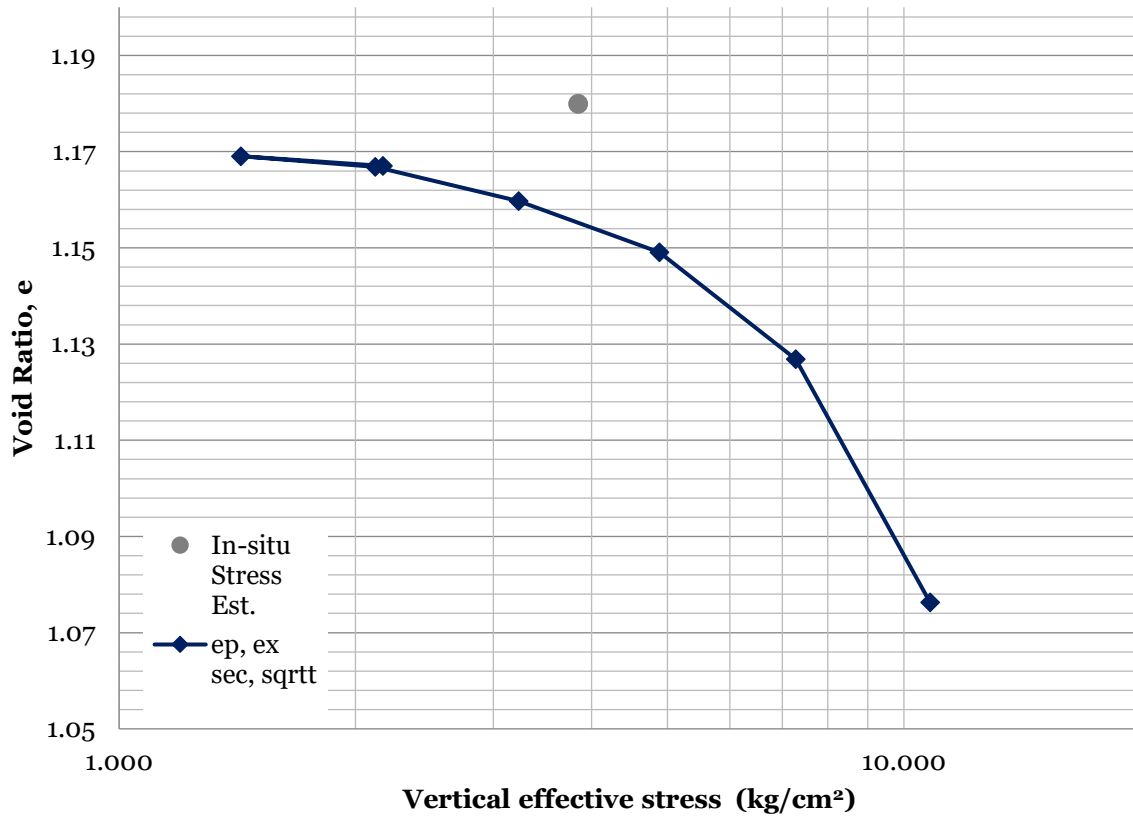
Increment	Effective stress (kg/cm²)	LIR	e₀	e₁₀₀	e_p, excluding secondary	C_v (m²/yr)	C_α
14	9.74	-0.5	0.949	0.956	1.085	10.9	0.0011
15	6.51	-0.5	0.958	0.958	1.085	6.7	0.0022
16	4.33	-0.5	0.972	0.987	1.099	2.3	0.0031
17	2.91	-0.5	0.989	1.007	1.117	1.3	0.0039



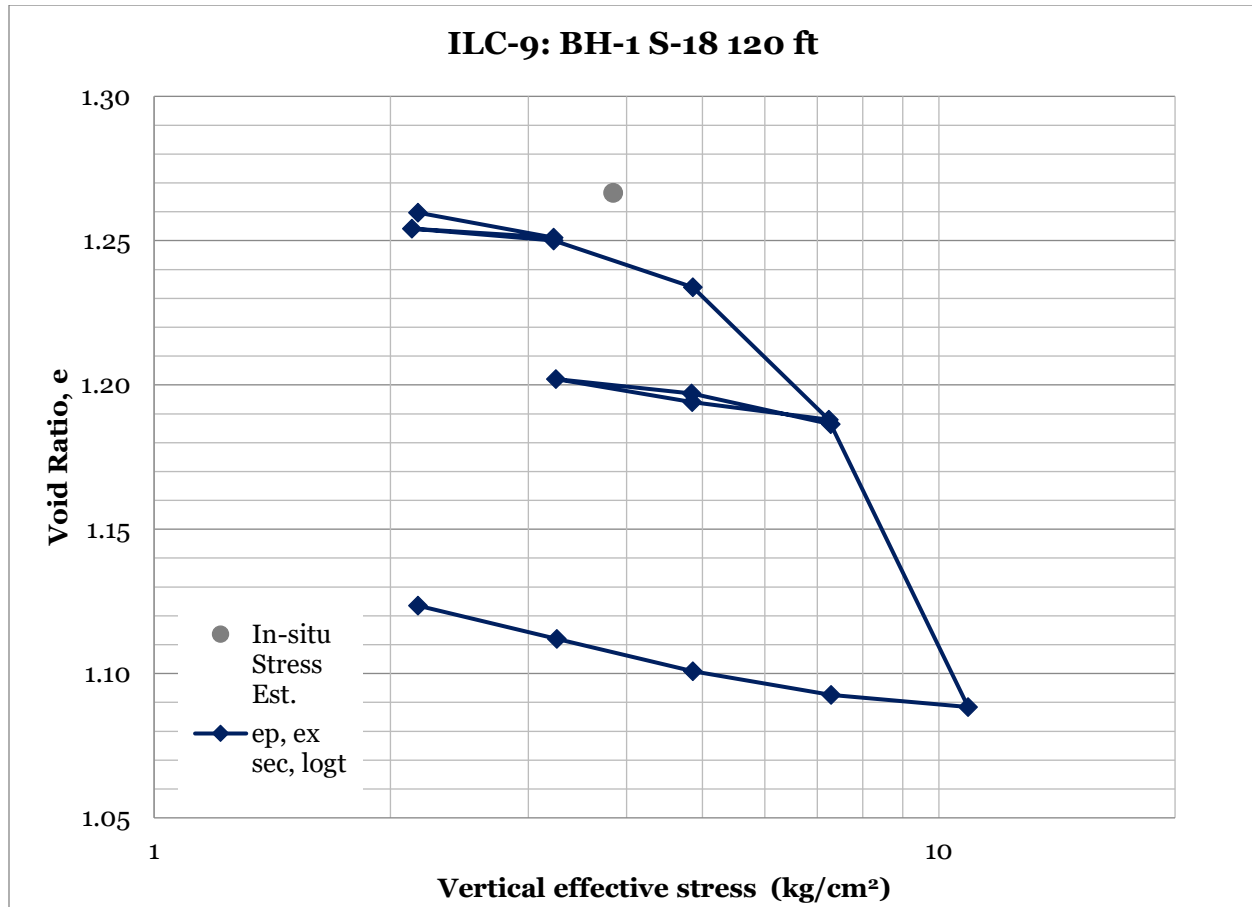
Increment	Effective stress (kg/cm ²)	LIR	e ₀	e ₁₀₀	e _p , excluding secondary	C _v (m ² /yr)	C _a
1	3.64		1.213	1.195	1.195	3.8	0.0037
2	5.26	0.4	1.184	1.159	1.169	1.8	0.0067
3	2.42	-1.2	1.152	1.163	1.180	7.2	0.0011
4	5.29	1.2	1.168	1.153	1.165	7.6	0.0032
5	7.94	0.5	1.146	1.113	1.131	2.0	0.0100
6	11.90	0.5	1.099	1.042	1.074	1.0	0.0120
7	14.37	0.2	1.012	0.996	1.058	1.4	0.0160
8	17.95	0.2	0.960	0.946	1.043	2.3	0.0180
9	14.43	-0.2	0.905	0.907	1.046	4.0	0.0004
10	11.86	-0.2	0.908	0.911	1.049	5.3	0.0042
11	7.96	-0.5	0.914	0.927	1.062	1.9	0.0028
12	12.00	0.5	0.932	0.922	1.052	3.3	0.0004

Increment	Effective stress (kg/cm ²)	LIR	e ₀	e ₁₀₀	e _p , excluding secondary	C _v (m ² /yr)	C _α
13	17.39	0.4	0.921	0.908	1.040	2.8	.00078 to .0089
14	12.04	-0.4	0.901	0.905	1.044	23.9	0.0008
15	7.97	-0.5	0.909	0.921	1.056	2.1	0.0018
16	5.35	-0.5	0.925	0.940	1.071	1.1	0.0033
17	3.62	-0.5	0.945	0.957	1.083	1.2	0.0052

ILC-8: BH-3 S-18 110 ft



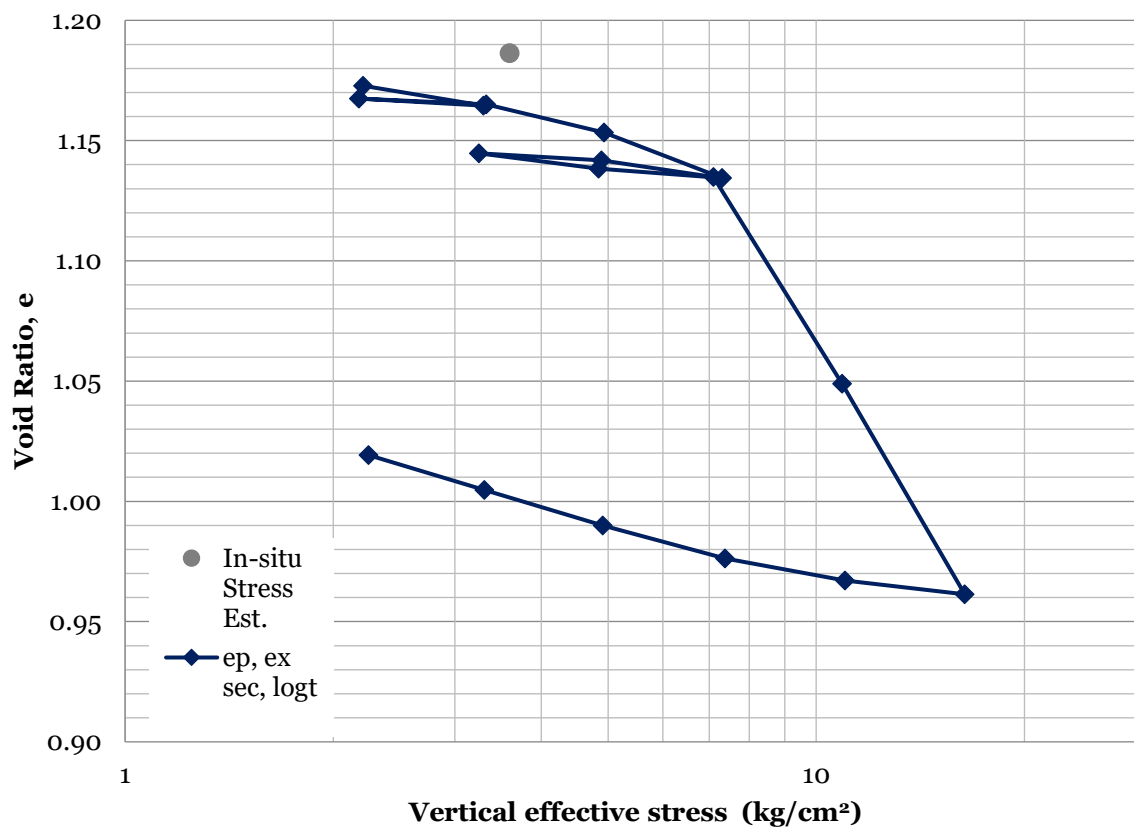
Increment	Effective stress (kg/cm^2)	LIR	e_0	e_{100}	e_p , excluding secondary	C_v (m^2/yr)	C_a
1	2.17		1.175	1.168	1.167	22.6	0.0020
2	1.43	-0.5	1.163	1.165	1.169	38.1	0.0004
3	2.12	0.5	1.165	1.163	1.167	163.2	0.0005
4	3.23	0.5	1.160	1.154	1.160	30.4	0.0020
5	4.88	0.5	1.144	1.134	1.149	19.9	0.0040
6	7.28	0.5	1.127	1.107	1.127	11.0	0.0170
7	10.80	0.5	1.053	1.008	1.076	4.0	0.0190



Increment	Effective stress (kg/cm ²)	LIR	e ₀	e ₁₀₀	e _p , excluding secondary	C _v (m ² /yr)	C _a
1	2.17		1.176	1.173	1.260	103.7	0.0010
2	3.23	0.5	1.174	1.165	1.251	28.7	0.0006
3	2.13	-0.5	1.165	1.168	1.254	49.1	0.0005
4	3.23	0.5	1.168	1.164	1.250	57.1	0.0003
5	4.86	0.5	1.162	1.145	1.234	8.5	0.0100
6	7.24	0.5	1.137	1.091	1.188	2.4	0.0300
7	4.85	-0.5	1.046	1.052	1.194	71.3	0.0005
8	3.25	-0.5	1.055	1.063	1.202	9.3	0.0006
9	4.84	0.5	1.063	1.058	1.197	42.5	0.0004
10	7.28	0.5	1.056	1.046	1.186	17.8	0.0030
11	10.90	0.5	1.040	0.942	1.088	0.8	0.0300
12	7.29	-0.5	0.918	0.922	1.093	48.1	0.0020
13	4.86	-0.5	0.926	0.934	1.101	8.3	0.0010

Increment	Effective stress (kg/cm²)	LIR	e₀	e₁₀₀	e_p, excluding secondary	C_v (m²/yr)	C_a
14	3.26	-0.5	0.938	0.949	1.112	6.0	0.0028
15	2.17	-0.5	0.953	0.965	1.124	4.2	0.0040

ILC-10: BH-3 S-18 110 ft



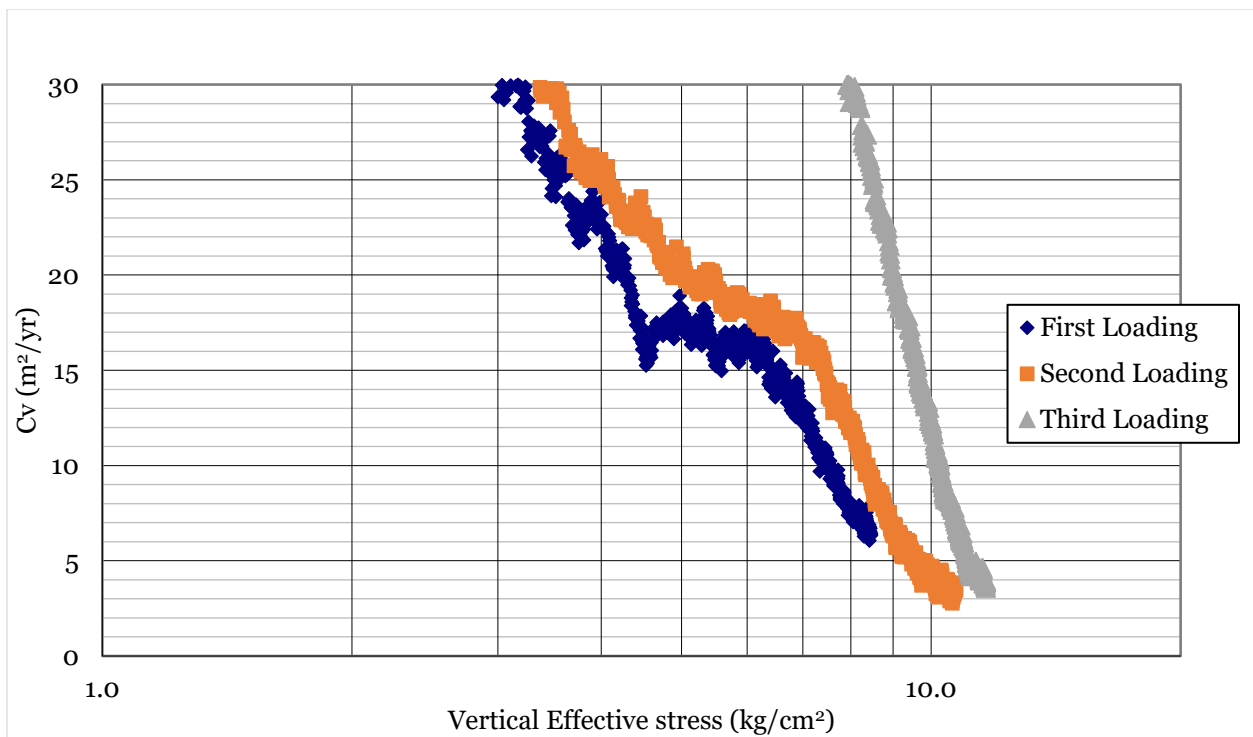
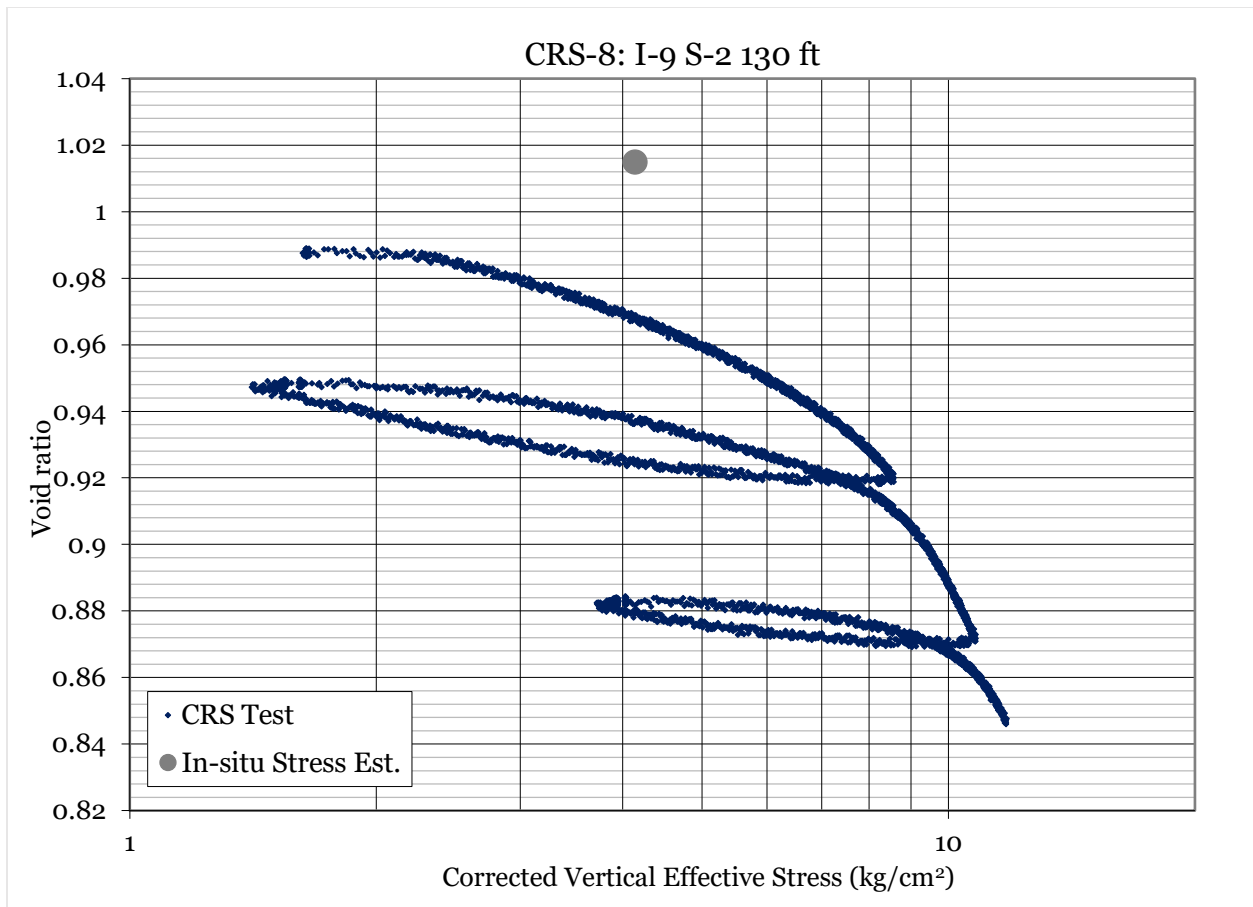
Increment	Effective stress (kg/cm ²)	LIR	e ₀	e ₁₀₀	e _p , excluding secondary	C _v (m ² /yr)	C _a
1	2.21		1.174	1.173	1.173	256.9	0.0006
2	3.30	0.5	1.173	1.165	1.165	34.0	0.0010
3	2.18	-0.5	1.161	1.164	1.168	102.1	0.0040
4	3.33	0.5	1.165	1.162	1.165	56.6	0.0004
5	4.93	0.5	1.162	1.150	1.153	45.6	0.0020
6	7.31	0.5	1.144	1.125	1.135	18.5	0.0070
7	4.84	-0.5	1.104	1.107	1.138	48.4	0.0003
8	3.25	-0.5	1.108	1.115	1.145	16.2	0.0014
9	4.89	0.5	1.117	1.114	1.142	33.6	0.0007
10	7.10	0.5	1.112	1.105	1.135	22.0	0.0006
11	10.90	0.5	1.104	1.018	1.049	0.9	0.0300
12	16.40	0.5	0.985	0.898	0.961	0.8	0.0230
13	11.00	-0.5	0.868	0.874	0.967	17.4	0.0005

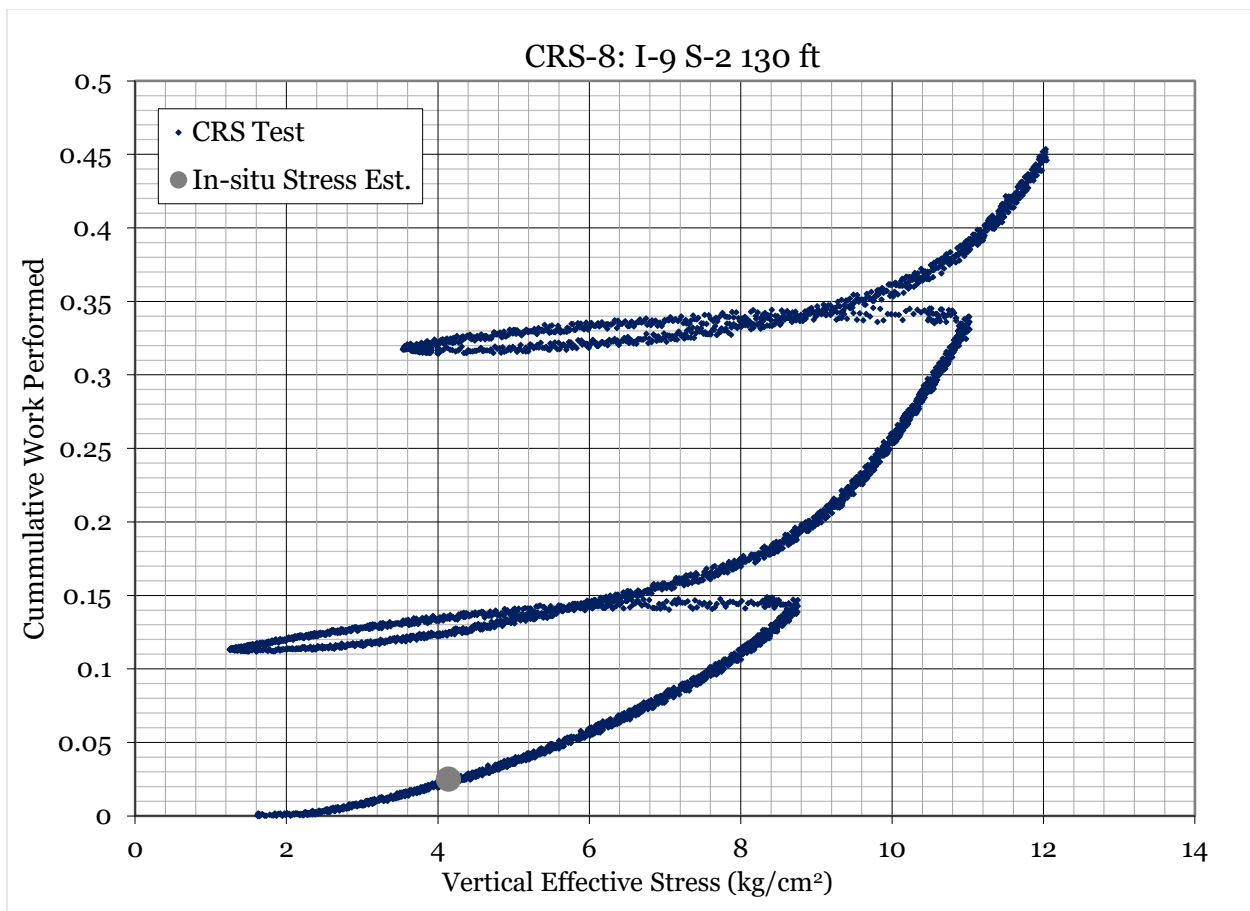
Increment	Effective stress (kg/cm²)	LIR	e₀	e₁₀₀	e_p, excluding secondary	C_v (m²/yr)	C_α
14	7.38	-0.5	0.875	0.884	0.976	5.5	0.0016
15	4.91	-0.5	0.885	0.898	0.990	2.6	0.0027
16	3.31	-0.5	0.901	0.916	1.005	1.3	0.0034
17	2.25	-0.5	0.919	0.933	1.019	0.9	0.0038

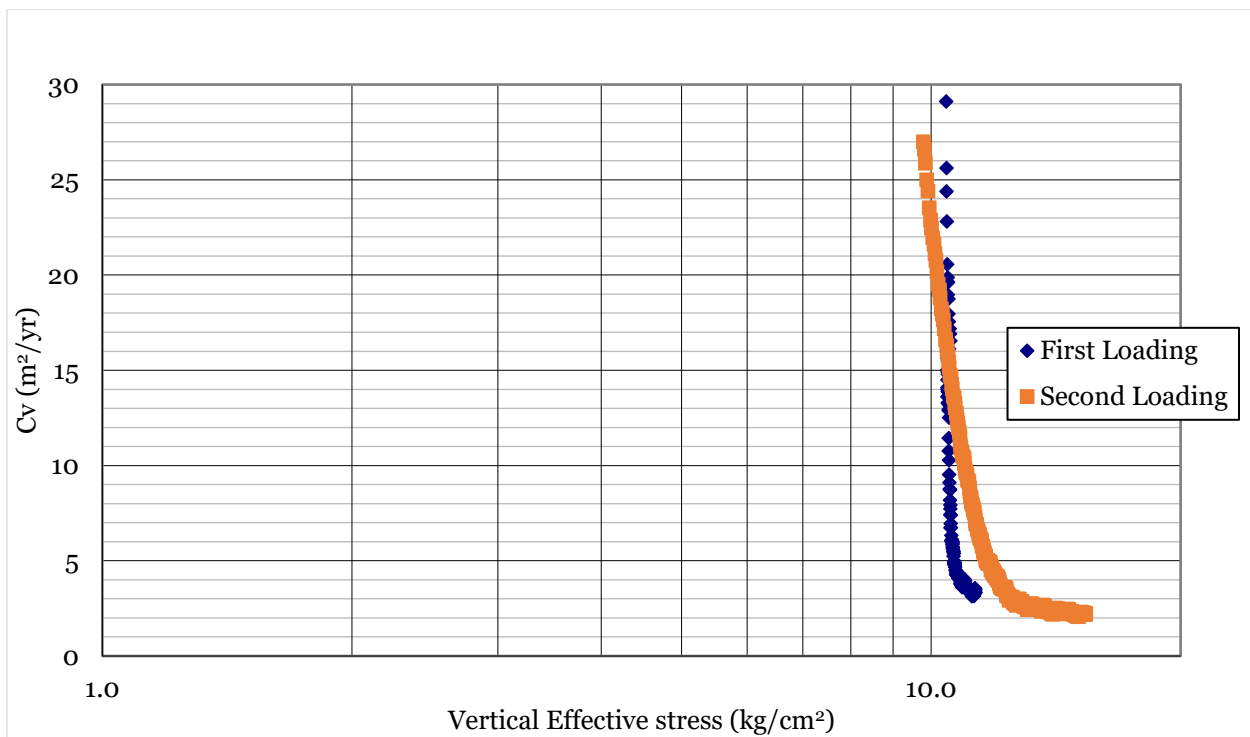
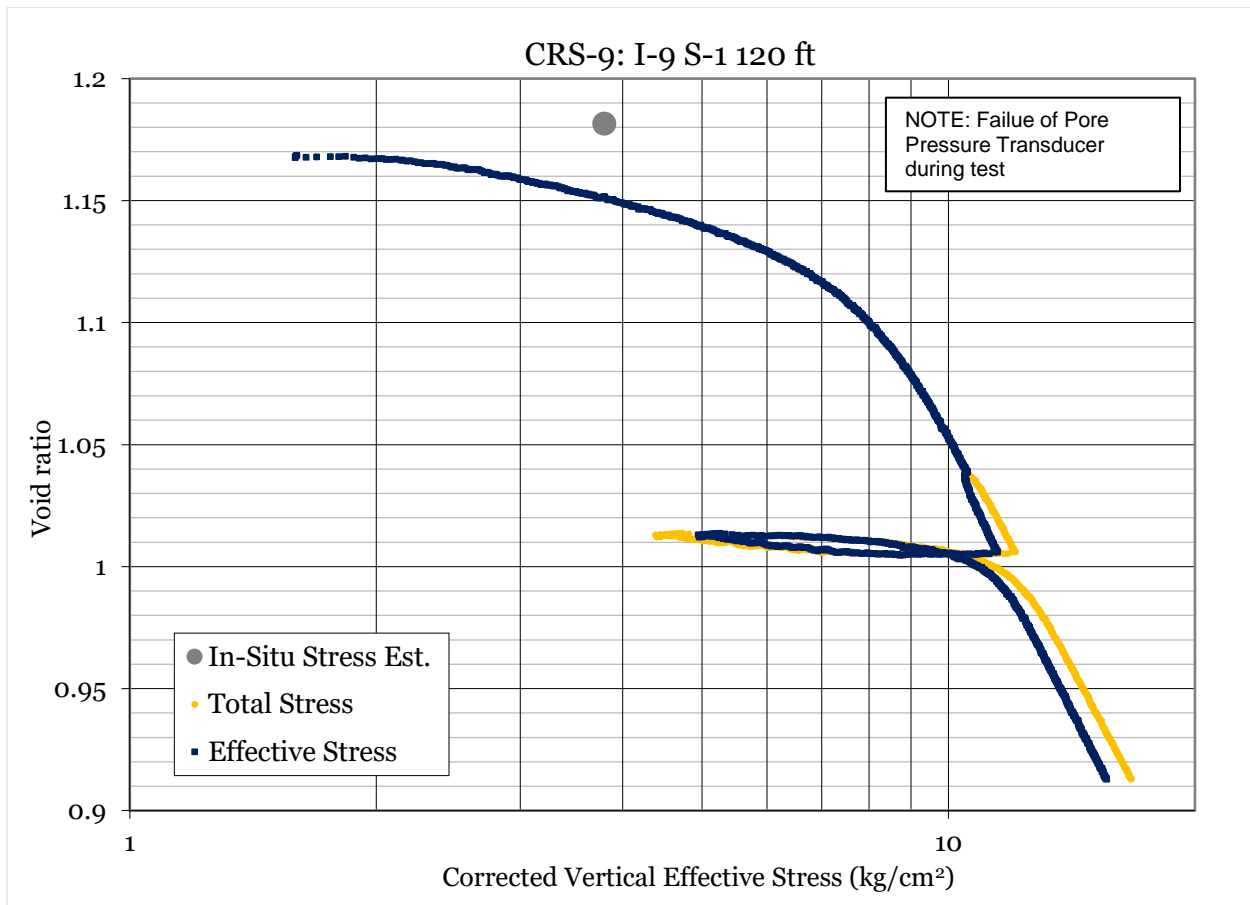
8.3 Constant Rate of Strain (CRS) Consolidation Testing

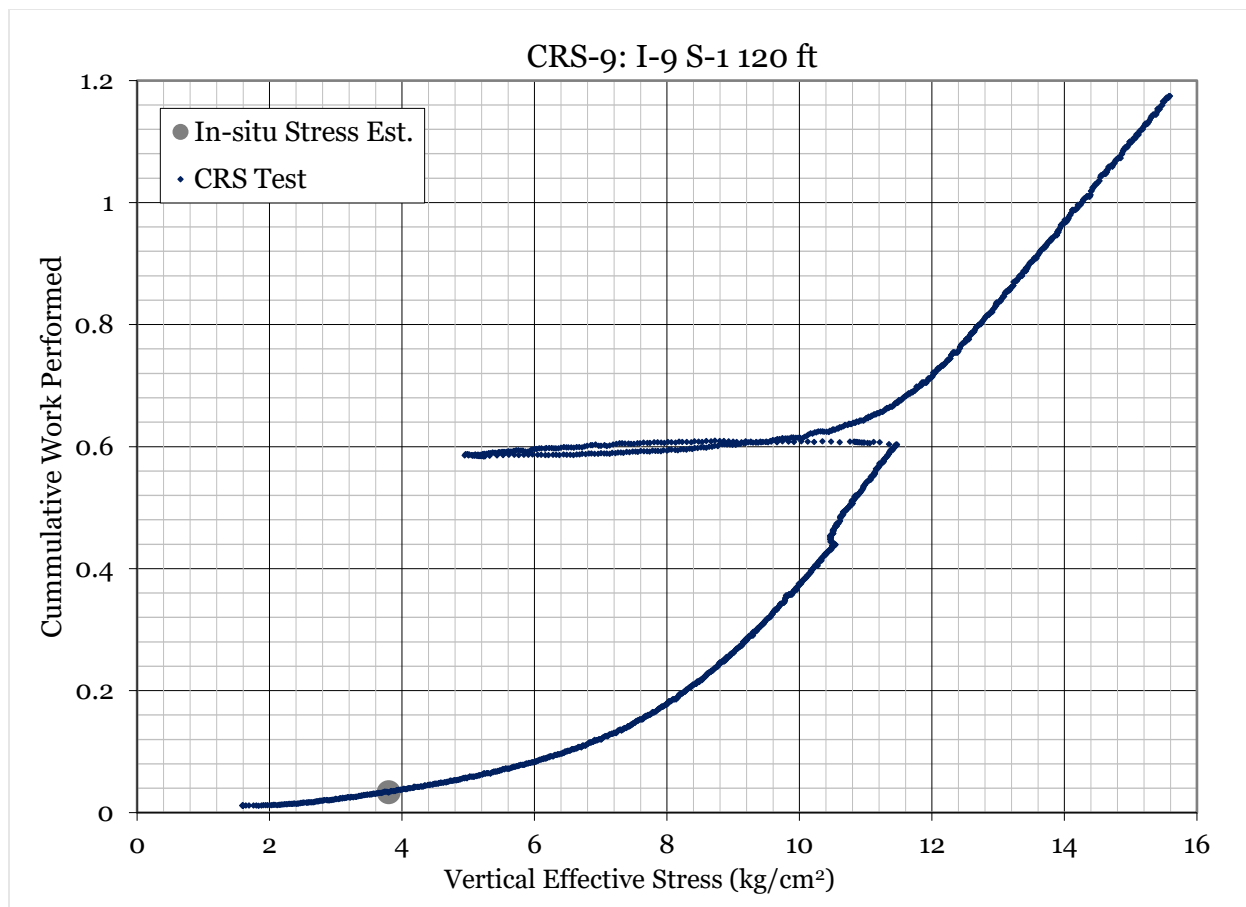
Table A- 4. Specimen properties and CRS test results for individual tests.

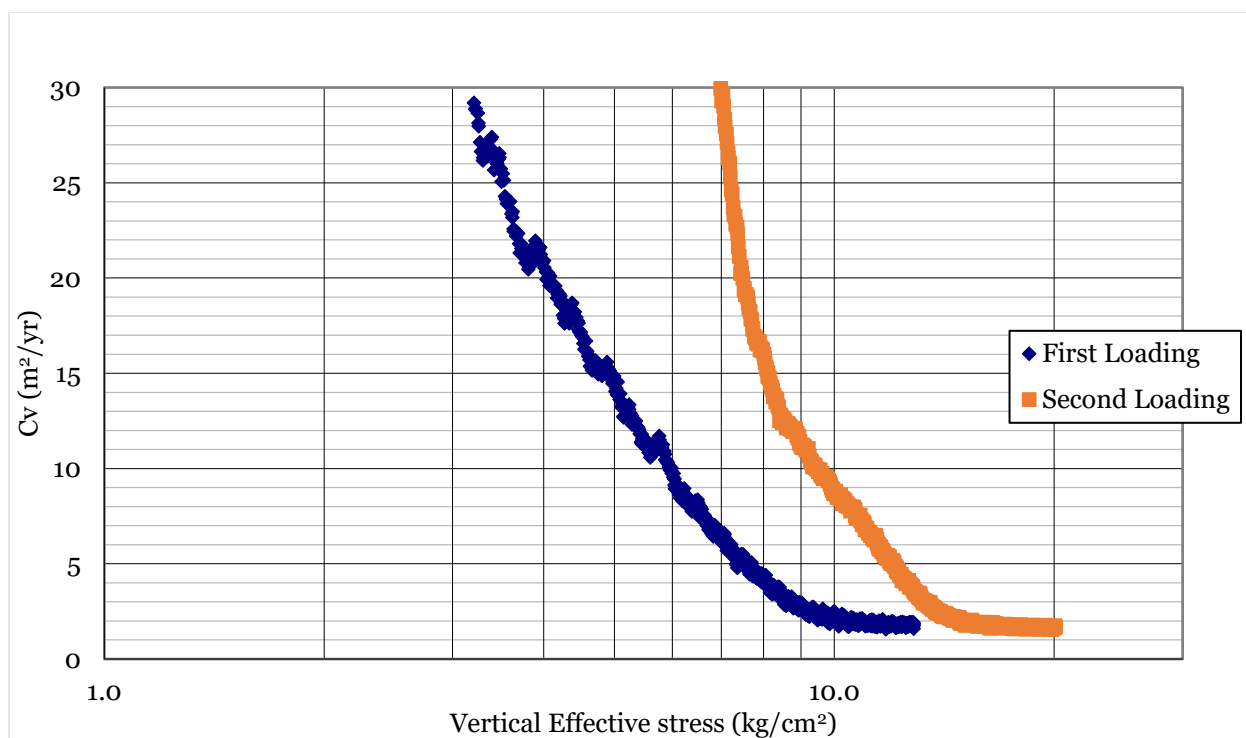
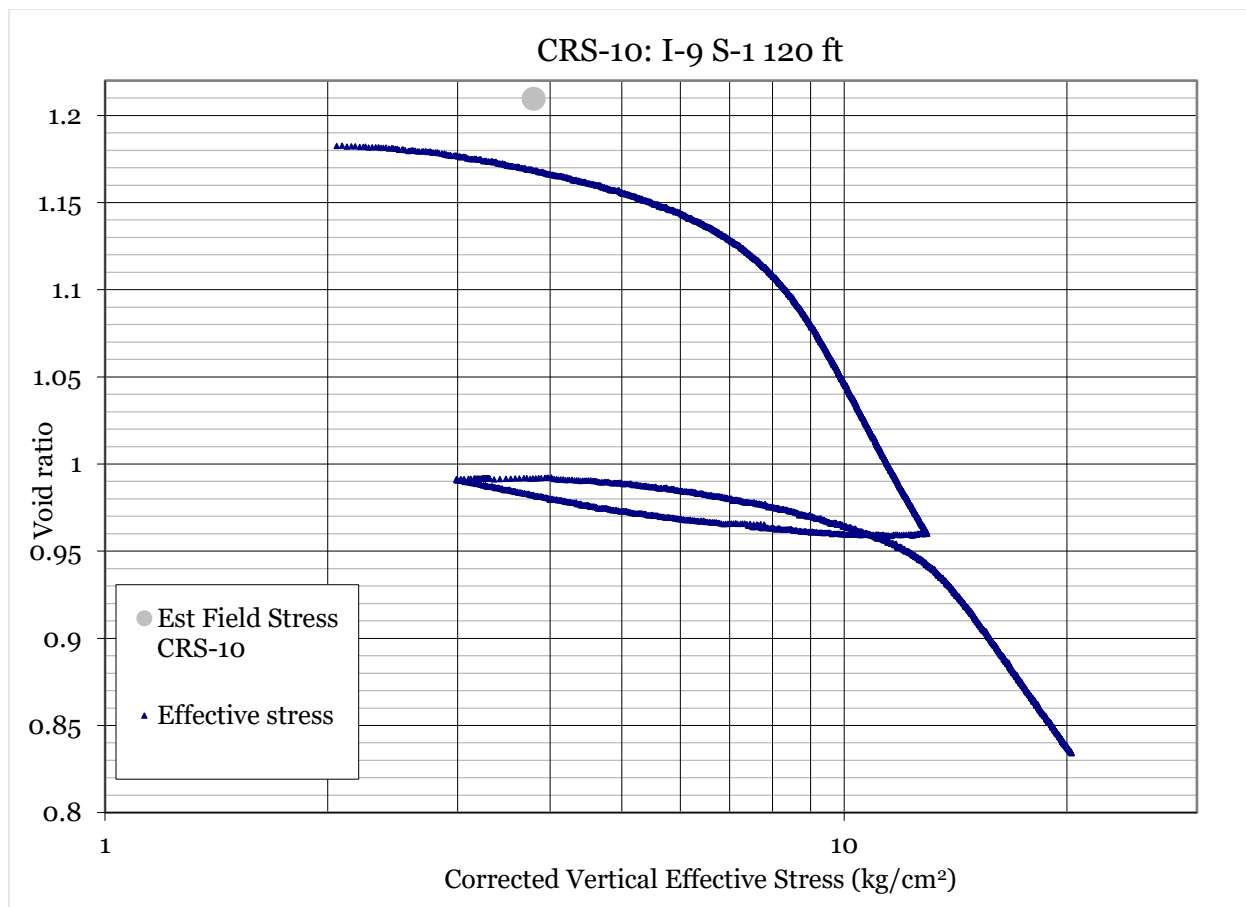
Test	Sample	Depth (ft)	Unit	e ₀	WC (%)	Dry Density (g/cm ³)	Unit Weight (pcf)	In situ Stress (kg/cm ²)	Pp (Pacheco-Silva) (kg/cm ²)	C _c	C _u , norm. consol.	C _v , norm. consol., (m ² /yr)
CRS-8	I-9 S-2	130	OBC	1.015	38.2	1.328	115.6	4.14	7.2	0.54	0.037	2.9
CRS-9	I-9 S-2	120	OBC	1.182	43.9	1.238	111.3	3.80	7.6	0.70	0.025	2.2
CRS-10	I-9 S-2	120	OBC	1.209	45.4	1.222	110.9	3.80	7.2	0.82	0.060	1.6
CRS-11	I-16 S-2	206	Alameda	1.095	42.0	1.289	114.5	6.10	10.0	0.70	0.056	0.9
CRS-12	I-16 S-1	200	Alameda	0.995	38.4	1.353	117.0	5.90	10.1	0.61	0.041	1.0
CRS-13	DSM-1 S-1	26	BM - W	1.813	66.1	0.960	99.2	1.10	4.2	1.05	0.090	0.4
CRS-14	DSM-1 S-1	26	BM - W	1.938	70.2	0.919	97.3	1.10	4.2	1.12	0.080	0.3
CRS-15	I-11 S-6	190	Alameda	0.873	33.0	1.441	119.6	5.60	12.0	0.46	0.024	1.4
CRS-17	I-11 S-6	190	Alameda	0.900	33.6	1.421	118.5	5.60	13.0	0.51	0.040	1.0
CRS-18	I-17A S-1	28	BM - E	0.805	30.4	1.496	115.8	1.28	1.4	0.25	0.010	19.0
CRS-19	I-35 S-4	135	OBC	1.163	43.5	1.272	113.9	3.80	9.0	0.70	0.023	1.8
CRS-20	I-11 S-3	135	OBC	1.097	41.1	1.311	115.4	4.27	7.3	0.73	0.015	1.6
CRS-21	I-17A S-3	109	OBC	1.015	37.4	1.365	117.0	3.54	8.4	0.59	0.013	4.4
CRS-22	I-11 S-3	135	OBC	1.128	42.2	1.293	114.7	4.27	7.8	0.69	0.015	1.4
CRS-23	EX-03 S-2	114.5	OBC	1.392	51.4	1.150	108.6	3.66	7.0	1.01	0.014	2.8
CRS-24	I-34 S-1	110	OBC	1.223	45.6	1.237	112.4	3.55	7.3	0.93	0.017	2.2
CRS-25	BH-2 S-35	195	Alameda	1.110	41.9	1.303	115.4	5.90	8.6	0.62	0.016	1.3
CRS-26	BH-1 S-18	120	OBC	1.153	42.4	1.277	113.2	3.85	6.3	0.73	0.010	2.1
CRS-27	BH-3 S-18	110	OBC	1.156	42.3	1.275	113.2	3.60	7.5	0.66	0.019	0.4
CRS-28	EX-04 S-2	100	OBC	1.192	43.9	1.254	112.5	3.30	6.3	0.74	0.016	1.7
CRS-29	BH-1 S-29	230	Alameda	1.082	40.3	1.321	115.6	6.84	8.0	0.66	0.037	0.5

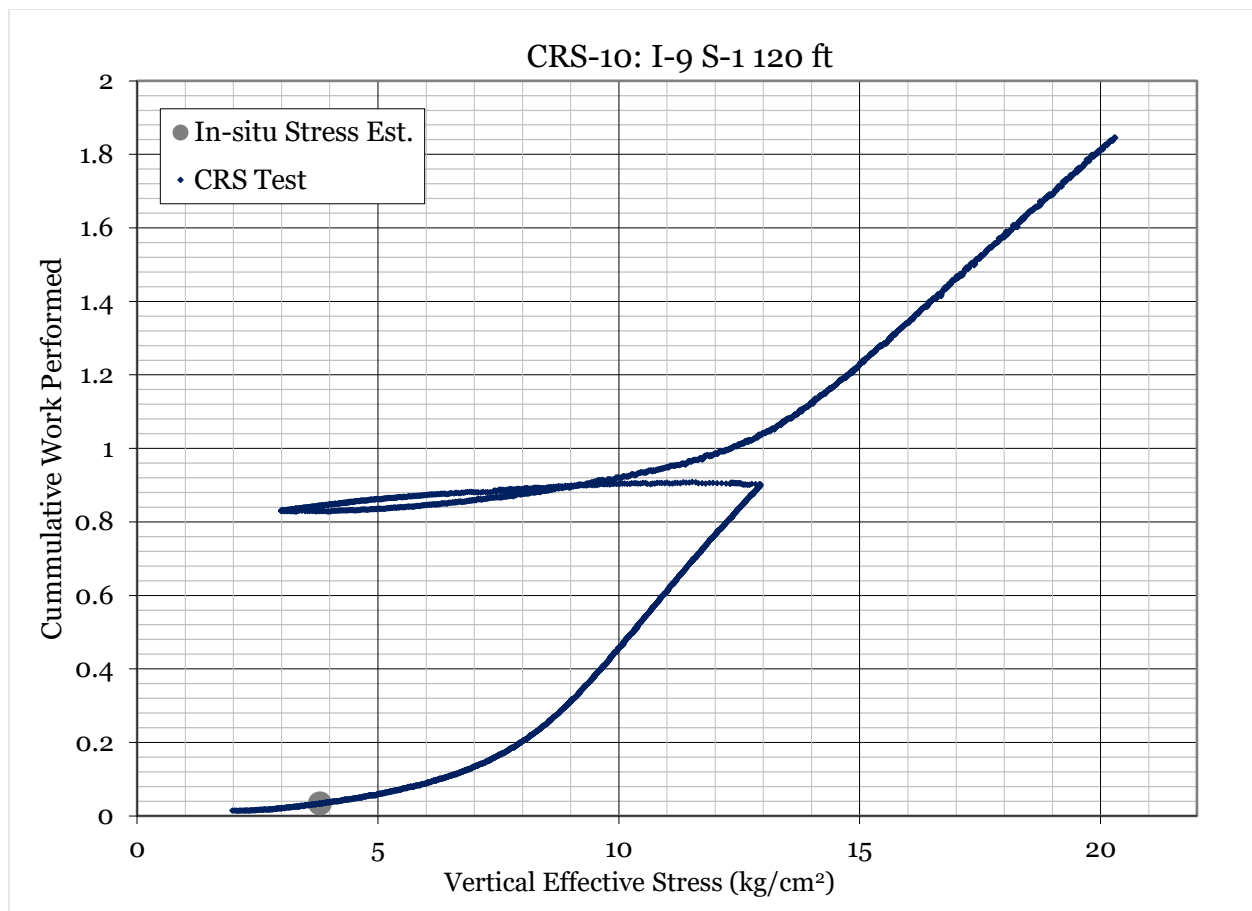


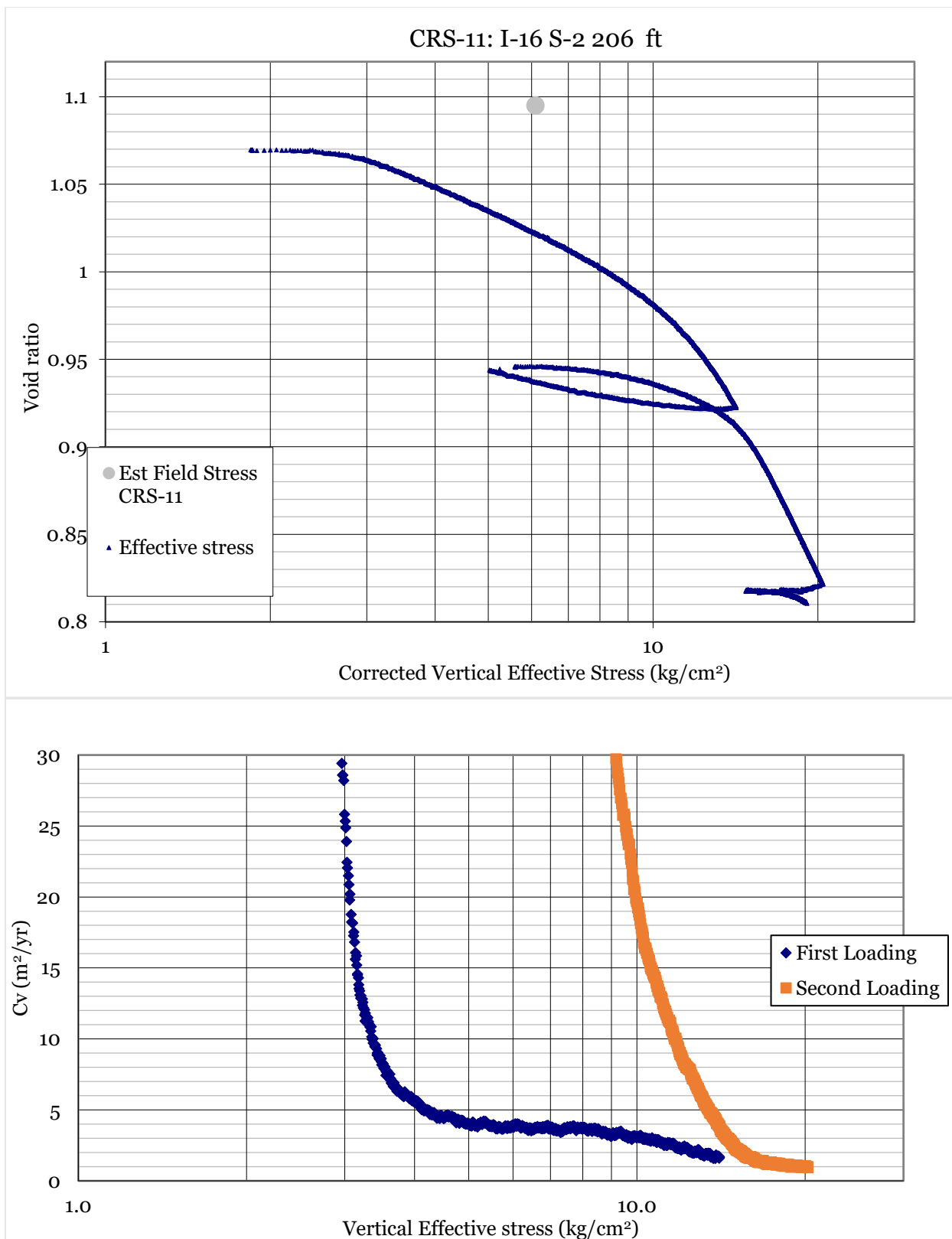


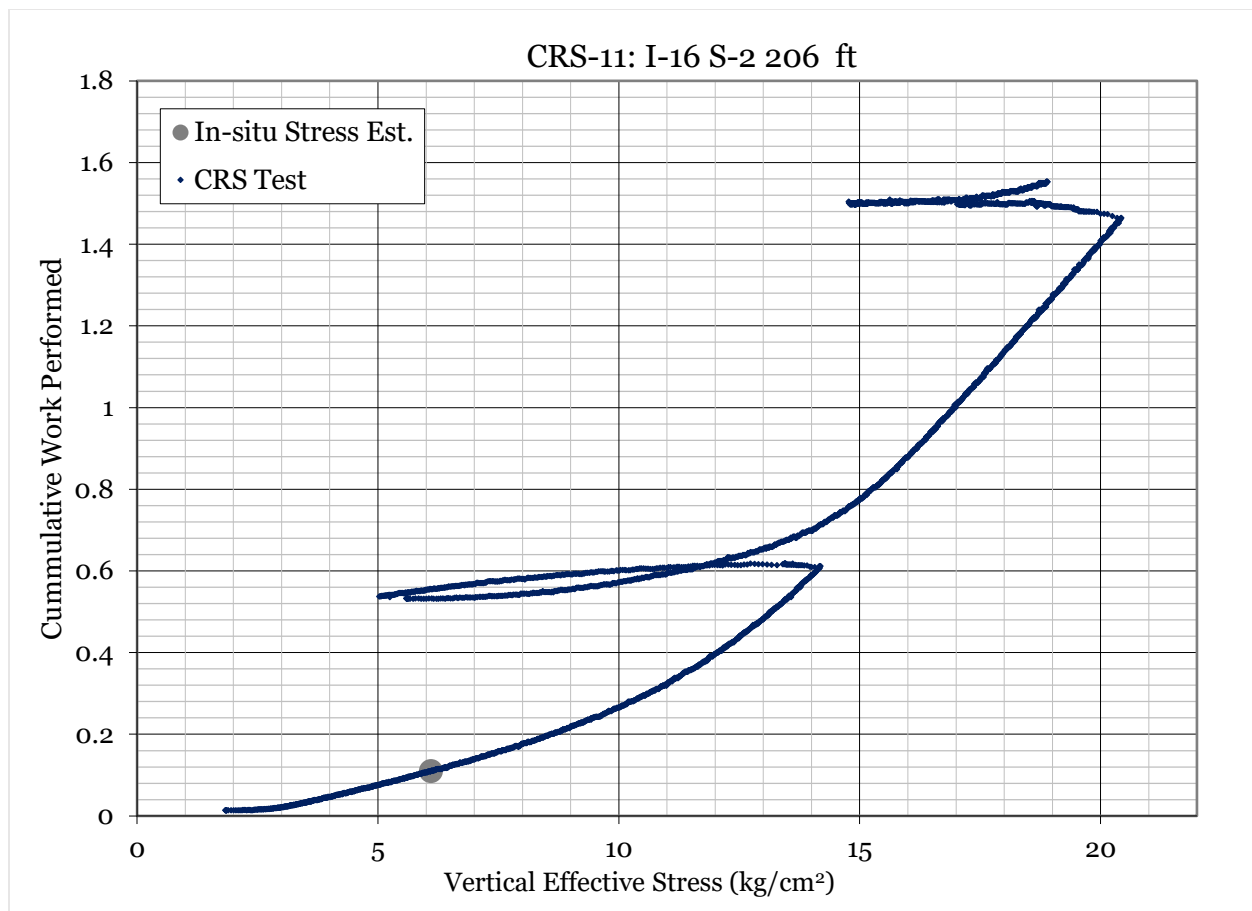


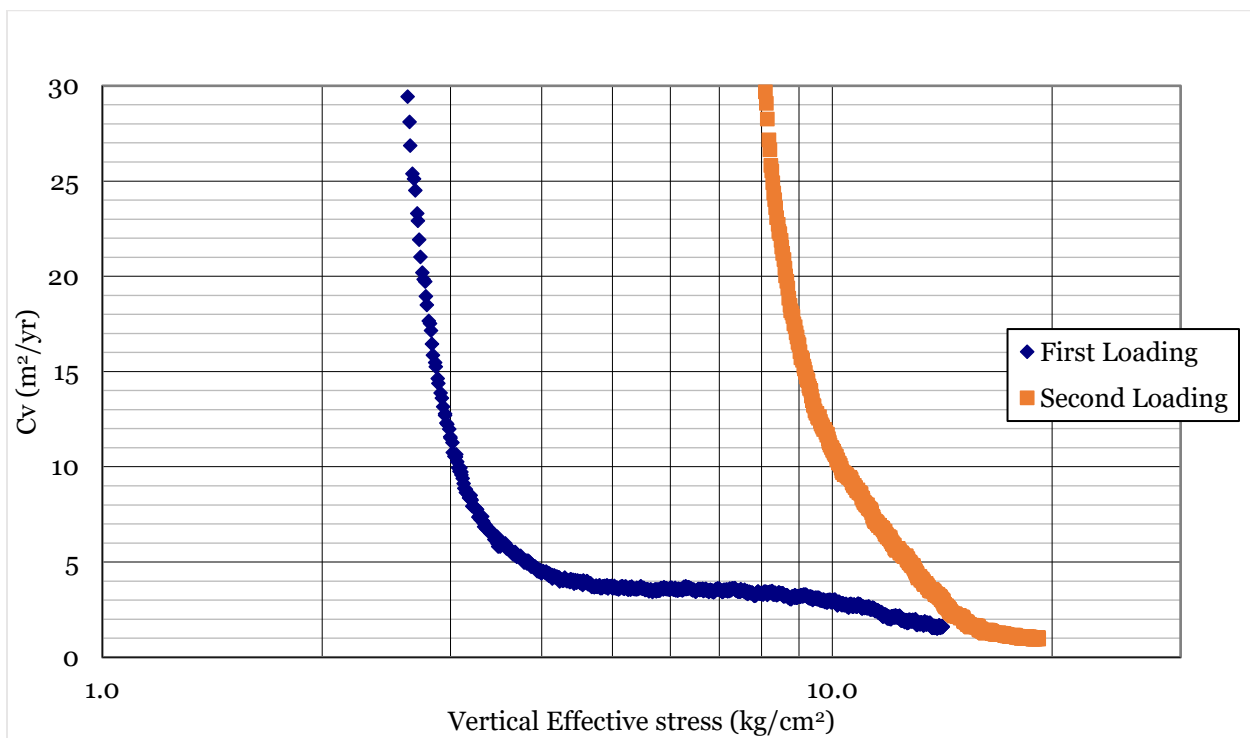
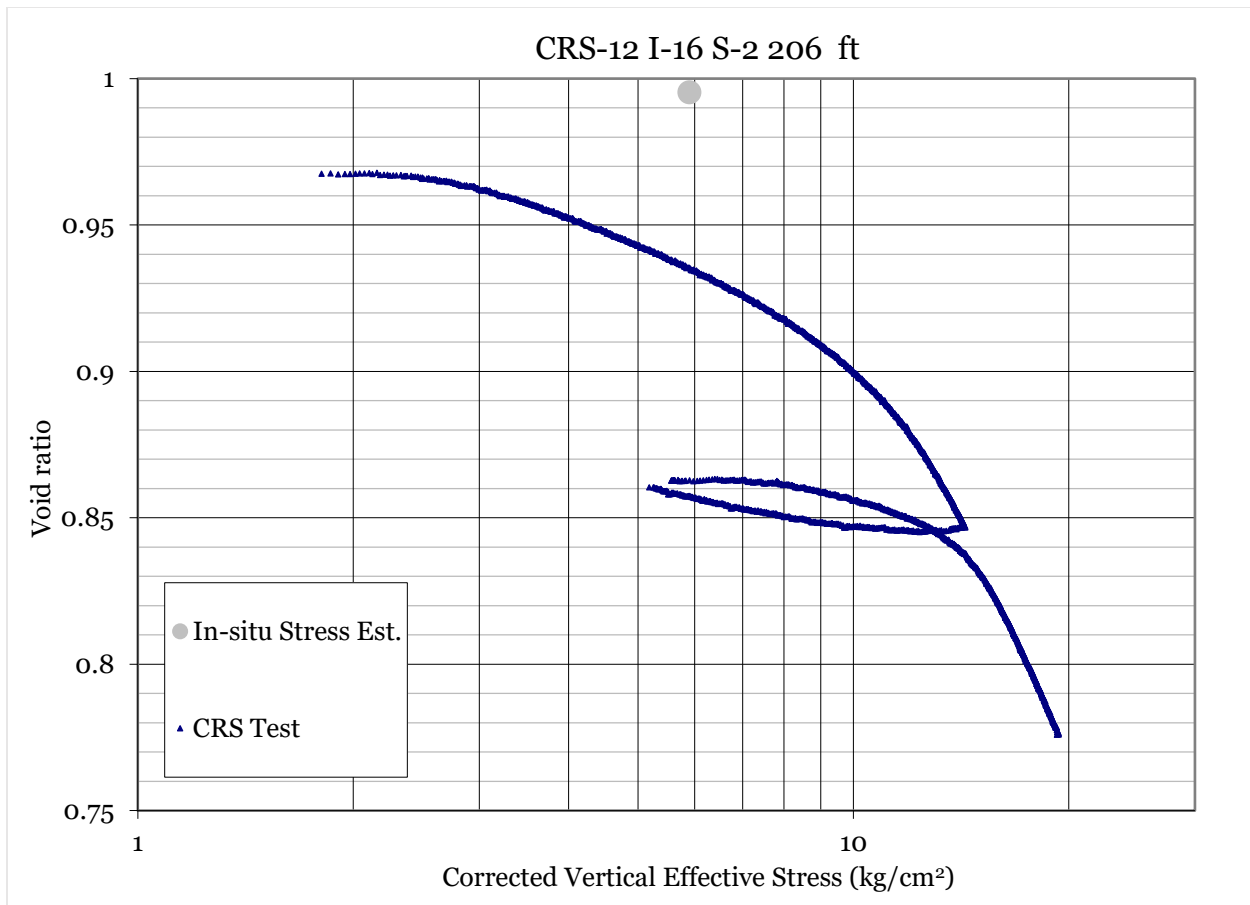


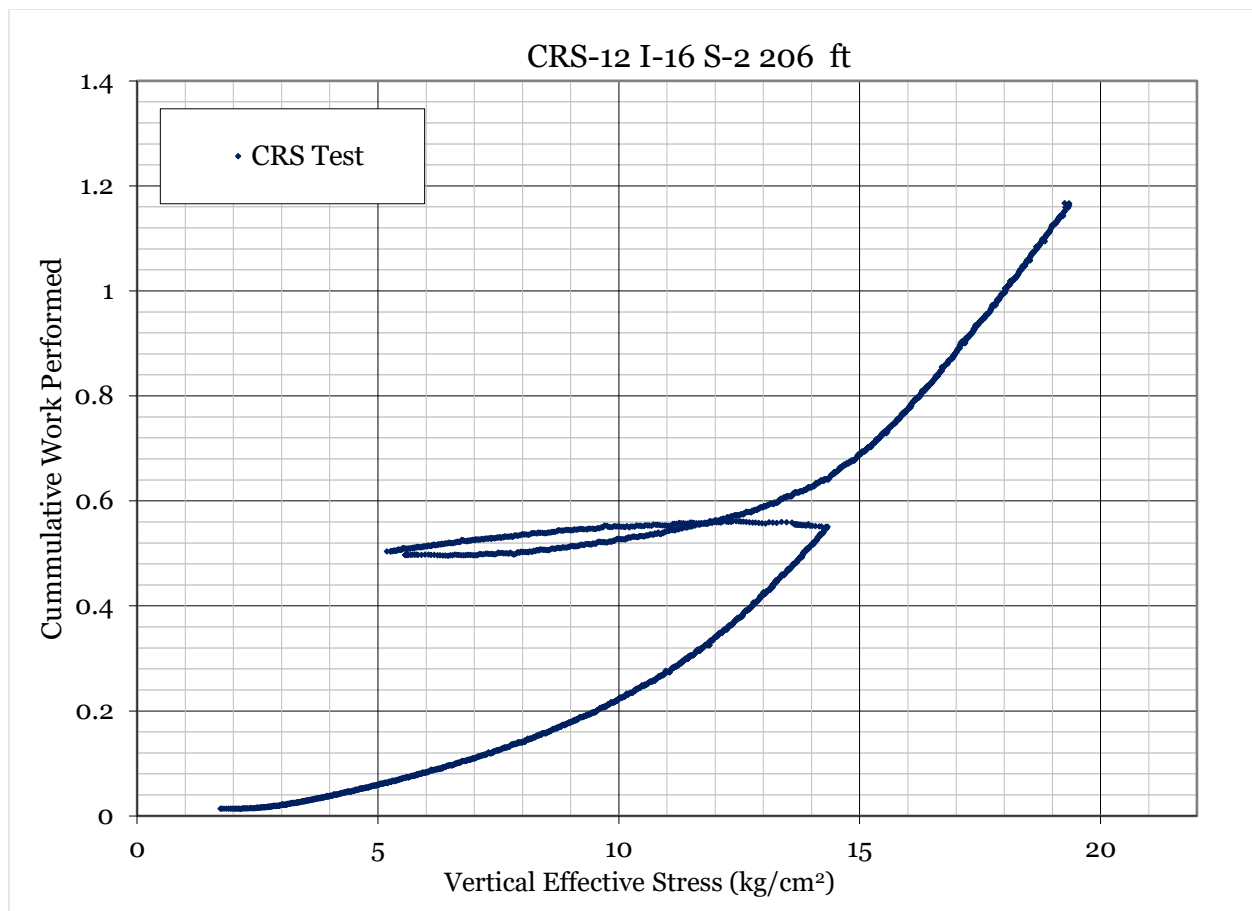


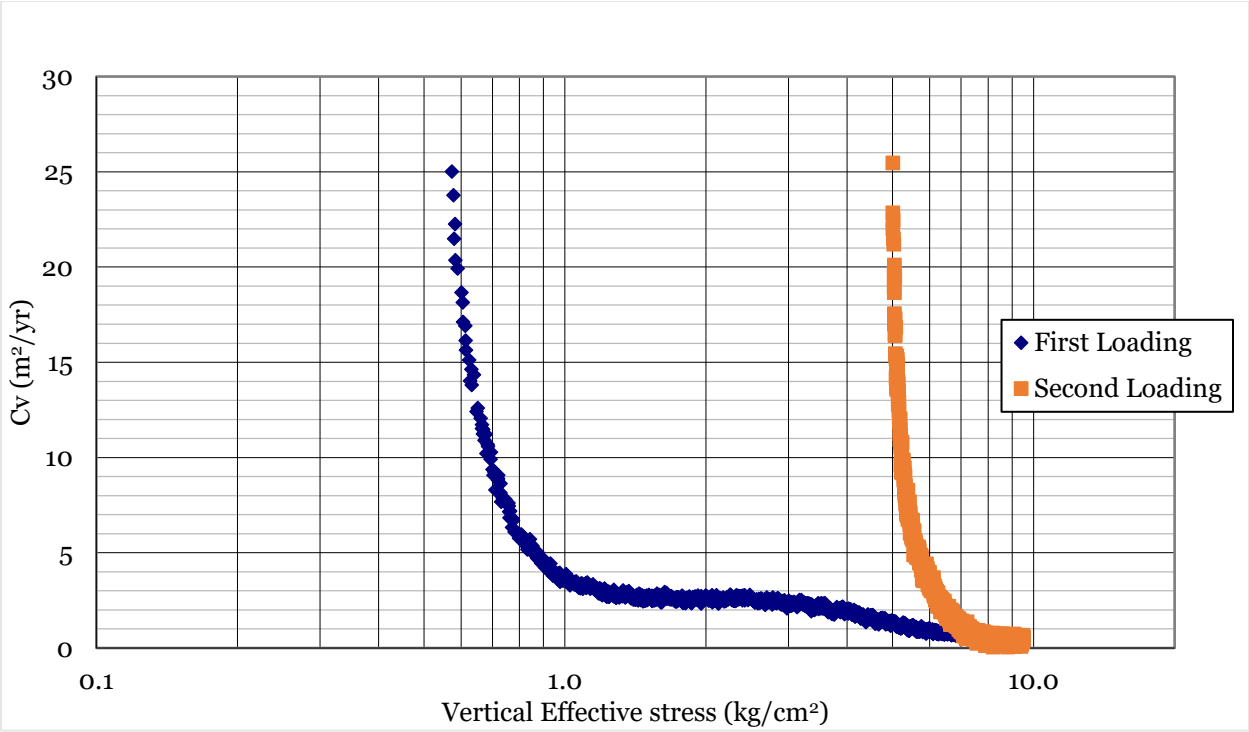
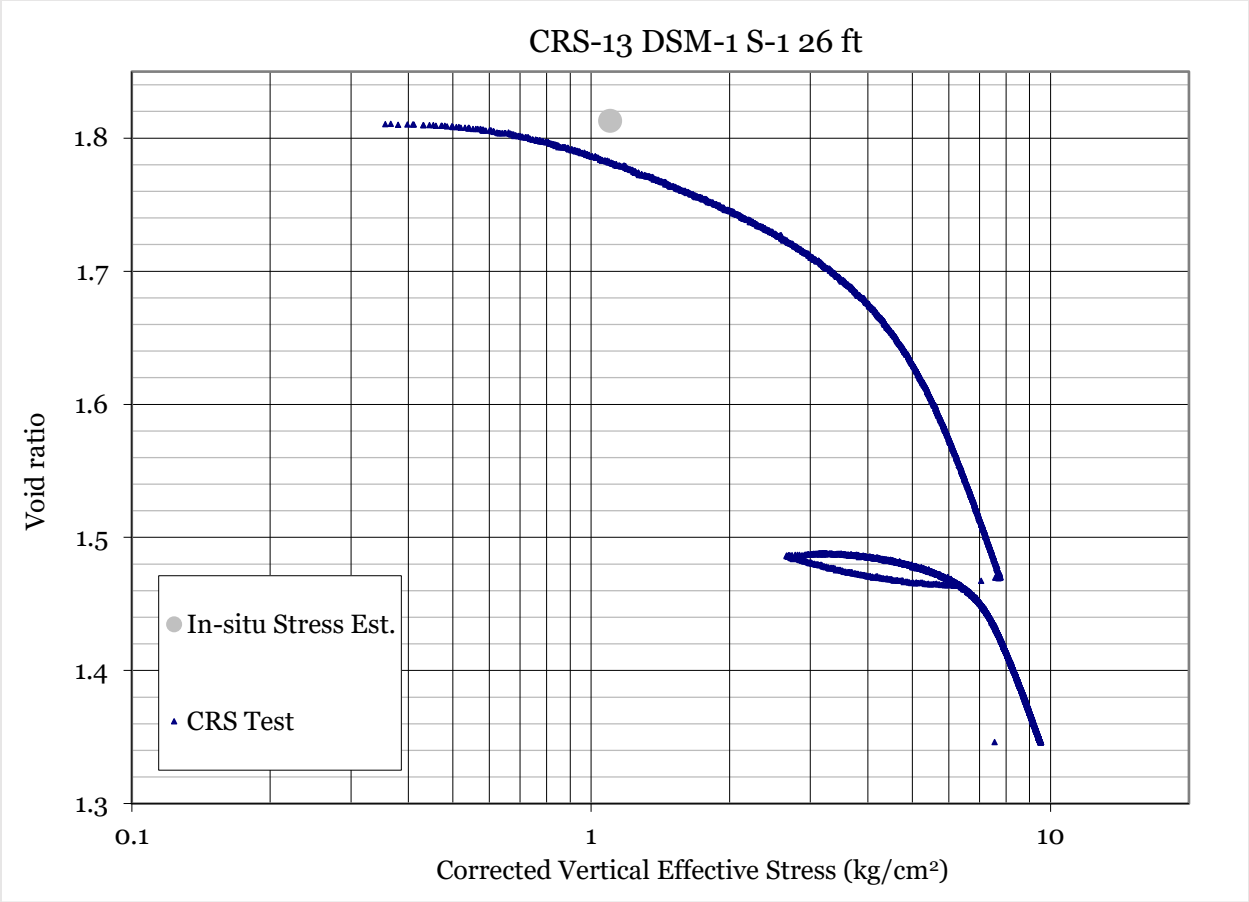


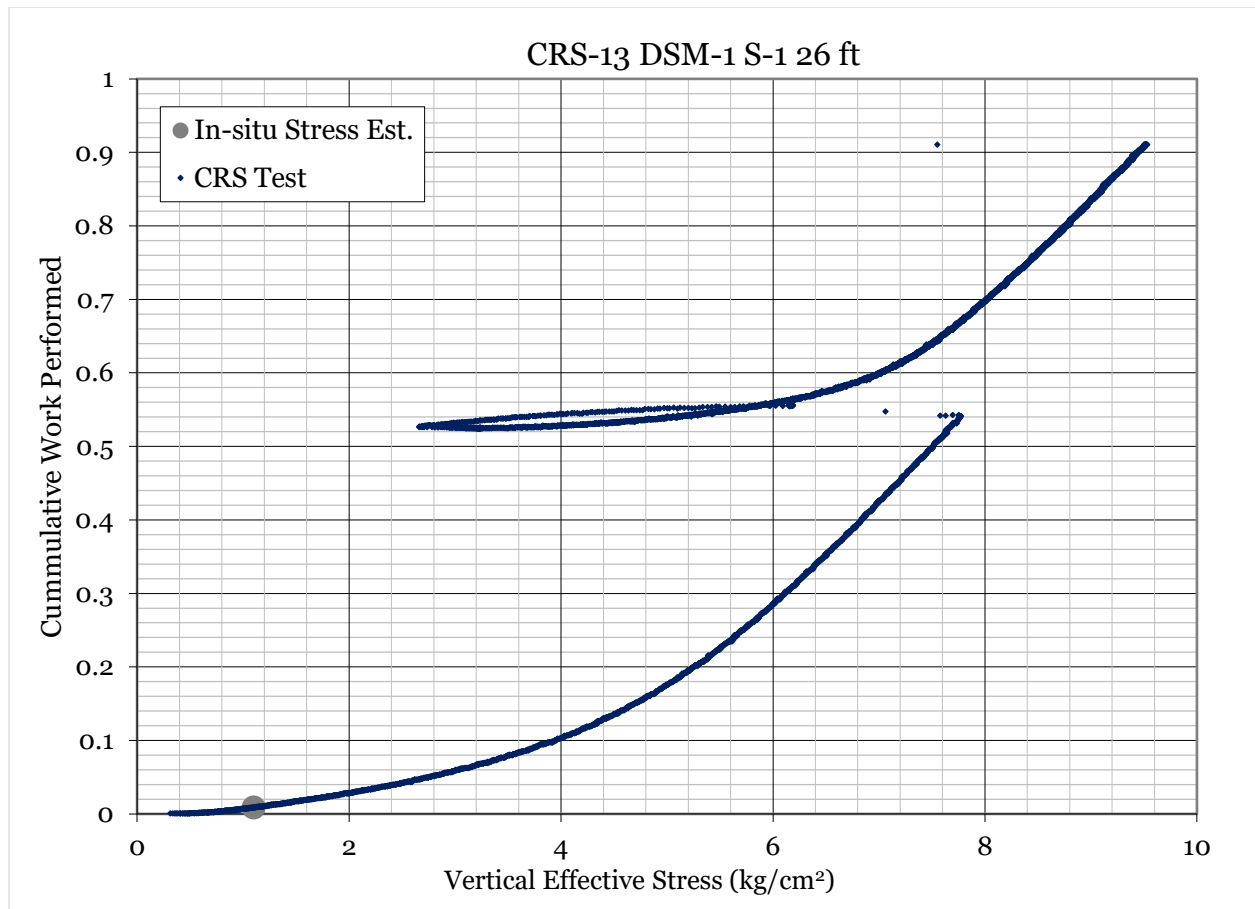


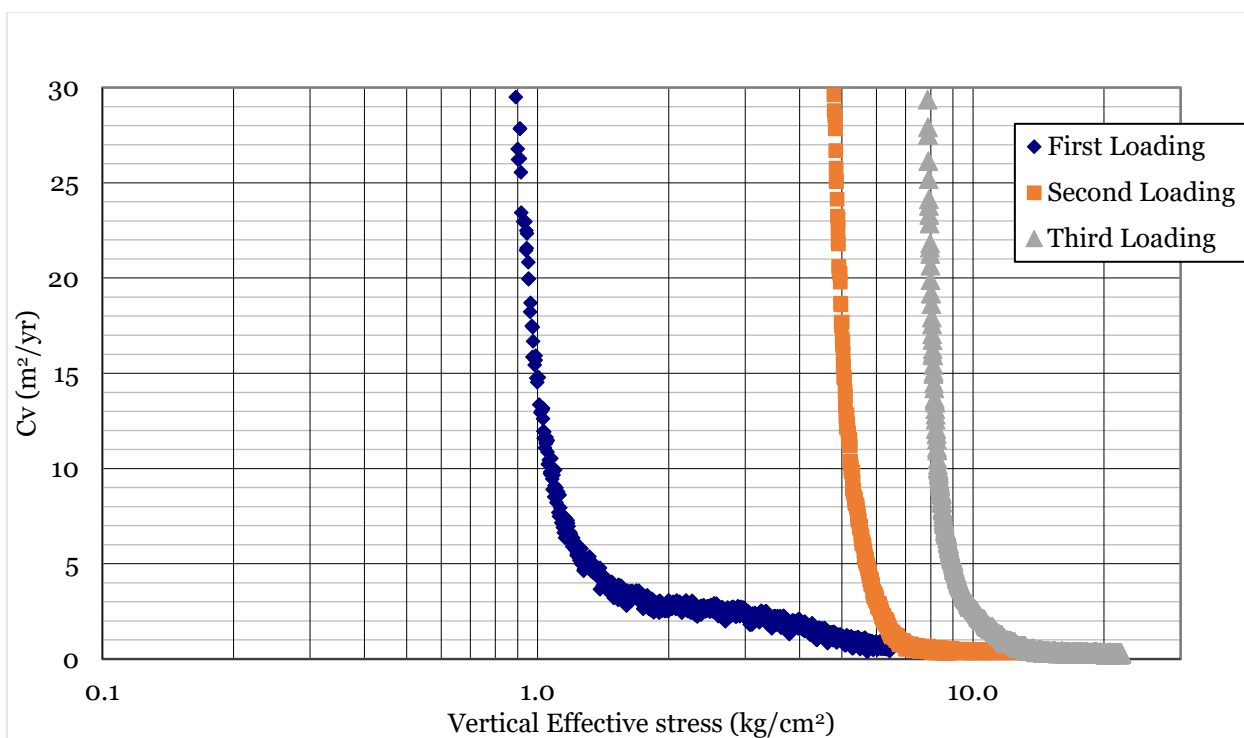
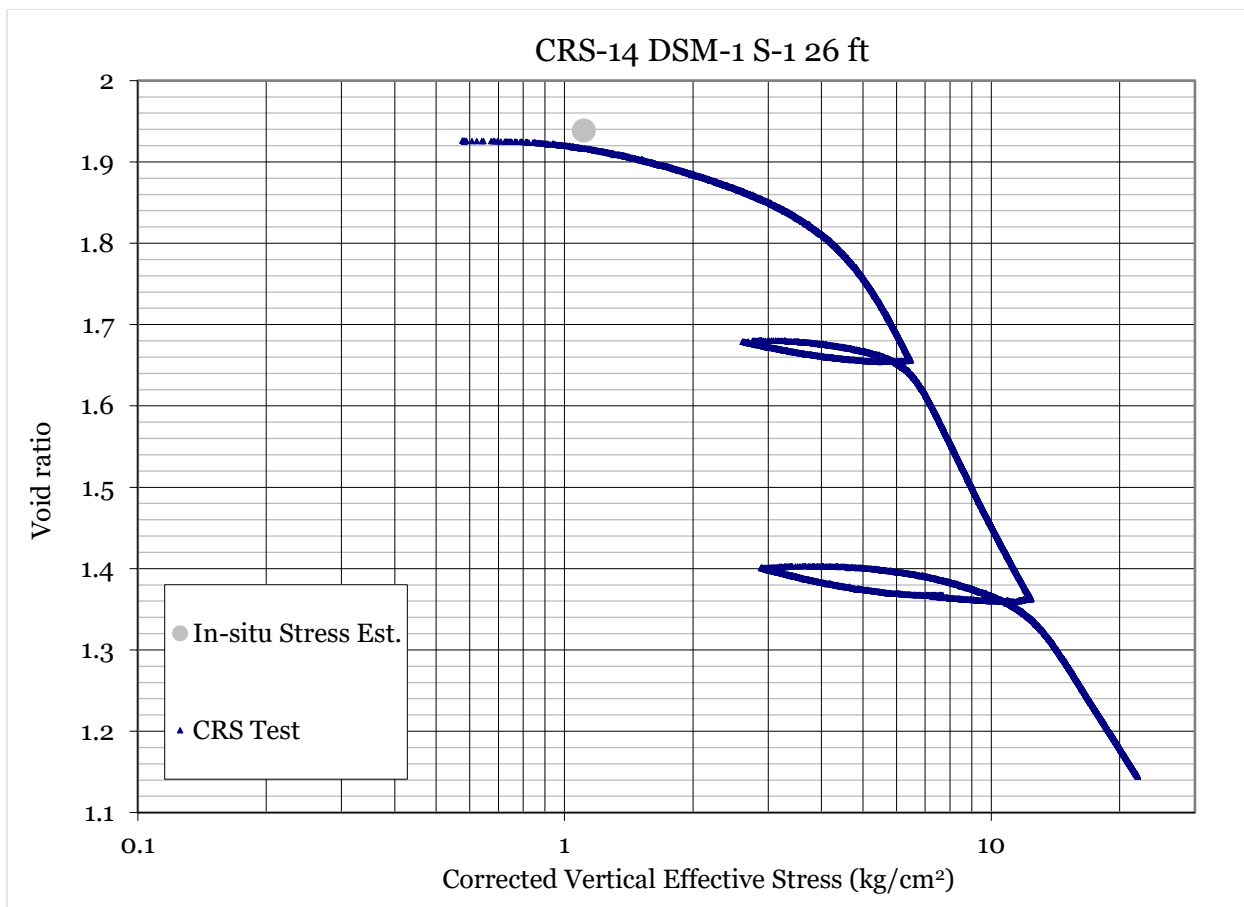


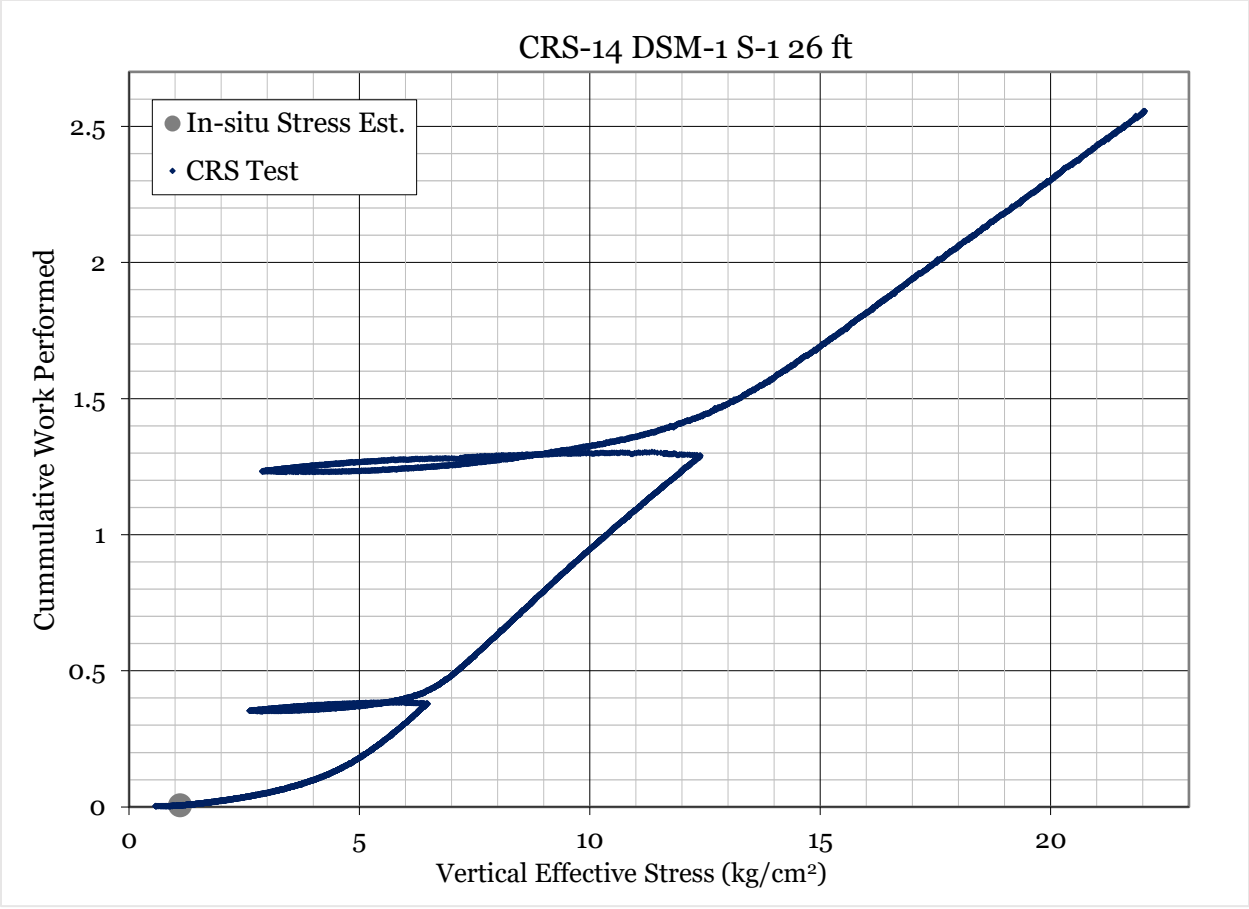


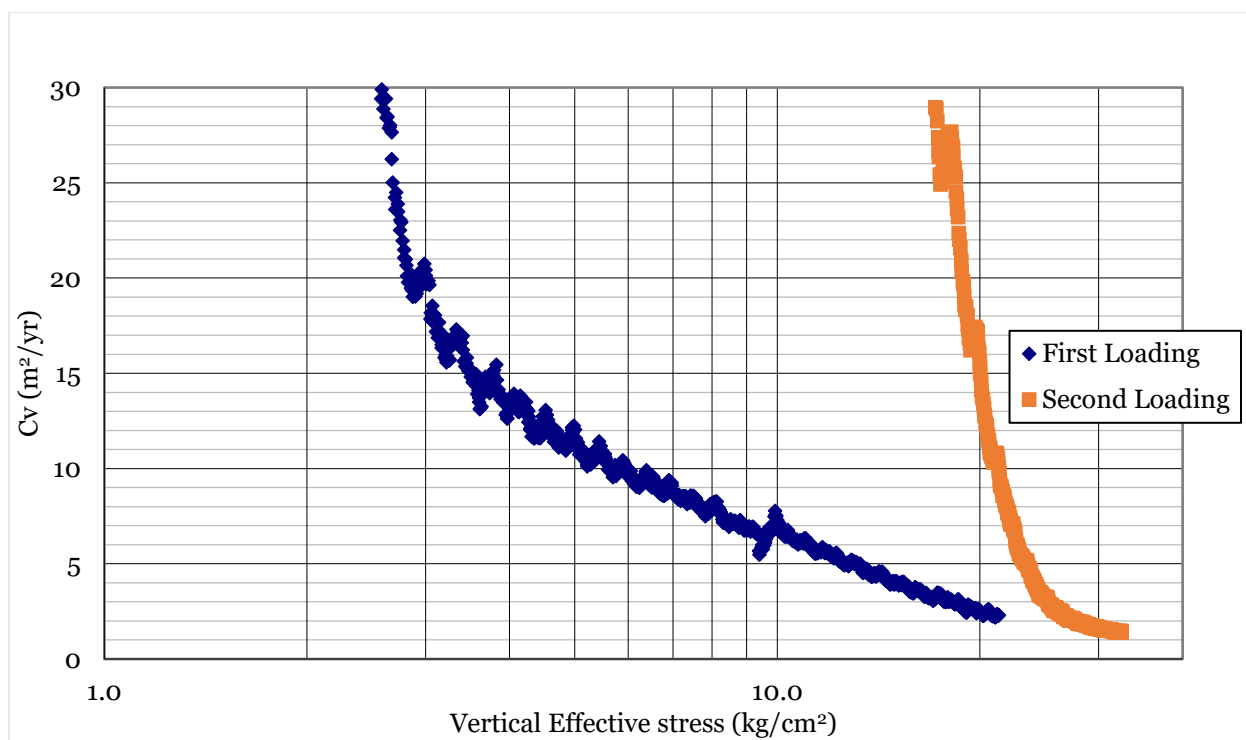
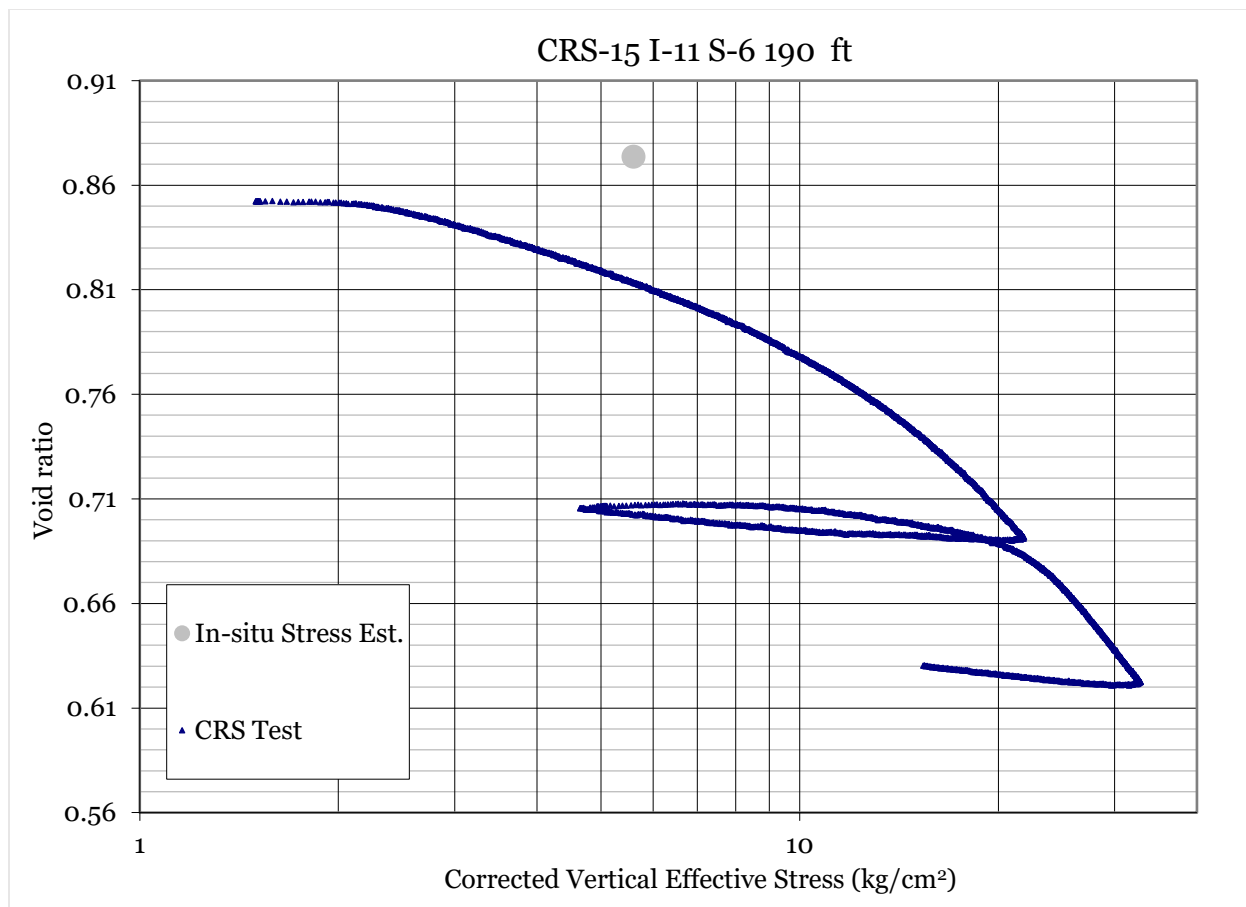


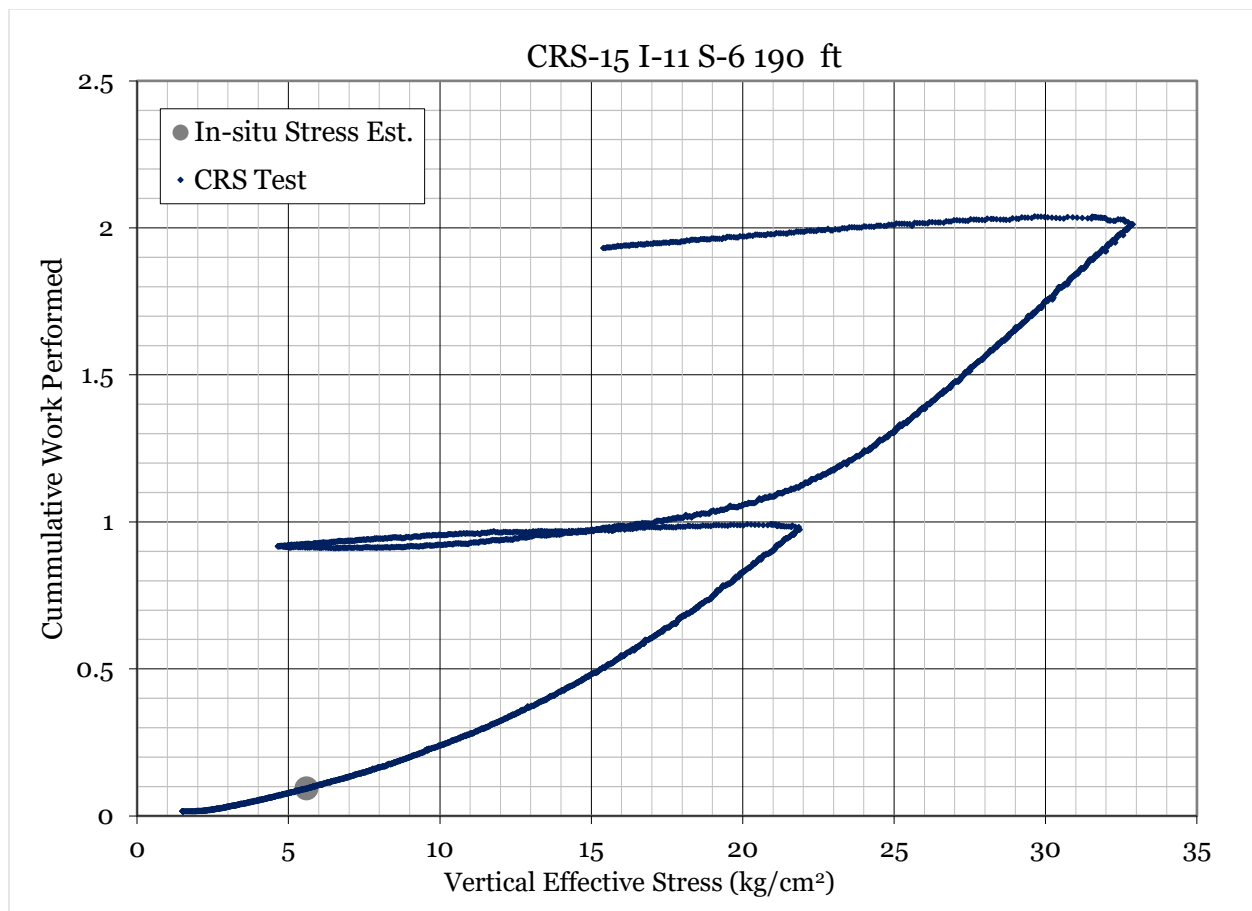


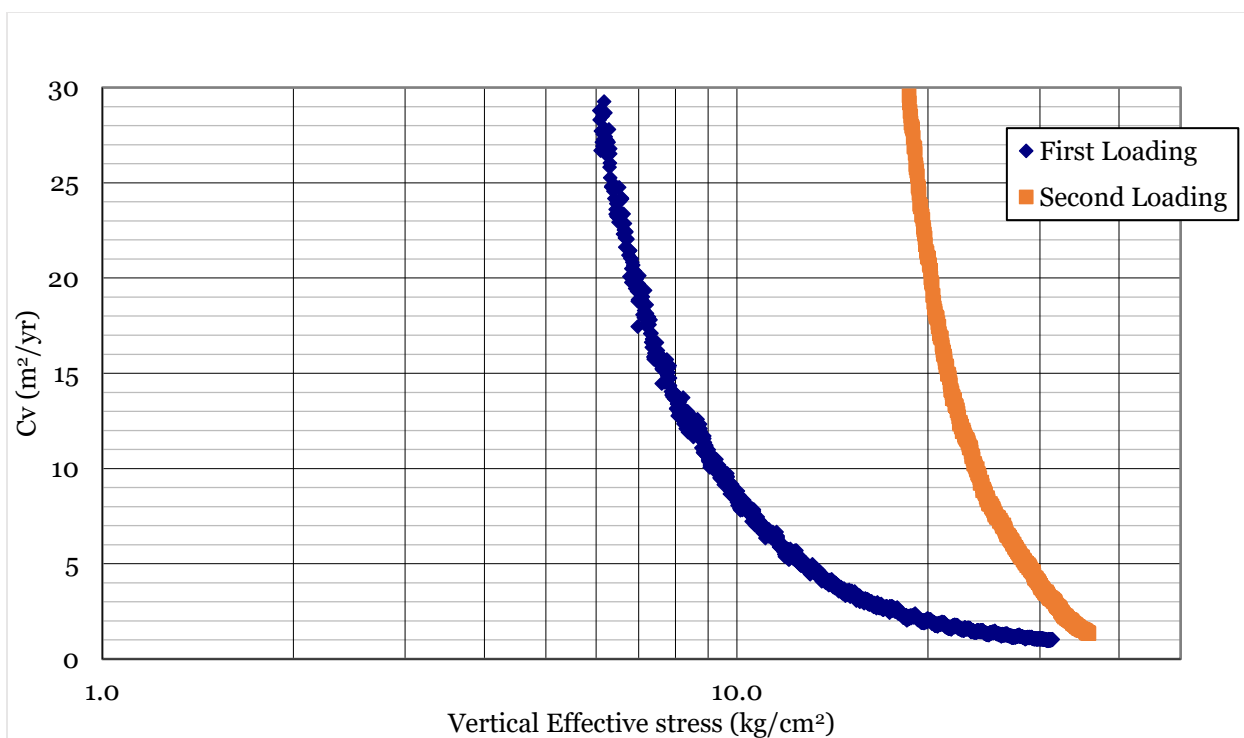
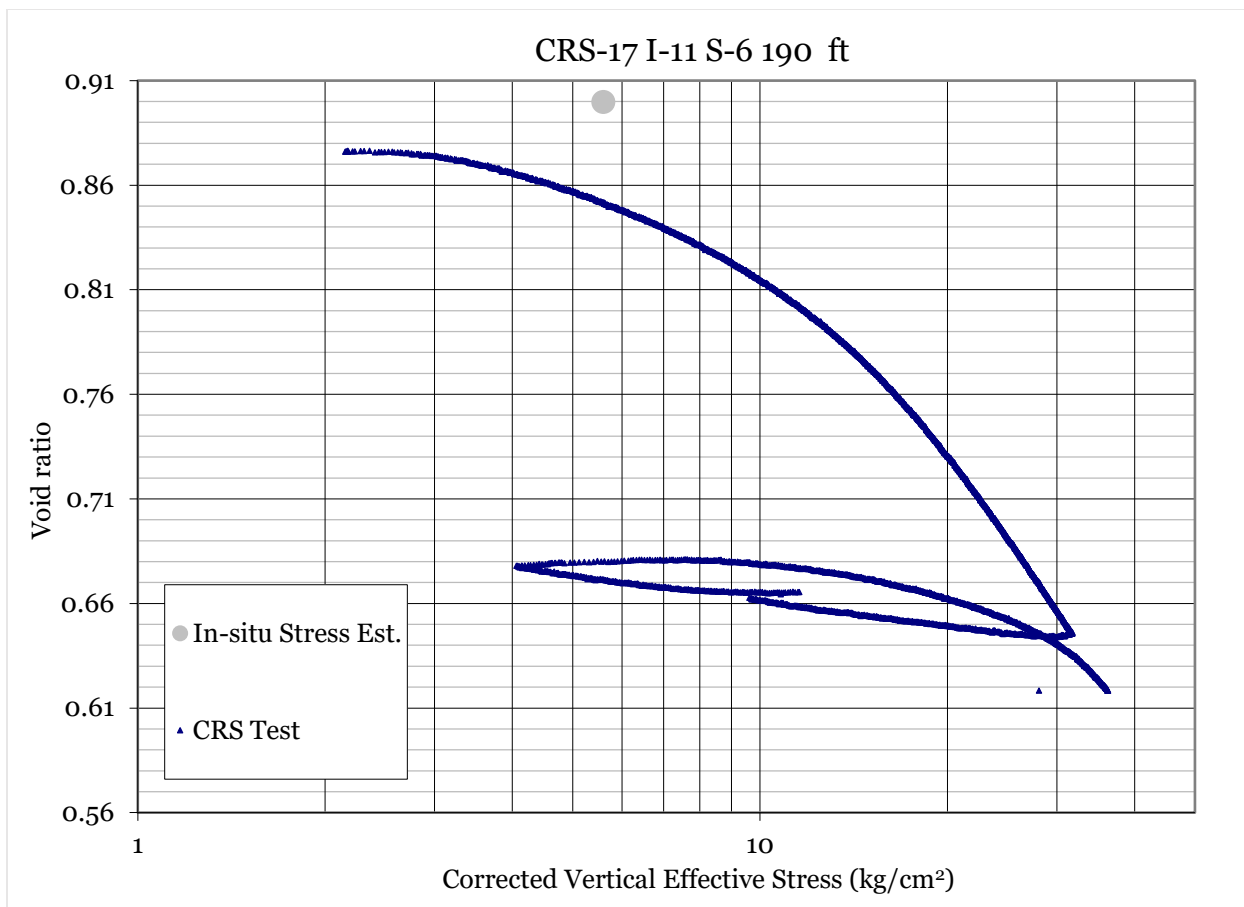


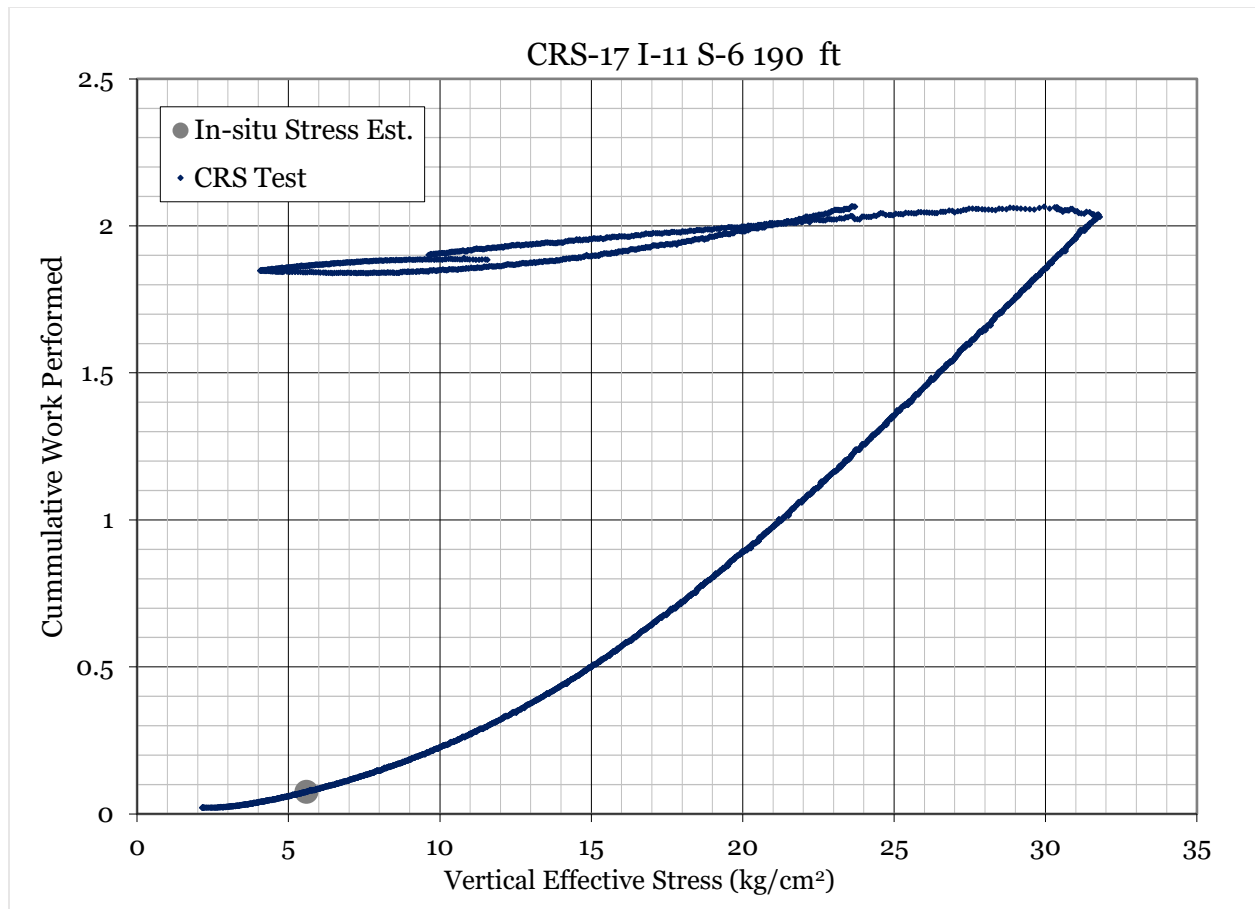


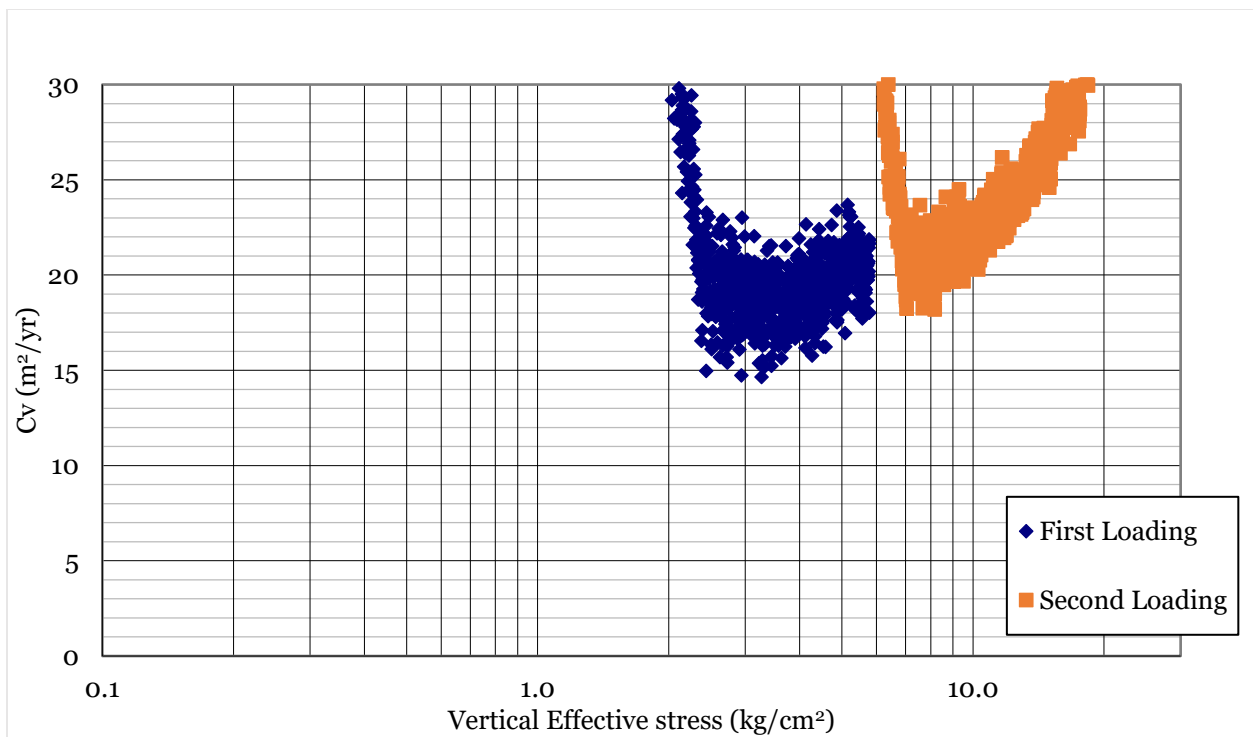
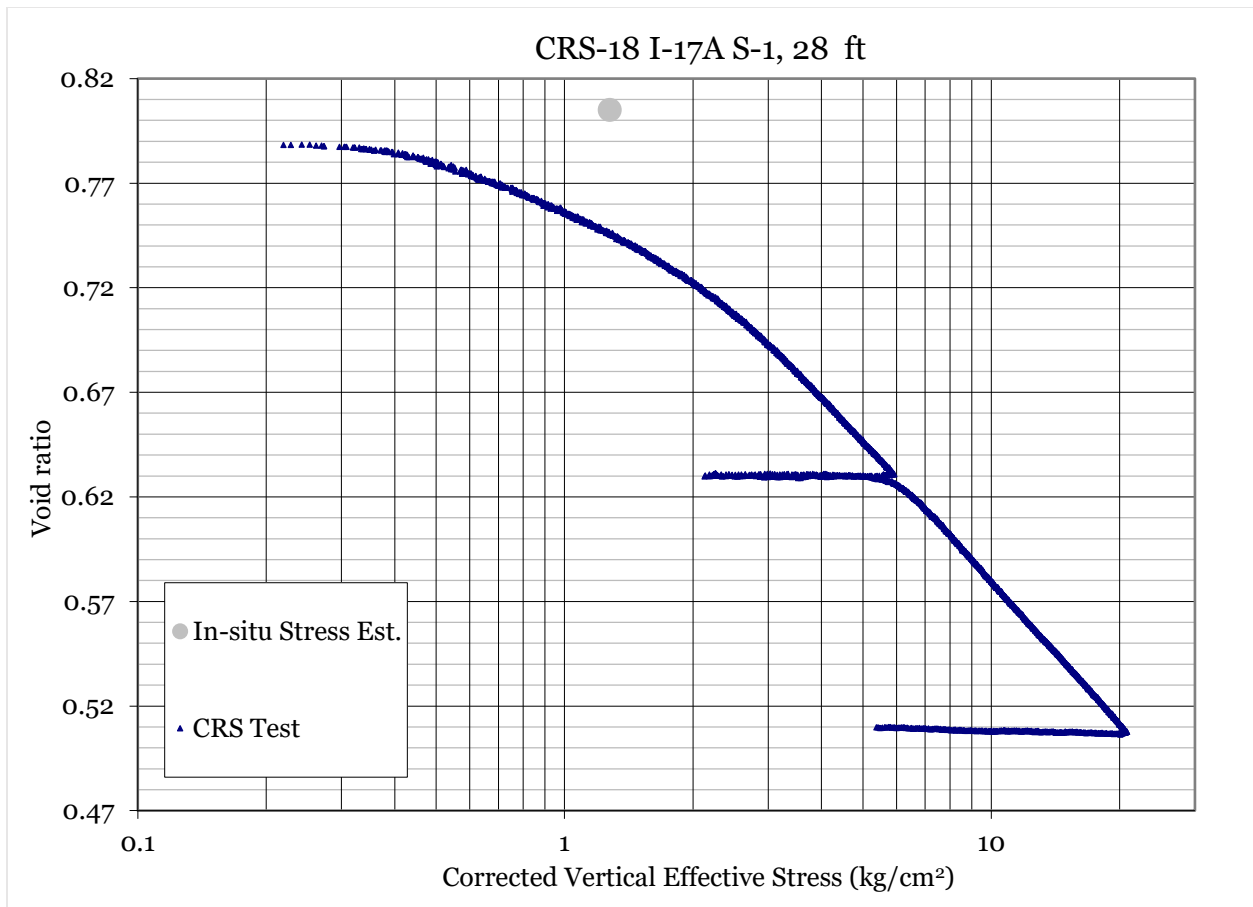


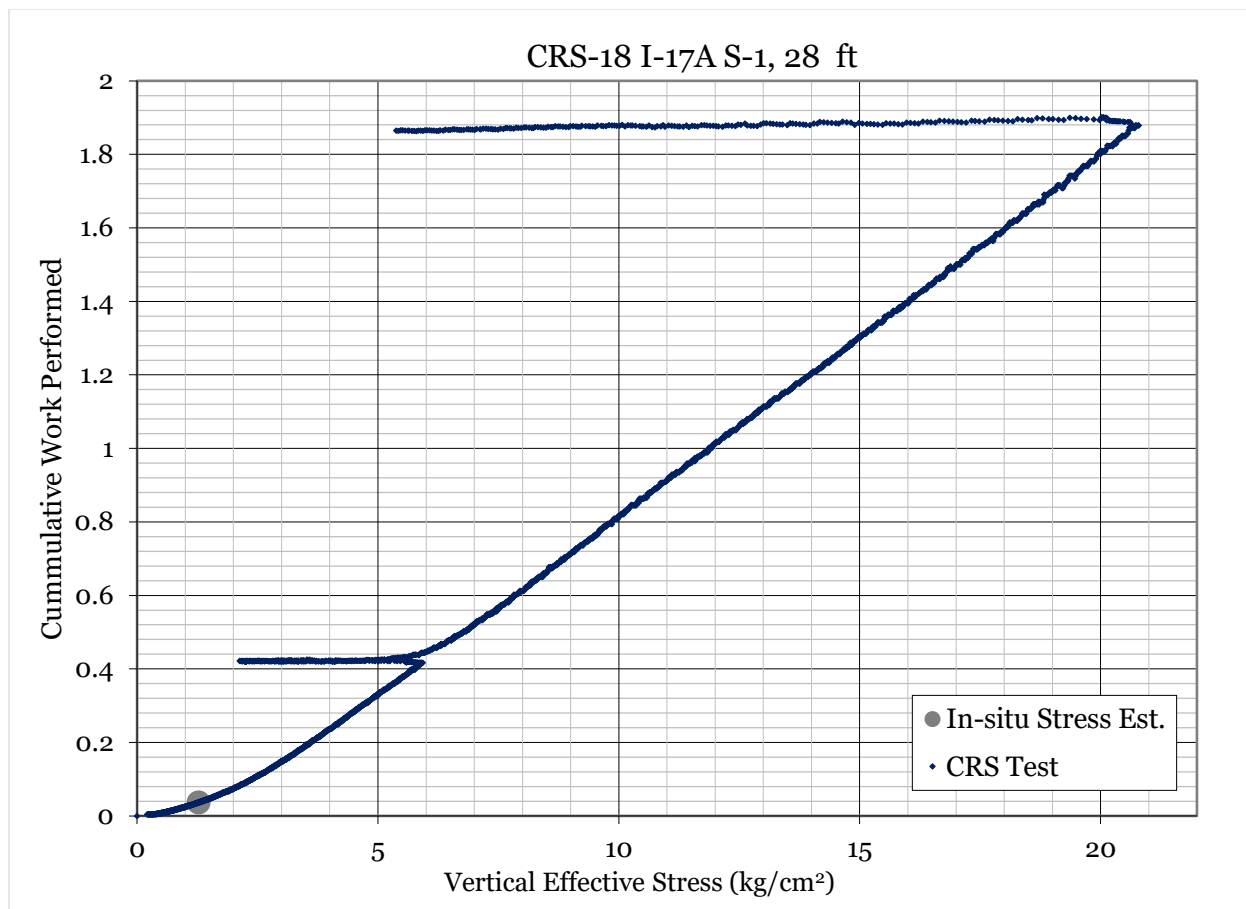


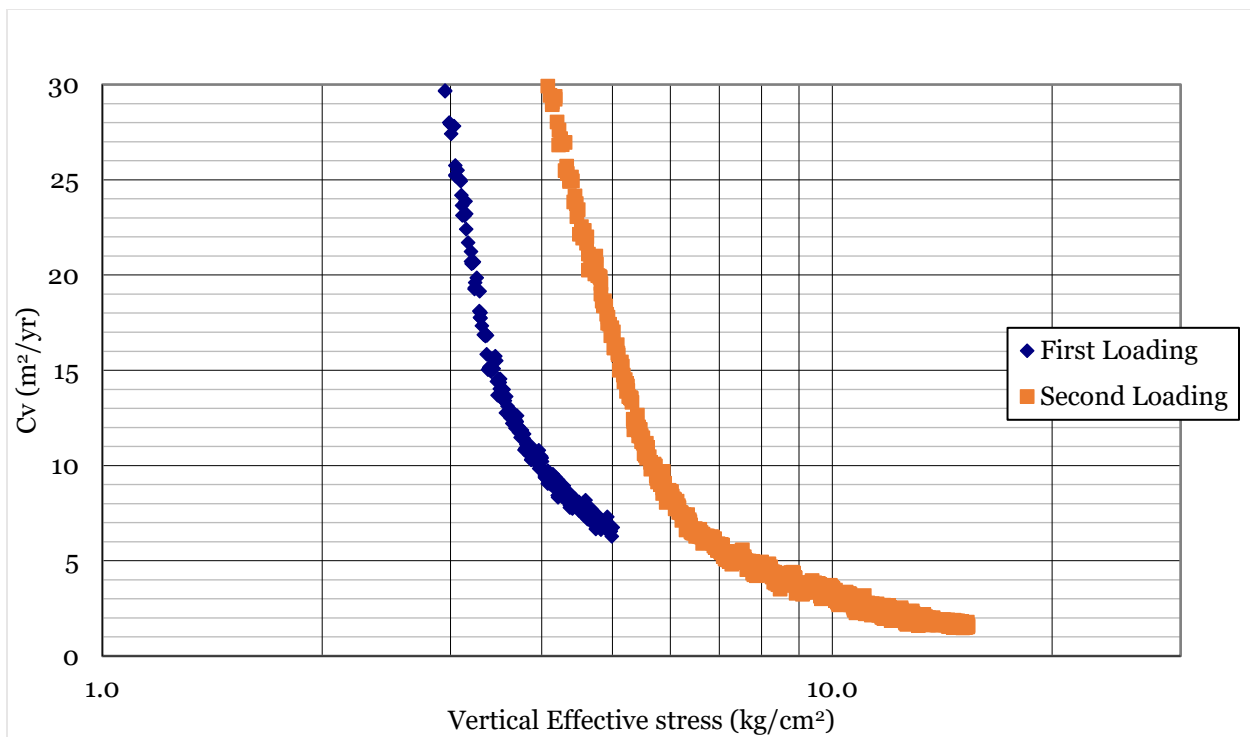
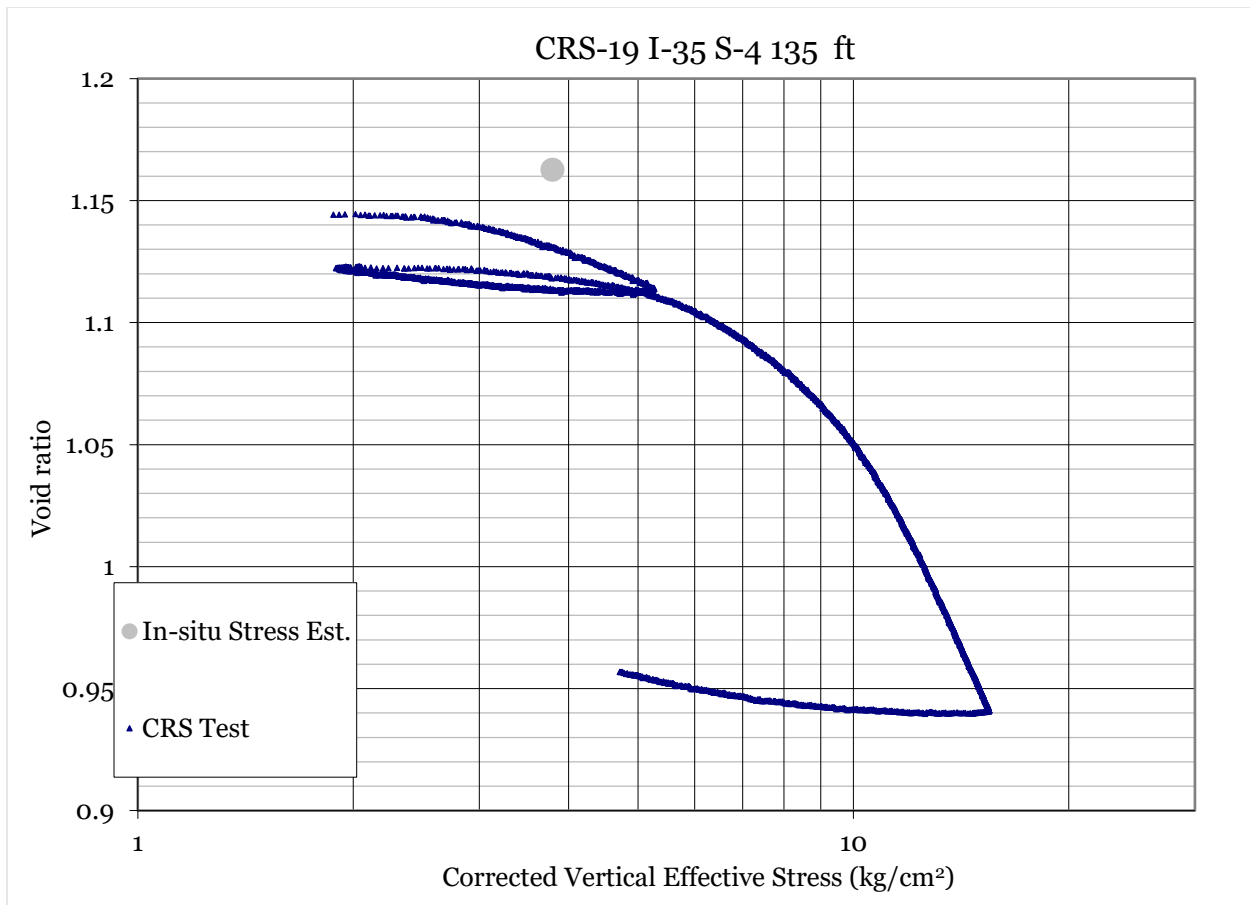


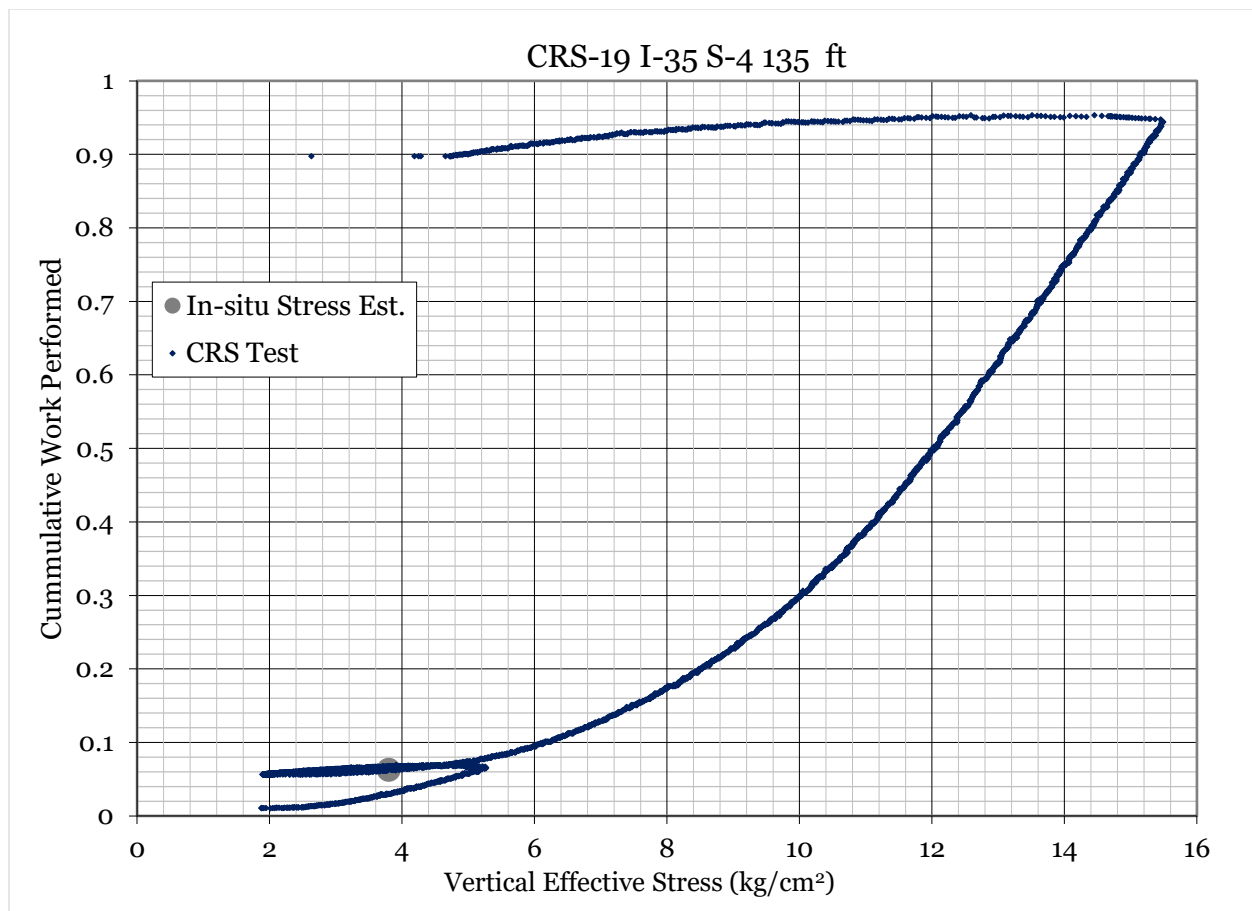


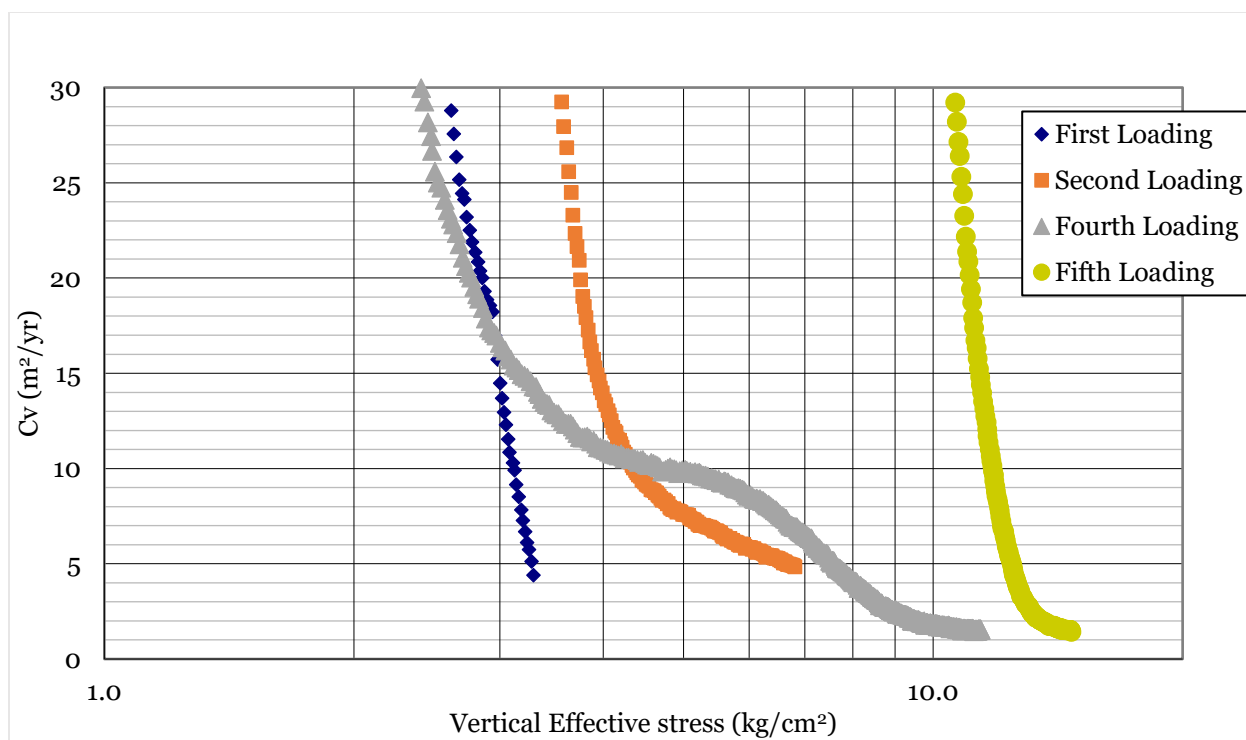
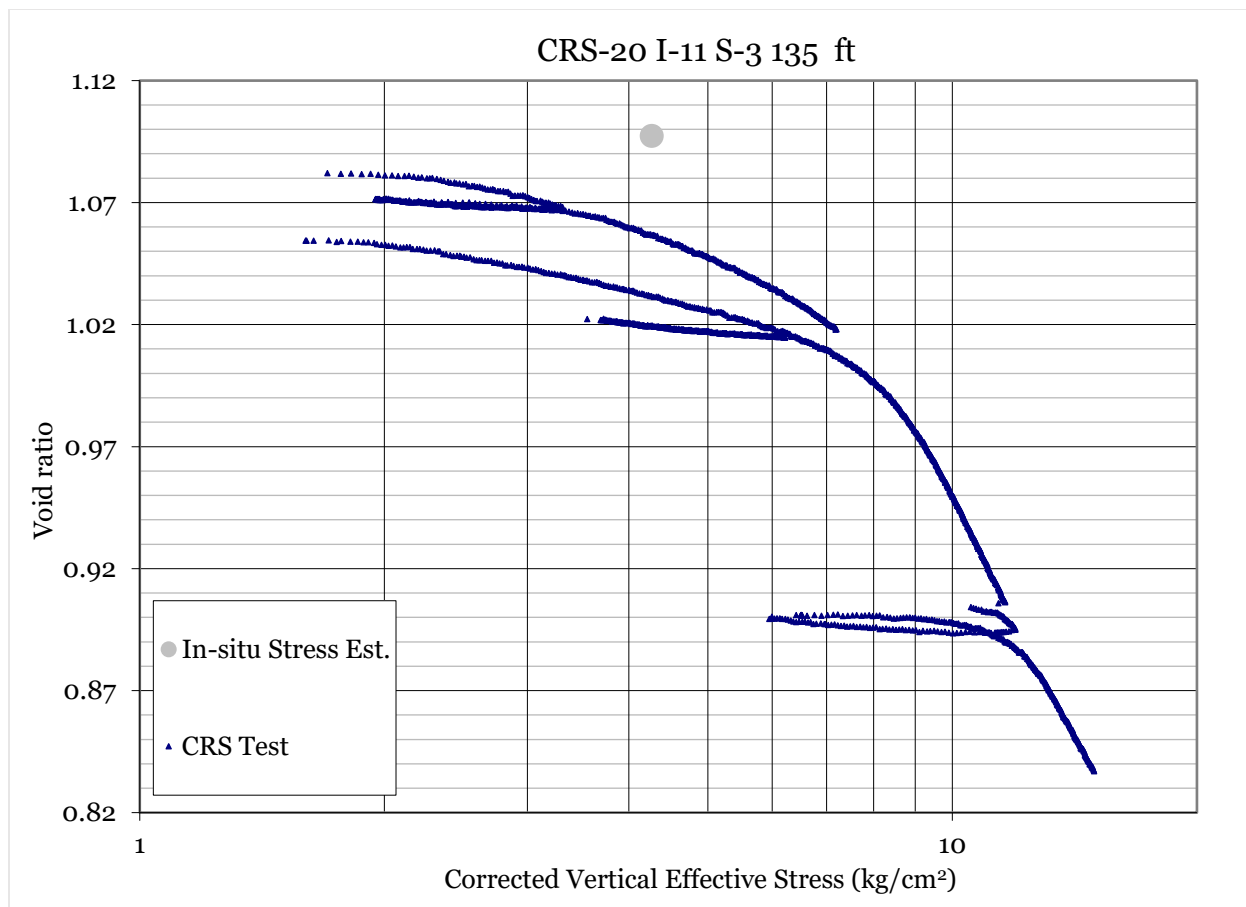


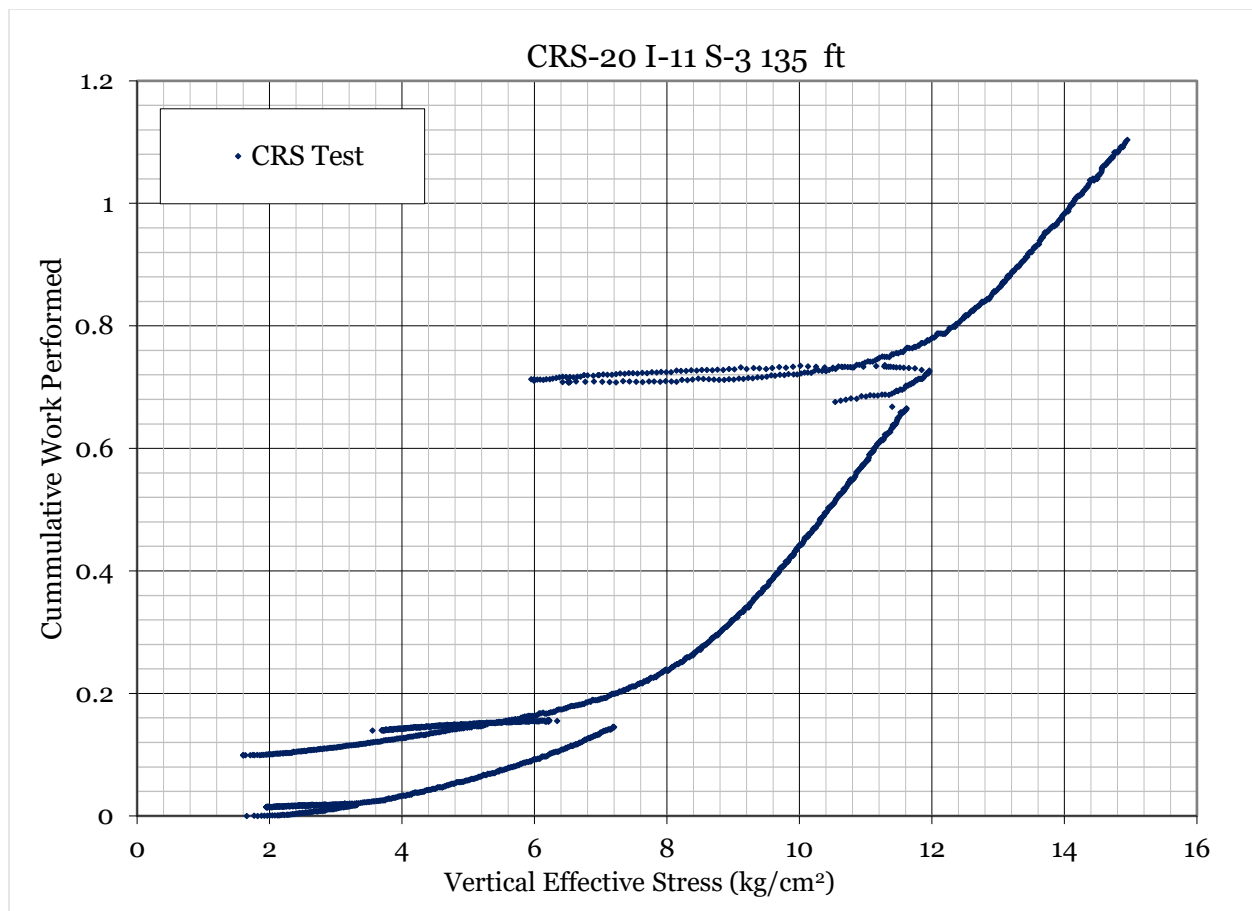


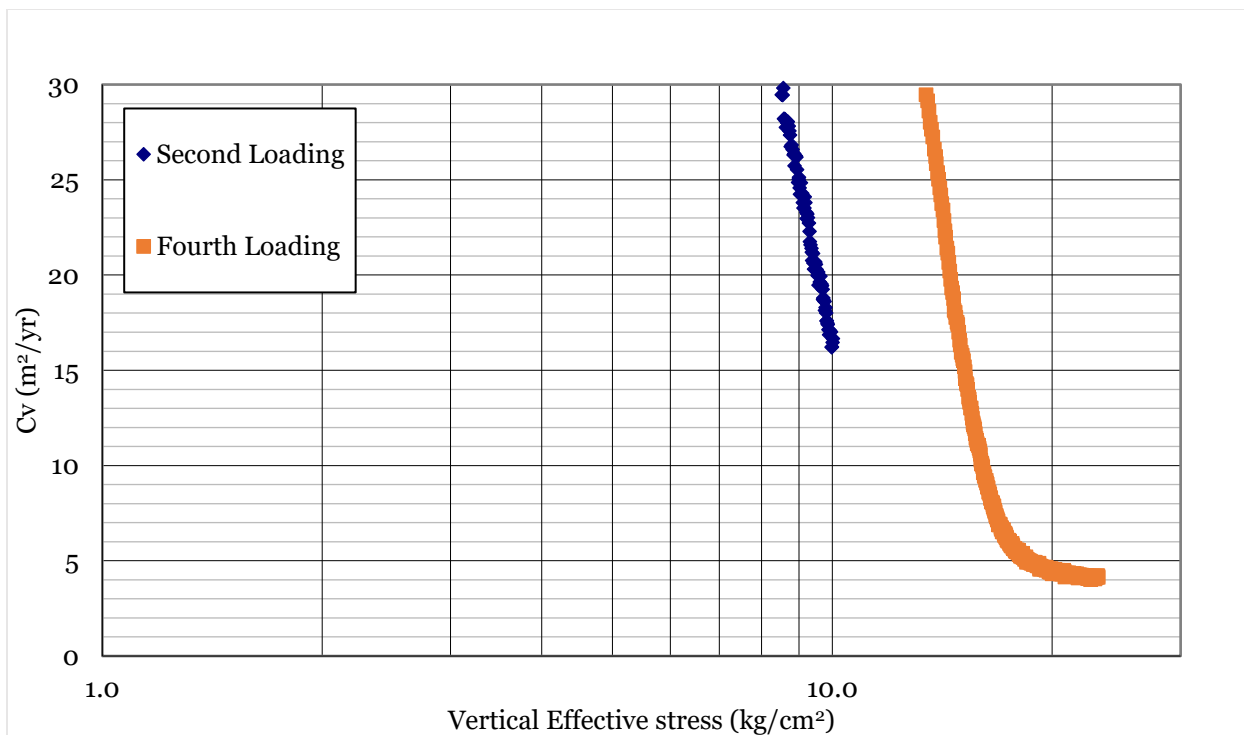
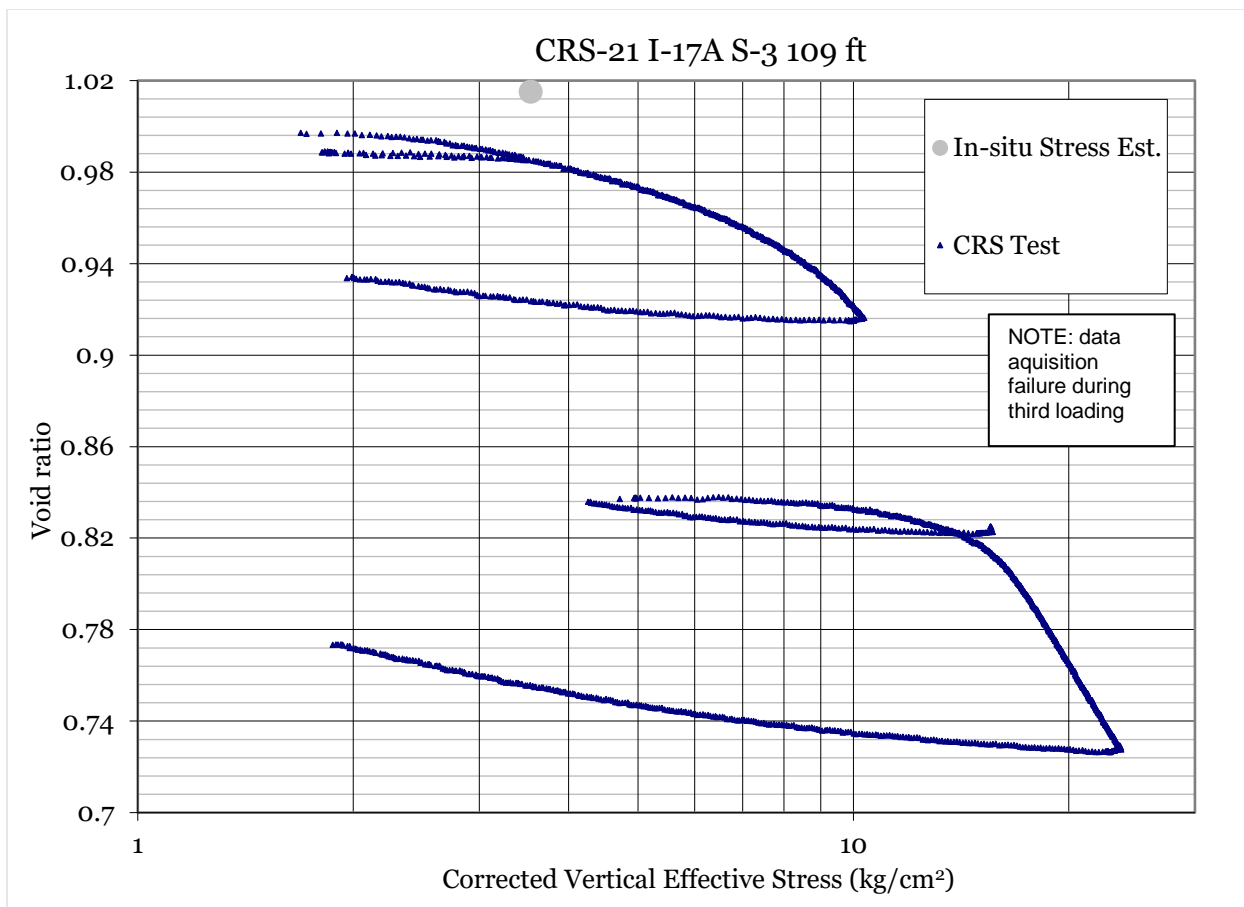


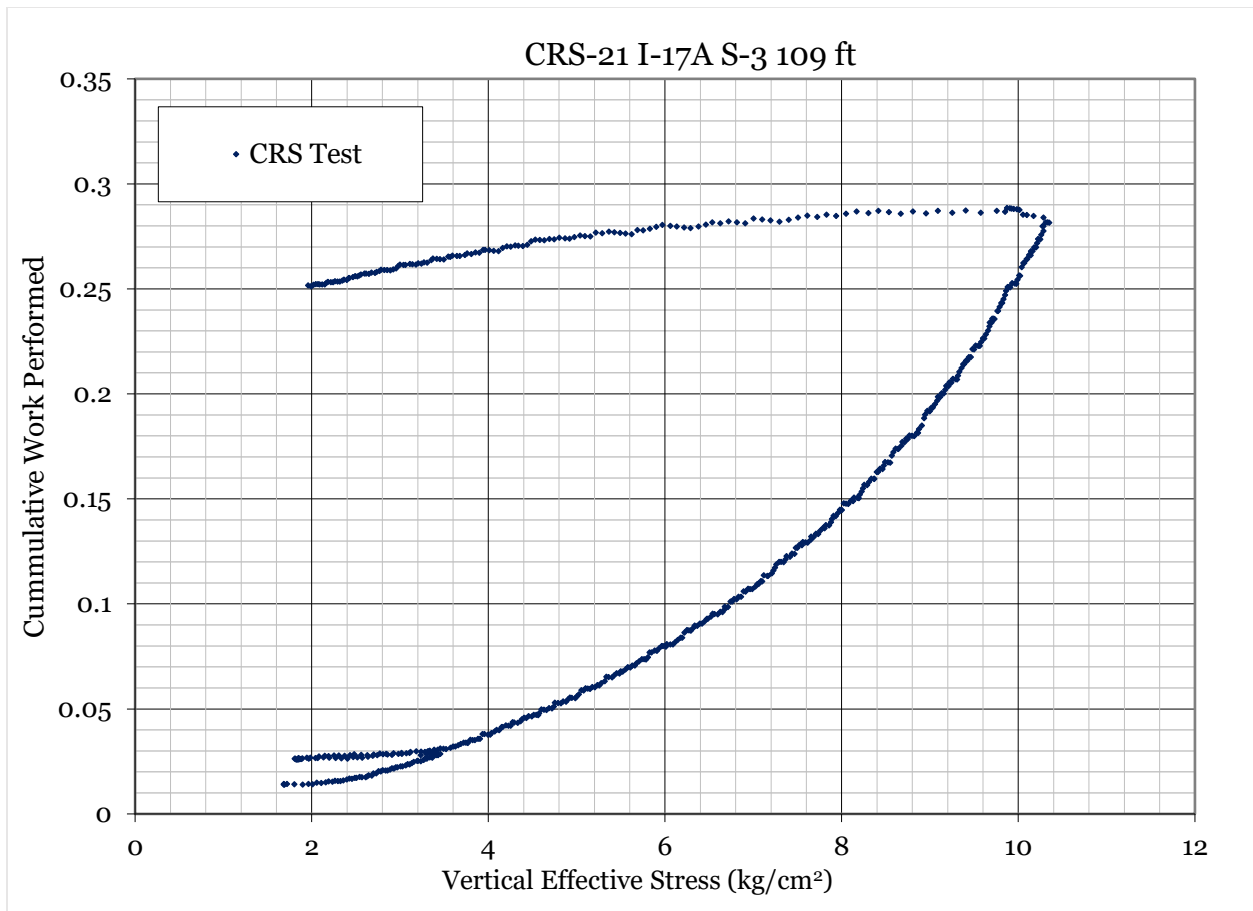


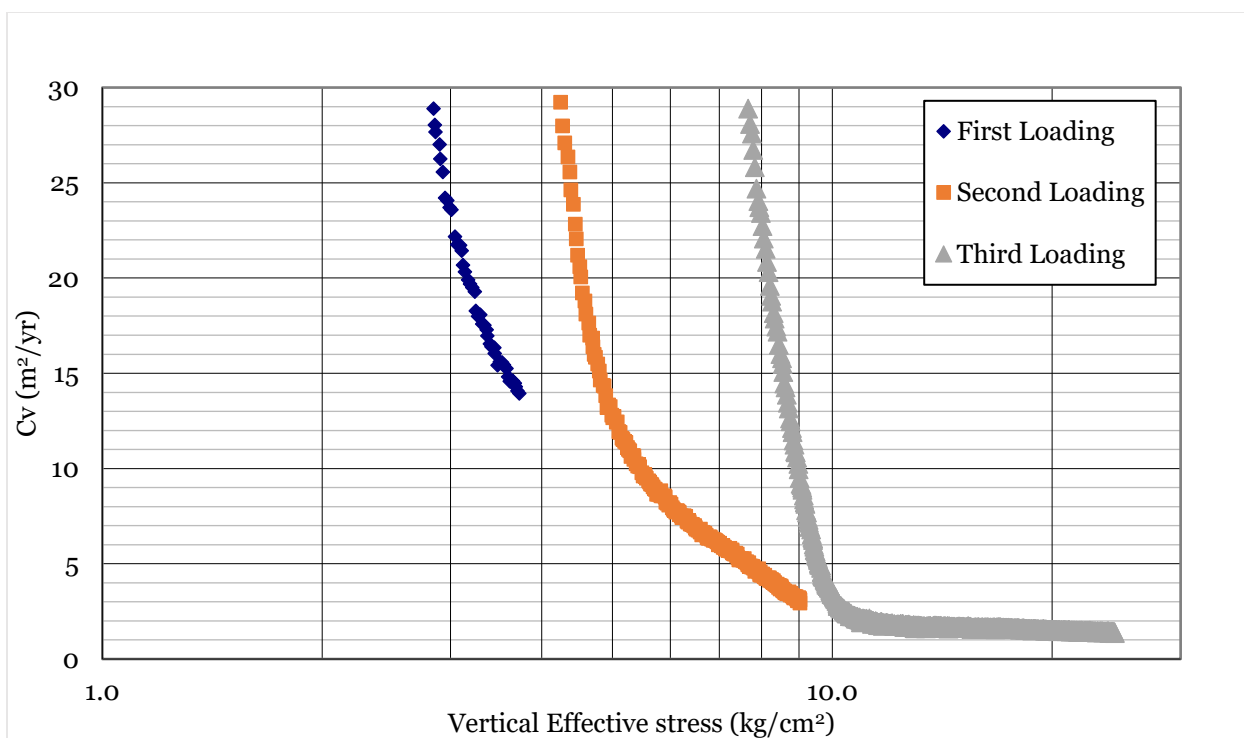
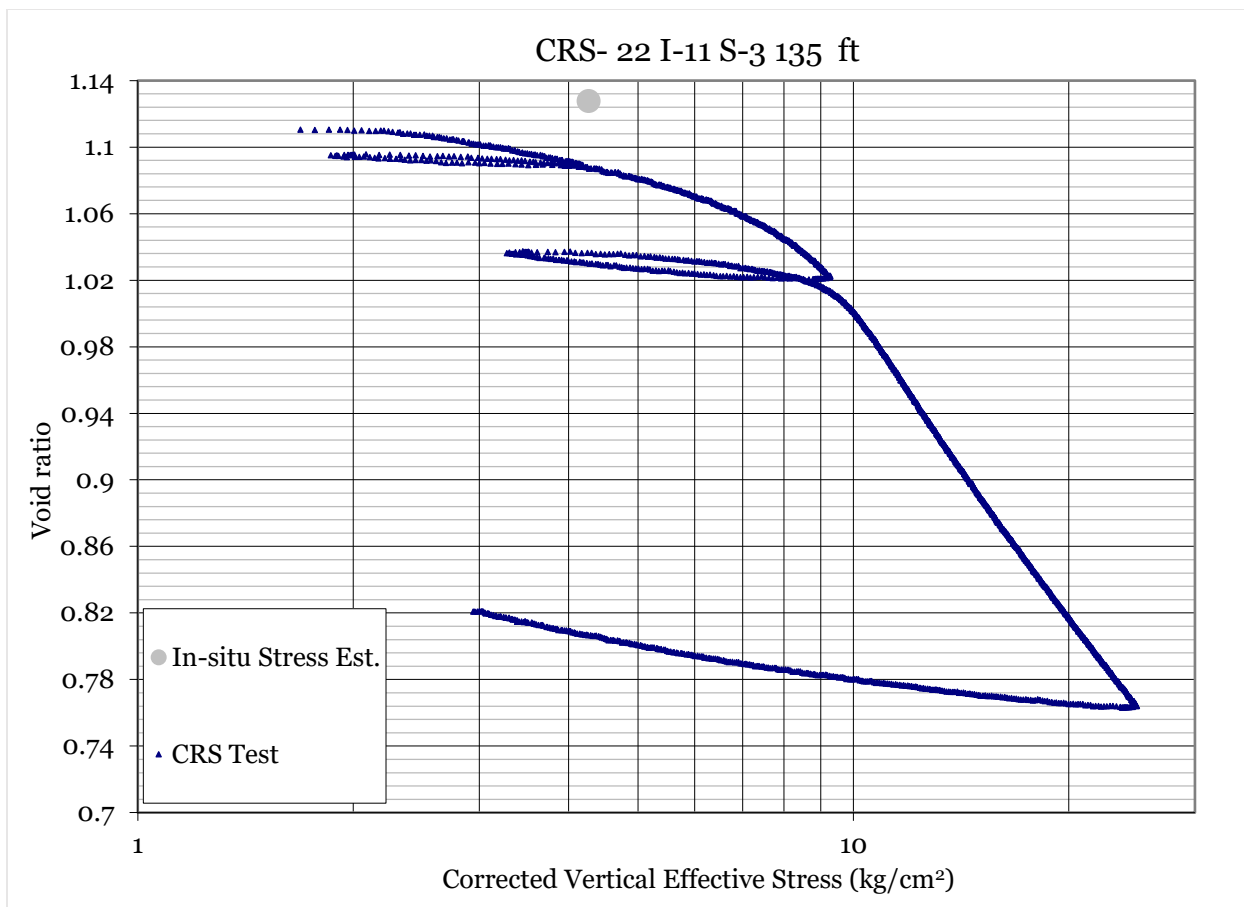


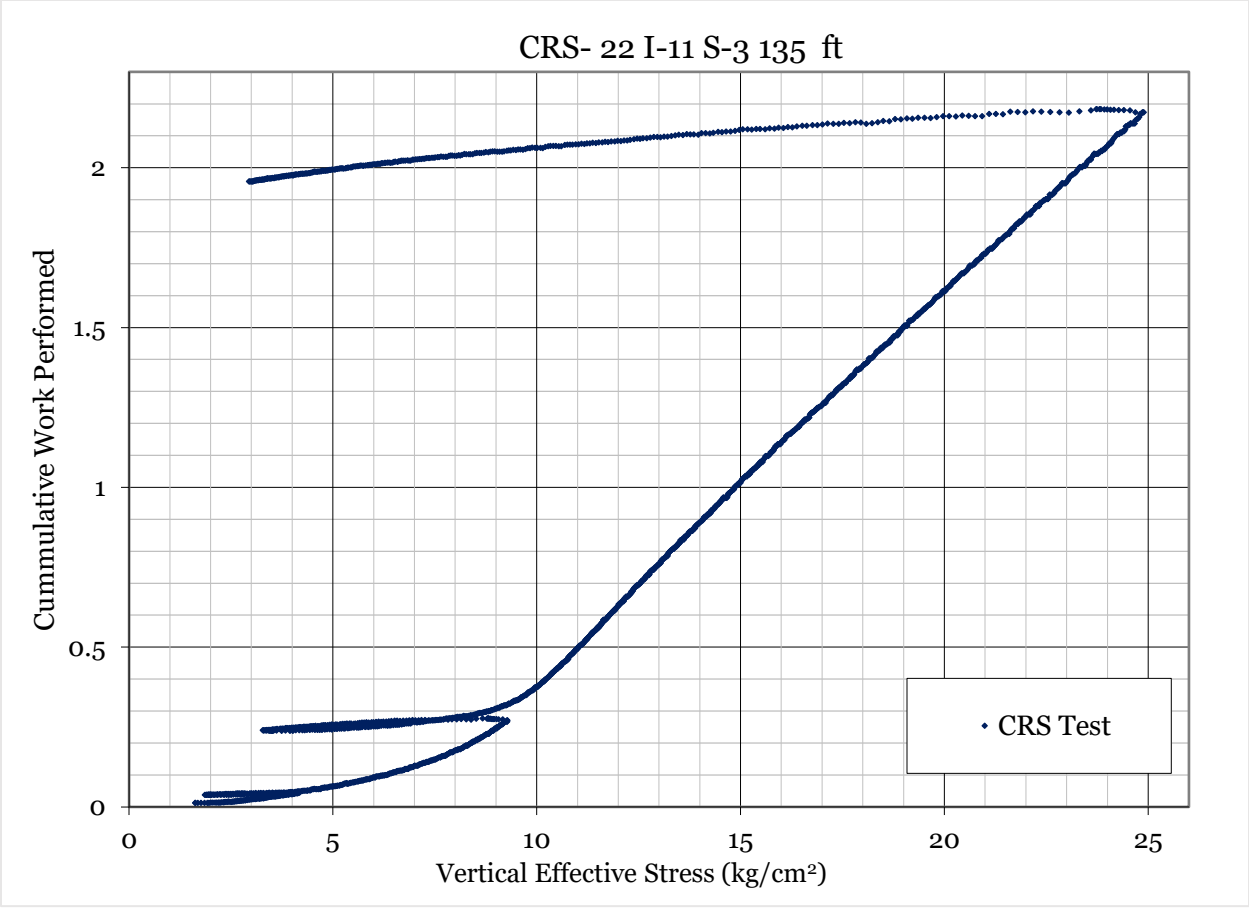


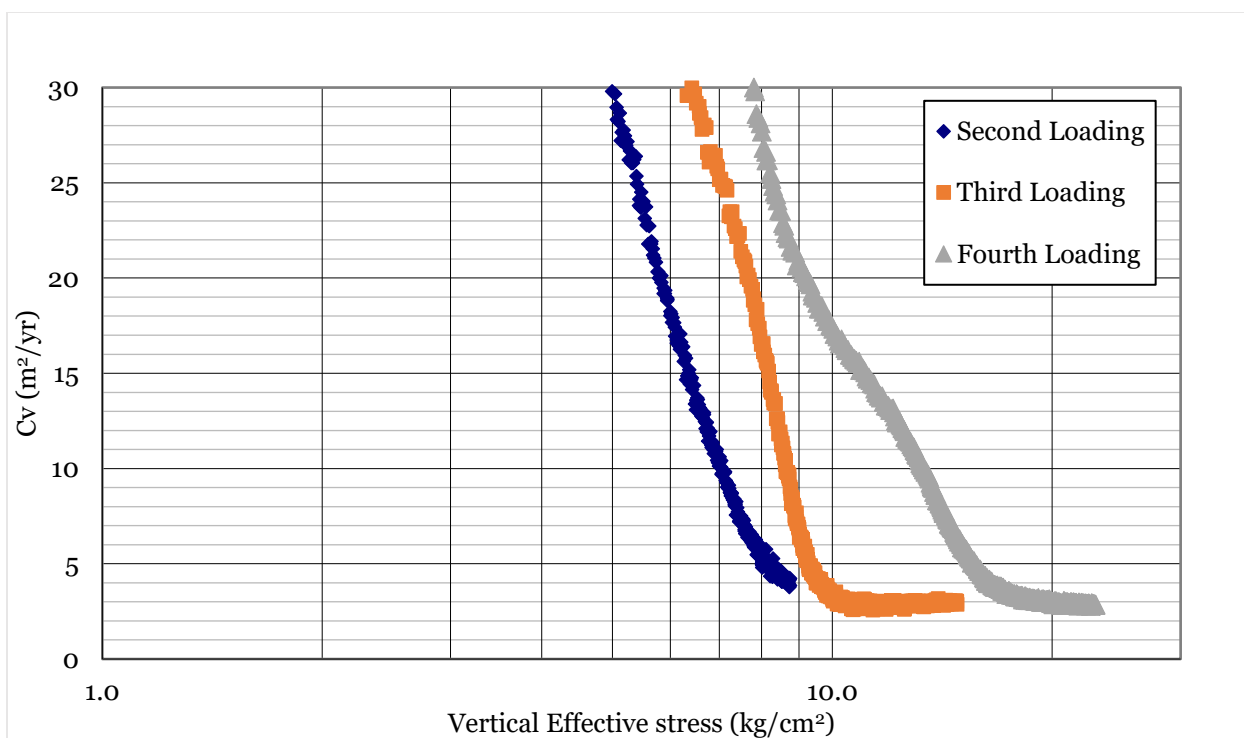
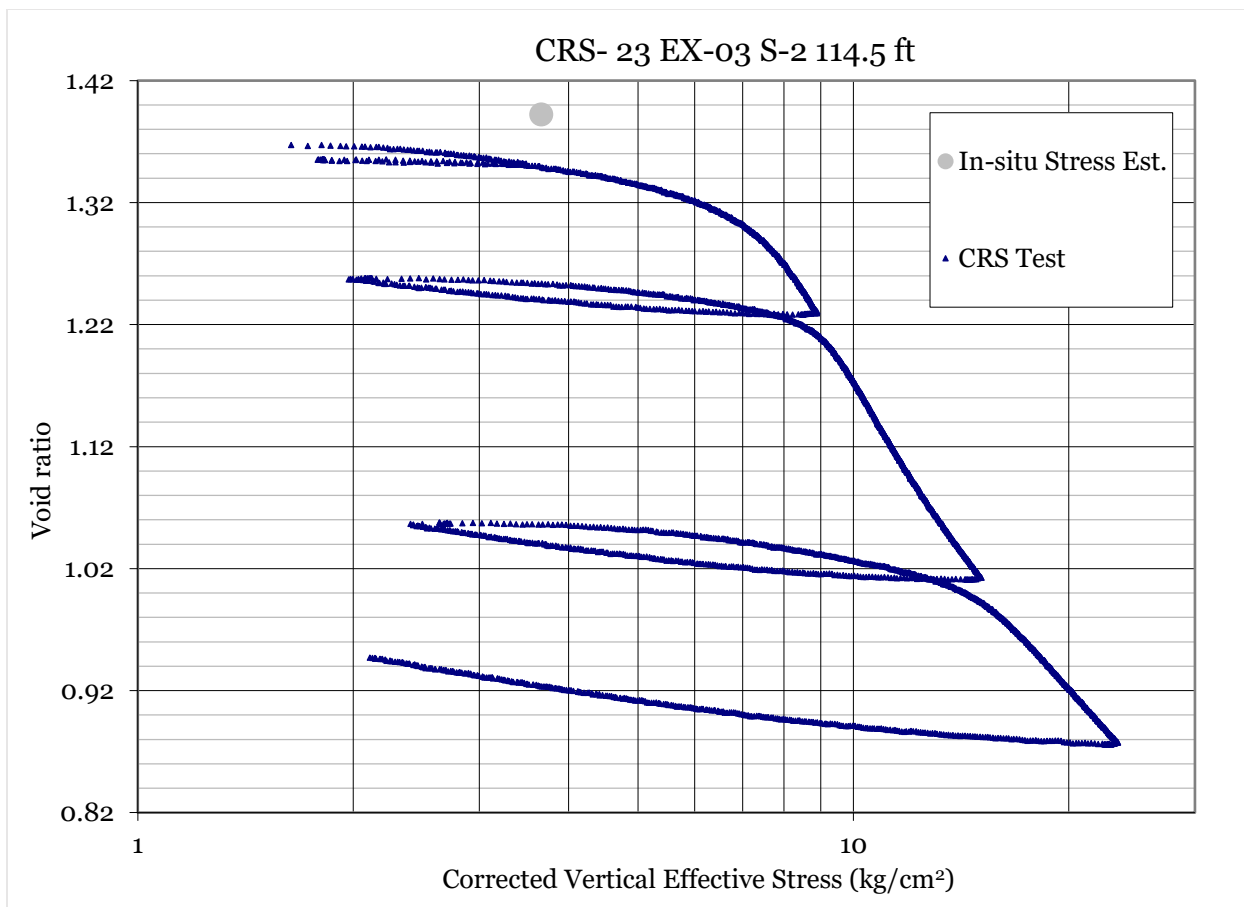


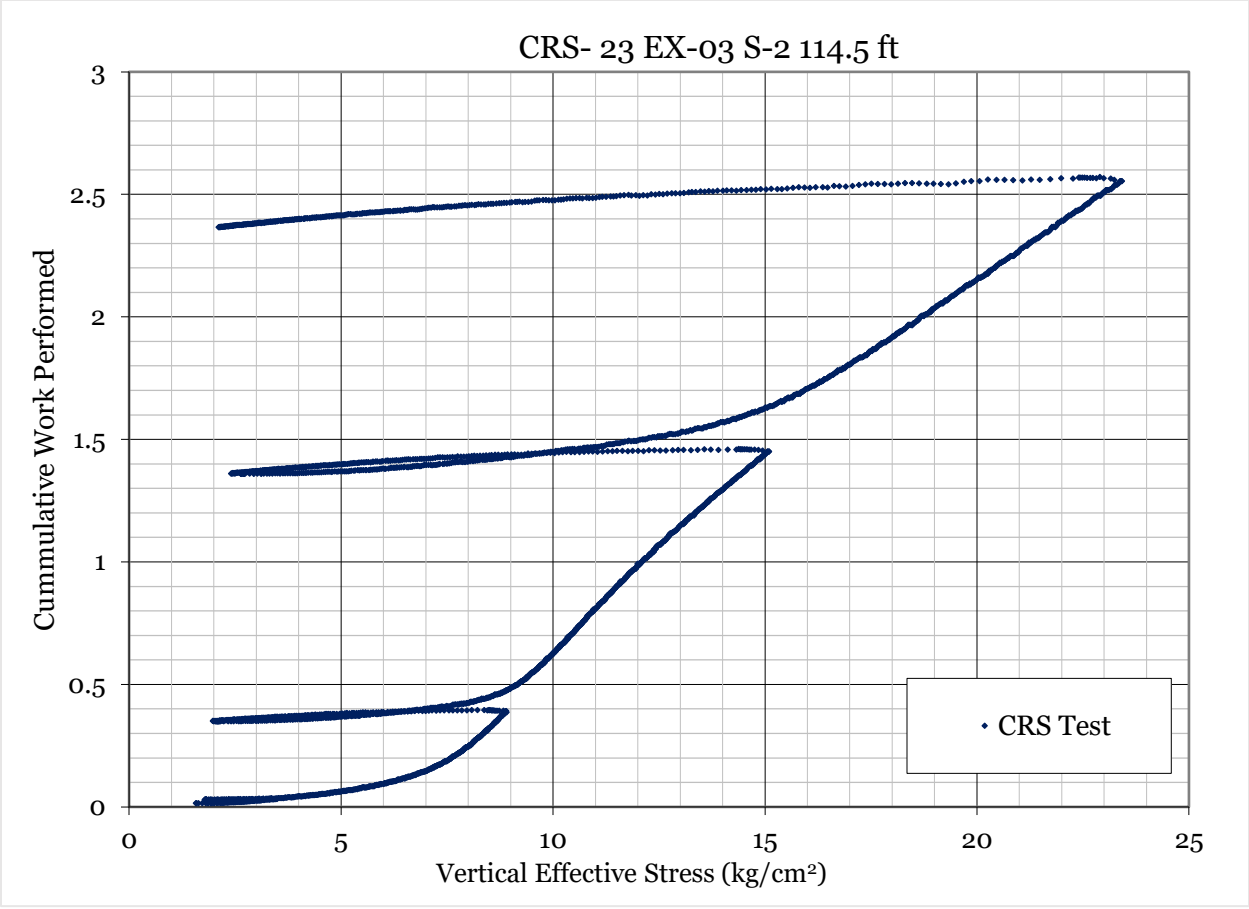


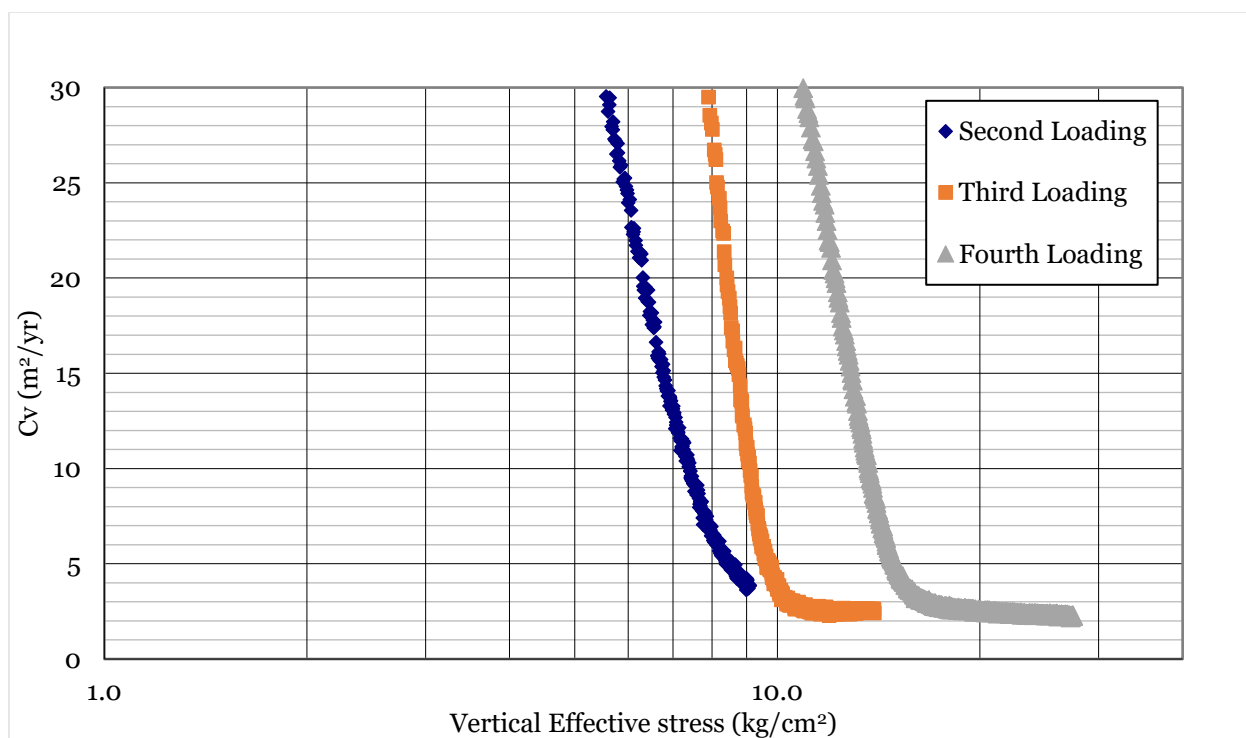
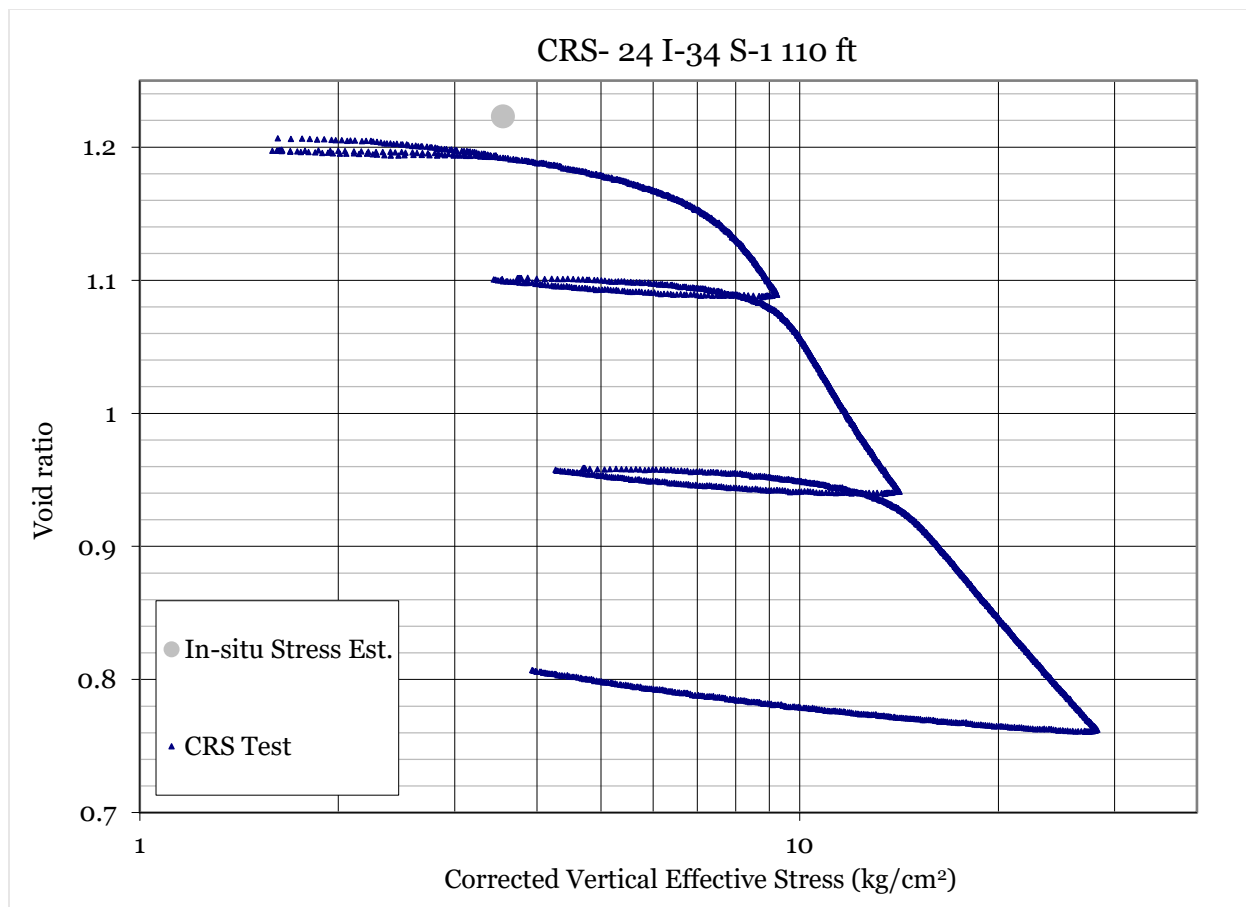


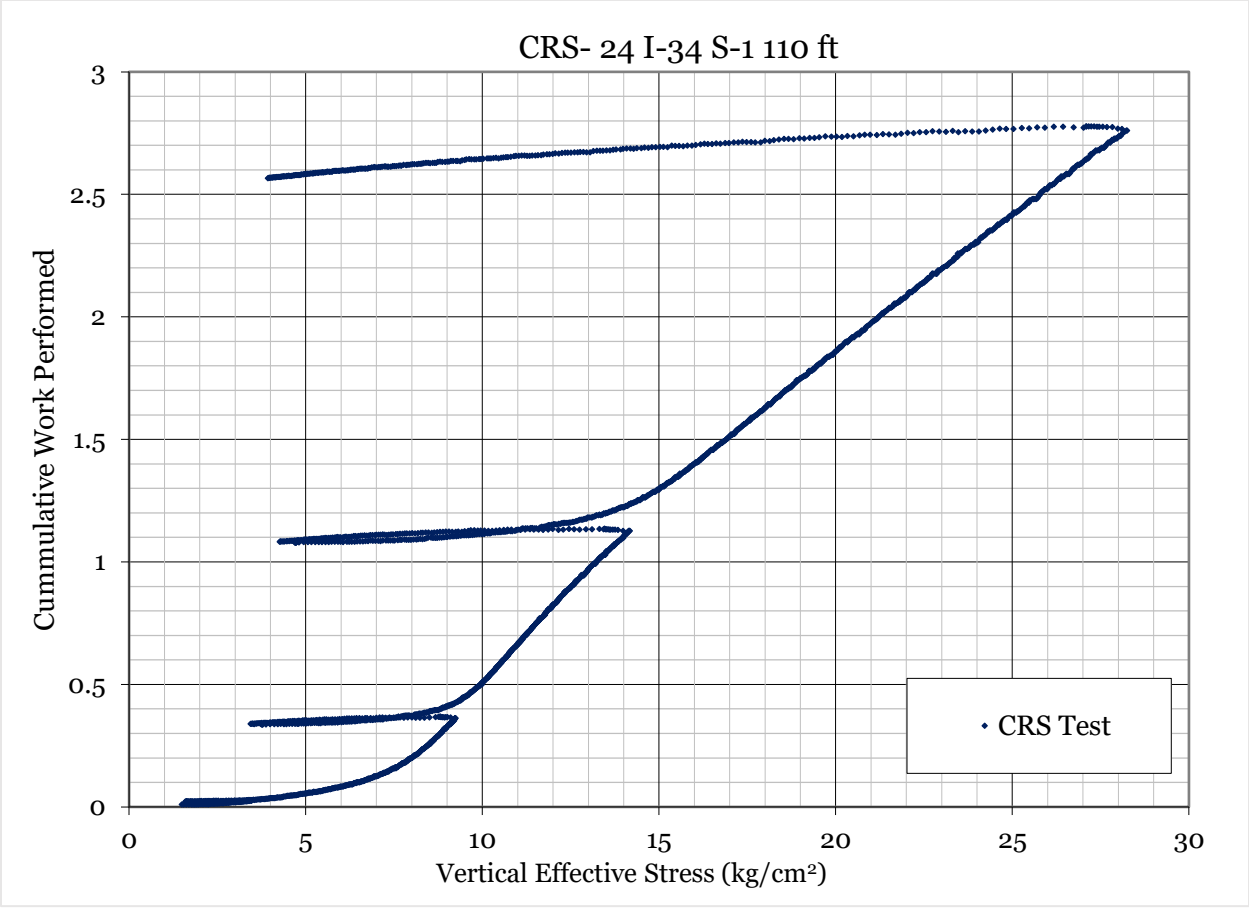


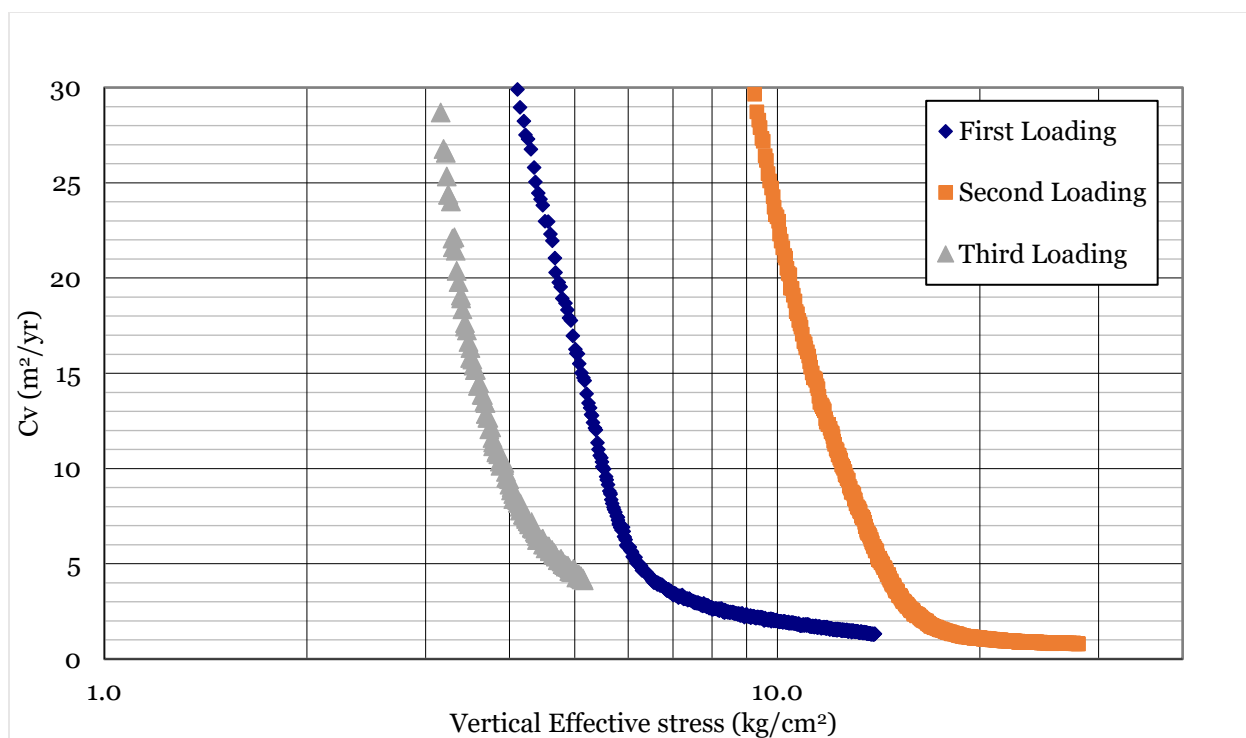
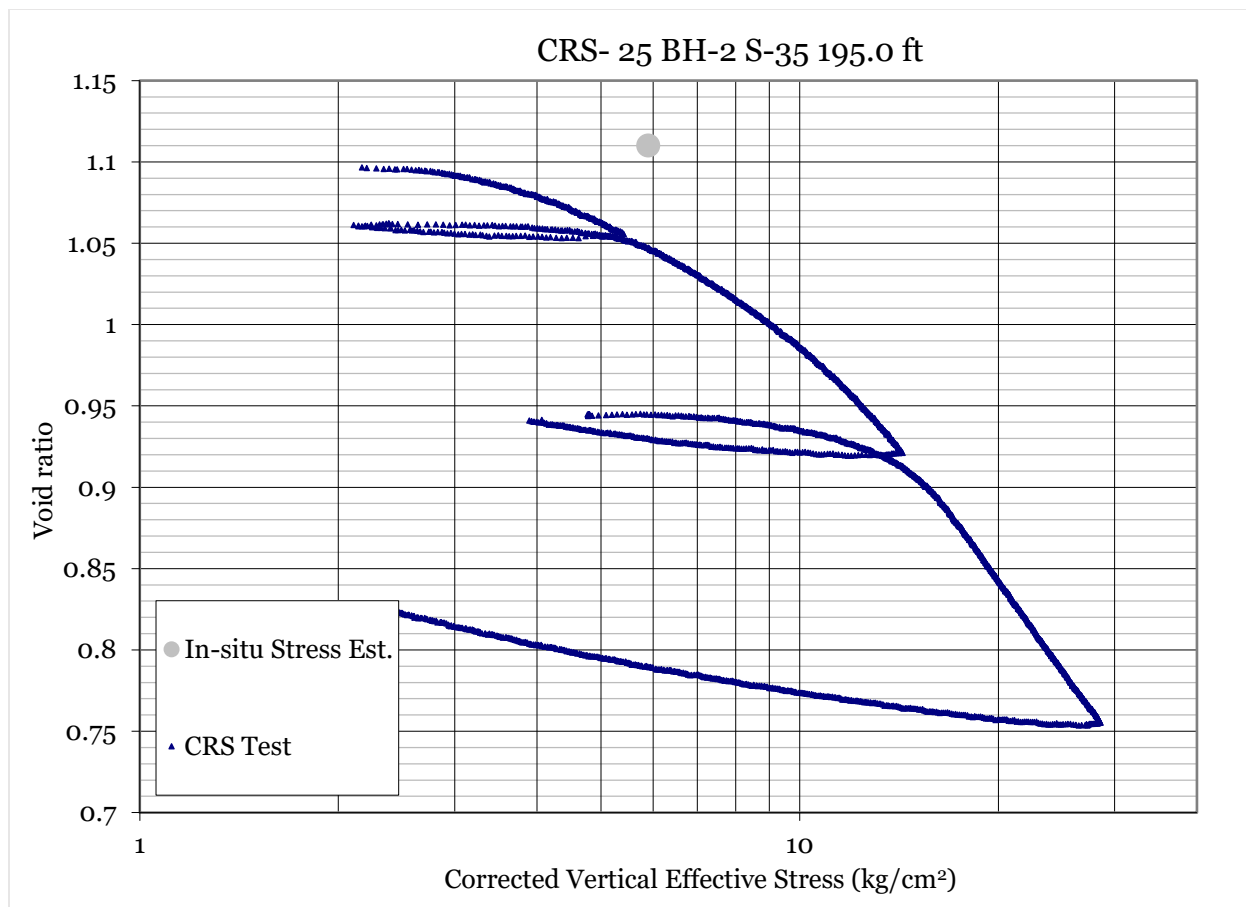


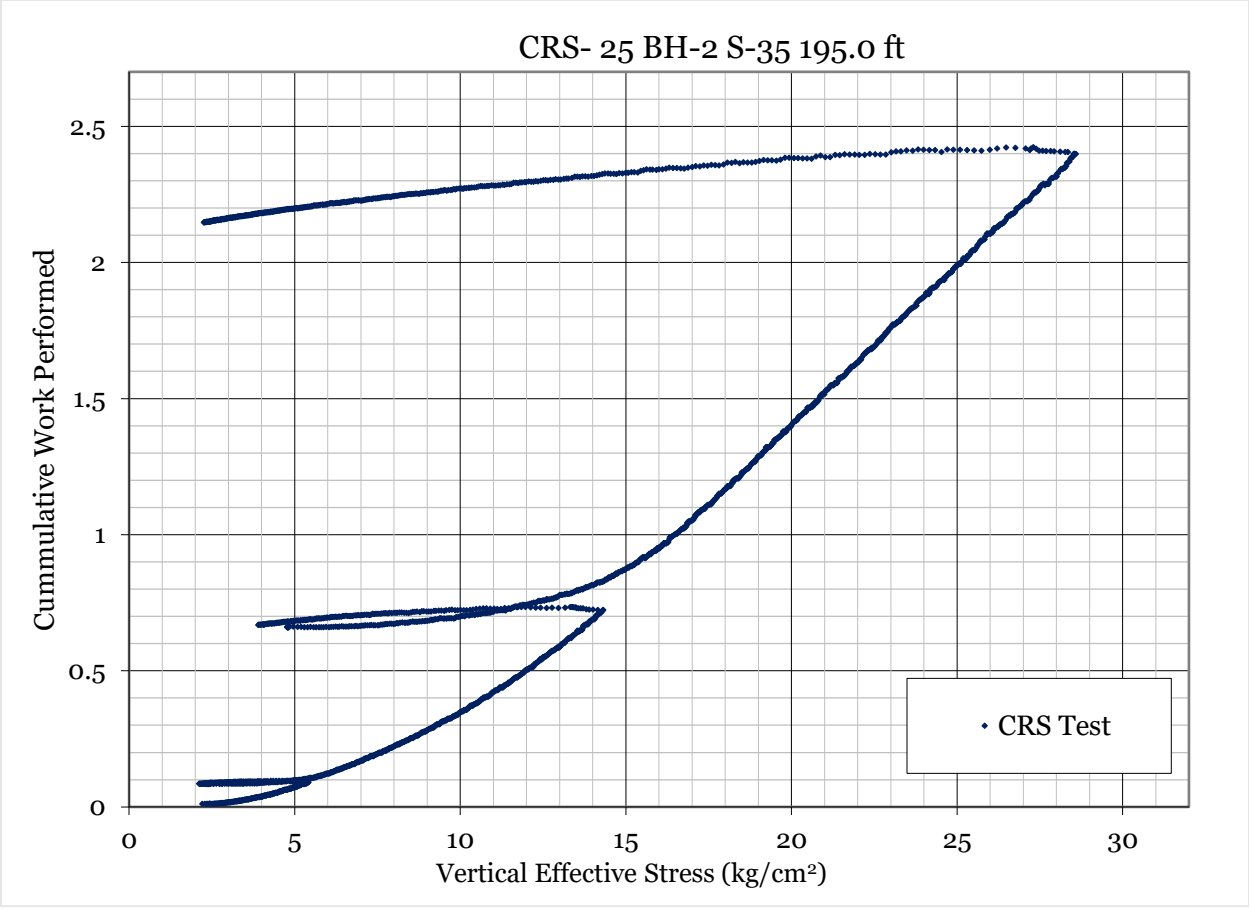


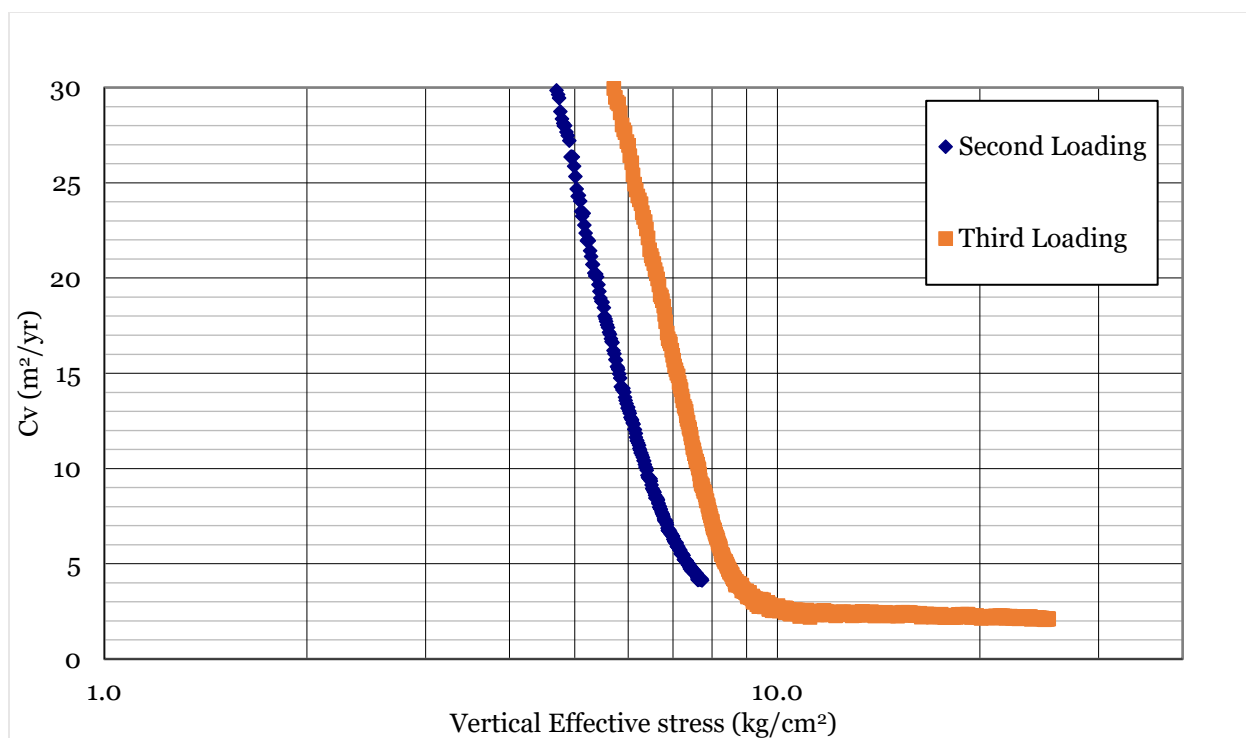
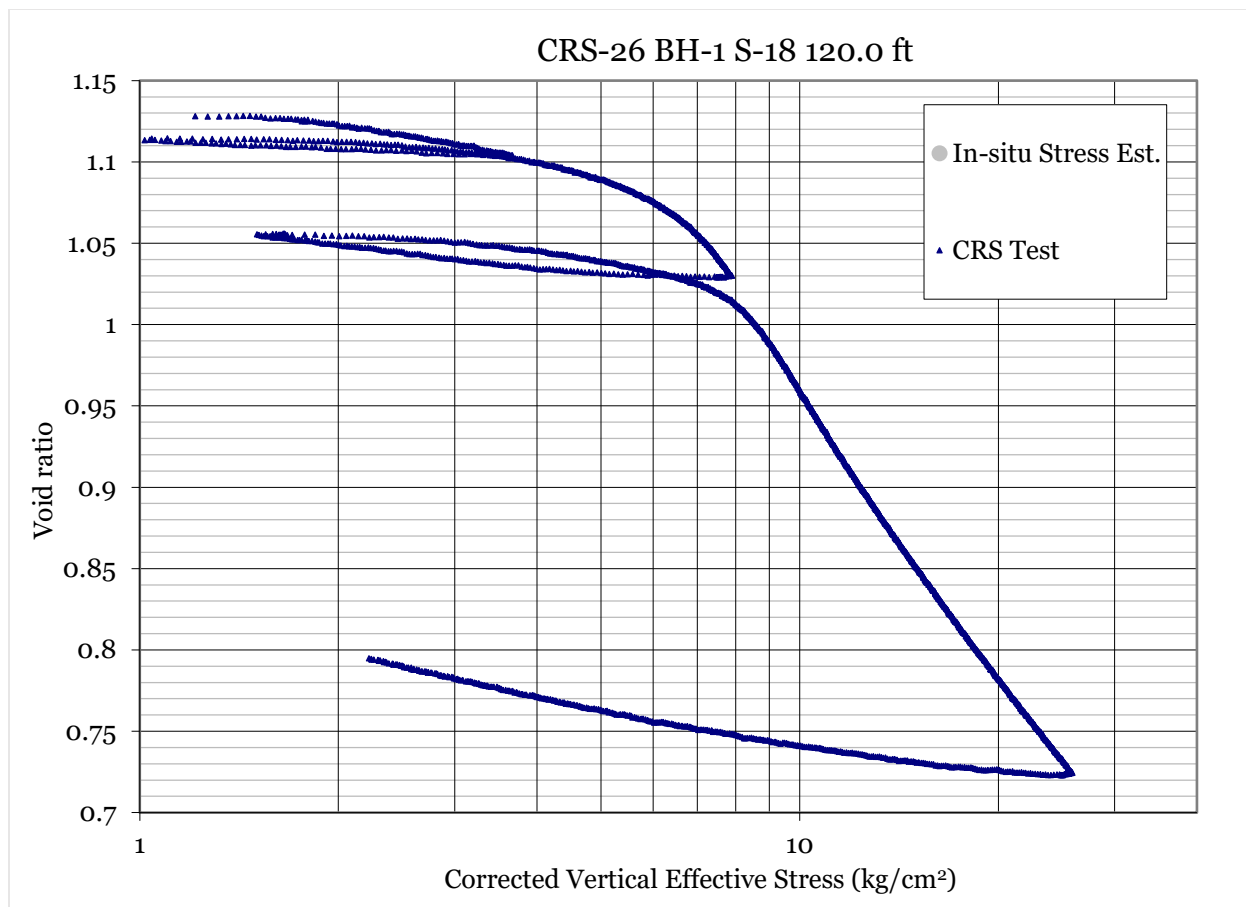


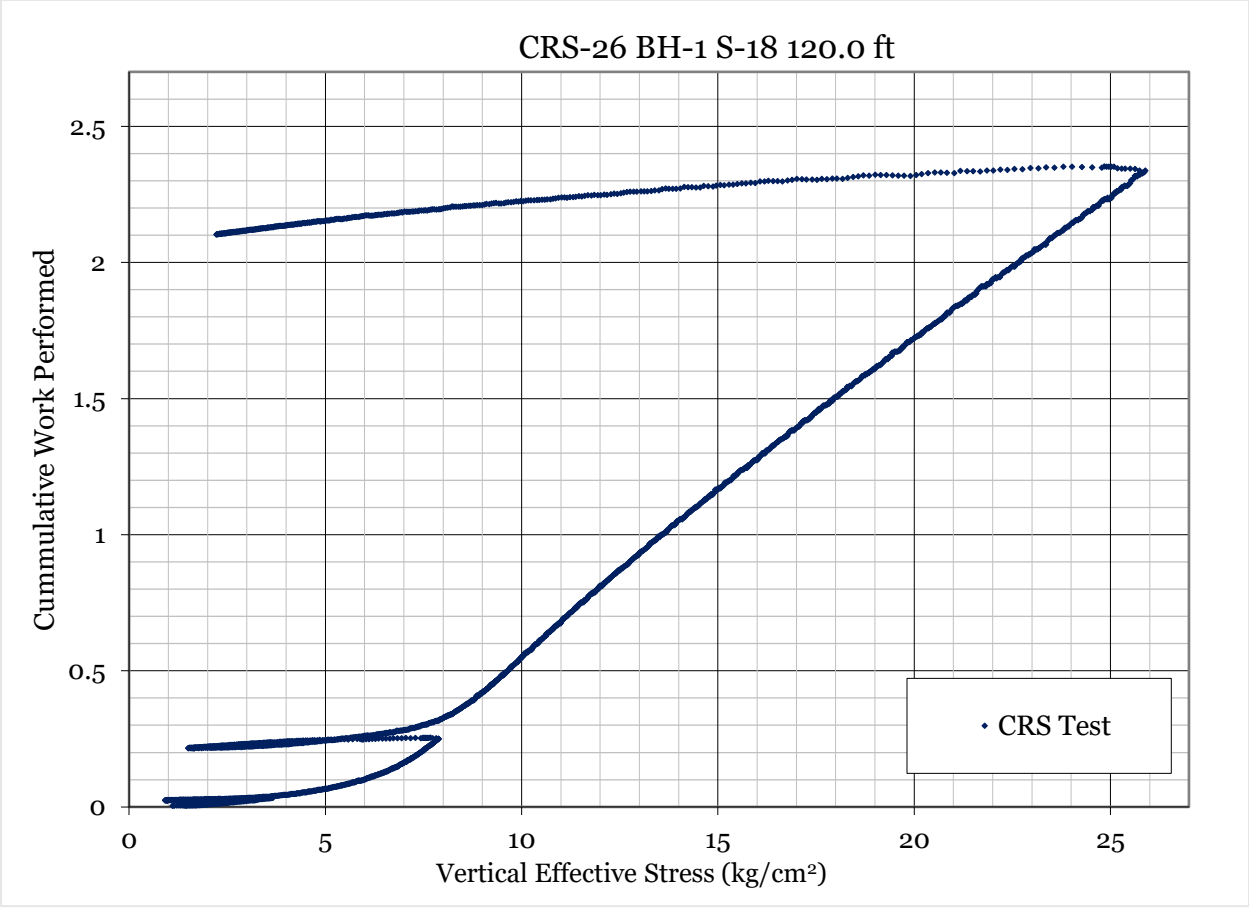


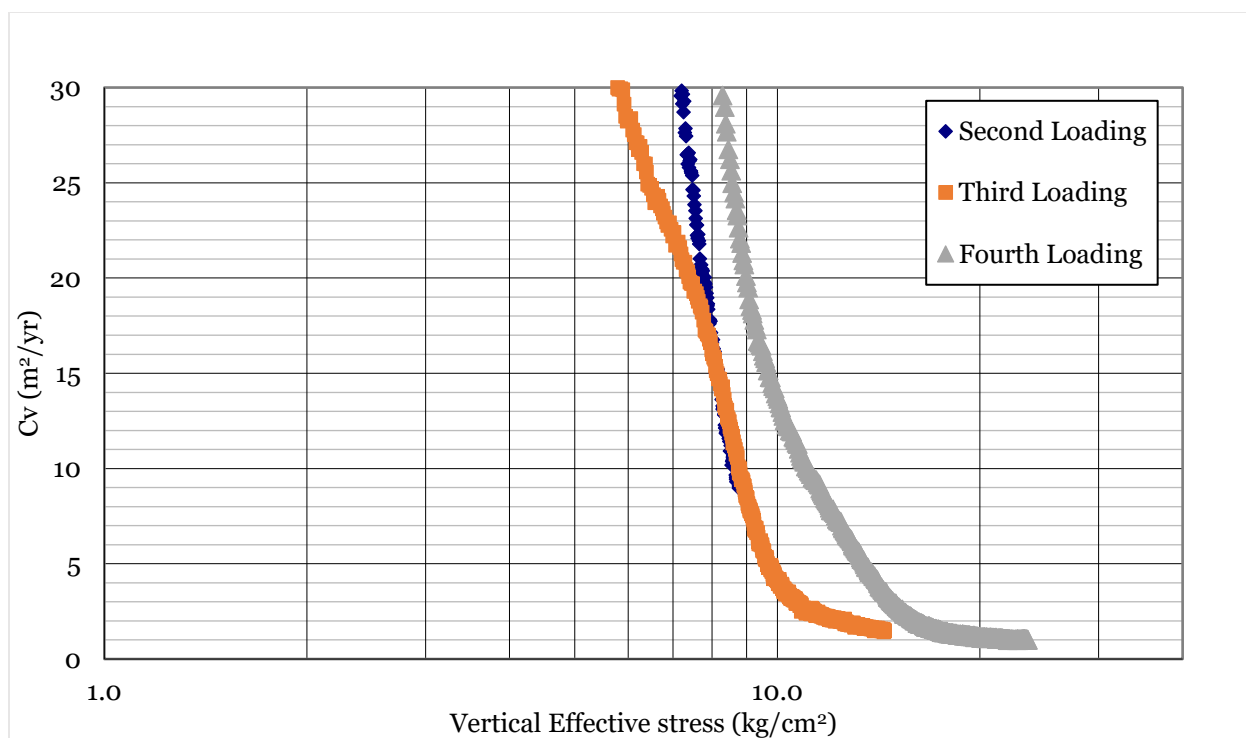
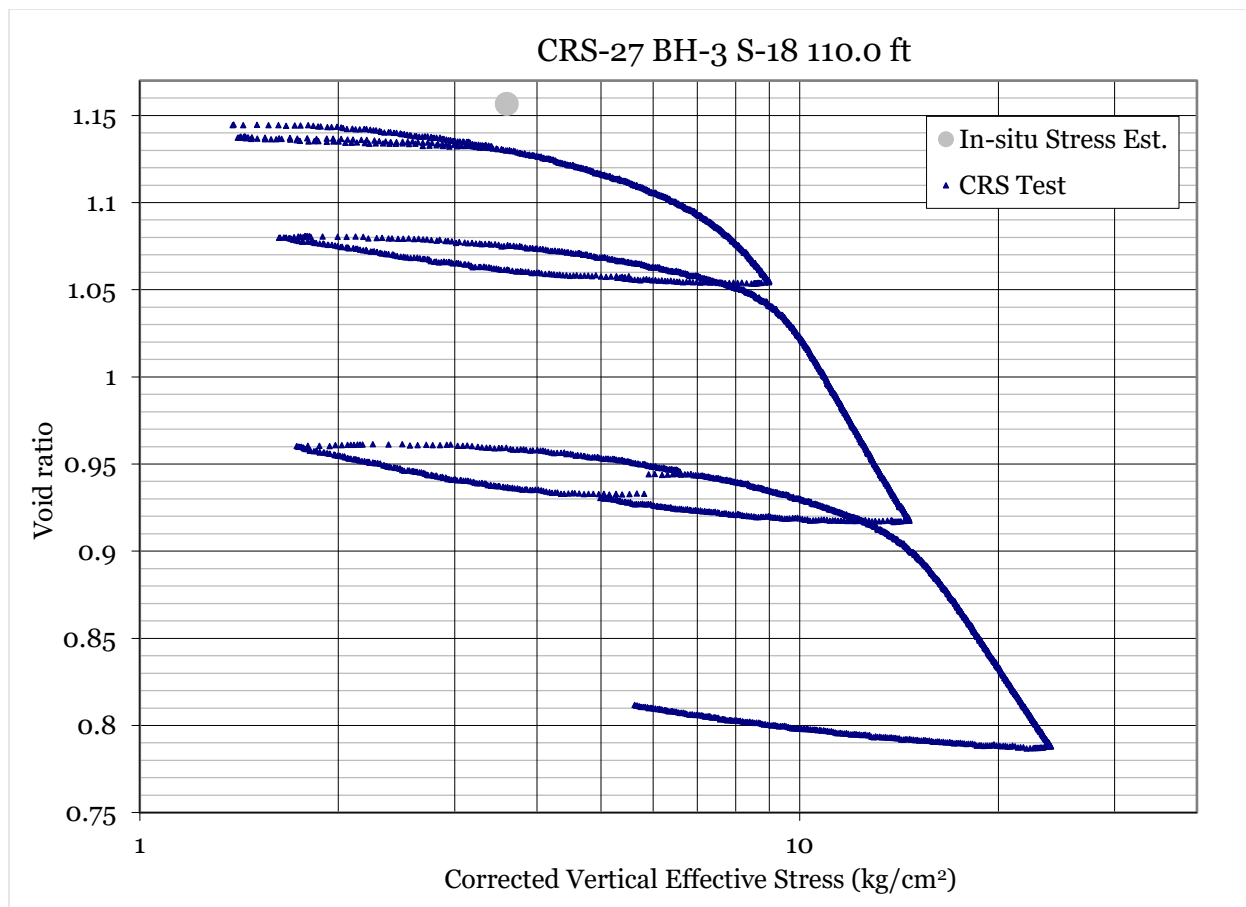


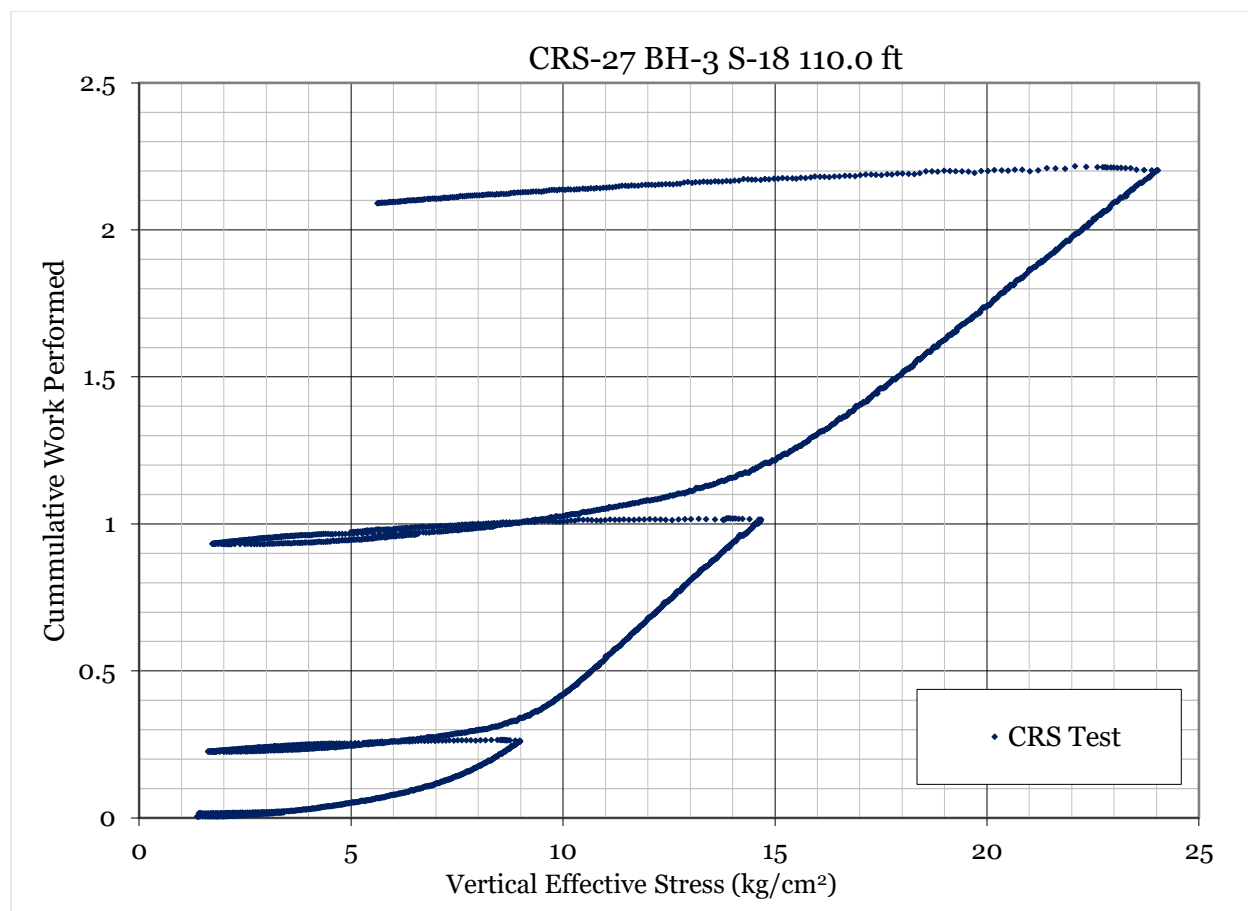


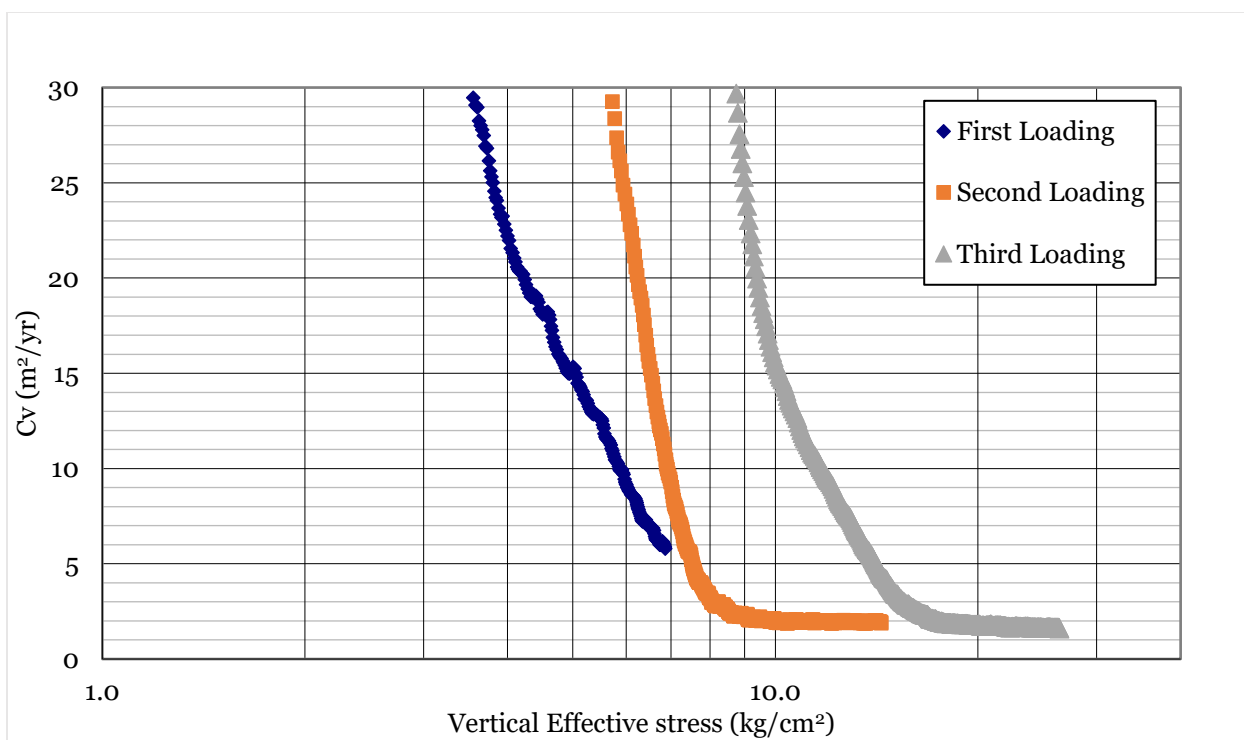
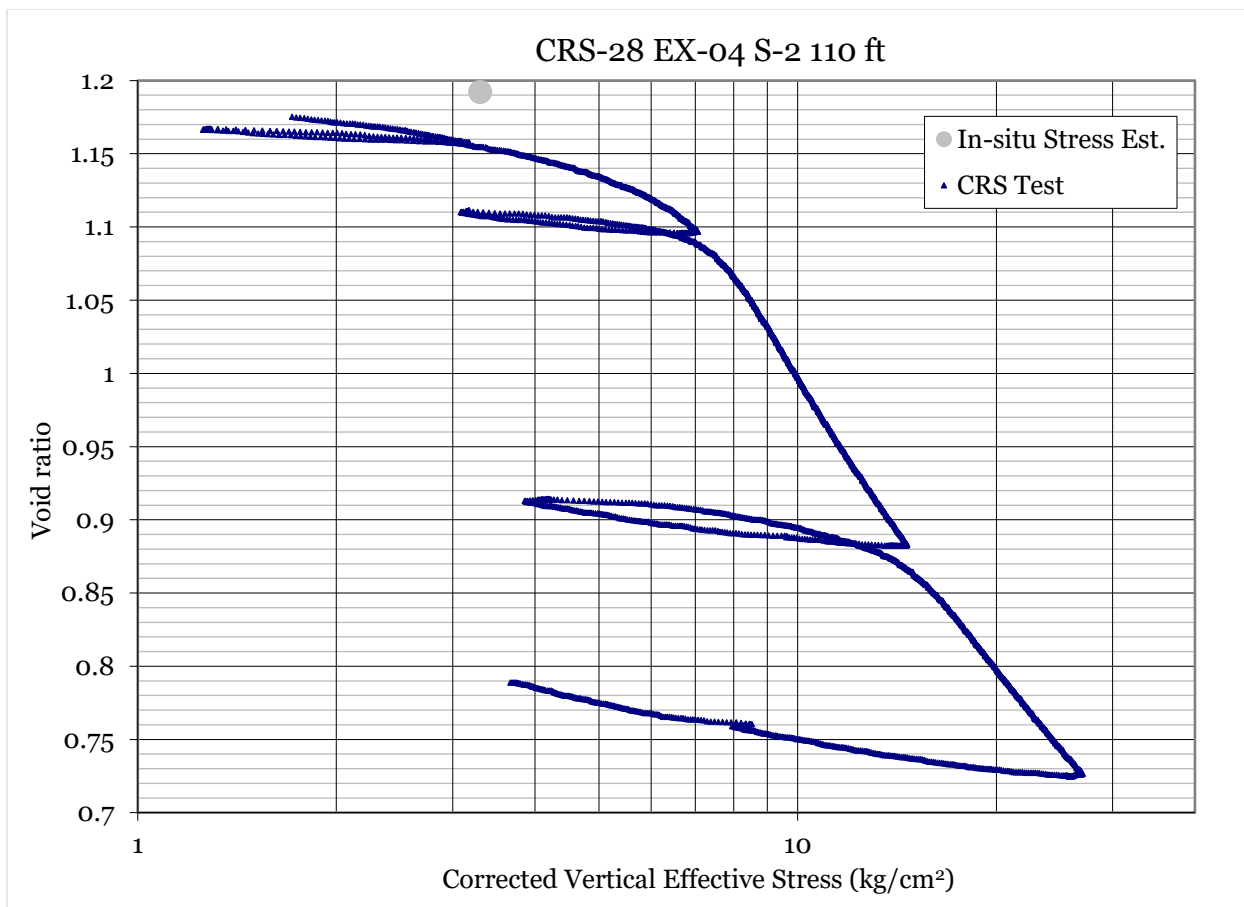


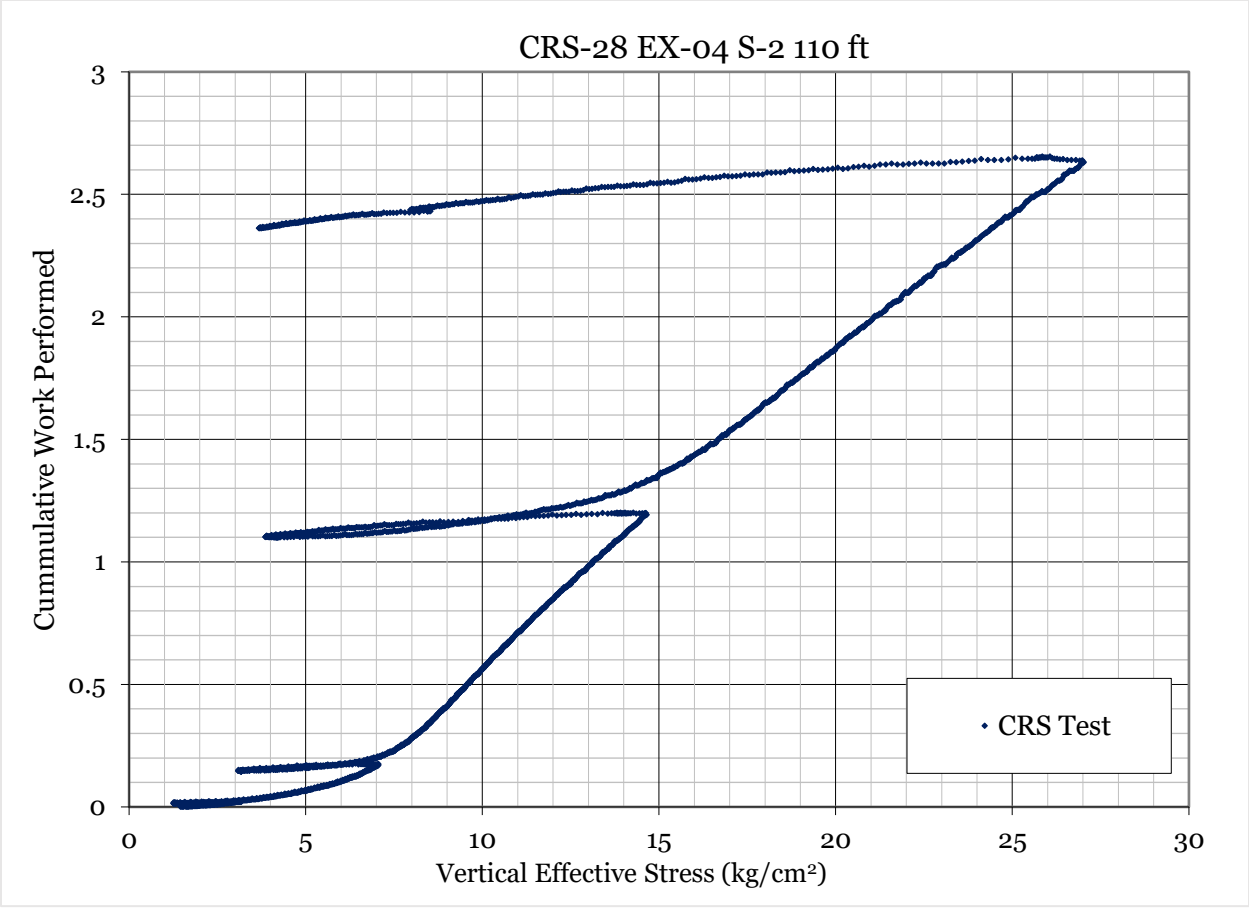


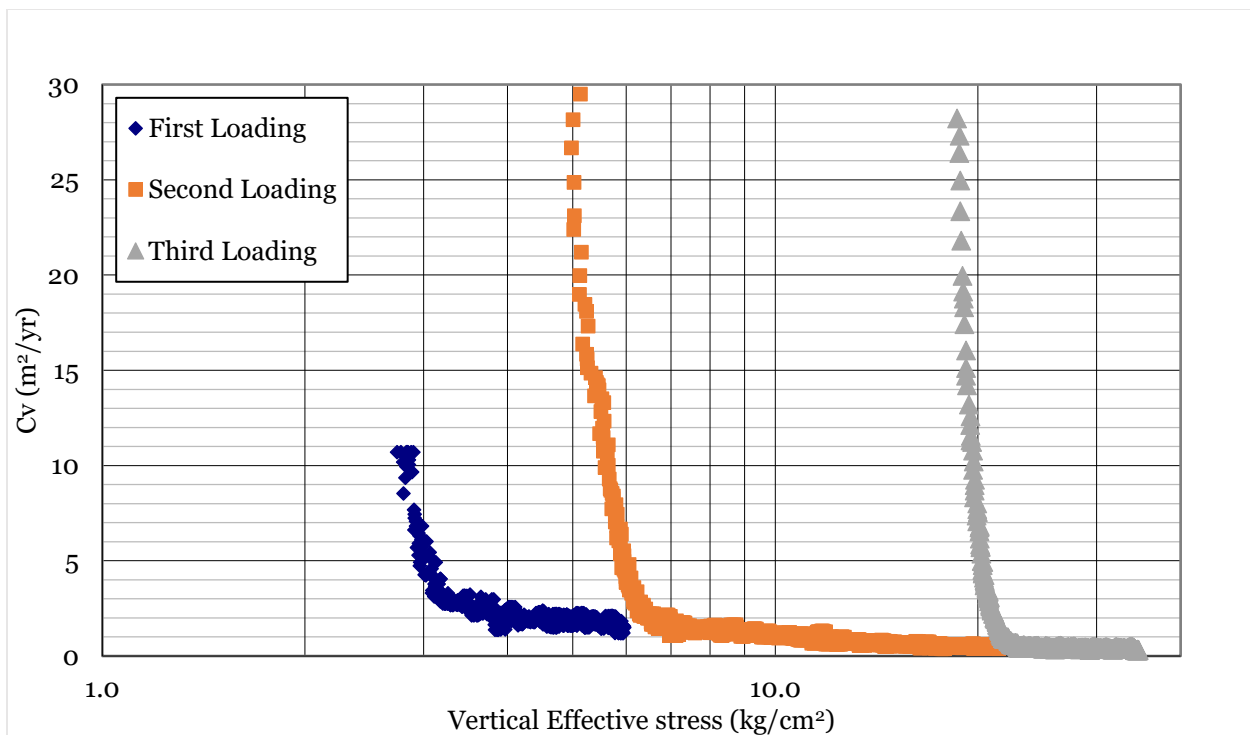
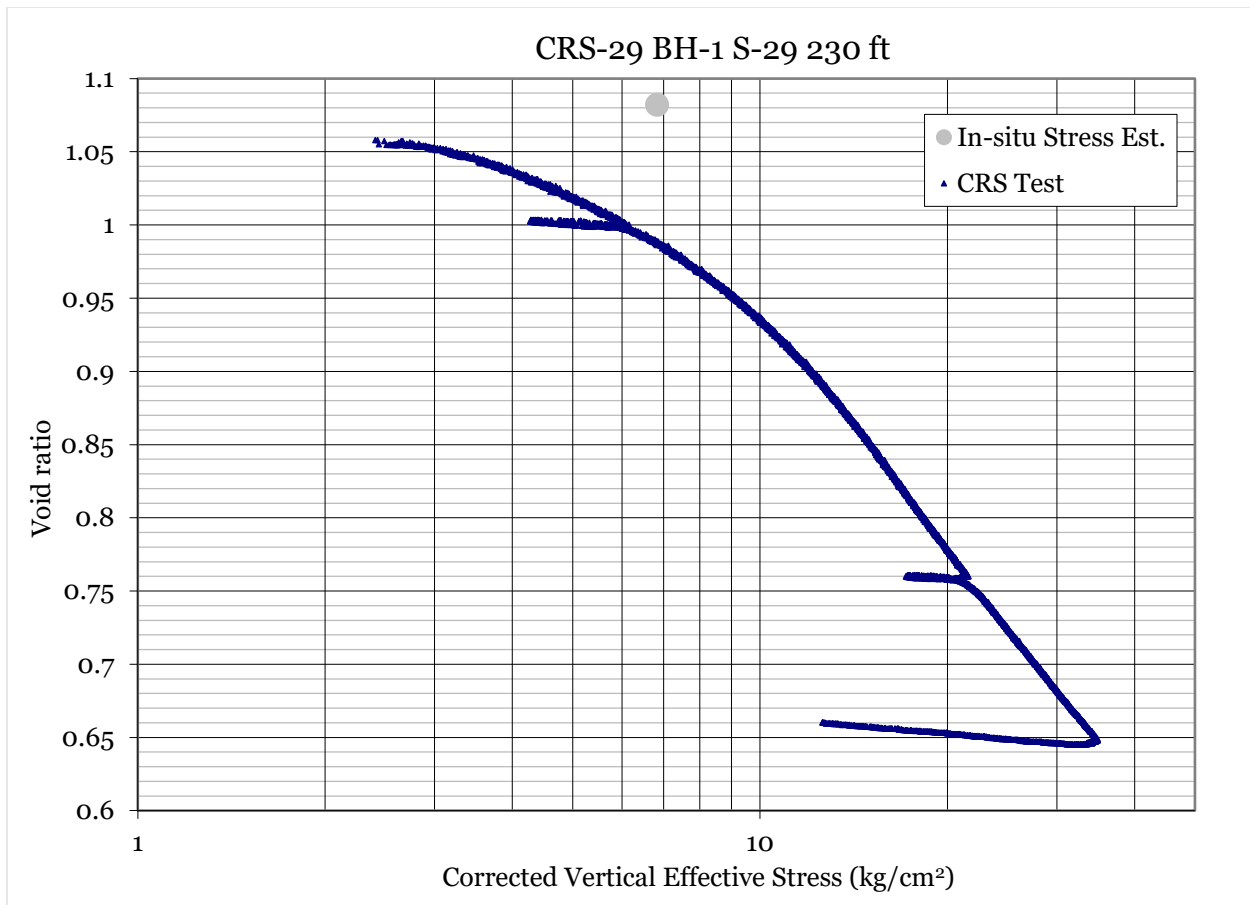


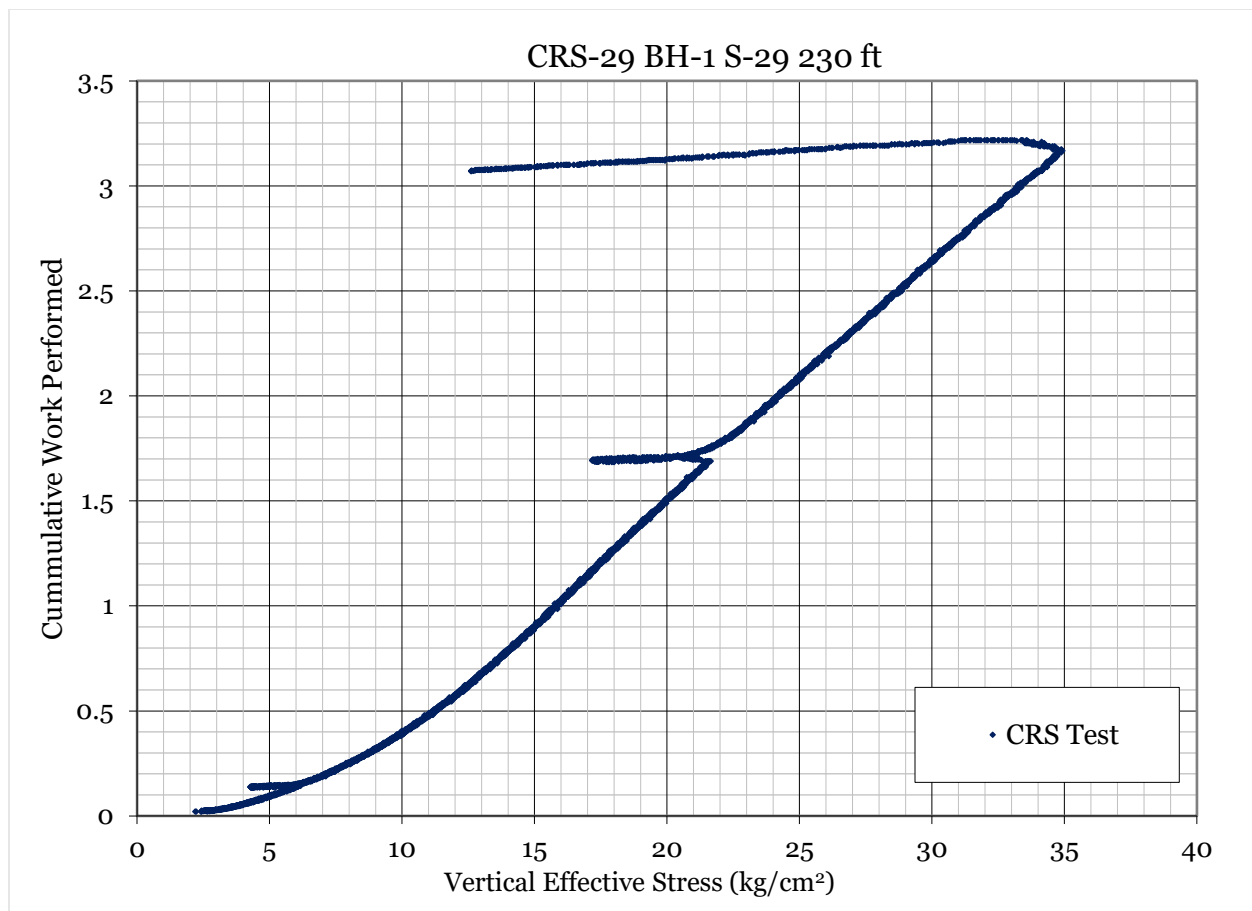












9 APPENDIX B

9.1 Anisotropically Consolidated Triaxial (CK_oUTX) Tests

Table on following page

Table B- 1. Anisotropically Consolidated Triaxial Tests.

Specimen Data						Consolidation Details		Testing Details		
Test	Sample	Depth (ft)	Unit	Consolidated Vertical Effective Stress, σ_v' (kPa)	K, during Consolidation	Test Name	Vertical Effective At Start of Test, σ_v' (kPa)	OCR at Start of Test	K, at Start of Test	
CUTX-1	I-9 S-2	120	OBC	350*	0.74	Compression 1	350	2	0.74	
						Dynamic 1	100	7	1	
						Compression 2	350	2	0.74	
						Dynamic 2	350	2	0.74	
						Extension 1	350	2	0.74	
						Extension 2	350	2	0.74	
CUTX-2	EX-03 S-2	114.5	OBC	400*	0.74	Compression 1	400	1.7	0.74	
CUTX-3	BH-2 S-35	195	Alameda	608*	0.65	Dynamic 1	570	1.4	0.72	
						Dynamic 2	570	1.4	0.72	
						Extension 1	570	1.4	0.72	
						Dynamic 3	604	1.3	0.65	
						Compression 1	604	1.3	0.65	
						Dynamic 4	616	1.3	0.65	
CUTX-4	I-34 S-18	110	OBC	800	0.55	Dynamic 1	373	2	0.67	
						Compression 1	373	2	0.67	
						Dynamic 2	373	2	0.67	
						Extension 1	373	2	0.67	
CUTX-5	I-35 S-4	135	OBC	800	0.55	Dynamic 1	400	2	0.67	
						Compression 1	400	2	0.67	
						Dynamic 1	700	1	0.55	
CUTX-6	BH-1 S-18	120	OBC	700	0.55	Compression 1	370	2	0.65	
						Dynamic 2	370	2	0.65	

Specimen Data				Consolidation Details		Testing Details			
Test	Sample	Depth (ft)	Unit	Consolidated Vertical Effective Stress, σ_v' (kPa)	K, during Consolidation	Test Name	Vertical Effective At Start of Test, σ_v' (kPa)	OCR at Start of Test	K, at Start of Test
						Extension 1	370	2	0.65
CUTX-7	BH-3 S-18	110	OBC	700	0.55	Compression 1	235	3	0.87
CUTX-8	BH-3 S-18	110	OBC	705	0.55	Compression 1	705	1	0.55
CUTX-9	BH-3 S-18	110	OBC	700	0.55	Compression 1	436	1.6	0.8
CUTX-10	BH-1 S-18	110	OBC	695	0.65	Dynamic 1	300	2.3	0.8
				900	Dynamic 2	900	1	0.65	
					Dynamic 3	450	0	0.8	
					Compression 1	451	2	0.8	

9.2 Lateral Unloading Triaxial Tests

Specimen Data				Consolidation Details		Testing Details		
Test	Sample	Depth (ft)	Unit	Consolidated Vertical Effective Stress, σ_v' (kPa)	K, during Consolidation	Vertical Effective At Start of Test, σ_v' (kPa)	OCR at Start of Test	K at Start of Test
VS-1	I-16 S-2	206	Alameda	100	1	-	-	-
VS-2	I-11 S-6	190	Alameda	100	1	-	-	-
VS-3	I-35 S-4	135	OBC	809	0.6	-	-	-
VS-4	I-9 S-2	130	OBC	809	0.6	677	1.2	0.63
VS-5	I-11 S-3	135	OBC	809	0.6	667	1.2	0.63